

Kinematic Evolution and Structural Styles of Fold-and-Thrust Belts

Edited by

J. Poblet and R. J. Lisle



Geological Society

Special Publication 349



Kinematic Evolution and Structural Styles of Fold-and-Thrust Belts

The Geological Society of London
Books Editorial Committee

Chief Editor

BOB PANKHURST (UK)

Society Books Editors

JOHN GREGORY (UK)

JIM GRIFFITHS (UK)

JOHN HOWE (UK)

RICK LAW (USA)

PHIL LEAT (UK)

NICK ROBINS (UK)

RANDELL STEPHENSON (UK)

Society Books Advisors

MIKE BROWN (USA)

ERIC BUFFETAUT (FRANCE)

JONATHAN CRAIG (ITALY)

RETO GIERÉ (GERMANY)

TOM McCANN (GERMANY)

DOUG STEAD (CANADA)

GONZALO VEIGA (ARGENTINA)

MAARTEN DE WIT (SOUTH AFRICA)

Geological Society books refereeing procedures

The Society makes every effort to ensure that the scientific and production quality of its books matches that of its journals. Since 1997, all book proposals have been refereed by specialist reviewers as well as by the Society's Books Editorial Committee. If the referees identify weaknesses in the proposal, these must be addressed before the proposal is accepted.

Once the book is accepted, the Society Book Editors ensure that the volume editors follow strict guidelines on refereeing and quality control. We insist that individual papers can only be accepted after satisfactory review by two independent referees. The questions on the review forms are similar to those for *Journal of the Geological Society*. The referees' forms and comments must be available to the Society's Book Editors on request.

Although many of the books result from meetings, the editors are expected to commission papers that were not presented at the meeting to ensure that the book provides a balanced coverage of the subject. Being accepted for presentation at the meeting does not guarantee inclusion in the book.

More information about submitting a proposal and producing a book for the Society can be found on its web site: www.geolsoc.org.uk.

It is recommended that reference to all or part of this book should be made in one of the following ways:

POBLET, J. & LISLE, R. J. (eds) 2011. *Kinematic Evolution and Structural Styles of Fold-and-Thrust Belts*. Geological Society, London, Special Publications, **349**.

TORRES CARBONELL, P. J., DIMIERI, L. V. & OLIVERO, E. B. 2011. Progressive deformation of a Coulomb thrust-wedge: the eastern Fuegian Andes Thrust–Fold Belt. In: POBLET, J. & LISLE, R. J. (eds) *Kinematic Evolution and Structural Styles of Fold-and-Thrust Belts*. Geological Society, London, Special Publications, **349**, 123–147.

GEOLOGICAL SOCIETY SPECIAL PUBLICATION NO. 349

Kinematic Evolution and Structural Styles of Fold-and-Thrust Belts

EDITED BY

J. POBLET

Universidad de Oviedo, Spain

and

R. J. LISLE

Cardiff University, UK

2011

Published by
The Geological Society
London

THE GEOLOGICAL SOCIETY

The Geological Society of London (GSL) was founded in 1807. It is the oldest national geological society in the world and the largest in Europe. It was incorporated under Royal Charter in 1825 and is Registered Charity 210161.

The Society is the UK national learned and professional society for geology with a worldwide Fellowship (FGS) of over 10 000. The Society has the power to confer Chartered status on suitably qualified Fellows, and about 2000 of the Fellowship carry the title (CGeol). Chartered Geologists may also obtain the equivalent European title, European Geologist (EurGeol). One fifth of the Society's fellowship resides outside the UK. To find out more about the Society, log on to www.geolsoc.org.uk.

The Geological Society Publishing House (Bath, UK) produces the Society's international journals and books, and acts as European distributor for selected publications of the American Association of Petroleum Geologists (AAPG), the Indonesian Petroleum Association (IPA), the Geological Society of America (GSA), the Society for Sedimentary Geology (SEPM) and the Geologists' Association (GA). Joint marketing agreements ensure that GSL Fellows may purchase these societies' publications at a discount. The Society's online bookshop (accessible from www.geolsoc.org.uk) offers secure book purchasing with your credit or debit card.

To find out about joining the Society and benefiting from substantial discounts on publications of GSL and other societies worldwide, consult www.geolsoc.org.uk, or contact the Fellowship Department at: The Geological Society, Burlington House, Piccadilly, London W1J 0BG: Tel. + 44 (0)20 7434 9944; Fax + 44 (0)20 7439 8975; E-mail: enquiries@geolsoc.org.uk.

For information about the Society's meetings, consult *Events* on www.geolsoc.org.uk. To find out more about the Society's Corporate Affiliates Scheme, write to enquiries@geolsoc.org.uk.

Published by The Geological Society from:

The Geological Society Publishing House, Unit 7, Brassmill Enterprise Centre, Brassmill Lane, Bath BA1 3JN, UK

(Orders: Tel. + 44 (0)1225 445046, Fax + 44 (0)1225 442836)

Online bookshop: www.geolsoc.org.uk/bookshop

The publishers make no representation, express or implied, with regard to the accuracy of the information contained in this book and cannot accept any legal responsibility for any errors or omissions that may be made.

© The Geological Society of London 2011. All rights reserved. No reproduction, copy or transmission of this publication may be made without written permission. No paragraph of this publication may be reproduced, copied or transmitted save with the provisions of The Copyright Licensing Agency Ltd, Saffron House, 6–10 Kirby Street, London EC1N 8TS, UK. Users registered with the Copyright Clearance Center, 222 Rosewood Drive, Danvers, MA 01923, USA: the item-fee code for this publication is 0305-8719/11/\$15.00.

British Library Cataloguing in Publication Data

A catalogue record for this book is available from the British Library.

ISBN 978-1-86239-320-2

Typeset by Techset Composition Ltd, Salisbury, UK

Printed by MPG Books Ltd, Bodmin, UK

Distributors

North America

For trade and institutional orders:

The Geological Society, c/o AIDC, 82 Winter Sport Lane, Williston, VT 05495, USA

Orders: Tel. + 1 800-972-9892

Fax + 1 802-864-7626

E-mail: gsl.orders@aidcvl.com

For individual and corporate orders:

AAPG Bookstore, PO Box 979, Tulsa, OK 74101-0979, USA

Orders: Tel. + 1 918-584-2555

Fax + 1 918-560-2652

E-mail: bookstore@aapg.org

Website: <http://bookstore.aapg.org>

India

Affiliated East-West Press Private Ltd, Marketing Division, G-1/16 Ansari Road, Darya Ganj, New Delhi 110 002, India

Orders: Tel. + 91 11 2327-9113/2326-4180

Fax + 91 11 2326-0538

E-mail: affiliat@vsnl.com

Contents

Acknowledgements	vi
POBLET, J. & LISLE, R. J. Kinematic evolution and structural styles of fold-and-thrust belts	1
MASINI, M., BIGI, S., POBLET, J., BULNES, M., DI CUIA, R. & CASABIANCA, D. Kinematic evolution and strain simulation, based on cross-section restoration, of the Maiella Mountain: an analogue for oil fields in the Apennines (Italy)	25
VIDAL-ROYO, O., HARDY, S. & MUÑOZ, J. A. The roles of complex mechanical stratigraphy and syn-kinematic sedimentation in fold development: insights from discrete-element modelling and application to the Pico del Águila anticline (External Sierras, Southern Pyrenees)	45
TANNER, D. C., BENSE, F. A. & ERTL, G. Kinematic retro-modelling of a cross-section through a thrust-and-fold belt: the Western Irish Namurian Basin	61
SIMÓN, J. L. & LIESA, C. L. Incremental slip history of a thrust: diverse transport directions and internal folding of the Utrillas thrust sheet (NE Iberian Chain, Spain)	77
ANTOLÍN, B., APPEL, E., MONTOMOLI, C., DUNKL, I., DING, L., GLOAGUEN, R. & EL BAY, R. Kinematic evolution of the eastern Tethyan Himalaya: constraints from magnetic fabric and structural properties of the Triassic flysch in SE Tibet	99
TORRES CARBONELL, P. J., DIMIERI, L. V. & OLIVERO, E. B. Progressive deformation of a Coulomb thrust wedge: the eastern Fuegian Andes Thrust–Fold Belt	123
FITZ-DIAZ, E., HUDLESTON, P. & TOLSON, G. Comparison of tectonic styles in the Mexican and Canadian Rocky Mountain Fold–Thrust Belt	149
GARCÍA-SANSEGUNDO, J., POBLET, J., ALONSO, J. L. & CLARIANA, P. Hinterland-foreland zonation of the Variscan orogen in the Central Pyrenees: comparison with the northern part of the Iberian Variscan Massif	169
FERNÁNDEZ, F. J., DÍAZ-GARCÍA, F. & MARQUÍNEZ, J. Kinematics of the Forcarei Synform (NW Iberian Variscan belt)	185
MANTERO, E. M., ALONSO-CHAVES, F. M., GARCÍA-NAVARRO, E. & AZOR, A. Tectonic style and structural analysis of the Puebla de Guzmán Antiform (Iberian Pyrite Belt, South Portuguese Zone, SW Spain)	203
REZ, J., MELICHAR, R. & KALVODA, J. Polyphase deformation of the Variscan accretionary wedge: an example from the southern part of the Moravian Karst (Bohemian Massif, Czech Republic)	223
POUL, I., MELICHAR, R. & JANEČKA, J. Thrust tectonics of the Upper Jurassic limestones in the Pavlov Hills (Outer Western Carpathians, Czech Republic)	237
Index	249

Acknowledgements

The editors of this Special Publication are deeply grateful to the authors of the manuscripts and to the following reviewers whose efforts and patience substantially improved the quality of this volume.

Antonio Azor
Josep M. Casas
Sébastien Castelltort
Ana Crespo-Blanc
Grenville Draper
Mary Ford
Wolfgang Franke
Richard H. Groshong Jr.
Bernie Housen
Michael Johnson
Keith A. Klepeis
Richard J. Lisle
Michael F. McGroder

Franz Neubauer
Emilio L. Pueyo
Víctor A. Ramos
António Ribeiro
François Roure
David J. Sanderson
Deborah A. Spratt
Stefano Tavani
Antonio Teixell
Jonathan P. Turner
Jaume Vergés
Wesley K. Wallace
various anonymous reviewers

Kinematic evolution and structural styles of fold-and-thrust belts

J. POBLET¹* & R. J. LISLE²

¹*Departamento de Geología, Universidad de Oviedo, C/Jesús Arias de Velasco s/n,
33005 Oviedo, Spain*

²*School of Earth and Ocean Sciences, Cardiff University, Park Place, Cardiff CF10 3YE, UK*

**Corresponding author (e-mail: jpoblet@geol.uniovi.es)*

Abstract: Fold-and-thrust (FAT) belts occur worldwide and have long been the focus of research of structural geologists who have devised a variety of techniques to image, characterize and model their main structural features. This introductory chapter reviews the principal geological features of FAT belts formed in different settings, emphasizing aspects related to their kinematic evolution and structural styles. Despite great advances, challenges remain, particularly in the understanding of the spatial and temporal evolution (4D) of FAT belts and their controlling factors. These research efforts are being assisted by the growing availability to researchers of relatively new tools to collect field data, high quality 3D seismic data, and computer and laboratory modelling tools. This volume includes technical papers presented in the conference 'International Meeting of Young Researchers in Structural Geology and Tectonics (YORSGET-08)' held in Oviedo (Spain), together with other papers on the same theme. These papers deal with FAT belts in different parts of the world and cover a broad range of different aspects, from detailed structural analysis of single structures to regional issues, and from studies based on classical field structural geology to modelling.

Fold-and-thrust belts, or FAT belts for short, have a worldwide distribution (see surveys in Nemcok *et al.* 2005; Cooper 2007), have formed in all eras of geological time, and are widely recognized as the most common mode in which the crust accommodates shortening. Generations of geologists have struggled to understand their origin, geometry, evolution and the control exerted on them by different structural, tectonic, stratigraphic and petrological parameters (see for instance monographic books such as McClay & Price 1981; MacQueen & Leckie 1992; McClay 1992a, 1994; Mitra & Fisher 1992; Nemcok *et al.* 2005; Lacombe *et al.* 2007).

A number of factors have contributed to our greater understanding of the structure of FAT belts; some of them derive from detailed analyses of prevalent patterns of faulting and folding and their related structural features, whereas others come from other earth science disciplines. Many important concepts were developed and applied to FAT belts as early as the 1970s, or even before, and have been subsequently modified. Since a comprehensive historical review of research progress is almost impossible here, only a few important landmarks are briefly described, starting with structural methods from small- to large-scale and following with techniques applied to these regions furnished by related disciplines such as petroleum geology, geophysics, geomorphology, petrology and sedimentology.

The application of classical methods of studying deformation mechanisms in rocks and of quantifying geological strain (e.g. Ramsay 1967; Durney & Ramsay 1973; Fry 1979a, b) to FAT belts has led to greater understanding of deformation on a small scale and has given insights into the mechanisms responsible for the development of individual structures such as folds and faults. A number of techniques were initially devised to analyze the structure of FAT belts, for example: (a) balanced and restored cross-sections (e.g. Dahlstrom 1969; Mitra & Namson 1989); (b) construction of geological cross-sections using techniques such as depth to detachment estimations (e.g. Chamberlin 1910; Mitra & Namson 1989) and the Busk and dip domain methods (Busk 1929; Suppe 1985, respectively); and (c) advances in the understanding of quantitative relationships between thrusts and their related folds and the rules to help to constrain the structural geometries (Suppe 1983; Jamison 1987; Mitra 1990; Suppe & Medwedeff 1990). These techniques have enabled construction and validation of admissible and retro-deformable geological sections across single structures, structural units and entire FAT belts. They have also provided guidelines for seismic interpretation, and proved to be essential tools in structural interpretation widely applied elsewhere, particularly in areas of scarce and/or poor quality data. The study of accretionary wedges played a key role in the development of the

Coulomb wedge theory (e.g. Davis *et al.* 1983; Dahlen *et al.* 1984). This theory, which incorporates the best of the gravity-driven v. surface force-driven motion hypotheses, was a major step forward in the understanding of the kinematics and dynamics of FAT belts because it allowed the inclusion of the effects of gravity and topography and provided answers to the problems of structure sequencing in these regions.

The contribution of geophysics has been hugely beneficial to FAT belt research. In particular, since many belts contain major oil and gas accumulations in structural traps, the geophysical explorations carried out by the hydrocarbon industry have supplied an enormous amount of subsurface data. From the early seismic experiments in the late 1920s in the Zagros FAT belt and in Oklahoma until the present day, seismic imaging has furnished additional constraints on the geological interpretation of the deep geometry of structures, which had previously relied on geological data collected at the surface. Seismic has, in some cases, also allowed mapping of subsurface structures that are decoupled from their surface structural expression. Without forgetting the important contribution made by some other branches of geophysics, such as gravimetry for constraining of the deep structural configuration, or palaeomagnetism in the understanding of rotations around vertical axes, one of the most important boons to mapping of FAT belts has been the development of 3D seismic survey methods. 3D seismic data volumes provide a continuous and more accurate image of the subsurface than can be obtained with 2D seismic methods (Hart 1999). Aided by the development of structural tools, for example, *Geosec 3D*, *3D Move*, *Lithotect* and *Gocad* software packages to visualize, characterize and model the 3D structure of folds and thrusts, 3D seismic is starting to supply answers, particularly with respect to the questions of the geometry of structures along strike and whether structures evolve in a self-similar fashion, that is, whether observed spatial variations in fold geometry reflect temporal geometric evolution (Elliott 1976; Means 1976), or whether they evolve through different structural forms.

The contributions of tectonic geomorphology and palaeo-seismology of mountain fronts (Bull 2007 and references therein) have helped to determine the development of structures through the study of the landscape evolution and offset/position of landforms. Furthermore, $P-T-t$ data (e.g. Spear & Selverstone 1983; England & Thompson 1984; Thompson & England 1984) collected from the interiors of FAT belts have been employed to interpret the burial, thermal and subsequent uplift histories operating during emplacement of thrust sheets. In addition, geochronology studies using

isotopes, magnetostratigraphy, fission tracks, cosmogenic nuclides, and so on (e.g. Vance & Müller 2003; Allègre 2008; Lisker *et al.* 2009; Dunai 2010) have enabled estimates to be derived for both the timing and the short- and long-term rates of motion of single structures and larger-scale tectonic processes. These have demonstrated, for instance, that synchronous movement of different thrusts is a significant feature in the kinematic evolution of FAT belts, which, in turn, has important implications for thrust sequences and the balancing/restoration of cross-sections and forward modelling of thrust terrains. A great deal of recent research has been focused on the dynamic interaction between FAT belt evolution and surficial processes such as syn-kinematic sedimentation, erosion, uplift and subsidence from lithosphere-scale (e.g. Beaumont *et al.* 1992; Kooi & Beaumont 1996) to individual structure-scale (e.g. Riba 1976; Suppe *et al.* 1992; Hardy & Poblet 1994). Thus, whereas the geometry of the syn-tectonic sediments and basins within the FAT belts is influenced by development of structures, the latter in turn are themselves strongly affected by sedimentation and erosion. In short, studies based on tectonic geomorphology and palaeoseismology, $P-T-t$ paths, geochronology and surficial processes in FAT belts sparked an increasing interest in quantitative modelling of the evolution of these belts at various scales.

Types of FAT belts

Summarizing the main features of FAT belts is not an easy task because they are remarkably diverse. Although they exhibit a number of common characteristics, no single map or cross-section can provide a universal portrayal of a FAT belt because many parameters exert an important influence on them (see, for instance, Fitz-Diaz *et al.* 2011). These factors include the plate tectonics setting in which they developed, whether only the cover or both the cover and basement rocks are involved in the structures, the role of mechanical stratigraphy, the presence, distribution and thickness of a salt/shale detachment, the occurrence of syn-orogenic erosion and deposition leading to burial, the depth to detachment and the effective elastic thickness of the lithosphere (e.g. Royden 1993), the occurrence of pre-existing basement structures, the timing and deformation rates, and so on. All of these factors are important, though a discussion of their effect is beyond the scope of this paper.

FAT belts are typical regions in most orogenic belts controlled by compressional tectonics and have been documented in environments resulting from plate convergence such as those formed at plate collision boundaries (e.g. Himalayas,

Apennines), at plate subduction boundaries (e.g. Andes, Zagros) and at intraplate locations influenced by neighbour plate convergence (e.g. Yinshan belt and Western Ordos belt in China). Accretionary prisms are a special type of FAT belt developed in subduction zones such as the Barbados prism. FAT belts known as toe thrust belts develop in deep water at the leading edge of large-scale gravitationally driven sedimentary prisms on continental margins such as those in the Gulf of Mexico and offshore Brazil, or in thick delta complexes such as the Niger delta or in deltas in northwest Borneo. FAT belts may also form due to transpression at oblique plate boundaries, where the overall plate convergence involves strike-slip components of motion, such as part of the southern Carpathians and the Central-South Trinidad thrust belt, or along large-scale transform or transcurrent faults at restraining bends or oversteps and at fault splays, such as the Transverse Ranges of the San Andreas transform fault and perhaps the Palmyride belt in Syria in relationship to the Dead Sea transform fault.

Foreland FAT belts and crystalline thrusts

One of the most well-known types of FAT belts are the foreland FAT belts that are 10 to 1000 kilometres wide and constitute the external zones of orogens (Figs 1 & 2). The Canadian Rocky Mountains zone (Price 1981) is one of the best examples of a foreland FAT belt. These FAT belts typically involve an unmetamorphosed or low-grade metamorphic sedimentary cover, whose thickness decreases towards the foreland (interior of a continent), deposited over a metamorphic/igneous basement, whose top usually dips towards the hinterland (ancient sea), that constitute the passive continental margin. They usually exhibit a wedge geometry in cross-sectional view and this shape is maintained throughout the deformational history of the belt. Deformation is confined to the uppermost part of the crust bounded by a sole thrust (basal detachment) that dips gently towards the hinterland and rises stratigraphically upwards towards the foreland; the sole thrust may be blind or may reach the topographic surface in some cases (Figs 1–3). There may be various detachments above the sole thrust that tend to rise up towards the foreland, but all of them ultimately branch off from the main sole fault. Many thrust surfaces are asymptotic at depth, forming imbricate thrust systems in which thrust surfaces may maintain an approximately regular spacing. However, other types of thrust systems such as duplex, antiformal stacks, triangle zones and intercutaneous wedges (Butler 1982; McClay 1992b) are common as well (Figs 1–4). The loading effect of a FAT belt creates accommodation space in the foreland basin developed in front

of the belt, which is usually filled in with debris eroded from the mountain belt and in some cases affected by the prograding thrust system which carries forward the older foreland basin. This uplifted, shortened and transported basin is known as a piggy-back basin.

Some FAT belts include a slate belt (Hobbs *et al.* 1976; Twiss & Moores 1992) such as that of Wales (e.g. Smith & George 1961), which mainly consists of a monotonous series of relatively unfossiliferous deep-water sediments, such as shales and slates. These sediments were deposited in relatively internal positions of the belt, such as the edge of passive continental margins or offshore volcanic environments. Slate belts are narrow, elongate features parallel to the orogenic belt. The stratigraphy and structure of slate belts is usually difficult to reconstruct due to poor exposure conditions, the lack of fossils and stratigraphic markers as well as the metamorphic conditions up to low grade. The low competence contrasts within these sedimentary piles results in tight to isoclinal flattened folds with thickened hinges which can possess near-similar geometry. They exhibit variably inclined axial surfaces, from upright to recumbent. They include parasitic folds and can form fold nappes, with more than one fold generation present in some cases. Pervasive continuous foliation such as a slaty cleavage and phyllitic foliations, overprinted by later spaced foliations in some cases accompanied by folding, and by kink bands, become dominant. Although thrusts are present, the lack of marker beds makes them difficult to map.

On the thickened side of the orogenic belts in the transition to the crystalline core of a mountain chain, metamorphic rocks, either as basement slices or as progressively metamorphosed sedimentary rocks, appear. The thrusts involving metamorphic and/or igneous rocks are usually known as crystalline thrusts (Hatcher 1995) and have been known for many decades in the Alps, Appalachians, Scandinavian and British Caledonides. Whereas the thrusts closer to the undeformed regions form under brittle conditions, those close to the metamorphic core develop under ductile to brittle conditions. Thus, the thrust surface may be initiated due to a local ductile behaviour, whereas the thrust sheet may be transported by brittle translation. In contrast to those FAT belts developed in regions occupied by sedimentary rocks where bedding is the main structural discontinuity, appropriately oriented pre-existing faults, well-developed foliations and ductile-brittle transitions are the main mechanical weaknesses that allow the propagation of crystalline thrusts. Crystalline thrust sheets are among the largest structures in orogenic belts and may form as large slabs or on the overturned limbs between recumbent folds because of continued transport

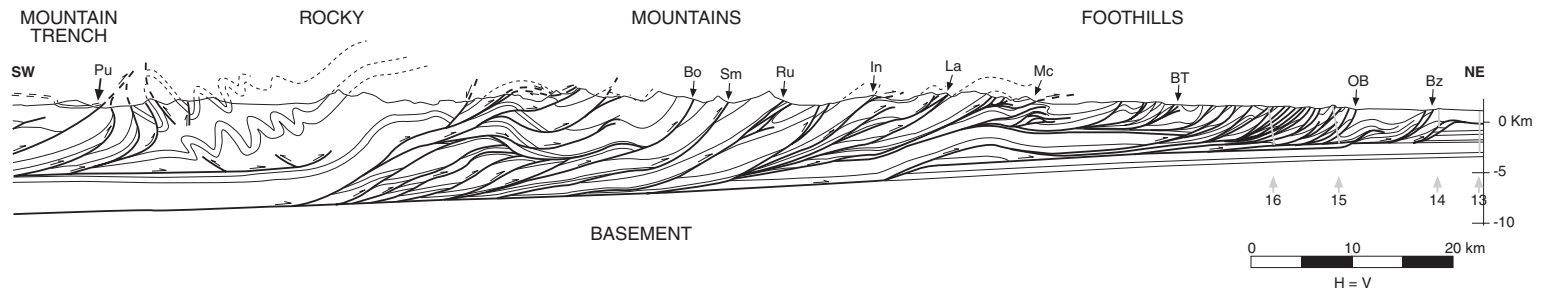


Fig. 1. Balanced geological section across the Rocky Mountains Foothills, Cordilleran FAT belt. Note the sub-vertical to overturned thrusts in the southwestern part of the cross-section, probably due to underlying folding and thrusting (modified from Price 1981).

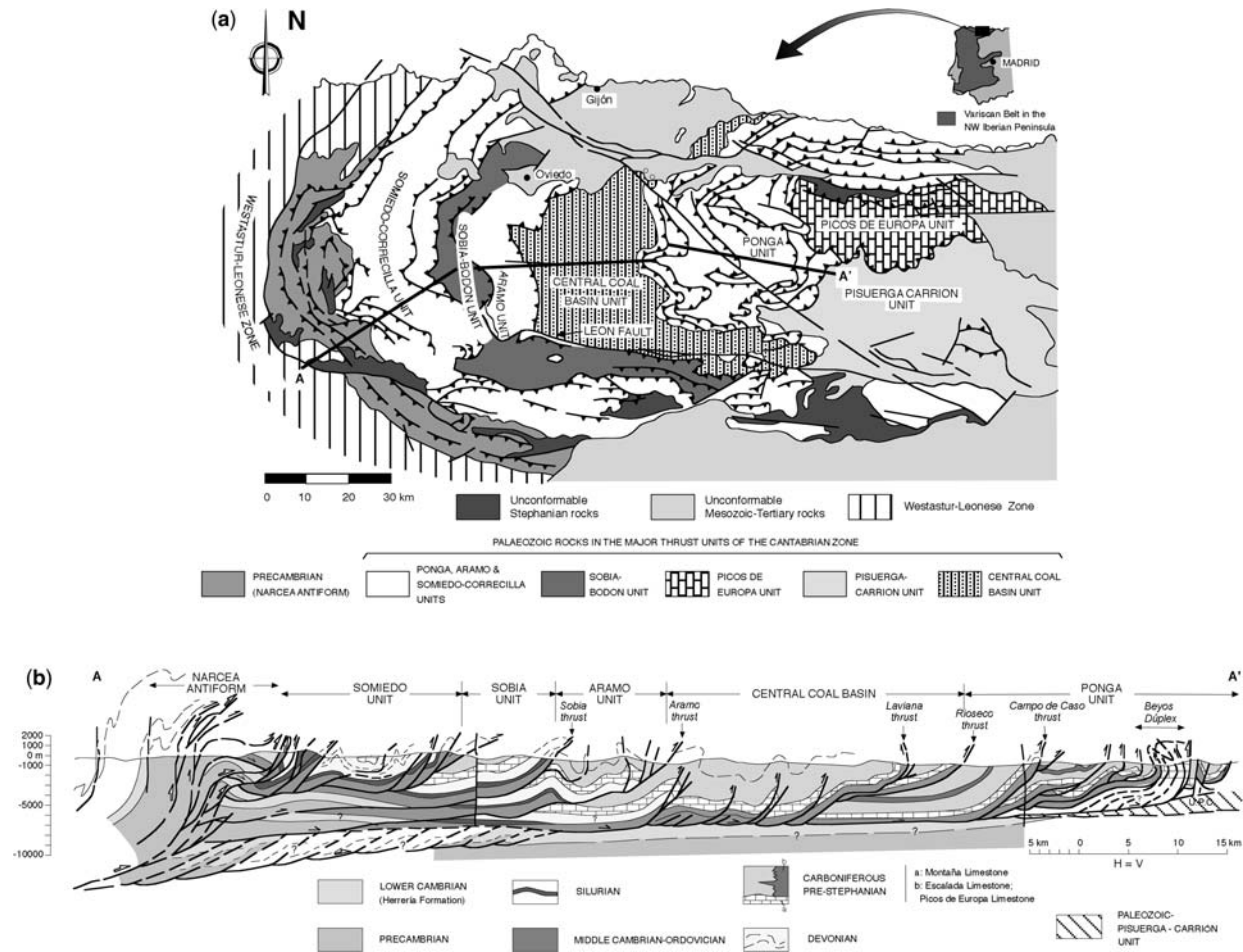


Fig. 2. (a) Simplified structural map of the foreland FAT belt of the Variscan Orogen in northwest Iberian Peninsula (Cantabrian Zone), which exhibits an orocline geometry (Ibero-Armorican or Asturian arc). Dominant thrusting style in the SW portion of the belt changes to a dominant folding style in the NW part of the belt. (b) Balanced geological section across the Cantabrian Zone. The cross-section line is located in Figure 2a. Note the sub-vertical to overturned thrusts in the east part of the cross-section probably due to thrust sheet stacking. Both figures are modified from Pérez-Estaún *et al.* (1988).

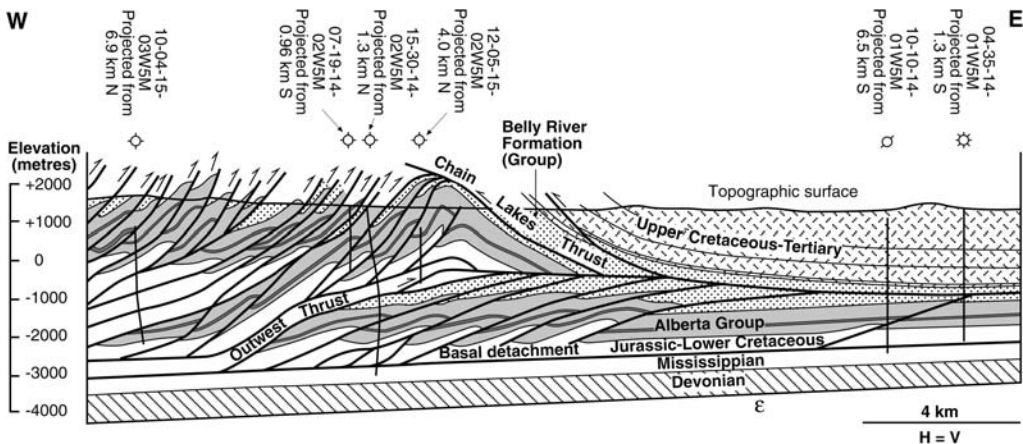


Fig. 3. Geological section across the south end of one of the largest structures within the leading edge of the southern Canadian Cordillera, called the Highwood structure, SW Alberta, which is relayed by the Turner Valley structure to the north (modified from MacKay 1996). The Highwood structure is interpreted as a sort of intracutaneous wedge including imbricate thrust systems, an antiformal stack, duplexes and backthrusts.

(fold nappes). Usually, multiple generations of folds, accompanied by foliations, produce a variety of fold interference structures. Thus, apart from thrusts, a frequent sequence of deformations observed in these regions includes recumbent isoclinal folds refolded by upright, more open folds, and finally deformed by smaller-scale kink bands.

Accretionary prisms

Accretionary prisms (e.g. Casey Moore & Silver 1987; von Huene & Scholl 1991) are the main locus of deformation in subduction zones, where the rock assemblages are mechanically scraped off the downgoing oceanic slab and accreted to the seaward edge of the upper advancing plate forming thrust sheets (Fig. 5). Many earthquakes that take place in subduction zones display thrust

fault focal mechanisms. The Nankai accretionary prism (Morgan & Karig 1995) is a classical example of this type of belt. Because they are composed of heterogeneous material, the internal structure of the prism is highly variable. Accretionary prisms have a wedge shape in cross-sectional view and their fronts are usually scalloped in map view. The bulk geometry of the prism and its detailed structure are strongly controlled by the thickness of the sedimentary pile of the subducting oceanic plate. The wedge is underlain by a detachment that ramps up to progressively shallower levels towards the trench, and propagates seaward decoupling mass from the downgoing slab that accretes to the overriding slab usually in the form of duplex (tectonic underplating). While this happens, the upper part of the trench fill or offscraped sequence is incorporated in the accretionary prism at the toe of the wedge (frontal accretion). Seaward of the emergent frontal thrust, blind thrusts emanate upwards from the detachment level while the detachment propagates leading to an imbricate thrust system with related folds. Sediments deposited in the synclinal troughs form piggy-back basins that usually evolve into asymmetrical tilted basins due to the general wedge tilting and may become incorporated into the prism as a result of thrust activity. In addition, deformation may reach the inner boundary of the accretionary prism leading to folding and backthrusting (rear accretion). Large-scale long-term margin subsidence observed in many wedges requires thinning of the upper plate, and since sedimentation continued during subsidence, erosion along the upper plate's base must have been occurred (subduction erosion). The processes that



Fig. 4. Folded repetitions of Devonian limestones caused by thrust sheet stacking in the Somiedo nappe (Juan Luis Alonso, pers. com.), foreland FAT belt, Variscan orogen, NW Iberian Peninsula (Cantabrian Zone).

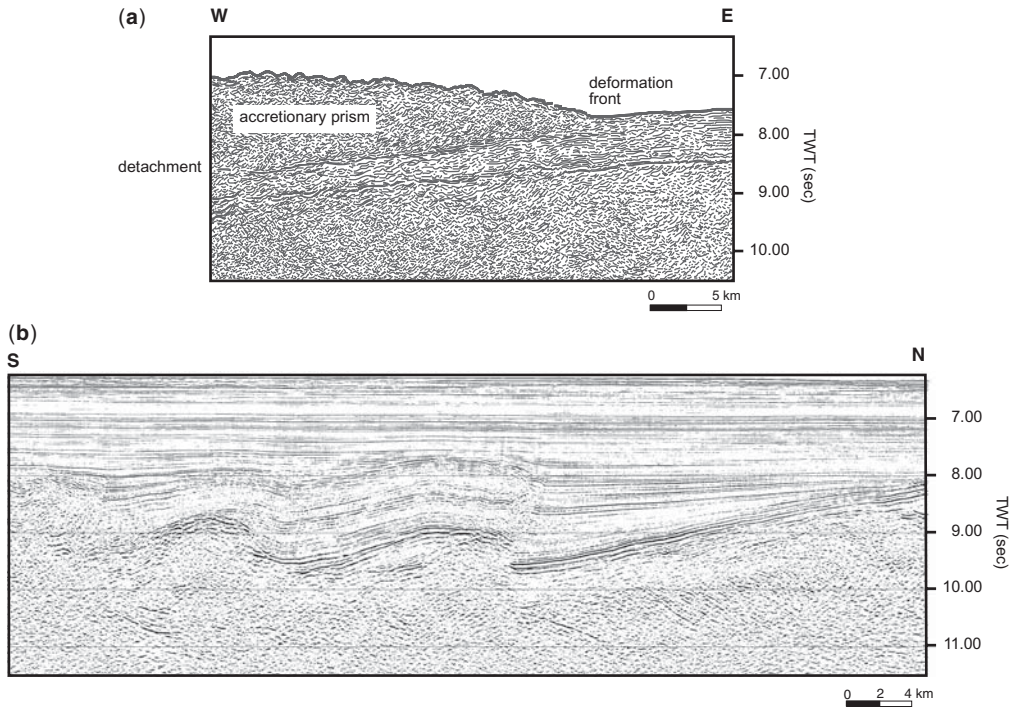


Fig. 5. (a) Line drawing of a seismic profile through the Barbados accretionary prism in which the detachment truncates some underlying horizons (modified from Westbrook *et al.* 1988). (b) Seismic profile showing the toe of the seaward frontal portion of the accretionary wedge in the North Iberian Atlantic margin, Bay of Biscay, developed as the western prolongation of the Pyrenees during Tertiary times (data courtesy of F. J. A. Pulgar and Marconi team, from Fernández-Viejo *et al.* in press). The section displays growth ramp anticlines and synclines including Mesozoic and Tertiary sediments deposited before, during (growth strata) and after fold development.

caused the erosion are still being discussed (see von Huene *et al.* 2004 for a summary): hydrofracturing of the upper plate due to elevated pore-fluid pressure or physical abrasion caused by horst and graben entering the trench axis. Accretionary prisms exhibit abundant small-scale folds, cleavages, boudins and veins. They usually include mud or serpentinite diapirs in sediment-dominated or igneous-basement prisms respectively. Thrust systems are often strongly affected by the collision of seamounts or fracture zones. Lateral faults commonly cut across the prisms and faulting of the lower lithospheric plate sometimes reflects pre-existing structure and may have some effect on the structure of the upper plate. Blueschists may form at the base of large accretionary prisms if pressures are high due to substantial lithostatic overburden and temperatures are low due to the relatively cold downgoing slab. However, if the subducting slab is not cool, then blueschists do not form and the wet sediment may melt creating small granitic intrusions. One of the main differences between the conventional FAT belts and those developed in

accretionary prisms is that in the latter there is a lack of rheological contrast among the different sedimentary beds and the generally weak, water-rich sediments of the accretionary prism become pervasively disrupted. Such chaotic deposits are called melanges.

Toe thrust belts

Toe thrust belts (e.g. Worrall & Snelson 1989; Cobbold *et al.* 1995) exhibit distinctive features. Unlike other FAT belts, they do not require lithospheric shortening, their deformation and transport are achieved entirely by gravity. They are generally detached on salt or overpressured shales and are, therefore, unrelated to the basement. In some cases, the down-slope advance of the glide complex is balanced by shortening in the frontal, lower portion located on the flat basin floor and by extension in the rear, upper part located on the inclined basin margin (Fig. 6). However in other cases the ductile substrate migrates forwards under the differential load to give extension on the delta top and

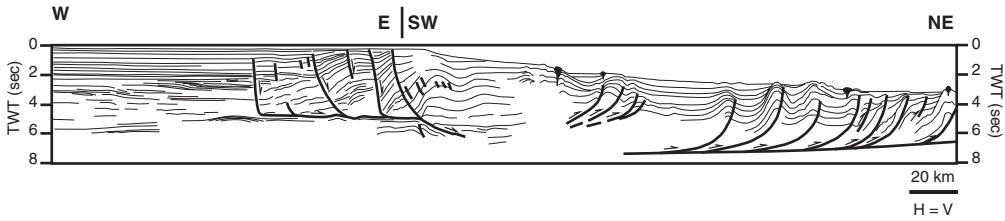


Fig. 6. Line drawing of a seismic profile through the offshore Eastern Venezuela basin deformed during Neogene times due to gravity collapse superimposed on a Mesozoic passive margin. Normal faulting and associated rollover anticlines in the rear part of the complex are balanced by thrusting and related folding in the frontal portion (modified from Di Croce 1995).

contraction at the delta toe (Fig. 7). The contractional structures developed include folds and thrusts as well as structures involving salt or shale such as tongues, wedges and canopies, and may accommodate significant amounts of shortening (100 km in the case of the Campos Basin, Brazil; Demercian *et al.* 1993) and may have travelled

considerable distances (60–160 km in the case of the Campos Basin; Nemcok *et al.* 2005). These FAT belts are controlled by the interaction of several parameters such as the width and dip of the basin margin, the distribution, thickness and rheology of the detachment horizon, the temporal and spatial variation of the sedimentary loading,

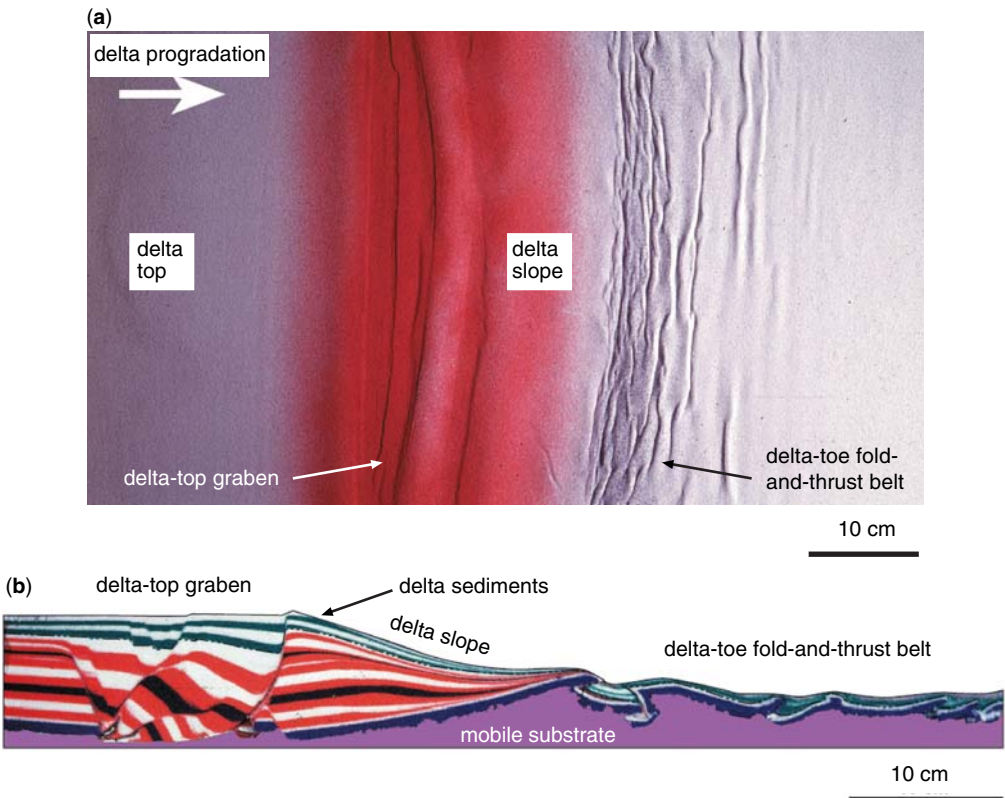


Fig. 7. (a) Top view and (b) cross-sectional view of an experimental sandbox model designed to simulate differential sedimentary loading in a progradational delta system developed on top of a ductile substrate. The structures developed during delta progradation are delta-top extensional faults giving rise to a graben and a FAT belt at the foot of the delta slope (modified from McClay *et al.* 2000).

and the occurrence of barriers to the gliding movement such as seamounts or tilted fault blocks. The main cause of the instability is the strongly reduced basal traction caused by an extremely weak layer at the base of the wedge.

Structural styles and evolution of FAT belts

Relationships between FAT belts and basement-involved belts

The style of deformation of FAT belts (see for instance the Canadian Rocky Mountains in Bally *et al.* 1966; Price 1981), in which thrusting involves only the sedimentary cover whereas the basement remains unaffected by the thrusting, is known as thin-skinned deformation (Figs 1–3 & 8b1). As we trace the thrusts back into the hinterland, basement rocks become involved in the thrust sheets (crystalline thrusts). These basement rocks may have been transported in a ‘thin-skinned’ manner on sub-horizontal thrusts over other basement or cover rocks. Eventually, the thrusts root down into crystalline basement rocks and lose their thin-skinned character. The thin-skinned structural style contrasts with the thick-skinned style of basement-involved belts (Coward 1983), in which both the basement and the cover are deformed due to contraction (Fig. 8b3), such as the Laramide uplifts (e.g. Schmidt *et al.* 1993). Usually, in contrast to FAT belts, rocks have not been transported over long distances in basement-involved belts. In these belts the basement is incorporated into the thrust sheets due to: (a) steep faults that penetrate the basement and create basement uplifts; and/or (b) reactivated inherited basement fabrics that control the subsequent thrust architectures such as inverted half-grabens. The basement uplifts of the thick-skinned belts may consist of fault blocks whose uplift and rotation caused forced folding of the cover sequences that drape relatively unfolded basement rocks (e.g. USA Rocky Mountain foreland, Prucha *et al.* 1965; Stearns 1971) or blocks formed by folded basement and cover rocks (Berg 1962; Blackstone 1983). The thick-skinned belts caused by reactivation of pre-existing faults exhibit different features depending mainly on whether all the faults were reactivated or only a few of them, the degree of reactivation, the angle between the direction of compression and the strike of the old faults, the main features of the inherited faults and the rheology of the involved sequences.

FAT and basement-involved belts coexist and are somehow related in many orogenic belts. These different structural styles may be distributed:

- (a) In different portions of the belt following a transversal pattern, such as the Rocky Mountains-USA Cordillera that exhibits thin-skinned styles in the interior and thick-skinned styles in the outer part (Hamilton 1988); in some cases the different structural styles are developed in adjacent regions, so that the steep faults that penetrate the basement rocks become sub-horizontal when they reach the cover and are responsible for its detachment such as in the Alps (e.g. Hayward & Graham 1989).
- (b) Along strike of the belt, such as the Andes (Fig. 8a) in which the structural style varies from thin-skinned styles in regions over inclined slab segments and thick sedimentary basins filled with cover rocks (Fig. 8b1) to transitional thin/thick-skinned styles (Fig. 8b2) to thick-skinned over flat segments of the subducted plate and little sedimentary cover on top of the crystalline basement (Fig. 8b3) (e.g. Mingham *et al.* 1979; Allmendinger *et al.* 1983).
- (c) Superimposed in the same region but developed during different times, such as the Bohemian Massif where an initial thin-skinned event is followed by a thick-skinned phase in which thrusts involve crystalline rocks and cross-cut older structures (Rez *et al.* 2011).

Some shortening-dominated regions formed by reactivation of inherited structures include elements from both FAT belts (thin-skinned) and basement-involved belts (thick-skinned). Thus, folds are related to steep faults that do not emanate from a detachment and cause relatively small displacements of the rocks. However, these belts are not proper thick-skinned belts because the basement rocks are not involved in the deformation similarly to thin-skinned belts (Fig. 9).

Amongst other factors, the presence of evaporites or shales at depth has a crucial impact on the structural style of the orogenic belt as a result of the efficiency of the detachment. The occurrence of basement fabrics exerts an essential control on the structural style as well; thus, passive margin basins filled by post-rift sedimentary prisms tapering onto the cratons favour the FAT belts (thin-skinned style), whereas intra-cratonic rift systems tend to give rise to basement-involved belts (thick-skinned structural style).

Along-strike geometry

On a large-scale in map view, FAT belts may be: (a) linear; (b) sinuous, when they show geometrical variations along-strike in the form of salients or virgations where the belt bulges into the undeformed region, and recesses, reentrants or syntaxis where

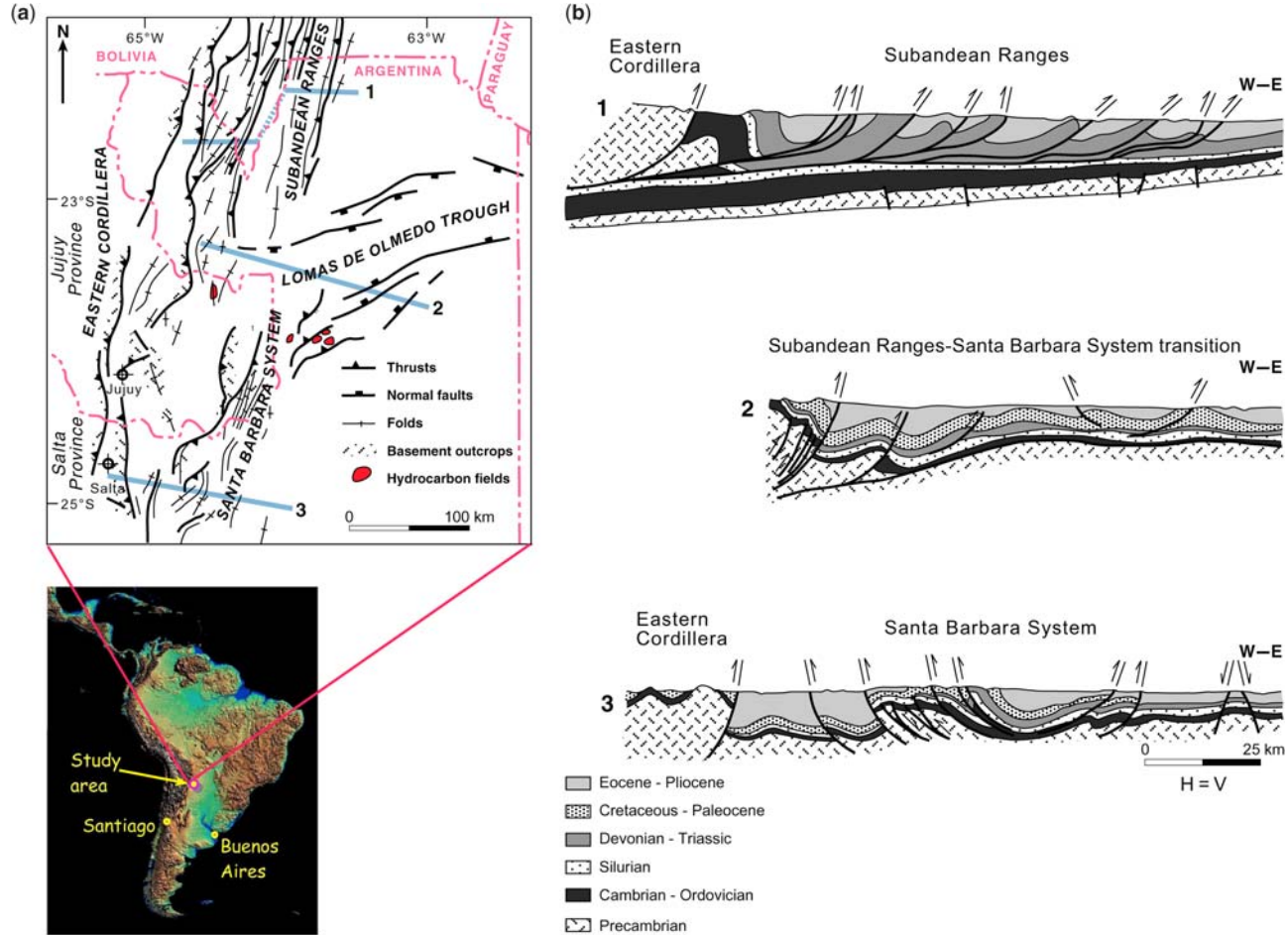


Fig. 8. (a) Simplified structural map of the frontal portion of the Andes, NW Argentina, showing the transition between the Subandean Ranges and the Santa Barbara System (modified from Uliana *et al.* 1995). (b) Three regional-scale geological cross-sections (modified from Mingramm *et al.* 1979) whose cross-section lines are located in Figure 1a. Section 1 across the Subandean Ranges exhibits a classical thin-skinned structural style, section 3 across the Santa Barbara System illustrates the typical thick-skinned style, and section 2 across the transition between both ranges interfered by the oblique Lomas de Olmedo Trough shows an intermediate structural style.

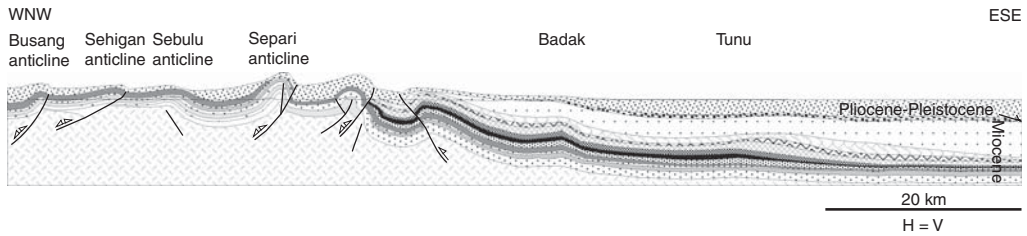


Fig. 9. Geological section across the Mahakam delta, Kalimantan, Indonesia, showing tight, anticlines whose steeper limb is bounded by a fault and broad synclines developed in sand, shale and coal-rich sequences of Miocene age. The folds developed due to regional-scale contractional reactivation of delta-top extensional growth faults produced during delta progradation. The faults root into the overpressured shale delta sequence (modified from McClay *et al.* 2000).

the belt has not propagated far into the undeformed region (salients and recesses may have experienced different kinematic evolutions); and (c) curved or arcuate, usually known as oroclines (Fig. 2a). The term ‘orocline’ was originally applied to curved mountain belts which were initially straight, or at least straighter than they are today. However, in the last few years, the definition has been broadened to include any curved mountain belt, regardless of its original shape. The Appalachians of eastern North America are a classical example of a sinuous mountain belt (e.g. Mitra 1997), whereas the Ibero-Armorican Variscan belt and its prolongation in the Variscan Pyrenees (García-Sansegundo *et al.* 2011) is a well-known example of an orocline. Many parameters influence the occurrence of curved geometries in map-view, for example, interaction of the propagating belt with basement highs, along-strike pinch-outs of favourable detachment horizons, lateral variations in stratigraphic thicknesses and/or lithologies, interaction of the belt with strike-slip faults, superposition of second deformation events with tectonic transport directions oblique or perpendicular to that responsible for the belt formation, and so on.

The non-straight geometry in map-view of some belts may be also caused by the fact that individual thrust sheets are not necessarily continuous along strike. Thrust surfaces may merge or be truncated by another thrust, but they can also transfer slip to another thrust fault through a transfer or relay zone, splay up and distribute movement among several smaller-scale thrusts, strike into the axial zones of folds that accommodate shortening or become segmented by sub-vertical faults, called tear or transfer faults, that separate different parts of the thrust sheet with distinct displacement, differential types of structures responsible for shortening accommodation (e.g. folding dominated in one tear fault block v. thrusting dominated in the other tear fault block) or connect non coplanar parts of a thrust surface.

Structural evolution

Most FAT belts exhibit an orogenic polarity which may vary along the belt, like the Himalayas (e.g. Antolín *et al.* 2011). Thus, folds verge usually towards the foreland in the case of foreland FAT belts (Figs 1–3 & 8b1), towards the trench in the case of accretionary wedges (Fig. 5b) and towards the basin in the case of toe thrust belts (Figs 6 & 7b), and thrusts show a sense of movement of top-to-the-foreland, and deformation becomes younger towards the foreland with thrusts developing in a break-forward or piggy-back sequence (Figs 10 & 11) defining a regional foreland-directed tectonic transport direction. Although a dominant orientation of the tectonic transport vector prevails, in detail the sense of motion of each thrust sheet may vary in its orientation spatially and/or through time (e.g. Simón & Liesa 2011). In addition to folds and thrusts vergent and directed respectively towards undeformed regions following a break-forward propagation sequence, other types of structures (backthrusts and back-vergent folds, out-of-sequence thrusts and/or reactivated thrusts) occur in many belts behind the deformation front (Figs 3 & 11). As new thrusts and related folds develop, unless the thrust ramp spacing is relatively large compared to the displacement along each thrust, early thrusts steepen due to rotation of the thrust imbricates (Figs 1, 2 & 10) accompanied by a certain amount of slip on the thrusts. Tilting and folding of the earliest thrusts makes continued slip on them increasingly difficult, and eventually they become inactive and too difficult to reactivate. New thrusts with their associated folds may propagate breaching, cutting through and/or folding the older thrust surfaces and related folds.

The kinematic evolution briefly described above is satisfactorily explained by the critical-taper theory. This requires the thrust wedges (Fig. 11) to maintain a critical taper angle (equal to the detachment surface dip plus surface-slope angle) to

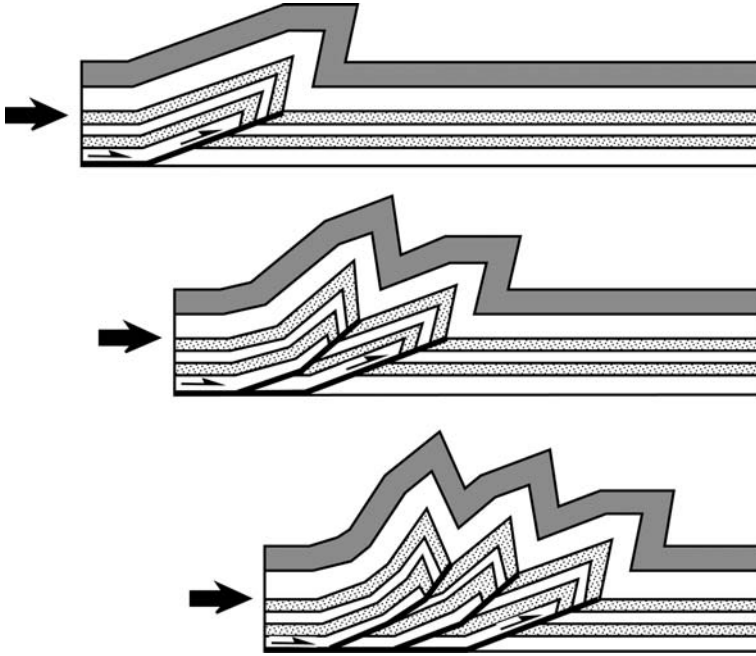


Fig. 10. Schematic development of an imbricate thrust system and related fault-propagation folds following a break-forward sequence and steepening of the earliest (hinterlandward) thrusts (modified from Mitra 1990).

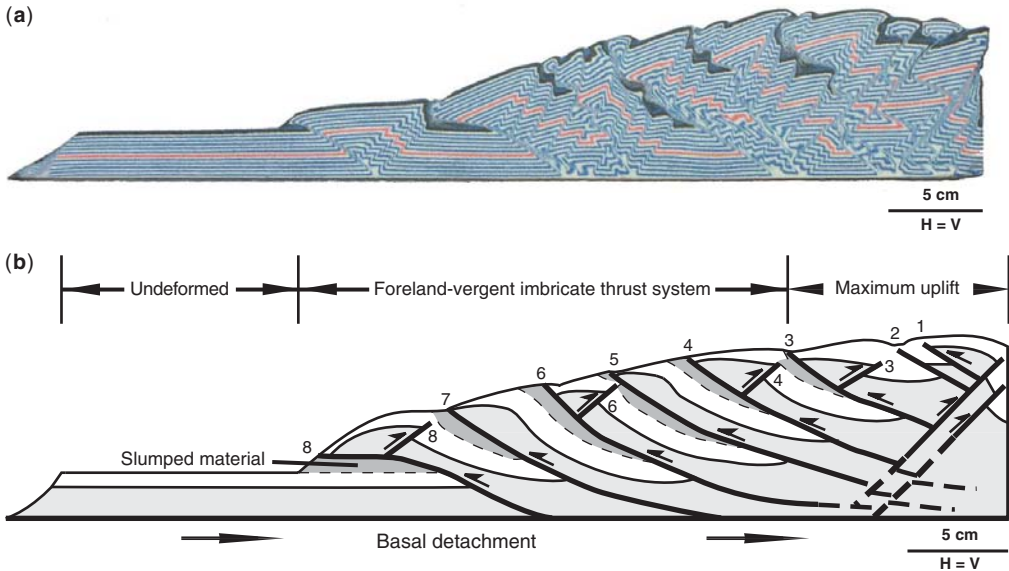


Fig. 11. (a) Cross-sectional view of an experimental sandbox model designed to simulate an orogenic wedge. The experiment was performed at the Fault Dynamics Laboratories conducted by K. R. McClay and is displayed at the Geological Museum—University of Oviedo (photograph courtesy of L. M. Rodríguez-Terente). (b) Schematic cross-section of an experimental thrust wedge derived from analysis of a series of scaled sandbox models showing three different regions and the general sequence of development of thrust faults. The backthrusts at the rear portion of the wedge were active during various growth stages. The scale is approximate (modified from Huiqi *et al.* 1992).

produce a dynamic equilibrium among different stresses: traction at the wedge base, compressive push at the back of the wedge, and the slope stress at the topographic surface. The wedge is thickened and shortened internally as thrusts override each other, folds develop, penetrative strain occurs and/or duplexes bounding rock packages are accreted from beneath the wedge. When the wedge reaches a critical taper angle, it slides stably along the detachment towards undeformed areas. During translation, the thrust wedge is lengthened as thrusts propagate towards undeformed regions and new material is added to its toe causing the taper angle to decrease because it distributes topographic elevation over a longer distance. When a subcritical taper angle is reached, stable sliding stops and internal deformation occurs again within the wedge. If the wedge reaches a temporary supercritical taper angle, the surface slope is decreased by wedge thinning due to erosion, collapses in a series of extensional faults, similar to large landslides, and/or slumps that remove material from the surface (Fig. 12). The subcritical, critical and supracritical stages may occur more than once during the evolution of a thrust wedge (e.g. Torres-Carbonell *et al.* 2011).

Fold-thrust interaction

The alternation of competent and incompetent lithologies exerts an important control on the geometry of thrust surfaces. Thus, thrust surfaces exhibit bedding-parallel segments, known as thrust

flats, usually within the incompetent horizons such as shales and evaporites, and bedding-oblique parts, called thrust ramps, so that they step up and cut across competent beds such as sandstones and limestones (Fig. 13a). After thrust movement, all sorts of situations are possible: hanging wall flats over footwall flats, hanging wall flats over footwall ramps, hanging wall ramps over footwall flats and hanging wall ramps over footwall ramps. Since the flats, that usually exceed the ramps in length, and the ramps are linked, overall the thrusts acquire staircase geometries. The occurrence of thrust ramps with strikes perpendicular to the tectonic transport vector (frontal ramps), forming an acute angle to the transport direction (oblique ramps) or with strikes parallel to the transport direction (lateral ramps) (Fig. 13b), leads to development of fault-bend folds (Rich 1934; Suppe 1983) due to the necessity of beds to conform to the thrust surface geometry (Fig. 14) and fault-propagation folds (Mitra 1990; Suppe & Medwedeff 1990) in those cases in which shortening is accommodated by both thrust ramp propagation and synchronous folding (Fig. 15). Although different types of ramp folds are the most typical modes of fold-thrust interaction in FAT belts, for example, the Iberian Variscan Massif (Mantero *et al.* 2011) or the Carpathians (Poul *et al.* 2011), not all folds in FAT belts are underlain by thrust ramps. Thus, simultaneously with propagation of a bedding-parallel thrust surface (detachment or décollement) or when a displacement gradient occurs along a detachment, detachment folds (Jamison 1987) form above or

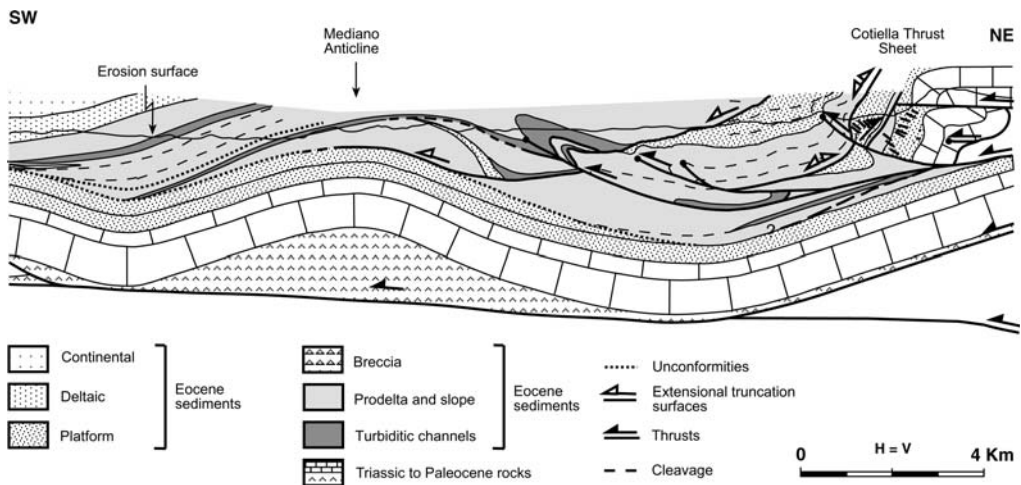


Fig. 12. Geological section across the Ainsa Basin, southern Pyrenees, showing thrusts and related folds (fault-bend, fault-propagation and detachment folds) partly truncated by extensional faults, which in turn, are cut and offset by part of the displacement along some thrusts. Since the relationships between thrusts and extensional faults indicate that they developed synchronously, the extensional surfaces are interpreted to reflect the episodic extensional collapse of the Pyrenean thrust wedge that advanced progressively into a marine foreland basin (modified from Muñoz *et al.* 1994).

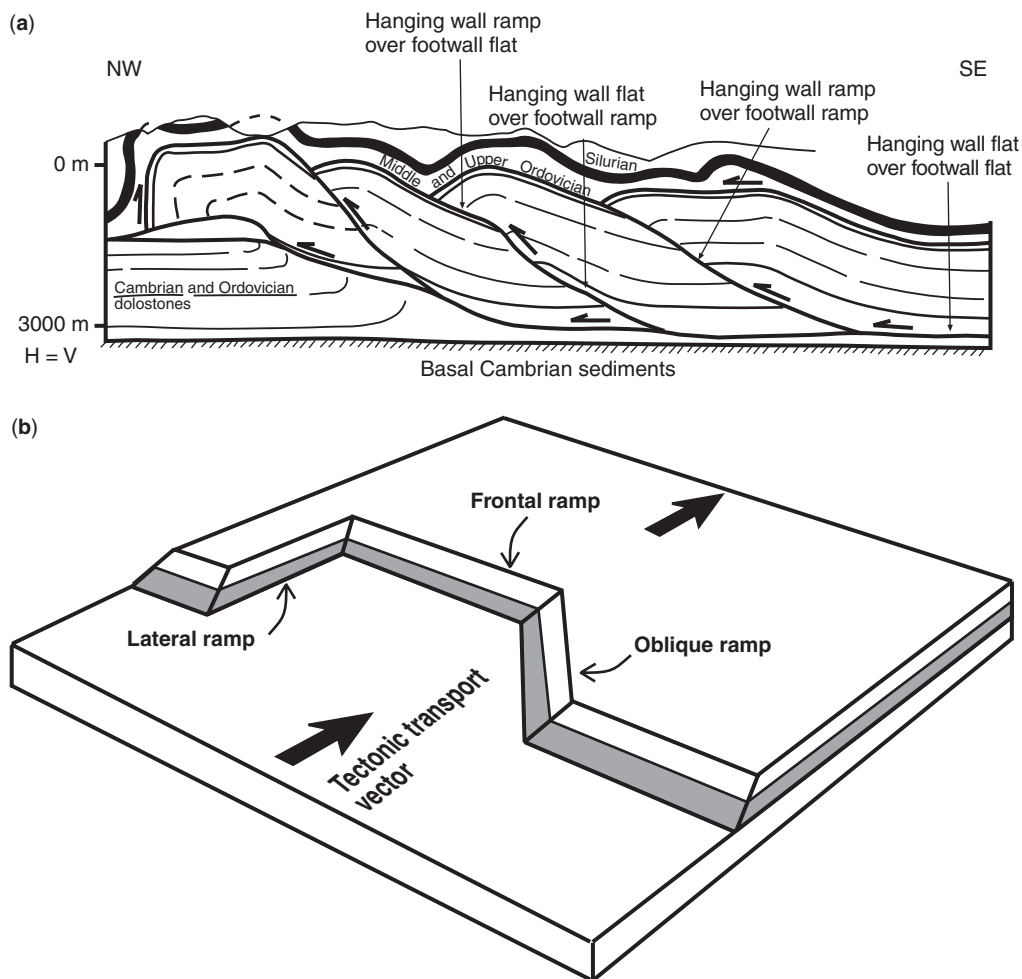


Fig. 13. (a) Geological section across the Nittany anticlinorium, Central Appalachians (section originally from Perry 1978 simplified by Geiser 1988) showing a staircase geometry of the thrust surfaces and all sorts of hanging wall and footwall ramp and flat situations. (b) 3D sketch showing the geometry of a thrust surface including frontal, oblique and lateral ramps.

below the detachment surface as in the case of the Pico del Águila detachment anticline in the southern Pyrenees (Vidal-Royo *et al.* 2011) (Fig. 16). Apart from ramp folds and detachment folds, other types of thrust-related folds develop for example, drag folds, and so on. All these folds can develop in the frontal part of thrust sheets (leading edge folds), in the rear portion of the thrust sheets (trailing edge folds), or within the thrust sheets (intraplate folds). As deformation increases, folds become tighter and overturned limbs may develop, and when they are too tight to accommodate more shortening they become locked-up and can be cut across by reverse faults (Fig. 17) giving rise to hybrid thrust-related folds (breakthrough and transported

fault-propagation and detachment folds) or to breakthrough folds such as the Maiella Mountain anticline in the Apennines (Masini *et al.* 2011) if folding developed before faulting. The dominant fold style is class 1B to 1C (Ramsay 1967) and most folds are asymmetric with a vergence towards undeformed regions. Usually in the hinge zones of folds cored by incompetent units such as argillaceous sediments, slaty cleavage may develop.

The folds described so far form under non-metamorphic or low-grade metamorphic conditions. In regions where the basement is involved in the thrust sheets and deformation takes place under medium to high-grade metamorphic conditions, large recumbent folds form with vergence towards

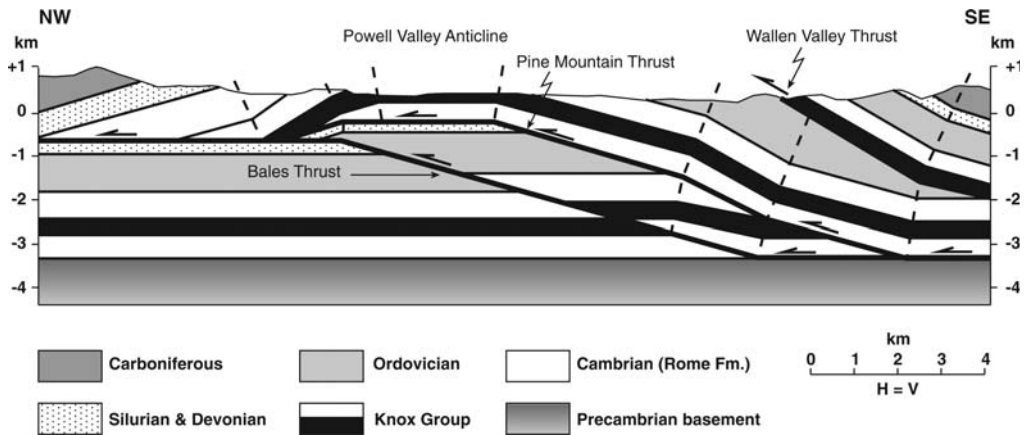


Fig. 14. Geological section across the Pine Mountain thrust system, southern Appalachians, in which the Powell Valley anticline is interpreted as a fault-bend fold cored by a duplex structure (modified from Suppe 1985).

the undeformed regions. These are accompanied by a pervasive cleavage. Various fold generations occur, for example, in the Iberian Variscan Massif (see Fernández *et al.* 2011).

Folding is a subordinate phenomenon related to thrusting in many belts in which imbricate thrust faults dominate, for example, in the Valley and Ridge province of the Appalachian Chain (Mitra 1988) or in the Southeastern Pyrenees (Muñoz 1992). However in other belts, folds dominate the tectonic architecture, for example, in Papua New Guinea (Smith 1965) or in the Western Irish Namurian Basin (Tanner *et al.* 2011). Along-strike

transitions from dominant folding to dominant thrusting have been reported in the Appalachians (Gwinn 1964), in the Canadian Rocky Mountains (Wheeler *et al.* 1972) and in the Cantabrian Mountains (Julivert & Arboleya 1984) amongst other FAT belts.

Contributions in this book

Much current research on the structure of FAT belts is focused on structural studies of regions or individual structures, and on the geometry and

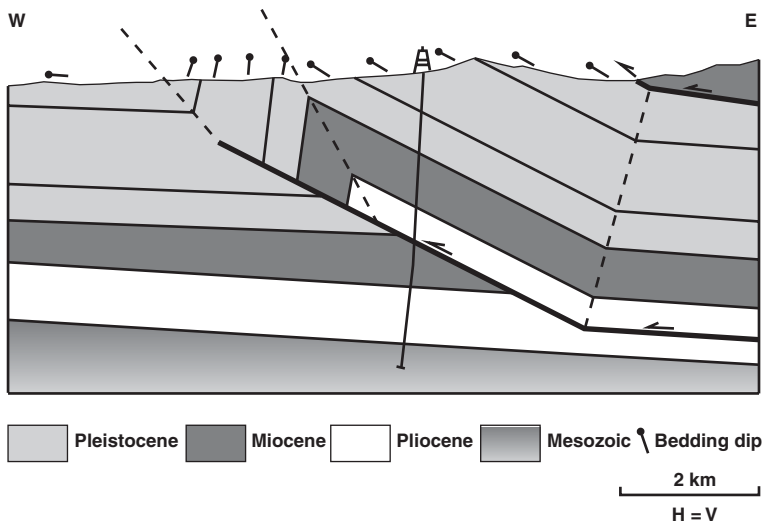


Fig. 15. Geological section across the Meilin anticline, western Taiwan, interpreted as a simple-step fault-propagation fold (modified from Suppe 1985).



Fig. 16. Satellite image of the External Sierras in the frontal part of the south Pyrenean foreland FAT belt showing a detachment fold train formed by narrow, rounded-hinge anticlines separated by wide, flat-bottom synclines affecting Triassic, Cretaceous, Paleocene, Eocene and Oligocene sedimentary rocks.

evolution of these regions employing kinematic, mechanical and experimental modelling. In keeping with the main trends of current research, this special publication is devoted to the kinematic evolution and structural styles of FAT belts. The topics of the papers included in this volume range from detailed structural analysis of individual structures to large-scale regional studies of FAT belts and from classical structural geology studies based on data collected in the field to numerical modelling. The papers included in this Special Publication are a selection of the works on FAT belts presented in various sessions at the 'International Meeting of Young Researchers in Structural Geology and Tectonics (YORSGET-08)' held at Oviedo (Asturias, Spain) in June–July 2008 together with others on the same topic matured over a similar period. This meeting was organized by M. Gutiérrez-Medina, C. López-Fernández, D. Pedreira and J. Poblet to jointly celebrate the 400 years anniversary of the foundation of the University of Oviedo and the

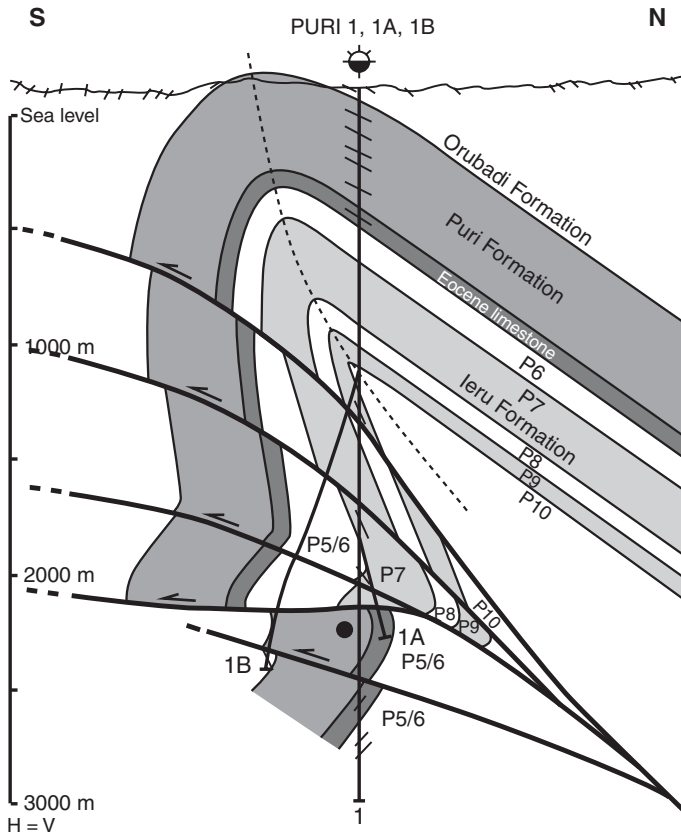


Fig. 17. Geological section across the Puri anticline, a long structure located in the leading edge of the Papua New Guinea FAT belt, showing out-of-sequence thrusting cutting across the steep forelimb of the fold and involving Eocene to Miocene rocks (modified from Medd 1996).

50 years anniversary of the Geology Faculty at Oviedo. The meeting attracted 53 oral presentations and 90 posters, and an audience of 201 participants from 25 countries, and included a field excursion to the Variscan FAT belt of NW Iberian Peninsula. This conference included a special session in memory of the structural geologist Martin Casey from the University of Leeds (UK) who died in 2008 and was a recognized authority on the modelling of natural deformation features and the author of papers fundamental to the understanding of the deformation responses of rock. In addition, this Special Publication includes the last article written by the structural geologist Florentino Díaz-García from the University of Oviedo (Spain) who devoted his research efforts to the study of the Variscan belt in northwestern Iberian Peninsula and who, unfortunately, died in 2009. This volume does not attempt to provide a comprehensive coverage of FAT belts, but puts together some contributions on specific topics of interest within this research theme, some of them presenting new concepts and techniques and others applying well-known concepts and techniques to new regions.

Internal deformation

The first two articles of this special publication describe the application of two different methods to analyze the internal deformation undergone by thrust-related anticlines. **Masini *et al.*** carried out field mapping and collected structural data in order to construct two sections across the Maiella Mountain anticline, a structure located in the Central Apennines, Italy, that resulted from Messinian–Early Pliocene extension and subsequent Late Pliocene shortening. They employed a strain simulation technique based on the inclusion of circular strain markers in the cross-sections, subsequent sequential restoration of the cross-section and the strain markers, and application of a mathematical model to obtain strain ellipses for each strain marker. According to their structural model, the Maiella structure is a break-thrust fold that underwent small amounts of extension associated with two main normal faults and subsequent shortening due to a major thrust and folding. The simulation of the strain distribution shows high strain intensity in both limbs and low deformation in the anticline crest and in part of the thrust footwall. In the anticline forelimb, where the strain is greater, high deformation is concentrated in two symmetric triangular zones separated by the thrust ramp. The distribution of strain intensity predicted in different structural positions of the Maiella structure is in broad agreement with the distribution of fracture density obtained from field data by previous authors. **Vidal-Royo *et al.*** employ 2D

discrete-element modelling to explore the evolution of the Pico del Águila anticline, a detachment fold formed during Eocene–Oligocene in the Spanish side of the Pyrenean FAT belt. This numerical technique treats the different units as an assemblage of circular elements that mutually interact with elastic forces influenced by gravity and obey Newton's equations of motion. Regarding the role of the mechanical stratigraphy, the competent beds experience rigid-body translation/rotation, localized faulting and minor shearing, whereas incompetent beds suffer high strain and are deformed by complex structures. The occurrence of extensional faults, stretching and gravitational instabilities in the crest of the anticline becomes substantially reduced when the model incorporates growth strata, and deformation is confined to the core of the structure leading to a tighter, narrower fold than in those situations in which growth strata is lacking.

3D data applications

This section contains two articles focussed on the determination of the kinematic evolution of folds and thrusts employing 3D data. **Tanner *et al.*** collected structural and stratigraphic data along the western Irish coast using high resolution GPS, constructed 3D geological surfaces and plotted the data onto a north–south vertical plane in order to obtain a balanced section parallel to the tectonic transport direction across the western Irish Namurian Basin. This basin is interpreted as a FAT belt developed in front of the northward propagating Variscan orogenic front in which folding predominates over thrusting. Subsequently, passive markers were included in the cross-section that was sequentially restored and decompacted to various Carboniferous syn-tectonic horizons. This allowed them to visualize variations in the folds' wavelength along the cross-section and to deduce how fold uplift evolved through time. Since accurate ages of the horizons are available, they were able to estimate folding- and thrusting-induced shortening rates and concluded that although the basin was subjected to comparatively very little shortening with respect to similar tectonic settings, the rates of orogenic shortening are within the typical ranges for FAT belts. They also found that the Western Irish Namurian Basin underwent an anomalous strong subsidence during its evolution. **Simón & Liesa** illustrate how construction of various geological sections through the Utrillas thrust sheet in the Iberian Chain, Spain, perpendicular and oblique to the frontal thrust trace, allows a 3D reconstruction of the geometry of the main thrust surface formed by ramps oriented in different directions. Detailed structural analysis and tectono-sedimentary relationships with the deposits of the adjacent foreland

and piggy-back Tertiary basins furnished data on the Eocene-Oligocene incremental motion history involving different tectonic transport directions. A schematic, plan-view retro-deformation of the distinctly oriented thrust ramps enabled estimation of the finite horizontal displacement along the thrust. The successive transport directions towards the ENE, NNE and north obtained are consistent with the development of two superposed main sets of folds and with the evolution of the intraplate stress fields through Tertiary times.

Tectonic and magnetic fabrics

This section deals with the information supplied by the magnetic fabrics to decipher the tectonic evolution of structures. **Antolín *et al.*** combined the anisotropy of magnetic susceptibility and structural analysis of a Triassic flysch to decipher the tectonic evolution of the Tethyan Himalaya FAT belt, Tibet. These authors defined a southern domain characterized by a magnetic foliation parallel to the first tectonic foliation in accordance with the south vergence of the belt, and a northern domain in which the magnetic foliation and the second tectonic foliation show a vergence opposite to that of the Himalayan system. Both domains are separated by a zone where both tectonic foliations coexist and where an intermediate magnetic fabric is developed. The magnetic lineation supplied information on the north-south transport direction of the thrust sheets. The different orientation of the magnetic foliations suggest a Middle Miocene clockwise rotation around a vertical axis which could be explained as a result of large-scale dextral shearing caused by eastward extrusion of the Tibetan Plateau or block rotations due to intrusion and exhumation of the North Himalayan domes.

Thrust wedges

The two articles in this section discuss the structural style and evolution of thrust wedges in various American FAT belts. The geological map and sections across the eastern Fuegian Andes FAT belt, Argentina, constructed by **Torres-Carbonell *et al.*** reveal that the structure of this region consists of various thrusts and backthrusts rooted at the base of the Cretaceous and within the Paleocene rocks. The occurrence of syn-tectonic sequences bounded by unconformities allowed them to perform a sequential cross-section restoration, decipher the kinematic evolution and timing of structural development and unravel the behaviour of the Coulomb wedge from Eocene to Oligocene times. The oldest stage was characterized by propagation of the basal detachment and formation of foreland-directed thrusts leading to a taper angle decrease.

During the subsequent period, corresponding to a subcritical Coulomb wedge stage, backthrusting accommodated significant shortening. The last period consisted of a new critical stage caused by renewed foreland-directed thrusting at the wedge front. **Fitz-Diaz *et al.*** compare the structural style of one traverse across the southern Canadian Rocky Mountains with another one across the Mexican FAT belt. Although the age of deformation, the overall structural pattern and the total amount of shortening are similar, the dominant tectonic style consists of imbricate thrust sheets with relatively little internal deformation in the former and individual thrust sheets with much more internal deformation, such as buckle folds, in the latter. One of the reasons for the differences in tectonic style is the facies distribution; massive platform limestone separated by thinly-bedded basinal limestone in the Mexico section, so that strain is concentrated toward the margins between platforms and basins, and thick platform carbonates forming continuous resistant units in Canada. Other possible reasons for the differences in tectonic style between the two sections include the taper angle of the tectonic wedges and the amount of friction along the basal detachment.

Structural evolution-case studies

The last section of this publication contains five articles that unravel the sequence of deformations in various belts located in Spain and in the Czech Republic. Based on field mapping and structural analysis of the Palaeozoic basement of the Central Pyrenees, France-Andorra-Spain, **García-Sansegundo *et al.*** propose a new division of this portion of the Variscan FAT belt into two different zones: non-metamorphic and metamorphic units, and a new sequence of Variscan deformations. The non-metamorphic units include thrust systems and related folds with a poorly developed cleavage, whereas in the metamorphic units two fold sets with axial plane cleavage and thrusts approximately coeval with the second fold generation occur. The structure of the Pyrenean non-metamorphic units has Variscan foreland affinities and is comparable to that of the Cantabrian Zone (foreland FAT belt of the Iberian Massif), whereas the deformation observed in the Pyrenean metamorphic units is characteristic of the Variscan hinterland and is consistent with the features of the West Asturian-Leonese Zone or Central-Iberian Zone. The relative position of the foreland and hinterland, with the non-metamorphic units located southwards of the metamorphic ones, and the south-directed motion of the Variscan thrusts, suggest that the Variscan Pyrenees may be equivalent to northern branch of the Ibero-Armorican or Asturian arc. Structural

analysis in the Palaeozoic rocks that constitute the Forcarei synform, located in the northwest part of the Iberian Variscan Massif, Spain, allowed **Fernández *et al.*** to conclude that two main Variscan deformation events occurred. The first event in this region caused a pervasive cleavage, a stretching lineation, the Forcarei Thrust and other related structures such as minor folds. The second event produced the large-scale Forcarei Synform and a sub-vertical crenulation cleavage parallel to its axial plane, an intersection lineation and minor folds which caused fold interference patterns with previous ones. The dominantly sinistral shear deduced from the analysis of quartz fabrics and kinematic indicators related to the first deformation is interpreted as a result of top-to-the-south displacement along the Forcarei Thrust combined with clockwise rotation along a sub-vertical axis evolving to dominant clockwise rotation in the last stages of thrust motion, subsequently folded into a synform during the second deformation event. **Mantero *et al.*** document two deformation phases in the Devonian and Carboniferous rocks of the Puebla de Guzmán antiform located in the Iberian Pyrite Belt in the south part of the Iberian Variscan Massif, Spain, which could be the result of a progressive deformation related to the growth of the South Portuguese Zone orogenic wedge. The first deformation phase gave rise to a widespread penetrative cleavage linked to thrusts at deep crustal levels and folds above them. The second deformation phase consists of thrusts, which constitute the most pronounced cartographic-scale structures, and two fold sets with axial plane crenulation cleavages. Despite the widespread presence of folds, the enveloping surfaces of bedding are sub-horizontal, and steep or overturned dips are restricted to the vicinity of frontal or lateral thrust ramps due to fault-propagation folds. The thrust displacement is distributed into a large number of thrusts and the important thickening produced in this region is due to thrust sheet stacking. Geological mapping, cross-section construction, structural analysis, and sedimentological and biostratigraphical data of Upper Devonian and Lower Carboniferous rocks allowed **Rez *et al.*** to establish a new Variscan sequence of deformations for the southern part of the Moravian Karst (Bohemian Massif, Czech Republic). Both deformation events involved northeast-directed thrusting suggesting progressive deformation during a constant stress orientation. The first event consisted of 'thin-skinned' thrusting and related folding and caused tectonic juxtaposition of two distinct facies of coeval sequences. The second deformational event led to 'thick-skinned' thrusting, which involved the crystalline rocks of the Brno Massif and cross-cut first phase thrusts, and folding of previous structures. Later

normal and strike-slip faults of probable Alpine age were responsible for the compartmentalization of the region into numerous small-scale blocks. **Poul *et al.*** present a new model for the controversial isolated ridges made up of Upper Jurassic limestones that constitute the Pavlov Hills located in the Outer Western Carpathians, Czech Republic. These uplands have been interpreted in the past as relicts of island ridges, exotic bodies derived from the basement, klippen, olistoliths and blocks bounded by faults. However, according to their new model based on geological mapping and geological interpretation of seismic lines, the present-day geometry and position of these ridges resulted from fault-bend folds related to antiformal stacks detached at the base of the Upper Jurassic limestones, subsequently offset by strike-slip faults sub-perpendicular to the thrusts trace. Unlike previous models for this region, this new interpretation including northwest-directed thrusts with flats and ramps is consistent with the structural style described for the Outer Western Carpathians.

Concluding remarks

If progress is to be made in the understanding of the evolution and styles of FAT belts, from small-scale to lithosphere-scale sections, and from both the pure scientific and applied points of view, detailed multi-disciplinary studies are required. These studies will need to integrate information from structural geology, stratigraphy-sedimentology, petrology, geochronology, geomorphology and geophysics, and take maximum advantage of all the new data that are being acquired by recently developed technologies. Accurate analyses of many aspects of individual fold-and-thrust structures located in different FAT belts, such as their 2D and 3D geometry, strain and fracture patterns, formation mechanisms and history (timing, uplift and shortening magnitudes and rates), have been carried out in recent times employing field and/or subsurface data, experimental and/or numerical models. If integrated into large-scale models of each FAT belt, these separate data collected in different parts of the belt would have an extraordinary impact on the understanding of the mechanisms responsible for the origin and evolution of these regions.

Due perhaps to interest from the economical point of view and the abundance of data derived, it seems that whilst the FAT belts located in external zones of cordilleras are relatively well studied, the FAT belts in interior parts of orogens have received less attention and require more detailed research on the more complex structures found therein, on the degree of basement involvement in the structures, on the control exerted by pre-existing structures,

and on the structural and temporal relationships between the inner and outer portions of FAT belts. A great deal of research is being done in offshore FAT belts because, although they are inaccessible, seismic imaging is excellent especially with modern technology. However seismic data may provide an incomplete picture. For instance, the initial attempts to contrast measurements of extension and contraction in a particular submarine toe thrust belt yielded different figures. This suggests that deformation is accommodated by other mechanisms apart from structures displayed in the seismic data. Existing kinematic algorithms for fold-thrust systems are not able to consider this, and therefore, they are likely to yield poor predictions of subseismic deformation and fault zone architecture. This means that current models need to incorporate the strain undergone by rocks amongst other parameters. Much less research is carried out in many onshore FAT belts because they are developed in severe terrains, the structures are complex and the subsurface data are poor in quality and/or quantity. This is the reason why understanding them has been strongly guided by geometrical models, fed by surface geological maps and sparse subsurface data, and which, in some cases, involve an important level of uncertainty rarely addressed in modern studies. Nowadays, since many geometrical models have been developed to predict the subsurface and 3D features of the structures, it would be essential to test them on well-known natural and experimental structures in which the complete geometry of the structure are available; this would permit magnitudes of errors in the structural interpretations to be quantified and would guide future improvements of these models. In addition, onshore FAT belts have to be revisited and detailed work carried out in order to revise the old interpretations in the light of the new concepts which, in turn, will provide additional conceptual and numerical models for this type of regions.

Contrasting the insights gained from analyzing active FAT belts, in which the structures are relatively well preserved and processes can be observed and quantified with a certain degree of confidence, with those gained from examining exhumed belts would contribute substantially to better constraint the 4D evolution of these regions. For instance, in recent years, the role of surficial processes has been emphasized in several studies on the evolution of FAT belts. The impact of erosion and sedimentation in controlling geomorphology, fold-thrust growth, exhumation processes and deformation history has been explored through numerical and experimental methods. More data, such as uplift estimates, and so on, collected in different FAT belts are needed to further elucidate the interactions

between the tectonic processes responsible for mountain building and climate-dependant surface processes on various time and space scales to maintain the dynamic equilibrium of orogenic wedges.

3D seismic data and precise analyses of folds and thrusts show that even simple structures are often far more complex than expected. For instance, many FAT belts exhibit faulted folds not well described by current theories; while some sections across individual structures may conform to proposed theories, the structures can exhibit rapid changes in 3D leading to a variety of complex fold-thrust architectures along strike. The capabilities of end-member fold-thrust interaction models, especially those embedded within many structural analysis software packages, are relatively restricted because they assume that deformation mainly causes displacement along faults and fold amplification. The models do not entertain other type of behaviours. However, discrete element modelling is beginning to allow us to build geologically realistic models. Geomechanics has to be the next step in structural geology research, to provide the additional constraints that geometry and kinematics do not, and needs to be applied at all scales, from small-scale deformational features to entire FAT belts. The last decades have seen a proliferation of quantitative approaches to studying FAT belts by means of geometrical, kinematical and some mechanical numerical modelling and physical experiments proving to be powerful tools for simulating the structural evolution of these belts. Although the present-day models of FAT belts have reached high levels of sophistication and are the subject of many present-day publications, detailed field and subsurface observations on FAT belts are still essential because natural examples based research is the ultimate test of the theoretical and physical models. We hope that this Special Publication will serve as a reference on future research and understanding of both the spatial and temporal evolution (4D) of FAT belts.

Comments by J. Turner substantially improved the initial version of this manuscript. We are indebted to the reviewers of the articles included in this Special Publication and of those manuscripts that, unfortunately, could not be part of this book. It was a pleasure to work with the efficient staff of the Geological Society of London, in particular A. Hills, T. Anderson and H. Floyd-Walker. Thanks to Carlos Olivares for reviewing the format of the manuscripts included in this publication and figure drafting, and Mayte Bulnes for critical reading of this manuscript and figure drafting. We acknowledge financial support by research grant CGL2008-03786/BTE (Mechanical analysis of deformation in folds) funded by the Spanish Ministry for Science and Innovation. J. Poblet is grateful to the Consolider programme project CSD2006-0041 (Topo-Iberia).

Referenes

- ALLÈGRE, C. J. 2008. *Isotope Geology*. Cambridge University Press, Cambridge.
- ALLMENDINGER, R. W., RAMOS, V. A., JORDAN, T. E., PALMA, M. & ISACKS, B. L. 1983. Paleogeography and Andean structural geometry, northwest Argentina. *Tectonics*, **2**, 1–16.
- ANTOLÍN, B., ERWIN, A., CHIARA, M., DUNKL, I., DING, L., GLOAGUEN, R. & EL BAY, R. 2011. Kinematic evolution of the eastern Tethyan Himalaya: constraints from magnetic fabric and structural properties of the Triassic flysch in SE Tibet. In: POBLET, J. & LISLE, R. J. (eds) *Kinematic Evolution and Structural Styles of Fold-and-Thrust Belts*. Geological Society, London, Special Publications, **349**, 99–121.
- BALLY, A. W., GORDY, P. L. & STEWART, G. A. 1966. Structure, seismic data, and orogenic evolution of southern Canadian Rocky Mountains. *Bulletin of Canadian Petroleum Geology*, **14**, 337–381.
- BEAUMONT, C., FULLSACK, P. & HAMILTON, J. 1992. Erosional control of active compressional orogens. In: MCCLAY, K. R. (ed.) *Thrust Tectonics*. Chapman & Hall, London, 377–390.
- BERG, R. R. 1962. Mountain flank thrusting in Rocky Mountain foreland, Wyoming and Colorado. *American Association of Petroleum Geologists Bulletin*, **46**, 2019–2032.
- BLACKSTONE, D. L. 1983. Laramide compressional tectonics, southern Wyoming. *University of Wyoming Contributions to Geology*, **19**, 105–122.
- BULL, W. B. 2007. *Tectonic Geomorphology of Mountains. A New Approach to Paleoseismology*. Blackwell Publishing, Oxford.
- BUSK, H. G. 1929. *Earth Flexures*. Cambridge University Press, London.
- BUTLER, R. W. H. 1982. The terminology of structures in thrust belts. *Journal of Structural Geology*, **4**, 239–245.
- CASEY MOORE, J. & SILVER, E. A. 1987. Continental margin tectonics: submarine accretionary prisms. *Reviews of Geophysics*, **25**, 1305–1312.
- COBBOLD, P. R., SZATMARI, P., DEMERCIAN, L. S., COELHO, D. & ROSSELLO, E. A. 1995. Seismic and experimental evidence for thin-skinned horizontal shortening by convergent radial gliding on evaporites, deep-water Santos Basin, Brazil. In: JACKSON, M. P. A., ROBERTS, D. G. & SNELSON, S. (eds) *Salt Tectonics: A Global Perspective*. American Association of Petroleum Geologists Memoir, **65**, 305–321.
- COOPER, M. 2007. Structural style and hydrocarbon prospectivity in fold and thrust belts: a global review. In: RIES, A. C., BUTLER, R. W. H. & GRAHAM, R. H. (eds) *Deformation of the Continental Crust: the Legacy of Mike Coward*. Geological Society, London, Special Publications, **272**, 447–472.
- COWARD, M. P. 1983. Thrust tectonics, thin-skinned or thick-skinned and the continuation of thrusts to deep in the crust. *Journal of Structural Geology*, **5**, 113–125.
- CHAMBERLIN, R. T. 1910. The appalachian folds of central Pennsylvania. *Journal of Geology*, **18**, 228–251.
- DAHLEN, F. A., SUPPE, J. & DAVIS, D. 1984. Mechanics of fold-and-thrust belts and accretionary wedges – cohesive Coulomb theory. *Journal of Geophysical Research*, **89**, 87–101.
- DAHLSTROM, C. D. A. 1969. Balanced cross sections. *Canadian Journal of Earth Sciences*, **6**, 743–757.
- DAVIS, D., SUPPE, J. & DAHLEN, F. A. 1983. Mechanics of fold/thrust belts and accretionary wedges. *Journal of Geophysical Research*, **88**, 1153–1172.
- DEMERCIAN, S., SZATMARI, P. & COBBOLD, P. R. 1993. Style and pattern of salt diapirs due to thin-skinned gravitational gliding, Campos and Santos basins, offshore Brazil. *Tectonophysics*, **228**, 393–433.
- DI CROCE, J. 1995. *Eastern Venezuela Basin: sequence stratigraphy and structural evolution*. PhD thesis, Rice University, Houston.
- DUNAI, T. 2010. *Cosmogenic Nuclides*. Cambridge University Press, Cambridge.
- DURNEY, D. W. & RAMSAY, J. G. 1973. Incremental strains measured by syntectonic crystal growth. In: DEJONG, K. A. & SCHOLTEN, R. (eds) *Gravity and Tectonics*. Wiley, New York, 67–96.
- ELLIOTT, D. 1976. The energy balance and deformation mechanisms of thrust sheets. *Philosophical Transactions of the Royal Society of London A*, **283**, 289–312.
- ENGLAND, P. C. & THOMPSON, A. B. 1984. Pressure temperature time paths of regional metamorphism. 1. Heat-transfer during the evolution of regions of thickened continental-crust. *Journal of Petrology*, **25**, 894–928.
- FERNÁNDEZ, F. J., DÍAZ-GARCÍA, F. & MARQUINEZ, J. 2011. Kinematics of the Forcarei Synform (NW Iberian Variscan belt). In: POBLET, J. & LISLE, R. J. (eds) *Kinematic Evolution and Structural Styles of Fold-and-Thrust Belts*. Geological Society, London, Special Publications, **349**, 183–198.
- FERNÁNDEZ-VIEJO, G., GALLASTEGUI, J., PULGAR, J. A., GALLART, J. & MARCONI TEAM. in press. The MARCONI project: a seismic view into the eastern part of the Bay of Biscay. *Tectonophysics*, doi: 10.1016/j.tecto.2010.06.020.
- FITZ-DIAZ, E., HUDESTON, P. & TOLSON, G. 2011. Comparison of tectonic styles in the Mexican and Canadian Rocky Mountain Fold–Thrust Belt. In: POBLET, J. & LISLE, R. J. (eds) *Kinematic Evolution and Structural Styles of Fold-and-Thrust Belts*. Geological Society, London Special Publications, **349**, 149–166.
- FRY, N. 1979a. Random point distribution and strain measurement in rocks. *Tectonophysics*, **60**, 89–105.
- FRY, N. 1979b. Density distribution techniques and strained line length method for determination of finite strain. *Journal of Structural Geology*, **1**, 221–229.
- GARCÍA-SANSEGUNDO, J., POBLET, J., ALONSO, J. L. & CLARIANA, P. 2011. Hinterland-foreland zonation of the Variscan orogen in the Central Pyrenees: comparison with the northern part of the Iberian Variscan Massif. In: POBLET, J. & LISLE, R. J. (eds) *Kinematic Evolution and Structural Styles of Fold-and-Thrust Belts*. Geological Society, London, Special Publications, **349**, 167–182.
- GEISER, P. A. 1988. The role of kinematics in the reconstruction and analysis of geological cross sections in deformed terranes. In: MITRA, G. & WOJTAŁ, S. F. (eds) *Geometries and Mechanisms of Thrusting, With*

- Special Reference To the Appalachians*. Geological Society of America, Special Paper, **222**, 47–76.
- GWINN, V. E. 1964. Thin-skinned tectonics in the plateau and northwestern Valley and Ridge provinces of the Central Appalachians. *Bulletin of the Geological Society of America*, **75**, 863–900.
- HAMILTON, W. B. 1988. Laramide crustal shortening. In: SCHMIDT, C. J. & PERRY, W. J. JR. (eds) *Interaction of the Rocky Mountain Foreland and the Cordilleran Thrust Belt*. Geological Society of America Memoir, **171**, 27–39.
- HARDY, S. & POBLET, J. 1994. Geometric and numerical model of progressive limb rotation in detachment folds. *Geology*, **22**, 371–374.
- HART, B. S. 1999. Definition of subsurface stratigraphy, structure and rock properties from 3-D seismic data. *Earth Science Reviews*, **47**, 189–218.
- HATCHER, R. D. JR. 1995. *Structural Geology. Principles, Concepts and Problems*. Prentice Hall Inc., Englewood Cliffs, NJ.
- HAYWARD, A. B. & GRAHAM, R. H. 1989. Some geometrical characteristics of inversion. In: COOPER, M. A. & WILLIAMS, G. D. (eds) *Inversion Tectonics*. Geological Society, London, Special Publications, **44**, 17–39.
- HOBBS, B. E., MEANS, W. D. & WILLIAMS, P. F. 1976. *An Outline of Structural Geology*. John Wiley & Sons, Inc., New York.
- HUIQI, L., MCCLAY, K. R. & POWELL, D. 1992. Physical models of thrust wedges. In: MCCLAY, K. R. (ed.) *Thrust Tectonics*. Chapman & Hall, London, 71–81.
- JAMISON, W. R. 1987. Geometric analysis of fold development in overthrust terranes. *Journal of Structural Geology*, **9**, 207–219.
- JULIVERT, M. & ARBOLEYA, M. L. 1984. A geometrical and kinematical approach to the nappe structure in an arcuate fold belt: the Cantabrian nappes (Hercynian chain, NW Spain). *Journal of Structural Geology*, **6**, 499–519.
- KOOI, H. & BEAUMONT, C. 1996. Large-scale geomorphology: classical concepts reconciled and integrated with contemporary ideas via a surface processes model. *Journal of Geophysical Research-Solid Earth*, **101**, 3361–3386.
- LACOMBE, O., LAVÉ, J., ROURE, F. & VERGÉS, J. 2007. *Thrust Belts and Foreland Basins*. Springer, Berlin.
- LISKER, F., VENTURA, B. & GLASMACHER, U. A. 2009. *Thermochronological Methods: From Palaeotemperature Constraints to Landscape Evolution Models*. Geological Society, London, Special Publications, **324**.
- MACKAY, P. A. 1996. The Highwood Structure: a tectonic wedge at the foreland edge of the southern Canadian Cordillera. *Bulletin of Canadian Petroleum Geology*, **44**, 215–232.
- MACQUEEN, R. W. & LECKIE, D. A. 1992. *Foreland Basins and Fold Belts*. American Association of Petroleum Geologists Memoir, **55**.
- MANTERO, E. M., ALONSO-CHAVES, F. M., GARCÍA-NAVARRO, E. & AZOR, A. 2011. Tectonic style and structural analysis of the Puebla de Guzmán Antiform (Iberian Pyrite Belt, South Portuguese Zone, SW Spain). In: POBLET, J. & LISLE, R. J. (eds) *Kinematic Evolution and Structural Styles of Fold-and-Thrust Belts*. Geological Society, London, Special Publications, **349**, 199–218.
- MASINI, M., BIGI, S., POBLET, J., BULNES, M., DI CUIA, R. & CASABIANCA, D. 2011. Kinematic evolution and strain simulation, based on cross-section restoration, of the Maiella Mountain: an analogue for oil fields in the Apennines (Italy). In: POBLET, J. & LISLE, R. J. (eds) *Kinematic Evolution and Structural Styles of Fold-and-Thrust Belts*. Geological Society, London, Special Publications, **349**, 25–44.
- MEANS, W. D. 1976. *Stress and Strain*. Springer-Verlag, New York.
- MEDD, D. M. 1996. Recent triangle zone deformation in Papua New Guinea. *Bulletin of Canadian Petroleum Geology*, **44**, 400–409.
- MCCLAY, K. R. 1992a. *Thrust Tectonics*. Chapman & Hall, London.
- MCCLAY, K. R. 1992b. Glossary of thrust tectonics terms. In: MCCLAY, K. R. (ed.) *Thrust Tectonics*. Chapman & Hall, London, 419–433.
- MCCLAY, K. R. 1994. *Thrust Tectonics and Hydrocarbon Systems*. American Association of Petroleum Geologists Memoir, **82**, Tulsa.
- MCCLAY, K. R. & PRICE, N. J. 1981. *Thrust and Nappe Tectonics*. Geological Society, London, Special Publications, **9**.
- MCCLAY, K., DOOLEY, T., FERGUSON, A. & POBLET, J. 2000. Tectonic evolution of the Sanga Sanga Block, Mahakam delta, Kalimantan, Indonesia. *American Association of Petroleum Geologists Bulletin*, **84**, 765–786.
- MINGRAMM, A., RUSSO, A., POZZO, A. & CAZAU, L. 1979. Sierras Subandinas. *II Simposio de Geología Regional Argentina, Córdoba (Argentina)*, **1**, 95–138.
- MITRA, G. 1997. Evolution of salients in a fold-and-thrust belt: the effects of sedimentary basin geometry, strain distribution and critical taper. In: SENGUPTA, S. (ed.) *Evolution of Geological Structures in Micro- to Macro-Scales*. Chapman & Hall, London, 59–90.
- MITRA, S. 1988. Effects of deformation mechanisms on reservoir potential in Central Appalachian overthrust belt. *American Association of Petroleum Geologists Bulletin*, **72**, 536–554.
- MITRA, S. 1990. Fault-propagation folds: geometry, kinematics and hydrocarbon traps. *American Association of Petroleum Geologists Bulletin*, **74**, 921–945.
- MITRA, S. & FISHER, G. W. 1992. *Structural Geology of Folds and Thrust Belts*. John Hopkins University Press, Baltimore.
- MITRA, S. & NAMSON, J. 1989. Equal area balancing. *American Journal of Science*, **289**, 563–599.
- MORGAN, J. K. & KARIG, D. E. 1995. Kinematics and a balanced and restored cross-section across the toe of the eastern Nankai accretionary prism. *Journal of Structural Geology*, **17**, 31–45.
- MUÑOZ, J. A. 1992. Evolution of a continental collision belt: ECORS-Pyrenees crustal balanced cross-section. In: MCCLAY, K. R. (ed.) *Thrust Tectonics*. Chapman & Hall, London, 235–246.
- MUÑOZ, J. A., MCCLAY, K. & POBLET, J. 1994. Synchronous extension and contraction in frontal thrust sheets of the Spanish Pyrenees. *Geology*, **22**, 921–924.
- NEMCOK, M., SCHAMEL, S. & GAYER, R. 2005. *Thrust-belts. Structural Architecture, Thermal Regimes and*

- Petroleum Systems*. Cambridge University Press, Cambridge.
- PÉREZ-ESTAÚN, A., BASTIDA, F. ET AL. 1988. A thin-skinned tectonics model for an arcuate fold and thrust belt: the Cantabrian Zone (Variscan Ibero-Armorican Arc). *Tectonics*, **7**, 517–537.
- PERRY, W. J. JR. 1978. Sequential deformation in the Central Appalachians. *American Journal of Science*, **278**, 518–542.
- PRICE, R. A. 1981. The Cordilleran foreland thrust and fold belt in the southern Canadian Rocky Mountains. In: McCAY, K. R. & PRICE, N. J. (eds) *Thrust and Nappe Tectonics*. Geological Society, London, Special Publications, **9**, 427–448.
- POUL, I., MELICHAR, R. & JANECKA, J. 2011. Thrust tectonics of the Upper Jurassic limestones in the Pavlov Hills (Outer Western Carpathians, Czech Republic). In: POBLET, J. & LISLE, R. J. (eds) *Kinematic Evolution and Structural Styles of Fold-and-Thrust Belts*. Geological Society, London, Special Publications, **349**, 233–244.
- PRUCHA, J. J., GRAHAM, J. A. & NICKELSEN, R. P. 1965. Basement-controlled deformation in Wyoming Province of Rocky Mountains Foreland. *American Association of Petroleum Geologists Bulletin*, **49**, 966–992.
- RAMSAY, J. G. 1967. *Folding and Fracturing of Rocks*. McGraw-Hill, New York.
- REZ, J., MELICHAR, R. & KALVODA, J. 2011. Polyphase deformation of the Variscan accretionary wedge: an example from the southern part of the Moravian Karst (Bohemian Massif, Czech Republic). In: POBLET, J. & LISLE, R. J. (eds) *Kinematic Evolution and Structural Styles of Fold-and-Thrust Belts*. Geological Society, London, Special Publications, **349**, 219–231.
- RIBA, O. 1976. Syntectonic unconformities of the Alto Cardener, Spanish Pyrenees: a genetic interpretation. *Sedimentary Geology*, **15**, 213–233.
- RICH, J. L. 1934. Mechanics of low-angle overthrust faulting as illustrated by Cumberland thrust block, Virginia, Kentucky, and Tennessee. *American Association of Petroleum Geologists Bulletin*, **18**, 1584–1596.
- ROYDEN, L. H. 1993. The tectonic expression slab pull at continental convergent boundaries. *Tectonics*, **12**, 303–325.
- SCHMIDT, C. J., CHASE, R. B. & ERSLEV, E. A. 1993. *Laramide Basement Deformation in the Rocky Mountain Foreland of the Western United States*. Special Paper Geological Society of America, **280**, Boulder.
- SIMÓN, J. L. & LIESA, C. L. 2011. Incremental slip history of a thrust: diverse transport directions and internal folding of the Utrillas thrust sheet (NE Iberian Chain, Spain). In: POBLET, J. & LISLE, R. J. (eds) *Kinematic Evolution and Structural Styles of Fold-and-Thrust Belts*. Geological Society, London, Special Publications, **349**, 77–97.
- SMITH, B. & GEORGE, T. N. 1961. *British Regional Geology, North Wales*. Institute of Geological Science, London.
- SMITH, J. G. 1965. Orogenesis in western Papua and New Guinea. *Tectonophysics*, **2**, 1–27.
- SPEAR, F. S. & SILVERSTONE, J. 1983. Quantitative p–t paths from zoned minerals – theory and tectonic applications. *Contributions to Mineralogy and Petrology*, **83**, 348–357.
- STEARNS, D. W. 1971. Mechanisms of drape folding in the Wyoming province. *Wyoming Geological Association 23rd Annual Field Conference Guidebook*, 125–144.
- SUPPE, J. 1983. Geometry and kinematics of fault-bend folding. *American Journal of Science*, **283**, 684–721.
- SUPPE, J. 1985. *Principles of Structural Geology*. Prentice-Hall, Englewood Cliffs, NJ.
- SUPPE, J. & MEDWEDEFF, D. A. 1990. Geometry and kinematics of fault propagation folding. *Eclogae Geologicae Helveticae*, **83**, 409–454.
- SUPPE, J., CHOU, G. T. & HOOK, S. C. 1992. Rates of folding and faulting determined from growth strata. In: McCAY, K. R. (ed.) *Thrust Tectonics*. Chapman & Hall, London, 105–121.
- TANNER, D. C., BENSE, F. A. & ERTL, G. 2011. Kinematic retro-modelling of a cross-section through a thrust-and-fold belt: the Western Irish Namurian Basin. In: POBLET, J. & LISLE, R. J. (eds) *Kinematic Evolution and Structural Styles of Fold-and-Thrust Belts*. Geological Society, London, Special Publications, **349**, 61–76.
- THOMPSON, A. B. & ENGLAND, P. C. 1984. Pressure temperature time paths of regional metamorphism. 2. Their inference and interpretation using mineral assemblages in metamorphic rocks. *Journal of Petrology*, **25**, 929–955.
- TORRES-CARBONELL, P. J., DIMIERI, L. V. & OLIVERO, E. B. 2011. Progressive deformation of a Coulomb thrust-wedge: the eastern Fugian Andes Thrust-Fold Belt. In: POBLET, J. & LISLE, R. J. (eds) *Kinematic Evolution and Structural Styles of Fold-and-Thrust Belts*. Geological Society, London, Special Publications, **349**, 123–147.
- TWISS, R. J. & MOORES, E. M. 1992. *Structural Geology*. W. H. Freeman & Company, New York.
- ULIANA, M. A., ARTEAGA, M. E., LEGARRETA, L., CERDÁN, J. J. & PERONI, G. O. 1995. Inversion structures and hydrocarbon occurrence in Argentina. In: BUCHANAN, J. G. & BUCHANAN, P. G. (eds) *Basin Inversion*. Geological Society, London, Special Publications, **88**, 211–233.
- VANCE, D. & MÜLLER, W. 2003. *Geochronology: Linking the Isotopic Record With Petrology and Textures*. Geological Society, London, Special Publications, **220**.
- VIDAL-ROYO, O., HARDY, S. & MUÑOZ, J. A. 2011. The roles of complex mechanical stratigraphy and syn-kinematic sedimentation in fold development: insights from discrete-element modelling and application to the Pico del Águila anticline (External Sierras, Southern Pyrenees). In: POBLET, J. & LISLE, R. J. (eds) *Kinematic Evolution and Structural Styles of Fold-and-Thrust Belts*. Geological Society, London, Special Publications, **349**, 45–59.
- VON HUENE, R. & SCHOLL, D. W. 1991. Observations at convergent margins concerning sediment subduction, subduction erosion, and the growth of continental crust. *Reviews of Geophysics*, **29**, 279–316.

- VON HUENE, R., RANERO, C. R. & VANNUCCHI, P. 2004. Generic model of subduction erosion. *Geology*, **32**, 913–916.
- WESTBROOK, G. K., LADD, J. W., BUHL, P., BANGS, N. & TILLEY, G. J. 1988. Cross section of an accretionary wedge: Barbados Ridge complex. *Geology*, **16**, 631–635.
- WHEELER, J. O., AITKEN, J. D. ET AL. 1972. The Cordilleran structural province. In: PRICE, R. A. & DOUGLAS, R. J. W. (eds) *Variations in Tectonic Styles in Canada*. Geological Association of Canada, Special Paper, **11**, 1–82.
- WORRALL, D. M. & SNELSON, S. 1989. Evolution of the northern Gulf of Mexico, with emphasis on Cenozoic growth faulting and the role of salt. In: BALLY, A. W. & PALMER, A. R. (eds) *The Geology of North America: an Overview*. Geological Society of America, Boulder, 97–138.

Kinematic evolution and strain simulation, based on cross-section restoration, of the Maiella Mountain: an analogue for oil fields in the Apennines (Italy)

MASSIMILIANO MASINI¹, SABINA BIGI^{2*}, JOSEP POBLET³, MAYTE BULNES³,
RAFFAELE DI CUIA⁴ & DAVIDE CASABIANCA^{5,6}

¹YPF S.A., Desarrollo Area Malargüe, UNAO, Av. España 955,
Mendoza 5500, Argentina

²Dipartimento di Scienze della Terra, Sapienza Università di Roma, P. le A Moro 5,
00183 Roma, Italy

³Departamento de Geología, Universidad de Oviedo, C/Jesús Arias de Velasco s/n,
33005 Oviedo, Spain

⁴G.E. Plan Consulting, Via Borgo dei Leoni 132, 44121 Ferrara (FE), Italy

⁵BP Exploration UK, Dyce, Aberdeen, AB21 7 PB, UK

⁶Present address: Marathon International Petroleum (GB) Ltd, Marathon House, Rubislaw Hill,
Anderson Drive, Aberdeen AB15 6FZ, UK

*Corresponding author (e-mail: sabina.bigi@uniroma1.it)

Abstract: Deformation predictive methods are useful for structural analysis from the scientific and industry point of view. We apply a strain simulation technique based on the inclusion of graphical strain markers in a cross-section, and subsequent cross-section restoration and numerical processing of strain markers, to the seismic-scale Maiella Mountain anticline (Central Apennines, Italy) considered a carbonate reservoir analogue for Apennines oil fields. The procedure followed involves field mapping and structural data collection, construction of cross-sections, sequential cross-section restoration, and application of the strain simulation technique. The cross-sections presented were constructed adopting one of the various structural interpretations proposed for this structure by different authors. According to this interpretation the Maiella Mountain structure resulted from Messinian–Early Pliocene extension and subsequent Late Pliocene shortening. According to our structural model the Maiella structure is a break-thrust fold and the comparison between the present-day and the restored cross-sections yields 1.3–4.6% of extension associated with two main normal faults and 21.5–22.1% and 2.5–3.4% of shortening due to a major thrust and folding respectively. The simulation of deformation distribution shows high deformation intensity in both limbs and low deformation in the anticline crest and part of the thrust footwall.

Deciphering the deformation undergone by rocks involved in tectonic structures has always received attention both from a theoretical and applied point of view. For instance, unravelling the amplification mechanisms that operated in a particular fold requires a profound knowledge of the strain all around the structure. In hydrocarbon exploration, the knowledge of the deformation history of geological bodies can help to understand migration and accumulation of oil and gas. Most methodologies developed to quantify strain employ strain markers recognizable directly in rocks (e.g. Ramsay 1967; Dunnet 1969; Fry 1979a, b; Ragan

1985), however, many predictive methods based on curvature analysis of folded surfaces, forward modelling, cross-section restoration, etc. have been developed in relatively recent times (e.g. Lisle 1994; Samson & Mallet 1997; Thorbjørnsen & Dunne 1997; Allmendinger 1998; Erickson *et al.* 2000; Hennings *et al.* 2000; Rouby *et al.* 2000; Roberts 2001; Bastida *et al.* 2003; Ormand & Hudleston 2003; Dunbar & Cook 2003; Allmendinger *et al.* 2004; Sanders *et al.* 2004; Moretti *et al.* 2007; Poblet & Bulnes 2007). These methods are able to predict strain in regions where directly measurable strain data are lacking. In many outcropping

structures, for example, strain markers are absent, poorly distributed or of insufficient quality; in other cases such as subsurface structures, data on deformation at sub-seismic scale are not accessible, or available only in scarce well-logs.

A strain simulation method, based on cross-section restoration techniques, has been recently proposed by Masini *et al.* (2010). The method consists of placing strain markers in the geological cross-section, subsequently restoring the section together with the strain markers, and finally obtaining strain ellipses for each strain marker through application of a mathematical model. The main parameters obtainable for each strain marker are the values and the orientation of the maximum and minimum elongation principal axes of the strain ellipse. By superimposing the simulated strain results on the structural cross-section it is possible to visualize the deformation distribution and the geological significance of the different deformation domains. Masini *et al.* (2010) analyzed a natural contractional structure, obtaining a good fit between the deformation architecture achieved

from this technique and the theoretical strain distribution for forward models of structures similar to the natural one.

In this paper we use the Masini *et al.* (2010) method to simulate the distribution of strain of the Maiella Mountain, a complex, kilometre-scale fault-related fold located in Central Apennines, Italy (Fig. 1). This structure involves Mesozoic and Tertiary marine carbonate sequences including a platform, its margin, and the associated pelagic deposits (Eberli *et al.* 1993; Lampert *et al.* 1997) (Fig. 2). It is considered an outcropping analogue for oil field reservoirs in the Apennines such as, for example, the one recently discovered offshore the Abruzzi region and the giant oil reservoirs located in Southern Italy (Mosca & Wavrek 2002; Shiner *et al.* 2004). The main features of the Maiella structure encouraged us to apply the deformation predictive method to this structure in order to test the validity of the method on a large-scale structure different from a fault-propagation fold and of economic interest since, up to now, the method has been only applied to an

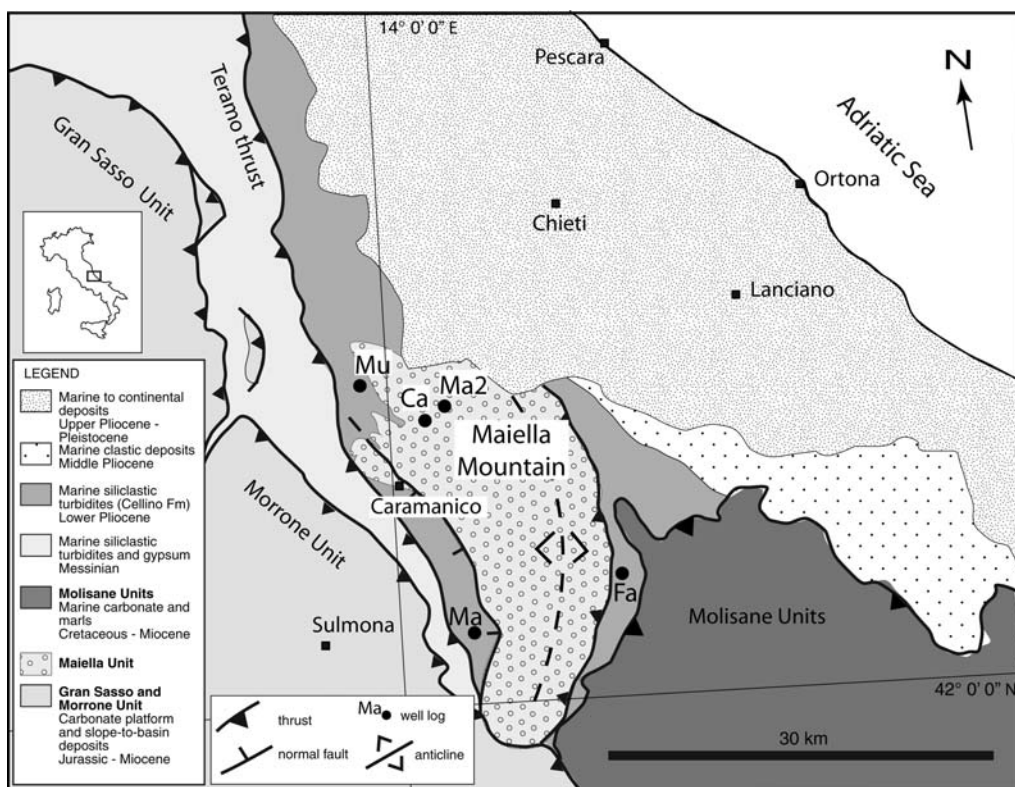


Fig. 1. Structural sketch of the eastern sector of central Apennines (Italy) showing the main tectonic units. Mu, Musella 1 well; Ca, Caramanico 1 well; Ma, Maiella 1 well; Ma2, Maiella 2 well; Fa, Fara 1 Well.

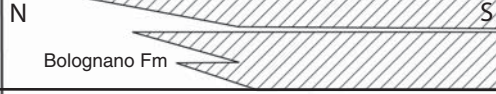



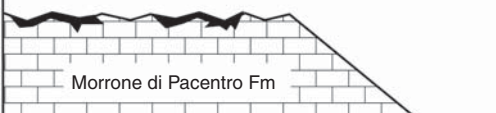
Age	MAIELLA STRATIGRAPHY	Depositional setting
Pliocene	Turrivalignani Fm	Sands, clays and conglomerates marine to continental shelf
	Argille Azzurre and Cellino Fm	Deep water muddy and sandy turbidites. Foredeep
Messinian	Gessoso Solifera Fm	Shallow water marginal marine evaporites
Miocene	N  S Bolognano Fm	Shallow marine shelf rudstones, grainstones, mudstones and marls. Carbonate ramp
	Oligocene	
Eocene	S.B.  S. Spirito Fm	Shallow marine shelf grainstones, mudstones and marls. Carbonate ramp
Paleocene		
Upper Cretaceous	S.B.  Orfento Fm (C) (PC)	Shallow marine shelf (PC) to deep water (C) rudstones, grainstones, mudstones and marls. Carbonate ramp
	S.B.  Cima delle Murelle Fm Tre Grotte Fm	Shallow marine platform boundstones (rudist biostromes), grainstones, wakestones to deep water rudstones (megabreccias), mudstones and marls. Carbonate platform to basin setting dissected by steep escarpment (faults)
	Valle dell'Inferno Fm	
Lower Cretaceous	 Morrone di Pacentro Fm	Shallow marine platform boundstones (rudist biostromes), grainstones, wakestones. At the top subareal bauxite deposits. Carbonate platform

Fig. 2. Chronostratigraphic scheme of the Maiella carbonate platform system from Lower Cretaceous–Pliocene.

outcropping metre-scale fault-propagation fold (Masini *et al.* 2010). In addition, the sections across the Maiella structure, their restorations and the deformation simulation will yield valuable information on the kinematic evolution of this debated structure.

The procedure adopted in this study consists of the following steps: (a) fieldwork mapping and collection of structural data of the Maiella Mountain structure; (b) construction of two geological cross-sections approximately perpendicular to the fold axis and parallel to the main tectonic transport direction; (c) restoration of the two geological cross-sections; (d) application of the deformation simulation technique; and (e) results, analysis and discussion.

Geological setting

The Maiella Mountain, located 40 km westwards of the Adriatic coast, is an *c.* 28 km long, 10–15 km wide, asymmetrical anticline with a gentle arc shape in map view (Fig. 1). This structure

exhibits a remarkable elevation above the sea level; the axial culmination corresponds to the Amaro Mount which is 2795 m high and is the second highest peak of the Apennines chain. To the north, the fold axial trace trends NW–SE, and bends in a NNE–SSW direction in the south. The fold axis plunges northwards in the northern part and southwards in the southern area (Patacca *et al.* 2008 and references therein). To the east, there is an east-directed thrust, approximately parallel to the major fold trace, formed in response to contractional Apennine deformation during the Pliocene. To the east and west bedding in the limbs of the anticline are offset by normal faults.

The Maiella structure is considered to be part of the northern edge of the Apulia Platform incorporated in the Apennines fold-and-thrust belt in Middle–Late Pliocene times. The stratigraphic succession in the area is constituted by Upper Triassic–Upper Miocene carbonates and Messinian evaporites (Gessoso Solifera Fm.) followed by Lower Pliocene siliciclastic turbiditic deposits (e.g. Donzelli 1969; Patacca *et al.* 1991 and references therein). The Upper Triassic–Upper Jurassic

portion of the succession is known only in the sub-surface (Musellaro 1, Caramanico 1 and Maiella 2 wells) (Figs 1 & 2).

In the central sector of the Maiella Mountain, a Barremian–Campanian (Cretaceous) platform-to-basin transition is exposed, whereas protected-platform carbonates crop out in the southern sector and coeval slope-to-basin deposits are present more to the north. The proximal basin in the north is separated from the external platform in the south by a steep non-depositional escarpment that dips *c.* 35° (Crescenti *et al.* 1969; Accarie 1988; Rusciadelli 2005). The slope-to-basin deposits progressively onlap this escarpment, and are characterized by re-cemented rudists grainstones and rudstones bodies (Stossel & Bernoulli 2000). Both platform and slope-to-basin deposits are overlain by Upper Cretaceous–Tertiary carbonate ramp deposits displaying proximal facies in the southern area and distal facies in the northern zones (Figs 2 & 3).

The sedimentary sequences and the stratigraphic evolution of the Maiella carbonate deposits are well-known due to biostratigraphic and sedimentological studies (e.g. Vecsei 1991; Eberli *et al.* 1993; Bernoulli *et al.* 1996; Vecsei & Sanders 1997, 1999; Vecsei *et al.* 1998; Casabianca *et al.* 2002; Morsilli *et al.* 2002; Rusciadelli 2005). The platform-basin differentiation occurred in Early Jurassic times in response to extensional tectonics widespread in the whole Central Mediterranean region. In the Musellaro 1 and Caramanico 1 wells (Fig. 1), Middle–Upper Liassic basinal deposits have been drilled; in the Caramanico 1 well these basinal deposits stratigraphically overlie shallow-water dolomites and limestones of Early Liassic and Late Triassic ages (Patacca *et al.* 2008 and references therein).

In the last decades, research projects in the Maiella Mountain area (e.g. Task Force Maiella Project (ENI), Crop 11 in Scrocca *et al.* 2003) have led to different interpretations of the structural style

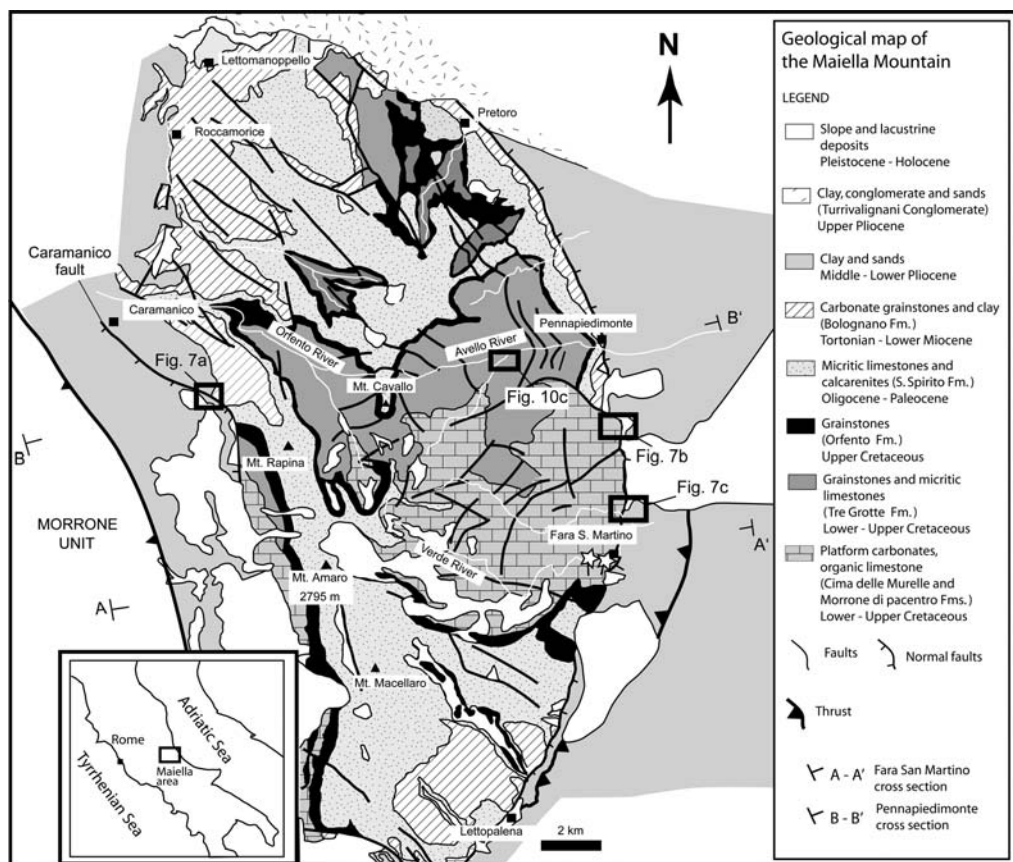


Fig. 3. Simplified geological map of the Maiella region with location of the two section lines corresponding to the geological cross-sections illustrated in Figures 5, 8, 9 and 11.

and tectonic evolution the Maiella Mountain (Fig. 4), based on stratigraphic and structural field data and on geological interpretations of available seismic lines (Scisciani *et al.* 2000a; Ghisetti &

Vezzani 2002; Casero 2004; Tavarnelli *et al.* 2004; Patacca *et al.* 2008).

The thin-skinned model for the Maiella Mountain, described in detail in Patacca *et al.* (2008)

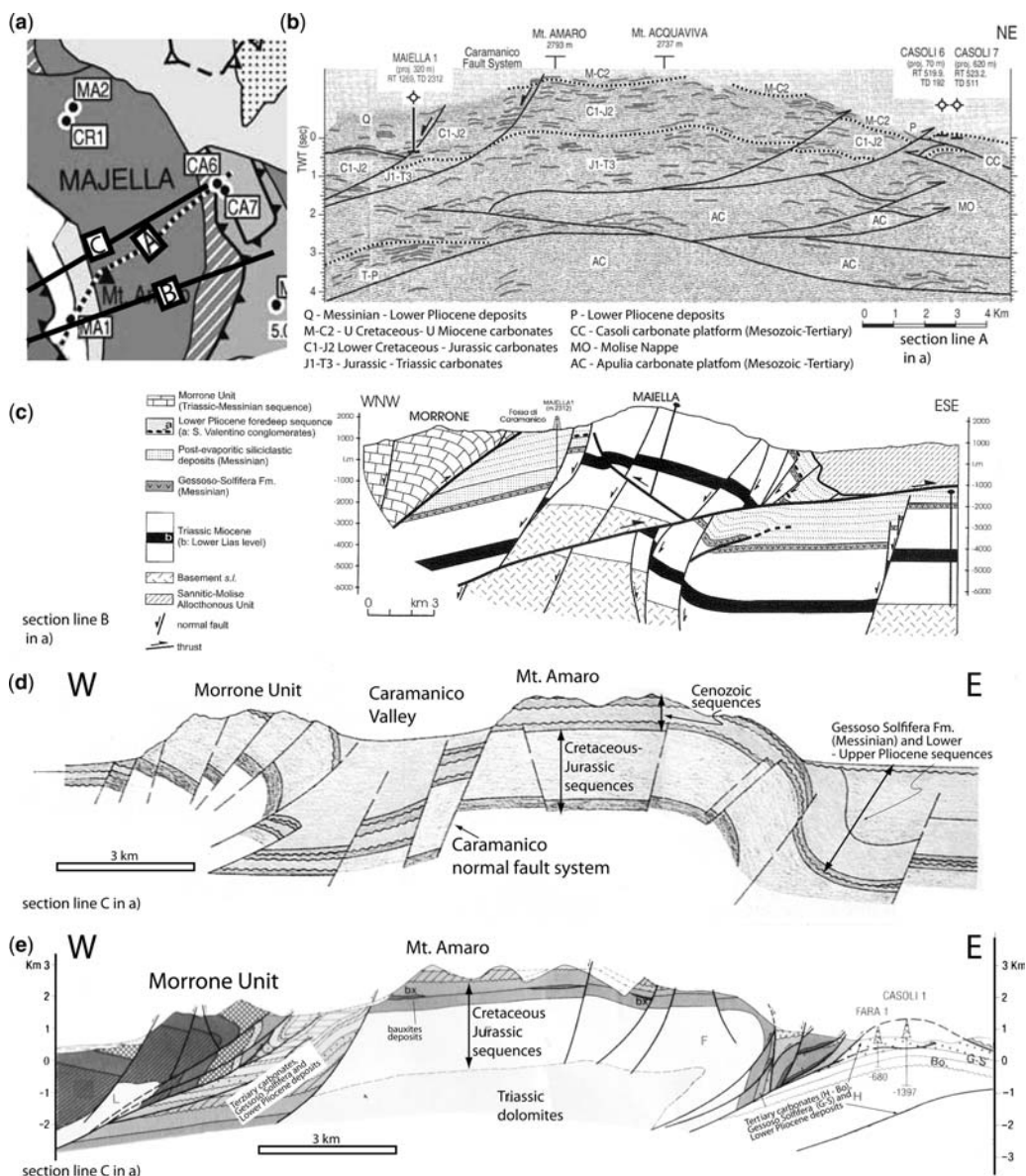


Fig. 4. Comparison among representative different published interpretations proposed from the late sixties up to now for the Maiella Mountain. This structure has been interpreted following two main models: a thin-skinned model in which thrusts detach at the Triassic rocks (b and e), and a thick-skinned model in which basement rocks are involved in the folded and thrust structure (c and d). Geological cross-sections from: (b) Patacca *et al.* (2008) modified, (c) Scisciani *et al.* (2000a) modified, (d) Donzelli (1969) modified and (e) Vezzani & Ghisetti (1998) modified. The section lines are located in the simplified geological map shown in (a). MA1, Maiella 1 well; MA2, Maiella 2 well; CR1, Caramanico 1 well; CA6, Casoli 6 well; CA7, Casoli 7 well.

(Fig. 4b), was already proposed for the Apennines (Bally *et al.* 1986; Mostardini & Merlini 1986; Patacca & Scandone 2004). Mostardini & Merlini (1986) considered the Maiella Massif to be the upper tectonic unit of an antiformal stack detached on Triassic evaporites. According to Patacca *et al.* (1991), the Maiella anticline is the upper horse of a huge duplex-like structure whose roof thrust is the basal detachment of the rootless Molise Allochthonous nappes, built up in the time span between the end of early Pliocene and the late Pliocene. Patacca *et al.* (2008) proposed that the Maiella anticline detachment was located below the Triassic dolomite and evaporitic beds, and lies within the Permo-Triassic terrigenous sequence found in the Puglia 1 and Gargano 1 deep wells, located more in the south in the Apulia Domain.

The thick-skinned model for the Maiella Mountain assumes that both the crystalline basement and the Permo-Triassic and younger rocks that belong to the cover are involved in the compressional deformation (Fig. 4d, e). In this model, the formation of the Maiella anticline resulted from a main thrust that cut through and offset a Late Miocene–Early Pliocene structural high, bounded by first-order normal faults linked to the foredeep development and penetrating into the crystalline basement (Donzelli 1969; Scisciani *et al.* 2000a). Such a structure would have experienced a modest horizontal displacement during Middle–Late Pliocene compression. Partial, or even severe, deformation of the basement was already postulated for the Northern Apennines (Barchi 1991; Lavecchia *et al.* 1994; Barchi *et al.* 1998; Coward *et al.* 1999) and for the Southern Apennines (Casero *et al.* 1988; Endignoux *et al.* 1989; Mazzoli *et al.* 2000; Menardi Noguera & Rea 2000; Speranza & Chiappini 2002).

Regarding the relative age of the normal faults and the anticline that crop out in the Maiella Mountain, basically two different interpretations have been proposed. Ghisetti & Vezzani (2002), Patacca *et al.* (2008) and many others support a late to post-folding age of the normal fault system, whereas according to Scisciani *et al.* (2000a, 2002) and others the normal faults show evidences of an intense activity before the contractional events responsible for the fold development.

Both the structural model for the Maiella Mountain and the age of the normal faults are discussed below.

Large-scale structure of the Maiella Mountain

A geological map (Fig. 3) and two WSW–ENE cross-sections, approximately perpendicular to the

Maiella anticline axis and parallel to the main tectonic transport direction (Fig. 5), have been constructed to characterize the main structural features of the Maiella Mountain, to unravel its kinematic evolution and to describe the distribution of deformation along the structure. The selected cross-sections run along river valleys, with relatively constant directions, cut through the mountain, and provide good exposition and accessibility to the outcrops. One cross-section line is located close to Fara San Martino town, in the southern sector of the Maiella Mountain, along the Verde River valley (Figs 3 & 5a). The internal platform sequences that crop out along this valley are made up predominantly of mudstones/grainstones with peritidal cycles (Morrone di Pacentro and Cima delle Murelle Fms) (Vecsei *et al.* 1998; Stossel & Bernoulli 2000; Patacca *et al.* 2008). The other cross-section line is close to Pennapedimonte town and runs across the main anticline in its central area along the Avello River valley (Figs 3 & 5b). This cross-section has been previously studied because of the continuity and quality of the outcrops where the slope-to-basin sequences are exposed (Antonellini *et al.* 2008 and references therein). These sequences comprise cross-bedded bioclastic grainstones and pelagic mudstones with resedimented calciturbidites and breccias (Valle dell'Inferno, Tre Grotte, Orfento and S. Spirito Fms.).

The cross-sections illustrated in Figure 5 integrate the surface stratigraphic and structural data we collected in the field, partly displayed on the simplified geological map in Figure 3; these data were contrasted with the data shown in the geological map of this region by Vezzani & Ghisetti (1998). The available subsurface data included in the cross-sections consists of the Maiella 1 well (2313 m) projected onto the western part of the cross-sections, and the Casoli 6 (192 m) and Casoli 7 (511 m) wells projected onto the eastern part of the cross-sections (Fig. 4a) (Vezzani & Ghisetti 1998). The geological interpretations of both confidential and published seismic lines across the area (Fig. 4b) (e.g. Scisciani *et al.* 2000a; Patacca *et al.* 2008) provided additional constraints on the geometry of beds and structures and the detachment depth. The two geological cross-sections constructed have been simplified, so that only the major structures are depicted, to facilitate the application of the strain simulation method and the subsequent interpretation of the results.

According to our interpretation, the macro-structure of this area consists of a slightly asymmetrical, east-vergent anticline with a double anticlinal hinge and an approximate box shape, and an east-directed thrust that dips moderately to the west (Fig. 5). The anticline is an approximately parallel fold whose west limb (backlimb) dips around 20°

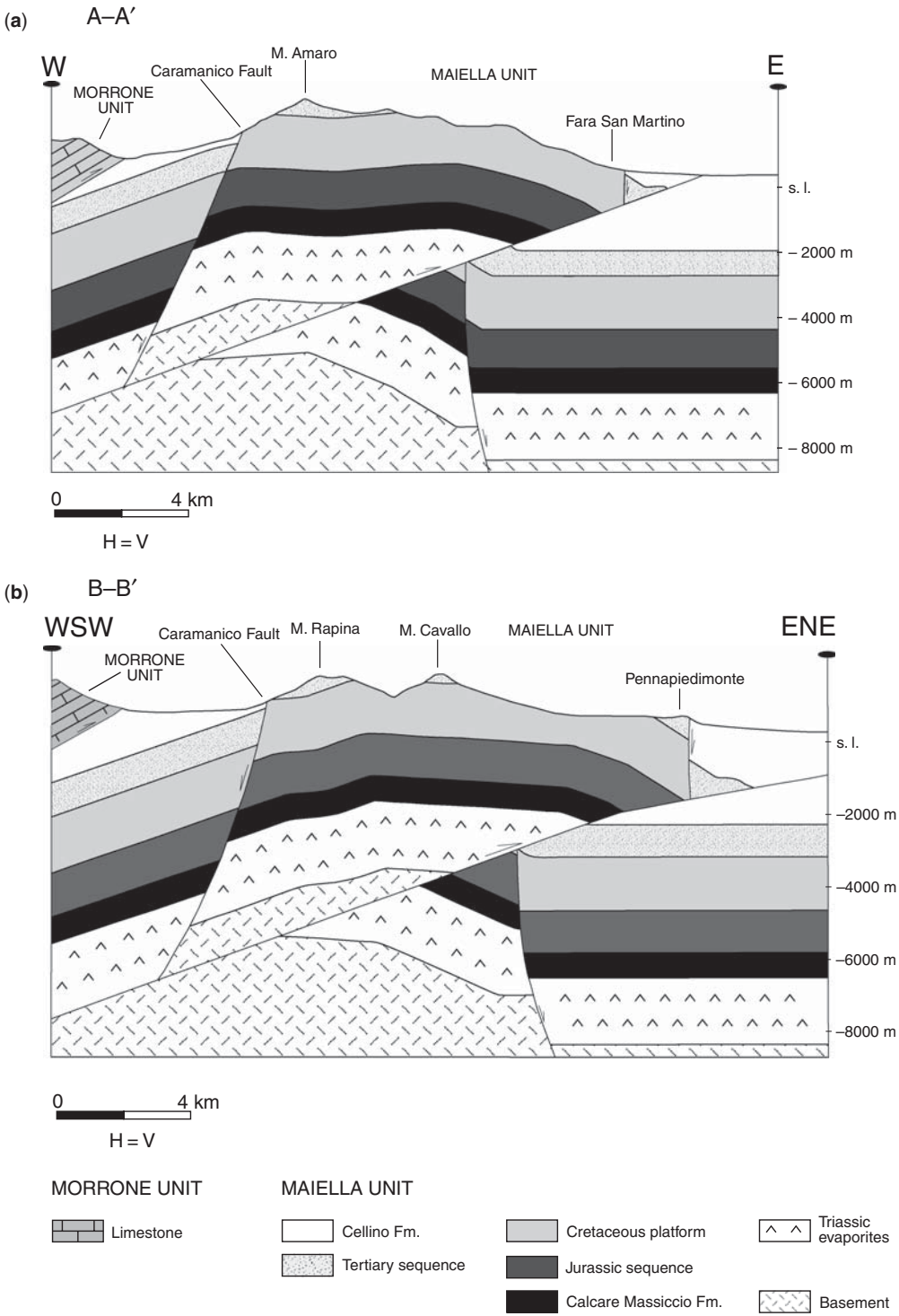


Fig. 5. Balanced geological sections across the Maiella Mountain. (a) Fara San Martino geological cross-section; and (b) Pennapiedimonte geological cross-section. See Figure 3 for location.

to the west and is longer than the east limb (forelimb) that dips 15° – 30° to east. The fold crest exhibits gentle undulations. Based on part of the interpretation of the seismic line displayed in Figure 4b, the thrust surface is assumed to be parallel to the backlimb bedding forming a moderate angle with the forelimb bedding. According to these angular relationships, this structure may be interpreted as a thrust ramp fold, that is, a fault-bend (e.g. Suppe 1983; Jamison 1987) or a fault-propagation fold (e.g. Jamison 1987; Mitra 1990; Suppe & Medwedeff 1990). However, the structural relationships between the fold and the thrust, with part of the forelimb in the thrust hanging wall and part in the thrust footwall, plus the fact that the thrust displacement for different beds is approximately equal in each cross-section (Fig. 6) suggest that this structure could be interpreted as a break-thrust fold (e.g. Fischer *et al.* 1992; McConnell *et al.* 1997), in which folding (at least partially) preceded thrusting. The portion of the fold above the thrust surface was passively transported and bent where a slight change in the thrust surface dip occur in the eastern part of the Pennapiedimonte cross-section (Fig. 5b).

In our interpretation, thrusting is responsible for displacement of two ancient normal faults (Fig. 5). One of these normal faults, the exhumed Caramanico fault, located in the anticline backlimb, dips moderately to the west and has not been interpreted in the footwall of the main thrust. The other normal fault, located in the anticline forelimb, is steeply dipping to the west near the topographic surface, and it is interpreted to become vertical in the thrust hanging wall and in the upper part of the thrust footwall and to dip steeply to the east at depth. We believe these normal faults bounded a structural high originated during Late Miocene,

subsequently cut and offset by the thrust, similarly to the cross-section of Scisciani *et al.* (2000a) (Fig. 4c).

Field data collected in the study area allowed us to decipher the age of the normal faults and the controversial timing relationships between them and the thrust. In the Caramanico valley, the Mesozoic–Miocene sequence within the backlimb of the Maiella anticline is truncated by two vertical to steeply WSW- to SW-dipping normal faults (Fig. 7a). The easternmost normal fault exhibits a Messinian succession in the eastern fault block (footwall) and a younger Messinian succession overlaid by Lower Pliocene conglomerates in the western fault block (hanging wall). The Messinian marls with olistoliths and slumps in the fault hanging wall do not display evidence of deformation related to the normal fault development and are interpreted to onlap a palaeo-fault escarpment. To the west, these Messinian and Lower Pliocene rocks are, in turn, truncated and offset by another normal fault, approximately parallel to the fault described above. The western block (hanging wall) of the westernmost normal fault is made up of a thick Lower Pliocene succession younger than the footwall Lower Pliocene rocks. The Lower Pliocene sandstones and clays that occur in the fault hanging wall are interpreted to onlap a palaeo-fault escarpment. These relationships between the faults and their associated hanging wall rocks indicate a Messinian age for the easternmost normal fault (Caramanico fault) in agreement with the observations of previous authors (Scisciani *et al.* 2000a, 2002) and a younger age (Lower Pliocene) for the westernmost fault.

The eastward dip of the beds that constitute the forelimb of the Maiella anticline varies from 60° – 70° to 30° along strike; these beds are truncated by a fault that displays relatively constant high cut-off angles to bedding, so that the fault dip also varies along strike becoming an east-dipping normal fault in those regions where beds dip gently to the east and a west-dipping apparently reverse fault in those regions where beds dip steeply to the east (southern and northernmost sectors of the Maiella Mountain) (Fig. 7b, c). At the surface, this fault is the tectonic contact between the Maiella carbonate succession and the Pliocene sequence to the east, and in the Pennapiedimonte area the fault exhibits an erosional fault escarpment onlapped by Lower Pliocene rocks (Scisciani *et al.* 2000a, 2002). The geometrical relationships between the dip of the Maiella forelimb and the fault dip suggest that the fault developed before folding, and the occurrence of a palaeo-fault escarpment evidences its Early Pliocene age. Variations in the dip of normal faults along the strike of structures because they maintain relatively constant cut-off angles with

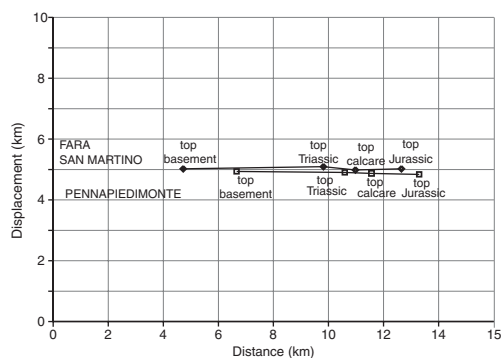


Fig. 6. Distance v. displacement graph for four beds offset by the east-directed thrust measured in the Fara San Martino and in the Pennapiedimonte geological cross-sections.

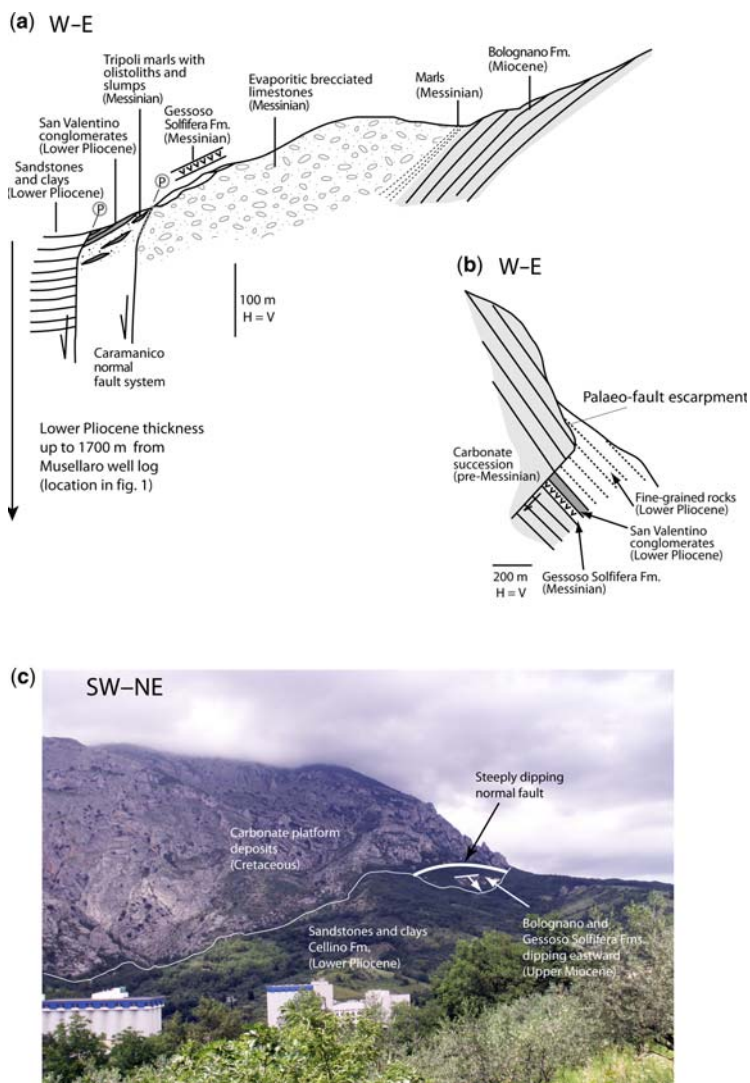


Fig. 7. Stratigraphic and structural evidence of the age of ancient normal faults in the backlimb and forelimb of the Maiella anticline. See Figure 3 for location. (a) Geological cross-section showing the Miocene–Lower Pliocene sequence that crops out in the vicinity of the Caramanico fault in the backlimb of the Maiella anticline. The Maiella 1 well log constrains the thickness (around 1.7 km) of Lower Pliocene siliciclastic deposits in the hanging wall of the westernmost normal fault (modified from Scisciani *et al.* 2000a). P, palaeo-fault escarpment. (b) Geological cross-section showing the faulted pre-Messinian–Lower Pliocene sequence that crops out in the forelimb of the Maiella anticline (modified from Scisciani *et al.* 2000a). (c) Photograph of a steeply dipping normal fault that affects the forelimb of the Maiella anticline north of the Fara S. Martino cross-section.

bedding have been documented for other normal faults in Central Apennines (e.g. Mazzoli *et al.* 2002; Scisciani *et al.* 2002; Bigi & Costa Pisani 2005). Studies carried out in recent years in the Apennines proved the activity of Messinian–Lower Pliocene syn-sedimentary normal faults, which controlled the foredeep architecture during

Early Pliocene, and the geometric and kinematic evolution of the subsequent contractional structures (Scisciani *et al.* 2000b) in accordance with the relative timing between the normal faults and the contractional structures proposed here.

The stratigraphic horizon at which thrusts detach is a matter of debate, but it is generally assumed to

be the Triassic evaporites located at a depth of several kilometres beneath the undeformed portions of the anticline (Casero *et al.* 1988; Scisciani *et al.* 2000a, 2002; Patacca *et al.* 2008). The occurrence of the structural high prior to thrusting caused that, underneath the anticline, the hanging wall of the thrust ramp includes basement rocks underlying the Triassic evaporites (Figs 4c & 5). The thrust surface has been interpreted to have a constant dip around 20°, except for the easternmost part of the Pennapiedimonte cross-section in which a lesser dip of 10° is assumed. The thrust surface is oblique to hanging wall and footwall bedding except for the backlimb of the anticline where it runs along the base of the Triassic evaporites in the hanging wall of the Caramanico normal fault and following partially a basement bedding surface in the footwall of this normal fault.

The interpretation of the geometry of the Maiella Mountain is a matter of debate as described in a previous section (Fig. 4). Amongst the different structural interpretations proposed for the Maiella Mountain, the thick-skinned model incorporating the basement into the structure (Vezzani & Ghisetti 1998; Scisciani *et al.* 2000b) (Fig. 4c, d) is the one that better fits our data and our interpretation. Thus, according to our interpretation the development of the Maiella structure started during the Messinian and lasted until the Late Pliocene, which is the age of the youngest undeformed deposits (Turrialgna Conglomerate of Upper Pliocene age) overlying the structure in the northern sector (Bigi *et al.* 1999; Rusciadelli 2005; Patacca *et al.* 2008).

Cross-section restoration

In order to validate the constructed cross-sections, to decipher the geometry of the structures during different deformation stages and their kinematics, and to quantify the amounts of displacement, the present-day, deformed cross-sections illustrated in Figure 5a, b were sequentially restored using the software 2DMove (Midland Valley). The sequential restorations were constructed in reverse order to the assumed chronology of the deformational events. The present-day Maiella structure (Figs 8a & 9a) resulted from two main tectonic events: extension during Late Miocene–Early Pliocene and contraction during Late Pliocene. Thus, the sequence of restoration employed was: (a) thrust restoration (Figs 8b & 9b); (b) fold restoration (Figs 8c & 9c); and (c) normal faults restoration (Figs 8d & 9d). Stages 1 and 2 correspond to the contractional phase, whereas stage 3 is the extensional phase.

Removal of the thrust displacement was performed assuming that deformation mainly consisted

of rigid hanging wall translation. This type of restoration required a slight adjustment of the easternmost upper portion of the thrust hanging wall in the Pennapiedimonte section because the thrust exhibits a subtle change in its dip.

According to our field observations layer-parallel shear (flexural slip/flow) is the main mechanism of distribution of strain in the folded Mesozoic and Tertiary layers, and therefore, this was the algorithm employed to restore the fold. Thus, a planar foliation, whose spacing is lithology dependent and its angle with bedding ranges from 60–90°, affects carbonate strata (Fig. 10a, b). The occurrence of insoluble material along the foliation surfaces suggests that it may correspond to a pressure/solution foliation and due to the high and relatively constant angle to bedding, this foliation may be interpreted as a result of an initial layer-parallel shortening. Many foliation surfaces have a sigmoidal shape in the well bedded marls within the slope-to-basin sequence of the Pennapiedimonte cross-section (Fig. 10c) and the stratification surfaces of some of these rocks exhibit striations and elongated calcite fibres. The striations and calcite fibres have approximately east–west directions, are parallel to dip of the bedding planes and the geometry of the sigmoidal foliation surfaces is consistent with the motion deduced from the striations and calcite fibres. Both the foliation sigmoidal geometry and the kinematic indicators on bedding surfaces indicate the occurrence of layer-parallel shear with a relative motion of top to the anticline hinge (Fig. 10c) consistent with theoretical fold amplification models in which layer-parallel shear is the mechanism of distribution of deformation within the folded layers. The fact that no significant variations in layer thickness have been observed is in agreement with this conclusion. Similar observations have been documented in equivalent stratigraphic sequences such as in the Mt. Catria anticline in the northern Apennines (Tavani *et al.* 2008).

The motion caused by the two normal faults was restored using inclined shear, assuming that the footwall remained undeformed, because this algorithm is currently employed in extensional tectonic settings with successful results in terms of both bed geometry and internal strain (e.g. Erickson *et al.* 2000; Poblet & Bulnes 2007 and references therein).

The restored sections show reasonable geometries of both beds and structures from the geological point of view starting from undeformed beds to a horst bounded by two opposite dipping normal faults, an east-vergent fold and eventually an east-directed thrust that cuts through the whole structural framework. Thus, the restorations validate our balanced cross-sections.

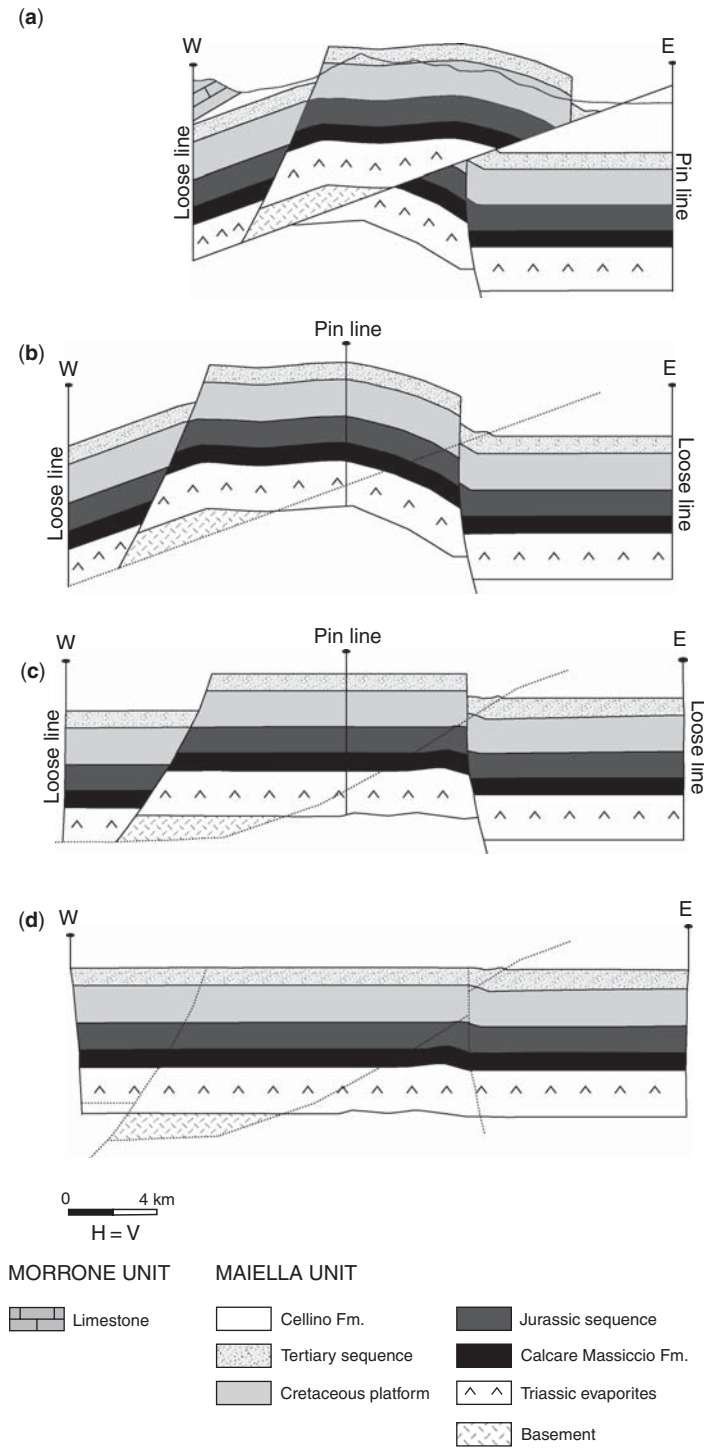


Fig. 8. Deformed, present-day section across the Fara San Martino area including the pin and loose lines employed in the thrust restoration (a) and different restoration stages following the reverse deformation chronology proposed: (b) thrust restoration including the pin and loose lines employed in the fold restoration, (c) fold restoration including the pin and loose lines employed in the horst restoration and (d) horst restoration.

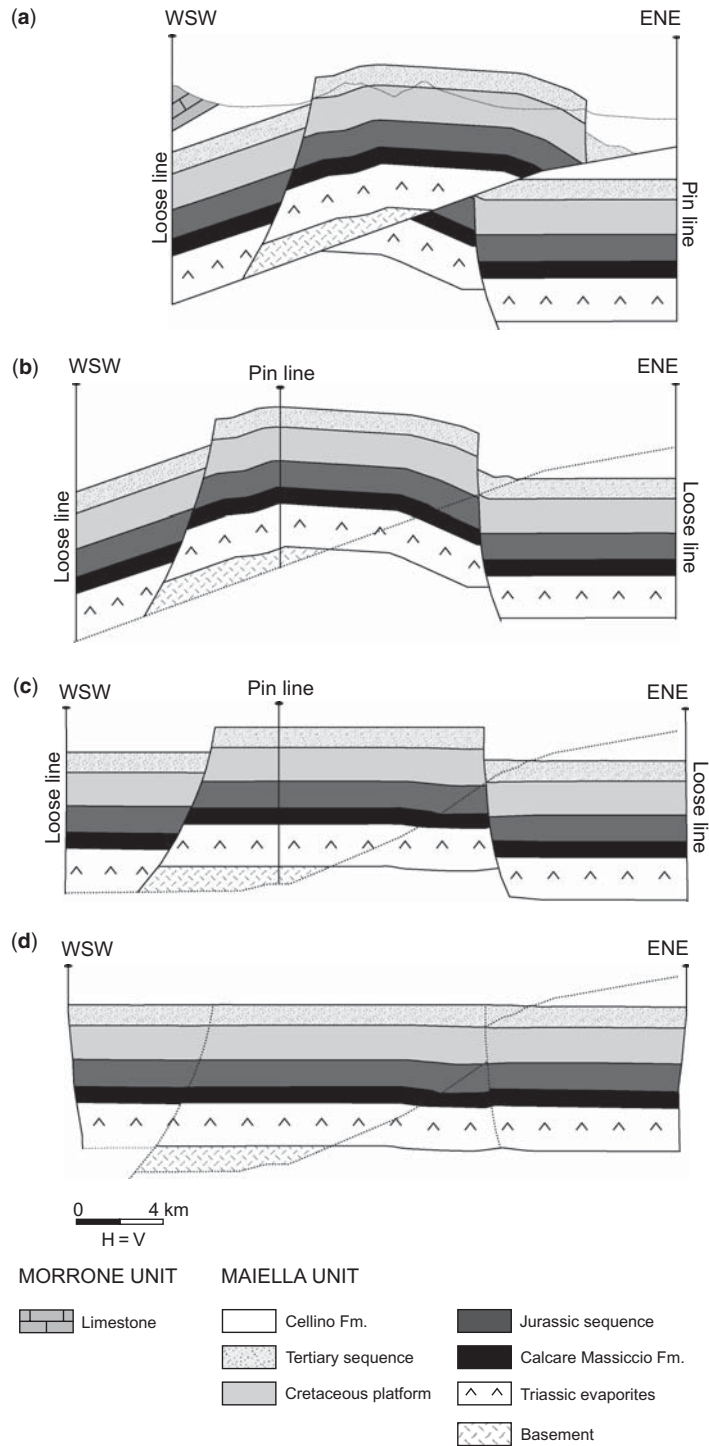


Fig. 9. Deformed, present-day section across the Pennapiedimonte area including the pin and loose lines employed in the thrust restoration (a) and different restoration stages following the reverse deformation chronology proposed: (b) thrust restoration including the pin and loose lines employed in the fold restoration, (c) fold restoration including the pin and loose lines employed in the horst restoration and (d) horst restoration.

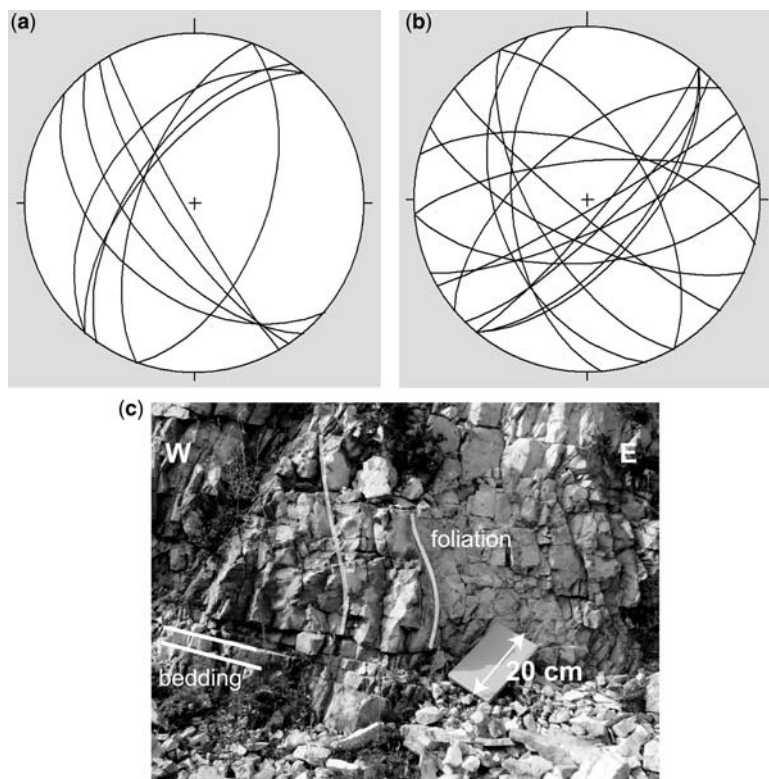


Fig. 10. (a) Equal area projection in the lower hemisphere of pressure/solution foliation surfaces measured in the Verde River valley (Fara San Martino cross-section), (b) equal area projection in the lower hemisphere of pressure/solution foliation surfaces measured in the Avello River valley (Pennapiedimonte cross-section) and (c) photograph of sigmoidal surfaces of pressure/solution foliation in the Avello River valley (Pennapiedimonte cross-section) that indicate top to the west motion along bedding surfaces consistent with layer-parallel shear as a mechanism of deformation distribution within the Maiella fold.

The sequential restorations constructed enable estimating the partial shortening, the total shortening, and the extension values undergone by this region. In both cross-sections, the shortening due to thrusting is around 21.5–22.1% (4.7–5.1 km), the shortening due to folding is around 2.7–3.4% (0.8–0.9 km), the value of total shortening is about 24.8–24.9% (5.6–5.9 km), and the extension due to pre-contractual normal faults is about 1.3–4.6% (0.4–1.2 km). The shortening caused by thrusting is greater in the Pennapiedimonte cross-section than in the Fara San Martino cross-section (Fig. 6), whereas the shortening caused by folding is slightly greater in the Fara San Martino cross-section than in the Pennapiedimonte cross-section, however the total shortening is slightly greater in the Pennapiedimonte cross-section. The fact that the amount of folding-induced shortening is greater in one cross-section and thrusting-induced shortening is greater in another cross-section agrees with the interpretation of the Maiella structure as a

break-thrust fold in which thrusting and folding are two separate processes. On the other hand, the extension is slightly greater in the Fara San Martino cross-section than in the Pennapiedimonte cross-section.

Strain simulation

We used a method based on cross-section restoration as a tool to simulate deformation patterns in the Maiella Mountain cross-sections. This method, described in Masini *et al.* (2010) who applied it to a fault-propagation fold from the Cantabrian fold-and-thrust belt in the NW Iberian Peninsula, requires the input of artificial strain markers in a retrodeformable, present-day section across a structure and subsequent restoration of the section including strain markers. Once the section is restored, the strain markers become the reciprocal strain ellipse and the real strain ellipse may be obtained using

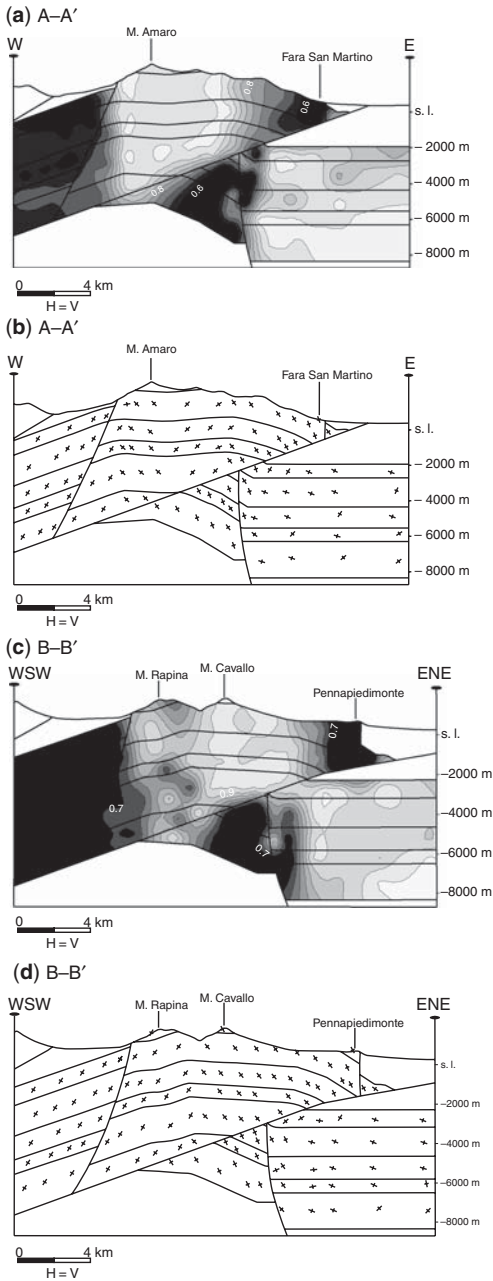


Fig. 11. (a) Contours obtained from the kriging interpolation algorithm of the ellipticity coefficient minimum/maximum elongation with the contour interval 0.04 and (b) orientation of the maximum and minimum elongation axis in the Fara San Martino cross-section. (c) Contours obtained from the kriging interpolation algorithm of the ellipticity coefficient minimum/maximum elongation with the contour interval 0.04 and (d) orientation of the maximum and minimum elongation axis in the Pennapiedimonte cross-section. White regions in figures (a) and (c) indicate values of the ellipticity coefficient close to 1 (undeformed regions), whereas dark regions point out values close to 0 (highly deformed regions). The fact that the ellipticity coefficient contours are continuous from the hanging wall to the footwall of the faults and are not offset is due to the methodology employed and does not indicate timing relationships between the deformation displayed and the faults. The length of the axes of maximum and minimum elongation in figures (b) and (d) is the same for all the strain markers and is not proportional to their value.

an algebraic transformation. The method outputs are the orientation and magnitude of the semi-axes of the strain ellipses for each strain marker at the present-day state. To display the distribution and magnitude of deformation these authors employed an ellipticity coefficient, consisting of the reverse of the ellipticity defined by Ramsay & Huber (1987). They defined this coefficient as the ratio between the minimum and maximum elongation of the strain ellipse; this coefficient varies from 0–1, so that highly deformed regions have values close to 0 and undeformed regions have a value equal to 1. The values of the ellipticity coefficient obtained for each strain marker may be contoured to obtain continuous deformation data all along the structure. It must be emphasized that: (a) the strain predicted is a simple function of the bedding dip (as in fig. 7–57 in Ramsay 1967), and therefore, the effect of competence contrasts between different stratigraphic units is ignored in the estimation of strain; and (b) the strain pattern obtained during flexural slip depends on the position of the pin line.

In the previous section we proved that the two geological sections across the Maiella Mountain, constructed parallel to the tectonic transport direction, were retro-deformable. This makes the Masini *et al.* (2010) method applicable to the sections across the Maiella Mountain presented here. The geometry and dimensions of the Maiella structure controlled the size, density and distribution of the strain markers we introduced in the deformed, present-day cross-sections, so that, in our opinion, the strain markers employed describe adequately, in terms of quantity and quality, the strain distribution along the structure (Fig. 11). The deformed, present-day cross-sections including strain markers were restored sequentially. The first step, consisting of thrust displacement restoration, did not cause substantial deformation of the strain markers, because it was simply a translation of the hanging wall along the thrust surface. During the second step, the fold restoration involved distortion and translation of the strain markers. The last step, removal of the two extensional faults, produced a local deformation of those strain markers close to the faults. Thus, the algorithms employed in the restoration sequence of the sections across the Maiella

structure allow quantifying mainly the deformation due to folding. Once the restorations were performed, a mathematical transformation was applied to the restored strain markers in order to obtain proper strain data for each strain marker. The values of the ellipticity coefficient calculated from each strain marker were contoured using the kriging interpolation algorithm and allowed the visualization of the strain distribution within the structure, whereas the axes of the maximum and minimum elongation were positioned in their corresponding place on the cross-sections and their orientation was displayed using lines (Fig. 11).

The contours of the predicted ellipticity coefficients (Fig. 11a, c) show a similar distribution of deformation in both cross-sections. The less deformed areas of both cross-sections are: (a) the flat-lying footwall relative to the thrust (this area corresponds to the hanging wall relative to the eastern normal fault); and (b) the gently folded crest of the box-shaped anticline in between the two main anticline hinges. The greatest values of strain are clustered on the limbs of the major anticline, especially in the forelimb, irrespective of their position in relation to the normal faults and the thrust. The thrust, emplaced after folding, runs parallel to bedding in the backlimb of the anticline but it is oblique to bedding in the forelimb. Thus, the most deformed area in the anticline forelimb is offset due to the thrust movement, forming two approximately symmetrical triangular zones: one in the thrust hanging wall more to the east and another one in the thrust footwall more to the west. The most deformed region in the portion of the forelimb located in the thrust hanging wall is connected with that in the thrust footwall in the Fara San Martino cross-section through a narrow zone of high deformation (11a), whereas these regions are separated by a narrow channel close to the thrust surface, with low to moderate values of deformation, in the Pennapedimonte cross-section (Fig. 11c).

This distribution of deformation is probably caused by the different thrust displacement values in both cross-sections (Fig. 6). Thrust displacement is less in the Fara San Martino cross-section where the inner part of the anticline forelimb in the hanging wall was thrust over the outer part of the anticline forelimb in the footwall (Fig. 5a). On the other hand, in the Pennapedimonte cross-section, where the thrust displacement is greater, a small portion of the anticline crest in the hanging wall, characterized by low to moderate deformation, was thrust over the anticline forelimb in the footwall (Fig. 5b).

While prediction of deformation at cross-section scale may be relatively successful employing kinematic models such as the one presented here,

prediction of the types and features of the structures that accommodate deformation probably demands a mechanical approach. However, some sort of correlation between the kinematical model employed and the occurrence of fractures could be established if we assume that: (a) deformation is accommodated through brittle mesostructures; and (b) zones with high values of strain may be statistically linked with zones of high probability of occurrence of systematic fractures, so that the greater the deformation the greater the fracture frequency and vice versa. We must keep in mind that the assumptions above, although geologically reasonable, they are not necessarily correct since: (a) ductile mesostructures, instead of brittle ones, may accommodate deformation; and (b) large amounts of deformation may be accommodated by a few faults of large displacement instead of by a large number of fractures. Irrespective of these considerations, if the assumptions above were true, possible paths of oil and/or gas migration could be determined identifying the connectivity or compartmentalization of areas with high values of deformation. Thus, in the frontal part of the Maiella anticline in the Fara San Martino cross-section, oil and gas might migrate from the deep Jurassic basinal sequence in the thrust footwall, that is, the potential source rocks, to the shallow Cretaceous and Tertiary rocks, that is, the potential reservoirs, located in the folded hanging wall relative to the thrust, a potential trap, because an approximately continuous band of high deformation extends from the source rocks to the trap. On the other hand this migration path is less likely to exist in the Pennapedimonte cross-section due to a channel of low deformation that separates the two high deformation triangular zones in the thrust hanging wall and in the footwall, and that could produce a compartmentalization between potential Jurassic source rocks and the trap formed by Cretaceous to Tertiary rocks. Unfortunately, the data available do not allow us to check this hypothesis, however, analyses of fracture data collected in the field within the Maiella structure have been carried out recently (see, for instance, Van Dijk *et al.* 2002; Graham *et al.* 2003; Marchegiani *et al.* 2006; Tondi *et al.* 2006; Antonellini *et al.* 2008; Di Cuia *et al.* 2009; Aydin *et al.* in press). In particular, Marchegiani *et al.* (2006) and Di Cuia *et al.* (2009) presented maps of fracture density obtained from field measurements in several locations within the study area (Fig. 12). Although the simulation of distribution of deformation intensity performed here (Fig. 11) does not match exactly the fracture density data collected in the field (Fig. 12) when compared in detail, the simulation of deformation, decreasing from the anticline forelimb towards the fold crest and increasing again towards the anticline backlimb, roughly agrees

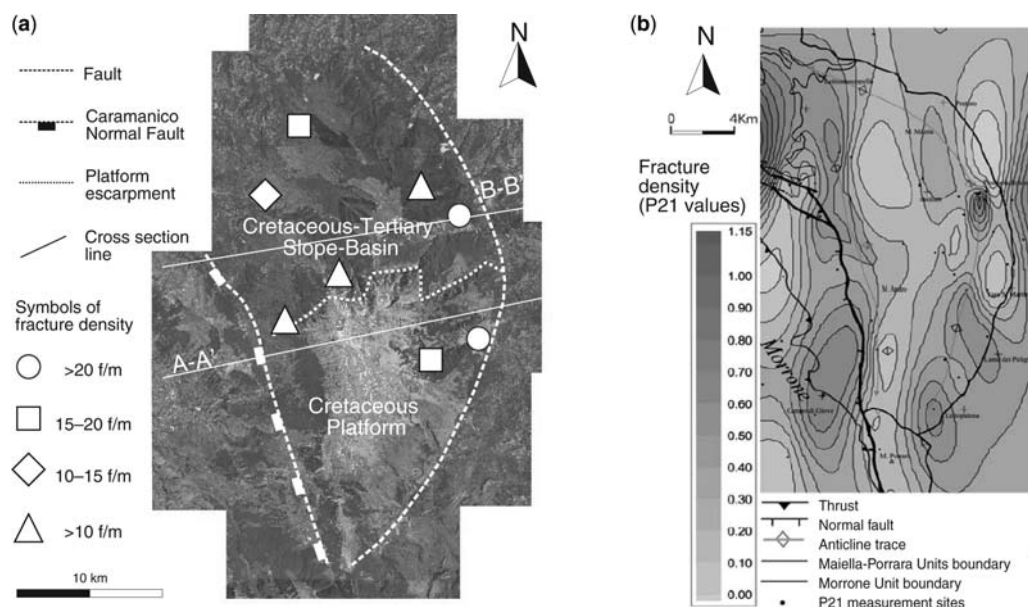


Fig. 12. Spatial distribution of fracture density across the Maiella structure. (a) Satellite image with superimposed fracture density values measured in some localities, slightly modified from Di Cuia *et al.* (2009). (b) Contour map obtained by interpolation of 50 values derived from scan area analysis, slightly modified from Marchegiani *et al.* (2006).

with the distribution of the fracture density values, and this supports to a certain extent our hypothesis of possible paths of oil and/or gas migration for the Maiella structure based on the connectivity or compartmentalization of areas with high values of deformation.

The orientation of the predicted elongation axes is rather similar in both cross-sections. The main difference lies in the crest of the large-scale box fold. In the Fara San Martino cross-section the orientation is more variable due to the occurrence of an open syncline in between the two anticlinal hinges, with an east limb gently dipping to the west and a west limb gently dipping to the east. In the Pennapiedimonte cross-section the anticlinal hinges are separated by a panel of beds slightly dipping to the east and this makes the orientation of the elongation axes more constant. The orientation of the elongation axes in the easternmost portion of the structure where beds are flat-lying is not representative due to the low amount of deformation undergone (Fig. 11a, c), which makes it difficult to determine the strain axes. Except for this region, in the rest of the structure the maximum elongation axes are oriented at about 45–60° to bedding whereas the minimum elongation axes and bedding average from 30–45° apart (Fig. 11b, d). The minimum elongation axes are not strictly perpendicular to the foliation because the strain ellipses compute the deformation undergone by beds due

mainly to folding, whereas the foliation could be the result of an early layer-parallel shortening event as suggested above. However, the strain ellipses defined by these elongation axes are compatible with the motion indicated by the sigmoidal pressure/solution foliation surfaces measured in the field.

The deformation pattern obtained for the Maiella structure is similar to that obtained in the classical card deck experiment used to demonstrate layer-parallel shear, when the card deck is flexed keeping the centre of the cards pinned and the circles drawn on one edge of the cards become ellipses as a result of the gliding motion between the cards (see for instance fig. 21.3 in Ramsay & Huber 1987). Thus, in both the Maiella structure and the experiment the maximum elongation axes of the strain ellipses converge with the anticline axial surfaces stratigraphically upwards and for low layer dip values (the ones observed in the Maiella structure) the dip of the maximum elongation axes increases as layer dip increases as well.

Conclusions

The Maiella Mountain (Central Apennines, Italy), an analogue model for hydrocarbon carbonate reservoirs in the Apennines, is made up of a Cretaceous/Miocene carbonate platform faulted during a

Miocene–Early Pliocene extensional event and exhumed during a contractional Late Pliocene episode involving folding and thrusting. The present-day structure consists of an asymmetrical, east-vergent box fold and an east-directed thrust ramp, interpreted as a break-thrust fold.

A geological map and two balanced sections across the structure were constructed, using field data and available wells and geological interpretations of seismic data, and subsequently restored. The sequential restoration from the present-day stage to the undeformed stage allowed us to visualize the main features of the Pliocene thrusting, Pliocene folding and Miocene–Pliocene normal faulting events. The restoration performed validated the geological interpretation of Maiella structure and supplied similar values of shortening around 24.8–24.9% (21.5–22.1% due to thrusting and 2.7–3.4% due to folding) and extension around 1.3–4.6% in the two cross-sections.

The strain distribution across the Maiella structure, estimated employing the two deformed, present-day geological cross-sections and their restorations, shows high deformation in both limbs of the anticline and low deformation in flat-lying beds forming the anticline crest and part of the thrust footwall. In the anticline forelimb, where the deformation is greater, high deformation is concentrated in two symmetric triangular zones separated by the thrust ramp. Because of the different displacement along the thrust, in the Fara San Martino cross-section the high deformation zones are connected, whereas in the Pennapiedimonte cross-section the high deformation zones are separated through a low deformation area. Considering the Maiella structure an analogue for carbonate reservoirs, our results suggest that, if deformation were recorded by fracturing, for the Fara San Martino cross-section (platform area), there would be high probability of fracture connectivity between Cretaceous limestones, making them potential reservoir rocks with the Jurassic rocks as potential source rocks. The distribution of strain intensity predicted in different structural positions of the Maiella structure is in broad agreement with the distribution of fracture density obtained from field data by previous authors. The orientations of the maximum and minimum elongation axes in both cross-sections and the distribution of deformation are consistent with the deformation pattern in sections across theoretical folds involving layer-parallel shear.

Up to now, the deformation simulation technique employed has been tested only on a metre-scale fault-propagation fold (Masini *et al.* 2010). The application of this relatively simple technique, which requires a few input parameters usually available, to the Maiella Mountain proved that it is able to simulate the internal deformation of

kilometre-scale break-thrust folds. Similarly to other restoration methods such as the ones presented by De Paor (1990), Erickson *et al.* (2000), Hennings *et al.* (2000), Rouby *et al.* (2000) and Dunbar & Cook (2003), in the approach used here, also based on cross-section restoration, strain is one of the results. Thus, in addition to validating the structures interpretation, deciphering the initial geometry and kinematic evolution of the structures, and quantifying the amount of contraction/extension, cross-section restoration is a valuable tool to visualize the distribution and quantify the amount of internal deformation throughout folded/thrusted rocks.

We would like to thank the editor of this volume R. Lisle, and S. Tavani and an anonymous reviewer for their comments and suggestions that substantially improved the initial version of this manuscript. C. Olivares is thanked for reviewing the format of the manuscript. M. Masini is grateful to the Royal Holloway, University of London research group and in particular to K. McClay and M. Sánchez for their useful scientific suggestions and to British Petroleum for its generous funding support. J. Poblet and M. Bulnes are grateful to projects CGL2008-03786/BTE, CGL2006-12415-C03-02/BTE, CSD2006-0041 and CGL2008-00463-E/BTE funded by the Spanish Ministry for Science and Innovation (MICIIN), and project CNG08-15 funded by the Asturian Foundation for the Scientific Research and Technology (FICYT).

References

- ACCARIE, H. 1988. *Dynamique Sédimentaire et Structurale au Passage Plate-Forme/Bassin. Les Facies Cretacées et Tertiaires: Massif de la Maiella. Mémoires des Sciences de la Terre*. Ecole des Mines de Paris, Paris.
- ALLMENDINGER, R. W. 1998. Inverse and forward numerical modelling of trishear fault-propagation folds. *Tectonics*, **17**, 640–656.
- ALLMENDINGER, R. W., ZAPATA, T., MANCADA, R. & DZELALIJA, F. 2004. Trishear kinematic modelling of structures, with examples from the Neuquén Basin, Argentina. In: McCLAY, K. R. (ed.) *Thrust Tectonics and Hydrocarbon Systems*. American Association of Petroleum Geologists Memoir, **82**, 356–371.
- ANTONELLINI, M., TONDI, E., AGOSTA, F., AYDIN, A. & CELLO, G. 2008. Failure modes in deep-water carbonates and their impact for fault development: Majella Mountain, Central Apennines, Italy. *Marine and Petroleum Geology*, **25**, 1074–1096, doi: 10.1016/j.marpetgeo.2007.10.008.
- AYDIN, A., ANTONELLINI, M., TONDI, E. & AGOSTA, F. in press. Deformation along the leading edge of the Maiella thrust sheet in central Italy. *Journal of Structural Geology*, **32**, doi: 10.1016/j.jsg.2008.10.005.
- BALLY, A. W., BURBI, L., COOPER, C. & GHELARDONI, R. 1986. Balanced sections and seismic reflection profiles across the central Apennines. *Memorie Società Geologica Italiana*, **35**, 257–310.
- BARCHI, M. N. 1991. Integration of a seismic profile with surface and subsurface geology in a cross-section

- through the Umbria-Marche Apennines. *Bollettino Società Geologica Italiana*, **110**, 469–479.
- BARCHI, M. R., MINELLI, G. & PIALLI, G. 1998. The CROP 03 profile: a synthesis of results on deep structures of the Northern Apennines. *Memorie Società Geologica Italiana*, **52**, 383–400.
- BASTIDA, F., BOBILLO-ARES, N. C., ALLER, J. & TOIMIL, N. C. 2003. Analysis of folding by superposition of strain patterns. *Journal of Structural Geology*, **25**, 1121–1139.
- BERNOULLI, D., ANSELMETTI, F. S., EBERLI, G. P., MUTTI, M., PIGNATTI, J. S., SANDERS, D. G. K. & VECSEI, A. 1996. Montagna della Maiella: the sedimentary and sequential evolution of a Bahamian-type carbonate platform of the South-Tethyan continental margin. *Memorie Società Geologica Italiana*, **51**, 7–12.
- BIGI, S. & COSTA PISANI, P. 2005. From a deformed Peri-Tethyan carbonate platform to a fold-and-thrust-belt: an example from the Central Apennines (Italy). *Journal of Structural Geology*, **27**, 523–539.
- BIGI, S., CALAMITA, F. ET AL. 1999. Tectonics and sedimentation within a Messinian foredeep in the Central Apennines, Italy. *Journal of Petroleum Geology*, **22**, 5–18.
- CASABIANCA, D., BOSENCE, D. & BECKETT, D. 2002. Reservoir potential of Cretaceous platform-margin breccias, Central Italian Apennines. *Journal of Petroleum Geology*, **25**, 1–24.
- CASERO, P. 2004. Structural setting of petroleum exploration plays in Italy. In: CRESCENTI, U. ET AL. (eds) *Geology of Italy*. Italian Geological Society, Florence, Italy, 189–199.
- CASERO, P., ROURE, F., EDIGNOUX, L., MORETTI, I., MULLER, C., SAGE, L. & VIALLY, R. 1988. Neogene Geodynamic evolution of the Southern Apennines. *Memorie Società Geologica Italiana*, **41**, 109–120.
- COWARD, M. P., DE DONATIS, M., MAZZOLI, S., PATRIGNIERI, W. & WEZEL, F. C. 1999. Frontal part of the northern Apennines fold and thrust belt in Romagna-Marche area (Italy): shallow and deep structural styles. *Tectonics*, **18**, 559–574.
- CRESCENTI, U., CROSTELLA, A., DONZELLI, G. & RAFFI, G. 1969. Stratigrafia della serie calcarea dal Lias al Miocene nella regione marchigiano-abruzzese (Parte II-litostratigrafia, biostratigrafia, paleogeografia). *Memorie Società Geologica Italiana*, **8**, 343–420.
- DE PAOR, D. G. 1990. Cross-section balancing in space and time. In: LETOUZEY, J. (ed.) *Petroleum Tectonics in Mobile Belts*. Editions Technip, Paris, 149–154.
- DI CUIA, R., SHAKERLEY, A., MASINI, M. & CASABIANCA, D. 2009. Integrating outcrop data at different scales to describe fractured carbonate reservoirs: example of the Maiella carbonates, Italy. *First Break*, **27**, 11–21.
- DONZELLI, G. 1969. Studio geologico della Maiella. In: CRESCENTI, U. (ed.) *Special volume*. Univ. degli Studi G. D'Annunzio, Chieti, Italy, 1–30.
- DUNBAR, J. A. & COOK, R. W. 2003. Palinspastic reconstruction of structure maps: an automated finite element approach with heterogeneous strain. *Journal of Structural Geology*, **25**, 1021–1036.
- DUNNET, D. 1969. A technique of finite strain analysis using elliptical particles. *Tectonophysics*, **7**, 117–136.
- EBERLI, G. P., BERNOULLI, D., SANDERS, D. & VECSEI, A. 1993. From aggradation to progradation: the Maiella platform (Abruzzi, Italy). In: SIMO, T., SCOTT, R. W. & MASSE, J. P. (eds) *Atlas of Cretaceous Carbonate Platforms*. AAPG, Tulsa, 213–232.
- ENDIGNOUX, L., MORETTI, I. & ROURE, F. 1989. Forward modelling of the Southern Apennines. *Tectonics*, **8**, 1095–1104.
- ERICKSON, S. G., HARDY, S. & SUPPE, J. 2000. Sequential restoration and unstraining of structural cross-sections: applications to extensional tectonics. *American Association of Petroleum Geologists Bulletin*, **84**, 234–249.
- FISCHER, M. P., WOODWARD, N. B. & MITCHELL, M. M. 1992. The kinematics of break-thrust folds. *Journal of Structural Geology*, **14**, 451–460.
- FRY, N. 1979a. Random point distribution and strain measurement in rocks. *Tectonophysics*, **60**, 89–105.
- FRY, N. 1979b. Density distribution techniques and strained line length method for determination of finite strain. *Journal of Structural Geology*, **1**, 221–229.
- GHISETTI, F. & VEZZANI, L. 2002. Normal faulting, extension and uplift in the outer thrust belt of the central Apennines (Italy): role of the Caramanico fault. *Basin Research*, **14**, 225–236.
- GRAHAM, B., ANTONELLINI, M. & AYDIN, A. 2003. Formation and growth of normal faults in carbonates within a compressive environment. *Geological Society of America Bulletin*, **31**, 11–14.
- HENNINGS, P. H., OLSON, J. E. & THOMPSON, L. B. 2000. Combining outcrop data and three-dimensional structural models to characterize fractured reservoirs: an example from Wyoming. *American Association of Petroleum Geologists Bulletin*, **84**, 830–849.
- JAMISON, W. R. 1987. Geometric analysis of fold development in overthrust terranes. *Journal of Structural Geology*, **9**, 297–219.
- LAMPERT, S. A., LOWRIE, W., HIRT, A. M., BERNOULLI, D. & MUTTI, M. 1997. Magnetic and sequence stratigraphy of redeposited uppercretaceous limestones in the Montagna della Maiella, Abruzzi, Italy. *Earth and Planetary Science Letters*, **150**, 79–93.
- LAVECCHIA, G., BROZZETTI, F., BARCHI, M., KELLER, J. & MENICHETTI, M. 1994. Seismotectonic zoning in east-central Italy deduced from the analysis of the Neogene to present deformations and related stress fields. *Geological Society of America Bulletin*, **106**, 1107–1120.
- LISLE, R. J. 1994. Detection of zones of abnormal strains in structures using Gaussian curvature analysis. *American Association of Petroleum Geologists Bulletin*, **78**, 1811–1819.
- MARCHEGIANI, L., VAN DIJK, J. P., GILLESPIE, P. A., TONDI, E. & CELLO, G. 2006. Scaling properties of the dimensional and spatial characteristics of fault and fracture systems in the Maiella Mountain, central Italy. In: CELLO, G. & MALAMUD, B. D. (eds) *Fractal Analysis for Natural Hazards*. Geological Society, London, Special Publications, **261**, 113–131.
- MASINI, M., POBLET, J. & BULNES, M. 2010. Cross-section restoration: a tool to simulate deformation. Application to a fault-propagation fold from the Cantabrian fold and thrust belt, NW Iberian Peninsula.

- Journal of Structural Geology*, **32**, 172–183, doi: 10.1016/j.jsg.2009.11.002.
- MAZZOLI, S., CORRADO, S. *ET AL.* 2000. Time and space variability of ‘thin-skinned’ and ‘thick-skinned’ thrust tectonics in the Italian Apennines. *Rendiconti Lincei: Scienze Fisiche e Naturali*, **9**, **11**, 5–39, doi: 10.1007/BF02904594.
- MAZZOLI, S., DEIANA, G., GALDENZI, S. & CELLO, G. 2002. Miocene fault controller sedimentation and thrust propagation in the previous faulted external zones of the Umbria-Marche Apennines, Italy. *EGU Stephan Mueller Special Publication Series*, **1**, 195–209.
- MCCONNELL, D. A., KATTERNHORN, S. A. & BENNER, L. M. 1997. Distribution of fault slip in outcrop-scale fault-related folds, Appalachian Mountains. *Journal of Structural Geology*, **17**, 257–267.
- MENARDI NOGUERA, A. & REA, G. 2000. Deep structure of the Campanian-Lucanian Arc (southern Apennines). *Tectonophysics*, **324**, 239–265.
- MITRA, S. 1990. Fault-propagation folds: geometry, kinematics and hydrocarbon traps. *American Association of Petroleum Geologists Bulletin*, **74**, 921–945.
- MORETTI, I., DELOS, V., LETOUZEY, J., OTERO, A. & CALVO, J. C. 2007. The use of surface restoration in Foothills exploration: theory and application to the Sub-Andean Zone of Bolivia. In: LACOMBE, O., LAVÉ, J., ROURE, F. & VERGÉS, J. (eds) *Thrust Belts and Foreland Basins*. Springer, Berlin, 149–162.
- MORSILLI, M., RUSCIADELLI, G. & BOSELLINI, A. 2002. Large-scale gravity-driven structures: control on margin architecture and related deposits of a Cretaceous carbonate platform (Montagna della Maiella, Central Apennines, Italy). *Bollettino Della Società Geologica Italiana*, **1**, 619–628.
- MOSCA, F. & WAVREK, D. A. 2002. *Petroleum system characteristics of the giant oil fields of Val D’Agri Region, Southern Apennines, Italy*. American Association of Petroleum Geologists Annual Meeting, Houston, Abstracts with Programs.
- MOSTARDINI, E. & MERLINI, S. 1986. Appennino centro-meridionale. Sezioni geologiche e proposta di modello strutturale. *Memorie Società Geologica Italiana*, **35**, 177–202.
- ORMAND, C. J. & HUDLESTON, P. J. 2003. Strain paths of three small folds from the Appalachian Valley and Ridge, Maryland. *Journal of Structural Geology*, **25**, 1841–1854.
- PATACCA, E. & SCANDONE, P. 2004. The Plio-Pleistocene thrust belt-foredeep system in the Southern Apennines and Sicily (Italy). In: CRESCENTI, U. *ET AL.* (eds) *Geology of Italy*. Italian Geological Society, Florence, Italy, 93–129.
- PATACCA, E., SCANDONE, P., BELLATALLA, M., PERILLI, N. & SANTINI, U. 1991. La zona di giunzione tra l’arco appenninico settentrionale e l’arco appenninico meridionale nell’Abruzzo e nel Molise. *Studi Geologici Camerti*, Vol. **Spec. 1991/2**, 417–441.
- PATACCA, E., SCANDONE, P., DI LUZIO, E., CAVINATO, G. P. & PAROTTO, M. 2008. Structural architecture of the central Apennines: interpretation of the CROP 11 seismic profile from the Adriatic coast to the orographic divide. *Tectonics*, **27**, TC3006, doi: 10.1029/2005TC001917.
- POBLET, J. & BULNES, M. 2007. Predicting strain using forward modelling of restored cross-section: application to rollover anticlines over listric fault. *Journal of Structural Geology*, **29**, 1960–1970.
- RAGAN, D. M. 1985. *Structural Geology: An Introduction to the Geometrical Techniques*. 3rd edn. Wiley, New York.
- RAMSAY, J. G. 1967. *Folding and Fracturing of Rocks*. McGraw-Hill, New York.
- RAMSAY, J. G. & HUBER, M. I. 1987. *The Techniques of Modern Structural Geology*. Vol. 2: 611 Folds and Fractures. Academic Press, London.
- ROBERTS, A. 2001. Curvature attributes and their application to 3D interpreted horizons. *First Break*, **19**, 391–412.
- ROUBY, D., XIAO, H. & SUPPE, J. 2000. 3-D restoration of complexly folded and faulted surfaces using multiple unfolding mechanisms. *American Association of Petroleum Geologists Bulletin*, **84**, 805–829.
- RUSCIADELLI, G. 2005. The Maiella Escarpment (Apulia platform, Italy): geology and modelling of an Upper Cretaceous scalloped erosional platform margin. *Bollettino Della Società Geologica Italiana*, **124**, 661–673.
- SAMSON, P. & MALLET, J. M. 1997. Curvature analysis of triangulated surfaces in structural geology. *Mathematical Geology*, **29**, 391–412.
- SANDERS, C., BONORA, M., RICHARDS, D., KOZŁOWSKI, E., SYLWAN, C. & COHEN, M. 2004. Kinematic structural restorations and discrete fracture modeling of a thrust trap: a case study from the Tarija Basin, Argentina. *Marine and Petroleum Geology*, **21**, 845–855.
- SCISCIANI, V., BIGI, S. & CALAMITA, F. 2000b. Shortcut geometry along the N–S-trending Gran Sasso and Morrone thrust front (Central Apennines). *Memorie Società Geologica Italiana*, **55**, 175–184.
- SCISCIANI, V., CALAMITA, F., BIGI, S., DE GIROLAMO, C. & PALTRINIERI, W. 2000a. The influence of synorogenic normal faults on Pliocene thrust system development: The Maiella structure (Central Apennines, Italy). *Memorie Società Geologica Italiana*, **55**, 193–204.
- SCISCIANI, V., TAVARNELLI, E. & CALAMITA, F. 2002. The interaction of extensional and contractional deformation in the outer zones of the central Apennines, Italy. *Journal of Structural Geology*, **24**, 1647–1658.
- SCROCCA, D., DOGLIONI, C. *ET AL.* (eds) 2003. *CROP Atlas: Seismic Reflection Profiles of the Italian Crust*. Memorie Descrittive Carta Geologica Italiana, **62**, 194, 71 tavole.
- SHINER, P., BECCACINI, A. & MAZZOLI, S. 2004. Thin-skinned v. thick skinned structural models for Apulian carbonate reservoirs: constraints from the Val d’Agri Fields, S Apennines, Italy. *Marine and Petroleum Geology*, **21**, 805–827.
- SPERANZA, F. & CHIAPPINI, M. 2002. Thick-skinned tectonics in the external Apennines (Italy): new evidence from magnetic anomaly analyses. *Journal Geophysical Research*, **107**(B11), 2290, doi: 10.1029/2000JB000027.
- STOSSEL, I. & BERNOULLI, D. 2000. Rudist lithosome development on the Maiella Carbonate platform

- margin. In: INSALACO, E., SKELTON, P. W. & PALMER, J. (eds) *Carbonate Platform Systems: Components and Interactions*. Geological Society, London, Special Publications, **178**, 177–190.
- SUPPE, J. 1983. Geometry and kinematics of fault-bend folding. *American Journal of Science*, **283**, 684–721.
- SUPPE, J. & MEDWEDEFF, D. A. 1990. Geometry and kinematics of fault propagation folding. *Eclogae Geologicae Helvetiae*, **8**, 409–454.
- TAVANI, S., STORTI, F., SALVINI, F. & TOSCANO, C. 2008. Stratigraphic v. structural control on the deformation pattern associated with the evolution of the Mt. Catria anticline, Italy. *Journal of Structural Geology*, **30**, 664–681.
- TAVARNELLI, E., BUTLER, R. W. H. ET AL. 2004. Implications of fault reactivation and structural inheritance in the Cenozoic tectonic evolution of Italy. In: CRESCENTI, U., D'OFFIZI, S., MERLINO, S. & SACCHI, L. (eds) *Geology of Italy*. Italian Geological Society, Florence, Italy, 209–222.
- THORBJORNSEN, K. L. & DUNNE, W. M. 1997. Origin of a thrust-related fold: geometric vs kinematic tests. *Journal of Structural Geology*, **19**, 303–319.
- TONDI, E., ANTONELLINI, M., AYDIN, A., MARCHEGIANI, L. & CELLO, P. 2006. The roles of deformation bands and pressure solution seams in fault development in carbonate grainstones of the Maiella Mountain, Italy. *Journal of Structural Geology*, **28**, 376–391.
- VAN DIJK, J. P., GILLESPIE, P. ET AL. 2002. *A New Faulting Mechanism in Carbonate Rocks*. Examples From Maiella Mountain Anticline, Italy SFERA Inaugural Meeting 2002, Abstracts Volume, Paper 9, 46–49.
- VECSEI, A. 1991. *Aggradation und Progradation eines Karbonat platform-Randes: Kreide bis mittleres Tertiär der Montagna della Maiella, Abruzzo*. PhD Thesis, Mitteilungen des Geologischen Institutes der Eidgenössischen Technischen Hochschule und der Universität Zürich.
- VECSEI, A. & SANDERS, D. G. K. 1997. Sea level high stand and low stand shedding related to shelf margin aggradation and emersion, Upper Eocene–Oligocene of Maiella carbonate platform, Italy. *Sedimentary Geology*, **112**, 219–234.
- VECSEI, A. & SANDERS, D. G. K. 1999. Facies analysis and sequence stratigraphy of a Miocene warm-temperate carbonate ramp, Montagna della Maiella, Italy. *Sedimentary Geology*, **123**, 103–127.
- VECSEI, A., SANDERS, D., BERNOULLI, D. & EBERLI, G. P. 1998. Evolution and sequence stratigraphy of the Maiella platform margin, Late Jurassic to Miocene, Italy. In: DE GRACIANSKY, P. CH., JACQUIN, T. & VAIL, P. R. (eds) *Mesozoic–Cenozoic Sequence Stratigraphy of Western European Basins*. Society of Economic Paleontologists and Mineralogists, Special Publication, **60**, 121–135.
- VEZZANI, L. & GHISSETTI, F. 1998. *Carta Geologica Dell'abruzzo. Scala 1:100 000*. SELCA, Firenze, Italy.

The roles of complex mechanical stratigraphy and syn-kinematic sedimentation in fold development: insights from discrete-element modelling and application to the Pico del Águila anticline (External Sierras, Southern Pyrenees)

OSKAR VIDAL-ROYO^{1*}, STUART HARDY^{1,2} & JOSEP ANTON MUÑOZ¹

¹*Geomodels Research Centre. GGAC, Departament de Geodinàmica i Geofísica, Facultat de Geologia, Universitat de Barcelona. C/ Martí i Franquès s/n, 08028, Barcelona, Spain*

²*ICREA (Institució Catalana de Recerca i Estudis Avançats), Catalonia, Spain*

**Corresponding author (e-mail: oskarvidal@ub.edu; vidal.oskar@gmail.com)*

Abstract: A 2D discrete-element modelling technique is used to explore the effects of complex mechanical stratigraphy and syn-kinematic sedimentation in the development of the Pico del Águila anticline (External Sierras, Southern Pyrenees). The stratigraphy (Middle Triassic–Oligocene in age) involved in this structure is characterized by a gross interlayering of competent and incompetent units, which leads to a striking variation in outcrop-scale deformation of the units observed in the field. The numerical model attempts to reproduce the stratigraphic variation seen in the field by using a mechanical stratigraphy that contains a complex interlayering of competent/incompetent units. Two experiments are presented. Model 1 tests the response of this complex mechanical stratigraphy to shortening under conditions that lead to the formation of a detachment fold. This experiment shows that folding mechanisms vary abruptly depending on the mechanical properties of the materials involved: the incompetent units are strongly internally deformed, accommodating much layer-parallel shearing; the competent units deform by rigid-body translation/rotation, localized faulting and minor internal shearing. Model 2 tests the effect of syn-kinematic sedimentation under identical boundary conditions: these sediments stabilize the fold against gravitational instabilities and cause a concentration of deformation in the core of the structure, leading to a tighter, narrower fold.

Many studies have considered mechanical stratigraphy as an important control on the present-day geometry of fault-related folds, influencing their evolution (e.g. Homza & Wallace 1995, 1997; Nalpas *et al.* 1999; Atkinson & Wallace 2003; Mitra 2003; Hardy & Finch 2005; Hardy & Finch 2007). However, most of these works treat mechanical stratigraphy in a qualitative manner, either considering it as a *possible* theoretical factor, or modelling a very simplified mechanical stratigraphy. In addition, growth strata – a common component of fault-related folds – have been mainly used as an indicator of folding mechanisms/kinematics, to estimate chronology and sedimentation/uplift rates, to reveal fold types and geometries or to recognize internal deformation features in the syn-kinematic package (e.g. Poblet & Hardy 1995; Poblet *et al.* 1997; Storti & Poblet 1997; Nigro & Renda 2004; Strayer *et al.* 2004; Casas-Sainz *et al.* 2005; Grando & McClay 2007; Tavani *et al.* 2007). However, most of these works neglect the effect of the syn-kinematic sedimentary load on the evolution of the fold itself.

The Pico del Águila is one of the best known north–south anticlines in the Central External Sierras (CES; Southern Pyrenees), which are interpreted to be in the hanging wall of the large-displacement South-Pyrenean thrust that places the Triassic décollement over a ramp that cuts far up-section through Tertiary syn-tectonic deposits. These anticlines are interpreted to have rotated clockwise *c.* 40° (Pueyo *et al.* 2002), towards the direction of tectonic transport. Previous numerical modelling techniques applied to the Pico del Águila anticline have used kinematic modelling (Poblet & Hardy 1995; Poblet *et al.* 1997) and inclined-shear restoration (Novoa *et al.* 2000). Based on accurate observations/mapping of the growth strata pattern, these studies focused on folding mechanisms/kinematics, and assumed a homogeneous pre-folding sequence. The main drawback of these works is that they consider the evolution of the structure only from geometrical and kinematical viewpoints, overlooking the importance of mechanical heterogeneities in the pre-folding sequence. As a result, even though the obtained geometries broadly agree with field data,

the proposed folding mechanisms may not fully represent the structural evolution of the Pico del Águila anticline and its expression in the field, which is far from being fully unravelled by those techniques alone.

In contrast to these studies, this work uses a discrete element model to explore the effects of a complex (non-trivial) mechanical stratigraphy and the syn-folding sedimentary load on the structural evolution of a detachment fold.

The Pico del Águila provides a well-exposed down-plunge view of a fold down to the Triassic core, with a well described mechanical stratigraphy and spectacular growth strata that record the fold development. This provides an excellent basis to compare how the mechanical stratigraphy behaved in the natural fold v. the model, and how the syn-kinematic sedimentation influenced the fold evolution. Although the numerical model does not purport to be a direct replica of the natural fold (i.e. it is constrained to deform by plane strain, does not contain vertical axis rotations, etc.), we compare the results to the Pico del Águila anticline, gaining insight on the folding mechanisms and structural evolution of this area.

Geological setting of the Pico del Águila anticline

The Pico del Águila is a widely studied anticline in the External Sierras of the Spanish Southern Pyrenees (Fig. 1). It grew from 42.67 ± 0.02 Ma (Upper Lutetian) until 34.8 ± 1.72 Ma (Lower Priabonian) (Poblet & Hardy 1995) and displays a spectacular growth strata record (Millán *et al.* 1994; Millán 1995; Poblet & Hardy 1995; Pueyo *et al.* 2002; Castelltort *et al.* 2003). A complete discussion on the regional geology is beyond the scope of this paper. The interested reader is referred to key works such as Puigdefàbregas (1975), IGME (1992), Millán *et al.* (1994) and Pueyo *et al.* (2002). Nevertheless, since this study models the effect of the mechanical stratigraphy in the fold development, a brief description of the geological setting and the stratigraphy of the Central External Sierras is provided (CES; Figs 2 & 3a).

The External Sierras constitute the frontal emergent part of the southernmost Pyrenean thrust sheets (Soler & Puigdefàbregas 1970; IGME 1992; Millán *et al.* 1994; Millán 1995; Pueyo *et al.* 2002) and consist of a system of imbricated thrust sheets detached on clayish, dolomitic and evaporitic Middle and Late Triassic facies (Keuper and Muschelkalk facies). The hanging wall of the frontal Pyrenean thrust involves an Upper Triassic–Lower Miocene sedimentary sequence (Puigdefàbregas 1975; Millán *et al.* 1994; Millán 1995) which was displaced

southwards over the Tertiary sediments of the Ebro foreland basin. During the early stages of the evolution of the External Sierras (Early Lutetian–Chattian), the thrust system was characterized by a south-directed main thrust and a set of arcuate north-eastward concave, oblique thrusts. Generated as detachment folds on a hanging wall flat over footwall flat thrust configuration, the north–south trending folds are interpreted as a more evolved stage of the initially arcuate oblique thrusts. In addition to a general translation towards the South, a regional clockwise rotation characterized the kinematics of the thrust system (up to 40° measured at the base of Arguis Fm, western limb of Pico del Águila anticline; Pueyo *et al.* 2002). However, during the Chattian to the Early Miocene, the structural evolution changed abruptly. The rotating thrust system was folded and truncated by the formation of the Santo Domingo detachment anticline and its associated south-directed thrust system, located in the western sector of the External Sierras (beyond the limits of Fig. 1, to the west). Consequently, the remaining north–south trending folds occurred at the hanging wall of the new Santo Domingo thrust system, representing the northernmost portion of those oblique structures (the rest of the structures are supposed to be either buried under the continental deposits of the Ebro foreland basin or isolated by erosion under the southern limb of the Santo Domingo anticline, according to Pueyo *et al.* (2002)). The emplacement of these north–south-trending folds in a hanging wall flat over footwall ramp position of the Santo Domingo thrust system caused their 30° plunge towards the hinterland (Millán 1995; Pueyo *et al.* 2002).

In common with other similar structures in Central External Sierras, the Pico del Águila has been commonly assessed to be either a detachment fold (Millán *et al.* 1994; Poblet & Hardy 1995; Pueyo *et al.* 2002; Castelltort *et al.* 2003) or a fault-propagation fold (McElroy 1990; Millán *et al.* 1994). Based on field and mapping observations as well as on ideas already suggested by previous authors (cf. Millán 1995; Pueyo *et al.* 2002), it is our hypothesis that the Pico del Águila anticline generated as a detachment fold (on a hanging wall flat over footwall flat thrust configuration according to Pueyo *et al.* 2002) and, with increasing shortening, the core of the anticline broke through, propagating upwards while folding the upper units of Guara Fm and overlying growth strata, finally evolving into a hybrid detachment/fault-propagation fold.

The stratigraphic record of the Pico del Águila anticline is composed by a pile of sedimentary rocks from Triassic to Oligocene in age (Fig. 2). The pre-folding stratigraphic sequence is made up of a relatively thin Mesozoic pile, consisting of Triassic limestone, dolomite and gypsum-bearing

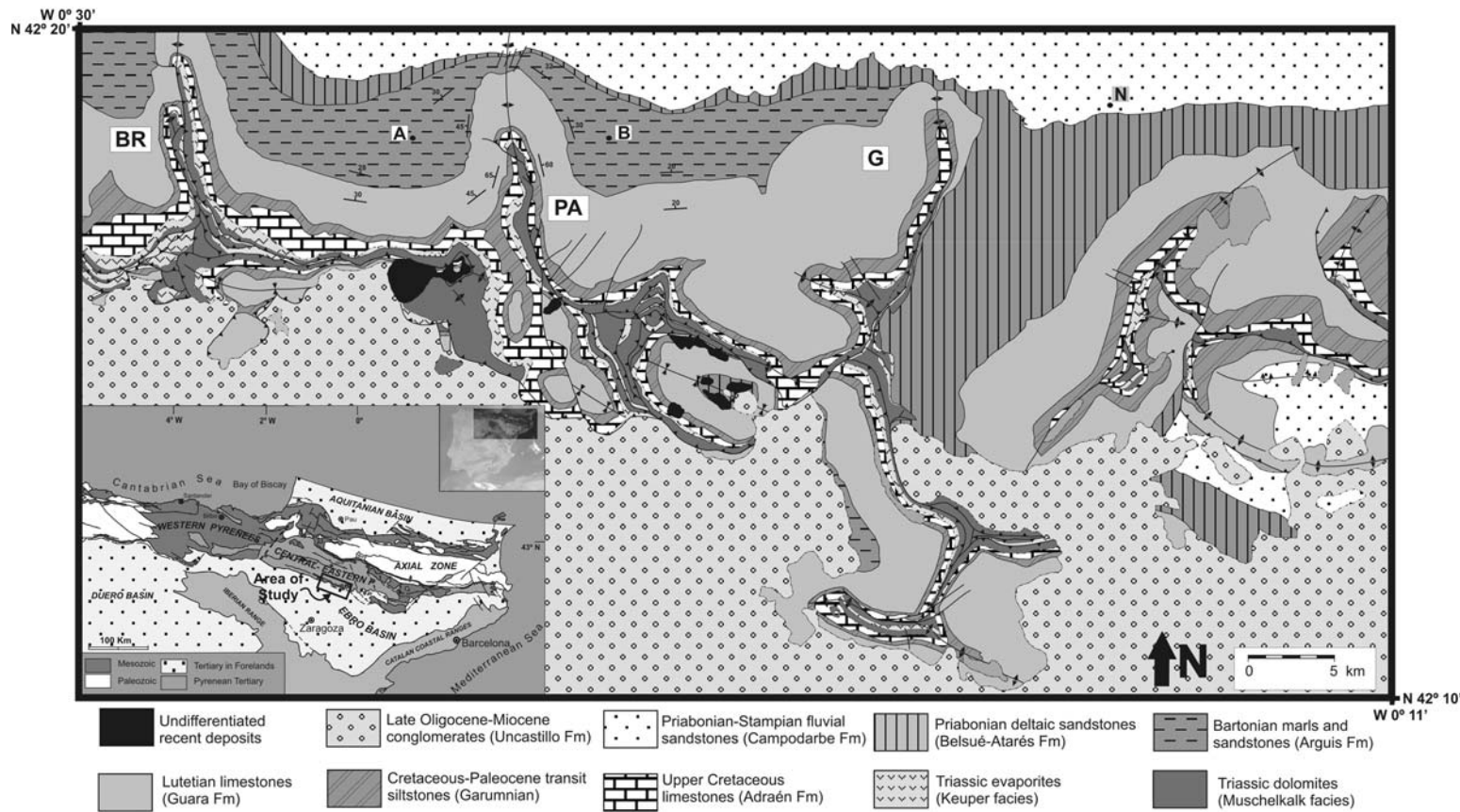


Fig. 1. Geological map of Central External Sierras (modified from IGME 1992). BR, Bentué de Rasal anticline; PA, Pico del Águila anticline; G, Gabardiella anticline complex; A, Arguis village; B, Belsué village; N, Nozito village.

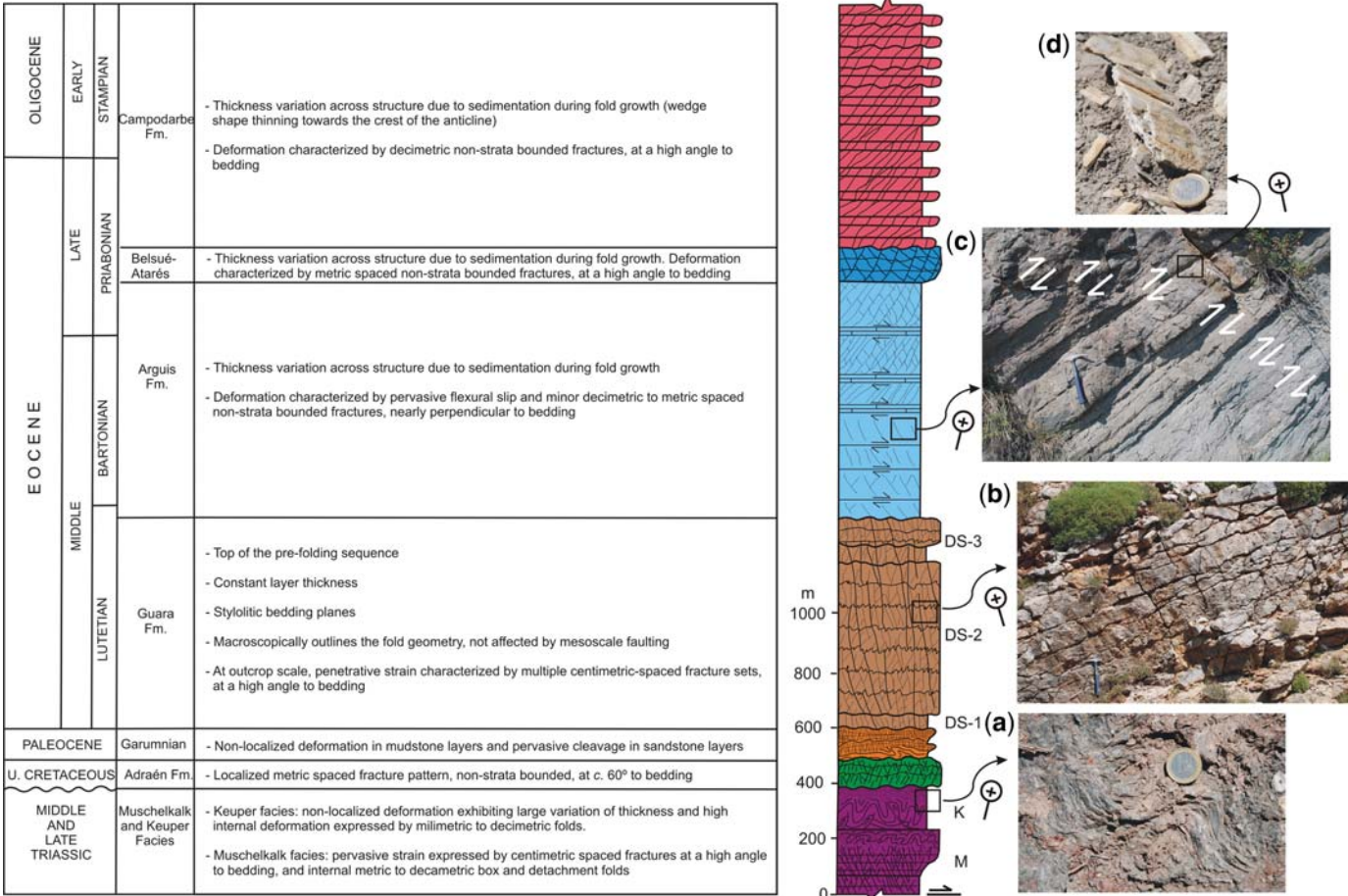


Fig. 2. Stratigraphic sequence cropping out in Central External Sierras (modified after Millán *et al.* 1994) showing the deformation style that characterizes each unit: (a) folded Keuper gypsiferous clays (photograph oriented east–west); (b) fracture pattern within the Guara limestones (photograph oriented NW–SE); (c) flexural slip and minor fractures within the Arguis marls (photograph oriented SW–NE); (d) detail of a remnant slickenslide parallel to bedding in the Arguis marls (dipping 29° to the north), indicating layer parallel displacement (c and d belong to different outcrops). Right side of the stratigraphic column: M is Muschelkalk, K is Keuper; DS-1, DS-2 and DS-3 are, respectively, Depositional Sequences 1, 2 and 3 within Guara Fm.

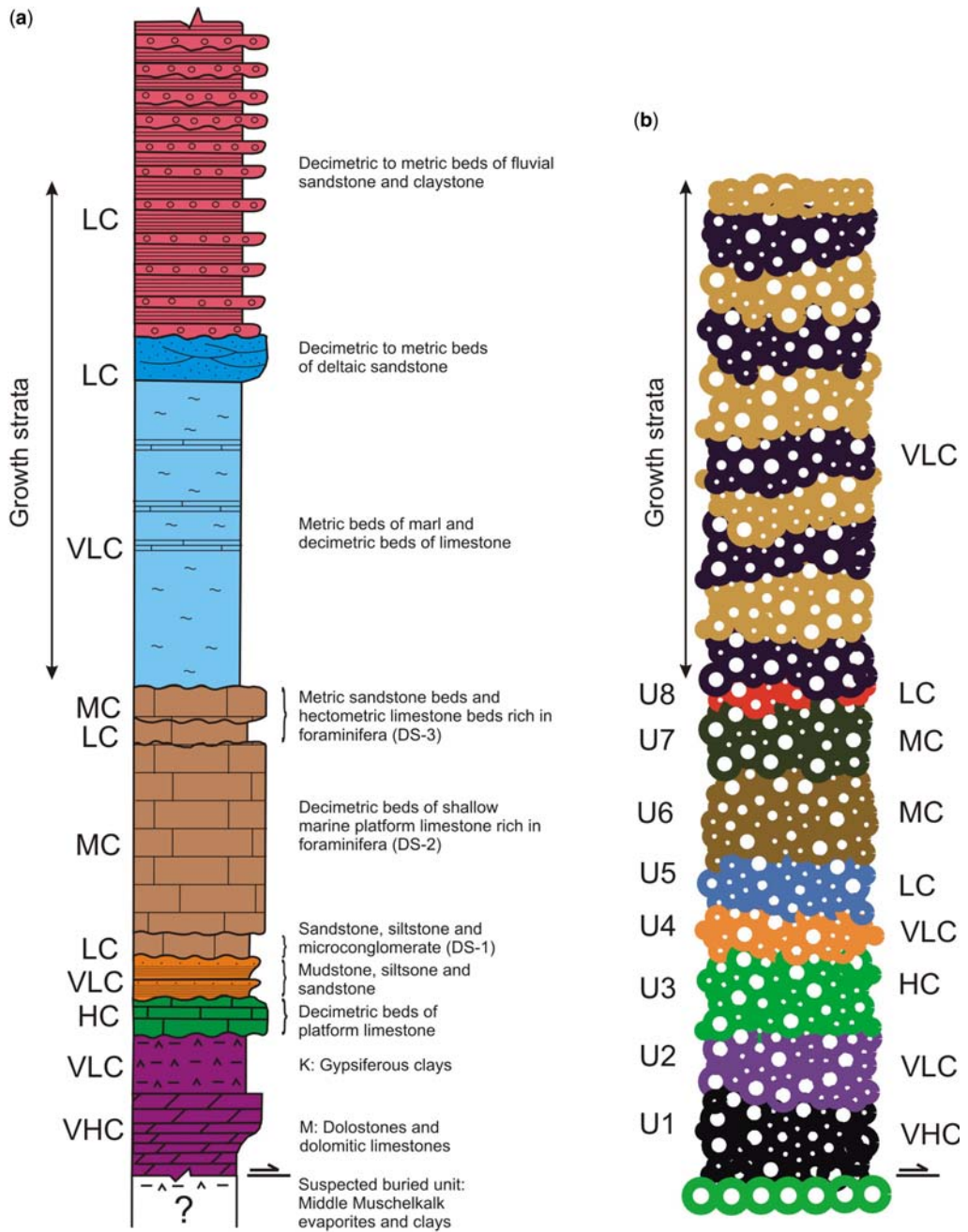


Fig. 3. Comparison between stratigraphic sequences: **(a)** sequence seen in the field (modified after Millán *et al.* 1994) with a brief description of the predominant lithologies observed in each unit (M, Muschelkalk; K, Keuper); and **(b)** sequence used to model the mechanical behaviour of the natural sequence. Next to each field/model unit there is an indication of its average mechanical behaviour: VHC, Very High Competence; HC, High Competence; MC, Medium Competence; LC, Low Competence; VLC, Very Low Competence.

clay (the oldest outcropping material), and Upper Cretaceous shallow marine limestone. This is followed by a thicker Palaeogene sequence comprising the continental sandstone, siltstone and lacustrine limestone of the Cretaceous–Paleocene transition (Garumnian facies), and the heterogeneous Lutetian shallow marine platform limestone of the Guara Formation. The syn-folding stratigraphic sequence comprises the uppermost part of the Guara Fm, the shallow marine and transitional marl, limestone and sandstone of the Arguis and Belsué-Atarés Fms (Upper Lutetian to Middle Priabonian), and the basal part of the fluvial mudstone, sandstone and conglomerate of the Campodarbe Fm (Middle Priabonian to Middle Oligocene).

It is important to highlight that the Muschelkalk dolomites and limestones are the oldest outcropping material exposed in the core of the anticline. However, data from the well Surpirenaica-1 located in the Ebro basin (to the South, beyond the limits of the studied area; IGME 1987) indicate the existence of an underlying thin Middle Muschelkalk material made up of clayish and evaporitic rocks, which might have behaved as a basal décollement in the CES. While we have no evidence of this material beneath the Muschelkalk limestones and dolomites, it is likely that the north–south anticlines of the CES are detached on a very thin sequence of Middle Muschelkalk claystone and evaporites. This unit is expected to be relatively thin (around dozens of metres) since it does not crop out in any of the north–south anticlines of the CES.

Summarizing, the whole stratigraphic sequence is an interlayering of competent and incompetent units (see Fig. 3; Millán *et al.* 1994). We use ‘competent’ and ‘incompetent’ in this paper *sensu lato*, that is we make the distinction between rocks that preferentially show discrete localized deformation and those that deform by more general distributed deformation. The stratigraphic sequence is characterized by the presence of at least two ‘incompetent’ levels that can accommodate the deformation by means of flexural slip/flow: the Upper Triassic evaporitic clay (Keuper facies) and the mudstone–siltstone of the Cretaceous–Paleocene transition (Garumnian facies). Although less important, the Guara Fm also presents mechanical heterogeneities with three differentiated depositional sequences (DS’s; Millán 1995): a decametric sequence of sandstone, marl, siltstone and microconglomerate (DS-1), interpreted as a material of low competence; a hectometric sequence of shallow marine platform limestone rich in foraminifera (DS-2; middle competence); and one hundred metres composed of a thin sequence of sandstone overlain by limestone rich in Nummulites and bivalves (DS-3; middle competence). As such, the stratigraphic record of Pico del Águila anticline shows large heterogeneities in terms of

mechanical behaviour which may have influenced the growth and evolution of the structure.

Modelling methodology

Discrete-element modelling

In this work, a two dimensional discrete-element modelling technique (DEM) has been used to test the effect of mechanical stratigraphy and syn-kinematic sedimentation on an idealized stratigraphic sequence. Discrete-element models have become commonly used in the description of the non-linear interaction of a large number of particles (e.g. Donzé *et al.* 1996; Kuhn 1999; Camborde *et al.* 2000; Finch *et al.* 2003; Hardy *et al.* 2009). Unlike continuum techniques, these discontinuum methods use simple particle interactions and, therefore, permit the dynamic evolution of a system to be modelled and observed. It is a technique well-suited to studying problems in which mechanical discontinuities (shear zones, faults, joints, or fractures) are important as it allows deformation involving large (unlimited) relative motion of individual elements, and by definition does not require the complex re-meshing at moderate to high strains that other techniques such as finite-element typically require.

This method treats a rock mass as an assemblage of circular elements (Fig. 4a) connected in pairs by breakable springs or bonds (Fig. 4b). Thus, it is possible to model different mechanical properties (e.g. a stratigraphic sequence) by assigning different values of breaking strains to each pair of elements (cf. Hardy & Finch 2005), allowing us to test the effect of a given mechanical stratigraphy on geometry, fold kinematics and folding mechanisms. As such, the method provides more information than previous kinematic modelling approaches. Furthermore, it allows for easy monitoring of displacement/location of the elements through time. In this way, the displacement path, the kinematic evolution and the strain distribution within the body can be easily tracked at any stage of the modelling.

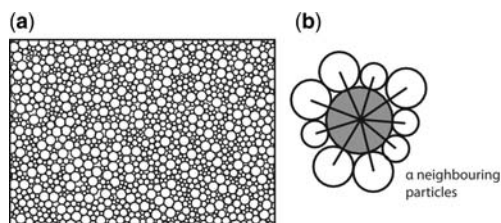


Fig. 4. Illustration of the discrete-element technique used in this work: (a) packing of particles with four different radii; (b) relationship between a given particle (grey shaded) and its neighbours (particles are connected by breakable elastic springs).

Given the competent/incompetent interlayering that characterizes the stratigraphic record (Fig. 3; Millán *et al.* 1994), we believe it to be an ideal method with which to model the Pico del Águila anticline. Finally, while sandbox models can be applied to similar complex boundary conditions, they are not ideally suited to modelling complex stratigraphic sequences and only rarely are model results analysed in a quantitative way to extract, for example, incremental shear strain.

Since this work aims to apply a DEM technique to understand the evolution of the Pico del Águila anticline, only a general overview of the method will be given. For a detailed description of the method as well as its mathematical background, we refer the reader to previous works such as Finch *et al.* (2003) or Hardy & Finch (2005, 2007). This modelling approach treats a rock mass as an assemblage of circular elements that interact in pairs, as if connected by breakable elastic springs. The behaviour of the elements assumes that the particles interact through a repulsive–attractive force (Mora & Place 1993; Hardy & Finch 2005), in which the resultant elastic-interaction force (F_s) between two elements is given by:

$$F_s = \begin{cases} K(r - R), & r < r_0, \text{ intact bond} \\ K(r - R), & r < R, \text{ broken bond} \\ 0, & r \geq R, \text{ broken bond} \end{cases} \quad (1)$$

where K is the elastic constant (spring stiffness) of the bond; R is the equilibrium separation between the particles (i.e. the initial distance); r_0 is a breaking separation that is a breaking threshold; and r is the current separation between particles.

Particles within the model remain bonded until the separation r exceeds the breaking threshold r_0 . From that time onwards, the bond becomes irreversibly broken and the particle pair will not experience an attractive force anymore. However, if the pair of elements return into a compressive contact ($r < R$), a repulsive force acts between them. The force acting on a bond at the breaking threshold is equivalent to the force necessary for a bond to fail (i.e. the stress acting on a particle at failure). Large values of the threshold (e.g. $0.05R$) produce ‘competent’ materials that fail by localized faulting. In contrast, low threshold values (e.g. $0.002R$) produce ‘incompetent’ materials that deform in a macroscopically ductile manner as a result of non-localized deformation (flow) caused by the relative motion of many hundreds of elements.

The total elastic force applied on a particle is the sum of the forces on each bond that links an element to its neighbours. A viscous damping term (proportional to the velocity of the particle) is also included, in order to dampen reflected waves from

the edges of the model. This avoids a build-up of kinetic energy within the system. In addition, gravitational forces are also considered, acting on each element only in the y vertical direction. Particles are displaced to their new positions within the model at each discrete time step, by integrating their equations of motion obeying Newtonian physics and using a velocity Verlet-based solution scheme.

Finally, to avoid any isotropy in the orientation of the strain/displacement fields of the particles (i.e. preferential predefined breaking planes between the particles) the assemblage is composed of particles of different sizes distributed at random. This reduces the likelihood for preferred planes of weakness and allows a non-predefined localization of deformation.

Model setup and experimental parameters

In this work, the method described above is used to test the role of both complex mechanical stratigraphy (Model 1) and syn-kinematic sedimentation (Model 2) in the evolution of the Pico del Águila anticline. The behaviour of the simulated rock mass is broadly elasto-plastic and frictionless (Place & Mora 2001; Finch *et al.* 2003, 2004; Hardy & Finch 2005, 2007), an approach used in previous studies to model the brittle deformation in sedimentary rocks in the upper crust. Deformation of the modelled sedimentary sequence occurs in response to shortening at a subduction slot at the base of the model (a common configuration in sandbox experiments). A velocity discontinuity is created at the subduction slot in the central basal part of the box, in which the right half of the model moves leftwards at a continuous rate of 0.001 m per time step (Fig. 5). A homogeneous rock density of 2500 kg m^{-3} has been used, a typical value of upper-crustal sedimentary rocks. A value of $5.5 \times 10^9 \text{ N m}^{-2}$ is used for the elastic constant (K) in the experiments. Experiments were run for 2 000 000 time steps with output of the assembly every 25 000 time steps (i.e. every 25 m shortening) for Model 1 and every 100 000 steps (i.e. every 100 m shortening) for Model 2. The total displacement in both experiments was 2 km. This provided a precise control on the structural evolution and variation of the strain distribution (Models 1 and 2) and a well constrained geometry of the syn-kinematic sedimentation (Model 2).

Within the modelling framework, one lattice unit (LU) corresponds to 250 m. The initial particle assembly contains 10 245 elements with four different radii of 0.125, 0.1, 0.075 and 0.05 LU (i.e. 31.25, 25, 18.75 and 12.5 m, respectively) distributed at random in an enclosed rectangular box. We believe these dimensions are suitable, since they provide enough resolution to model a kilometric-scale structure like the Pico del Águila

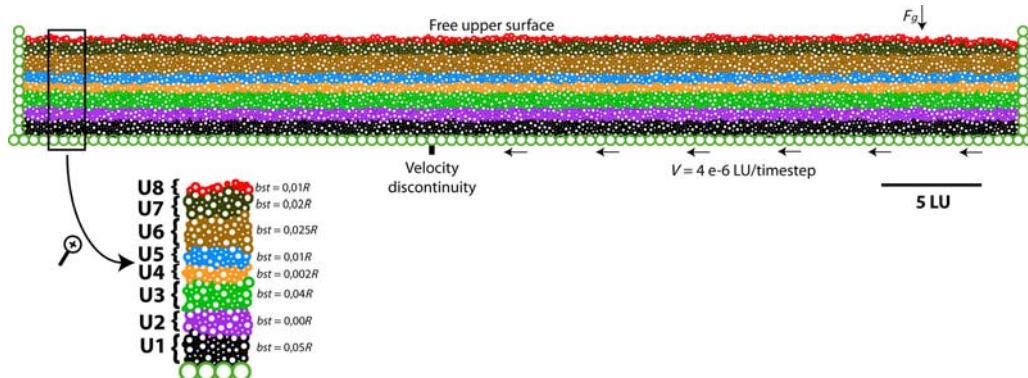


Fig. 5. Initial setup and boundary conditions applied in both Models 1 & 2. The initial assembly contains 10 245 elements with radii of 31.25, 25, 18.75 and 12.5 m, positioned at random in a box that measures 12.5×1.25 km. The assemblage is composed of 32 flat-lying layers that are later grouped in eight units with different mechanical properties. Displacement is increased at 0.001 m/time-step. F_g corresponds to the force of gravity.

anticline, avoiding the generation of preferred planes of weakness and allowing a non-predefined localization of deformation that a homogeneous particle size would imply. After initial generation, the elements are allowed to relax to a stable equilibrium and are left to settle under gravity for *c.* 2 000 000 time steps to obtain a stable, well-packed initial assemblage and to further minimize void space. The resulting initial assembly is 12.5 km long and *c.* 1.25 km thick, simulating a continuous rock mass that can deform by progressive bond breakage (fracturing/faulting) and bulk motion of unbroken pairs of elements (folding). In addition, in Model 2 the syn-kinematic sedimentary sequence was modelled by adding incrementally a total of 11 708 elements.

The initial particle assembly was composed of 32 flat layers grouped into units with different mechanical properties to create a complex mechanical stratigraphy (Figs 3 & 5). We have constructed a mechanical stratigraphy that we believe is suitable to model the behaviour of that observed in the field (see Fig. 3 and Table 1 for a comparison between the sequence in the field and the model), reproducing a complex interlayering of competent/incompetent units as described below (from bottom to top; Fig. 5):

- Unit U1 – Highly competent unit. Five layers. Breaking separation (bst) = $0.05R$
- Unit U2 – Highly incompetent unit. Four layers. bst = $0.00R$
- Unit U3 – Competent unit. Five layers. bst = $0.04R$
- Unit U4 – Incompetent unit. Three layers. bst = $0.002R$
- Unit U5 – Low competence unit. Three layers. bst = $0.01R$

Table 1. Correlation between field and model stratigraphic units

Field units	Model units
Campodarbe	Growth strata
Belsué Atarés	Growth strata
Arguis	Growth strata
Guara DS-3	U7 and U8
Guara DS-2	U6
Guara DS-1	U5
Garumnian	U4
Upper Cretaceous	U3
Keuper	U2
Muschelkalk	U1

- Unit U6 – Medium competence unit. Six layers. bst = $0.025R$
- Unit U7 – Medium competence unit. Four layers. bst = $0.02R$
- Unit U8 – Low competence unit. Two layers. bst = $0.01R$

The mechanical behaviour of the stratigraphy observed in the field is used to guide that of the modelled units. In this sense, U1 simulates the behaviour of the M3 Muschelkalk facies; U2 models Keuper facies; U3 models Upper Cretaceous rocks; U4 models Garumnian facies; U5 models DS-1 of Guara Fm; U6 models DS-2 of Guara Fm; U7 models DS-3 of Guara Fm; and U8 models the top of the Guara Fm. The syn-kinematic materials deposited during shortening of Model 2 are regarded as being highly incompetent (i.e. bst = $0.00R$).

The breaking strain values have been chosen based on the expected mechanical behaviour of each unit guided by field observations (cf. Fig. 2).

Our previous work has discussed in detail the effect of larger and smaller values of the breaking separation (see Finch *et al.* 2003, 2004). Large values of the threshold (e.g. $0.05R$), equivalent to high elastic moduli, produce ‘competent’ materials which fail by localized faulting, whereas low values (e.g. $0.002R$) produce ‘incompetent’ materials which deform in a macroscopically ductile manner as a result of non-localized deformation. It is important to note that we have set up the elements of U1 to be unlinked to the base of the box, in an attempt to reproduce the geological setting of the Muschelkalk dolomites and limestones, which are bounded by two ductile materials: the Keuper evaporitic claystone above and tentatively the unreported thin Middle Muschelkalk claystone and evaporites below: as such the basal décollement is the boundary between U1 and the base of the model. Maps of the shear strain distribution at every stage of the model have also been generated, in order to identify the loci of deformation during shortening. To do so, we have used a free academic version of SSPX[®] developed by N. Cardozo (Cardozo & Allmendinger 2009). SSPX calculates best-fitting strain tensors given displacement or velocity vectors at a minimum of three points in 2D. The shear strain

plots presented here were generated by SSPX using a Delaunay algorithm to construct a mesh of triangles (at the start and end of the considered period) using the centre of each discrete element as a vertex.

Experimental results

Two experiments have been carried out: Model 1 tests the effect of a complex mechanical stratigraphy on fold development; Model 2 explores the additional influence of growth strata. Both experiments have the same initial configuration with the aforementioned mechanical properties.

Model 1: Complex interlayering of competent/incompetent units

In this experiment, we only consider a pre-kinematic sequence with the mechanical properties described above (Fig. 5). The geometry and the shear strain distribution of the model at five stages are shown in Figure 6 and are discussed below.

As expected, the structure starts to grow above the velocity discontinuity. After 4% bulk shortening (500 m; Fig. 6b) an open, gentle fold has

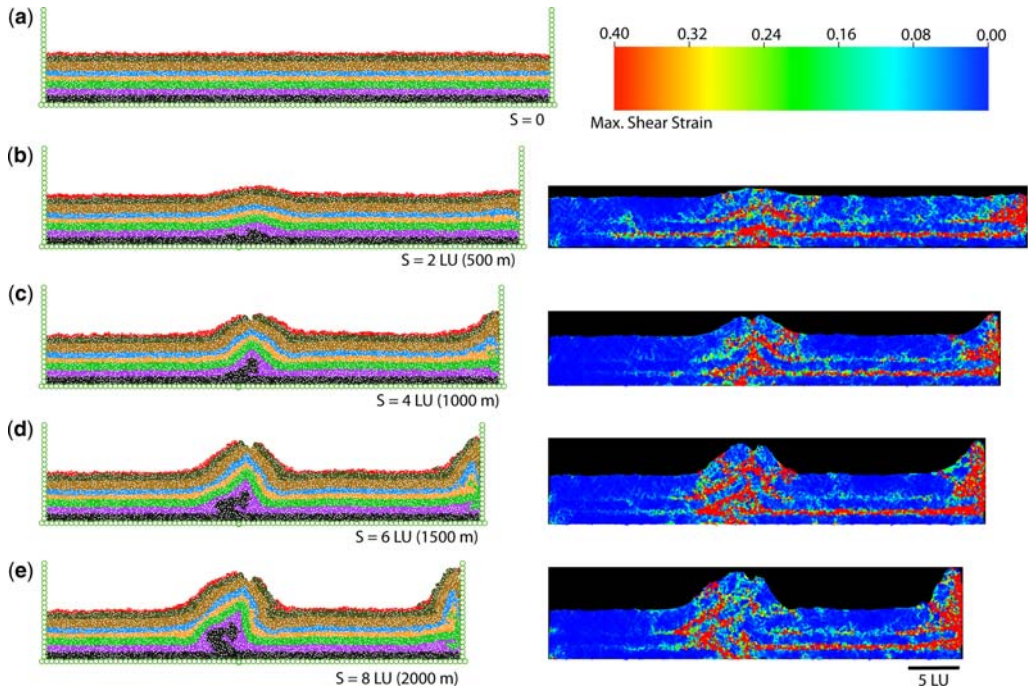


Fig. 6. Evolution of Model 1 shown at: (a) 0 m, (b) 500 m, (c) 1000 m, (d) 1500 m and (e) 2000 m. The left column illustrates the geometrical evolution of the model as shortening continues. The right column shows the distribution of the incremental shear strain at the reported stages. Scale at the top-right of the figure illustrates the range of shear strain considered.

developed: in the lower parts of the stratigraphic sequence it can be seen that a right-dipping fault has developed within U1 in the core of the fold, and that U2 has thickened in both flanks of the structure. In contrast, the upper units U3–U8 display a parallel, open anticline with no thickness variations or faulting. At the right border of the model, a small perturbation/fold has also formed due to the boundary effect of the nearby moving wall and this continues growing throughout the model run. However, it does not propagate from the right edge at any time and remains far from the central detachment fold of interest. The shear strain distribution map shows that shear strain (i.e. faulting) is concentrated in the incompetent units U2 and U4, and in the basal competent unit U1 (Fig. 6b). In U2 and U4 shear strain is continuous and high across much of the model from the right wall to the growing structure and towards the left wall. In the other units (U3 and U5–U8), shear strain is more diffuse and discontinuous. After 8% bulk shortening (1000 m; Fig. 6c) the disharmonic nature of the fold has been accentuated. Units U1 and U2 are now highly deformed, with marked hinge thickening and rightward thrusting of U1 on top of U2. However, above U2 an almost symmetric anticline continues to grow. Normal faulting is now seen in the crest of the structure, particularly in units U7 and U8. As before, U2 and U4 display high shear strain, particularly in the right-hand limb of the structure. In the other units (U3 and U5–U8), shear strain is more diffuse and discontinuous (Fig. 6c). After 12% bulk shortening (1500 m; Fig. 6d) the lower units, U1 and U2, are now complexly deformed. The wavelength of the anticline has increased, and the fold is now asymmetric with slight vergence towards the right. Deformation in U4 (as illustrated by incremental shear strain) is mainly concentrated in the left-hand limb, in contrast to the previous stage. During this stage fold growth is complex: the left-hand limb grows by a combination of limb-rotation and lengthening (this last one due to transport of material into the limb through the bounding synclinal hinge), with evident hinge migration of the left-hand syncline towards the left. Large hinge thickening of the anticline is observed, particularly in U2. On the other hand, the right-hand limb appears to grow mainly by rotation. Stretching in the outer arc persists, as indicated by continued normal faulting in the crestal region (Fig. 6d). Finally, after 16% bulk shortening (2000 m; Fig. 6e), the anticline appears to lock and the right-hand limb shows evidence of rightward thrusting cutting this limb. The right-hand limb is now vertical in U3 and almost overturned in U5. Crestal normal faulting has not developed further, suggesting a cessation of outer arc stretching. However, the hinge and the crestal normal faults have

rotated clockwise (around 10°) with respect to the previous stage. Shear strain is particularly concentrated in the core of the structure (U1 and U2), but also along the limbs in units such as U3 and U5 (Fig. 6e).

The final structure is shown after 2000 m of total (boundary) shortening. At that stage, the central structure had reached the maximum amount of shortening that it could accommodate by folding. However, of this total, only c. 1080 m of shortening were needed to form the central structure. The rest of the boundary displacement is consumed in layer-parallel shortening and in the formation of the right-border structure which in a regional/field sense can be thought of as an earlier or contemporaneous structure.

Model 2: Inclusion of syn-kinematic sedimentation

This experiment explores the effect of the syn-kinematic sedimentation on the structural evolution of a growing fold. The initial setup (Figs 5 & 7a) comprises the same mechanically-interlayered (pre-kinematic) sequence as before. The geometrical and shear strain evolution of this model are shown in Figure 7.

After 4% bulk shortening (500 m; Fig. 7b) a small, low amplitude, structure has started to grow above the velocity discontinuity, as a perturbation with layer-parallel geometry. The incompetent units U2 and U4 exhibit high shear strain in both the structure itself and some distance across the model. Competent unit U1 shows high shear strain and is complexly deformed in the core of the anticline. The other pre-kinematic units only exhibit low shear strain which is slightly accentuated in the fold (Fig. 7b). On the other hand, the growth strata show high but variable amounts of shear strain. However, two types of strain within the growth strata package must be distinguished. Firstly, the shear strain due to the recent deposition and ongoing compaction of the recently deposited units, essentially restricted to the uppermost two layers of the assembly (i.e. the thin horizontal red area at the top of the strain distribution maps; Fig. 7). Secondly, the shear strain exhibited by the growth pile due to shortening and consequent fold development. As in Model 1, a border-effect is generated at the right-hand edge of the model due to the displacement of this wall towards the left. After 8% bulk shortening (1000 m; Fig. 7c), the central structure has grown significantly, its limbs have steepened and now it verges slightly towards the right. Disharmonic folding is now observed in the stratigraphic sequence. Below U4 minor folds have developed, particularly in U2–U4 towards the right-hand edge of the model, and the core of the structure

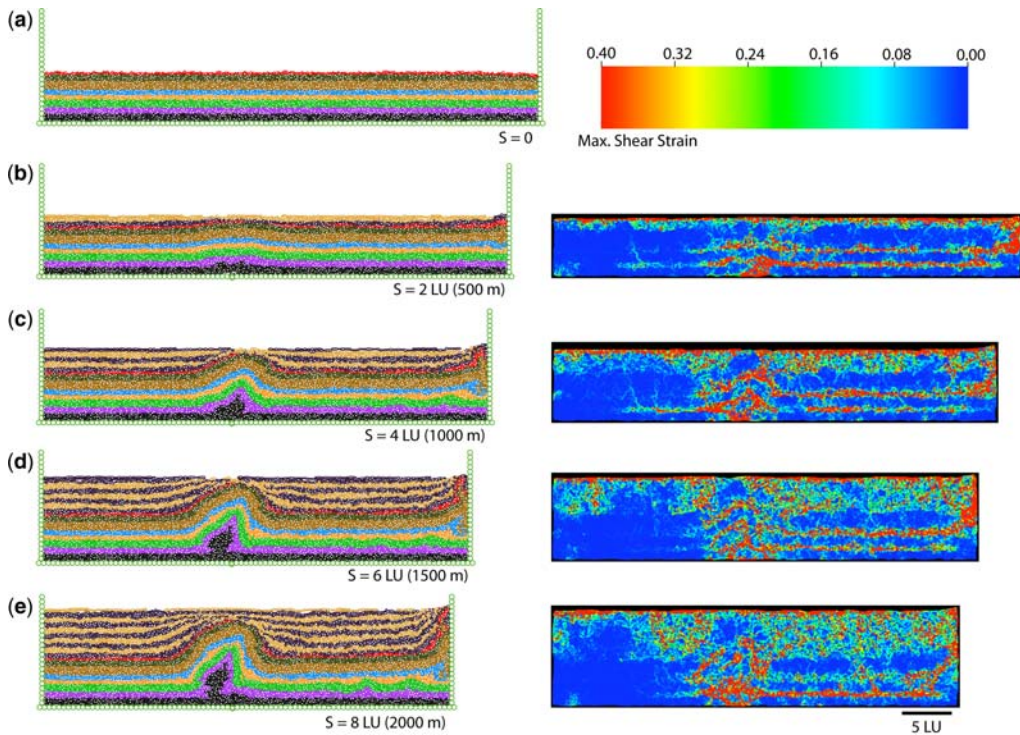


Fig. 7. Evolution of Model 2 shown at: (a) 0 m, (b) 500 m, (c) 1000 m, (d) 1500 m and (e) 2000 m. The left column illustrates the geometrical evolution of the model as shortening continues. The right column shows the distribution of the incremental shear strain at the reported stages. Scale at the top-right of the figure illustrates the range of shear strain considered.

is now becoming complexly deformed in U1. Above U4, the pre-kinematic units define a gentler fold geometry, with no thickness changes or minor folds observed. The syn-kinematic sequence now shows marked thickness variations producing flanking sedimentary wedges which thin towards the crest of the anticline. In contrast to Model 1, no normal faulting is observed in the crest of the structure. Within the growth strata package, moderate to high shear strain is observed and a distinct contrast in shear strain is observed at the base of the growth strata package. After 12% bulk shortening (1500 m; Fig. 7d), thickening of the incompetent units is seen in the hinge of both flanking synclines and the core of the fold becomes highly deformed. In particular, U1 starts to become dramatically deformed, displaying a bottle-neck geometry. Small folds continue to grow in U2 between the anticline and the right-hand model border. Disharmonic folding is observed in the hinge of the anticline, with folding style above and below U4 differing markedly. Shear strain continues to be concentrated within the incompetent units involved in the fold and their continuation towards the right-hand wall.

Growth strata continue to rotate and thin against the growing structure displaying much internal shear strain. At 16% bulk shortening (2000 m; Fig. 7e) the anticline appears to cease to grow upwards (note that growth strata now overlap the structure) with the fold tightening by limb rotation. However, the model shows a shift in the distribution of shortening from the central fold to the right edge, manifested by propagation of folding from the right edge, and giving rise to small décollement folds detached on U2. In the main fold, shear strain continues to be concentrated in the core of the structure, together with shear of the fold limbs particularly in U4 and U5. In the core of the fold U1 is further 'pinched' into a bottle-neck structure. At this stage, the growth strata package is about 1.2 km thick, similar to the one observed in nature at Pico del Águila.

Discussion

The aim of this work has been to test the effect of a complex mechanical stratigraphy and growth strata

on the development of detachment folds and compare the results to the Pico del Águila anticline (Central External Sierras, Southern Pyrenees). This was the primary motivation for this work: in the core of this anticline, field observations and geological mapping suggest a potentially complex structure and only scarce, poor-quality seismic data are available. In addition, outcrop data do not help to reveal much of the structure at depth (Fig. 8). Our objective was therefore to use the discrete element approach to provide new insights into the geometry and evolution of this structure.

In general, the modelling results have proven informative and the approach successful. In particular, model results have highlighted the dramatic change in structural style between units U1–U2 and the overlying stratigraphic sequence. The model results re-emphasize that the structural evolution of a growing fold strongly depends on the mechanical behaviour of the stratigraphic sequence involved. The presence of multiple incompetent levels (U2 and U4 in Models 1 and 2; and, less importantly, the syn-kinematic package in

Model 2), leads to a complex partitioning of shear strain within the stratigraphic sequence. As a consequence, disharmonic folding is seen in both Models 1 and 2.

In both models fold growth started at an early stage above the velocity discontinuity as a nearly symmetric, constant-thickness, open fold with gently-dipping limbs. Further shortening resulted in fold growth by a combination of limb lengthening and limb rotation. This development, however, is not homogeneous throughout the stratigraphic sequence. The upper units above U4 grew mainly by limb lengthening whereas the units below grew mainly by limb rotation. This led to disharmonic folding, as the upper, outer layers dip more gently than the inner ones, which reach vertical and overturned dip values. It appears that folding mechanisms do not solely depend on the mechanical behaviour of a given unit, but they are also driven by its relationship with the immediately adjacent units (i.e. the mechanical contrast between a unit and its neighbours, or brittle–ductile coupling in the sense of Smit *et al.* 2003).

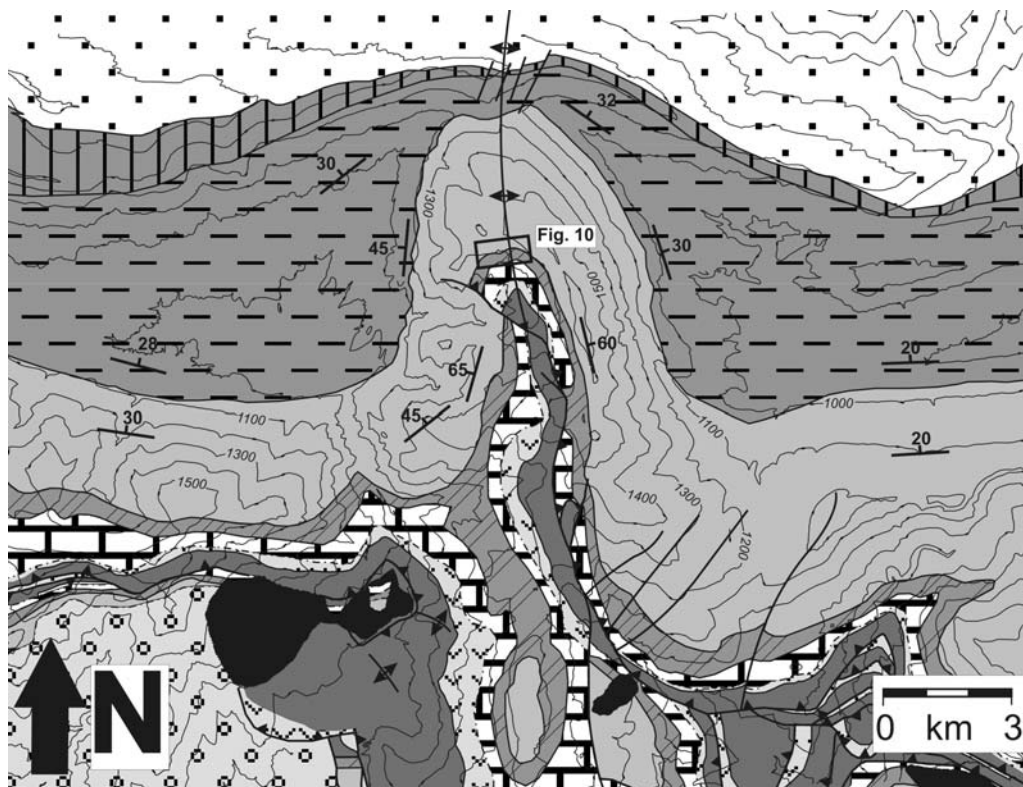


Fig. 8. Geological map of the Pico del Águila anticline (modified from IGME 1992). Notice the geometrical similarities between the model results and the structure in nature: growth strata sedimentary prism, folding in the upper units, and faulting in the lower units. See Figure 1 for legend.

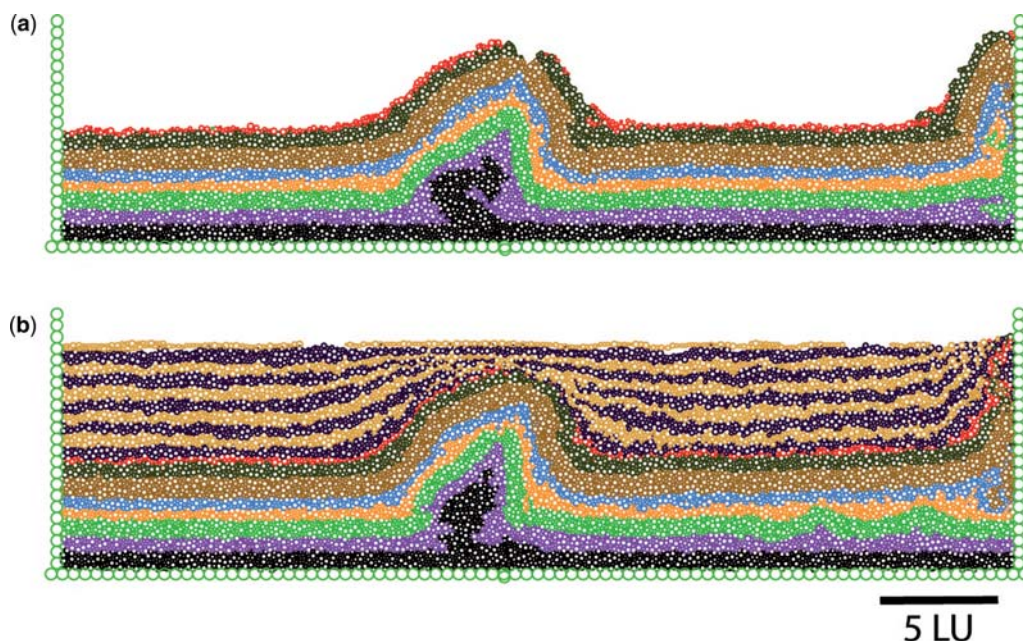


Fig. 9. Final geometries of Model 1 (a) and Model 2 (b) after 2000 m of shortening. Both experiments had identical initial configurations (see Fig. 5) and mechanical properties. However, Model 2 included sedimentation during shortening, producing the observed growth strata pattern.

It is notable that small-scale extensional faulting took place at the crest of the anticline in Model 1 (Fig. 9a). This was mainly due to the stretching produced in the outer layers and to the gravitational instability of the structure produced as its amplitude increased. This effect was diminished in Model 2 as flanking sedimentation took place during shortening and fold growth (Fig. 9b). Since the pre-kinematic outer arc was buried under the growth strata, the syn-kinematic sedimentary load minimized the stretching and supported the fold, reducing any potential gravitational instabilities.

Syn-kinematic materials have been modelled as a mass of cohesionless elements and, thus, have acted as an incompetent level on top of the pre-kinematic sequence. Syn-kinematic materials are thus deformed pervasively, as observed in the shear strain distributions shown in Figure 7. This deformation has been mainly by small-scale folding and distributed faulting. However, due to the additional load, the syn-kinematic pile also influences the deformation within the pre-growth sequence. In other words, this additional load confines the deformation to the core of the structure, which is tighter in Model 2 compared to in Model 1 (Fig. 9), by means of multiple faults and disharmonic folding (see the bottle-neck structure in Fig. 9b). As observed in Model 1 (Figs 6 & 9a), the lack of a syn-kinematic load leads to a fold which is more

open, and which widens with increasing shortening. Summarizing, the effect of syn-kinematic sedimentation in the development of a growing fold is double: firstly, it minimizes stretching in the upper, outer units of the structure; and secondly, it influences growth of the anticline generating a tighter, more complex and upright structure in the inner, lower units.

In both models, it is also noticeable that shortening produces a detachment fold in a stratigraphic sequence in which the basal unit is not a simple, homogeneous ductile unit. Both competent and incompetent units (U1 and U2) are involved and highly deformed in the core of the anticline. The lack of any bonding between U1 and the base of the box (modelling the suspected interaction between Muschelkalk dolomites and the underlying evaporitic clays) as well as the presence of the incompetent U2 above it means that the basal highly competent unit is bordered by two ductile materials and thus it can fold freely.

Most of the features described above have parallels in the Pico del Águila anticline. Given that the anticline plunges towards the north up to 40° , the down-plunge view offered by the geological map can be considered as an equivalent to a cross-section of the structure (Fig. 8), comparable to the results obtained in Models 1 and 2. The stratigraphic record of the area is characterized by an



Fig. 10. Photograph illustrating the disharmonic folding observed in the hinge of the Pico del Águila anticline (see Fig. 8 for location): upper layers showing minor associated folds correspond to the base of Guara Fm, whereas lower highly-vegetated layers correspond to the top of the Garumnian facies.

interlayering of competent/incompetent units (Figs 2 & 3), which appear to have exerted a strong influence on the generation and development of the fold. As observed in Figure 8, a dramatic change in structural style exists between the lower and the upper units: the Muschelkalk-middle Guara sequence is faulted and complexly deformed whereas the overlying upper Guara-Campodarbe sequence is more simply folded. Model 2 (Fig. 9b) has reproduced this behaviour since the U1–U4 sequence is complexly faulted and folded whereas the overlying strata are more simply folded. Such disharmonic folding is observed in the hinge area of Pico del Águila (Fig. 10). Model results suggest a non-concentric geometry for the Pico del Águila, in which some pre-kinematic units (U6, U5 and U3) show minor disharmonic folds in the crest of the anticline whereas U2 does not display such behaviour. An almost identical phenomenon is observed in Figure 10, where Guara Fm shows minor metric folds in the crest of the Pico del Águila, above the Garumnian, which does not exhibit such disharmonic folding. In addition, the geometry of the growth strata bears a striking resemblance to that seen in Model 2, including small scale reverse faulting along the limbs (observed in the field) and very local normal faulting in the crest of the anticline (see Fig. 8). This crestal normal faulting, however, is not well represented in Model 2 since the scale of these faults in the field (*c.* 50 m) is within the order of magnitude of the element sizes used in the models (*c.* 12–31 m).

Summarizing, the modelling indicates that it is unlikely that the complex interplay of parameters occurring in nature can be easily explained in terms

of simple, single folding mechanisms/kinematics. Limb rotation, limb lengthening, faulting, hinge migration, hinge thickening, among others, usually act coevally depending on the mechanical properties of individual units and their stratigraphic position. In addition, this contribution indicates that growth strata, when present during the evolution of a structure, are not just simple passive markers – rather they are mechanically important in the evolution of a structure.

Conclusions

A 2D discrete-element modelling technique has been used to test the influence of complex competent/incompetent interlayering and the presence of growth strata in the generation and development of the Pico del Águila anticline. The model simulates the sedimentary sequence as an assemblage of circular elements that interact in pairs with elastic forces influenced by gravity and obey Newton's equations of motion. The mechanical interlayering leads to high shear strain and complex deformation within the incompetent units, whereas the competent units are subject to more distributed shear strain and simple folding. As a result of the differing mechanical responses to shortening, it is difficult to explain the evolution of such a structure in terms of simple kinematic models. Furthermore, the addition of growth strata reduces the effects of stretching, extensional faulting and gravitational instabilities on the crest of the anticline. Finally, the load of the syn-kinematic package also led the deformation to be more confined to the core of the structure, which is thus tighter than in the case where growth strata are lacking.

We would like to thank N. Cardozo for the free academic use of SSPX to generate the shear strain distribution maps presented in this work. In addition, discussions with Stefano Tavani are gratefully acknowledged. The Group of Geodynamics and Basin Analysis (GGAC) at Universitat de Barcelona is also acknowledged for their support (2005SGR 00397 and 2009 SGR 1198). This research has also been supported by ICREA, StatoilHydro, the Geomod 3D project (CGL2004-05816-C02-01/BTE), the MODES-4D project (CGL2007-66431-C02-01/BTE) and the Geomodels Institute Consortium. O. Vidal-Royo is grateful to Agència de Gestió d'Ajuts Universitaris i a la Recerca (AGAUR) for providing a PhD grant (2005 FI 00200). Dr W. Wallace, Dr S. Castelltort, Dr J. Poblet and Dr R. J. Lisle are gratefully acknowledged for thorough reviews that have definitely improved the quality of this work.

References

- ATKINSON, P. A. & WALLACE, W. K. 2003. Competent unit thicknesses in detachment folds in the Northeastern Brooks Range, Alaska: geometric analysis and a conceptual model. *Journal of Structural Geology*, **25**, 1751–1771.
- CAMBORDE, F., MARIOTTI, C. & DONZÉ, F. V. 2000. Numerical study of rock and concrete behaviour by discrete element modelling. *Computers and Geotechnics*, **27**, 225–247.
- CARDOZO, N. & ALLMENDINGER, R. W. 2009. SSPX: a program to compute strain from displacement/velocity data. *Computers and Geosciences*, **35**, 1343–1357.
- CASAS-SAINZ, A. M., SOTO-MARIN, R., GONZÁLEZ, A. & VILLALAIN, J. J. 2005. Folded onlap geometries: implications for recognition of syn-sedimentary folds. *Journal of Structural Geology*, **27**, 1644–1657.
- CASTELLTORT, S., GUILLOCHEAU, F., ROBIN, C., ROUBY, D., NALPAS, T., LAFONT, F. & ECHARD, R. 2003. Fold control on the stratigraphic record: a quantified sequence stratigraphic study of the Pico del Aguila anticline in the south-western Pyrenees (Spain). *Basin Research*, **15**, 527–551.
- DONZÉ, F., MAGNIER, S. A. & BOUCHEZ, J. 1996. Numerical modelling of a highly explosive source in an elastic–brittle rock mass. *Journal of Geophysical Research*, **101**, 3103–3112.
- FINCH, E., HARDY, S. & GAWTHORPE, R. L. 2003. Discrete element modelling of contractional fault-propagation folding above rigid basement blocks. *Journal of Structural Geology*, **25**, 515–528.
- FINCH, E., HARDY, S. & GAWTHORPE, R. L. 2004. Discrete element modelling of extensional fault-propagation folding above rigid basement fault blocks. *Basin Research*, **16**, 489–506.
- GRANDO, G. & MCCLAY, K. R. 2007. Morphotectonics domains and structural styles in the Makran accretionary prism, offshore Iran. *Sedimentary Geology*, **196**, 157–179.
- HARDY, S. & FINCH, E. 2005. Discrete-element modelling of detachment folding. *Basin Research*, **17**, 507–520.
- HARDY, S. & FINCH, E. 2007. Mechanical stratigraphy and the transition from trishear to kink-band fault-propagation fold forms above blind basement thrust faults: a discrete-element study. *Marine and Petroleum Geology*, **24**, 75–90.
- HARDY, S., MCCLAY, K. R. & MUÑOZ, J. A. 2009. Deformation and fault activity in space and time in high resolution numerical models of doubly vergent thrust wedges. *Marine and Petroleum Geology*, **26**, 232–248.
- HOMZA, T. X. & WALLACE, W. K. 1995. Geometric and kinematic models for detachment folds with fixed and variable detachment depths. *Journal of Structural Geology*, **17**, 475–488.
- HOMZA, T. X. & WALLACE, W. K. 1997. Detachment folds with fixed hinges and variable detachment depth, Northeastern Brooks Range. *Journal of Structural Geology*, **19**, 337–354.
- IGME 1987. *Contribución De La Exploración Petrolífera Al Conocimiento De La Geología De España*. Instituto Geológico y Minero de España. Published report plus maps.
- IGME 1992. *Mapa Geológico De España*. Map 248 (Apiés), Instituto Geológico y Minero de España, Madrid, Unpublished 36 pp report + 1:50 000 map.
- KUHN, M. R. 1999. Structured deformation in granular materials. *Mechanics of Materials*, **31**, 407–429.
- MCÉLROY, R. 1990. *Thrust kinematics and syntectonic sedimentation: the Pyrenean frontal ramp, Huesca, Spain*. PhD thesis, University of Cambridge, UK.
- MILLÁN, H. 1995. *Estructura y Cinemática del frente de cabalgamiento surpirenaico en las Sierras Exteriores Aragonesas*, PhD thesis, Universidad de Zaragoza, Spain.
- MILLÁN, H., AURELL, M. & MELÉNDEZ, A. 1994. Synchronous detachment folds and coeval sedimentation in the Prepyrenean External Sierras (Spain): a case study for a tectonic origin of sequences and system tracts. *Sedimentology*, **41**, 1001–1024.
- MITRA, S. 2003. A unified kinematic model for the evolution of detachment folds. *Journal of Structural Geology*, **25**, 1659–1673.
- MORA, P. & PLACE, D. 1993. A lattice solid model for the non-linear dynamics of earthquakes. *International Journal of Modern Physics C*, **4**, 1059–1074.
- NALPAS, T., GYÖRFI, I., GUILLOCHEAU, F., LAFONT, F. & HOMEWOOD, P. 1999. Influence de la charge sédimentaire sur le développement d'anticlinaux synsédimentaires. Modélisation analogique et exemple du terrain (bordure sud du bassin de Jaca). *Bulletin de la Société Géologique de France*, **170**, 733–740.
- NIGRO, F. & RENDA, P. 2004. Growth patterns of underlithified strata during thrust-related folding. *Journal of Structural Geology*, **26**, 1913–1930.
- NOVOA, E., SUPPE, J. & SHAW, J. H. 2000. Inclined-shear restoration of growth folds. *AAPG Bulletin*, **84**, 787–804.
- PLACE, D. & MORA, P. 2001. A random lattice solid model for simulation of fault zone dynamics and fracture processes. In: MULHAUS, H. B., DYSKIN, A. V. & PASTERNAK, E. (eds) *Bifurcation and Localisation Theory for Soils and Rocks '99*. A. A. Balkema, Rotterdam/Brookfield.
- POBLET, J. & HARDY, S. 1995. Reverse modelling of detachment folds, application to the Pico del Aguila anticline in the South Central Pyrenees (Spain). *Journal of Structural Geology*, **17**, 1707–1724.

- POBLET, J., MCCLAY, K. R., STORTI, F. & MUÑOZ, J. A. 1997. Geometries of syntectonic sediments associated with single-layer detachment folds. *Journal of Structural Geology*, **19**, 369–381.
- PUEYO, E. L., MILLÁN, H. & POCOVÍ, A. 2002. Rotation velocity of a thrust: a paleomagnetic study in the External Sierras (Southern Pyrenees). *Sedimentary Geology*, **146**, 191–208.
- PUIGDEFÀBREGAS, C. 1975. La Sedimentación Molásica en la Cuenca de Jaca. *Monografías Del Instituto De Estudios Pirenaicos. Número Extraordinario De Revista Pirineos*, **104**, Instituto de Estudios Pirenaicos, Jaca.
- SMIT, J. H. W., BRUN, J. P. & SOKOUTIS, D. 2003. Deformation of brittle-ductile thrust wedges in experiments and nature. *Journal of Geophysical Research*, **108**, 2480, doi: 10.1029/2002JB002190.
- SOLER, M. & PUIGDEFÀBREGAS, C. 1970. Líneas generales de la geología del Alto Aragón Occidental. *Pirineos*, **96**, 5–20.
- STORTI, F. & POBLET, J. 1997. Growth stratal architectures associated to décollement folds and fault-propagation folds. Inferences on fold kinematics. *Tectonophysics*, **282**, 353–373.
- STRAYER, L. M., ERICKSON, S. G. & SUPPE, J. 2004. Influence of growth strata on the evolution of fault-related folds: distinct-element models. In: MCCLAY, K. (ed.) *Thrust Tectonics and Hydrocarbon Systems*. American Association of Petroleum Geologists Memoir, **82**, 413–437.
- TAVANI, S., STORTI, F. & SALVINI, F. 2007. Modelling growth stratal architectures associated with double edge fault-propagation folding. *Sedimentary Geology*, **196**, 119–132.

Kinematic retro-modelling of a cross-section through a thrust-and-fold belt: the Western Irish Namurian Basin

DAVID C. TANNER^{1,2*}, FRITHJOF A. BENSE¹ & GABRIELE ERTL^{1,3}

¹*Geoscience Centre, University of Göttingen, Department of Structural Geology and Geodynamics, Goldschmidtstr. 3, D-37077 Göttingen, Germany*

²*Present address: Leibniz Institute for Applied Geophysics, Stilleweg 2, D-30655 Hannover, Germany*

³*Present address: Lower Saxony State Authority for Mining, Energy and Geology, Stilleweg 2, D-30655 Hannover, Germany*

**Corresponding author (e-mail: DavidColin.Tanner@liag-hannover.de)*

Abstract: The Western Irish Namurian Basin (WINB) developed into a fold-and-thrust belt at the front of the northward-propagating Variscan orogenic wedge. Part of this basin is well exposed along the coast of County Clare, Ireland. From a detailed study that used an integrated GPS mapping approach, we produced a c. 50 km long, balanced cross-section, parallel to the tectonic transport vector. We sequentially decompacted and retro-deformed the Namurian strata in 7 stages to evaluate the palinspastic situation of the basin and the amount of shortening. By using passive markers in the model and a highly-detailed timescale, we were able to determine that shortening of the WINB, from the onset of Central Clare Group sedimentation was 7.44% (or 4.07 km) of which shortening due to folding accounts for c. 2.64% (c. 1.37 km), and therefore c. 4.80% (c. 2.69 km) was solely because of thrusting. The rate of horizontal shortening ranges from 1–34 mm a⁻¹; this is within typical orogenic values.

The south-western coast of Ireland, especially the Munster Province, excellently exposes the Irish Variscides and the sediments in front of the orogen (Ford *et al.* 1991; Bresser 2000). In particular, the Late Carboniferous (foreland) basin, mainly exposed in County Clare, has attracted sedimentologists and petroleum industry workers (e.g. Pulham 1989; Collinson *et al.* 1991; Wignall & Best 2000). Most balanced cross-sections that were drawn across the Irish Variscides (e.g. Cooper *et al.* 1984; Ford 1987) did not include the weaker deformed sediments north of the Variscan front, until the position of the front itself was questioned (Klemperer *et al.* 1991; Bresser & Walter 1999). The Namurian sediments of the Variscan Orogen in County Clare are known as the Western Irish Namurian Basin (WINB; Fig. 1; Wignall & Best 2000). It is one of a number of interlinked basins that existed from the southern North Sea to Nova Scotia during the Late Carboniferous (Maynard *et al.* 1997).

In this paper we present new mapping of the outcrops of the WINB using a method consisting of highly-accurate GPS positioning and structural analysis. These data were then used to construct a balanced cross-section of the area, parallel to the tectonic transport vector. In a process we term ‘retro-deformation’, we sequentially backstripped

the sediments and removed folding and fault movement using two restoration algorithms. In this fashion, we were able to follow the change in sediment thicknesses over time (due to decompaction), reconstruct the palinspastic situation of the basin, decipher the folding history (which was coeval with sedimentation), and, using passive markers in the model, determine horizontal shortening rates of deformation.

Geological setting

During the Middle–Late Devonian and probably Early Carboniferous, thick alluvial Old Red sandstone successions (up to 6 km) accumulated in the WSW–ENE-oriented Munster Basin to the south of the study area (in the Counties of Kerry and Cork, Fig. 1). The Munster Basin was a half-graben, controlled by a major ENE-striking basin margin fault to the north at Dingle Bay (Graham 1983; Sanderson 1984; Price 1989; Bresser 2000; Williams 2000), which probably coincides with the Killarney–Mallow Fault (Williams *et al.* 1990; Ford *et al.* 1991; Bresser 2000). North of the Dingle Bay and, therefore outside of the Munster Basin, reduced successions of Old Red Sandstone accumulated (Williams 2000).

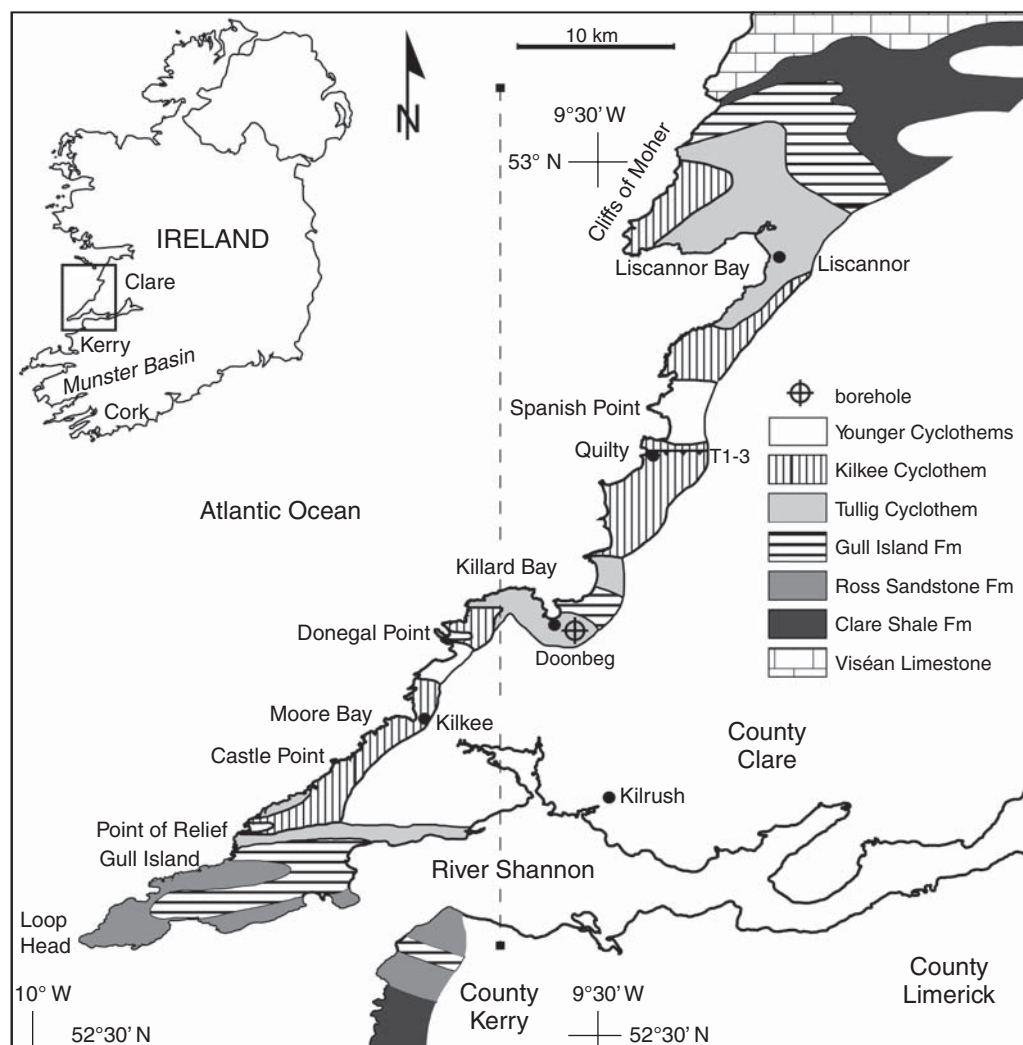


Fig. 1. Geological map of the WINB (after Wignall & Best 2000). Dashed line represents the location of the cross-section in Figure 6. Barbed line marked T1–3 is the position of the Quilty duplex, barbs on the hanging wall.

During the Late Devonian a marine transgression began in the south, advancing further north during the Early Carboniferous (Tournaisian and Viséan). During this time a new basin developed just south of the former and now completely-filled Munster Basin. This new basin was the South Munster Basin and accumulated up to 2.5 km of Culm facies marine siliciclastics (George *et al.* 1976; Clayton & Higgs 1979; Price 1989). Both the Munster and the South Munster Basin probably developed due to heterogeneous stretching during crustal extension of a passive continental margin (Price 1989).

During the Variscan Orogeny, the sediments on the ancient passive continental margin of SE

Laurussia (Old Red Continent), namely the deposits of the Munster Basin (Old Red sandstones), the South Munster basin (Culm facies), the Western Irish Namurian Basin (Tournaisian, Viséan and Namurian siliciclastics), as well as the Munster Shelf (Tournaisian and Viséan limestones), were folded and thrust. Therefore the Irish Variscides, as part of the Rhenohercynian belt of Europe, represent a typical foreland fold-and-thrust belt (Franke 1989; Bresser & Walter 1999; Graham 2001; Sevastopulo 2001; Sevastopulo & Wyse Jackson 2001).

The WINB developed during Early Carboniferous times (Dinantian) as a result of extension and subsidence on the Shannon Lineament (which coincides with the present-day Shannon Estuary,

Fig. 1), and probably represents the Iapetus Suture (Collinson *et al.* 1991; Klemperer *et al.* 1991). It is still unclear whether the WINB began as a foreland flexural basin or an extensional basin (Collinson *et al.* 1991; Wignall & Best 2000). Nevertheless, the deformation of the WINB was a result of the Variscan Orogeny, which occurred during ongoing sedimentation.

Based on biostratigraphical work (Hodson 1954*a, b*; Hodson & Lewarne 1961; Rider 1974) the Namurian successions of the WINB have been subdivided into the Shannon Group and the Central Clare Group (Fig. 2).

The Clare Shale Formation is an up to 180 m thick succession of mudstones (Figs 1 & 2; Martinsen & Bakken 1990). In the region of the Shannon Estuary, goniatite zones from Pendleian

(E1a) to mid-Chokerian (H1b) frame the period of sedimentation (Collinson *et al.* 1991). In the north of County Clare the base was determined as Lower Chokerian (H1a) and the top as base Kinderscoutian age (Fig. 2; Wignall & Best 2000).

There is a controversial discussion whether the Ross Sandstone Fm is a time-equivalent of the Clare Shale Fm (Rider 1974; Pulham 1989) or over-lays the same (Hodson & Lewarne 1961; Wignall & Best 2000). We accept that the latter is the case. The Ross Sandstone Fm comprises centimetre to several metres thick, sheet-like sandstones interbedded with fine layers of silty mudstones (Wignall & Best 2000). It obtains a maximum thickness of 250 m in the area of Loop Head.

The turbiditic deposits of the Ross Sandstone Formation pass into the up to 550 m thick delta

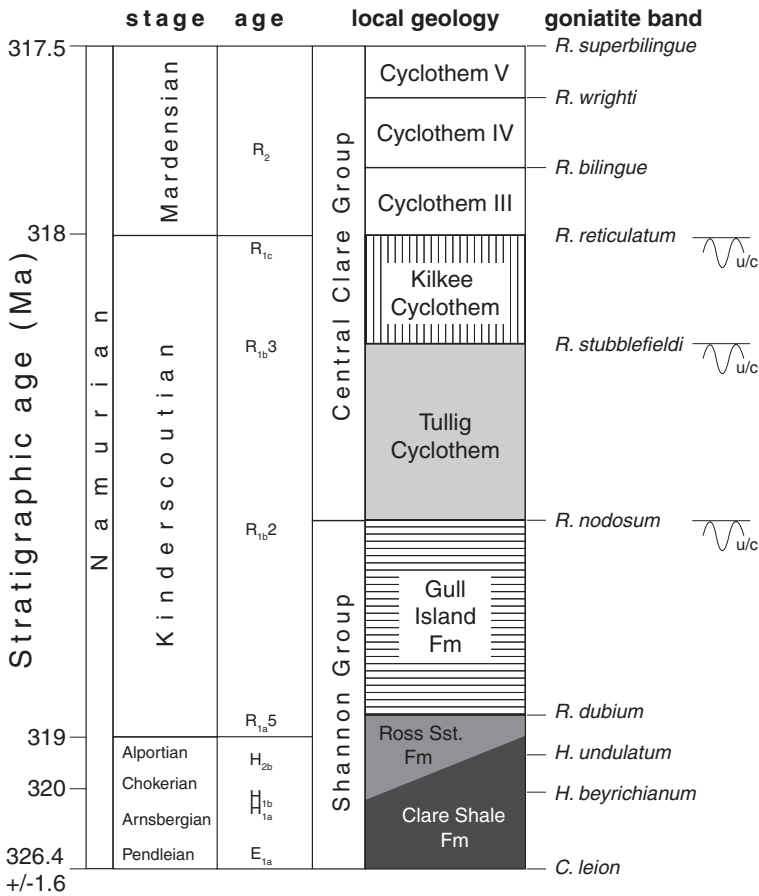


Fig. 2. Stratigraphic overview of the Namurian sediments in the WINB. Note the age scale is not linear. Colours of the geological units are used throughout this work; Cyclothem III–V are combined as Younger Cyclothem. R, Reticuloceras; C, Cravenoceras; H, Homoceras; u/c, unconformity. After Stanislawski *et al.* (2007); stratigraphic ages from Menning *et al.* (2006); local geological names from Pulham (1989).

slope succession of the Gull Island Formation (Fig. 2; Wignall & Best 2000). While turbiditic sandstones persist in the lower 400 m of the formation, siltstones and minor mudstones domain the upper part (Collinson *et al.* 1991). Many of the deposits were highly deformed by soft-sediment deformation (e.g. Fig. 3; Martinsen & Bakken 1990). An unconformity marks the boundary to the Central Clare Group (Fig. 3d).

The c. 900 m thick Central Clare Group consists of five deltaic cyclothems, which were deposited from Kinderscoutian to Marsdenian (Fig. 2). The thickness of each cyclothem is about 100–200, up to 250 m (Rider 1974; Wignall & Best 2000). Note the existence of the unconformities at the base of each cyclothem (Fig. 2). In principle, the whole of the Central Clare Group shows three types of depositional sequences (Pulham 1989). Firstly 25–120 m thick, large-scale, coarsening-upward sequences represent delta-front progradation; secondly 2.5–14 m thick, small-scale coarsening-upward sequences are interpreted as sediments of interdistributary bays, and thirdly up to 70 m thick channel sequences with erosive bases and mainly sandstone infill. Synsedimentary deformation structures (e.g. slumps, slides, mudstone

diapirs and growth faults) within the Central Clare Group are mainly attributed to the fine-grained nature of Namurian strata and the resulting instability (Pulham 1989; Fig. 3). Growth faults appear in this group due to delta progradation (Pulham 1989; Wignall & Best 2000). The top of each cyclothem is marked by the presence of a marine band (Fig. 2).

In the model of Wignall & Best (2000), sediment supply during the Namurian sedimentation was consistently from the south, i.e. Variscan Orogen, and subsidence was always greater in the south (Shannon area). Delta migration in the Tullig Cyclothem was towards the north.

Method

GPS mapping

We collected data in the field with a 12-channel, dual frequency GPS receiver. The dual frequency capability of the receiver meant both L1- and L2-carrier phases, as well as the L1 C/A code, could be received (United States Naval Observatory 2008). In addition, an external antenna was used to increase the performance of the receiver. Digital

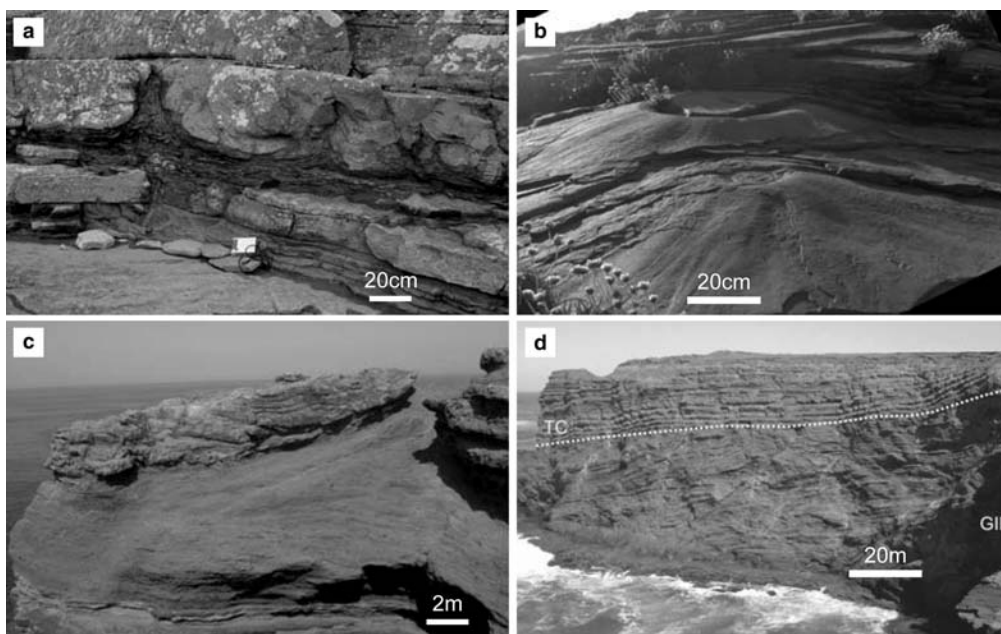


Fig. 3. Evidence of sediment overpressuring and synsedimentary deformation. (a) Shale dykes in sandstone, Killard Bay, Tullig Cyclothem (view west). (b) Sand volcanoes, Liscannor Bay near Green Island, Kilkee Cyclothem (view east). (c) Shale diapir, Moore Bay, Younger Cyclothem (view north). (d) Unconformity between the intensely-deformed Gull Island Fm (GIF) and the overlying undeformed Tullig Cyclothem (TC), Point of Relief, (view north).

data recording was achieved using a field computer with field acquisition software. After post-processing, 97.5% of all data had a vertical and horizontal accuracy between 1–5 m.

An input mask was created with the field acquisition software that allowed the user to first specify the type of geological object, for example, bedding surface, unconformity, and so on. Depending on this choice, the user is then asked to enter particular data for that location. For instance, with bedding data, the user is prompted to enter the stratigraphic unit, and dip direction and dip of the bedding. The software then saved the geographical position and the structural data to a text file.

There were two main types of data: point and line data. For the former, the user entered new data for each locality. This was used mainly for discrete data such as bedding traces, slickenside localities, and so on. For the latter, the type of geological object was first specified and then the GPS device was taken over, for example, a bedding surface, while the GPS registered the position every second, in such a way that the surface was covered by an irregular grid of points. This method was used wherever appropriate, because it enabled a direct three-dimensional image of the geological object to be produced.

Data projection

We collected data from a total of 276 outcrops. All data were manipulated in the first instance by scripts written in the Python programming language (Python Software Foundation 2010). Line files were directly converted into GOCAD 'point sets' (Association Scientifique pour la Géologie et ses Applications 1997), and then converted into surfaces made of irregular triangles, to visualize the structure and for further analysis. Point data were projected first in the strike and then in the dip directions, by a distance set by the user and the file saved as a GoCAD 'point set'. The projection distances were preferably recorded in the field to avoid inaccurate model building. In this fashion, three-dimensional surfaces were generated for all the data of the outcrops analysed.

From the kinematic data, for example slickenside lineations, we determined that the transport direction of the WINB was north–south (Fig. 4a). Furthermore, we also determined in the field and in the model that the folds were cylindrical and that fold axes plunge statistically horizontal (Fig. 4b). Because we assume that all the folds are cylindrical, we were able to project all the outcrop data along a horizontal, east–west vector onto a north–south striking cross-section. This means that data had to be projected over a maximum distance of *c.* 15 km onto the cross-section (Fig. 1).

Cross-section construction

The cross-section was constructed using the 'Busk method' (Busk 1929), which is applicable to folded terrains, especially for parallel folds (Ramsay & Huber 1987), and the 'dip domain method', which is more appropriate for kink fold geometries. In the WINB, the Ross Sandstone Fm, with its thick sandstone beds, is folded in box folds, whereas folds within higher stratigraphic units form parallel folds (Fig. 5). Therefore we constructed the

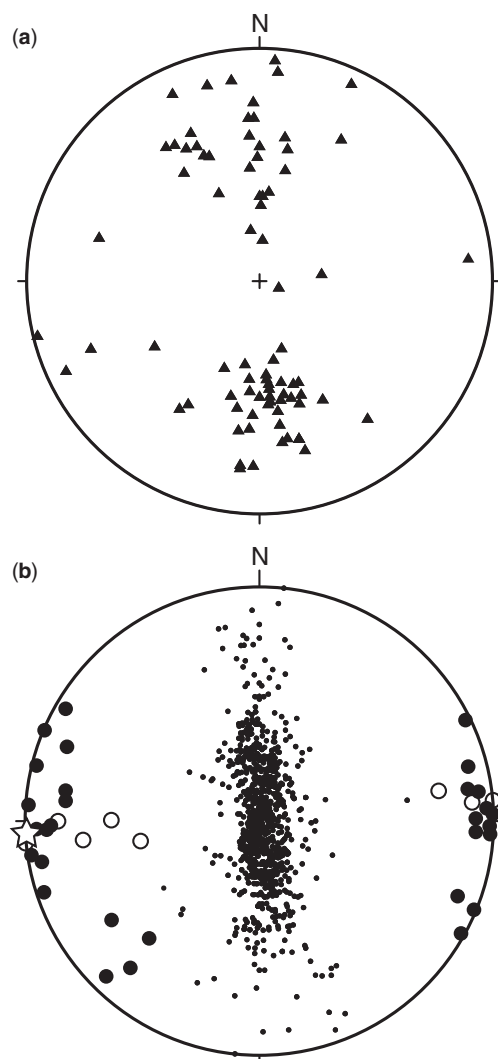


Fig. 4. Lower hemisphere, equal-area stereonet projections of (a) all slickenside lineations ($n = 81$), (b) poles to all bedding planes (small full circles, $n = 1048$), folds axes measured in the field (open circles, $n = 7$) and those constructed in GoCAD (full circles, $n = 30$) and minimum eigenvector of bedding plane poles (star).

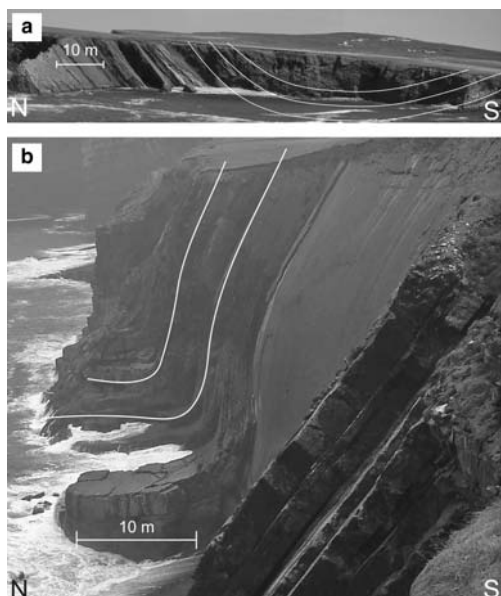


Fig. 5. Comparison of folding styles, as seen in the field. (a) Open, parallel syncline within the Younger Cyclothem (north of Point of Relief, see Fig. 1 for location), (b) Southern flank of a synclinal box fold in the Ross Sandstone Fm (Loop Head, see Fig. 1 for location).

cross-section using the dip domain method for the Ross Sandstone Fm and the Busk construction for higher units. We believe that geometrical differences between the folds were accommodated by the Gull Island Fm, which is very pelitic, especially in the upper half (see Geological Setting section). This leads mainly to thinning of the Gull Island Fm in the limbs of the folds.

It is important to note that we had to deviate from the Busk method in two ways. Firstly, a number of unconformities were measured in the field; these data were used to construct the unconformities in the modelled section (this is the particular case of the Gull Island Fm/Tullig Cyclothem and

Kilkee/Younger Cyclothem contacts, see Fig. 2). Secondly, where a formation was exposed at the surface its thickness could be determined. All of the formations vary greatly in thickness and this variation was incorporated into the section. The Busk construction explicitly produces cross-sections with beds of constant thickness, so that we could only truly use the method in small segments. In segments where the thicknesses changed greatly, the section was drawn by hand, keeping as close to the Busk solution as possible. One borehole (Doonbeg, see Fig. 1; Sleeman & Pracht 1999; Bresser 2000) was also used to build the cross-section.

In the vicinity of Quilty (Fig. 1), the structure is such that it was impossible to achieve a balanced cross-section without a duplex (described from now on as the Quilty Duplex) which consists of three thrust faults (Fig. 6), which reach down to a detachment in the basement at around 2.5 km depth. A similar solution was chosen by Bresser (2000).

Retro-deformation

We used two tools in Move 2008.1 (Midland Valley Exploration Ltd 2008) to retro-deform the model; fault-parallel flow (FPF) to restore displacement on faults and flexural-slip unfolding (FSU) to restore folding (e.g. Tanner *et al.* 1998, 2003). FPF is often used in compressional settings, especially over (fault-bend fold) ramp structures (Suppe 1983; Savage & Cooke 2003). FSU is applicable in this case because we recognized slickenside lineations on bedding surfaces in the field, perpendicular to the fold axes (Fig. 4), which are indicative of flexural slip.

FPF is a relatively newly-developed algorithm for moving beds along fault surfaces (Egan *et al.* 1999). The node points of beds are fixed such that they can only move along flow planes that are parallel to the fault surface and in the plane of the tectonic transport vector (Tanner *et al.* 2003). Bed length and thickness are not maintained as beds pass over

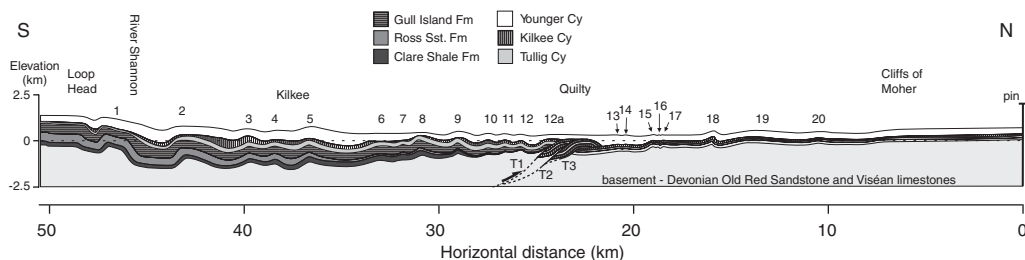


Fig. 6. The constructed cross-section through the WINB. Anticlines are numbered for further reference. Dashed line is sea-level.

angular changes in the fault surface, but this can be corrected by bed-parallel shear (Tanner *et al.* 2003).

The FSU algorithm is designed to unfold a three-dimensional surface (Griffiths *et al.* 2002). Unfolding is carried out away from a foreland pin, in a particular kinematic direction (typically perpendicular to the fold axis). The advantage of this method is that passive surfaces can also be included, so that unfolding the template bed removes the same amount of deformation from the passive surfaces, while maintaining bed thickness. Thus the method lends itself to incremental retro-deformation (Griffiths *et al.* 2002). Bed length is maintained in the kinematic transport direction, even if bed thicknesses vary (Griffiths *et al.* 2002). For this work, the kinematic direction was southwards, perpendicular to the typical fold axes (Fig. 4).

Decompaction

As sediments are covered by new sediments, they are subject to gravitational load (Allen & Allen 1990). This causes compaction of the underlying sediments by loss of pore volume (i.e. porosity), which occurs mainly by water expulsion. In general, the rate of porosity loss (and therefore gain in rock density) with increasing depth follows a negative exponential curve (Athy 1930; Sclater & Christie 1980). According to these authors, the porosity of a rock at depth (Φ) is equal to its initial porosity (Φ_0) multiplied by the exponential to the negative power of the depth coefficient (c) multiplied by the depth (in kilometres).

Decompaction is the reverse process to compaction. The top bed is removed and the thicknesses of the underlying beds are modified according to their new depths. Move 2008.1 applies decompaction by appropriating c and Φ_0 values to stratigraphic units. After backstripping the top bed, the other beds are adjusted using ray tracing to find their new porosity and therefore new bed elevations and thicknesses.

Porosity data were not available from the Doonbeg borehole or other Irish Namurian strata, so we estimated the percentages of sand, silt and clay in the different geological units in the field. By combining these data with typical values for the same lithologies from the North Sea (from Sclater & Christie 1980), we estimated values of c and Φ_0 for the WINB strata (Table 1). The Tullig, Kilkee and Younger Cyclothem all gave such similar estimates that they were given the same values. Figure 7 shows these data plotted as porosity/depth curves. One can see that clay-rich units, such as the Clare Shale, have high starting porosities, but lose porosity quickly with depth, whereas the opposite is true for the sand-rich Ross Sandstone Fm. The other curves fall between these end-members.

Table 1. Derived decompaction parameters for the different units

	CS	RS	GIF	TKY
Initial porosity Φ_0 (%)	63.0	53.9	58.8	55.0
Depth coefficient c (km ⁻¹)	0.51	0.35	0.44	0.38

Abbreviations: CS, Clare Shale Fm; RS, Ross Sandstone Fm; GI, Gull Island Fm; TKY, Tullig, Kilkee and Younger Cys.

To model the overpressuring of the sediments, evidence of which was seen in the field (see above, Fig. 3), we gave zero c values to all beds in the last step before decompaction. This is represented as the zone of no water expulsion in Figure 7.

Horizontal and vertical displacement analysis

We placed markers (spheres of 30 m diameter) on the crests and troughs of folds on each layer in the model (a total of 246 markers). These markers were passively retro-deformed with the model. The centre coordinates of the markers were then used to evaluate the horizontal shortening of the section and as triplets to determine individual fold amplitude variations.

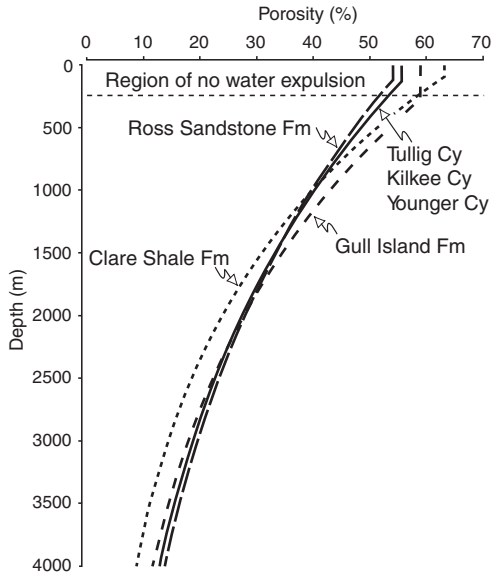


Fig. 7. Graph of modelled sediment porosity against depth for decompaction. See text for method. Region of no water expulsion is where sediments cannot lose water and therefore their porosity remains constant (see text for details).

Results

Figure 6 shows the present-day cross-section through the WINB. Note the onlapping of the beds and the unconformities. Note also how the Younger and Kilkee Cyclothems thin and thicken above anticlines and synclines, respectively, which is indicative of syntectonic sedimentation. The hinterland-dipping duplex around the town of Quilty comprises three thrusts. The roof thrust is developed at the top of the Kilkee Cyclothem. Thrusts T2 and T3 merge at a depth of 1 km. Both thrusts 1 and 2 emerge from a basal detachment, which we presume to be situated in pre-Namurian successions and is not shown in the model. Both southern thrusts have single ramp geometries. They step up with maximum angles of 45° and 41° (T1 and T2, respectively). The footwall of the youngest and northernmost thrust T3 has a flat-ramp-flat structure (dips: 19° – 37° – 4°). On T2, the hanging wall ramp has overridden the footwall flat.

Fold shape ranges from kink geometries (*sensu* Woodward *et al.* 1989) in the south to concentric in the north; the transition is around anticline 3–5 (Fig. 6). In addition, as pointed out in the Method Section, folds in the Ross Sandstone Fm are box

folds while folds above the Gull Island Fm are parallel, open folds (Fig. 5). This information was incorporated into the cross-section, with geometrical differences accommodated within the Gull Island Fm, which is very pelitic. Fold interlimb angles vary from 65 – 160° in the Ross Sandstone Fm to 120 – 170° in the Younger Cyclothems.

Figure 8 demonstrates the cross-section at various stages of retro-deformation back to the commencement of deposition of the Gull Island Fm. The stages of retro-deformation are listed in Table 2. Typically the top of a formation was first unfolded, then the formation (and the layers below) were decompacted and backstripped, and finally removed. Note that although each top layer is unfolded, the lower formations remain partly folded. This is evidence of the syndimentary nature of the deformation. It is not an artifact of the restoration algorithms, because bed thickness is maintained during FSU, even if the bed thicknesses vary over the fold (Griffiths *et al.* 2002), nor is it due to the cross-section construction. At Donegal Point (Fig. 1), for instance, we directly observed Younger Cyclothem beds unconformably onlapping onto the Kilkee Cyclothem. The unconformity is due to open folding of the Kilkee

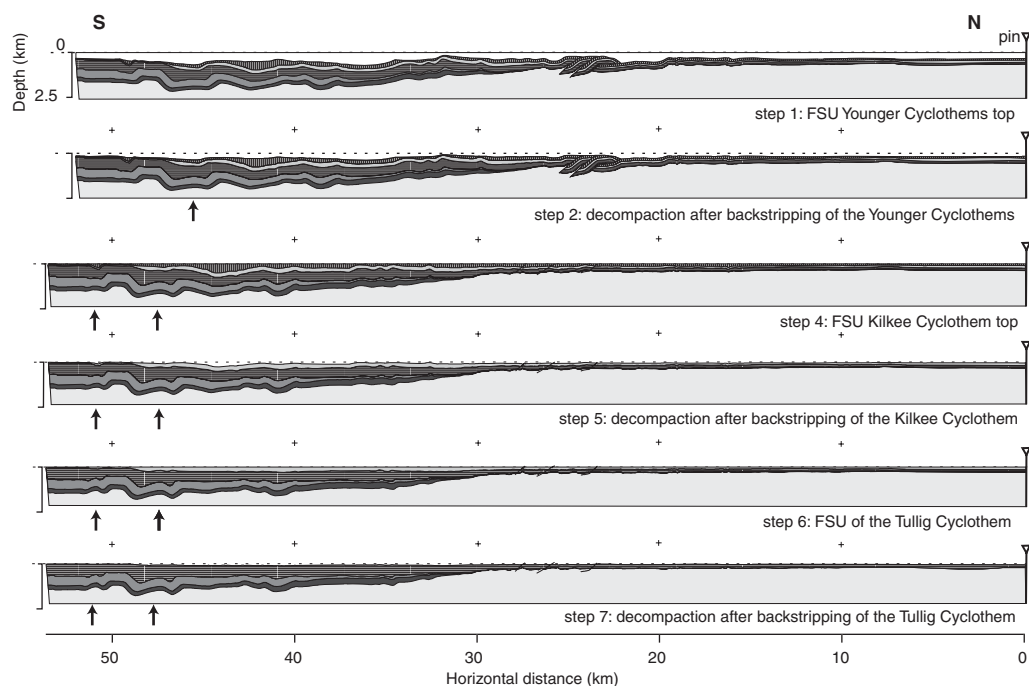


Fig. 8. Cross-sections after the retro-deformation steps 1–7, as listed in Table 2. Some steps are not shown for clarity of the figure. Patterns and colours are as in Figure 6. FSU, Flexural slip unfolding. Arrows point to spurious folds that occurred during the retro-deformation as a result of geometrical differences between folds above and below the Gull Island Fm.

Table 2. *Retro-deformation stages*

No.	Stage	Method
1	UF Younger Cy	FSU
2	BS Younger Cy	D
3	R Quilty Duplex (T1–3*)	FPF
4	UF Kilkee Cy	FSU
5	BS Kilkee Cy	D
6	UF Tullig Cy	FSU
7	BS Tullig Cy	D

*Displacements: 690, 940 and 1280 m, respectively.

Abbreviations: FSU, flexural slip unfolding; FPF, fault parallel flow; UF, unfolding; BS, backstripping; R, restoration; D, decompaction; Cy, cyclothem.

Cyclothem, which is not apparent in the upper cyclothem, that is, these are growth folds (in the sense of Suppe *et al.* 1992). The onlapping is not laterally extensive, but illustrates ongoing folding during deposition.

It should be noted that our method of cross-section construction, in particular the use of two construction methods, caused some additional folding artifacts to occur during the restoration (see Fig. 8; arrows). This effect is only apparent south of anticline 2. As this is a result of the geometry of the Gull Island Fm, we only show the effect of retro-deformation down to stage 7, that is, backstripping of the Tullig Cyclothem.

During the retro-deformation, we measured the wavelength of folds, that is, the wavelength of the fold before limb rotation took place, at the stage at which they had just begun to develop (Fig. 9). The result shows that initial wavelength decreases almost linearly from south to north, as far as the Quilty Duplex, after which it increases again toward the north.

The initial thicknesses of the sedimentary formations, based on the retro-deformation and

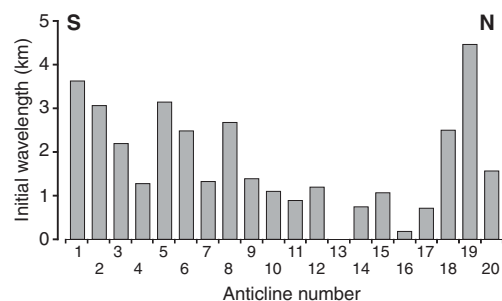


Fig. 9. Wavelengths of anticlines since Gull Island Fm deposition, as determined at the stage of retro-deformation at which the fold began to develop, measured at the Base Gull Island Fm horizon. Anticline numbers are as shown in Figure 6.

decompaction, are shown in Table 3. For thick, clay-rich formations, such as the Gull Island Fm, decompaction resulted in over 50% gain in thickness. Because many of the formations, especially the Ross Sandstone and Clare Shale Formations, thin towards the north, the thickness changes are further pronounced by decompaction (see Fig. 8).

By following passive particles within the model over time, from Gull Island deposition onwards (see Method section), we were able to calculate the precise vertical evolution of fold limbs. Three examples are shown in Figure 10. Typically, folding began with fold limb rotation, as shown by the acceleration of the markers after the onset of vertical movement. This is in agreement with the theoretical models of Hardy & Poblet (1994). Fold limbs always developed symmetrically at first, but asymmetry occurs in some folds at a later stage (Fig. 10).

The finite horizontal orogenic shortening values of the WINB section for each layer of the model, calculated from retro-deformation, are shown in Table 4. The increase in shortening over time is clear evidence of progressive shortening. Furthermore, the large increase in shortening at the boundary between the Kilkee and Younger Cyclothem shows that this is when major shortening occurred with respect to the whole section.

From the restoration back to Base Tullig Cyclothem, we obtained a shortening value of 7.44% (or 4.07 km). Shortening due to folds accounts for *c.* 2.64% (or *c.* 1.37 km), and therefore shortening of *c.* 4.80% (or *c.* 2.69 km) is solely due to thrusting. We were able to separate these values because thrusting was removed in a different step to folding. Using FPF, we were able to remove displacement on the thrusts and most of the fold-bend related folding above the thrust ramps, before the section was unfolded with FSU. Therefore, the value for thrust-related shortening includes fold-bend fold shortening.

A number of authors have concerned themselves with structural models of the Irish Variscides (Cooper *et al.* 1984, 1986; Ford 1987; Le Gall 1991; Bresser & Walter 1999; Bresser 2000), however only two works have included the WINB. Le Gall (1991), from his modelling of seismic offshore data, estimated 15% shortening within the area from Ballybunnon (in County Kerry) to the Cliffs of Moher. Bresser & Walter (1999), from a more detailed structural model, but on the scale of the whole Irish Variscides, calculated 11.5% shortening for the section north of the Killarney–Mallow Fault (in County Kerry), which includes the more highly deformed rocks of County Kerry. Nevertheless, this value of shortening correlates well with our results.

The process of retro-deformation, in combination with an exact timescale (Fig. 2), also allowed

Table 3. *Finite change in thicknesses (Δ_t) of the geological units after decompaction*

	t_0 (north)	Δ_t (m)	Δ_t (%)	t_0 (south)	Δ_t (m)	Δ_t (%)
Younger Cy	375	–	–	334	–	–
Kilkee Cy	91	9	11	30	5	20
Tullig Cy	130	7	6	66	26	65
Gull Island Fm	154	46	43	643	106	20
Ross Sandstone Fm	<20*	c. 5*	c. 20*	590	116	24
Clare Shale Fm	<20*	c. 16*	c. 60*	350	139	66

*Approximate values because of the error involved when measuring small distances.
 t_0 is thickness of the unit before decompaction.

a detailed examination of the horizontal shortening rate over time (Fig. 11). Clearly the major pulse of shortening took place between 318.6 to 317.5 Ma, mostly by displacement on the Quilty Duplex; but this was also the peak time of folding (Fig. 8). At c. 318.6 Ma shortening by folding began at c. 1 mm a⁻¹, which rose to 30 mm a⁻¹ during peak deformation (Fig. 11). This higher shortening rate is defined by seven stratigraphic time markers, so that we are sure of this rate being attained for less than 0.5 Ma.

Figure 12 shows the lateral distribution of the horizontal shortening through the cross-section, as derived from the passive markers. In this figure, two observations can be made; firstly, the greatest acceleration of displacement vectors occurs between 318.25–317.75 Ma, and secondly, a line can be drawn that divides displaced from undisplaced markers. This represents an incremental ‘deformation front’, which migrated from south to north over time (Fig. 12).

Discussion

Error estimates

Errors can occur during data measurement, the construction of the cross-section, and during modelling. Inaccuracy caused by measurements was negligible due to the use of a highly accurate GPS device. The

greatest sources of errors in construction were consequently avoided. We projected 1024 bedding data. However, due to the fact that exposure is only present along the SW–NE trending coast, we had to project the structural data onto the cross-section (over distances of up to 15 km). This is probably the highest source of error. Although the east–west projection is geometrically valid (see previous section), small deviations from perfect fold cylindricity would mean data would be laterally transposed. Wignall & Best (2000) estimated regional erosion of about 30 m by erosive surfaces. This amount of error is acceptable and negligible for a cross-section of c. 60 km length.

We noted that spurious folds occurred during the restoration due to our construction of box folds in the Ross Sandstone Fm, but parallel folds in higher stratigraphic units. Our emphasis in the cross-section construction was to maintain fold geometries as seen in the field. We believe that geometrical differences in the folds were accommodated by the pelitic Gull Island Fm. This implies that material was moved towards the fold hinge during folding. The FSU algorithm is not able to cope with this, so that extra ‘folds’ are left after restoration (Fig. 8). We considered this more appropriate than constructing the folds in the Ross Sandstone Fm in an incorrect manner. This meant that we were only able to correctly restore syn-sedimentary folding back to the Gull Island Fm.

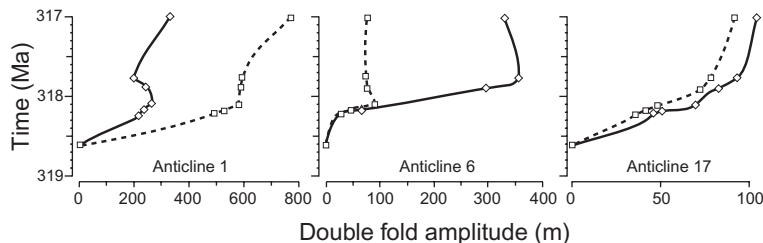


Fig. 10. Vertical development of three anticlines over time, since Gull Island Fm deposition (anticline numbers as in Fig. 6), measured at the Base Clare Shale Fm horizon. The dashed and solid lines are the northern and southern limbs of the folds, respectively.

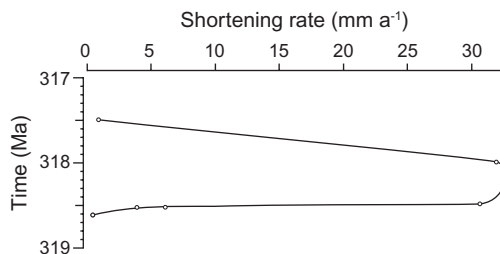
Table 4. Finite shortening values (%) for each layer

Horizon	Shortening* (%)
Younger Cy. Top	1.1
Younger Cy. Base	6.6
Kilkee Cy. Base	7.2
Tullig Cy. Base	7.4

*Includes shortening due to spurious folds (see Fig. 8).

During modelling, the passive markers generally account for an error less than 30 m due to their size. Mismatches at the cutoffs of the duplex after retro-deformation were less than 20 m, which were due to the construction of the model and strain during FPF over the thrusts. This is less than 2% of average displacement on the thrusts, and therefore it is negligible compared with other errors. From Figure 8, one can see that the loose pin at the southern end of the model is sheared by *c.* 3° anticlockwise by the first stage of FSU and by approximately a further 2° anticlockwise by step 4, that is, due to FPF retro-deformation of the Quilty Duplex. Further stages do not produce noticeable effects. The former effect is mainly due to the large unconformity between the Younger and Kilkee Cyclothems. The latter effect is due to (shear) strain being passed on to the hinterland during FPF, and occurs because there are more positive than negative angular changes in ramp angle (e.g. Tanner *et al.* 2003). Both effects cause overestimation of the shortening values by a maximum of 130 m for the Kilkee Cyclothem (compared to those obtained for the underlying stratigraphic units), or less than one quarter of a percent.

Decompaction values (i.e. *c* and Φ_0) in this model were derived from lithological values ostensibly used for the North Sea sediments (Sclater & Christie 1980). These authors show that their porosity curves for shale are also close to those obtained

**Fig. 11.** Horizontal shortening rate of the cross-section over time.

for shales on the east coast of USA and the Gulf coast, but steeper than those obtained for shales in Oklahoma and Venezuela. Similarly, sandstone values were close to those obtained from Louisiana. Williams (2000), in his modelling of the Munster Basin, SW Ireland, used decompaction values for shale, silt- and sandstone that are within $\pm 2\%$ of our values. This would change the values in Table 3 by a maximum of $\pm 5\%$, for example, the finite change in thickness of the Gull Island Fm (north) was 106 ± 5 m. During decompaction, we restored the particular template surfaces to sea-level (0 m), which is a real scenario for sedimentation of the beds of an overfilled molasse stage, but may not be for an underfilled flysch period. Water depth during this critical phase is still in discussion (see Wignall & Best 2000).

Comparison with other foreland and thrust and fold belts

Compared with other foreland basins that have undergone shortening and deformation, it is apparent that although the WINB was subject to comparatively very little shortening, the rate of shortening was high, especially during thrusting (Table 5). This is even more surprising because the WINB is

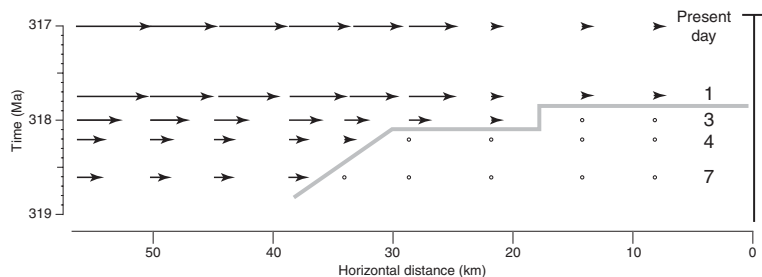
**Fig. 12.** Horizontal displacement of nine passive markers in the cross-section (at base Clare Shale Fm) over the seven stages of retro-deformation (Table 2). Circles represent displacements of less than the measurement error (*c.* 100 m). Grey line represents the incremental deformation front (see text). Stage numbers (see Fig. 8 and Table 2) are on the right-hand side of the figure in the column next to the pin line.

Table 5. Comparison of shortening rates from different fold-and-thrust belts (FTB)

FTB	Shortening rate (mm a ⁻¹)	Method	References
Altiplano and Eastern Cordillera	Max 8	SB	Elger <i>et al.</i> (2005)
Andes	c. 8–10	SB/SR	McQuarrie <i>et al.</i> (2005)
Barrême Basin (Alps)	0.003–0.2	SR	Artori & Meckel (1998)
	Average 0.03		
Bolivian Subandes	>1.5	3D-SB	Hinsch (2001)
Central Apennines	5.3 (±1)	SB (thick-skinned)	Tozer <i>et al.</i> (2002)
Central Apennines	24.6 (±5)	SB (thin-skinned)	Ghisetti <i>et al.</i> (1993)
Eastern Pyrenees (Aquitaine Basin)	Min <0.5	SB	Mascle & Puigdefabregas (1998)
	Max >4.5		
East Carpathian foredeep	c. 20	Elastic thin-plate model	Leever <i>et al.</i> (2006)
Pyrenees (Ebro Basin)	>4	SR	Vergés <i>et al.</i> (1998)
Hellenides	c. 1	SB	Sotiropoulos <i>et al.</i> (2003)
Himalayan front	14 (±2)	SB	Powers <i>et al.</i> (1998)
Pindos FTB, Greece	c. 6	SB	Skourlis & Doutsos (2003)
Pyrenees	2.4	SB	Muñoz (1992)
Taiwan	11–82	GPS	Yu <i>et al.</i> (1997)
Tian Shan	3.3 (max. 4.4)	MC	Chen <i>et al.</i> (2002)
WINB	Max 34	SR	This study
Zagros fold belt	3–4	SB	Oveisi <i>et al.</i> (2007)

Abbreviations: FTB, Fold-and-thrust belt; SB, cross-section restoration; SR, sequential restoration; MC, magnetochronology.

a thin-skinned deformation belt, which typically show larger shortening values than thick-skin variants (e.g. Ghisetti *et al.* 1993; Tozer *et al.* 2002). There are two possible reasons for this:

- (1) The quickly-deposited flysch sediments of the WINB more readily folded than thrust, thus limiting the total amount of finite shortening (see next section). Evidence for this is the lack of thrusting, except at Quilty; no other thrusts were recognized in the field; and
- (2) The high pore pressure (due to fast sedimentation) within the sediments reduced the effective stress, so that strain rate could be higher. This is a hypothesis, not readily tested, although it has often been postulated that high pore pressure (of which there is ample evidence) reduces the effective stresses (Ramsay 1967). The first products of this were frequent slides and syn-sedimentary deformation (e.g. normal faults) apparent in these rocks (Martinsen 1989; Martinsen & Bakken 1990). We propose this behaviour continued in response to the tectonic stresses of the Variscan Orogeny.

Folding and sedimentation

The WINB clearly shows a higher proportion of folding than many other published fold-and-thrust

belts (cf. references in Table 5). Notable exceptions from Table 5 include the Jura Mountains of France and Switzerland, because folding is accommodated in the Jura by detachment on Triassic salt at a very shallow depth (Laubscher 1965, 1977), which is not comparable with the WINB.

The higher proportion of folding in the WINB is probably due to the rheological properties of the Namurian deposits, such as the Young's Modulus. The most suggestive explanation is given by the sedimentation. The sedimentation rate during the Gull Island Formation and the Tullig Cyclothem was 2 mm a⁻¹, and the average sedimentation for all the formations was 0.7 mm a⁻¹, as estimated by Martinsen (1987, 1989). Thus the WINB documents very fast deposition. This fast sedimentation led to high water retention of the sediment, which is evidenced by soft-sediment deformation features (Fig. 3). We suggest the soft sediments were anomalously less able to thrust than sediments of other foreland basins. Jamison (1992) suggested that the tendency for a rock package to deform by buckling or faulting is determined by the stress path within the respective stability fields. Increasing the fluid pressure by water retention reduces the vertical stress. Vertical stresses were very low in any case because tectonics occurred during sedimentation. After horizontal (tectonic) stresses are applied, the rock will therefore impinge the buckling field before it reaches the faulting envelope (Jamison 1992).

Style of folding

Since we were only able to retro-deform the cross-section back to Base Tullig Cyclothem (Step 7, Fig. 8), we can only postulate whether the Gull Island, Ross Sandstone and Clare Shale Fms were pre-tectonic. However, Figure 3d shows that the Gull Island Fm is more deformed than the overlying Tullig Cyclothem, which we suggest means the former was also syn-sedimentarily deformed. It is probable that the Ross Sandstone and Clare Shale Fms were deposited before folding commenced, but there is insufficient outcrop of these units throughout the cross-section to substantiate this.

Fold growth accelerated after the initiation of the folding, between 319–318.6 Ma (Fig. 10).

The change in fold style in the WINB from south to north can be explained in terms of the stratigraphy. The turbiditic Ross Sandstone Fm, with a thickness of over 500 m in the south, appears to function as the controlling member. With its decrease in thickness to the north, it loses this dominance. We believe there is a positive relationship of fold wavelength against thickness of the Ross Sandstone Fm. Therefore the kink-style and asymmetrical folds of southern County Clare are replaced by more symmetrical, concentric folds in the middle and north of the county.

Over the whole section of the WINB buckling was not followed by flattening, *sensu* Ramsay (1967) and Hudleston (1973), but instead we believe strain was transferred progressively to the north, resulting in new buckle folds in the foreland, as shown by passive markers in the model, which we followed during the retro-deformation (Fig. 12). This resulted in parallel fold geometry and explains the low fold amplitudes and long wavelengths.

Basin geometry

The results of the retro-deformation show the palinspastic basin geometry over time (Fig. 8). The southern part of the basin was always deeper than the northern part, and the basin floor always sloped towards the south. During deposition of the Younger Cyclothem, the southward-dipping slope nearly vanished. The decrease in slope angle is an indication for slowing of subsidence and the initiation of the final basin-evolution stage; that is, the filling of the entire basin accommodation space.

In our opinion, the occurrence of folding and thrusting coeval with sedimentation does not support an extensional origin for the WINB. The proximity of the Variscan Orogen (Ford 1987) to the south is only circumstantial evidence for a foreland basin. To test this hypothesis further, we compared the palinspastic data with the theoretical curve of foreland basin subsidence as modelled as

a two-dimensional lithospheric plate under a linear end-load (Walcott 1970; Turcotte & Schubert 2002), assuming the forebulge (DeCelles & Giles 1996) was located just north of the Cliffs of Moher (Figs 1 & 6). We discovered that the actual subsidence at the southern edge of the cross-section was five-fold that predicted by the modelled subsidence curve for a foreland basin, even with the weakest flexural rigidity (10^{21} N; Walcott 1970; Turcotte & Schubert 2002) and smallest dimensions. This suggests that the WINB is not a classical foreland flexural basin, but it is not feasible to further define the origin of the subsidence on the available evidence. It is possible that anomalously strong subsidence occurred on a fault under the Shannon Estuary, but this was not proven by offshore seismics (Le Gall 1991). Thermal subsidence of the basin is possible, since very high temperatures have been reported from vitrinite reflection data for the WINB, which was interpreted as evidence of a late Variscan plume (Goodhue & Clayton 1999).

Conclusions

The Western Irish Namurian Basin (WINB), exposed on the west coast of County Clare, Ireland, comprises eight formations and cyclothem in two groups. Sedimentation occurred very fast, which lead to soft-sediment deformation and overpressuring of the sediments. We constructed a c. 50 km long cross-section through the WINB, based on GPS based structural mapping of the outcrops. The section is parallel to the north–south tectonic transport vector.

We retro-deformed the cross-section in 7 steps, that is, removed the deformation caused by faulting and folding in the reverse order to their formation. We also decompacted the strata at each stage of the retro-deformation. We included strategic passive markers in the model to follow the evolution of folds and faults. From this analysis, we are able to show that:

- (1) The shortening of the section back to Base Tullig Cyclothem was 7.44% (4.07 km), of which 2.64% (1.37 km) is due to folding and 4.8% (2.69 km) due to thrusting;
- (2) The rate of orogenic shortening ranged from 0.1 to 6.0 mm a⁻¹, which is typical for fold-and-thrust belts, although very high. Peak shortening happened during thrusting, where 30 mm a⁻¹ occurred over 1 Ma. Presumably the high deformation rates were encouraged by low effective stresses caused by high pore pressure; and
- (3) Decompaction shows that the bed true thickness at the time of deposition was up to 50% more than at present. The palinspastic

implications are that the WINB developed on a faulted basement, which subsided far more than is typical for foreland basin flexure. The highest subsidence occurred around the River Shannon area.

This work is part of the Masters theses of FB and GE at the University of Göttingen. We thank Nancy for providing accommodation during the fieldwork. R. Groshong, J. Poblet, R. Lisle, and M. Ford are thanked for their thorough reviews which markedly improved the manuscript.

References

- ALLEN, P. A. & ALLEN, J. R. 1990. *Basin Analysis: Principles and Applications*. Blackwell Publishing, Oxford.
- ARTONI, A. & MECKEL, L. D. I. 1998. History and deformation rates of a thrust sheet top basin: the Barrême basin, western Alps, SE France. In: MASCLE, A., PUIG-DEFABREGAS, C., LÜTERBACHER, H. P. & FERNANDEZ, M. (eds) *Cenozoic Foreland Basins of Western Europe*. Geological Society, London, Special Publications, **134**, 213–237.
- ASSOCIATION SCIENTIFIQUE POUR LA GÉOLOGIE ET SES APPLICATIONS 1997. *GoCAD – User's Manual 1.4*. ASGA, Nancy, France.
- ATHY, L. F. 1930. Density, porosity, and compaction of sedimentary rocks. *Association of American Petroleum Geologists Bulletin*, **14**, 1–24.
- BRESSER, G. 2000. An integrated structural analysis of the SW Irish Variscides. *Aachener Geowissenschaftliche Beiträge*, **35**, 190.
- BRESSER, G. & WALTER, R. 1999. A new structural model for the SW Irish Variscides; the Variscan front of the NW European Rhenohercynian. *Tectonophysics*, **309**, 197–209.
- BUSK, H. G. 1929. *Earth Flexures*. Cambridge University Press, Cambridge.
- CHEN, J., BURBANK, D. W., SCHARER, K. M., SOBEL, E., YIN, J., RUBIN, C. & ZHAO, R. 2002. Magnetochronology of the upper Cenozoic strata in the southwestern Chinese Tian Shan; rates of Pleistocene folding and thrusting. *Earth and Planetary Science Letters*, **195**, 113–130.
- CLAYTON, G. & HIGGS, K. 1979. The Tournaisian marine transgression in Ireland. *Journal of Earth Sciences Royal Dublin Society*, **2**, 1–10.
- COLLINS, J. D., MARTINSEN, O., BAKKEN, B. & KLOSTER, A. 1991. Early fill of the Western Irish Namurian Basin: a complex relationship between turbidites and deltas. *Basin Research*, **3**, 223–242.
- COOPER, M. A., COLLINS, D., FORD, M., MURPHY, F. X. & TRAYNER, P. M. 1984. Structural style, shortening estimates and the thrust front of the Irish Variscides. In: HUTTON, D. H. & SANDERSON, D. J. (eds) *Variscan Tectonics of the North Atlantic Region*. Geological Society, London, Special Publications, **14**, 167–175.
- COOPER, M. A., COLLINS, D., FORD, M., MURPHY, F. X., TRAYNER, P. M. & O'SULLIVAN, M. 1986. Structural evolution of the Irish Variscides. *Journal of the Geological Society, London*, **143**, 53–61.
- DECELLES, P. G. & GILES, K. A. 1996. Foreland basin systems. *Basin Research*, **8**, 105–123.
- EGAN, S. S., KANE, S., BUDDIN, R., WILLIAMS, G. D. & HODGETTS, D. 1999. Computer modelling and visualisation of the structural deformation caused by movement along geological faults. *Computers and Geosciences*, **25**, 283–297.
- ELGER, K., ONCKEN, O. & GLODNY, J. 2005. Plateau-style accumulation of deformation: Southern Altiplano. *Tectonics*, **24**, TC4020.
- FORD, M. 1987. Practical application of the sequential balancing technique – an example from the Irish Variscides. *Journal of the Geological Society, London*, **144**, 885–891.
- FORD, M., BROWN, C. & READMAN, P. 1991. Analysis and tectonic interpretation of gravity data over the Variscides of southwest Ireland. *Journal of the Geological Society, London*, **148**, 137–148.
- FRANKE, W. 1989. Variscan plate tectonics in Central Europe – current ideal and open questions. *Tectonophysics*, **169**, 221–228.
- GEORGE, T. N., JOHNSON, G. A. L., MITCHELL, M., PRENTICE, J. E., RAMSBOTTOM, W. H. C., SEVASTOPOULO, G. & WILSON, R. B. 1976. A correlation of the Dinantian rocks of the British Isles. *Geological Society London Special Report*, **7**, 101–123.
- GHISETTI, F., BARCHI, M., BALLY, A. W., MORETTI, I. & VEZZANI, L. 1993. Conflicting balanced structural sections across the Central Apennines (Italy): problems and implications. In: SPENCER, A. M. (ed.) *Generation, Accumulation and Production of Europe's Hydrocarbons III*. Special Publication of the European Association of Petroleum Geoscientists, **3**, 219–231.
- GOODHUE, R. & CLAYTON, G. 1999. Organic maturation levels, thermal history and hydrocarbon source rock potential of the Namurian rocks of the Clare Basin, Ireland. *Marine and Petroleum Geology*, **16**, 667–675.
- GRAHAM, J. R. 1983. Analysis of the Upper Devonian Munster basin, an example of a fluvial distributary system. In: COLLINSON, J. D. & LEWIS, J. (eds) *Modern and Ancient Fluvial Systems*. International Association of Sedimentologists, Special Publication, **6**, 473–483.
- GRAHAM, J. R. 2001. Variscan Structures. In: HOLLAND, C. H. (ed.) *The Geology of Ireland*. Dunedin Academic Press, Edinburgh, 313–330.
- GRIFFITHS, P., JONES, S., SALTER, N., SCHAEFER, F., OSFIELD, R. & REISER, H. 2002. A new technique for 3-D flexural-slip restoration. *Journal of Structural Geology*, **24**, 773–782.
- HARDY, S. & POBLET, J. 1994. Geometric and numerical model of progressive limb rotation in detachment folds. *Geology*, **22**, 371–374.
- HINSCH, R. 2001. *Frontale Akkretion und Verformungsauftteilung eines gebogenen Falten- und Überschiebungsgürtels: Räumliche Strukturanalyse im Subandin Bolivians*. PhD thesis, Freie Universität Berlin.
- HODSON, F. 1954a. The beds above the Carboniferous Limestone in northwest County Clare, Eire. *Quarterly Journal of the Geological Society of London*, **109**, 259–283.
- HODSON, F. 1954b. The Carboniferous rocks of Foynes Island, County Limerick. *Geological Magazine*, **91**, 153–160.

- HODSON, F. & LEWARNE, G. C. 1961. A mid-Carboniferous (Namurian) basin in parts of the counties Limerick and Clare, Ireland. *Quarterly Journal of the Geological Society of London*, **117**, 307–333.
- HUDLESTON, P. J. 1973. Fold morphology and some geometrical implications of theories of fold development. *Tectonophysics*, **16**, 1–46.
- JAMISON, W. R. 1992. Stress controls on fold thrust style. In: McCLAY, K. R. (ed.) *Thrust Tectonics*. Chapman & Hall, London, 155–164.
- KLEMPERER, S. L., RYAN, P. D. & SNYDER, D. B. 1991. A deep seismic reflection transect across the Irish Caledonides. *Journal of the Geological Society, London*, **148**, 149–164.
- LAUBSCHER, H. P. 1965. Ein kinematisches Modell der Jurafaltung. *Eclogae Geologicae Helveticae*, **58**, 231–318.
- LAUBSCHER, H. P. 1977. Fold development in the Jura. *Tectonophysics*, **37**, 337–362.
- LE GALL, B. 1991. Crustal evolutionary model for the Variscides of Ireland and Wales from SWAT seismic data. *Journal of the Geological Society, London*, **148**, 744–759.
- LEEVE, K. A., BERTOTTI, G., ZOETEMEIJER, R., MATENCO, L. & CLOETINGH, S. A. P. L. 2006. The effects of a lateral variation in lithospheric strength on foredeep evolution: implications for the East Carpathian foredeep. *Tectonophysics*, **421**, 251–267.
- MARTINSEN, O. J. 1987. *Sedimentology and Syndepositional Deformation of the Gull Island Formation (Namurian R1), Western Irish Namurian Basin, Ireland – With Notes on the Basin Evolution*. PhD thesis, University of Bergen.
- MARTINSEN, O. J. 1989. Styles of soft-sediment deformation on a Namurian (Carboniferous) delta slope, Western Irish Namurian Basin, Ireland. In: WHATELEY, M. K. & PICKERING, K. T. (eds) *Deltas: Sites and Traps for Fossil Fuels*. Geological Society, London, Special Publications, **41**, 167–177.
- MARTINSEN, O. J. & BAKKEN, B. 1990. Extensional and compressional zones in slumps and slides – examples from the Namurian of County Clare, Ireland. *Journal of the Geological Society, London*, **147**, 153–164.
- MASCLE, A. & PUIGDEFÀBREGAS, C. 1998. Tectonics and sedimentation in foreland basins: results from the Integrated Basin Studies project. In: MASCLÉ, A., PUIGDEFÀBREGAS, C., LÜTERBACHER, H. P. & FERNÁNDEZ, M. (eds) *Cenozoic Foreland Basins of Western Europe*. Geological Society, London, Special Publications, **134**, 1–28.
- MAYNARD, J. R., HOFMAN, W., DUNAY, R. E., BENTHAM, P. N., DEAN, K. P. & WATSON, I. 1997. The Carboniferous of western Europe: the development of a petroleum system. *Petroleum Geoscience*, **3**, 97–115.
- MCQUARRIE, N., HORTON, B., ZANDT, G., BECK, S. & DECELLES, P. 2005. Lithospheric evolution of the Andean fold-thrust belt, Bolivia, and the origin of the central Andean plateau. *Tectonophysics*, **399**, 15–37.
- MENNING, M., ALEKSEEV, A. S. ET AL. 2006. Global time scale and regional stratigraphic reference scales of Central and West Europe, East Europe, Tethys, South China, and North America as used in the Devonian–Carboniferous–Permian Correlation Chart 2003 (DCP 2003). *Palaeogeography, Palaeoclimatology, Palaeoecology*, **240**, 318–372.
- MIDLAND VALLEY EXPLORATION LTD 2008. Move2008.1 software package. <http://www.mve.com>.
- MUÑOZ, J. A. 1992. Evolution of a continental collision belt: ECORS Pyrenees crustal balanced cross-section. In: McCLAY, K. R. (ed.) *Thrust Tectonics*. Chapman & Hall, London, 235–246.
- OVEISI, B., LAVÉ, J. & VAN DER BEEK, P. 2007. Rates and processes of active folding evidenced by Pleistocene terraces at the Central Zagros Front (Iran). In: LACOMBE, O., LAVÉ, J., ROURE, F. & VERGÉS, J. (eds) *Thrust Belts and Foreland Basins from Fold Kinematics to Hydrocarbon Systems: Frontiers in Earth Sciences*. Springer, Berlin, 267–288.
- POWERS, P. M., LILLIE, R. J. & YEATS, R. S. 1998. Structure and shortening of the Kangra and Dehra Dun reentrants, Sub-Himalaya, India. *Geological Society of America Bulletin*, **110**, 1010–1027.
- PRICE, C. A. 1989. Some thoughts on the subsidence and evolution of the Munster Basin, southern Ireland. In: ARTHURTON, R. S., GUTTERIDGE, P. & NOLAN, S. C. (eds) *The Role of Rection in Devonian and Carboniferous Sedimentation in the British Isles*. Special Publication of Yorkshire Geological Society, **6**, 111–121.
- PULHAM, A. J. 1989. Controls on internal structure and architecture of sandstone bodies within Upper Carboniferous fluvially-dominated deltas, County Clare, western Ireland. In: WHATELEY, M. H. & PICKERING, K. T. (eds) *Deltas – Sites and Traps of Fossil Fuels*. Geological Society, London, Special Publications, **41**, 179–203.
- PYTHON SOFTWARE FOUNDATION 2010. *The Python Language Reference*. <http://docs.python.org/reference/index.html>
- RAMSAY, J. G. 1967. *Folding and Fracturing of Rocks*. McGraw-Hill, New York.
- RAMSAY, J. G. & HUBER, M. I. 1987. *The Techniques of Modern Structural Geology, Vol. 2: Folds and Fractures*. Academic Press, London.
- RIDER, M. H. 1974. The Namurian of West County Clare. *Proceedings of the Royal Irish Academy*, **74B**, 125–142.
- SANDERSON, D. J. 1984. Structural variation across the northern margin of the Variscides in NW Europe. In: HUTTON, D. H. W. & SANDERSON, D. J. (eds) *Variscan Tectonics of the North Atlantic Region*. Geological Society, London, Special Publications, **14**, 149–165.
- SAVAGE, H. & COOKE, M. 2003. Can flat-ramp-flat fault geometry be inferred from fold shape?: a comparison of kinematic and mechanical folds. *Journal of Structural Geology*, **25**, 2023–2034.
- SCLATER, J. G. & CHRISTIE, P. A. F. 1980. Continental stretching: an explanation of the post-mid Cretaceous subsidence in the central North Sea Basin. *Journal of Geophysical Research*, **85**, 3711–3739.
- SEVASTOPULO, G. E. 2001. Carboniferous (Silesian). In: HOLLAND, C. H. (ed.) *The Geology of Ireland*. Dunedin Academic Press, Edinburgh, 289–312.
- SEVASTOPULO, G. E. & WYSE JACKSON, P. 2001. Carboniferous (Dinantian). In: HOLLAND, C. H. (ed.)

- The Geology of Ireland*. Dunedin Academic Press, Edinburgh, 241–267.
- SKOURLIS, K. & DOUTSOS, T. 2003. The Pindos Fold-and-thrust belt (Greece): inversion kinematics of a passive continental margin. *International Journal of Earth Sciences*, **92**, 891–903.
- SLEEMAN, A. G. & PRACHT, M. 1999. Geology of the Shannon Estuary, 1:100 000. Geological Society of Ireland, Dublin.
- SOTIROPOULOS, S., KAMBERIS, E., TRIANTAPHYLLOU, M. V. & DOUTSOS, T. 2003. Thrust sequences in the central part of the External Hellenides. *Geological Magazine*, **140**, 661–668.
- STANISLAWSKA, M., SELBY, D. & CHEW, D. 2007. Re and Os isotopic systematics in organic-rich shales from the Clare Basin, Ireland – preliminary results. *50th Annual Irish Geological Research Meeting*. University of Ulster, Coleraine, 42–43.
- SUPPE, J. 1983. Geometry and kinematics of fault-bend folding. *American Journal of Science*, **283**, 684–721.
- SUPPE, J., CHOU, G. T. & HOOK, S. C. 1992. Rates of folding and faulting determined from growth strata. In: McCLAY, K. R. (ed.) *Thrust Tectonics*. Chapman & Hall, London, 105–121.
- TANNER, D. C., BEHRMANN, J. H. & DRESMANN, H. 2003. Three-dimensional retro-deformation of the Lechtal Nappe, Northern Calcareous Alps. *Journal of Structural Geology*, **25**, 737–748.
- TANNER, D. C., BEHRMANN, J. H., ONCKEN, O. & WEBER, K. 1998. Three-dimensional retro-modelling of transpression on a linked fault system: the Upper Cretaceous deformation on the western border of the Bohemian Massif, Germany. In: HOLDSWORTH, R. E., STRACHAN, R. A. & DEWEY, J. F. (eds) *Continental Transpressional and Transtensional Tectonics*. Geological Society, London, Special Publications, **135**, 275–287.
- TOZER, R. S. J., BUTLER, R. W. H. & CORRADO, S. 2002. Comparing thin- and thick-skinned thrust tectonic models of the Central Apennines, Italy. *Stephan Mueller Special Publication Series*, **1**, European Geosciences Union, 181–194.
- TURCOTTE, D. L. & SCHUBERT, G. 2002. *Geodynamics: Applications of Continuum Physics to Geological Problems*. 2nd edn. John Wiley & Sons, New York.
- UNITED STATES NAVAL OBSERVATORY 2008. NAVSTAR – Global Positioning System. Available online at: <http://tycho.usno.navy.mil/gps.html>
- VERGÉS, J., MARZO, M., SANTAELÀRIA, T., SERRA-KIEL, J., BURBANK, D. W., MUÑOZ, J. A. & GIMÉNEZ-MONTSANT, J. 1998. Quantified vertical motions and tectonic evolution of the SE Pyrenean foreland basin. In: MASCLÉ, A., PUIGDEFÀBREGAS, C., LUTERBACHER, H. P. & FERNÁNDEZ, M. (eds) *Cenozoic Foreland Basins of Western Europe*. Geological Society, London, Special Publications, **134**, 107–134.
- WALCOTT, R. I. 1970. Flexural rigidity, thickness and viscosity of the lithosphere. *Journal of Geophysical Research*, **75**, 3941–3954.
- WIGNALL, P. B. & BEST, J. L. 2000. The Western Irish Namurian Basin reassessed. *Basin Research*, **12**, 59–78.
- WILLIAMS, E. A. 2000. Flexural cantilever models of extensional subsidence in the Munster Basin (SW Ireland) and Old Red Sandstone fluvial dispersal systems. In: FRIEND, P. F. & WILLIAMS, B. P. J. (eds) *New Perspectives on the Old Red Sandstone*. Geological Society, London, Special Publications, **180**, 239–268.
- WILLIAMS, E. A., FORD, M. & EDWARDS, H. E. 1990. Discussion of a model for the development of the Irish Variscides. *Journal of the Geological Society, London*, **147**, 566–571.
- WOODWARD, N. B., BOYER, S. & SUPPE, J. 1989. *Balanced Geological Cross-Sections: An Essential Technique in Geological Research and Exploration*, **6**. American Geophysical Union, Washington.
- YU, S.-B., CHEN, H.-Y. & KUO, L.-C. 1997. Velocity field of GPS stations in the Taiwan area. *Tectonophysics*, **274**, 41–59.

Incremental slip history of a thrust: diverse transport directions and internal folding of the Utrillas thrust sheet (NE Iberian Chain, Spain)

J. L. SIMÓN* & C. L. LIESA

Departamento de Ciencias de la Tierra, Universidad de Zaragoza, Pedro Cerbuna, 12. 50009 Zaragoza, Spain

**Corresponding author (e-mail: jsimon@unizar.es)*

Abstract: A kinematical model for the Utrillas thrust is proposed, including reconstruction of the incremental slip history, progressive internal deformation and tectono-sedimentary relationships at the Montalbán (foreland) and Aliaga (piggy-back) Tertiary basins. A 3D geometrical model of the main thrust surface, defined by ramps oriented NE–SW, east–west, NW–SE and north–south, is reconstructed from cross-sections. Besides, the thrust sheet is internally deformed by two main, frequently superposed fold sets, trending NW–SE to NNW–SSE (earlier) and east–west (later), respectively. A total ‘arrow’ (finite horizontal displacement) of about 5.9 km towards N032°E is estimated by means of schematic, plan-view retrodeformation of the distinctly oriented ramps making its front. Orientation and cross-cut relationships of mesoscopic kinematical indicators at the thrust front provide a scenario of successive transport directions towards the ENE, NNE and north, which is consistent with the progressive development of internal folding, as well as with the evolution of intraplate compressive stress fields through Tertiary times.

Our knowledge of thrusts, as master structures in the architecture of mountain chains, has significantly increased in the last tens of years. After the development of 2D reconstructions based on balanced cross-sections (e.g. Suppe 1983; Butler 1992; Zoete-meijer & Sassi 1992), 3D geometric models have been improved by acquiring precise subsurface data from deep boreholes and high-resolution seismic profiles, and using new techniques of numerical processing (Calcagno *et al.* 2007). In general, kinematical analysis has not made the same advance. The reconstruction of deformation paths and the achievement of balanced sections usually assume, either explicitly or implicitly, a plane-deformation model with the cross-section being the true movement plane of the whole structures, that is, the cross-section being parallel to the transport direction (e.g. Marshak & Mitra 1988, p. 312). Alternatively, a cross-section oblique to the movement plane could be admitted if the transport direction is approximately constant in its vicinity (Elliott 1983; Groshong 1999, fig. 8.4).

The transport direction of thrust sheets is frequently inferred on maps assuming non-contrasted hypotheses: (a) vector orthogonal to the average or the preferred orientation of the thrust trace and the associated folds (e.g. Cartwright 1989; Marshak & Mitra 1988, p. 312); and (b) application of the ‘bow-and-arrow rule’ proposed by Elliott (1976). On the other hand, the relationships between such

transport direction and the regional direction of shortening or compression (not necessarily parallel to each other) are frequently neglected. As a consequence, values of separation between markers measured in cross-section can be erroneously interpreted as values of net slip or absolute shortening, and assigned as relevant kinematical attributes to the studied structures.

The Utrillas thrust, in the northeastern Iberian Chain (eastern Spain, see Fig. 1), is an important structure in which this problem can be confronted. Owing to its particular location within the Iberian Plate, this region underwent distinct remote tectonic compressions transmitted from the active plate margins, which combined in a complex stress history (Capote *et al.* 2002; Liesa & Simón 2007, 2009). Most thrust structures within the Iberian Chain are Mesozoic extensional faults inverted under such heterogeneous stress conditions (Casas & Simón 1992; Casas *et al.* 2000; Salas *et al.* 2001), so they probably moved along variable transport directions whose time sequence has not been adequately discerned.

A broadly northward transport direction is accepted for the Utrillas thrust (Canérot 1974; Guimerà 1988; González & Guimerà 1993; Casas *et al.* 2000), although this is not supported by precise kinematical data. As an example, González & Guimerà (1993) propose an evolutionary model, based on the tectono-sedimentary relationships at

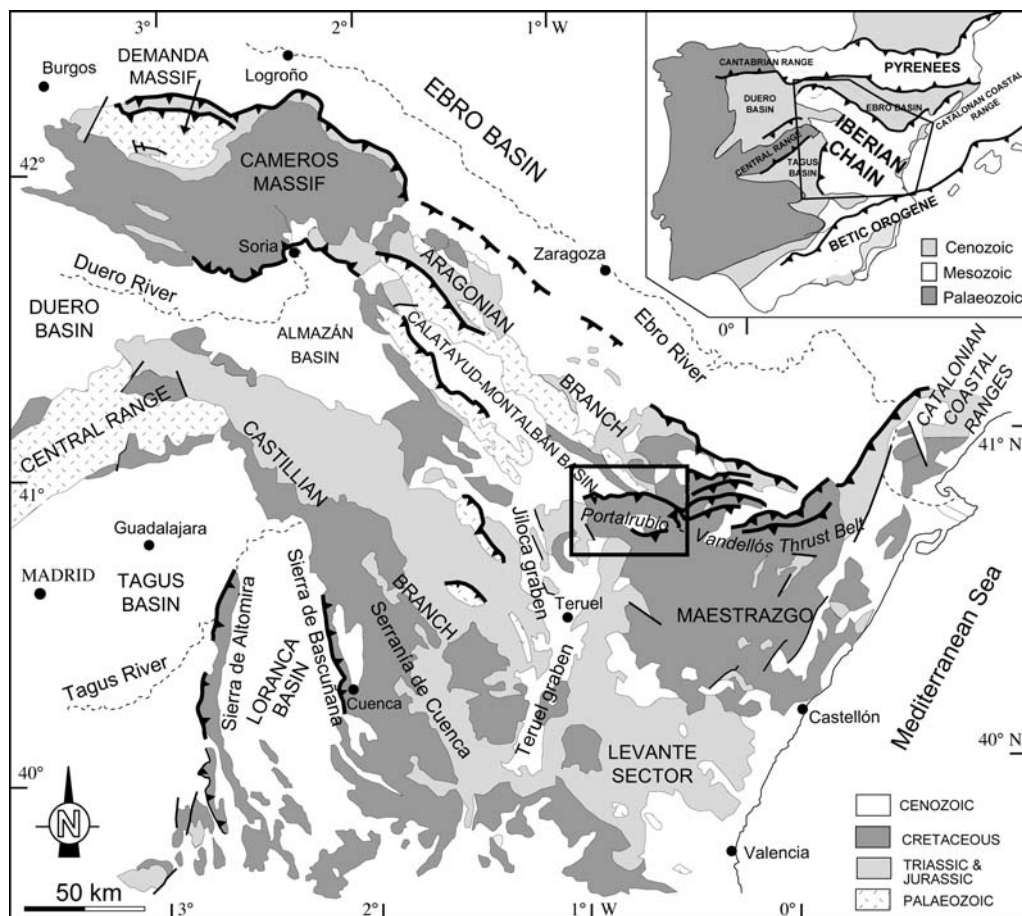


Fig. 1. Geological location of the Utrillas thrust within the Iberian Chain, eastern Spain.

the piggy-back Aliaga basin, with two main stages of movement (Late Eocene and Late Oligocene–Early Miocene, respectively). According to this model, a single $N10^{\circ}E$ transport direction, orthogonal to the average thrust trace, persisted during the whole process. Nevertheless, Liesa (1999, 2000) observed diversely oriented kinematical indicators at a mesostructural scale (several striations on main thrust planes, S-C structures) that suggest at least two non-coeval movement directions towards the NE and NNW.

Within such changing kinematical scenario, it seems not reasonable to determine the total ‘arrow’ (both direction and magnitude) of the Utrillas thrust by using geometric procedures such as the ‘vector orthogonal to the fault trace’ or the ‘bow-and-arrow rule’. These cannot be generally applied in the case of fault reactivation (McClay & Buchanan 1992; Coward 1994), in which oblique movements frequently occur (determined, according to

Bott’s equation, by the orientation of fault planes and the remote deviatoric stress tensor; Bott 1959). On the other hand, a more satisfactory estimate of the net slip can be obtained by kinematical analysis based on the following bases: (a) the existence of distinctly oriented ramps bounding the thrust sheet; (b) the assumption that this consistently moved on these ramps as a rigid block (in spite of the existence of significant internal deformation); and (c) the evidence of diverse transport directions during the Tertiary orogenic period.

In this paper we present a complete kinematical model for the Utrillas thrust, including reconstruction of the progressive displacement and internal deformation of the sheet, the changes in transport direction, as well as a realistic estimation of the total resultant ‘arrow’. We will analyse overall macrostructural information and, specifically, mesoscopic kinematical indicators directly observed either on the main fault surfaces or in their vicinity.

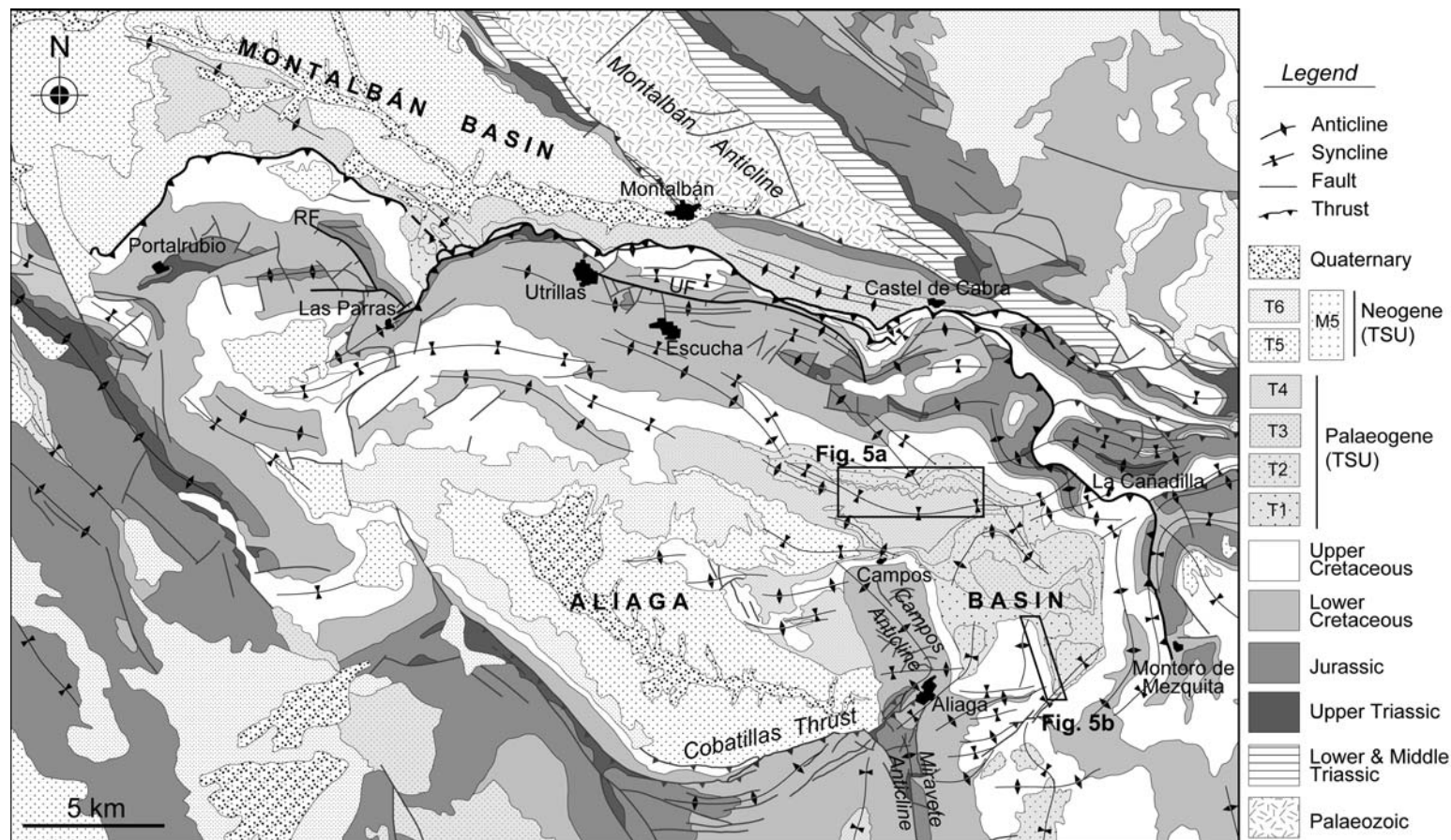


Fig. 2. Geological map of the Utrillas thrust. RF, La Rambla normal fault; UF, Utrillas normal fault.

The results will be contrasted with 3D features of internal folding of the thrust sheet, and with tectono-sedimentary relationships at two Tertiary basins involved in thrust evolution: the Montalbán (foreland) and Aliaga (piggy-back) basins (Fig. 2). Finally, we will briefly discuss the compatibility of the proposed model with the dynamic tectonic framework.

Geological setting

The Iberian Chain, with an overall NW–SE trend, is an intraplate mountain range located in eastern Iberia (Fig. 1). It was developed during Tertiary times from positive inversion of a Mesozoic basin (the Iberian Basin) connected to Tethys (Álvaro *et al.* 1979; Guimerà & Álvaro 1990; Salas & Casas 1993; Capote *et al.* 2002).

Mesozoic sedimentation took place within an intraplate extensional basin (Álvaro *et al.* 1979; Salas & Casas 1993; Capote *et al.* 2002), following two main rift stages (Late Permian to Hettangian and Late Jurassic to Early Cretaceous) related to Tethys and Central Atlantic spreading (Salas & Casas 1993). The Mesozoic series includes (see Fig. 3 for more detail): (a) Triassic in Germanic facies (Garrido & Villena 1977), with sandstones and claystones (Buntsandstein facies), dolostones and marlstones (Muschelkalk facies), and lutites and evaporites (Keuper facies); (b) Jurassic marine calcareous deposits of shallow epicontinental seas (Aurell *et al.* 2002); (c) Lower Cretaceous (Salas 1987), including a continental series (Weald facies) made of sandstones, lutites and lacustrine limestones and marls, followed by marine limestones and marls (Urgon facies), and topped by shales with coal of the transitional Escucha Formation; and (d) Upper Cretaceous, with a basal siliciclastic aeolian formation (Utrillas Fm.) (Rodríguez-López *et al.* 2008), followed by dolostones, limestones and marls of shallow marine realms (Martin-Chivelet *et al.* 2002).

The overlying Tertiary units were deposited in continental basins (Figs 1 & 2) bounding the Iberian Chain (e.g. Ebro, Duero and Tajo basins), as well as in intramountain basins (e.g. Almazán, Calatayud, Montalbán or Aliaga basins). They mainly include alluvial conglomerates, sandstones, shales and lacustrine carbonates (Villena *et al.* 1996). Most of these units were syntectonic with respect to inversion of the Mesozoic basin.

The Iberian Chain is characterized by a moderate deformation, with very little magmatism and metamorphism, and a very contrasting behaviour of the Variscan basement and the Mesozoic–Tertiary cover, both separated by a regional detachment level at the Middle–Upper Triassic Muschelkalk

and mainly Keuper facies (Álvaro *et al.* 1979; Salas & Casas 1993; Capote *et al.* 2002). The Tertiary structure of the eastern Iberian Chain shows the superimposition of two orthogonal, fold-and-thrust structural trends striking NW–SE and NE–SW, respectively (Guimerà 1988; Simón 2004) (Fig. 1). Both structural trends represent the rejuvenation and inversion of previous normal faults, inherited essentially from the Mesozoic extension and/or post-Variscan fracturing (Guimerà & Salas 1996; Soria 1997; Simón *et al.* 1998; Liesa & Simón 2004; Liesa *et al.* 2004).

As a result of the successive, partially superposed tectonic compressions transmitted from the Pyrenean and Betic active margins of Iberia, the intraplate Iberian Chain was submitted to a complex palaeostress history during Tertiary times (Capote *et al.* 2002). Based on a broad compilation of compression directions inferred from mesostructural data (faults, stylolites and shear fractures), Liesa & Simón (2007, 2009) proposed a model that includes three independent Intraplate Stress Fields (ISF) whose maximum compression trajectories roughly trend NE–SW, ESE–WNW to SSE–NNW and NNE–SSW, respectively. The ages of these stress fields have been constrained from relative timing of related mesostructures, relationships between meso- and macrostructures, and ages of the involved, both pre- and syn-deformational materials. The NE–SW ISF probably was the most intense one, acting since Middle Eocene to Late Oligocene times. The ESE–WNW to SSE–NNW ISF was partially coeval with the former one, although it underwent fluctuations resulting in two peaks of activity at the Eocene *sensu lato* (ESE–WNW compression) and the Late Oligocene to Early Miocene (SE–NW to SSE–NNW). The NNE–SSW ISF was active since latest Oligocene times.

The Utrillas thrust is the westernmost structure of one of the major structural domains within the eastern Iberian Chain (Fig. 1): the east–west-trending, N-verging Portalrubio–Vandellós fold-and-thrust belt. This belt, which represents the link of this chain with the NE–SW structures of the Catalanian coastal ranges (Guimerà 1988, 2004), resulted from the inversion of the Late Jurassic–Early Cretaceous Maestrazgo Basin. Thus, the belt shows several changes in trend, with three major inflections where the structures veers from NW–SE to NE–SW (Fig. 1), that mimics the northern margin of the extensional basin (Liesa *et al.* 2004; Antolín-Tomás *et al.* 2007). The basal thrust was detached in the Middle–Upper Triassic (Muschelkalk and Keuper facies), although towards the south and west the Variscan basement is also involved (Casas *et al.* 2000; Liesa *et al.* 2000; Guimerà 2004).

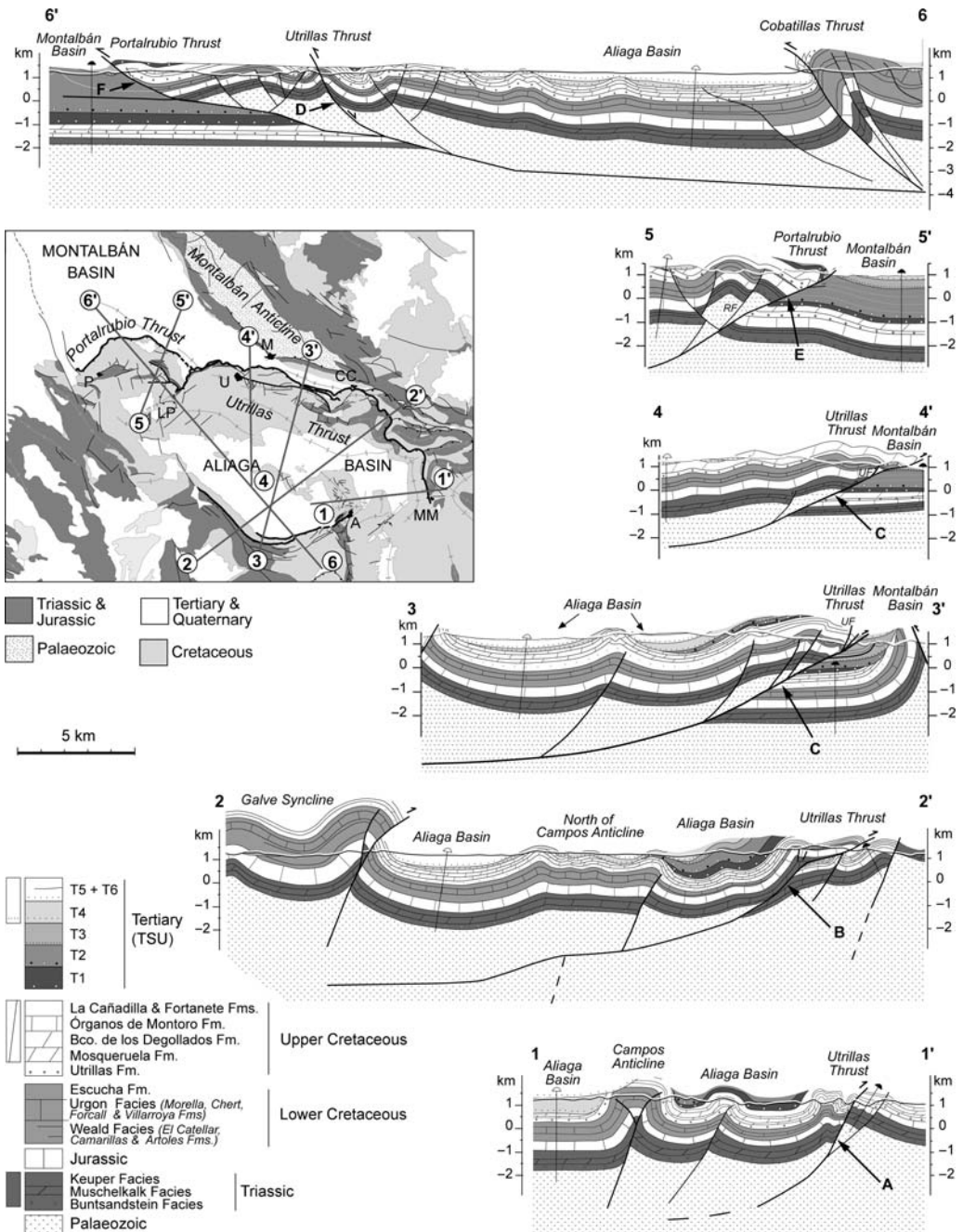


Fig. 3. Cross-sections of the Utrillas and Portalrubio thrust sheets. 1-1', 2-2', 3-3' and 6-6': original in this work; 4-4': modified from Casas *et al.* (2000); 5-5': modified from Liesa *et al.* (2000). RF, La Rambla normal fault; UF, Utrillas normal fault. A to F on cross sections: thrust ramps, as labelled on Figure 4. On the map: P, Portalrubio; LP, Las Parras de Martín; U, Utrillas; M, Montalbán; CC, Castel de Cabra; MM, Montoro de Mezquita; A, Aliaga.

Overall geometry of the Utrillas thrust

The Utrillas thrust is a 50 km long, northward verging structure that displays a curved and winding trace, with NE–SW to east–west, NW–SE and north–south trends (Fig. 2). González & Guimerà (1993) and Casas *et al.* (2000) estimated a maximum displacement between 6 and 8 km for this structure. The whole thrust is divided into two major thrust sheets: (i) the western Portalrubio sheet, with an arc-shaped front oriented NE–SW to NW–SE, and (ii) the Utrillas sheet, with a NE–SW-trending front at the westernmost sector (Las Parras), a broadly east–west front at the central sector (Utrillas–Castel de Cabra), and a sinuous NW–SE to north–south trace at the eastern sector (Castel de Cabra–Montoro de Mezquita). Most of the thrust front (except the easternmost sector, east of Castel de Cabra) overlaps the Tertiary rocks of the Montalbán basin.

The Utrillas thrust is inherited from the east–west to ESE–WNW striking faults that made the northern margin of the Early Cretaceous Las Parras subbasin (Liesa *et al.* 2000, 2004). The geometry of the thrust surface has been reconstructed in this work from four newly constructed cross-sections (1–1', 2–2', 3–3' and 6–6' in Fig. 3), and another two that were modified from Casas *et al.* (2000) (section 4–4') and Liesa *et al.* (2000) (section 5–5'). Unfortunately, neither seismic reflection profiles nor deep boreholes are available for this region, so that the cross-sections are mainly based on published geological maps (Almela *et al.* 1975;

Canérot *et al.* 1977; Martín & Canérot 1977; Martín *et al.* 1977; Gautier 1979; Hernández & Anadón 1982–83; Ferreiro & Ruiz 1986–87; Guimerà & Salas 1996; Simón *et al.* 1998; Casas *et al.* 2000; Liesa *et al.* 2000, 2004), and on our field data. The current knowledge about the normal faults bounding the Mesozoic extensional basins (Soria 1997; Liesa *et al.* 2000, 2004, 2006), as well as about thickness variations of the Cretaceous syn-rift series (Soria 1997; Clariana *et al.* 2000; Peropadre *et al.* 2005, 2007), have allowed us to constrain fault geometries at depth and the location of their detachment levels. Figure 4 summarizes the 3D geometric model for the thrust surface by means of a schematic contour map. It has been constructed based on the cross-sections shown in Figure 3, by reading the inferred depths of the main thrust and interpolating their values. Its purpose is to show the position, orientation and articulation of the footwall ramps, labelled as A to F. Owing to the lack of subsurface information, the quantitative aspects of this map should be taken only as an estimate.

The Portalrubio and Utrillas thrust sheets behaved as two independent thrust sheets during most of their evolution. At present, the Portalrubio thrust sheet is cut by the westernmost, NE–SW striking ramp of the Utrillas thrust sheet (Fig. 2; ramp D in cross-section 6–6' of Fig. 3).

At the central sector, the Utrillas thrust shows a S-dipping gentle (20–25°) ramp (Fig. 3, cross-sections 3–3' and 4–4'; Fig. 4), which cuts both the Mesozoic series and the Palaeozoic basement. At

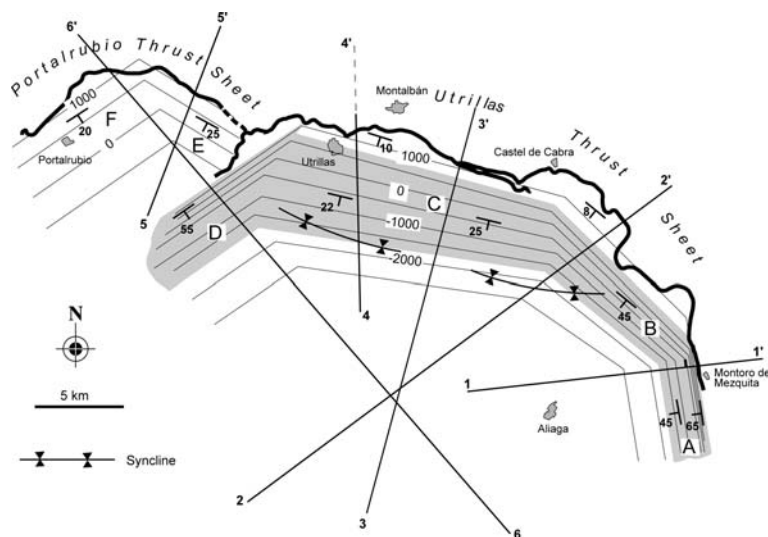


Fig. 4. Schematic contour map showing the 3D geometrical model of the thrust surface, constructed from cross-sections of Figure 3. A to F: footwall ramps. Contours in metres (datum: see level). Shaded: main ramps of the Utrillas thrust sheet.

its eastern sector, the dip and the WNW–ESE strike of this ramp are marked at the surface by an extent WNW–ESE monocline affecting Upper Cretaceous and Tertiary (T1 to T3) units at the northern margin of the Tertiary Aliaga basin (Fig. 5a; location in Fig. 2). At the thrust front, the ramp dip decreases up to become locally a footwall flat with an overturned anticline (mainly detached at the Utrillas sandy unit) in the hanging wall. This sector of the Utrillas thrust represents a short-cut fault developed at the hanging wall of the Utrillas normal fault (UF in Figs 2 & 3), which was active during the Early Cretaceous (Soria 1997; Casas *et al.* 2000). The upper segment of this fault has been passively transported within the Utrillas sheet (Fig. 2; cross-sections 3-3' and 4-4' in Fig. 3).

The western sector of the Utrillas thrust is defined by the above-mentioned, NE–SW-trending ramp (D in Fig. 4), which is significantly steeper (up to 55° , as observed at the surface) than the central ramp (Fig. 3, cross-section 6-6'). This thrust ramp represents the partial inversion of the southeast-dipping Las Parras normal fault (Liesa & Simón 2004), which segmented the northern margin of the Early Cretaceous Las Parras subbasin (Soria 1997; Liesa *et al.* 2000, 2004) and allowed the Utrillas sheet to overthrust the Portalrubio sheet (Fig. 2).

At the eastern sector, the thrust shows a sinuous trace (trending NNW–SSE on average) that extends from Castel de Cabra to Montoro de Mezquita. Two

ramps have been distinguished (A and B in Fig. 4). Ramp B strikes NW–SE to NNW–SSE and dips about 45° SW, and is marked by similar attitudes in the Mesozoic and Tertiary units of the hanging wall (section 2-2' in Fig. 3). Its dip diminishes to approximately 8° towards the thrust front, where the thrust sheet shows a nearly flat structure except for the frontal overturned anticline (see Fig. 6a). Ramp A also shows a steep dip (45 to 65°) at the surface, which is consistent with the narrow belt of close, upright folds developed nearby the thrust front at the hanging wall (Fig. 3, cross-section 1-1'). Ramp A can be interpreted as a high-angle basement fault, which constituted both the eastern margin of the Cretaceous extensional Las Parras subbasin (note the difference in thickness of the Lower Cretaceous at both fault blocks in sections 1-1' and 2-2') and of the Tertiary Aliaga Basin.

The Portalrubio thrust front is characterized by two ramps (E and F; cross-sections 5-5' and 6-6' in Fig. 3) with gentle dip (20 – 25°) to the south, which cut the Tertiary and Mesozoic rocks and the Variscan basement. The WNW–ESE ramp (E) has been interpreted as a short-cut thrust generated in the footwall of the reactivated WNW–ESE La Rambla normal fault (Liesa *et al.* 2000, 2004; Liesa & Simón 2004). The upper segment of this normal fault was passively transported within the thrust sheet (RF in cross-section 5-5' and Fig. 2). Its surface expression is the relatively large

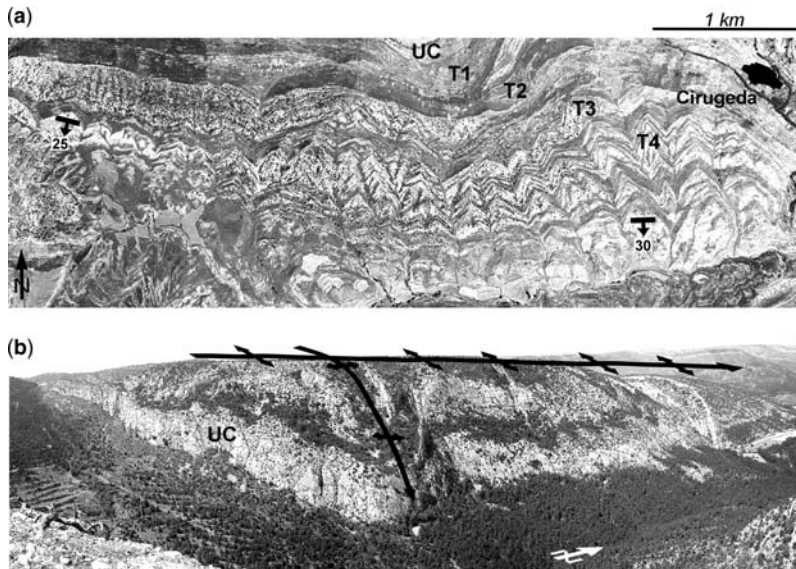


Fig. 5. Field view of internal folds within the Utrillas thrust sheet (see location in Fig. 2). (a) Accommodation monocline at the northern margin of the Tertiary Aliaga Basin, related to the main ramp of the central sector of the Utrillas thrust. (b) Type 1 fold superposition east of Aliaga: an east–west-trending anticline overprints a north–south-trending one. UC, Upper Cretaceous; T2, Late Eocene; T4, Late Oligocene.

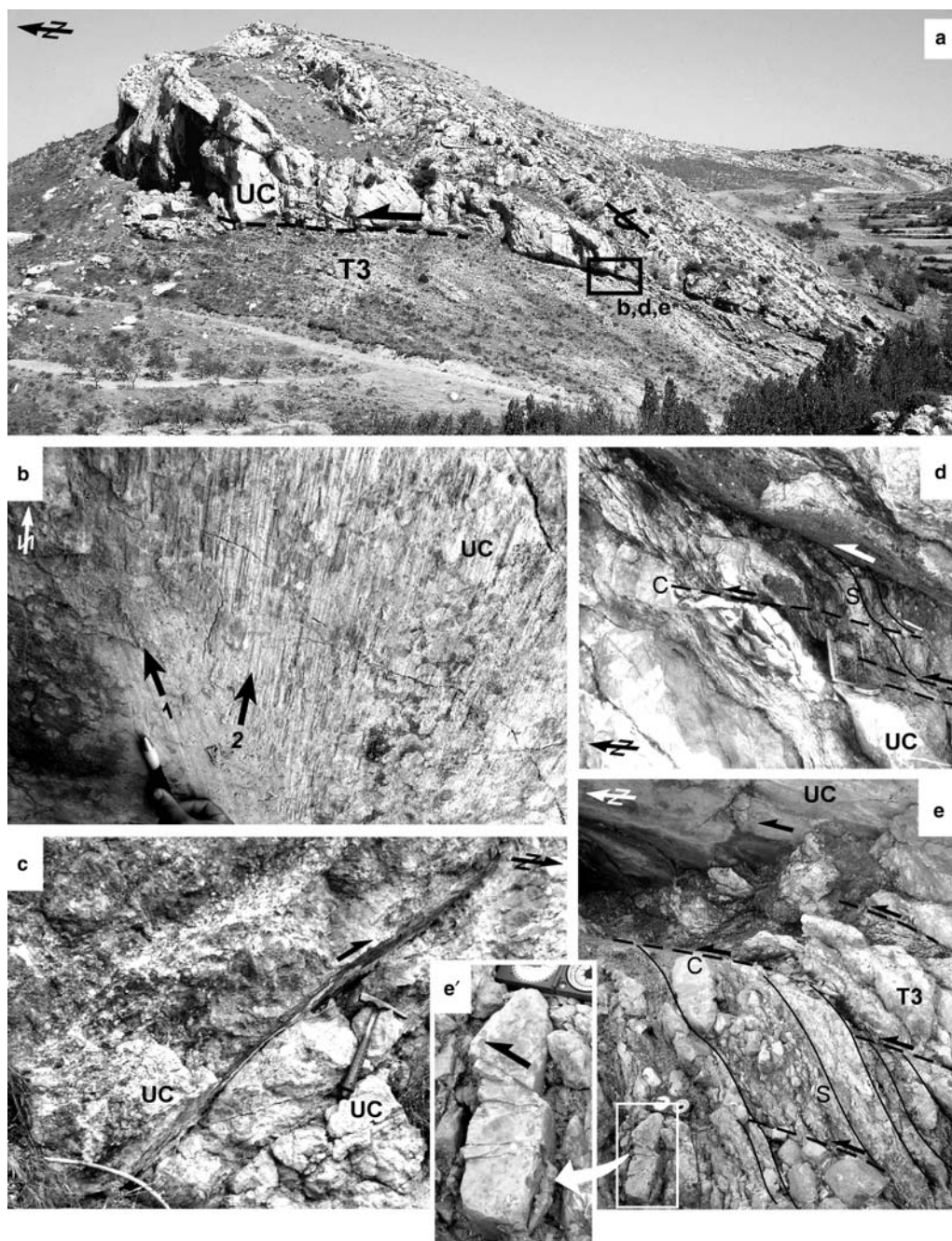


Fig. 6. Types of meso-scale structures used as kinematical indicators. (a) General field view of the Utrillas thrust front at Castel de Cabra (meso-structural site 8), where most of the following examples (b, d, e) are located. (b) Main thrust surface at site 8, showing two striation sets: towards the NNE (1, earlier) and towards the N (2, younger). (c) Minor reverse fault planes; site 12. (d) S-C structure in Upper Cretaceous limestones; site 8. (e) Rough S-C structure and sheared pebbles (see detail in e') in Tertiary calcareous conglomerate; site 8. UC, Upper Cretaceous dolostones; T3, Early Oligocene calcareous conglomerates. Arrows indicate relative movement of the hanging wall.

southern limb, dipping 30°S on average, of an accommodation anticline that shows Jurassic and Early Cretaceous units cropping out in its core; Figure 3, cross-section 5-5'. In any case, a higher level of uncertainty exists in this sector about the thrust surface geometry, depth of the detachment level (generally interpreted as being located in Silurian and Precambrian slates), and its relationship with other shallower detachments.

In a general view (Fig. 3), it can be seen how the Aliaga and Montalbán Tertiary basins represent, respectively, the piggy-back and the foreland basin with respect to the Utrillas thrust (González & Guimerà 1993; Casas *et al.* 2000). The Aliaga basin partially lies on a basal flat (or maybe on a S-dipping low-angle ramp) located between 3.5 and 4 km below sea level. Some previously published cross-sections (e.g. Guimerà 1988, 2004; González & Guimerà 1993; Casas *et al.* 2000, cross-section 4-4') proposed a more irregular thrust surface made of two ramps and two flats; the most important (basal) detachment level would be located at the shale and gypsum facies of the middle Muschelkalk (Middle Triassic), at about 1 km below sea level. In our interpretation (based on numerous lines of evidence concerning the thickness of Triassic and Lower Cretaceous units, and the location and geometry of observed fault detachments) the thrust is detached within the basement, so that the hanging wall incorporates Palaeozoic and Triassic rocks (Fig. 3). This interpretation is also upheld by Casas *et al.* (2000) in their cross-section 3-3'.

Internal deformation of the thrust sheet

The Utrillas thrust sheet displays noticeable internal deformation, both in the Mesozoic and Tertiary units (see Figs 2, 3 & 5). Two main fold sets can be distinguished (Fig. 2), mainly including fault-propagation and detachment folds, with a lesser proportion of fault-bend folds. The first set is made of NW–SE-trending folds (predominant at the northern part of the thrust sheet and northward of it), and NNW–SSE to north–south-trending folds (located at the southern part and larger in scale than the former ones). Among the NNW–SSE to north–south structures, the Campos–Aliaga–Villarroya anticline stands out. This is a 20 km long box fold with estimated amplitude of 2 km, which is associated with the inversion of the Cretaceous Miravete fault (Soria 1997; Liesa *et al.* 2006). The second fold set is formed by ENE–WSW-trending folds, which are mainly concentrated into a 5-km wide band in the vicinity of Aliaga. Likewise, this fold band is located on another basement fault that made the boundary between Las Parras and Galve

extensional subbasins from the Kimmeridgian to the Early Albian (Guimerà & Salas 1996; Soria 1997; Liesa *et al.* 2006). This band of traverse structures crosses and divides the Campos–Aliaga–Villarroya anticline into a northern segment (Campos anticline, which separates the eastern and western sectors of the Tertiary Aliaga basin) and a southern segment (Miravete anticline; Fig. 2).

The NNW–SSE and ENE–WSW-trending fold sets show a great variety of superposition structures (Fig. 5b), belonging to both Type 1 and Type 2 of the Thiessen & Means' (1980) classification; they indicate that the ENE–WSW folds are younger than NW–SE to north–south-trending folds (Simón 2004, 2005). The same relationships are found with respect to NW–SE and east–west-trending segments of the Utrillas thrust front. First, NE–SW to east–west segments of the thrust cut folds of the NW–SE-trending set. In the western sector (Las Parras area, Fig. 2), the NE–SW western ramp of the Utrillas sheet overthrusts the NW–SE segment of the Portalrubio sheet, as well as hanging wall and footwall folds associated with the latter (Liesa *et al.* 2004). In the central sector, the east–west thrust front overthrusts Triassic materials of the core of the NW–SE-trending Montalbán anticline, which involves folding and erosion of this anticline previous to displacement of the thrust sheet (Guimerà 1988). Second, later ENE–WSW folds deform NW–SE oriented segments of the Utrillas thrust front. The most conspicuous example appears at the eastern ramp (La Cañadilla area, Fig. 2), where both the thrust surface and a parallel hanging wall anticline are folded by ENE–WSW traverse folds, defining a Type 2 superposition (Simón 2004).

Tectono-sedimentary relationships within the Tertiary basins

Two Tertiary basins bound the Utrillas thrust sheet: the Montalbán foreland basin and the Aliaga piggy-back basin (Fig. 2). Both contain a quite continuous sedimentary infill made of alluvial, fluvial and lacustrine deposits, which records the whole orogenic and early post-orogenic periods, between the Paleocene and mid Miocene times (Pardo *et al.* 1989).

These Tertiary series have been divided into several tectono-sedimentary units (TSU), limited by unconformities at the basin margins that correlate with sedimentary breaks throughout the basin centre (Garrido-Megías 1973, 1982; González *et al.* 1988; Pardo *et al.* 1989). Five TSU (M1 to M5) have been defined in the Montalbán basin, with a total thickness of c. 2000 m (Pérez 1989; Casas *et al.* 2000). In the Aliaga basin, six units (A1 to A6) totalize

1700 m (González 1989; González & Guimerà 1993). The megasequential evolution of both series shows sufficient similarity to allow correlation of most TSU units (González *et al.* 1988; Pardo *et al.* 1989), always bearing in mind the cautions required in internally-drained basins (Santanach 1989). As a result, a single regional succession of TSU units can be used (T1–T6; González *et al.* 1988; Pardo *et al.* 1989), with T1–T4 representing the whole Palaeogene, and T5–T6 being attributed to the Lower Miocene *s.l.* Although some ambiguity remains with respect to the uppermost units (T5 and T6), following the stratigraphic divisions used by Villena *et al.* (1991) and Casas *et al.* (2000) we assume that both are grouped into M5 at the Montalbán basin.

Using this TSU succession as a relative chronological reference, the structural evolution of the Utrillas thrust can be constrained by analysing relationships between deformation and sedimentation at both neighbouring basins. The results of a number of sedimentological, palaeogeographical and structural works (Pardo *et al.* 1984; González 1989; Pérez 1989; Guimerà *et al.* 1990; González & Guimerà 1993; Simón *et al.* 1998; Casas *et al.* 2000; Simón 2004) have been used for this purpose, paying special attention to those sedimentary units that either are deformed or lie unconformably on each generation of tectonic structures. We next summarize the main stages of that evolution, which have been retained for constructing the final model of progressive deformation.

- (i) Deposition of T2 was controlled by NW–SE to NNW–SSE-trending structures such as the anticlines located to the north (e.g. Montalbán anticline), whose exhumed Palaeozoic cores supplied quartzitic clasts to conglomerates of this unit in both the Montalbán and the Aliaga basins, and the eastern limb of the Campos–Aliaga anticline, which supplied sediments to the eastern sector of the Aliaga basin.
- (ii) The T2–T3 transition recorded the beginning of the northward displacement of the Utrillas thrust: both the Montalbán and the Aliaga basins received sediments from an east–west-trending palaeogeographic high that can be identified with the main hanging wall anticline that separated them.
- (iii) Around the T3–T4 limit, the Aliaga basin expanded to the west. The sedimentary imprint of the aforementioned hanging wall anticline separating the Montalbán and Aliaga basins disappeared, which suggests a decline of the dip slip component (i.e. episodic dominance of the strike-slip component) on ramp C of the Utrillas thrust or, otherwise, a marked

decrease of the displacement rate. This situation remained up to mid T4.

- (iv) During the T4–T5 transition, the pattern of the Aliaga basin underwent an abrupt change: intense folding (with NW–SE to north–south trends) occurred close to the eastern ramp, accompanied by overall rise of the eastern sector of the basin and erosion of its Palaeogene infill. Sedimentation migrated to the western sector, bounded by the newly developed western limb of the Campos–Aliaga anticline.
- (v) The end of T4 and the entire T5 unit recorded new activity of the Utrillas thrust. Conglomerates of T4 attached to the thrust front are then cut by minor hanging wall thrusts developed in a break-back sequence (Liesa *et al.* 2004). The Cobatillas thrust that makes the southern boundary of the piggy-back basin underwent coeval displacement, and new ENE–WNW-trending folds develop in its vicinity.
- (vi) No evidence of movement exists since the beginning of T6.

Transport directions from meso-scale kinematical indicators

A specific field survey has provided a wide compilation of kinematical data at a mesostructural scale, on 14 data sites located within or near the thrust surface. This allows us to reconstruct the precise transport directions at the frontal zone, as well as their variations during thrust history.

We have measured and analysed (Fig. 6):

- (1) Orientations of striations on the main thrust surface. They provide direct evidence of the local slip direction. In some cases, the occurrence of two or more striation sets showing cross-cutting relationships indicates a sequence of distinct, diversely oriented slip increments (Fig. 6b).
- (2) Striations on planes parallel to the main thrust and located close to it (within a few metres; Fig. 6c). We supposed these to represent minor individual discontinuities within the fault zone sharing the same movement plane.
- (3) Shear-induced solution cleavage and incipient S-C fabrics, developed either in Mesozoic carbonates or in Tertiary clastic deposits (Fig. 6d, e). The transport vector on the shear plane is taken as the normal to the intersection line with cleavage planes (e.g. Marshak & Mitra 1988, p. 235).
- (4) Sheared pebbles in Tertiary conglomerates (Fig. 6e'). Offset marker points on their surfaces allow us to reconstruct the precise slip vectors.

The ensemble of orientations of mesostructures obtained within each data site is treated statistically in order to infer significant transport directions. Specific tools included in *Stereonet* software ($6.3.2 \times$ version; Allmendinger 2004) have been used for this purpose.

The orientations of mesoscopic structures and the results of our kinematical analysis on thrust transport directions are shown in Figure 7 and Table 1. In the case of some large data sites where a number of different outcrops were studied (sites 5, 6 and 8), the results for each outcrop are presented separately. The map in Figure 7 compiles the inferred local transport directions (arrows), and summarizes them for each sector and for the whole thrust sheet (rose diagrams).

Transport directions show high variability, with a marked polymodal distribution. The dominant direction is towards the north (azimuth range from $340-010$), accompanied by two secondary modes towards the NNE ($020-040$) and ENE ($060-080$). These frequency maxima are quite persistent all over the thrust front independently of its orientation: (a) in the central sectors (oriented NW–SE and east–west), where data are more abundant and representative, all three mentioned transport directions are recorded; (b) in the eastern sector (oriented north–south), the north and ENE directions are recorded; and (c) in the western sector (NE–SW striking ramps), transport indicators towards the north and NNW prevail.

A number of studied sites show several distinct transport directions. Among 98 striated thrust planes that were measured, 27 planes exhibit two or more distinctly oriented striations. Cross-cutting relationships have been discerned in 7 of them, which allow us to characterize relative timing of local movements (Table 1). Almost all of them are consistent with a time sequence that describes an anti-clockwise rotation of transport directions for the Utrillas sheet: ENE \rightarrow NNE \rightarrow north. The only exception is the sequence between directions 030 and 053 recorded at Site 8.8.

Interpretation and discussion

Consistence of macro- and mesoscopic structures and their time relationships

Our mesoscopic kinematical results suggest that the three dominant transport directions recorded within the Utrillas thrust sheet represent successive episodes of incremental rigid-block translation (although accompanied by significant internal folding). It is true that the reliability of meso-scale kinematical indicators is not universally accepted; some authors maintain that they provide less representative results than those obtained from

macrostructural reconstructions (e.g. Marshak & Mitra 1988, p. 312), whereas others use the latter only as a preliminary approach (Groshong 1999, p. 182). Besides, we should be aware of the likelihood that deflection of local transport directions could occur on oblique ramps (as quantitatively analysed by Apotria *et al.* 1992), which surely contributes to scattering of the recorded slip vectors. Bearing these difficulties in mind, the consistency of results from different sources (macro- and mesostructural geometry and kinematics, tectono-sedimentary relationships) should be considered as a key test for the proposed evolutionary model.

Within the Utrillas thrust sheet, transport directions inferred from mesostructural indicators, as well as their relative time sequence, are in good agreement with the evolution of internal folding. The early transport episodes towards the ENE and NNE were approximately orthogonal to the early fold hinges (trends ranging from NNW–SSE to WNW–ESE), while the late movement towards the north is orthogonal to the superposed, transverse (east–west to ENE–WSW) folds. It is usually assumed that detachment folds accommodating differential movement within a thrust sheet have the same movement plane as the thrust, that is, their hinge lines are nearly orthogonal to the transport direction (e.g. Marshak & Mitra 1988, p. 312). Since most of the flexural folds deforming the Utrillas thrust sheet belong to this type, the described geometric relationship between hinge lines and transport vectors are kinematically meaningful and can be taken as a basis for the proposed evolutionary model.

The fold and transport sequence is corroborated (and chronologically constrained) by tectono-sedimentary relationships in the neighbouring Tertiary basins (particularly in the Aliaga basin). Briefly, NW–SE to NNW–SSE-trending folds deform units T1–T4 (Eocene–Late Oligocene in age), while east–west-trending folds and related northward displacement on both the Utrillas and the Cobatillas thrusts are coeval or younger than the Early Miocene T5 unit.

Finally, the evolution of regional palaeostress fields (Simón 2006; Simón & Liesa 2008; Liesa & Simón 2009) has been also taken into account in order to propose a kinematical scenario dynamically consistent with the tectonic framework. In summary, the early thrust displacement towards the ENE and NNE fits well the NE–SW intraplate stress field, active from Middle Eocene–Late Oligocene times. Late transport towards the north is consistent with two stress fields active by the Miocene, with maximum compression trajectories trending SSE–NNW and NNE–SSW, respectively.

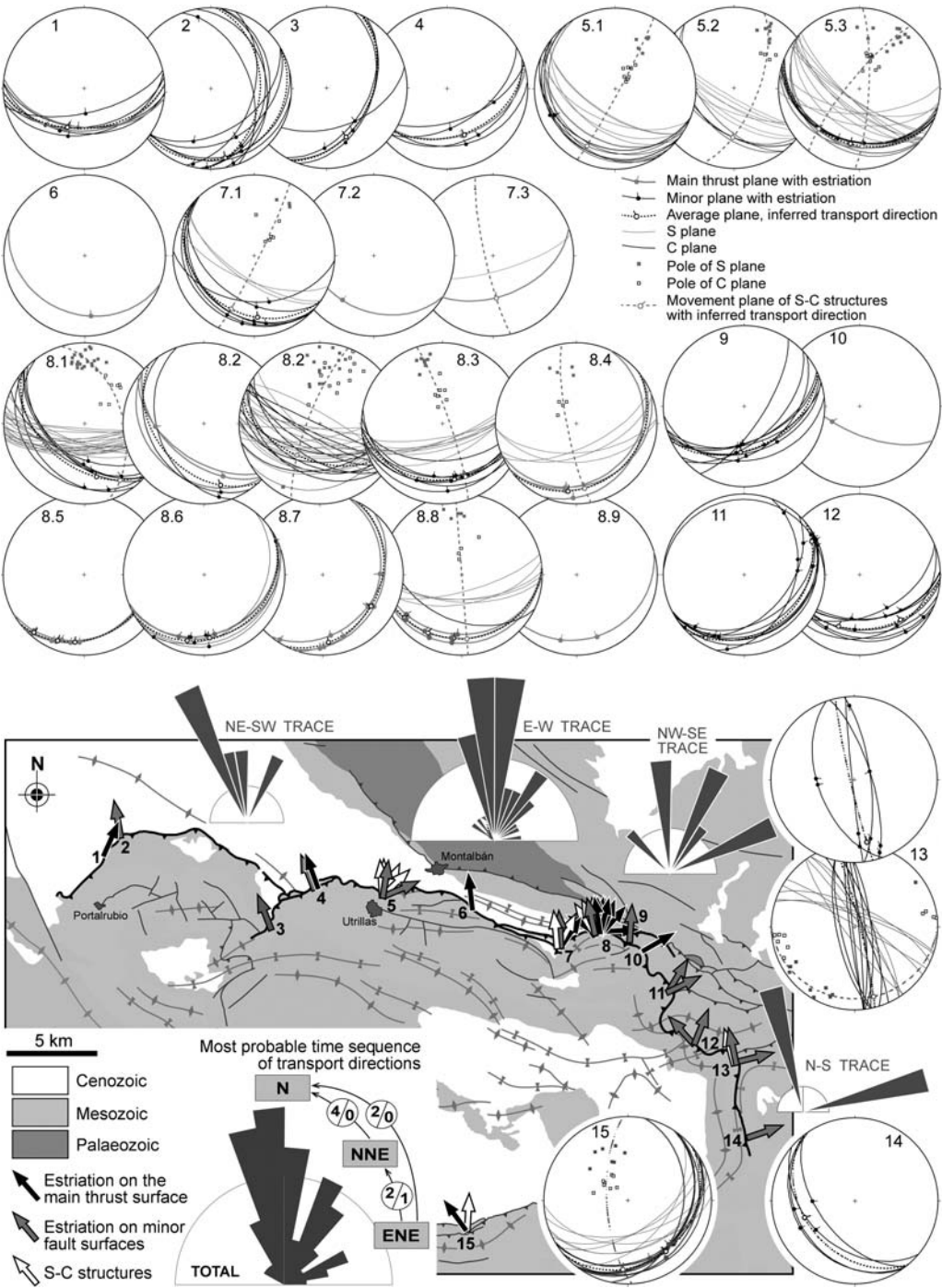


Fig. 7. Results of kinematical analysis from meso-scale structures at the Utrillas thrust front. Equal-area plots (lower hemisphere) 1 to 15: orientation of structures and inferred transport directions at each structural site. Arrows on the map: horizontal projection of local transport directions. Rose diagrams: frequency distribution of transport directions for each distinctly oriented sector of the thrust front, and for the total data base (radius represents 10% of the total data). Accompanying the synthetic rose diagram: sketch of time relationships between the three preferred transport directions; circles enclose the total number of local cross-cut relationships compatible/incompatible with each binary time sequence (curved arrows).

Table 1. *Results of kinematical analysis*

Site	Unit, position	Meso-structures			Average plane with pitch of transport direction	Azimuth of transport direction (hanging wall)
		M.p	m.p	S-C		
1	Upper Cret. hanging wall	X			087, 49S; 72W	023
2	Upper Cret. hanging wall		X		061, 24S; 70W 004, 39E; 18S	350
3	T1 footwall		X		025, 43E; 55S	339
4	Upper Cret. + T4 both blocks		X		071, 40S; 89E	339
		X			075, 39S; 86E	340
5.1	T4 both blocks		X		125, 24S; 60W	067
				X	129, 20S; 77E	026
5.2	T4 both blocks			X	136, 48S; 55E	001
5.3	T4 both blocks		X		113, 32S; 77E	009
				X	111, 32S; 68W	046
				X	111, 32S; 69E	177
6	Upper Cret. hanging wall	X			110, 28S; 66E	354
7.1	T3 footwall		X		123, 29S; 56E	357
				X	133, 24S; 72E	023
7.2	Upper Cret. hanging wall	X			120, 33S; 86W	034
7.3	Upper Cret. hanging wall			X	070, 48S; 79W	355
8.1	T3 footwall		X		129, 45S; 48E	348
				X	130, 46S; 25E	328
8.2	Upper Cret. + T3 both blocks	X	X		137, 41W; 32S 130, 49S; 55W	345 087
				X	137, 41W; 79S	032
8.3	T3 footwall		X		084, 28S; 84E	349
				X	086, 30S; 73E	337
8.4	T3 footwall	X			050, 23S; 46W	006
				X	050, 23S; 60W	352
8.5	Upper Cret. hanging wall	X			052, 24S; 13W 37W 51W	041 (1) 022 (2) 008 (3)
8.6	Upper Cret. hanging wall	X			059, 23S; 47W 65W	014 (1) 355 (2)
8.7	Upper Cret. hanging wall	X			027, 29 E; 85S 35S	303 (1) 355 (2)
8.8	Upper Cret. + T3 both blocks	X			085, 22S; 35W 57W 80W	053 (1) 030 (2) 007 (3)
				X	085, 22S; 90	355
8.9	T3 footwall	X			072, 21S; 60W 072, 21S; 90	014 (1) 342 (2)

(Continued)

Table 1. *Continued*

Site	Unit, position	Meso-structures			Average plane with pitch of transport direction	Azimuth of transport direction (hanging wall)
		M.p	m.p	S-C		
9	Upper Cret. hanging wall	X			065, 46S; 68W	004
10	Upper Cret.	X			115, 63S; 72W	060
11	Lower Jura. hanging wall		X		049, 27S; 16E 049, 27S; 21W	064 (1) 031 (2)
12	Upper Cret. hanging wall		X		092, 33S; 51E 092, 33S; 72W	318 022
13	Upper Cret. hanging wall		X		167, 86W; 24S pl. M: 076, 86N	348 (1?) 076 (2?)
				X	166, 85E; 14S	345
14	Jurassic footwall		X		140, 38W; 74N	071
15	Lower Cret. hanging wall	X		X	050, 28W; 87W 48W	144 005

Transport directions inferred from meso-scale kinematical indicators at fifteen sites along the Utrillas thrust front (see location in Fig. 8). M.p, striations on main thrust plane; m.p, striations on minor reverse fault planes close to the main thrust; S-C, S-C structures associated to the main thrust movement. (1), (2), (3): local time sequence of transport directions based on cross-cut relationships.

An integrated model of incremental slip and progressive deformation for the Utrillas thrust

The following seven episodes (with approximate chronology) can be distinguished within our proposed evolutionary scheme (1 to 7 in Fig. 8):

- (1) During the Early Eocene (early T2 unit), a NNW–SSE-trending, E-verging monocline developed at the Aliaga area, due to positive inversion of the Miravete fault. This fold controlled and bounded the eastern Aliaga basin. Other NW–SE-trending folds developed NW of our region, their exhumed Palaeozoic cores supplying sediments to the newly created Montalbán basin.
- (2) During the Late Eocene (T2–T3 boundary), translation of the Utrillas thrust (including the Portalrubio block) initiated. An east–west hanging wall bending monocline developed on the eastern sector of the main deep ramp, giving rise to a disconnection between the Montalbán and Aliaga basins. Since direct kinematical evidence of such early movement is not available, its transport direction remains imprecise.
- (3) By the Early Oligocene (end of T3), the movement was probably restricted to the central sector (Utrillas–Castel de Cabra), the rate of relief uplift decreased and the palaeogeographical high separating both Tertiary basins

vanished. This scenario is consistent with the early transport direction towards the ENE, the central segment of the thrust therefore acting as an oblique or nearly lateral ramp with only minor upthrow component. Blockage at the eastern, steep ramp avoided displacement of the thrust front towards the east, the internal deformation being accommodated by the Miravete monocline and newly created detachment and propagation, north–south-trending folds. The Montalbán anticline began to develop and controlled the northeastern boundary of the Montalbán basin.

- (4) During the Middle–Late Oligocene (T4), the whole thrust sheet underwent displacement towards the NE or NNE. Development of the whole NW–SE-oriented set of propagation and detachment folds was in progress. Sedimentation continued in the Montalbán basin and expanded to the western Aliaga basin.
- (5) By the Late Oligocene (T4–T5 boundary), the thrust sheet probably underwent a short episode of eastwards movement, which amplified the north–south folds of the Aliaga–Montoro de Mezquita sector by buttressing against the steep, north–south-trending ramp. Back-thrusting at the Miravete fault zone gave rise to development of the western limb of the Campos–Aliaga anticline. This episode could explain the anomalous time relationship between local transport directions recorded at Site 8.8 (see section on meso-scale kinematical analysis).

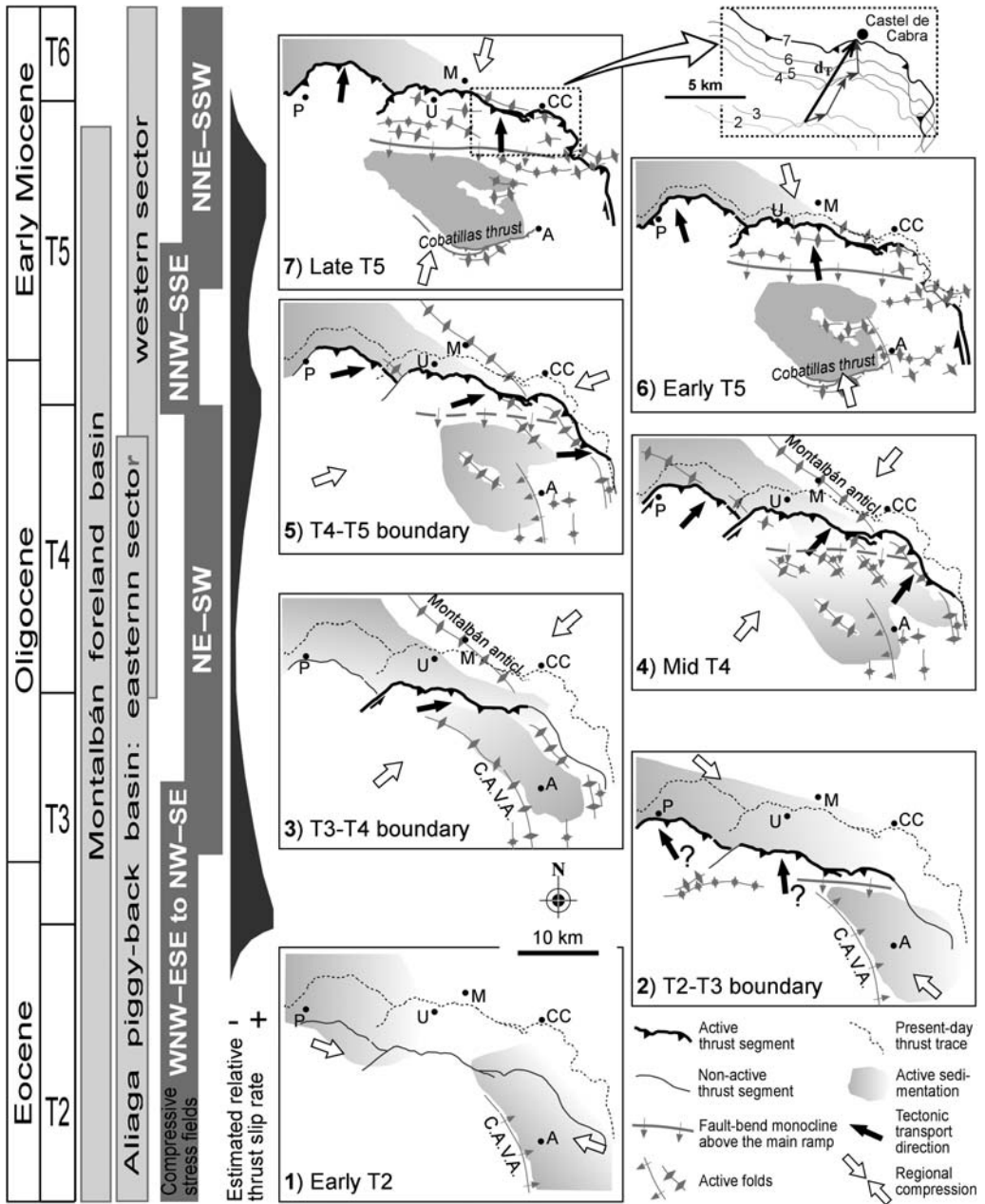


Fig. 8. Evolutionary model proposed for the Utrillas thrust, including: slip history, progressive internal deformation, relationships with the evolution of the Montalbán (foreland) and Aliaga (piggy-back) Tertiary basins, and relationships with the intraplate compressive stress fields defined by Liesa & Simón (2009). (1) to (7): sketches of the successive evolutionary episodes. Inset on top: summary of the incremental translation of the Utrillas thrust sheet since stage 2 to stage 7, represented by successive displacement vectors that result in the total finite arrow d_T (see Fig. 9). On the maps: P, Portalrubio; U, Utrillas; M, Montalbán; CC, Castel de Cabra; A, Aliaga; C.A.V.A., Campos–Aliaga–Villarroya anticline.

- (6) By the Oligocene–Miocene boundary (early T5), the Palaeogene infill of the eastern sector of the Aliaga basin had been strongly eroded owing to previous, intense north–south folding close to the north–south ramp; sedimentation was then confined west of the Campos–Aliaga anticline. The whole Utrillas thrust sheet now moved towards the north or NNW, accompanied by intense east–west to ENE–WSW internal folding (main hanging wall accommodation monocline, detachment folds all over the sheet and, occasionally, propagation folds close to the frontal ramps) as well as displacement of the Cobatillas thrust (southern boundary of the Aliaga basin). The new folds overprinted the NW–SE to NNW–SSE previous folds, and even affected the main thrust surface at its north-eastern segment (La Cañadilla).
- (7) During the Early Miocene (end of T5), the Utrillas thrust concluded its emplacement, with a persisting transport direction towards the north. The rest of east–west to ENE–WSW contractional structures completed their development as well.

The question of the total ‘arrow’

Our proposal of progressive displacement and deformation of the Utrillas thrust refines previous models by Guimerà (1988), Guimerà *et al.* (1990), González & Guimerà (1993) and Casas *et al.* (2000). Our model does not give, on its own, an answer to the basic question of the total ‘arrow’ (horizontal component of the net slip vector), which needs the contribution of map and macro-structural analysis. However, it allows us to constrain the overall kinematical reconstruction.

The Utrillas thrust front combines distinctly oriented segments, as a result of its Mesozoic structural heritage, which provides a more helpful marker than a straight trace in order to estimate the net slip. The total ‘arrow’ that could be obtained by applying the ‘bow-and-arrow rule’ depends on whether the complete trace or the traces of the best-defined arcs (Portarubio and Las Parras–Castel de Cabra) are utilized. The results would be 9.8 km towards N022°E in the first case, and c. 4.0 km towards 000 in the second one (arrows 1 and 2/2’ in Fig. 9a, respectively). These hypothetical transport directions closely approximate the most prominent

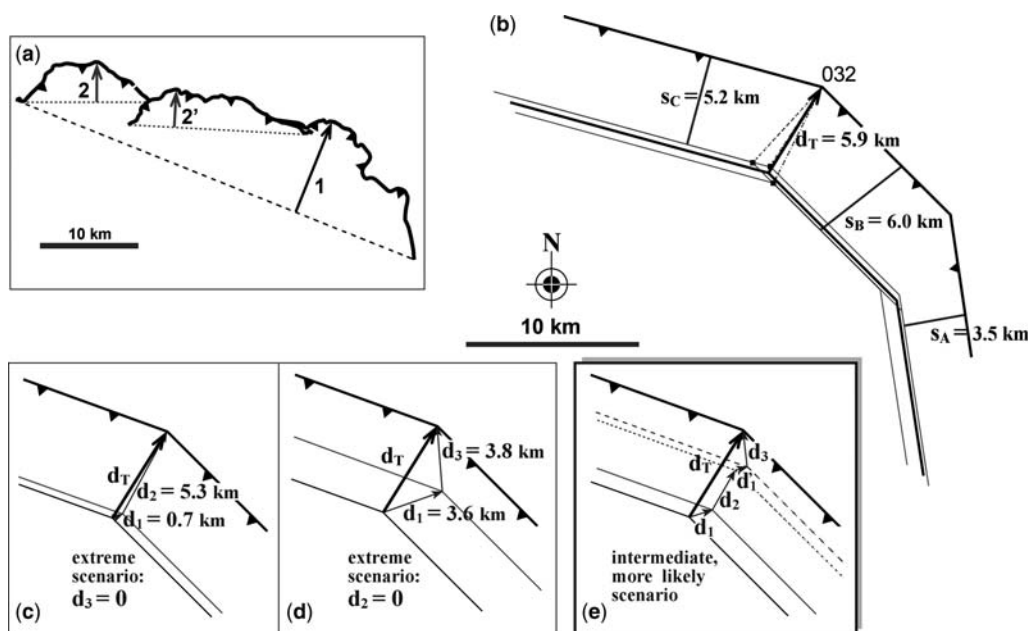


Fig. 9. Different kinematical approaches of the total finite displacement (‘total arrow’, d_T) and the three distinct transport components (d_1 , d_2 , d_3) of the Utrillas thrust. (a) Simple approaches by applying the ‘bow-and-arrow rule’. (b) 2D procedure based on calculation of three finite shortening values along cross-sections 1-1’, 2-2’ and 3-3’ of Figure 3. (c) and (d) Two extreme scenarios for assessing the distinct transport components, assuming $d_3 = 0$ and $d_2 = 0$, respectively. (e) An intermediate, tentative, likely scenario assuming $d_2 \geq d_3 > d_1 > d'_1 > 0$. Azimuths of d_1 , d_2 and d_3 are taken as the means of the corresponding maxima in the synthetic rose diagram of Figure 7: 070, 030 and 355, respectively.

maxima in the synthetic rose diagram of Figure 7. However, such coincidence does not give direct support to the conjecture that either of these two vectors represents the real translation vector, that is, the finite resultant of the whole displacement history.

Alternatively, we can apply the following, simple geometric procedure in order to constrain the total 'arrow' of the Utrillas thrust (Fig. 9b):

- (i) Draw a simplified sketch of the present-day thrust front. Only the central and eastern sectors (ramps A, B and C in Fig. 4) have been taken into account, owing to the relative independence of the Portalrubio sheet.
- (ii) Calculate total absolute shortening values in the thrust sheet on cross-sections 1-1', 2-2' and 3-3' of Figure 3, traverse to ramps A, B and C, respectively (s_A , s_B and s_C in Fig. 9b). Each value represents the total convergence of two extreme points within the footwall and the hanging wall, respectively, along a cross-section. It integrates horizontal fault separation and shortening produced by internal folding (see Table 2). In order to avoid the extensional deformation that took place during the early Cretaceous, shortening and thrust heave in each cross-section have been measured using different horizons of the post-rift sequence (usually the base and top of the Upper Cretaceous series). Total shortening values express the differences between the average length of those horizons, measured between the pin and loose lines, and the present-day distance between these lines in each cross-section. Thrust heave and its horizontal component were calculated using bed cut-off points of these horizons in each cross-section. The results are very similar for both horizons, the mean of them being included in Table 2.
- (iii) Schematic, plan-view retrodeforming the whole thrust by simultaneous, 2D restoration of the three shortening values. This kinematical exercise has been carried out graphically by using the simplified, three-segment sketch of the thrust front as a 'virtual marker' (only

in the case of no internal folding, the retrodeformed position of this marker would have matched the real position of the material line representing the present-day front). This operation is the reverse one of that used for measuring opening of veins: in absence of fibrous infill, the finite opening vector can be determined from precise marker points provided by matching bent walls (Hobbs *et al.* 1976, pp. 292–293). In our sketch, the intersection points between oblique segments represent such marker points (solid squares in Fig. 9b). Since we have three segments and three potential marker points, the procedure will result in three distinct solution vectors (thin dashed lines joining marker points of the thrust trace before and after displacement; Fig. 9b). These closely constrain the total finite arrow, ranging from 027 to 043 in azimuth, and from 5.5 to 6.2 km in length. The mean vector has been taken as the optimum solution: \mathbf{d}_T = displacement at the thrust front + internal deformation = 5.9 km towards N032°E.

Our results are not far from those published by González & Guimerà (1993) and Casas *et al.* (2000), who proposed broadly northward transport directions with maximum displacement of 6–8 km. Their estimates, based only on unidirectional cross-sections (i.e. '1D' strain), are now modified by our independent 2D kinematical analysis. The adjustment mainly concerns the finite transport direction, which fits the NNE secondary frequency mode obtained from mesoscopic kinematical indicators instead of being oriented towards the north. Besides, the resulting direction closely approaches that obtained by applying the 'bow-and-arrow rule' to the complete thrust trace (022), although this procedure would have overestimated the magnitude of the actual net displacement (9.8 km v. 5.9 km). Such misfit probably occurs because we are not dealing with a single thrust front, but with a complex one made of several distinct ramps.

Table 2. Separation and absolute shortening calculated on three representative cross-sections traverse to ramps A, B and C of the Utrillas thrust

Ramp	Cross-section	Total shortening (S, km)	Dip separation (km)	Horizontal separation (heave, km)	Shortening due to internal deformation (km)
A	1-1'	3.5	0	0	3.5
B	2-2'	6.0	2.8	2.0	4.0
C	3-3'	5.2	4.8	4.3	0.9

Characterizing the various components of the total displacement vector and their tectonic framework

After reconstructing the progressive displacement of the Utrillas thrust, with at least three distinct transport directions towards the ENE (070), NNE (030) and north (355), an estimate to the relative magnitude of each of these components (d_1 , d_2 and d_3 , respectively) could be made. Using a simple vector construction, two extreme hypotheses can be envisaged by making virtually null either d_3 or d_2 (no combination is feasible considering $d_1 = 0$). With $d_3 = 0$, a maximum value of 5.3 km can be assigned to d_2 , and a minimum of 0.7 km to d_1 (Fig. 9c). By making d_2 null, maximum values of 3.6 and 3.8 km could be assigned to d_1 and d_3 , respectively (Fig. 9d). An intermediate, more likely scenario can be considered by assuming that (a) none of the three components is null; and (b) according to our evolutionary model, the displacement component d_1 was recorded at two distinct episodes: 3 and 4 in Figure 8. This would result in a tentative model of progressive deformation made of four incremental vectors, each one being in the order of 1–3 km long (Fig. 9e).

In summary, the net slip vector of the Utrillas thrust is the finite result of a complex slip history. In particular, the displacement episodes towards the ENE and NNE, prior to the northward one, are essential pieces of the evolutionary model that were not previously considered. These episodes are consistent with the orientation (NE–SW) and age (Oligocene *sensu lato*) of the apparently most intense compressive stress field within the region (Liesa & Simón 2009), responsible for the main, NW–SE to NNW–SSE-trending folds within the thrust sheet. Moreover, such slip episodes should be necessarily invoked for explaining the buttressing folds at the easternmost sector (Montoro de Mezquita).

The relative importance of the earlier thrust movements (Eocene–Early Oligocene) and the later ones (Late Oligocene–Early Miocene) has been differently assessed by previous authors, depending on whether it has been analysed from the perspective of the Montalbán basin or the Aliaga basin. In this way, Casas *et al.* (2000) interpret that most of the total displacement occurred during the first episode, and only 1.5 km of the total slip (estimated at about 8 km) took place after T3 sedimentation in the Montalbán basin. In contrast, González & Guimerà (1993, fig. 10) attribute around 75% of their total 6–7 km-long arrow to the second period, based on the evolution of the piggy-back Aliaga basin. Unfortunately, our results do not allow us to discriminate between these two

possibilities, since no evidence has been found about the relative magnitude of the later, northward oriented transport component.

Conclusions

Reconstructing progressive deformation during thrust development, including incremental slip vectors and development of internal fold sets, should be considered as an essential piece of an integrated, ‘4D’ model of thrusting. This target is crucial in the case of thrusts that result from positive inversion of inherited, diversely oriented extensional faults. In contrast to the newly propagated thrusts, no precise relationship between geometry and transport direction should be assumed in that case; fault reactivation will follow a slip vector controlled by the orientation of the fault surface as well as by the average deviatoric stress tensor in the surrounding rock body (Bott 1959). Therefore, a wide range of transport directions could be expected, as well as, eventually, distinct successive slip vectors as a response to changing stress conditions.

The Utrillas thrust resulted from inversion of the extensional structure of the northern margin of the Early Cretaceous Las Parras subbasin, in the NW of the Cretaceous Maestrazgo basin. It is made of two distinct thrust sheets, Utrillas and Portalrubio sheets, separated by Las Parras fault. Both thrust sheets are bounded by diversely oriented, S-dipping ramps that cut both the Mesozoic series and the Variscan basement, which are inherited from extensional Early Cretaceous faults. They show dominant strikes ENE–WSW to WNW–ESE (Fig. 4) and, in most cases, gentle dips (20–25°), except for the two steeper ramps that laterally enclose the Utrillas thrust sheet.

The whole Utrillas thrust sheet behaved as an undivided block during most of the Tertiary orogenic period, although it underwent strong coeval internal deformation. Its positive inversion did not follow a single slip vector. Meso-scale kinematical indicators at the thrust front, and their time relationships, record successive transport directions of the hanging wall towards the ENE, NNE and north. This incremental slip history is consistent with the dominant trends of internal folds and their time sequence: the earlier transport directions (ENE and NNE) are approximately orthogonal to the earlier, NNW–SSE to WNW–ESE-trending folds, while the later transport towards the north is nearly orthogonal to the younger, transverse fold generation. Such progressive deformation model is also in agreement with (a) tectono-sedimentary interactions at the Montalbán (foreland) and Aliaga (piggy-back) basins; and (b) the framework of palaeostress field evolution.

Dating of involved sedimentary units provides a chronological frame for the proposed evolutionary model, as we next summarize. Late Eocene: beginning of the thrust movement, with development of an east–west hanging wall anticline disconnecting the Montalbán and Aliaga basins. Early Oligocene: movement towards the ENE, probably restricted to the central ramp, with blockage of effective displacement at the eastern, steep ramp and strong internal, north–south-trending folding. Middle–Late Oligocene: displacement towards the NE or NNE, and development of the whole NW–SE-trending fold set. Late Oligocene: probable short episode of eastwards movement, which amplified the north–south folds by buttressing against the steep eastern ramp. Oligocene–Miocene transition: movement towards the north or NNW, accompanied by intense east–west to ENE–WSW internal folds that locally overprint the NW–SE to NNW–SSE previous folds and the thrust surface. Early Miocene: last transport episode towards the north.

The ‘arrow’ (total finite horizontal displacement) of the Utrillas thrust has been estimated by means of 2D, plan-view schematic retrodeformation of the whole trace, taking into account shortening values measured on three distinctly oriented cross-sections. The most likely result is a hanging wall transport vector pointing towards N032°E with a modulus of c. 5.9 km. According to our model of progressive deformation, this total vector would represent the sum of three main components parallel, respectively, to the three distinct transport directions defined above: ENE (070; probably acting at two distinct episodes: 3 and 4 in Fig. 8), NNE (030) and north (355). This kinematical model, although based on necessary simplifications concerning the geometry of the thrust front and the deformational history, represents a more detailed calculation than that based on the simple ‘bow-and-arrow rule’.

Precise identification of the transport directions of thrust sheets, reconstruction of their time sequence, and interpretation of the total net slip as a sum of such components is necessary for both characterizing the tectonic evolution and constraining the geometric models. Defining the transport direction based on empirical evidences should be considered as an essential part of thrust research. Any quantitative estimate of the displacement of a thrust sheet should be corrected according to such actual transport directions, avoiding automatic conversion of fault separation measured on cross-section to net displacement.

We are very grateful to the editors, J. Poblet and R. J. Lisle, and two anonymous reviewers for their useful suggestions. The Spanish Ministerio de Educación y Ciencia and FEDER (projects CGL2006-09670, CGL2008-05418 and

CGL2009-13390), as well as the Aragón Government (Geotransfer research group), provided financial support for this work.

References

- ALLMENDINGER, R. W. 2004. Stereonet for Macintosh. Stereonet for Windows. Available online at: <http://www.geo.cornell.edu/geology/faculty/RWA/main-text.html>.
- ALMELA, A., MANSILLA, H., QUINTERO, I. & GÓMEZ, E. 1975. Cartografía geológica. In: *Mapa Geológico De España 1:50.000, Hoja no. 493* (Oliete), Instituto Geológico y Minero de España, Madrid (publ. 1977).
- ÁLVARO, M., CAPOTE, R. & VEGAS, R. 1979. Un modelo de evolución geotectónica para la Cadena Celtibérica. *Acta Geológica Hispánica*, **14**, 172–177.
- ANTOLÍN-TOMÁS, B., LIESA, C. L., CASAS, A. M. & GIL-PEÑA, I. 2007. Geometry of fracturing linked to extension an basin formation in the Maestrazgo basin (Eastern Iberian Chain, Spain). *Revista de la Sociedad Geológica de España*, **20**, 351–365.
- APOTRIA, T. G., SNEDDEN, W. T., SPANG, J. H. & WILTSCHKO, D. V. 1992. Kinematic models of deformation at an oblique ramp. In: McCLAY, K. R. (ed.) *Thrust Tectonics*. Chapman & Hall, London, 141–154.
- AURELL, M., MELÉNDEZ, G. ET AL. 2002. Jurassic. In: GIBBONS, W. & MORENO, T. (eds) *The Geology of Spain*. Geological Society, London, 213–253.
- BOTT, M. H. P. 1959. The mechanics of oblique slip faulting. *Geological Magazine*, **96**, 109–117.
- BUTLER, R. W. H. 1992. Structural evolution of the western Chartreuse fold and thrust system, NW French Subalpine Chains. In: McCLAY, K. R. (ed.) *Thrust Tectonics*. Chapman & Hall, London, 287–298.
- CALCAGNO, PH., LAZARRE, J., COURRIOUX, G. & LEDRU, P. 2007. 3D geometric modelling of an external orogenic domain: a case history from the western Alps (massif de Morges, Pelvoux). *Bulletin de la Societe Géologique de France*, **178**, 263–274.
- CANÉROT, J. 1974. *Recherches géologiques aux confins del chaînes Ibérique et Catalane*. PhD thesis, Université de Toulouse, France. Publ. ENADIMSA, Madrid.
- CANÉROT, J., CRESPO, A. & NAVARRO, D. 1977. Cartografía geológica. In: *Mapa Geológico De España 1:50 000, Hoja No. 518 (Montalbán)*. Instituto Geológico y Minero de España, Madrid (publ. 1979).
- CAPOTE, R., MUÑOZ, J. A., SIMÓN, J. L., LIESA, C. L. & ARLEGUI, L. E. 2002. Alpine tectonics I: The Alpine system north of the Betic Cordillera. In: GIBBONS, W. & MORENO, T. (eds) *The Geology of Spain*. Geological Society, London, 367–400.
- CARTWRIGHT, J. A. 1989. The kinematics of inversion in the Danish Central Graben. In: COOPER, M. A. & WILLIAMS, G. D. (eds) *Inversion Tectonics*. Geological Society, London, Special Publications, **44**, 153–175.
- CASAS, A. & SIMÓN, J. L. 1992. Stress field and thrust kinematics: a model for the tectonic inversion of the Cameros Massif (Spain). *Journal of Structural Geology*, **14**, 521–530.
- CASAS, A. M., CASAS, A., PÉREZ, A., TENA, S., BARRIER, L., GAPAIS, D. & NALPAS, TH. 2000. Syn-tectonic sedimentation and thrust-and-fold kinematics at the

- intra-mountain Montalbán Basin (northern Iberian Chain, Spain). *Geodinamica Acta*, **1**, 1–17.
- CLARIANA, M. P., MELÉNDEZ, A. & SORIA, A. R. 2000. Sedimentología y paleogeografía de la secuencia de depósito Aptiense inferior (Facies Urgon) en la subcuenca de Las Parras (Teruel). *Geogaceta*, **27**, 47–50.
- COWARD, M. 1994. Inversion tectonics. In: HANCOCK, P. L. (ed.) *Continental Deformation*. Pergamon Press, Oxford, 289–304.
- ELLIOTT, D. 1976. The energy balance and deformation mechanisms of thrust sheets. *Philosophical Transactions of the Royal Society of London*, **A-283**, 289–312.
- ELLIOTT, D. 1983. The construction of balanced cross sections. *Journal of Structural Geology*, **5**, 101.
- FERREIRO, E. & RUIZ, V. 1986–87. Cartografía geológica. In: GABALDÓN, V. (coord) *Mapa Geológico De España 1:200 000, Hoja No. 40 (Daroca)*. Instituto Tecnológico GeoMinero de España, Madrid (publ. 1991).
- GARRIDO-MEGÍAS, A. 1973. *Estudio geológico y relación entre tectónica y sedimentación del Secundario y Terciario vertiente meridional pirenaica en su zona central (provincias de Huesca y Lérida)*. PhD thesis, Universidad de Granada, Spain.
- GARRIDO-MEGÍAS, A. 1982. Introducción al análisis tectosedimentario: aplicación al estudio dinámico de cuencas. *Actas V Congreso Latinoamericano de Geología*, 385–402.
- GARRIDO, A. & VILLENA, J. 1977. El Trías germánico en España: Paleogeografía y estudio secuencial. *Cuadernos de Geología Ibérica*, **4**, 37–56.
- GAUTIER, F. 1979. Cartografía geológica. In: BARNOLAS, A. (coord) *Mapa Geológico De España 1:50 000, Hoja No. 543 (Villarluengo)*. Instituto Geológico y Minero de España, Madrid (publ. 1980).
- GONZÁLEZ, A. 1989. *Análisis tectosedimentario del Terciario del borde sur de la depresión del Ebro (sector bajo-aragonés) y de las cubetas ibéricas marginales*. PhD thesis, Universidad de Zaragoza, Spain.
- GONZÁLEZ, A. & GUIMERÀ, J. 1993. Sedimentación sintectónica en una cuenca transportada sobre una lámina de cabalgamiento: la cubeta terciaria de Aliaga. *Revista de la Sociedad Geológica de España*, **6**, 151–165.
- GONZÁLEZ, A., PARDO, G. & VILLENA, J. 1988. El análisis tectosedimentario como instrumento de correlación entre cuencas. *Actas II Congr. Geológico de España*, Sociedad Geológica de España, Granada, Vol. Simposios, 175–184.
- GROSHONG, R. H. 1999. *3-D Structural Geology*. Springer Verlag, Berlin.
- GUIMERÀ, J. 1988. *Estudi estructural de l'enllaç entre la Serralada Ibérica y la Serralada Costanera Catalana*. PhD thesis, Universidad de Barcelona, Spain.
- GUIMERÀ, J. 2004. La Zona de Enlace. In: VERA, J. A. (ed.) *Geología De España. Sociedad Geológica De España-IGME*, Madrid, 605–606.
- GUIMERÀ, J. & ÁLVARO, M. 1990. Structure et évolution de la compression alpine dans la Chaîne ibérique et la Chaîne côtière catalane (Espagne). *Bulletin de la Société Géologique de France*, **6**, 339–348.
- GUIMERÀ, J., GONZÁLEZ, A. & PÉREZ, A. 1990. Evolución del cabalgamiento de la Muela de Montalbán (Cordillera Ibérica, Teruel). *Geogaceta*, **8**, 47–49.
- GUIMERÀ, J. & SALAS, R. 1996. Inversión terciaria de la falla normal mesozoica que limitaba la subcuenca de Galve (cuenca del Mastrazgo). *Geogaceta*, **20**, 1701–1703.
- HERNÁNDEZ, A. & ANADÓN, P. 1982–83. Cartografía geológica. In: HERNÁNDEZ, A. *Mapa Geológico De España 1:200 000, Hoja No. 47 (Teruel)*. Instituto Geológico y Minero de España, Madrid (publ. 1986).
- HOBBS, B. E., MEANS, W. D. & WILLIAMS, P. F. 1976. *An Outline of Structural Geology*. John Wiley & Sons, New York.
- LIESA, C. L. 1999. Estructura y cinemática del arco de cabalgamientos Portalrubio-Vandellós en el sector de Castellote (Teruel). *Revista Mas de las Matas*, **18**, 9–37.
- LIESA, C. L. 2000. *Fracturación y campos de esfuerzos compresivos alpinos en la Cordillera Ibérica y el NE peninsular*. PhD thesis, Universidad de Zaragoza, Spain.
- LIESA, C. L. & SIMÓN, J. L. 2004. Modelos de inversión positiva en sistemas de fallas normales en graderío: los márgenes de las cuencas extensionales cretácicas en la Cordillera Ibérica centro-oriental. *Geotemas*, **6**, 229–232.
- LIESA, C. L. & SIMÓN, J. L. 2007. A probabilistic approach for identifying independent remote compressions in an intraplate region: the Iberian Chain (Spain). *Mathematical Geology*, **39**, 337–348.
- LIESA, C. L. & SIMÓN, J. L. 2009. Evolution of intraplate stress fields under multiple compressions: The case of the Iberian Chain (NE Spain). *Tectonophysics*, doi: 10.1016/j.tecto.2009.02.002.
- LIESA, C. L., SORIA, A. R. & MELÉNDEZ, A. 2000. Estructura extensiva cretácica e inversión terciaria del margen noroccidental de la subcuenca de Las Parras (Cordillera Ibérica, España). *Geotemas*, **1**, 231–234.
- LIESA, C. L., CASAS, A. M., SORIA, A. R., SIMÓN, J. L. & MELÉNDEZ, A. 2004. Estructura extensional cretácica e inversión terciaria en la región Aliaga-Montalbán. In: COLOMBO, F., LIESA, C. L., MELÉNDEZ, G., POCOVÍ, A., SANCHO, C. & SORIA, A. R. (eds) *Itinerarios Geológicos Por Aragón*. Sociedad Geológica de España, Zaragoza. Geo-Guías, **1**, 151–180.
- LIESA, C. L., SORIA, A. R., MELÉNDEZ, N. & MELÉNDEZ, A. 2006. Extensional fault control on the sedimentation patterns in a continental rift basin: El Castellar Formation, Galve sub-basin, Spain. *Journal of the Geological Society, London*, **163**, 487–498.
- MARSHAK, S. & MITRA, G. 1988. *Basic Methods of Structural Geology*. Prentice Hall, New Jersey.
- MARTÍN, M. & CANÉROT, J. 1977. Cartografía geológica. In: *Mapa Geológico De España 1:50 000, Hoja No. 517 (Argente)*. Instituto Geológico y Minero de España, Madrid (publ. 1979).
- MARTÍN, M., CANÉROT, J. & LINARES-RIVAS, A. 1977. Cartografía geológica. In: *Mapa Geológico De España 1:50 000, Hoja No. 492 (Segura De Los Baños)*. Instituto Geológico y Minero de España, Madrid.
- MARTÍN-CHIVELET, J. (coord), BERÁSTEGUI, X. ET AL. 2002. Cretaceous. In: GIBBONS, W. & MORENO, T.

- (eds) *The Geology of Spain*. Geological Society, London, 255–292.
- McCLAY, K. R. & BUCHANAN, P. G. 1992. Thrust faults in inverted extensional basins. In: McCLAY, K. R. (ed.) *Thrust Tectonics*. Chapman & Hall, London, 93–104.
- PARDO, G., VILLENA, J., PÉREZ, A. & GONZÁLEZ, A. 1984. El Paleógeno de los márgenes del umbral de Montalbán: relación tectónica-sedimentación. *Publicaciones de Geología, Univ. Autónoma de Barcelona*, **20**, 355–363.
- PARDO, G., VILLENA, J. & GONZÁLEZ, A. 1989. Contribución a los conceptos y a la aplicación del análisis tectosedimentario. Rupturas y unidades tectosedimentarias como fundamento de correlaciones estratigráficas. *Revista de la Sociedad Geológica de España*, **2**, 199–219.
- PÉREZ, A. 1989. *Estratigrafía y sedimentología del Terciario del borde meridional de la Depresión del Ebro (sector riojano-aragonés) y cubetas de Muniesa y Montalbán*. PhD thesis, Universidad de Zaragoza, Spain.
- PEROPADRE, C., MELÉNDEZ, N. & LIESA, C. L. 2005. Niveles de tormenta en un intervalo siliciclástico costero aptiense de la subcuenca de Las Parras (Teruel): consideraciones paleogeográficas y estratigráficas. *Geo-Temas*, **8**, 81–84.
- PEROPADRE, C., MELÉNDEZ, N. & LIESA, C. L. 2007. Heterogeneous subsidence and paleogeographic elements in an extensional setting revealed through the correlation of a store deposit unit (Apitan, E Spain). *Journal of Iberian Geology*, **33**, 79–91.
- RODRÍGUEZ-LÓPEZ, J. P., MELÉNDEZ, N., DE BOER, P. L. & SORIA, A. R. 2008. Aeolian sand-sea development along the mid-Cretaceous western Tethyan margin (Spain); erg sedimentology and paleoclimate implications. *Sedimentology*, **55**, 1253–1292.
- SALAS, R. 1987. *El Malm i el Cretaci inferior entre el Massís de Garraf i la Serra d'Espadà*. PhD thesis, Universidad de Barcelona, Spain.
- SALAS, R. & CASAS, A. 1993. Mesozoic extensional tectonics, stratigraphy, and crustal evolution during the Alpine cycle of the eastern Iberian basin. *Tectonophysics*, **228**, 33–55.
- SALAS, R., GUIMERÀ, J., MÁS, R., MARTÍN-CLOSAS, C., MELÉNDEZ, A. & ALONSO, A. 2001. Evolution of the Mesozoic Central Iberian Rift System and its Cenozoic inversion (Iberian Chain). In: ZIEGLER, P. A., CAVAZZA, W., ROBERTSON, A. F. H. & CRASQUIN-SOLEAU, S. (eds) *Peri-Tethys Memoir 6: PeriTethyan Rift/Wrench Basins and Passive Margins*. Mémoires du Muséum national d'Histoire naturelle, **186**, 145–185.
- SANTANACH, P. 1989. Reflexiones sobre los mecanismos de incidencia de la tectónica en la división estratigráfica de rellenos de cuenca. Implicaciones en la correlación estratigráfica. *Revista de la Sociedad Geológica de España*, **2**, 223–234.
- SIMÓN, J. L. 2004. Superposed buckle folding in the eastern Iberian Chain, Spain. *Journal of Structural Geology*, **26**, 1447–1464.
- SIMÓN, J. L. 2005. Erosion-controlled geometry of buckle fold interference. *Geology*, **33**, 561–564.
- SIMÓN, J. L. 2006. El registro de la compresión intraplaca en los conglomerados de la cuenca terciaria de Aliaga (Teruel, Cordillera Ibérica). *Revista de la Sociedad Geológica de España*, **19**, 163–179.
- SIMÓN, J. L. & LIESA, C. L. 2008. Evolución de los campos de esfuerzos a partir del registro mesoestructural en las cuencas terciarias de Montalbán y Aliaga (Teruel, Cordillera Ibérica). *Geo-Temas*, **10**, 1531–1534.
- SIMÓN, J. L., ARENAS, C. ET AL. 1998. *Guía Del Parque Geológico De Aliaga*. Ayto. de Aliaga-CEDEMA-Dep. Geología Universidad de Zaragoza.
- SORIA, A. R. 1997. *La sedimentación en las cuencas marginales del surco Ibérico durante el Cretácico Inferior y su control tectónico*. PhD thesis, Universidad de Zaragoza, Spain.
- SUPPE, J. 1983. Geometry and kinematics of fault-bend folding. *American Journal of Science*, **283**, 684–721.
- THIESSEN, R. L. & MEANS, W. D. 1980. Classification of fold interference patterns: a reexamination. *Journal of Structural Geology*, **2**, 311–316.
- VILLENA, J., PÉREZ, A., PARDO, G. & GONZÁLEZ, A. 1991. Terciario. In: GABALDÓN, V. (coord) *Mapa Geológico De España 1:200 000, Hoja No. 40 (Daroca)*. Instituto Tecnológico GeoMinero de España, Madrid, 138–176.
- VILLENA, J., PARDO, G., PÉREZ, A., MUÑOZ, A. & GONZÁLEZ, A. 1996. The Tertiary of the Iberian margin of the Ebro basin: sequence stratigraphy. In: FRIEND, P. F. & DABRIO, C. J. (eds) *Tertiary Basins of Spain: The Stratigraphic Record of Crustal Kinematics*. Cambridge University Press, Cambridge, 77–82.
- ZOETEMEIJER, R. & SASSI, W. 1992. 2-D reconstruction of thrust evolution using the fault-bend fold method. In: McCLAY, K. R. (ed.) *Thrust Tectonics*. Chapman & Hall, London, 133–140.

Kinematic evolution of the eastern Tethyan Himalaya: constraints from magnetic fabric and structural properties of the Triassic flysch in SE Tibet

BORJA ANTOLÍN^{1*}, ERWIN APPEL¹, CHIARA MONTOMOLI², ISTVÁN DUNKL³, LIN DING⁴, RICHARD GLOAGUEN⁵ & RACHIDA EL BAY¹

¹*Institute for Geosciences, University of Tuebingen, Sigwartstrasse 10, 72076 Tuebingen, Germany*

²*Department of Earth Sciences, University of Pisa, via S. Maria 53, 56126 Pisa, Italy*

³*Institute for Geosciences, University of Göttingen, Goldschmidtstrasse 3, D-37077 Göttingen, Germany*

⁴*Institute of Tibetan Plateau Research, Chinese Academy of Sciences, Shuangqing Rd. 18, Beijing 100085, China*

⁵*Department of Geology, Technical University of Freiberg, Bernhard-von-Cottastrasse 2, 09596 Freiberg, Germany*

**Corresponding author (e-mail: borjapinzas@hotmail.com)*

Abstract: Anisotropy of magnetic susceptibility (AMS) combined with structural analysis are used in this work with the aim to characterize the tectonic evolution of the Triassic flysch within the eastern Tethyan Himalaya Thrust Belt in SE Tibet. The attitude of the magnetic foliation and lineation are concordant with the planar and linear structures of tectonic origin defined by the preferred orientation of the iron-bearing silicates. Two different tectonic domains can be defined: (a) the southern domain is controlled by the Eohimalayan tectonic foliation (S1) recorded in the magnetic foliation which trends east–west and dips to the north; (b) the northern domain is dominated by the Neohimalayan magnetic foliation with WNW–ESE strike and dips to the south opposite to the vergence of the main structures. A slightly prolate magnetic ellipsoid has been found in between the two domains recording the intersection of S1 and the subtle development of the S2 tectonic foliation. Hinterland propagation of the deformation lead to the Great Counter backthrust generation, pointed out by the SSW steeply plunging magnetic lineation. Furthermore different orientations of magnetic foliation may indicate an Early Miocene c. 20° clockwise vertical-axis rotation.

The collision of India into Eurasia resulted in large-scale shortening of ‘Greater India’ and the consequent development of the Himalayan chain in the Early Tertiary (c. 55–50 Ma) (e.g. Searle 1986; Gaetani & Garzanti 1991; Patzelt *et al.* 1996; Najman *et al.* 2005). The Tibetan Plateau and its bordering orogenic mountain belts like the Himalaya provide one of the best natural laboratories to study continental collision processes. The Himalayan orogen has a length of c. 2500 km between the Nanga Parbat and the Namche Barwa peaks. These extreme points are geologically called Western and Eastern Syntaxis respectively (Fig. 1a, b).

The present study is focused in a key area of the eastern Himalayan belt in SE Tibet, close to the

Eastern syntaxis, where the structural style changes from frontal collision along the Himalaya to dextral shear between Indian and Asian plates as indicated by GPS observations and Quaternary fault slip rates (Holt *et al.* 1991). Furthermore the study area belongs to the Tethyan Himalaya which represents the carapace to mid-crustal rocks whose exhumation mechanism is under discussion (e.g. Godin *et al.* 2006; Kellett & Godin 2009). To better understand the processes we focus our study in the Triassic flysch of the Tethyan Himalaya in order to obtain better constraints on the kinematic evolution and structural style of folds and thrusts since the India–Asia collision. In the remote area of SE Tibet a very long (c. 80 km) and continuous section of Triassic flysch of Tethyan Himalaya

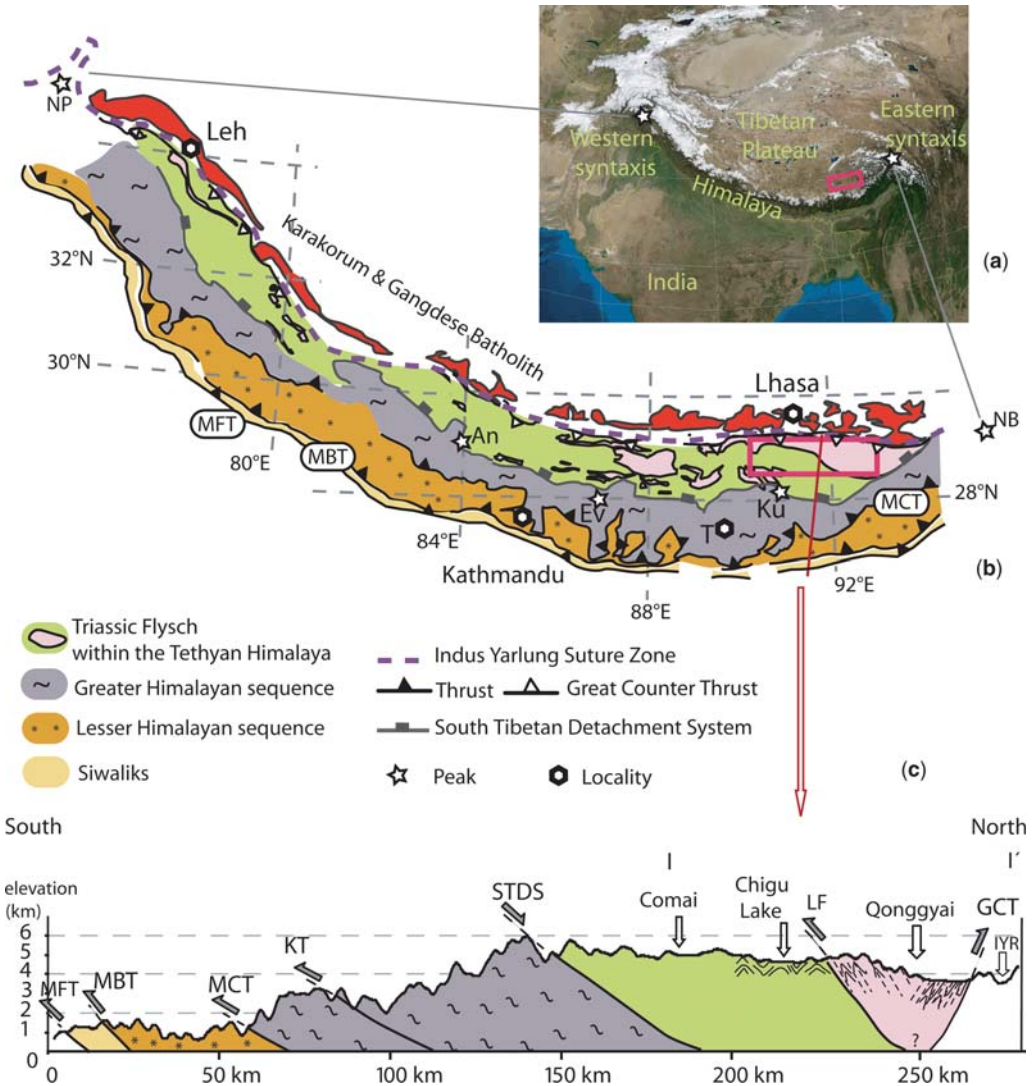


Fig. 1. (a) Satellite image of the Himalayan-Tibetan orogen and surrounding area. (b) Geological sketch map of the Himalayan chain after Steck (2003), Pan *et al.* (2004) and Yin (2006). A rectangle shows the location of the studied area. MFT, Main Frontal Thrust; MBT, Main Boundary Thrust; MCT, Main Central Thrust; NP, Nanga Parbat; An, Annapurna; E, Everest; Ku, Khula Kangri; NB, Namche Barwa; T, Timphu. (c) Simplified cross-section of the eastern Himalayas; location in Figure 1b; topographic profile from DEM data. STDS, South Tibetan Detachment System; LF, Lhunze Fault; GCT, Great Counter Thrust and IYR, Indus-Yarlung River. MFT, MBT, MCT, KT (Kakhtang thrust) and STDS attitude from Grujic *et al.* (2002) and McQuarrie *et al.* (2008); Tethyan Himalayan (I-I') features from Figure 3 (this study).

crops out perpendicular to the main east–west trend of the belt, where little work has been done until now (Fig. 1b, c).

The present work combines the analysis of anisotropy of magnetic susceptibility (AMS) and structural data. The usefulness of AMS has been widely proved for studying deformation in weakly

deformed rocks like mudstones or granites with an incipient deformation (e.g. Borradaile & Tarling 1981; Tarling & Hrouda 1993; Bouchez 1997; Borradaile & Jackson 2004; Román-Berdiel *et al.* 2004). Moreover in deformed rocks, with a dominant paramagnetic signal of the tensor, AMS can be a reliable and fast tool for quantifying the

preferred orientation of elongated particles or structural elements or crystallographic alignment of minerals (e.g. Hirt *et al.* 1988; Averbuch *et al.* 1992; Parés & van der Pluijm 2002; Oliva-Urcia *et al.* 2009). The study of AMS in slightly deformed rocks has been recently emphasized by Burmeister *et al.* (2009) and it seems that it is able to highlight strain distributions more efficiently than measurements techniques of finite strain analyses.

Major Himalayan tectonic elements

The Himalayan belt is the result of the complex superposition of two main tectonic and metamorphic phases: the Eohimalayan phase related to the first stages of the collision (Middle Eocene–Late Oligocene) and the Neohimalayan phase responsible for the main structure of the orogen (Early Miocene–present) (Hodges 2000; Fig. 2). Looking at the major Neohimalayan tectonic elements the Himalaya can be divided into four litho-tectonic units (Fig. 1b, c) (Gansser 1964; Le Fort 1975; Hodges 2000; Yin 2006). These are, from bottom to top and from south to north:

- (1) The Siwalik molasses in the footwall of the Main Boundary Thrust (MBT) made up of Himalayan foreland basin sediments of Miocene to Pliocene–Pleistocene age (Gansser 1964) (Fig. 1b, c).
- (2) The Lesser Himalayan Sequence (LHS) in the footwall of the Main Central Thrust (MCT) (Fig. 1b, c), consisting of sediments from Proterozoic to Cambrian reaching the Paleocene age in the more eastern sectors of the belt (Stöcklin 1980; Valdiya 1980). Sediments were deposited in a proximal position on the Indian shelf and deformed by thrusts and folds under very low-grade metamorphic conditions (Colchen *et al.* 1986; Hodges 2000).
- (3) The Greater Himalayan sequence (GHS) cropping out between the MCT and the set of north-dipping normal faults of the South Tibetan Detachment System (STDS) (Pêcher 1991; Burchfiel *et al.* 1992). It represents the metamorphic core of the Himalayas with high grade metasediments and meta-igneous rocks (Le Fort 1975; Grujic *et al.* 2002). Leucogranitic intrusions are common in the contact zone with the STDS, for example, the Manaslu granite (e.g. Guillot *et al.* 1993). The contemporaneous activity of the MCT and the STDS, confined between 23–17 Ma (Godin *et al.* 2006) led to the exhumation of the GHS (Figs 1b, c & 2).
- (4) The Tethyan Himalaya sequence (THS) is a typical passive margin sequence deposited

on the Indian passive margin. It crops out between the south-dipping Great Counter Thrust (GCT) in the north and the STDS in the south (Fig. 1b, c). The Great Counter Thrust is a south-dipping thrust system (Heim & Gansser 1939; Searle 1986; Ratschbacher *et al.* 1994; Ding *et al.* 2005) which can be detected along the entire Himalaya from Zaskar to east of Gyaca (Fig. 1). North of the Great Counter Thrust the Indus Yarlung Suture Zone (IYSZ) marks the contact with the southern margin of Eurasia represented by the Lhasa Block. Moreover the Tethyan Himalayan sequences are affected by an Oligocene–Miocene discontinuous belt of metamorphic rocks and leucogranitic bodies named the North Himalayan gneiss domes (e.g. Hodges 2000; Lee *et al.* 2000).

The Tethyan Himalayan Sequence, deformation and metamorphism

The Tethyan Himalayan Sequence crops out along c. 150 km between the South Tibetan Detachment System and the Indus Yarlung Suture Zone with approximately the same width from Annapurna to the East of Khula Kangri (Fig. 1b). The Tethyan Himalaya is built up of a continuous sedimentary sequence ranging from Cambro-Ordovician to Eocene and deposited on the passive northern margin of the Indian continent (Fuchs 1967; Willems *et al.* 1996; Garzanti 1999; Dupuis *et al.* 2006). The central Tethyan Himalaya can be divided in two sub-zones which are separated by the Gyirong-Kangmar Thrust (Liu 1992; Liu & Einsele 1994; Willems *et al.* 1996). The southern sub-zone is formed by slightly metamorphosed carbonate platforms and the northern sub-zone is defined by clastic sediments indicating the separation of the Indian plate from Gondwana and the following abyssal sedimentation conditions (Gaetani & Garzanti 1991; Brookfield 1993; Liu & Einsele 1994; Willems *et al.* 1996).

The sequence has experienced a complex structural history (see Fig. 2 for correlation of tectonic features in the Tethyan Himalaya). Godin (2003) defined five main phases of deformation, in the south Tethyan Himalaya in central Nepal, which can be partially or completely recognized along strike of the THS (Fig. 2). The first phase (D1) is defined by south-vergent small-scale folds (F1) with related low-grade axial planar foliation (S1) (e.g. Godin 2003; Carosi *et al.* 2007; Fig. 2). The D2 phase is characterized by large asymmetrical north-vergent megascopic backfolds (Kellett & Godin 2009) and a penetrative axial plane foliation (S2) defined by the preferred orientation of biotite,

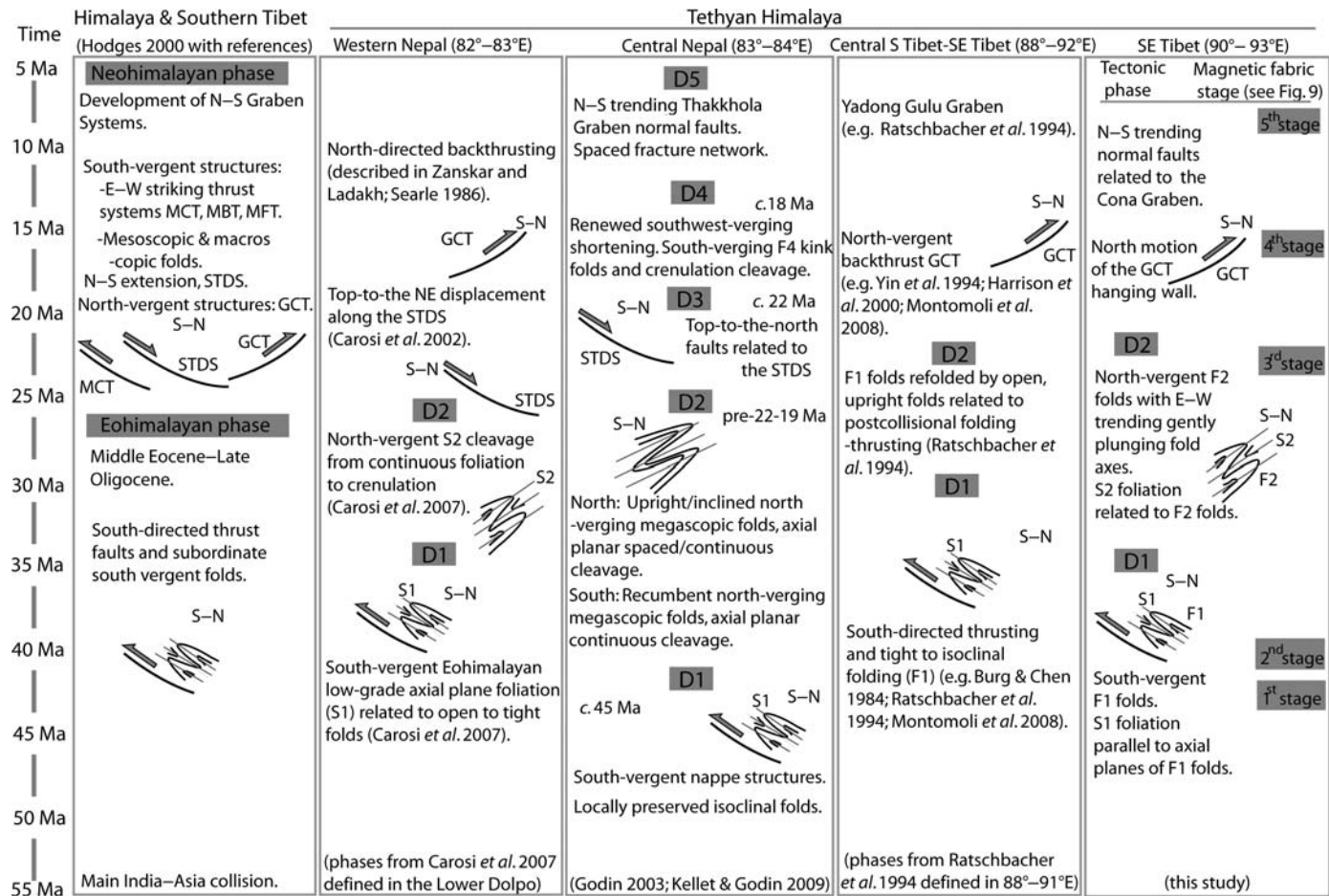


Fig. 2. Simplified synthesis of main deformation events in the Tethyan Himalaya from west to east. Left column refers to previous synthesis proposed by Hodges (2000) including general Himalayan events.

muscovite and elongated quartz grains in pelitic layers (Godin 2003; Carosi *et al.* 2007; Fig. 2). Crouzet *et al.* (2007) found K/Ar ages around 30–25 Ma interpreted as ages of recrystallized K-white micas newly formed during metamorphism and D2 in central Nepal. Moreover secondary pyrrhotite remanences show that F2 folding took place about 35–32 Ma (Appel *et al.* 1991; Crouzet *et al.* 2001; Schill *et al.* 2003). The third phase is related to the development of the South Tibetan Detachment system at *c.* 23–17 Ma for the whole belt (Godin *et al.* 2006 and references therein; Fig. 2). In the eastern Himalaya near Khula Kangri (Fig. 1b), Edwards & Harrison (1997) found an age <12.5 Ma for the STDS development. D4 deformation phase is characterized by SW–NE shortening recorded in post-peak metamorphic F4 kink folds associated with a regional crenulation cleavage S4 and SW directed thrusts (Godin 2003). Since at least the late Miocene (*c.* 8 Ma) east–west extension affected the Tethyan Himalaya sequence (D5 phase; Fig. 2) giving rise to north–south Graben structures, for example, the Takkhola Graben in central Himalaya and the Cona Graben in the eastern Himalaya (Armijo *et al.* 1986; Garzione *et al.* 2003). The Tethyan Himalaya sequence experienced low-grade metamorphic conditions (Garzanti *et al.* 1994; Crouzet *et al.* 2007; Aikman *et al.* 2008; Dunkl *et al.* 2008) characterized by peak palaeotemperatures ranging from 250–450 °C (Crouzet *et al.* 2007). The age of the metamorphism decreases from the west to the east Himalaya ranging from 44–47 Ma in Zanskar to 30–25 Ma in central Himalaya (Bonhomme & Garzanti 1991; Crouzet *et al.* 2007).

Study area: the Triassic flysch of the eastern Tethyan Himalaya

The present study is focused on the Triassic flysch of the Tethyan Himalaya with a sedimentation age of Middle Triassic to Early Jurassic (Chang 1984; Pan *et al.* 2004). Our work is concentrated in an area geographically located south of the Yarlung Tsangpo River that extends from Nagarze in the west as far as east of Gyaca (Fig. 3). Here the flysch consists of turbidites and carbonate flysch (Dupuis *et al.* 2005) and it is represented by black shales interbedded with sandstone/siltstone and locally some limestone. The organic-rich pelitic lithologies always contain early diagenetic pyrite crystals. The sequence is intruded by mafic dykes and contains small ultramafic intrusions. The dominant structures are folds and imbricate thrusts involving the whole passive continental margin sequence of the Tethyan Himalaya (Yin & Harrison 2000; Aikman *et al.* 2008).

In the north the Great Counter Thrust separates the Triassic flysch from the *mélange* complex and the Cretaceous clastic rocks (Fig. 3). The *mélange* complex (constituted by cherts, shales, marbles, andesites, diorites, mafic and ultramafic bodies, limestones and phyllites) has been deposited on the growing Neo-Tethys ocean floor and incorporated in a subduction complex *mélange* (Searle 1986). The Cretaceous clastic rocks were deposited in the active palaeomargin of the Indus Yarlung Suture Zone (Harrison *et al.* 2000; Pan *et al.* 2004; Dupuis *et al.* 2005). In the eastern Himalaya the Renbu-Zedong Thrust (Yin *et al.* 1994; Harrison *et al.* 2000) has been correlated with the Great Counter Thrust. The Great Counter Thrust in the Ringbung area is dated by K/Ar in a phyllite as 17.5 Ma old (Ratschbacher *et al.* 1994). This age coincides with the interval of activity from 18–10 Ma of the Great Counter Thrust in the Zedong area dated by Ar/Ar analyses on K-feldspar analysis (Quidelleur *et al.* 1997; Harrison *et al.* 2000).

Towards the south the Triassic flysch is in contact with the Upper Jurassic (continental clastic rocks, marls and marine limestones) and Cretaceous clastic rocks which represent the platform sequence of the Indian passive margin (e.g. Liu & Einsele 1996). The southern contact between the Triassic flysch and the Jurassic–Cretaceous rocks (Fig. 3) is marked by the Lhunze Fault which is likely comparable with the east–west-trending and north-dipping Gyrong-Kangmar Thrust cropping out around 50 km west of the Yadong Gulu Graben (Chen *et al.* 1990; Liu 1992; Yin 2006; Aikman *et al.* 2008).

Two kinds of intrusions have affected the Triassic flysch in the study area: the Dala granitoids of Eocene age (Aikman *et al.* 2008) and the Neogene North Himalayan gneiss domes (Fig. 3). The latter are represented by the Mt. Jangsang Lhamo south of Nagarze and the Yala Xiangbo south of Qusum (Fig. 3). Preliminary thermochronological data indicate that the Yala Xiangbo leucogranite was emplaced at *c.* 18 Ma, and cooled through the muscovite closure window at *c.* 13.5 Ma (Aikman *et al.* 2004; Zhang *et al.* 2005). The Neogene domes have been interpreted as metamorphic core complex owing to the fact that the granites are surrounded by detachment faults and shear zones (e.g. Zhang *et al.* 2005). Afterwards the east–west Neogene extension played a key role in the deformation of the eastern Tethyan Himalaya giving rise to the NNE–SSW Cona Graben that can be followed from the north of the Indus Yarlung Suture Zone as far as the South Tibetan Detachment System, with *c.* 210 km length and 8 km width (Fig. 3). The Cona Graben is the easternmost graben that crosses the Tethyan Himalaya and GPS velocities

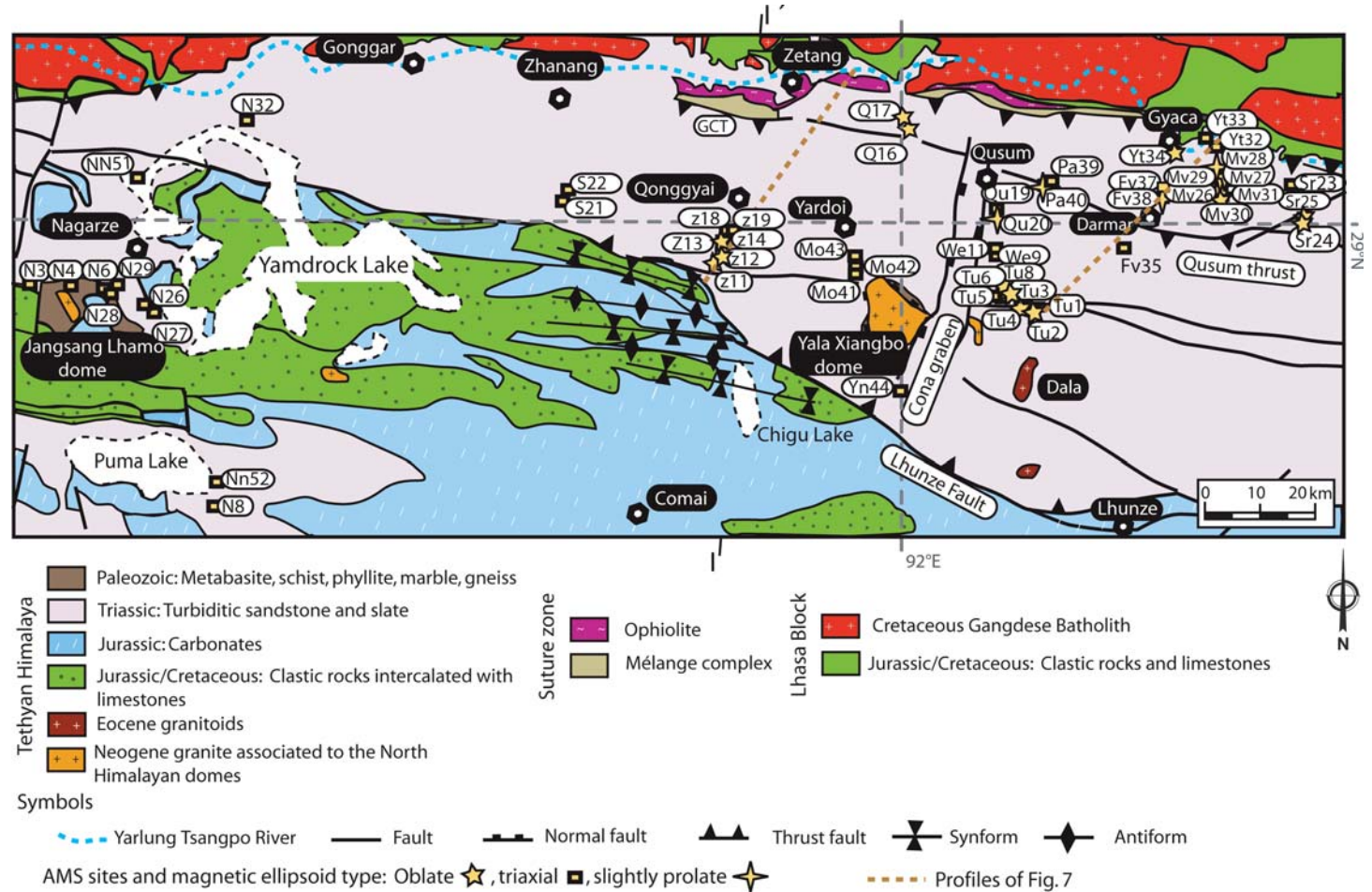


Fig. 3. Simplified geological map of SE Tibet. Modified from Pan *et al.* (2004), Yin (2006) and Aikman *et al.* (2008). The studied sites are marked in function of the type of AMS ellipsoid. Line I-I' indicates the cross-section in Figure 1c. Dashed orange lines indicate the two cross-sections of Figure 7.

have indicated no significant ($0.3 \pm 0.9 \text{ mm a}^{-1}$) fault opening at present-day (Gan *et al.* 2007).

Structural and metamorphic data

A polyphase tectonic history has been recognized in the study area characterized by two main tectonic phases named hereafter D1 and D2 (see Fig. 2 for correlation between Tethyan Himalayan deformation phases). During the first D1 tectonic phase, referred to the Eohimalayan event (Hodges 2000), metric to kilometric asymmetrical F1 folds developed. F1 folds face to the south and their axes trend ENE–WSW. Parallel to axial planes of F1 folds, a S1 axial plane foliation can be recognized (see stereograms of sector 1, south of sector 2 and sector 3 in Fig. 4a). In the southern parts of the studied area S1 is the dominant planar structure in the field (Fig. 4b). In the Nagarze area (sector 1; Fig. 4a) the mean vector of the S1 poles trends 220° and plunges 70° ($\alpha_{95} = 22^\circ$; $k = 4.9$) and in the Qonggyai valley (south of Zetang in sector 2; Fig. 4a) the S1 pole mean vector trends 182° and plunges 30° ($\alpha_{95} = 24^\circ$; $k = 13.8$; Fig. 4a). East of the Cona Graben, in sector 3, S1 poles mean vector trends 210° and plunges 35° ($\alpha_{95} = 5.6^\circ$; $k = 7.3$; Fig. 4c). S1 is a low grade foliation and microstructural observations show that moving from south to north, S1 foliation varies from a disjunctive spaced stylolitic cleavage with no dynamic recrystallization to a fine continuous foliation (Montomoli *et al.* 2008) marked by syn-kinematic recrystallization of very fine-grained phyllosilicates (Fig. 4d). Object lineations, trending NW–SE, are well represented by strain fringes, mainly composed of quartz around pyrite crystals. D1 deformation occurred in diagenetic or lower anchizonal conditions probably in Paleogene times (Dunkl *et al.* 2008).

A later D2 deformation phase is superimposed on D1 structures (Fig. 2). D2 is represented by a weak crenulation cleavage in the southern portions but moving towards the GCT it gives rise to decimetre to decametre-scale F2 folds (Fig. 4e). F2 folds have east–west-trending gently plunging axes and verge to the north. Associated with F2 folds a S2 foliation was generated. Axial plane foliation S2 strikes WNW–ESE with moderate dips towards the south (see stereograms north of sector 2 and sector 4 in Fig. 4a). Equal area projection of S2 poles of sector 4 show a grouping ($\alpha_{95} = 14.6^\circ$; $k = 3.2$; Fig. 4c) with a mean vector trending 007° and plunging 43° (Fig. 4a, c). Foliation S2 varies from a discrete zonal crenulation with well defined cleavage domains near the Qusum Thrust (Fig. 4f) to a fine continuous foliation in a more strained area in the vicinity of the Great Counter Thrust,

where S2 is the most visible structural element in the outcrop. In some cases, in the more northern areas S2 is associated with the dynamic recrystallization of illite-sericite (Montomoli *et al.* 2008). East of the Cona Graben the WNW–ESE-trending thrust fault with south to south–SW dip described in Yin (2006), that we name the Qusum Thrust, represents the boundary between S1 and S2 foliations.

Top-to-the-N or NE brittle–ductile shear zones are developed in the overturned limbs of F2 folds with kinematic indicators such as C–S fabric (Berthé *et al.* 1979). On C surfaces stretching lineations strike north–south and plunge gently to the south (Montomoli *et al.* 2008; see Fig. 4a stereogram with stretching lineation within S2 at site Yt32). D2 took place at higher anchizonal to greenschist facies conditions in Miocene times and the process culminated around 24 Ma as Dunkl *et al.* (2008) have shown.

AMS analysis

AMS was measured in 516 cylindrical rock specimens with a standard size of 2.5 cm diameter and 2.1 cm length. Samples were collected from 53 sites distributed along north–south valleys between Yamdrock lake and east of Gyaca (Fig. 3), with an average of 10 cores at each site. A portable gasoline powered rock drill machine was used and cores were oriented *in situ* with a magnetic compass. The study of AMS was carried out with an AGICO KLY-2 Kappabridge at Tuebingen University. The AMS ellipsoid was determined from 15 different directional measurements. The results can be characterized by the bulk susceptibility (K_m) given as arithmetic mean of the three principal axes of the AMS ellipsoid: $K_m = 1/3(K_{\max} + K_{\text{int}} + K_{\min})$ and the orientations and magnitudes of the $K_{\max} > K_{\text{int}} > K_{\min}$ axes of the AMS ellipsoid. The statistical procedure to obtain the directional data was based on tensor analysis by Jelinek (1977), using the program anisoft42 developed by Chadima and Jelinek (last version of 2008). The mean values for areas were calculated by Fisher statistics (Fisher *et al.* 1987) with the program Stereogram v. 1.2 (R. Allmendinger). In numerous tectonic and AMS studies it has been shown that in rocks where iron-rich silicates control magnetic susceptibility the cluster of minimum axes of the magnetic ellipsoid (K_{\min}) is related to the magnetic foliation because the minimum susceptibility axis is nearly perpendicular to the basal cleavage of phyllosilicates crystals (e.g. Kneen 1976; Borradaile & Werner 1994; Martín-Hernández & Hirt 2003). A cluster of maximum axes (K_{\max}) or magnetic lineation can reflect either the extension direction, the intersection of two competing subfabrics (because the

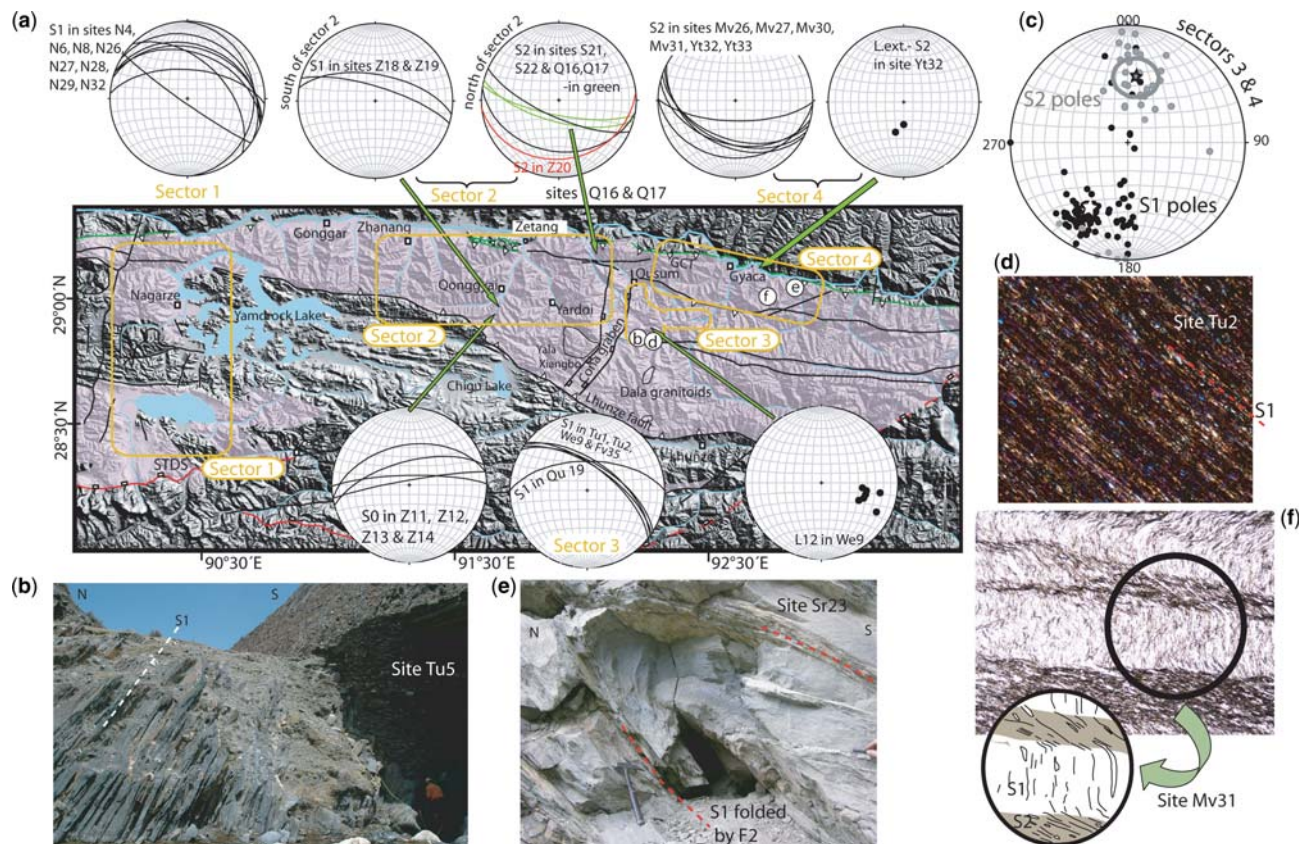


Fig. 4. (a) SRTM topography overlapped with the Triassic flysch (pink colour) and the structural elements of Figure 3. The orange rectangles show the sectors described in the structural and magnetic fabric sections; b, d, e and f letters correspond to the position of the outcrop and thin section images. Lower-hemisphere, equal-area stereogram of the general trend of tectonic foliations per site and stretching lineation (L.ext.) within S2 foliation from site Yt32 and intersection lineations of foliation S1 and S2 (L12) in site We9. (b) Outcrop view of site Tu5, dashed line shows S1 foliation. (c) Lower-hemisphere, equal-area stereogram of the poles of S1 and S2 tectonic foliations of sector 3 and 4, stars indicate mean vectors. (d) Photomicrograph of S1 foliation developed in the slates of the site Tu2 (field of view 5 mm). (e) Example of F2 fold in site Sr23. (f) Thin section photomicrograph from the slates of the site Mv31 and geological interpretation; both S1 and S2 foliations are recognizable (field of view 7 mm).

maximum susceptibility axis is the intersection axis between the phyllosilicates crystals), or an orientation in between (Borradaile & Tarling 1981; Housen *et al.* 1993; Parés *et al.* 1999; Parés & van der Pluijm 2002; Soto *et al.* 2003).

Furthermore Jelinek's method gives different scalar parameters which are very useful to describe the magnetic fabrics: the corrected anisotropy degree (P') can be related to the intensity of the preferred orientation of minerals in rocks in which the susceptibility is mainly carried by paramagnetic minerals. The shape parameter (T) indicates the form of the magnetic ellipsoid. T can range from -1 (prolate ellipsoid) to 1 (oblate ellipsoid). The magnetic foliation parameter ($F = K_{\text{int}}/K_{\text{min}}$) and magnetic lineation parameter ($L = K_{\text{max}}/K_{\text{int}}$) can be plotted in a Flinn type plot (Flinn 1962) normally used in structural geology. We used also Jelinek's elliptical confidence angles as markers of the quality of AMS data (Jelinek 1977).

Magnetic mineralogy and carriers of the magnetic fabric

The determination of the minerals that contribute to the anisotropy of magnetic susceptibility is an essential step in order to understand the origin of the magnetic fabric and their structural interpretation. In the following we predominantly utilize median values and quartiles for concentration-dependent parameters because these are more representative than mean values and standard deviation in data sets with some significant outliers.

The bulk susceptibility median of the 53 studied sites is 232×10^{-6} SI (1st quartile = 187×10^{-6} SI, 3rd quartile = 372×10^{-6} SI, mean = 334×10^{-6} SI and STD = 314×10^{-6} SI) (Table 1; Fig. 5a). Around 89 % of the sites show a low bulk susceptibility median $< 500 \times 10^{-6}$ SI typical for rocks where the magnetic fabric is usually controlled by the crystal lattice orientation of the paramagnetic fraction (Rochette 1987). Similar values of magnetic susceptibility have been found in other studies where paramagnetic minerals controlled the AMS ellipsoid (e.g. Tarling & Hrouda 1993). Sites N6, Tu5, Tu6 and Mv30 have higher values ($K_m > 800 \times 10^{-6}$ SI) probably related to a significant contribution of the ferro(i)magnetic fraction to the total magnetic susceptibility and they will be analysed separately. Natural Remanent Magnetization (NRM) was measured in 10 samples per site with a 2 G RF-SQUID magnetometer. The NRM median is low, 0.4 mA/m (1st quartile = 0.26 mA/m, 3rd quartile = 1.4 mA/m, mean = 10.8 mA/m and STD = 43.3 mA/m) (Table 1). Around 72% of the sites give median values of NRM < 1 mA/m and there is no

correlation of K_m and NRM ($R^2 = 0.12$) likely indicating a low content of ferro(i)magnetic minerals (Fig. 5a). A similar analysis was carried out on 41 samples from 24 sites, looking at the relation between the K_m and saturation isothermal remanent magnetization (SIRM) at 2.4 T (SIRM imparted by a MMPM9 pulse magnetizer). Also for SIRM and K_m no significant dependence was found. Variation of magnetic susceptibility was measured for 14 sites between -196°C and room temperature using a low temperature unit attached to a KLY-3 Kappa-bridge (AGICO). The measured thermomagnetic curves, after free furnace correction, show a temperature dependence of susceptibility following the Curie Law (Nagata 1961) characteristic for paramagnetic minerals (Fig. 5b). Moreover variation of magnetic susceptibility was measured for 7 sites between room temperature and 700°C using a high temperature unit attached to a KLY-3 Kappa-bridge (AGICO). The measured thermomagnetic curves, after free furnace correction, show no presence of pyrrhotite and a minor contribution of magnetite indicated by decay around 580°C .

In thin sections and in outcrop views we observed pyrite crystals inside the slates. Pyrite influence on the total magnetic susceptibility is small but it is an important source for the creation of pyrrhotite during the metamorphism (Rochette 1987; Borradaile & Sarvas 1990; Crouzet *et al.* 2001). The main decay of intensity of the SIRM around 325°C indicates the presence of pyrrhotite in all the studied samples (Fig. 5c). IRM acquisition in a direct field up to a maximum of 1.8 T shows near saturation at 0.3 T suggesting that the pyrrhotite grains are in a rather low coercive multidomain state. It is also noted that in site Yt32 additional magnetite was observed by its Curie temperature around 580°C .

The aforementioned results were further examined quantitatively by means of hysteresis properties. Hysteresis properties were measured in 28 sites with an Alternating Gradient Force Magnetometer AGFM 2900 (Princeton Measurements Corp.). The maximum applied field was 800 mT in which the ferro(i)magnetic phase is fully saturated. All samples show a straight line at high fields due to the intrinsic high field susceptibility of the paramagnetic minerals (Borradaile & Werner 1994). The ferro(i)magnetic component shows a low coercivity ($H_c < 10$ mT) confirming the presence of a very low coercive MD pyrrhotite or some contribution of magnetite (Fig. 5d). In order to quantify the paramagnetic and ferro(i)magnetic contribution to the total magnetic susceptibility we calculated the bulk specific susceptibility of the paramagnetic fraction from the slope of the hysteresis loop at high fields and compared it with the total bulk specific susceptibility at low fields of the same sample as

Table 1. NRM and AMS data

Site	NRM (mA/m)	n	AMS type	Km (*10E-6 SI)	K _{max} (T/P)	CA	K _{min} (T/P)	CA	P'	T
Tu1	28.44 ± 21.10	16	2	432.8 ± 372.8	114/30	26/6	215/18	15/6	1.56	0.65
Tu2	0.35 ± 0.18	12	2	180.4 ± 50.6	314/20	60/11	217/17	15/8	1.23	0.82
Tu3	64.18 ± 115.6	8	1	463.0 ± 797.1	121/17	36/6	223/35	8/4	1.41	0.74
Tu4	0.33 ± 0.28	11	1	239.5 ± 39.7	310/10	31/8	215/27	14/7	1.28	0.94
Tu5	349.6 ± 269.6	10	2	1395.0 ± 1079.0	345/44	30/18	212/35	22/10	2.12	0.44
Tu6	98.85 ± 121	10	2	1304 ± 1079.0	342/47	22/12	210/31	14/7	2.08	0.59
Tu8	11.95 ± 14.48	10	1	239.7 ± 38.3	310/18	19/6	215/14	36/17	1.24	0.60
We9	9.04 ± 12.23	10	2	470.7 ± 198.7	113/22	12/6	217/31	17/6	1.30	0.43
We11	23.63 ± 58.19	10	1	623.5 ± 467.0	082/33	13/5	207/42	7/5	1.54	0.61
Qu19	0.29 ± 0.11	11	2	246.8 ± 23.8	284/9	14/5	187/34	9/3	1.17	0.30
Qu20	0.78 ± 0.63	9	3	214.4 ± 15.8	280/9	19/14	168/67	27/11	1.16	-0.13
Sr23	0.34 ± 0.36	9	2	243.7 ± 99.3	277/11	12/4	014/33	12/5	1.15	0.61
Sr24	0.58 ± 0.37	7	1	166.8 ± 45.1	103/15	81/17	003/33	19/7	1.15	0.59
Sr25	0.84 ± 1.09	10	1	105.3 ± 38.8	124/19	39/7	019/38	8/6	1.17	0.70
Mv26	0.61 ± 0.25	9	1	199.7 ± 73.1	140/12	49/13	031/57	30/18	1.21	0.30
Mv27	0.49 ± 0.15	7	3	276.5 ± 27.5	262/29	8/6	004/19	34/5	1.16	0.09
Mv28	0.33 ± 0.18	9	1	357.1 ± 83.4	141/65	34/15	032/9	15/12	1.26	0.58
Mv29	0.45 ± 0.24	13	3	411.6 ± 69.0	271/9	12/10	179/13	36/7	1.18	0.14
Mv30	157.7 ± 184.80	13	1	1684 ± 1521.0	167/44	48/11	014/43	13/6	2.35	0.39
Mv31	22.56 ± 28.78	10	3	520.7 ± 477.8	285/14	9/4	188/25	47/9	1.46	-0.07
Yt32	0.54 ± 0.91	9	2	282.1 ± 42.2	193/70	10/4	003/20	11/4	1.18	0.61
Yt33	0.49 ± 0.30	10	2	246.2 ± 23.5	189/64	24/16	030/24	23/15	1.37	0.85
Yt34	23.97 ± 35.00	9	1	377.8 ± 277.2	109/24	56/7	006/26	8/5	1.38	0.40
Fv35	1.66 ± 1.29	10	2	216.1 ± 51.0	122/7	33/5	216/28	7/5	1.16	0.54
Fv37	0.01 ± 0.05	7	2	160.0 ± 20.9	149/48	20/4	024/27	7/4	1.28	0.70
Fv38	0.47 ± 0.55	11	3	119.6 ± 27.6	281/2	14/6	015/68	22/6	1.15	0.43
Pa39	0.30 ± 0.14	10	2	247.3 ± 105.4	091/36	28/15	190/13	19/14	1.28	0.58

Pa40	0.13 ± 0.06	11	3	171.6 ± 43.9	283/6	15/6	125/83	39/10	1.23	0.49
N3	10.20 ± 18.34	14	1	370.0 ± 277.0	298/3	13/4	095/86	5/3	1.20	0.44
N4	45.64 ± 106.60	11	1	203.0 ± 178.0	332/8	4/3	161/82	6/2	1.33	0.50
N6	216.70 ± 357.90	14	2	857 ± 702.0	344/13	4/2	198/75	3/1	2.29	0.02
N8	1.13 ± 2.35	9	1	264.0 ± 38.5	298/14	25/1	143/74	7/2	1.15	0.61
N26	3.08 ± 2.12	12	2	232.0 ± 38.4	331/50	12/6	177/37	10/3	1.15	0.65
N27	1.22 ± 1.45	11	2	112.0 ± 28.5	297/66	6/3	205/1	8/3	1.17	0.68
N28	3.03 ± 3.11	10	2	113.0 ± 14.5	329/33	8/5	215/32	7/3	1.17	0.63
N29	0.96 ± 0.55	9	2	200.0 ± 75.1	356/33	16/7	210/52	13/7	1.07	0.27
N32	0.35 ± 0.32	9	1	189.0 ± 30.5	123/24	58/28	220/15	30/17	1.07	0.31
Nn51	0.08 ± 0.04	5	2	278.0 ± 20.1	164/54	19/2	339/36	5/3	1.12	0.56
Nn52	1.84 ± 3.14	10	2	406.0 ± 77.4	339/30	10/4	211/47	20/3	1.12	-0.09
Q16	0.29 ± 0.22	10	1	167.0 ± 40.0	253/51	22/3	011/20	5/3	1.21	0.83
Q17	0.36 ± 0.43	7	1	140.0 ± 64.3	248/53	38/5	010/22	9/6	1.14	0.59
S21	0.26 ± 0.16	5	2	142.0 ± 17.5	219/22	11/1	350/58	15/2	1.05	0.37
S22	0.36 ± 0.23	8	2	189.0 ± 12.6	228/78	9/8	007/10	10/6	1.08	0.41
Z11	0.21 ± 0.08	10	1	213.0 ± 16.5	083/4	24/5	175/17	7/2	1.08	0.65
Z12	1.73 ± 3.32	11	1	194.0 ± 25.6	285/29	30/7	179/27	19/12	1.20	0.80
Z13	0.23 ± 0.29	11	2	223.0 ± 23.3	012/47	7/3	173/41	17/2	1.21	0.83
Z14	1.04 ± 0.95	10	1	202.0 ± 46.9	081/12	21/7	174/16	8/6	1.11	0.79
Z18	0.27 ± 0.25	12	2	136.0 ± 45.2	056/55	18/5	185/23	7/1	1.09	0.45
Z19	0.29 ± 0.20	12	2	158.0 ± 16.7	015/69	5/4	189/21	7/4	1.10	0.29
Mo41	3.40 ± 5.74	9	2	463.0 ± 291.0	348/40	11/3	160/50	6/3	1.07	-0.07
Mo42	0.28 ± 0.16	9	2	257.0 ± 22.9	005/43	10/5	157/44	10/3	1.19	0.68
Mo43	0.26 ± 0.36	10	2	218.0 ± 36.9	340/46	10/5	147/44	6/4	1.17	0.65
Yn44	0.27 ± 0.04	7	2	201.0 ± 10.3	279/16	11/3	169/50	10/4	1.07	0.28

NRM, natural remanent magnetization mean (mA/m); STD, Standard deviation. AMS data (Jelinek's statistics, 1977): n, number of measured samples; Km, Bulk magnetic susceptibility ($\times 10^{-6}$ SI); K_{\max} and K_{\min} mean (trend/plunge) with the 95% confidence angle (CA). P', corrected degree of anisotropy; T, shape parameter.

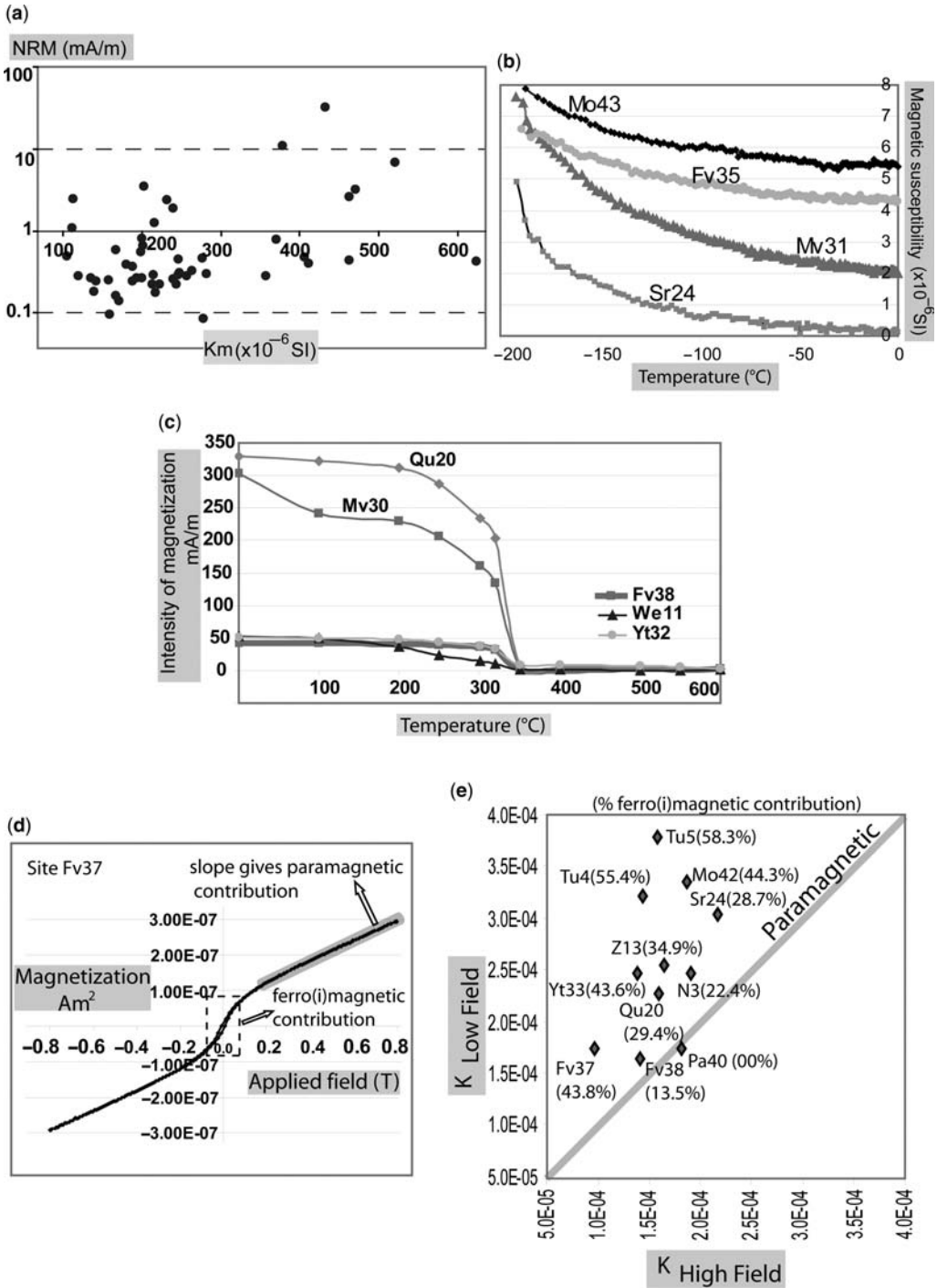


Fig. 5. Magnetic mineralogy analysis. (a) Km v. NRM plot without sites Tu5, Tu6, Mv30 and N6 with important ferro(i)magnetic contribution, see discussion in the text. (b) Curves of magnetic susceptibility v. the temperature. (c) Thermal demagnetization curves of the SIRM. (d) Hysteresis curve from site Fv37. (e) High field bulk magnetic susceptibility v. low field bulk magnetic susceptibility essays.

was previously done by other authors (e.g. Richter & van der Pluijm 1994). The values obtained in 11 samples from different homogeneously distributed sites indicate that in five samples (sites Pa40, Fv38, N3, Qu20, Sr24) the ferro(i)magnetic contribution is less than 30% and in six samples (sites Fv37, Z13, Yt33, Mo42, Tu4, Tu5) the ferro(i)magnetic contribution to the total magnetic susceptibility is in between 30% and 60% (Fig. 5e).

However, one has to be cautious with these results as they are based on very small samples and thus reliability of upscaling is dependent on the homogeneity of the rocks.

Consequently all these results in conjunction with the well defined magnetic foliation parallel to the tectonic foliation plane and the fact that P' values are characteristic of rocks governed by phyllosilicates (Fig. 6a) point out that a predominating

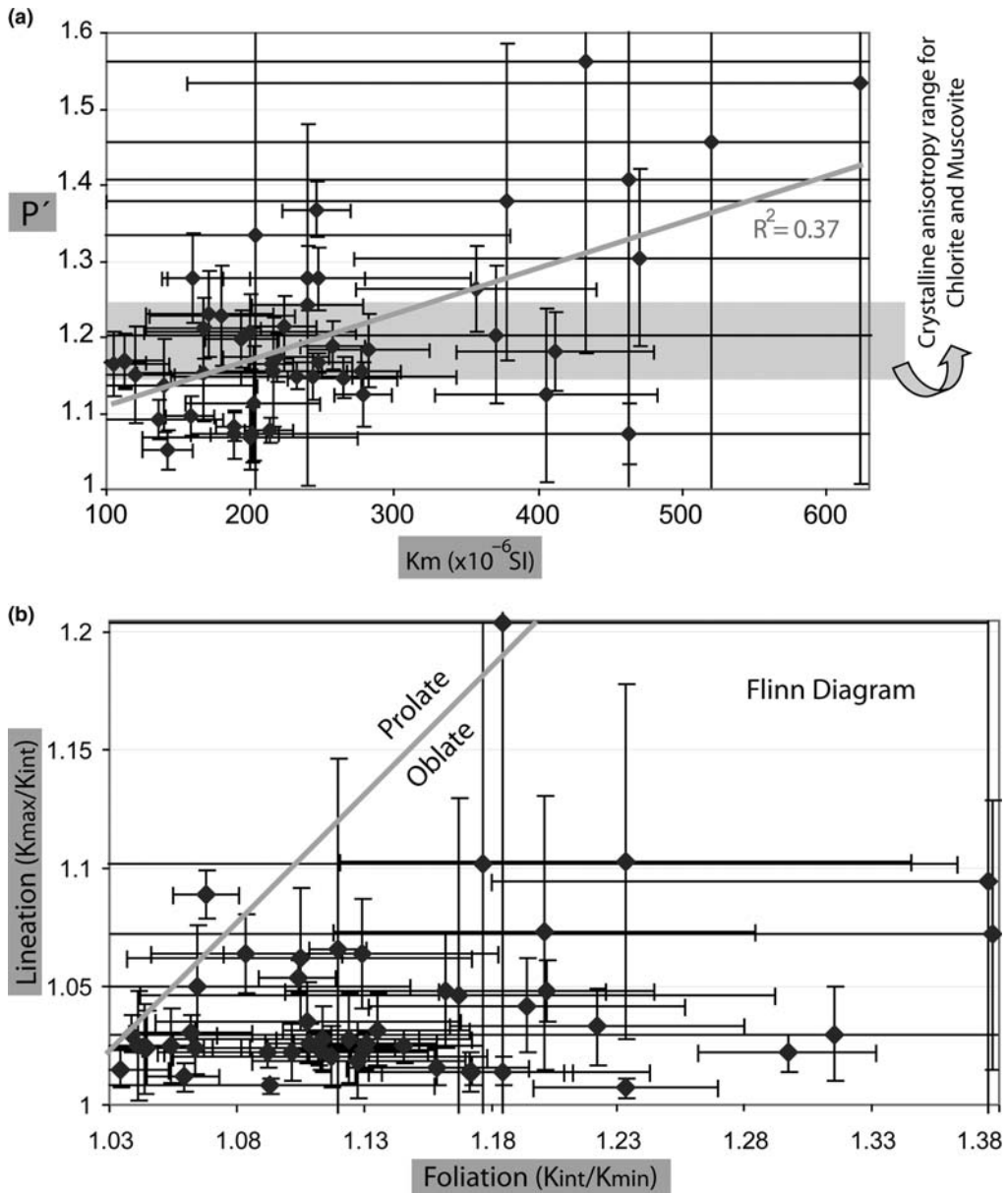


Fig. 6. AMS scalar parameters plots. (a) Km v. P' . (b) Flinn diagram.

paramagnetic control of the total anisotropy of magnetic susceptibility can be expected in most sampled sites. For this reason the geographical distribution of the axes of the ellipsoid of magnetic susceptibility can be interpreted in terms of the preferred orientation of the phyllosilicates in relation to their structural location. However, there might be also some small contribution from subordinate pyrrhotite or magnetite mainly in sites Tu5, Tu6, Mv30 and N6 which have not been included in the scalar parameter plots and in the tectonic interpretation. Although these four sites show K_{\min} axis nearly perpendicular to the tectonic foliation (Table 1 & Fig. 4a) as in the sites controlled by the paramagnetic mineral fraction, may be related to a co-axiality of magnetic fabrics and petrofabrics, as was previously noted by Borradaile & Sarvas (1990) in the slates west of Atikokan (Canada).

AMS ellipsoid: the corrected degree of anisotropy and shape parameters

The corrected degree of anisotropy (P') in the slates of SE Tibet is in the range of P' characteristic for slates where the main carriers of the AMS are phyllosilicates (Tarling & Hrouda 1993; Parés & van der Pluijm 2002). The sites show a median value of 1.18 (1st quartile = 1.14; 3rd quartile = 1.27; Mean = 1.28, STD = 0.30) (Fig. 6a & Table 1). Moreover these values are similar to the crystalline anisotropies of chlorite ($P' = 1.15$ – 1.19) or muscovite ($P' = 1.15$ – 1.27) (values of P' given by Martín-Hernández & Hirt 2003 and Borradaile & Werner 1994 respectively). In order to detect the dependence of the corrected degree of anisotropy on the rock composition (iron content) we studied the relation between the corrected degree of anisotropy and K_m at site scale and regional scale. Only two sites (We9 and Sr23) indicate dependence of the corrected degree of anisotropy on the magnetic susceptibility at site scale. The plot of K_m v. P' mean site values indicates no correlation between the magnetic susceptibility (iron content) and the degree of anisotropy ($R^2 = 0.37$; Fig. 6a). These data corroborate the magnetic mineralogy analysis suggesting that the phyllosilicates predominantly control the AMS signal.

The shape of the magnetic ellipsoid is oblate in 92% of the sites; only sites N6, Qu20, Nn52 and Mo41 show a slightly prolate ellipsoid. The shape parameter mean is 0.5 (STD = 0.26) suggesting the dominance of a planar fabric controlled by the foliation (Fig. 6b & Table 1). Likewise the F parameter (F mean = 1.18, STD = 0.16) and the L parameter (L mean = 1.06, STD = 0.08) distribution in the Flinn diagram confirms the control of the foliation (Fig. 6b).

Different shapes of AMS ellipsoids, definition of magnetic foliation and lineation

Equal area plots of the principal AMS axes show three typical shapes of AMS ellipsoids (Figs 3, 7 & Table 1). The first type is an oblate ellipsoid with a cluster of K_{\min} perpendicular to the foliation plane and K_{\max} and K_{int} distributed along the foliation plane (e.g. site Q16 in Fig. 7a). The fact that K_{\max} is not grouped prevents the definition of the magnetic lineation (e.g. Pueyo *et al.* 2004). The second type and most common one shows a triaxial ellipsoid with all three axes well grouped; K_{\min} axes are perpendicular to the foliation plane and K_{\max} axes represent different structural elements. They can be parallel to the F1 or F2 fold axes, related to the intersection of S1 and S2 as previously documented Housen *et al.* (1993) (e.g. see Fig. 4a intersection lineation of S1 and S2, L12, in site We9 is nearly parallel to K_{\max} orientation of We9; Table 1) or parallel to the stretching lineation (e.g. site Yt32 in Fig. 7b). The third type presents a slightly prolate ellipsoid characterized by a semi-girdle distribution of K_{\min} axes and a cluster of K_{\max} axes, magnetic lineation, which is related the intersection lineation of S1 and S2 foliations as can be seen in the site Qu20 in Figure 7b. How these ellipsoids are spatially distributed in the studied area as well as the orientation and relation with the structural elements is discussed below.

Magnetic foliation and lineation in the Triassic flysch of SE Tibet

Four sectors like in the structural section have been distinguished in order to understand the relation between the magnetic fabric and the structural data (Fig. 8).

Sector 1 mainly corresponds to the Nagarze area, which is located east of the Yadong Gulu Graben and in the vicinity of the Jangsang Lhamo North Himalayan gneiss dome (Figs 4 & 8). These nine sites show a triaxial magnetic ellipsoid described above. Magnetic foliation strikes WNW–ESE with moderate dips towards the north and parallel to S1 tectonic foliation (Fig. 8a). It is also noted that the dip varies from very gentle angles beside the Jangsang Lhamo Dome to near vertical moving to the east. Magnetic lineation has a NNW–SSE trend and north–NW plunge approximately parallel to gneiss dome elongation (Fig. 8b). Like the magnetic foliation the plunge values of the magnetic lineation increase from the Jangsang Lhamo dome to the east. Furthermore two sites were drilled in the east side of the Puma Lake and c. 40 km north of the South Tibetan Detachment System (Fig. 3; sites N7 and N8).

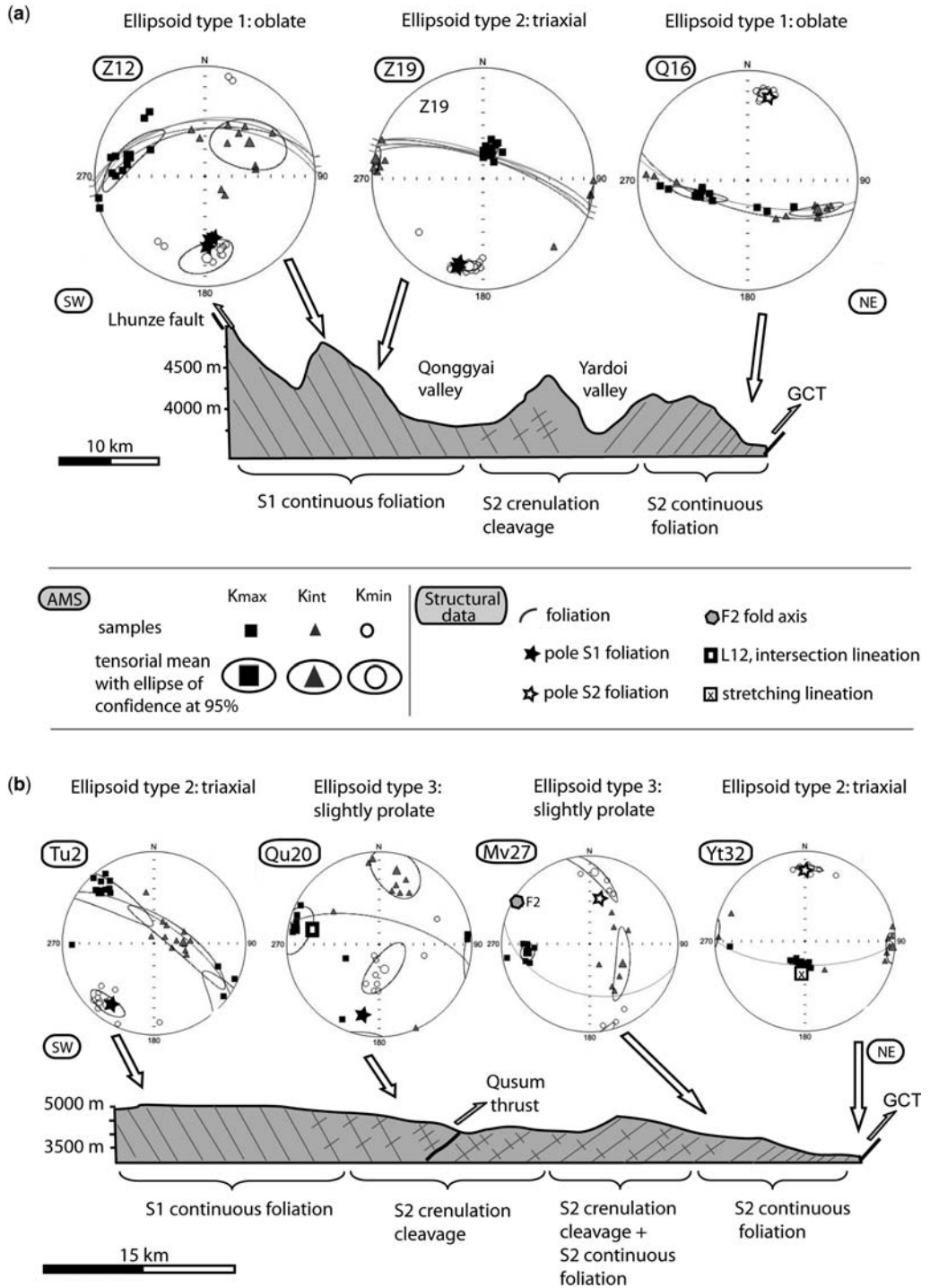


Fig. 7. Types of AMS ellipsoids within two simplified cross-sections indicated in Figure 3 with the schematic stages of cleavage development. (a) Cross-section from the Lhunze fault to the Great Counter thrust along the Qonggyai valley. (b) Cross-section crossing sectors 3 and 4.

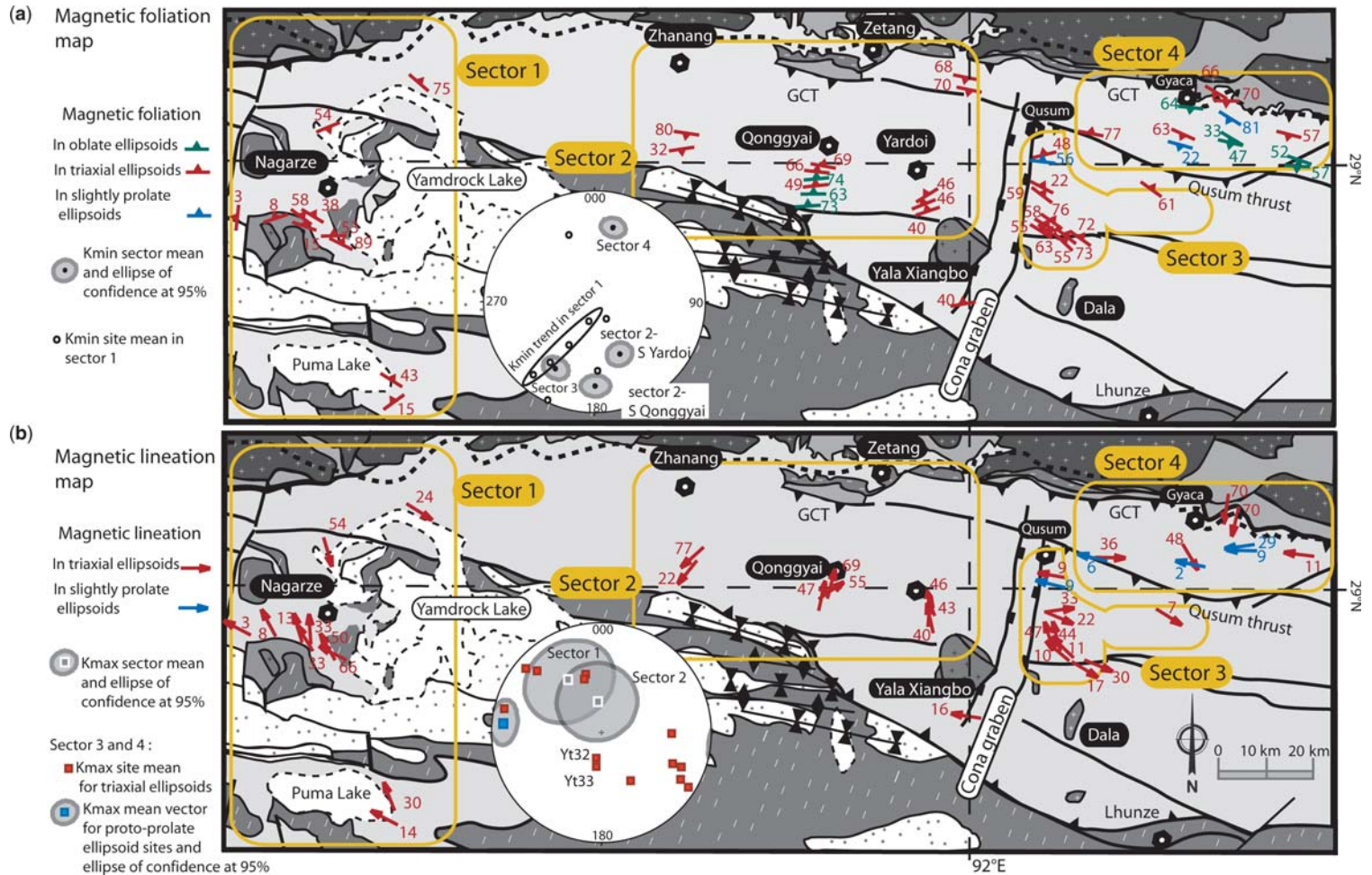


Fig. 8. (a) Magnetic foliation map and lower-hemisphere, equal-area stereogram with the K_{\min} mean vector for sector 2 south of Yardoi, sector 2 south of Qonggyai, sector 3, sector 4 and scattered distribution of single sites K_{\min} mean vector of sector 1. (b) Magnetic lineation map and lower-hemisphere, equal-area stereogram of K_{\max} mean vector for sector 1 and 2, and K_{\max} mean vector for sites within sectors 3 and 4. Both maps follow the same map legend of Figure 3 with greyscale colours.

These two sites have directions and plunges of the magnetic lineation and foliation that follow the general trend of the magnetic axes at Nagarze.

Sector 2 covers the valleys south of Zhanang and Zetang towards Yala Xiangbo dome (Figs 4 & 8). Sites S21 and S22 in the Zhanang valley present triaxial magnetic ellipsoids with magnetic foliation trending east–west with moderate dip to the south parallel to S2 tectonic foliation. Magnetic lineation trends NNE–SSW with plunge towards the south–SW. The Qonggyai profile (location in Fig. 3) presents AMS ellipsoids that change from oblate in the south to triaxial in the central part and magnetic foliation strikes east–west and dips to the north analog to tectonic foliation S1 (Fig. 7a site Z12). The magnetic lineation contained in the magnetic foliation and S1, trends NNE–SSW with moderate north–NE plunge (K_{\max} mean vector = 028/59, $\alpha_{95} = 26.7^\circ$, $k = 33.5$) (Fig. 7a site Z19). North-west of Yala Xiangbo and south of Yardoi three sites describe triaxial ellipsoids and magnetic foliation striking SW–NE with moderate dip values towards the NW. The cluster of K_{\max} values describes a magnetic lineation trending NNW–SSE with 43° plunge towards the north–NW (Fig. 8b). Moving towards Zetang and the Great Counter Thrust the AMS ellipsoid is oblate (sites Q16 and Q17) and magnetic foliation strikes WNW–ESE but with southward dip similar to S2 tectonic foliation (Figs 7a site Q16 & 8a). From these results we can define two domains within sector 2 with opposite dip of the magnetic foliation and tectonic foliation (Figs 7a & 8a).

Sector 3 lies geographically between north of the Dala pass and Qusum. Tectonically this area is east of the Cona Graben and south of the Qusum Thrust. Eastward of the Yala Xiangbo (sites Tu and We) AMS ellipsoids are triaxial, the magnetic foliation has a NW–SE strike and dips about 60° to the NE parallel to S1 (Fig. 7a site Tu2). The magnetic lineation trends NW–SE and plunges to the NW and SE. Moving to the north the magnetic foliation changes to east–west strike and the magnetic lineation becomes east–west with a gentle plunge to the east parallel to the intersection of S1 and S2 tectonic foliations. In the proximity of the Qusum Thrust and the S2 domain, the magnetic ellipsoid switches to be more prolate (e.g. $T = -0.13$ in site Qu20). Here magnetic lineation trends east–west with almost horizontal plunge, parallel to the intersection of S1 and S2 tectonic foliations (Fig. 7b site Qu20 & Fig. 8b).

Sector 4 is located between the Great Counter Thrust and the Qusum Thrust where S2 is the main tectonic foliation. The southern and central parts present AMS ellipsoids which are slightly prolate (sites Mv27, Mv29, Fv38, Pa40) or oblate AMS ellipsoids (Fig. 7b site Mv27). The magnetic

foliation reflected in the oblate ellipsoids (sites Sr24, Sr25, Mv26, Mv28, Mv30 & Yt34) has WNW–ESE strike and south–SW dips parallel to S2 tectonic foliation. The slightly prolate ellipsoids present magnetic lineations with east–west direction and gentle plunges towards the west and are parallel to the F2 fold axes and the lineation defined by the intersection of S1 and S2 foliation. Towards the north, close to the Great Counter Thrust and the Indus Yarlung Suture Zone (sites Sr23, Yt32 & Yt33), ellipsoids turn to triaxial shape. Magnetic foliation trends west–east with steep dips towards the south and the magnetic lineation trends north–south with a 67° plunge to the south (sites Yt32 & Yt33), parallel to the stretching lineation and perpendicular to the Great Counter Thrust surface (Fig. 7b site Yt32 & Fig. 8a, b).

Tectonic interpretation and sequence of magnetic fabric development

Magnetic foliation and lineation in the slates of the Triassic flysch are the result of a complex sum of tectonic and metamorphic phases from the India–Asia collision until present. We suggest a 5-stage-evolution of the magnetic fabric supported by the structural properties to constraint the kinematic evolution of the eastern Tethyan Himalaya. Magnetic foliation and lineation have been analysed referred to their present-day orientation (see Fig. 9 for kinematic model proposed here and Fig. 2 to comparison with other kinematic models previously proposed).

1st Stage

During the Eohimalayan or D1 phase (Middle Eocene–Late Oligocene; Hodges 2000; Fig. 2) the collision of India and Asia produced the development of east–west-trending south facing isoclinal folds with related axial planar foliation (S1). This is shown south of Qonggyai (sector 2; Figs 4a & 8a) by well grouping K_{\min} directions and K_{\max} and K_{int} axes scattered within the tectonic S1 foliation plane (Fig. 9a).

2nd Stage

Near the locality of Qonggyai where D1 phase governs the orientation of the structures, the magnetic lineation is interpreted as the direction of stretching lineation of the phyllosilicates, under the prevailing stress field, during thrust sheet emplacement as has been described in other thrust structures (Oliva-Urcia *et al.* 2009). The plunge of the magnetic lineation indicates thrust emplacement towards the south–SW (Himalayan foreland)

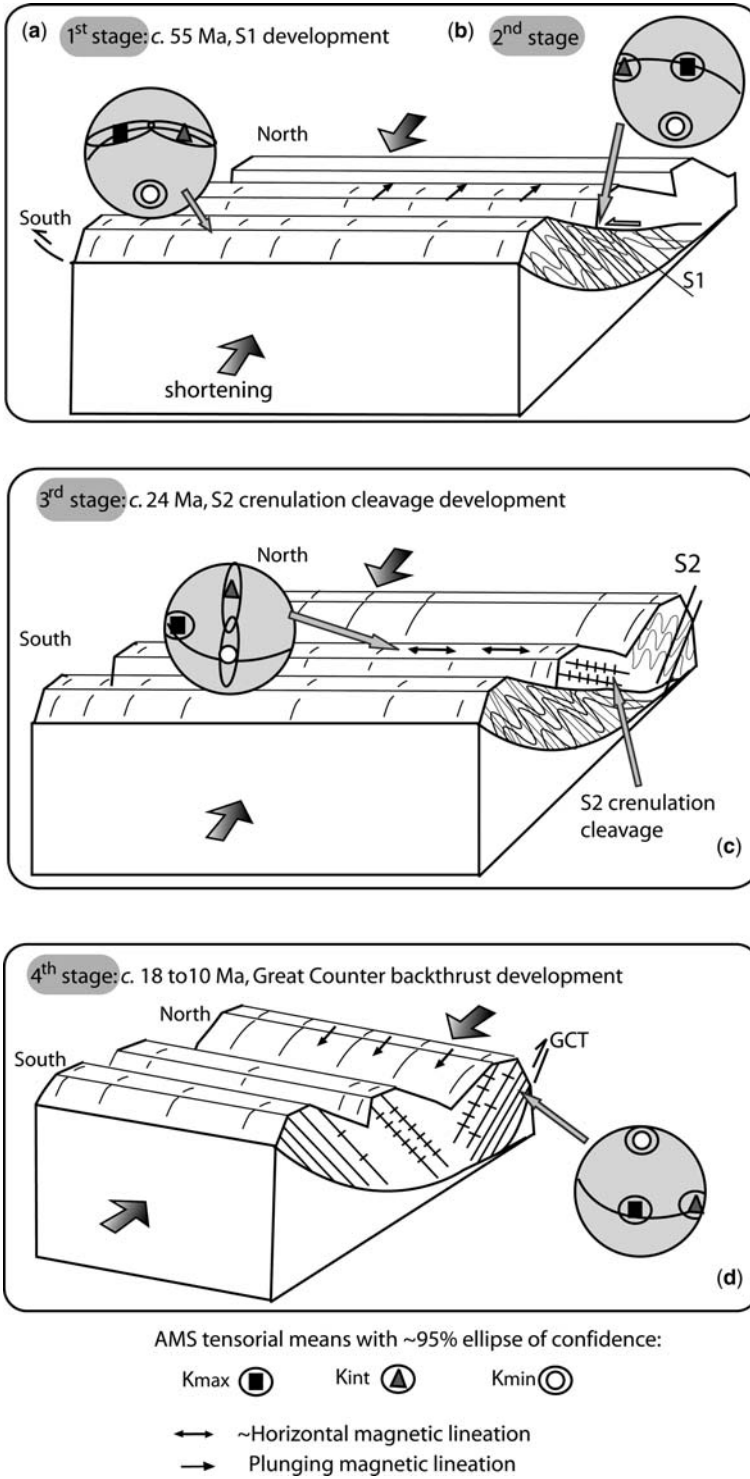


Fig. 9. Block diagrams showing the successive stages of the magnetic fabric evolution and the kinematics of the Triassic flysch in the eastern Tethyan Himalaya: (a) 1st stage, (b) 2nd stage, (c) 3rd stage and (d) 4th stage.

(Fig. 9b) in agreement with the south-directed displacement along the Lhunze fault, 15 km south of the studied sites (Aikman *et al.* 2008). Detailed structural and thermochronological analysis should be carried on the Lhunze Fault to closely constraint the timing and local and regional importance of this fault.

3rd Stage

Continuous deformation in the flysch thrust-wedge produced a change in the fold vergence around 20 km south of the Indus Yarlung Suture Zone and the Gangdese granite. This north-vergent deformation starts with the incipient development of the north-vergent F2 folds and related S2 crenulation cleavage (Fig. 2). This switch of vergence in the structures is recorded in the magnetic fabric by a subtle prolate ellipsoid with K_{\min} axes distributed in a semigirdle (Figs 7b sites Qu20, Mv27; Fig. 9c). This stage of magnetic fabric is similar to the stage of pencil cleavage (e.g. Borradaile & Tarling 1981; Housen *et al.* 1993; Parés *et al.* 1999) characterized by the incipient development of a new planar feature, in our case the foliation S2. This composite fabric reflects a combination of the S1 and the younger S2 foliation with K_{\max} axes strikingly east–west with gentle plunge, parallel to the intersection lineation between S1 and S2 (L12). The reason for this parallelism is that this direction is the intersection axis between the iron sheet silicates (Parés *et al.* 1999). As the foliation S2 becomes pervasive it transposes the older S1 and K_{\min} cluster parallel to the pole of S2 tectonic foliation. K_{\max} and K_{int} axes are distributed in a girdle that coincides with the S2 foliation plane. The time interval for the S2 foliation development can be related to the *c.* 24 Ma K/Ar ages found in illites (Dunkl *et al.* 2008), which we relate to an authigenic origin linked to the formation of the foliation S2. As deformation increases K_{\max} and K_{\min} axes become tightly clustered (triaxial ellipsoid) and magnetic lineation trends east–west parallel to F2 axes and the intersection lineation of S1 and S2 foliations (e.g. Fig. 8b sites Fv35 and Sr23).

4th Stage

Continuation of backward deformation towards higher structural levels was probably responsible for the formation of the north-directed Great Counter backthrust around 18 to 10 Ma (Quidelleur *et al.* 1997; Harrison *et al.* 2000; Fig. 2) which placed the Triassic flysch over the mélange complex or the Cretaceous rocks. This event is reflected in the north–south direction and 67° southward plunge of the magnetic lineation that is strikingly coincident with the stretching lineation in

sites Yt32 and Yt33. The magnetic lineation is the expression of the strain undergone by the hanging wall of the Great Counter backthrust during its emplacement (Fig. 9d).

5th Stage

From a more speculative point of view the 5th stage suggests two possible processes, which during the Middle Miocene resulted in the change of the east–west trend of the Eohimalayan magnetic foliation preserved in the Qonggyai valley to the NW–SE trend of the post-Eohimalayan magnetic foliation near Nagarze (sector 1) and east of the Cona Graben (sectors 3 and 4). The first possibility is an *c.* 20° clockwise rotation of the magnetic foliation related to vertical-axis rotations during the eastward extrusion of the Tibetan plateau (Tapponnier *et al.* 1982). Schill *et al.* (2004) also reported clockwise rotation in the central Tethyan Himalaya based on secondary remanence directions which were probably acquired during the last metamorphic cooling in Late Oligocene or Early Miocene times. Gan *et al.* (2007) describe a NE trend of GPS velocities in SE Tibet. Their data furthermore indicate that the GPS velocity east of the Cona Graben is more eastward directed which implies a clockwise rotation of this area relative to the adjacent area in the west. The second possibility can be associated with the doming of the North Himalayan domes. The magnetic foliation around the Yala Xiangbo describes a slight bend that is parallel to the contact of the dome with the flysch and in Nagarze area the inclination of the magnetic foliation and lineation decreases towards east of the flank of the Jangsang Lhamo dome. These two facts can suggest that the Triassic flysch had passively accommodated the doming around 18–13.5 Ma (Aikman *et al.* 2004) producing block rotations and tilting of the neighbouring structural elements.

Conclusions

The AMS and structural data collected in the Triassic flysch of the Tethyan Himalaya indicate that the magnetic fabric is an indicator of progressive deformation when the original foliation is overprinted, and allow us to reconstruct the fabric and tectonic evolution processes in SE Tibet.

In the studied slates magnetic susceptibility is predominantly carried by the paramagnetic fraction. This is shown by temperature dependence of the susceptibility following the $\sim 1/T$ Curie law, the comparison between the high field *v.* the low field susceptibilities and the parallelism between tectonic and magnetic foliation.

AMS provides quantitative information about the orientation of phyllosilicates alignment and the degree and shape of the AMS ellipsoid. Directions of stretching and intersection of the two foliations have been detected even when it is difficult to identify them in the field or only possible to measure them with extensive time consumption. AMS combined with structural studies allow us to gain a deeper structural insight on the evolution of the Triassic flysch within the eastern Tethyan Himalaya. Two different tectonic domains can be defined. East of the Cona graben these domains are separated by the Qusum Thrust. The southern domain is structurally dominated by east–west-striking and north-dipping magnetic foliation parallel to the Eohimalayan S1 tectonic foliation in accordance with the characteristic south vergence of the orogen. North of the Qusum Thrust ‘backward’ deformation is reflected in the magnetic foliation and tectonic S2 foliation which have WNW–ESE direction and dips to the south, opposite to the main vergence of the Himalayan system. In between the two domains an intermediate magnetic fabric is found where the incipient S2 foliation overlaps the S1 foliation and K_{\max} cluster roughly parallel to the intersection of S1 and S2 tectonic foliations. K/Ar age of *c.* 24 Ma (Dunkl *et al.* 2008) have been related to new micas with an authigenic origin linked to the formation of the S2 foliation. The two domains described in this study are the result of D1 and D2 deformation phases which can be observed in other north–south sections along the fold-thrust belt (Fig. 2), indicating no major changes in deformation features along east–west strike of the Tethyan Himalaya.

Magnetic lineation is interpreted as the transport direction of thrust structures in two locations within the study area. Near Qonggyai we identified a north–NE plunging magnetic lineation that is related to the phyllosilicates elongation direction, and could be the expression of the strain caused in the footwall of the Lhunze basement thrust. Close to the Yarlung Tsangpo, the magnetic lineation shows north–south trend and steep south plunge, and recorded the transport direction of the Neohimalayan Great Counter backthrust about 18 to 10 Ma (Quidelleur *et al.* 1997; Harrison *et al.* 2000) synchronous with the activity on the MCT and STDS (Yin *et al.* 1994).

Different orientations of magnetic foliations may indicate a Middle Miocene *c.* 20° clockwise vertical-axis rotation. This result would be in accordance with clockwise block rotations in the central Himalaya observed in secondary remanence directions (Schill *et al.* 2004) and present GPS velocities (e.g. Gan *et al.* 2007) that point out large-scale dextral shearing caused by the eastward extrusion of the Tibetan Plateau. Likewise intrusion and

exhumation of the North Himalayan domes can have induced block rotations and tilting of the adjacent tectonic elements. However these hypotheses need additional structural and palaeomagnetic analyses to be verified.

The authors thank the German Research Foundation (DFG) for financial support; Institute of Tibetan Plateau Research (ITP) and the Chinese Academy of Sciences (CAS) for logistic support. We thank Taba, Puchum, Nobu, and Xu Qiang for helping us during the field work. The authors are grateful to Zanist Hama-Aziz and Liu Yang for support in the magnetic measurements. We wish to thank B. Oliva-Urcia and R. Carosi for constructive comments. We deeply acknowledge the revisions from E. Pueyo, B. Housen, J. Poblet and R. Lisle which helped to improve the first version of the manuscript.

References

- AIKMAN, A., HARRISON, T. M. & DING, L. 2004. Preliminary results from the Yala-Xiangbo Leucogranite dome, SE Tibet. *Himalaya Journal of Sciences*, **2**, 91.
- AIKMAN, A., HARRISON, T. M. & DING, L. 2008. Evidence for Early (>44 Ma) Himalayan Crustal Thickening, Tethyan Himalaya, southeastern Tibet. *Earth and Planetary Science Letters*, **274**, 14–23.
- APPEL, E., MÜLLER, R. & WIDDER, R. W. 1991. Palaeomagnetic results from the Tibetan Sedimentary Series of the Manang area (north central Nepal). *Geophysical Journal International*, **104**, 255–266.
- ARMJO, R., TAPPONNIER, P., MERCIER, J. L. & TONGLIN, H. 1986. Quaternary extension in southern Tibet: field observations and tectonic implications. *Journal of Geophysical Research*, **91**, 13 803–13 872.
- AVERBUCH, O., FRIZON DE LAMOTTE, D. & KISSEL, C. 1992. Magnetic fabric as a structural indicator of the deformation path within a fold-thrust structure: a test case from the Corbières (NE Pyrenees, France). *Journal of Structural Geology*, **14**, 461–474.
- BERTHÉ, D., CHOUKROUNE, P. & JEGOUZO, P. 1979. Orthogneiss, mylonite and non coaxial deformation of granites: the example of the South Armorican Shear Zone. *Journal of Structural Geology*, **1**, 31–42.
- BONHOMME, M. & GARZANTI, E. 1991. Age of metamorphism in the Zaskar Tethys Himalaya (India). *Géologie Alpine*, **16**, 15–16.
- BORRADAILE, G. J. & JACKSON, M. 2004. Anisotropy of magnetic susceptibility (AMS): magnetic petrofabric of deformed rocks. In: MARTÍN-FERNÁNDEZ, F., LÜNEBURG, C. M., AUBOURG, C. & JACKSON, M. (eds) *Magnetic Fabric: Methods and Applications*. Geological Society, London, Special Publications, **238**, 299–360.
- BORRADAILE, G. J. & SARVAS, P. 1990. Magnetic susceptibility fabrics in slates: structural, mineralogical and lithological influences. *Tectonophysics*, **172**, 215–222.
- BORRADAILE, G. J. & TARLING, D. H. 1981. The influence of deformation mechanism on magnetic fabrics in weakly deformed rocks. *Tectonophysics*, **77**, 151–168.
- BORRADAILE, G. J. & WERNER, T. 1994. Magnetic anisotropy of some phyllosilicates. *Tectonophysics*, **235**, 223–248.

- BOUCHEZ, J. L. 1997. Granite is never isotropic: an introduction to AMS studies of granitic rocks. In: BOUCHEZ, J. L., HUTTON, D. H. W. & STEPHEN, W. E. (eds) *Granite: From Segregation of Melt to Emplacement Fabrics*. Kluwer Academic Publishers, Dordrecht, 95–112.
- BROOKFIELD, M. 1993. The Himalayan passive margin from Precambrian to Cretaceous. *Sedimentary Geology*, **84**, 1–35.
- BURCHFIEL, B. C., ZHILIANG, C., HODGES, K. V., YUPING, L., ROYDEN, L. H., CHANGRONG, D. & JIENE, X. 1992. *The South Tibetan Detachment System, Himalaya Orogen: Extension Contemporaneous with and Parallel to Shortening in a Collisional Mountain Belt*. Geological Society of America, Special Papers, 269.
- BURG, J. P. & CHEN, G. M. 1984. Tectonics and structural zonation of southern Tibet, China. *Nature*, **311**, 219–223.
- BURMEISTER, K. C., HARRISON, M. J., MARSHAK, S., FERRÉ, E. C., BANNISTER, R. A. & KODAMA, K. P. 2009. Comparison of Fry strain ellipse and AMS ellipsoid trends to tectonic fabric trends in very low-strain sandstone of the Appalachian fold-thrust belt. *Journal of Structural Geology*, doi: 10.1016/j.jsg.2009.03.010.
- CAROSI, R., MONTOMOLI, C. & VISONÀ, D. 2002. Is there any detachment in the Lower Dolpo (western Nepal)? *Comptes Rendus Geoscience*, **334**, 933–940.
- CAROSI, R., MONTOMOLI, C. & VISONÀ, D. 2007. A structural transect in the Lower Dolpo: Insights on the tectonic evolution of Western Nepal. *Journal of Asian Earth Sciences*, **29**, 407–423, doi: 10.1016/j.jseas.2006.05.001.
- CHANG, C. 1984. Les caractéristiques tectoniques et l'évolution de la zone de suture du Yarlung-Zangbo. In: MERCIER, J. L. & LI, G. C. (eds) *Mission Franco-Chinoise Au Tibet 1980: Étude Géologique Et Géophysique De La Croûte Terrestre Et Du Manteau Supérieur Du Tibet Et De L'Himalaya*. Editions du Centre National de la Recherche Scientifique, Paris, France, 341–350.
- CHEN, Z., LIU, Y., HODGES, K. V., BURCHFIEL, B. C., ROYDEN, L. H. & DENG, C. 1990. The Kangmar dome: A metamorphic core complex in southern Xizang (Tibet). *Science*, **250**, 1552–1556.
- COLCHEN, M., LE FORT, P. & PÉCHER, A. 1986. *Annapurna-Manaslu-Ganesh Himal Notice De La Carte Géologique Au 1/200.000* (bilingual Edition, French–English). Centre National de la Recherche Scientifique, Paris.
- CROUZET, C., STANG, H., APPEL, E., SCHILL, E. & GAUTAM, P. 2001. Detailed analysis of successive pTRMs carried by pyrrhotite in Himalayan metacarbonates: an example from Hidden Valley Central Nepal. *Geophysical Journal International*, **146**, 607–618.
- CROUZET, C., DUNKL, I., PAUDEL, L., ARKAI, P., RAINER, T. M., BALOGH, K. & APPEL, E. 2007. Temperature and age constraints on the metamorphism of the Tethyan Himalaya in Central Nepal: a multidisciplinary approach. *Journal of Asian Earth Sciences*, **30**, 113–130, doi: 10.1016/j.jseas.2006.07.014.
- DING, L., KAPP, P. & WAN, X. 2005. Paleocene-Eocene record of ophiolite obduction and initial India–Asia collision, south central Tibet. *Tectonics*, **24**, TC3001, doi: 10.1029/2004TC001729.
- DUNKL, I., LIN, D. ET AL. 2008. Diagenetic and metamorphic overprint and deformation history of Permo-Triassic Tethyan sediments, SE Tibet. *Himalayan Journal of Sciences*, **5**, 49.
- DUPUIS, C., HÉBERT, R., DUBOIS-COTÉ, V., WANG, C. S., LI, Y. L. & LI, Z. J. 2005. Petrology and geochemistry of mafic rocks from mélange and flysch units adjacent to the Yarlung Zangbo Suture Zone, southern Tibet. *Chemical Geology*, **214**, 287–308.
- DUPUIS, C., HÉBERT, R., DUBOIS-COTÉ, V., GUILMETTE, C., WANG, C. S. & LI, Z. J. 2006. Geochemistry of sedimentary rocks from mélange and flysch units south of the Yarlung Zangbo suture zone, southern Tibet. *Journal of Asian Earth Sciences*, **26**, 489–508.
- EDWARDS, M. A. & HARRISON, T. M. 1997. When did the roof collapse? Late Miocene north–south extension in the high Himalaya revealed by Th–Pb monazite dating of the Khula Kangri granite. *Geology*, **25**, 543–546.
- FISHER, N. I., LEWIS, T. & EMBLETON, B. J. J. 1987. *Statistical Analysis of Spherical Data*. Cambridge University Press, Cambridge.
- FLINN, D. 1962. On folding during three-dimensional progressive deformation. *Quarterly Journal of the Geological Society of London*, **118**, 385–433.
- FUCHS, G. 1967. *Zum Bau Des Himalaya*. Österreichische Akademie der Wissenschaften, Mathematisch-Naturwissenschaftliche Klasse, Denkschriften, **113**, 1–211.
- GAETANI, M. & GARZANTI, E. 1991. Multicyclic history of the northern Indian continental margin (northwestern Himalaya). *American Association of Petroleum Geologists, Bulletin*, **75**, 1427–1446.
- GAN, W., ZHANG, P. ET AL. 2007. Present-day crustal motion within the Tibetan Plateau inferred from GPS measurements. *Journal of Geophysical Research*, **112**, B08416, doi: 10.1029/2005JB004120.
- GANSSE, A. 1964. *Geology of the Himalayas*. Wiley Interscience, London.
- GARZANTI, E. 1999. Stratigraphy and sedimentary history of the Nepal Tethys Himalaya passive margin. *Journal of Asian Earth Sciences*, **17**, 805–827.
- GARZANTI, E., GORZA, M., MARTELLINI, L. & NICORA, A. 1994. Transition from diagenesis to metamorphism in the Paleozoic to Mesozoic succession of the Dolpo-Manang synclorium and Thakkola graben (Nepal Tethys Himalaya). *Eclogae Geologicae Helvetiae*, **87**, 613–632.
- GARZIONE, C. N., DECELLES, P. G., HODKINSON, D. G., ORHA, T. P. & UPRETI, B. N. 2003. East-west extension and Miocene environmental change in the southern Tibetan plateau: Thakkhola graben, central Nepal. *Geological Society of America Bulletin*, **115**, 3–20.
- GODIN, L. 2003. Structural evolution of the Tethyan sedimentary sequence in the Annapurna area, central Nepal Himalaya. *Journal of Asian Earth Sciences*, **22**, 307–328.
- GODIN, L., GRUJIC, D., LAW, R. D. & SEARLE, M. P. 2006. Channel flow, extrusion and exhumation in continental collision zones: an introduction. In: LAW, R. D., SEARLE, M. P. & GODIN, L. (eds) *Channel Flow, Ductile Extrusion and Exhumation in Continental*

- Collision Zones*. Geological Society, London, Special Publications, **268**, 1–23.
- GRUJIC, D., HOLLISTER, L. & PARRISH, R. R. 2002. Himalayan metamorphic sequence as an orogenic channel: insight from Bhutan. *Earth and Planetary Science Letters*, **198**, 177–191.
- GUILLLOT, S., PÉCHER, A., ROCHETTE, P. & LEFORT, P. 1993. The emplacement of the Manaslu granite of central Nepal: field and magnetic susceptibility constraints. In: TRELOAR, P. J. & SEARLE, M. P. (eds) *Himalayan Tectonics*. Geological Society, London, Special Publications, **74**, 413–428.
- HARRISON, T. M., YIN, A., GROVE, M. & LOVERA, O. M. 2000. The Zedong Window: a record of superposed Tertiary convergence in southeastern Tibet. *Journal of Geophysical Research*, **105**, 19 211–19 320.
- HEIM, A. & GANSSER, A. 1939. Central Himalaya. Geological Observations of the Swiss Expedition 1936. *Mémoires de la Société Helvétique des Sciences Naturelles*, **7/31**, 1–245.
- HIRT, A. M., LOWRIE, W., CLENDENEN, W. S. & KLIGFIELD, R. 1988. The correlation of magnetic anisotropy with strain in the Chelmsford Formation of the Sudbury Basin, Ontario. *Tectonophysics*, **145**, 177–189.
- HODGES, K. V. 2000. Tectonics of the Himalaya and southern Tibet from two perspectives. *Geological Society of America Bulletin*, **112**, 324–350.
- HOLT, W. E., NI, J. F., WALLACE, T. C. & HAINES, A. J. 1991. The Active Tectonics of the Eastern Himalayan Syntaxis and Surrounding Regions. *Journal of Geophysical Research*, **96**, 14 595–14 632.
- HOUSEN, B. A., RICHTER, C. & VAN DER PLUIJM, B. A. 1993. Composite magnetic anisotropy fabrics: experiments, numerical models, and implications for the quantification of rock fabrics. *Tectonophysics*, **220**, 1–12.
- JELINEK, V. 1977. *The statistical theory of measuring anisotropy of magnetic susceptibility of rocks and its application*. Geofyzika Brno.
- KELLETT, D. A. & GODIN, L. 2009. Pre-Miocene deformation of the Himalayan superstructure, Hidden valley, central Nepal. *Journal of the Geological Society, London*, **166**, 261–275.
- KNEEN, S. 1976. The relationship between the magnetic and strain fabrics of some haematite-bearing Welsh slates. *Earth and Planetary Science Letters*, **31**, 413–416.
- LEE, J., HACKER, B. R. ET AL. 2000. Evolution of the Kangmar Dome, southern Tibet: structural, petrologic, and thermochronologic constraints. *Tectonics*, **19**, 872–895.
- LEFORT, P. 1975. Himalayas, the collided range. Present knowledge of the continental arc. *American Journal of Science*, **275-A**, 1–44.
- LIU, G. 1992. Permian to Eocene sediments and Indian passive margin evolution in the Tibetan Himalayas. *Tübinger Geowissenschaftliche*, **A13**, 1–268.
- LIU, G. & EINSELE, G. 1994. Sedimentary history of the Tethyan basin in the Tibetan Himalayas. *Geologische Rundschau*, **83**, 32–61.
- LIU, G. & EINSELE, G. 1996. Various types of olistostromes in a closing ocean basin, Tethyan Himalaya (Cretaceous, Tibet). *Sedimentary Geology*, **104**, 203–226.
- MARTÍN-HERNÁNDEZ, F. & HIRT, A. M. 2003. The anisotropy of magnetic susceptibility in biotite, muscovite and chlorite single crystals. *Tectonophysics*, **337**, 13–28.
- MCQUARRIE, N., ROBINSON, D., LONG, S., TOBGAY, T., GRUJIC, D., GEHRELS, G. & DUCEA, M. 2008. Preliminary stratigraphic and structural architecture of Bhutan: Implications for the along strike architecture of the Himalayan system. *Earth and Planetary Science Letters*, **272**, 105–117.
- MONTOMOLI, C., APPEL, E., ANTOLÍN, B., DUNKL, I., EL BAY, R., LIN, D. & GLOAGUEN, R. 2008. Polyphase deformation history of the 'Tibetan Sedimentary Sequence' in the Himalaya chain (South-East Tibet). *Himalayan Journal of Sciences*, **5**, 91.
- NAGATA, T. 1961. *Rock Magnetism*. Maruzen, Tokyo.
- NAJMAN, Y., CARTER, A., OLIVER, G. & GARZANTI, E. 2005. Provenance of Eocene foreland basin sediments, Nepal: Constraints to the timing and diachroneity of early Himalayan orogenesis. *Geology*, **33**, 309–312.
- OLIVA-ÚRCIA, B., LARRASOÑA, J. C. ET AL. 2009. Disentangling magnetic subfabrics and their link to deformation processes in cleaved sedimentary rocks from the Internal Sierras (west central Pyrenees, Spain). *Journal of Structural Geology*, **31**, 163–176.
- PAN, G., DING, J., YAO, D. & WANG, L. 2004. *Geological Map of Qinghai-Xizang (Tibet) Plateau and Adjacent Areas (1:1,500,000)*. Chengdu Institute of Geology and Mineral Resources, China Geological Survey. Chengdu Cartographic Publishing House.
- PARÉS, J. M. & VAN DER PLUIJM, B. 2002. Evaluating magnetic lineations (AMS) in deformed rocks. *Tectonophysics*, **350**, 283–298.
- PARÉS, J. M., VAN DER PLUIJM, B. A. & DINARÈS-TURELL, J. 1999. Evolution of magnetic fabric during incipient deformation of mudrocks (Pyrenees, northern Spain). *Tectonophysics*, **307**, 1–14.
- PATZELT, A., LI, H., WANG, J. & APPEL, E. 1996. Paleomagnetism of Cretaceous to Tertiary sediments from southern Tibet: evidence for the extent of the northern margin of India prior to the collision with Eurasia. *Tectonophysics*, **259**, 259–284.
- PÉCHER, A. 1991. The contact between the higher Himalayan crystalline sediments and the Tibetan sedimentary series: Miocene large-scale dextral shearing. *Tectonics*, **10**, 587–598.
- PUEYO, E. L., ROMÁN-BERDIEL, T., BOUCHEZ, J. L., CASAS, A. M. & LARRASOÑA, J. C. 2004. In: MARTÍN-FERNÁNDEZ, F., LÜNEBURG, C. M., AUBOURG, C. & JACKSON, M. (eds) *Magnetic Fabric: Methods and Applications*. Geological Society, London, Special Publications, **238**, 395–420.
- QUIDELLEUR, X., GROVE, M., LOVERA, O. M., HARRISON, T. M. & YIN, A. 1997. Thermal evolution and slip history of the Renbu-Zedong Thrust, southeastern Tibet. *Journal of Geophysical Research*, **102**, 2659–2679.
- RATSCHBACHER, L., FRISCH, W., LIU, G. & CHEN, C. 1994. Distributed deformation in southern and western Tibet during and after the India–Asia collision. *Journal of Geophysical Research*, **99**, 19 917–19 945.
- RICHTER, C. & VAN DER PLUIJM, B. A. 1994. Separation of paramagnetic and ferrimagnetic susceptibilities using low temperature magnetic susceptibilities and

- comparison with high field methods. *Physics of the Earth and Planetary Interiors*, **51**, 113–123.
- ROCHETTE, P. 1987. Metamorphic control of the magnetic mineralogy of black shales in the Swiss Alps: toward the use of 'magnetic isograds'. *Earth and Planetary Science Letters*, **84**, 1015–1020.
- ROMÁN-BERDIEL, T., CASAS, A. M., OLIVA-URCIA, B., PUEYO, E. & RILLO, C. 2004. The main Variscan deformation event in the Pyrenees: new data from the structural study of the Bielsa granite. *Journal of Structural Geology*, **17**, 1337–1346.
- SCHILL, E., APPEL, E., GODIN, L., CROUZET, C., GAUTAM, P. & REGMI, K. 2003. Record of deformation by secondary magnetic remanences and magnetic anisotropy in the Nar/Phu valley (central Himalaya). *Tectonophysics*, **377**, 197–209.
- SCHILL, E., APPEL, E., CROUZET, C., GAUTAM, P., WEHLAND, F. & STAIGER, M. 2004. Oroclinal bending v. regional significant clockwise rotations in the Himalayan arc—Constraints from secondary pyrrhotite remanences. In: SUSSMAN, A. J. & WEIL, A. B. (eds) *Orogenic Curvature: Integrating Paleomagnetic and Structural Analyses*. Geological Society of America, Special Paper, **383**, 73–85.
- SEARLE, M. 1986. Structural evolution and sequence of thrusting in the High Himalayan, Tibetan-Tethys and Indus suture zones of Zaskar and Ladakh, Western Himalaya. *Journal of Structural Geology*, **8**, 923–936.
- SOTO, R., MATTEI, M. & CASAS, A. M. 2003. Relationship between AMS and folding in an area of superimposed folding (Cotiella-Bóixols nappe, Southern Pyrenees). *Geodinamica Acta*, **16**, 171–185.
- STECK, A. 2003. Geological Map of the NW Himalaya. *Eclogae Geologicae Helvetiae*, **96**, 147–U13.
- STÖCKLIN, J. 1980. Geology of Nepal and its regional frame. *Journal of the Geological Society, London*, **137**, 1–34.
- TAPPONNIER, P., PELTZER, G., LE DAIN, A. Y., ARMIJO, R. & COBBOLD, P. 1982. Propagating extrusion tectonics in Asia: New insights from simple experiments with plasticine. *Geology*, **10**, 611–616.
- TARLING, D. H. & HROUDA, F. 1993. *The Magnetic Anisotropy of Rocks*. Chapman & Hall, London.
- VALDIYA, K. S. 1980. *Geology of the Kumaun Lesser Himalaya*. Wadia Institute of Himalayan Geology, Dehra Dun.
- WILLEMS, H., ZHOU, Z., ZHANG, B. & GRÄFE, K. U. 1996. Stratigraphy of the Upper Cretaceous and Lower Tertiary strata in the Tethyan Himalayas of Tibet (Tingri area, China). *Geologische Rundschau*, **85**, 723–754.
- YIN, A. 2006. Cenozoic evolution of the Himalayan Orogen as constrained by along strike variations of structural geometry, exhumation history, and foreland sedimentation. *Earth-Science Reviews*, **76**, 1–131.
- YIN, A. & HARRISON, T. M. 2000. Geologic evolution of the Himalayan–Tibetan orogen. *Annual Review of Earth and Planetary Sciences*, **28**, 211–280.
- YIN, A., HARRISON, T. M., RYERSON, F. J., WENJI, C., KIDD, W. & COPELAND, P. 1994. Tertiary structural evolution of the Gangdese thrust system, southeastern Tibet. *Journal of Geophysical Research*, **99**, 18 175–18 201.
- ZHANG, B., ZHANG, J., GUO, L. & WANG, W. 2005. Microstructural and deformational studies on mylonite in the detachment faults of Yalashangbo dome, North Himalayan domes zone. *Progress in Natural Science*, **15**, 1005–1013.

Progressive deformation of a Coulomb thrust wedge: the eastern Fuegian Andes Thrust–Fold Belt

PABLO J. TORRES CARBONELL^{1*}, LUIS V. DIMIERI² & EDUARDO B. OLIVERO¹

¹*Centro Austral de Investigaciones Científicas (CADIC), CONICET, Bernardo Houssay 200, (9410) Ushuaia, Tierra del Fuego, Argentina*

²*Instituto Geológico del Sur (INGEOSUR), CONICET and Departamento de Geología, Universidad Nacional del Sur, San Juan 670, (8000) Bahía Blanca, Argentina*

**Corresponding author (e-mail: polmacleod@hotmail.com)*

Abstract: Time-calibrated balanced-cross sections of the eastern Fuegian Thrust–Fold Belt reveal many complex pro- and retro-vergent structures, rooted at the base of Cretaceous and within Paleocene rocks. These structures involve the unconformity-bounded syntectonic sequences of the Austral foreland basin, and accommodate a minimum shortening of c. 41.8 km. The complex kinematics of the thrust–fold belt are recorded by: (1) propagation of the basal décollement into the foreland, and forward-directed thrusting during the Ypresian; (2) out-of-sequence thrusting in the Lutetian; (3) subsidence and sedimentation from the Late Lutetian to the Oligocene; (4) backthrusting during the Oligocene; and (5) a renewed stage of forward-directed thrusting between the latest Oligocene and the Early Miocene, probably related to accretion below the sole fault in the hinterland. This thrust sequence is interpreted as the result of critical Coulomb wedge behaviour during the first stage of thrust–fold belt expansion, with accretion of new material that led to a taper decrease. The subsequent period of internal deformation corresponds to a subcritical stage, during which backthrusting accommodates significant shortening (c. 15%). After growth and taper increase, the last period of forward thrusting at the wedge's front marks the inception of a new critical stage.

The Fuegian Andes form the southernmost extremity of the South American Andean Cordillera. The mountain front of this portion of the Andes is formed by the Fuegian Thrust–Fold Belt, which has been described in isolated parts of Tierra del Fuego as a thin-skinned wedge that involves Upper Cretaceous to Miocene sequences (Álvarez-Marrón *et al.* 1993; Klepeis 1994a; Klepeis & Austin 1997; Ghiglione *et al.* 2002; Torres Carbonell *et al.* 2008a). The location of the Fuegian Andes in a complex and still poorly understood geotectonic setting (Dalziel *et al.* 1975; Kraemer 2003; Eagles *et al.* 2005) makes the Fuegian Thrust–Fold Belt a key area for the study and better comprehension of the tectonic evolution of southern South America and Antarctica. In addition, the hydrocarbon significance of the Austral Basin, genetically related to this thrust wedge (Biddle *et al.* 1986; Galeazzi 1998; Rosello *et al.* 2008), strongly encourages further analysis of its detailed structure and stratigraphy.

Even though the geometry and kinematics of the Fuegian Thrust–Fold Belt have been described and analysed in some areas, the timing of its overall structural evolution is still poorly known. Based on the stratigraphic framework known at that time (Olivero & Malumíán 1999; Olivero *et al.* 2002,

2003) and on fieldwork in the southeastern part of Tierra del Fuego, Ghiglione & Ramos (2005) proposed the only chronological scheme of thrust front migration known for the area. In this paper, new field data and interpretations are examined, leading to an improved stratigraphic framework (Torres Carbonell *et al.* 2009a) and structural database, which allows better constraints on the geometry and kinematics of structures and their age of development.

This work focuses on the tectonics of northern Península Mitre, in SE Tierra del Fuego (Fig. 1), where the best exposures of the eastern Fuegian Thrust–Fold Belt are located. Balanced cross-sections were constructed on the basis of detailed maps of selected sectors in this area, which permit a well-constrained structural geometry for the thrust–fold belt to be established. The kinematic evolution of these cross-sections is time-calibrated with the chronostratigraphy of the syntectonic successions affected by the contractional structures (Olivero & Malumíán 2008, and references therein; Torres Carbonell *et al.* 2009a). Based on the structural analysis, a comprehensive kinematic model for the thrust–fold belt between Península Mitre and its leading edge at Punta Gruesa (Torres

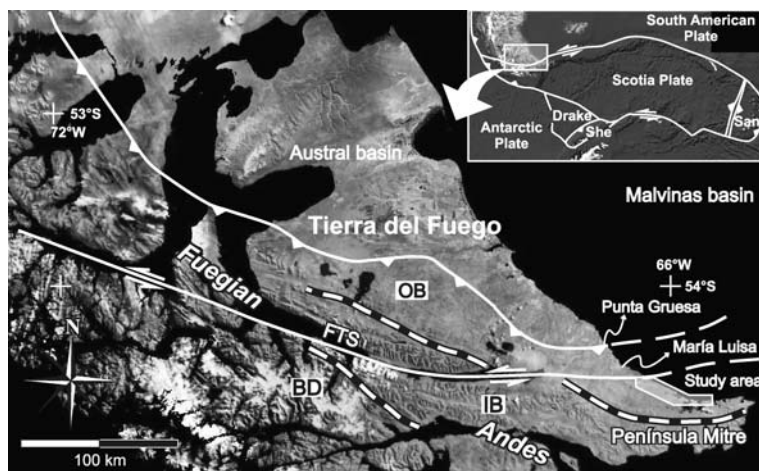


Fig. 1. Location of the study area (see Fig. 3) in Tierra del Fuego, and its tectonic setting (inset). Drake, Drake Plate; San, Sandwich Plate; She, Shetland Plate. The dashed heavy lines mark the approximate boundaries between the Upper Palaeozoic–Middle Jurassic basement domain (BD), the Upper Jurassic–‘mid’ Cretaceous inner orogenic belt (IB), and the Upper Cretaceous–Cenozoic outer orogenic belt (OB). The Neogene sinistral Fagnano Transform System (FTS) cuts the entire Fuegian Andes.

Carbonell *et al.* 2008a) is proposed, highlighting the progressive growth history of the Fuegian Andes. This growth history, far from adjusting to standard thrust-sequences, reveals a complex episodic evolution characterized by stages of forward thrusting and interposed out-of-sequence thrusting and back-thrusting stages. The episodic progression of the deformation in the eastern Fuegian Thrust–Fold Belt is explained here in terms of the Coulomb wedge theory. The improved kinematic model developed, plus the complex and distinct thrust-sequence analyzed in terms of a widely applied theory, gives both a local and global topical significance to this work.

The studied area (Fig. 1) is located between Cabo Malengüena (54°32'S; 66°13'W) and Punta Donata (54°39'S; 65°33'W). This remote area is difficult to access, and the outcrops are limited to the coastal cliffs, wave-cut platforms, inland river valleys, and to sectors of nearby hills not covered by vegetation.

Fuegian Thrust–Fold Belt

The Fuegian Andes evolved since the ‘mid’ Cretaceous, when a marginal retro-arc basin that had formed from the Late Jurassic–Early Cretaceous closed against the South American southwestern margin (Dalziel *et al.* 1974, 1987; Kraemer 2003). Closure led to intense deformation and tectonic thickening of the marginal basin fill between a parautochthonous magmatic arc and the cratonic

margin (Nelson *et al.* 1980; Dalziel 1986; Klepeis 1994a). The orogenic belt is separated here into three domains, according to the degree of deformation involved (Fig. 1): The basement domain, located in southwestern Tierra del Fuego, comprises Upper Palaeozoic to Middle Jurassic high to low grade metamorphic rocks affected by several folding stages, and is thrust over the inner belt with a NE vergence (Nelson *et al.* 1980; Dalziel & Brown 1989; Klepeis 1994a). The inner orogenic belt, composed of Upper Jurassic to ‘mid’ Cretaceous rocks, forms the core of the Fuegian Cordillera and reveals polyphase deformation, isoclinal to tight folding, and slaty cleavage (Bruhn 1979; Caminos 1980; Klepeis 1994a). A thin-skinned thrust–fold belt forms the outer orogenic belt, affecting the Upper Cretaceous–Cenozoic sediments deposited in a foreland basin, known as Austral Basin (Biddle *et al.* 1986; Wilson 1991; Álvarez Marrón *et al.* 1993; Klepeis 1994a; Ghiglione & Ramos 2005).

The stratigraphic successions involved in the thrust–fold belt have been divided into unconformity bounded sequences (Olivero & Malumíán 2008). The bounding unconformities have been recognized throughout the thrust–fold belt and beyond, in the stable cratonic margin of the foreland basin (Malumíán *et al.* 1971), and have been linked to tectonic events in the Fuegian Andes (Martinioni *et al.* 1999; Ghiglione & Ramos 2005; Malumíán & Olivero 2006; Torres Carbonell *et al.* 2008a, 2009a).

The youngest structures recognized in the Fuegian Thrust–Fold Belt are the thrust imbricates that crop out at Punta Gruesa (Fig. 1; Torres Carbonell

et al. 2008a), which affect Early Miocene syntectonic strata (Ghiglione 2002; Malumíán & Olivero 2006; Ponce *et al.* 2008). Cessation of contractional deformation and freezing of the thrust–fold belt is presumed to have occurred throughout its eastern part by Early Miocene times, according to the age and stratigraphic architecture of undeformed sequences in the foredeep of the Austral Basin, adjacent to the thrust-front (Ponce *et al.* 2008). The end of the contractional tectonics was followed by a period characterized by strike-slip faulting, associated with the development of the transform boundary between the Scotia and South American plates, expressed as the major Fagnano Transform System in Tierra del Fuego (Klepeis 1994b; Torres Carbonell *et al.* 2008b).

Stratigraphy

The stratigraphic framework of the studied area is here briefly described, based on the generalized section shown in Figure 2. Most of the sedimentary successions recognized are part of the wedge-top depocenter of the Austral Basin (cf. Torres Carbonell *et al.* 2008a, 2009a), and therefore they are unconformity-bounded sequences that constrain the age of the contractional stages in the thrust–fold belt.

Policarpo Formation (Maastrichtian–Danian)

The Policarpo Formation (Furque & Camacho 1949; Olivero *et al.* 2002) consists of a mudstone-dominated turbidite succession at least 300 m thick, with ammonites and microfossils from the Maastrichtian–Danian (Fig. 2) (Olivero *et al.* 2002, 2003). It crops out at Punta Donata, Punta Duquesa, and at the northern shore of Laguna Río Bueno (Figs 3 & 4). The base of this unit is not exposed, and the top is formed by an unconformity overlain by the Río Bueno Formation (Lutetian). In other parts of Tierra del Fuego, the Policarpo Formation is unconformably covered by Paleocene strata (Martinioni *et al.* 1999; Olivero *et al.* 2003; Torres Carbonell *et al.* 2008b). The unconformity with the Río Bueno Formation reveals an angular relationship of up to 20°, but the magnitude decreases to almost zero in some places.

Cabo Leticia and La Barca Formations (Paleocene)

The Paleocene sedimentary rocks comprise the base of the Río Claro Group, composed of the Cabo Leticia and La Barca Formations, which are separated by a transitional contact (Fig. 2) (Olivero

et al. 2002; Olivero & Malumíán 2008). These formations form a turbidite system with a minimum thickness of 370 m, composed of tuffaceous breccia, conglomerate and sandstone at the base, and mudstone at the top (Olivero *et al.* 2002; Olivero & Malumíán 2008). The age of this sedimentary package is constrained by post-Danian foraminiferal and palynological assemblages in the La Barca Formation (Malumíán & Caramés 2002; Olivero *et al.* 2002; Torres Carbonell *et al.* 2009a). The Cabo Leticia and La Barca Formations crop out at Cabo Leticia and surrounding areas, and at Río Malengüena (Figs 3 & 5).

The base of the Cabo Leticia Formation is not exposed at the studied area, and the contact of the La Barca Formation with the immediately youngest Punta Noguera Formation (Ypresian) is a N-verging gently dipping thrust revealed at Punta Ainol (see below). The La Barca Formation is also covered through an angular unconformity by the Leticia Formation (Upper Lutetian–Priabonian) at Punta Ainol, and by the Río Bueno Formation (Lutetian) at the southern part of Cabo Leticia (Figs 3 & 5).

Punta Noguera and Cerro Ruperto Formations (Ypresian)

The Punta Noguera and Cerro Ruperto Formations form part of the upper Río Claro Group (Fig. 2) (Olivero *et al.* 2002; Olivero & Malumíán 2008). The Punta Noguera Formation consists of tuffaceous, sandy gravity flow deposits with a minimum thickness of 380 m at the type area, in the eponymous site (Figs 3 & 4). The age of the Formation is constrained by Ypresian microfossils (Malumíán *et al.* 2009; Torres Carbonell *et al.* 2009a). The Punta Noguera Formation is also recognized at Río Malengüena, at Punta Ainol, at the wave-cut bench between Punta Noguera and Cabo Leticia, and at the Punta Ancla cliffs (Figs 3–5). The base of the Formation is not exposed, although an unconformity is inferred based on the strong facies and microfaunal differences with the turbidites of the La Barca Formation (Torres Carbonell *et al.* 2009a). The top of the Punta Noguera Formation is marked by an angular unconformity with the Río Bueno Formation (Lutetian), exposed at Punta Noguera.

The Cerro Ruperto Formation consists of a minimum of 200 m of marine sandstone and siltstone with an Ypresian palynological content (Olivero *et al.* 2002). The outcrops are restricted to the type area, located between Cerro Ruperto and Punta Cuchillo. The siltstones poorly exposed in the northern foothills of Cerro Las Vacas and eastern foothills of Cerro Piedra are here tentatively assigned to this Formation (Fig. 4). The base of

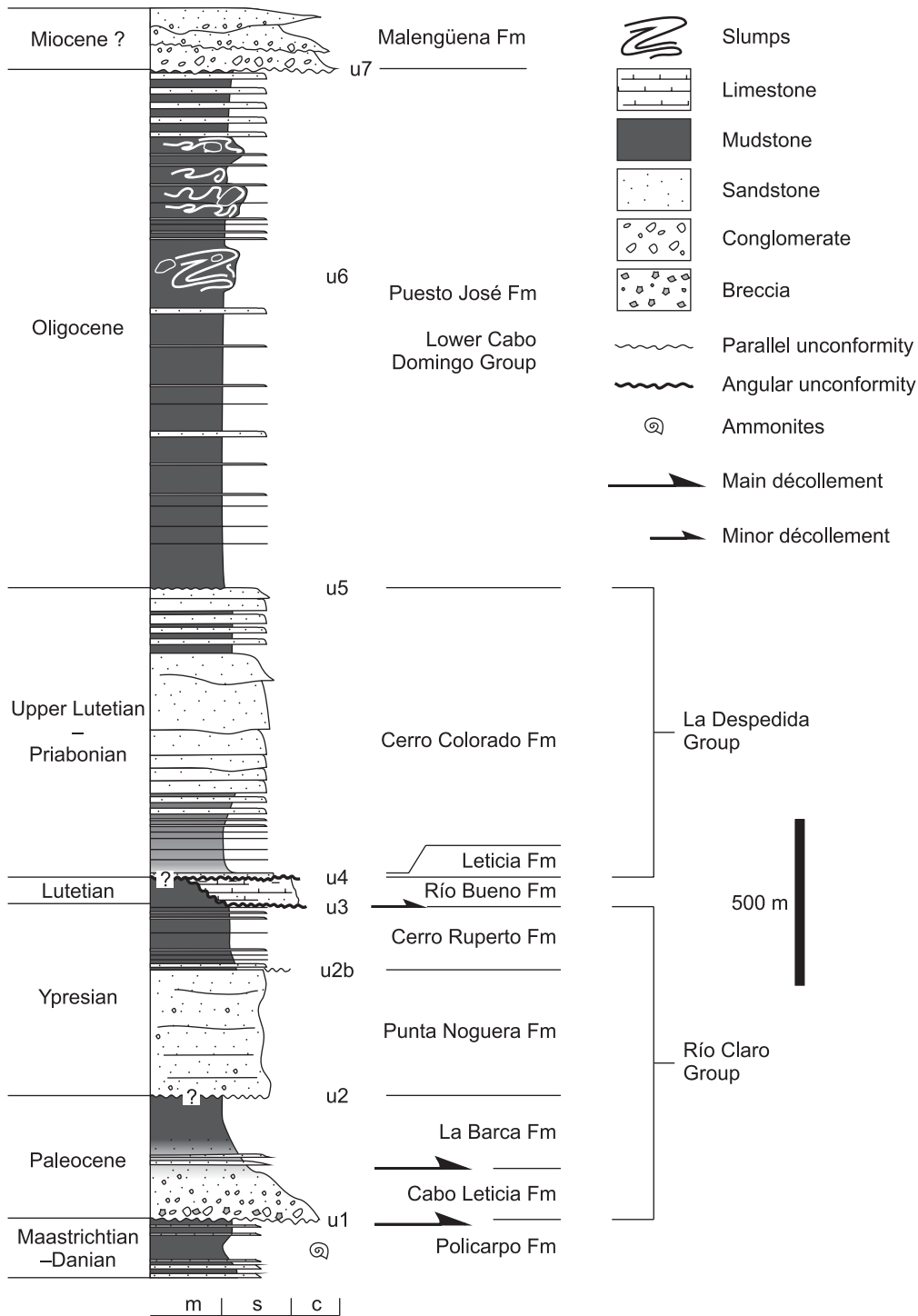


Fig. 2. Idealized stratigraphic section of the studied area. m, mudstone; s, sandstone; c, conglomerate. Unconformities (u) 1–7 are shown.

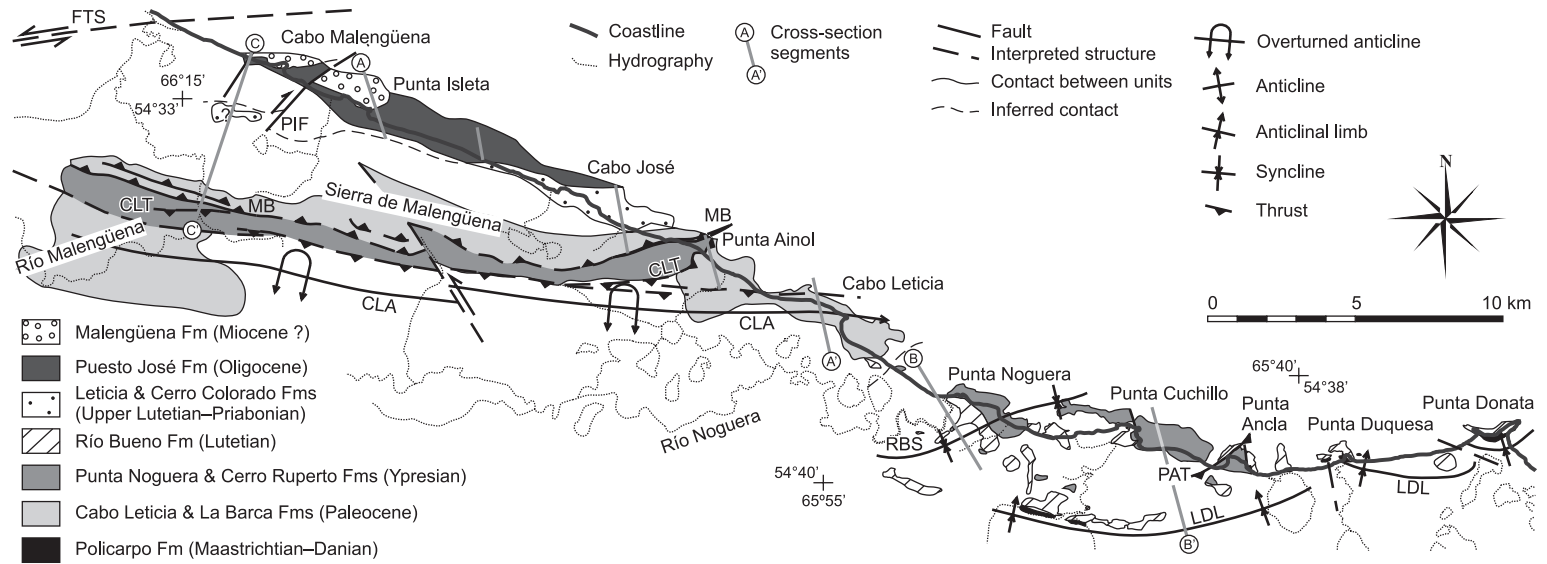
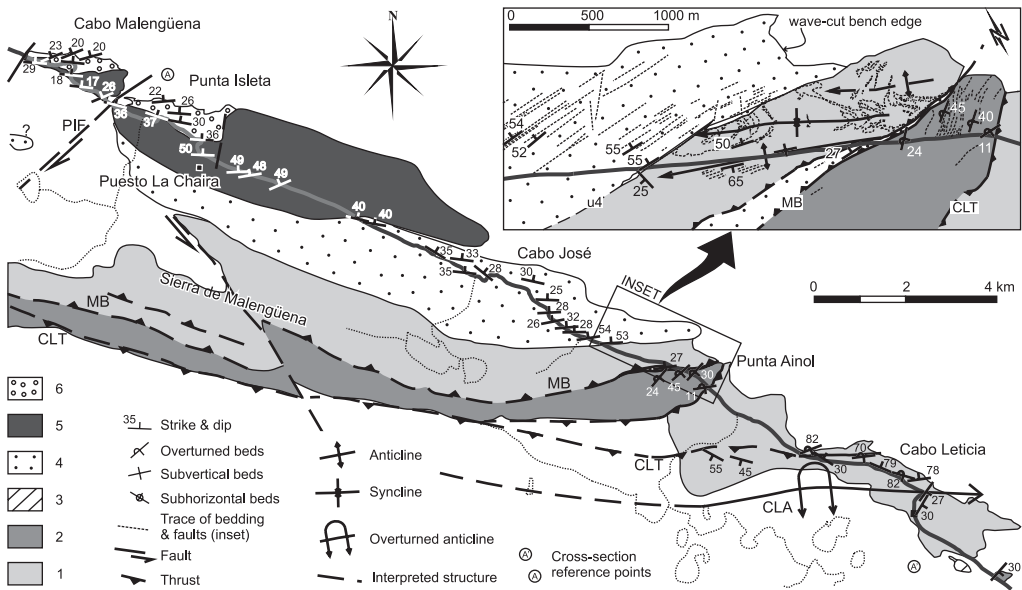
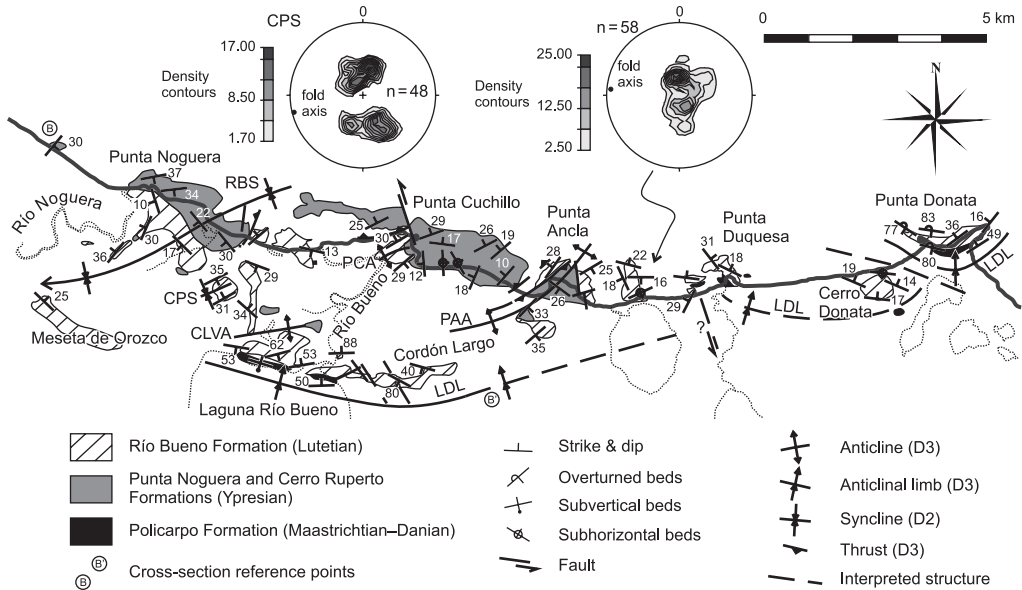


Fig. 3. Main geological features of the studied area. FTS, Fagnano Transform System; MB, Malengüena Backthrust; PIF, Punta Isleta Fault; CLT, Cabo Leticia Thrust; CLA, Cabo Leticia Anticline; RBS, Río Bueno Syncline; PAT, Punta Ancla Thrust; LDL, Cordón Largo–Punta Donata Anticlinal Limb. The area is accessed through a track along the coast. The segments of cross-sections in Figures 6 and 7 are indicated. Enlarged maps of the eastern and western portions of the area are shown in Figures 4 and 5, respectively.



the Cerro Ruperto Formation is not exposed, but on the basis of facies differences with the older Punta Noguera Formation (Olivero *et al.* 2002), a minor unconformity is inferred between both successions. The top of the Cerro Ruperto Formation is an angular unconformity with the Río Bueno Formation, well exposed at Punta Cuchillo (Fig. 4).

Río Bueno Formation (Lutetian)

The Río Bueno Formation (Furque & Camacho 1949) consists of more than 80 m of shelfal grainstone, calcareous sandstone, marl and micrite (Fig. 2) (Olivero *et al.* 2002; Olivero & Malumíán 2008). Its Lutetian age is constrained by microfossils and, according to recent estimations, could be extended to the latest Ypresian (N. Malumíán, pers. comm.).

The Formation crops out discontinuously from Punta Donata to the south of Cabo Leticia, and is also exposed along Cordon Largo, at Cerro Las Vacas and at Meseta de Orozco (Figs 3–5). The Río Bueno Formation unconformably covers the Policarpo, La Barca, Punta Noguera and Cerro Ruperto Formations with varying angular relationships at the different outcrops. This feature was interpreted as the evidence of significant contractional deformation prior to the deposition of the Río Bueno Formation (Olivero *et al.* 2002). The top of the unit is not exposed.

Leticia and Cerro Colorado Formations (Upper Lutetian–Priabonian)

The Leticia and Cerro Colorado Formations consist of a coarsening-upwards succession of more than 950 m of sandstone and minor mudstone, with Late Lutetian–Priabonian foraminifers. Both formations form part of the La Despedida Group (Fig. 2) (Olivero & Malumíán 1999; Torres Carbonell *et al.* 2009a). This succession, as well as the younger units to be described below, were all previously assigned to the Cerro Colorado Formation (Olivero *et al.* 2002), but recent fieldwork and micropaleontological analysis led to a reorganization of the original stratigraphic framework (Torres Carbonell *et al.* 2009a).

The Leticia and Cerro Colorado Formations crop out from Punta Ainol to Cabo José. Poor sandstone exposures on a hill a few kilometres SSW of Cabo Malengüena are preliminarily assigned to this package (Fig. 5). The base of the Leticia Formation is an angular unconformity with the La Barca Formation at Punta Ainol, while its contact with the Cerro Colorado Formation is a parallel transgressive unconformity (Torres Carbonell *et al.* 2009a). The top of this last formation is an unconformity with the Oligocene Puesto José Formation.

Puesto José Formation (Oligocene)

The Puesto José Formation is composed of a minimum thickness of 1600 m of mudstone at the base and mudstone with turbidite sandstone intercalations at the middle and upper sections (Torres Carbonell *et al.* 2009a) (Fig. 2). It bears Oligocene foraminifers that correlate it with the lower Cabo Domingo Group (Malumíán & Olivero 2006; Torres Carbonell *et al.* 2009a). The Puesto José Formation crops out along the coast between Cabo José and Cabo Malengüena (Fig. 5). Its base is a parallel unconformity with the Cerro Colorado Formation and the top is an erosive unconformity with the Malengüena Formation (Miocene?).

Malengüena Formation (Miocene?)

The Malengüena Formation consists of a minimum of 216 m of marine conglomerate and sandstone with abundant lithic fragments of sedimentary rocks, amongst other lithologies (Torres Carbonell *et al.* 2009a) (Fig. 2). Its age resolution is poor, but estimated as Miocene on the basis of the preserved microfossils (Torres Carbonell *et al.* 2009a). The Formation crops out at Cabo Malengüena and Punta Isleta, sites where its unconformable basal contact with the Puesto José Formation is exposed. The top of the Malengüena Formation does not crop out.

Structure at Península Mitre

Unconformities and contractional stages

The age constraints for the structures exposed at the study area are determined by syntectonic unconformities calibrated with microfossils (mainly foraminiferal assemblages). Otherwise, a relative age (oldest) for the structures is determined by the age of the affected sedimentary packages. The unconformities and related contractional stages recognized are summarized as follows:

Maastrichtian/Danian–Paleocene unconformity (u1). An unconformity (u1) between the Policarpo Formation and Paleocene rocks not exposed at the study area has been recognized widely in Tierra del Fuego (Martinioni *et al.* 1999; Olivero *et al.* 2003; Torres Carbonell *et al.* 2008b). The u1 unconformity was recognized in eastern Península Mitre, at least 20 km from the study area (Olivero *et al.* 2003), with an apparently angular character (Ghiglione & Ramos 2005).

The development of a pencil structure and incipient foliation in the Policarpo Formation (Torres Carbonell *et al.* 2008b, 2009b), not recognized in the Paleocene rocks above the u1, reveals more intense strains in the older unit leading to interpret

that the unconformity is related to contractional tectonics. Therefore, a contractional period older than the Middle–Late Paleocene (D1) is inferred (Ghiglione & Ramos 2005), although not discussed in this work since it is prior to the development of the structures here described. In the study area, the u1 is inferred to be present in subsurface, at the contact between the Policarpo Formation and the Cabo Leticia and La Barca Formations.

Base of the Ypresian unconformity (u2). The contact between the La Barca Formation and the Punta Noguera Formation is not exposed, but an unconformity (u2) is inferred on the basis of significant facies and microfaunal differences between both formations (Malumíán & Caramés 2002; Torres Carbonell *et al.* 2009a).

A minor unconformity is also inferred within the Ypresian package between the Punta Noguera and the Cerro Ruperto Formations (u2b), whose contact is also not exposed. In this case there is a facies change from gravity-flow deposits to suspensive fall-out deposits and a different palynological content inferred as a shift to shallower, or more restricted depositional environments (Olivero *et al.* 2002).

Both u2 and the minor u2b unconformities are here related to a contractional stage that started at the Paleocene–Eocene boundary and acted in the Ypresian (D2). The early pulses of deformation of the D2 stage are recorded by thrust imbrications in more internal parts of the orogenic belt (Martinioni *et al.* 1999; Torres Carbonell *et al.* 2008b). The u2 and u2b may be the expression in the basin of tectonic-related erosion and syntectonic deposition during the formation of those structures. Further deformation during the D2 generated structures that affected both unconformities (Río Bueno Syncline and Cabo Leticia Anticline) described later in this paper. The u2 unconformity is tentatively correlated with the unconformity at the top of the P1 sequence of the western Malvinas Basin (Galeazzi 1998).

Another possible evidence of contractional tectonics during the end of the Paleocene near the study area are clastic dykes exposed at Río Malenguena. These affect the La Barca Formation at the frontal limb of the Cabo Leticia Anticline, and are oriented approximately east–west, parallel to the fold axis, with dips around 65°N (Ghiglione & Ramos 2005). Ghiglione & Ramos (2005) considered the intrusions as seismically induced, relating them to the proximity of the thrust front to this area at the Late Paleocene, although the criteria used to determine the seismic character of the dykes is not discussed in detail in their article.

Base of the Lutetian unconformity (u3). The Río Bueno Formation unconformably overlies the

older packages (Maastrichtian–Danian to Ypresian) with an angular relationship that varies between 20° with the Policarpo Formation and 5–20° with the Punta Noguera Formation (u3). While the rest of the unconformities described here, except the u4, separate parallel sedimentary packages and are indicated by micropaleontological and sedimentological features, the u3 is an angular unconformity that involves significant hiatuses. This feature is considered the evidence of significant contractional deformation before the deposition of the Río Bueno Formation (Olivero *et al.* 2002). According to our interpretation, this also indicates that while most of the rest of the unconformities recognized were developed synchronously with the contractional stages, the u3 formed by sedimentation after a deformation episode, in this case the D2 stage. The u3, therefore, constrains the earliest age of that stage. The recent estimations of a possible Late Ypresian age for the Río Bueno Formation (N. Malumíán pers. comm.), which covers the u3, further constrains the D2 stage to the Ypresian. The u3 is here tentatively correlated with the top of the P2 sequence of the western Malvinas basin (Galeazzi 1998).

Base of the Upper Lutetian unconformity (u4). The base of the Upper Lutetian is an unconformity (u4) widely recognized in the Austral Basin (Malumíán *et al.* 1971; Biddle *et al.* 1986). In the María Luisa area (c. 25 km NW from the study area, Fig. 1) u4 is an angular unconformity at the base of the Leticia Formation (with an age estimated in c. 43.7 Ma, Olivero & Malumíán 1999; Torres Carbonell *et al.* 2009a), which overlies the Ypresian Punta Torcida Formation (Olivero & Malumíán 2008). At the study area, the u4 is recognized at Punta Ainol, defined by the strongly angular contact (up to 85°) between the La Barca and the Leticia Formations (Fig. 5).

The unconformities u2 to u4 are here related to a period of enhanced growth of the Fuegian Andes between the Paleocene and the Lutetian (60–40 Ma, Klepeis 1994a; Kohn *et al.* 1995), associated with the D2 and D3 stages. The u4 is the expression of erosion after the last pulse of contraction (D3) at the end of this orogenic period. As well as the u3 unconformity, the u4 is covered by a succession (Leticia and Cerro Colorado Formations) that does not show evidence of synchronous contractional deformation. The u4 is here correlated with the top of the P3 sequence of Galeazzi (1998).

Uppermost Priabonian–lowermost Oligocene unconformity (u5). The parallel unconformable contact between the Cerro Colorado and the Puesto José Formations is related to a significant facies change from channelized sandstones to

massive mudstones, and is also indicated by a shift in paleoenvironments recorded by the microfossil assemblages (Torres Carbonell *et al.* 2009a). This unconformity (u5) is correlated with the one mentioned by Malumián & Olivero (2006) between the Cerro Colorado Formation and the earliest Oligocene Tchat-chii Conglomerate at central Tierra del Fuego and at the coastal sector in the María Luisa area (Fig. 1).

The u5 unconformity was related to a shift to deep marine settings in the foreland basin due to eustatic and tectonic processes (Malumián & Olivero 2006; Scarpa & Malumián 2008), and was locally associated with the development of the Campo del Medio Anticline, a fault-bend fold formed above a backthrust (Torres Carbonell *et al.* 2008a). Uplift and erosion in the hinterland during development of the u5 is inferred from the provenance analysis of the Tchat-chii Conglomerate (Jurassic, Cretaceous and Palaeogene source rocks; cf. Malumián & Olivero 2006). Therefore, a contractional stage (D4) that occurred at the thrust front near María Luisa and at the inner Fuegian Cordillera, is related to the development of the u5 in the latest Priabonian–earliest Oligocene.

Oligocene syntectonic strata (u6). Several large syndimentary folds are recognized at the upper section of the Puesto José Formation, within a coarsening-upwards succession with turbidites and chaotic sandstones (slumps) in its uppermost part (Torres Carbonell *et al.* 2009a). These features are interpreted as a syntectonic package deposited during a new contractional stage (D5). Although there are no exposures of a discrete unconformity surface, the slumps occur in a stratigraphic interval of at least 500 m, and define the boundary (u6) between massive mudstones at the base of the Puesto José Formation to gravelly and sandy turbidites at the top. The age of the D5 contractional stage is estimated at the ‘mid’ Oligocene on the basis of foraminiferal biostratigraphic markers (Torres Carbonell *et al.* 2009a).

Miocene ? unconformity (u7). The youngest unconformity recognized in the study area (u7) separates the Puesto José and Malengüena Formations, with significant erosion of the top of the former. Although the unconformity is apparently parallel, it laterally involves a hiatus of at least the entire Upper Oligocene succession (Torres Carbonell *et al.* 2009a), and is related to a contractional stage (D6) that uplifted part of the older sedimentary packages. Erosion of these previous successions is indicated by the composition of coarse facies above the unconformity, with abundant clasts and reworked microfossils from the Upper Cretaceous–Palaeogene beds (Torres Carbonell *et al.*

2009a). The age of the D6 is younger than the Late Oligocene, and most probably Miocene.

Geometry and kinematics of the structures

A detailed structural survey allowed the construction of 1:50 000 scale maps, from which a regional-scale north–south balanced cross-section was made, depicting the subsurface geometries of the major structures across northern Península Mitre. The studied part of the thrust–fold belt is separated in five distinctive structural zones (Fig. 3): (1) to the north, a north-dipping backthrust sheet (Malengüena Backthrust) involves Paleocene to ?Miocene strata, and is affected by (2) a strike-slip fault system at its northern termination (Punta Isleta Fault System); (3) in the north-central zone, a north-verging fault-propagation fold (Cabo Leticia Anticline) is formed above a major thrust that affects the Paleocene and Ypresian packages (Cabo Leticia Thrust); (4) in the south-central zone, a syncline at the rear of the Cabo Leticia Anticline is formed in the Ypresian succession and is covered unconformably by the Lutetian package (Río Bueno Syncline); and finally (5) in the southernmost zone, an arcuate roughly east–west, north-dipping structure forms the northern limb of an anticline cored by the Maastrichtian–Danian succession (Cordón Largo–Punta Donata Anticlinal Limb).

The balanced cross sections (Figs 6 & 7) show a décollement for these structures located within the Paleocene. This layer has been identified as a décollement in the Cerro Malvinera sector, less than 50 km WNW from northern Península Mitre (Torres Carbonell *et al.* 2008b), and in previous schematic cross-sections of the study area that show a décollement for the main structures around the same level (Ghiglione & Ramos 2005). In the study area the mudstones of the La Barca Formation act as a décollement for the Malengüena backthrust (Figs 5 & 6), supporting the interpretation of a regional sole fault associated with this suitable level.

Malengüena Backthrust. The Malengüena Backthrust (Figs 3 & 5) is the base of a south-vergent thrust sheet composed of the La Barca, Leticia, Cerro Colorado, Puesto José and Malengüena Formations, and is exposed as a fault that cuts the frontal limb of the Cabo Leticia Anticline. The backthrust was previously interpreted as an out-of-sequence thrust (Ghiglione & Ramos 2005), but it is reinterpreted in this paper on the basis of the improved structural mapping (Fig. 5) and biostratigraphical ages recently obtained for the successions involved in deformation (Torres Carbonell *et al.* 2009a).

At Punta Ainol, the Malengüena Backthrust dips c. 27°N, and is exposed as a couple of splays that

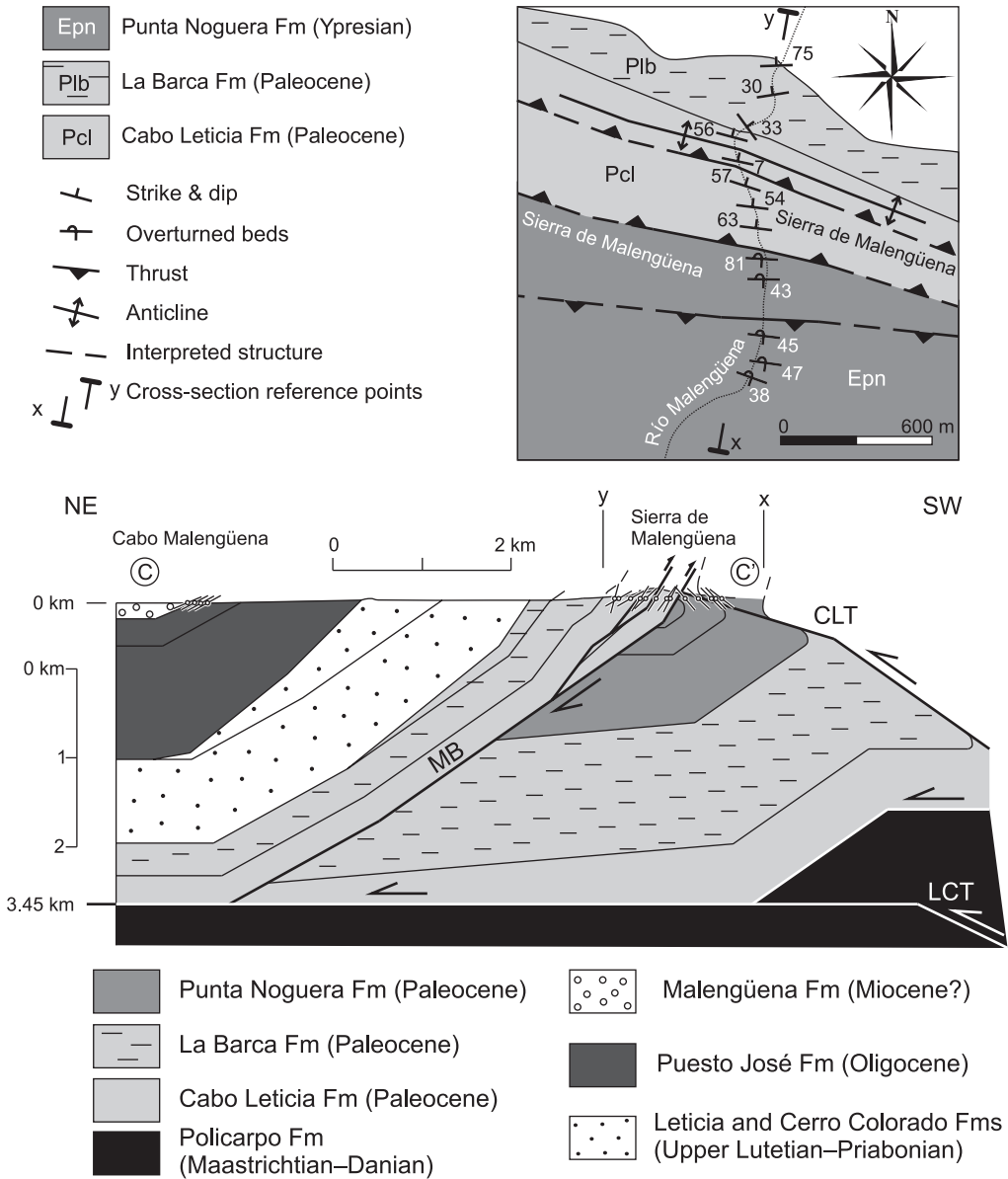


Fig. 6. Geological map and balanced cross-section of the valley of the Río Malengüena. See location of cross section (C–C') in Figure 3. Basemap key as in Figure 3. LCT, La Chaira Thrust; CLT, Cabo Leticia Thrust; MB, Malengüena Backthrust.

locally repeat the La Barca and Leticia Formations (Fig. 5). At this site, the Leticia Formation is thrusts above overturned beds of the Punta Noguera Formation, leading to the problem of explaining younger beds thrusts over older beds. This feature is interpreted assuming significant erosion of the Punta Noguera Formation to the north of the Cabo Leticia Anticline, followed by

deposition of the Leticia Formation directly above the La Barca Formation (covering the u4 unconformity). After its deposition, the Leticia Formation was thrusts over the Punta Noguera Formation due to the Malengüena Backthrust (Figs 7 & 11).

At Río Malengüena, the backthrust is also exposed as a set of fault splays that dip between 60°NE and 30°NE (Fig. 6). There, the Cabo Leticia

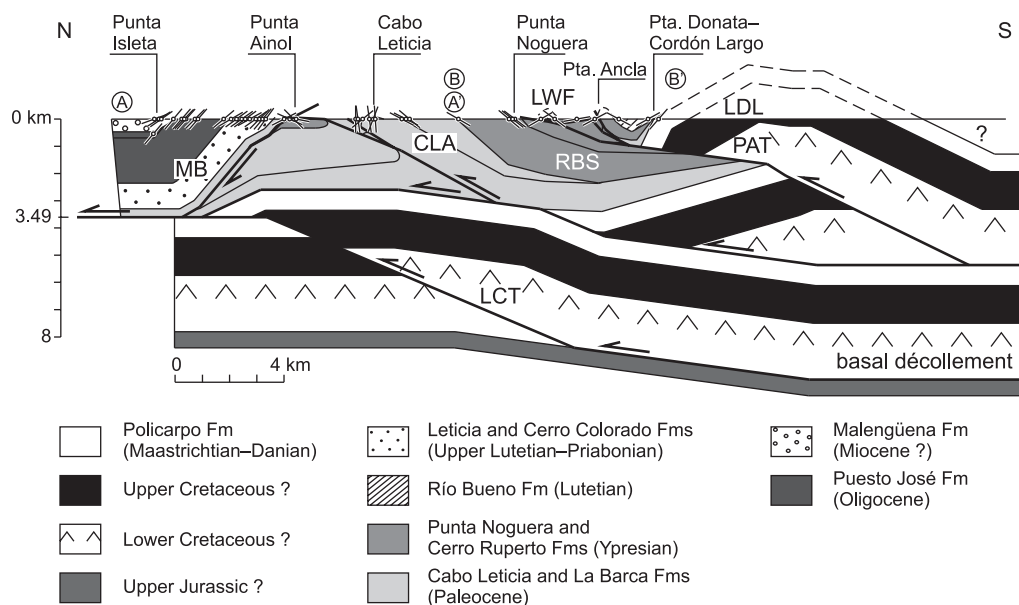


Fig. 7. Balanced cross-section between Punta Isleta and Punta Donata-cordón Largo. See location of reference points (A-A' and B-B') in Figures 3-5. The parts A-A' and B-B' were constructed combining partial segments normal to the main structures, as shown in Figure 3. MB, Malengüena backthrust; CLA, Cabo Leticia Anticline; RBS, Río Bueno Syncline; PAT, Punta Ancla Thrust; LDL, Cordón Largo-Punta Donata Anticlinal Limb; LCT, La Chaira Thrust; LWF, Low-wavelength folds.

and La Barca Formations are thrust over south-dipping overturned beds of the Punta Noguera Formation.

Only the backlimb of the Malengüena Backthrust sheet is exposed, with beds consistently dipping to the north with moderate angles (30-40°N) except in its northernmost part, where the Puesto José Formation dips 50°N just south of Punta Isleta (Fig. 5). These steep dip angles, higher than the moderate dips expected in the backlimbs of simple thrust-sheets (Boyer & Elliott 1982; Suppe 1983; Suppe & Medwedeff 1990), are suggestive of further rotation of the original backthrust sheet. Successive thrust imbrications, frequent in piggyback thrust sequences, normally generate partial rotation of the original moderately dipping thrust sheets. Since no evidence of minor scale (parasitic) folds is seen in the well exposed backlimb of the Malengüena Backthrust sheet between Punta Ainol and Punta Isleta, we consider the interpretation of rotation by multiple thrusting stages as the most effective way to explain the recognized geometry. The structure responsible for partial rotation of the Malengüena Backthrust sheet is further described and discussed later in this article.

The balanced cross-section (Figs 6 & 7) shows a décollement for the Malengüena Backthrust at

c. 3.5 km below sea level, within the Paleocene succession, associated with the La Barca Formation as seen at Punta Ainol.

Punta Isleta Fault System. At Cabo Malengüena and Punta Isleta, a system of subvertical faults (Punta Isleta Fault System) affects the Puesto José and Malengüena Formations, disconnecting the outcrops of both sites (Fig. 8). The fault system is composed of three sets of faults, each with a strike-slip apparent displacement in map view. These sets strike NNE, NE and NNW.

The NNE set, exposed in the cliffs and wave-cut bench of Cabo Malengüena and Punta Isleta, has a dominant right-lateral slip sense with a minor (apparent) normal component, determined by stratigraphic offsets in plan view (tens of metres) and cross-section (metre scale), respectively (Fig. 8). The faults of this set also affect the terrain near Cabo Malengüena, generating a fault scarp of about a kilometre length and one metre height. The scarp affects the post-glacial deposits (Holocene, cf. Heusser 2003), apparently playing an important role on the hydrographic control of the area. A dry circular lake adjacent to the coast (less than 500 m in diameter) was probably drained towards the sea due to activity of the fault system (Fig. 8). This inference is supported by a rectilinear stream that flows

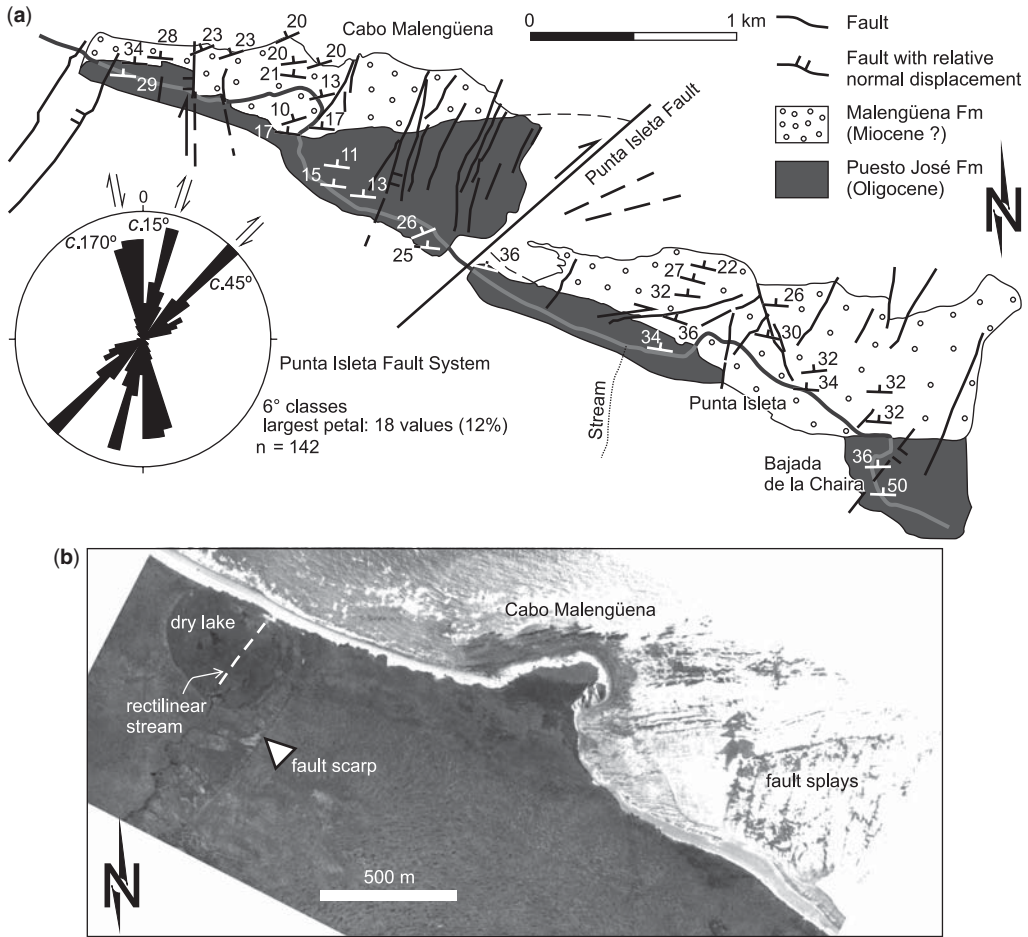


Fig. 8. (a) Geological map of the Cabo Malengüena–Punta Isleta area, basemap key as in previous figures. The rose diagram shows the strikes of the three fault sets that compose the Punta Isleta Fault System, n : number of measurements. (b) Aerial photograph of Cabo Malengüena, showing major morphological features related to the Holocene NNE fault set.

to the sea crossing the dry lake along a fault splay, which is exposed continuously up to the wave-cut platform. The age of the NNE fault set, therefore, is younger than the Malengüena Formation (?Miocene), most probably Holocene, according to the control of the faults on the terrain morphology.

The NE set includes a main fault located at the bay between Punta Isleta and Cabo Malengüena, which combined with the NNE set produces, in map view, a right-lateral offset of at least 600 m, and probably up to 1000 m, to the contact of the Puesto José and Malengüena Formations (Fig. 8).

The NNW faults are also exposed in the cliffs and wave-cut bench at both sites, although they are less frequent. Both the NNW and NNE sets bound blocks formed by the Puesto José and Malengüena Formations, which reveal attitude changes

from block to block interpreted as relative rotations due to the apparent minor oblique-slip observed in the NNE faults.

Following Coulomb fracture criterion (Twiss & Moores 2007), the maximum compressive stress (σ_1) has a different orientation for each of the three fault sets analyzed separately, which in turn may suggest that they formed diachronously. Assuming dominant strike-slip, the σ_1 direction for the NNE faults should be approximately oriented N225°; for the NE faults N255°; and for the NNW faults N200°. These three maximum compression directions are SW–NE oriented, which is consistent with the approximately NW–SE strike of the major contractional tectonic features in the region. On the other hand, if a regional north–south right-lateral shear is assumed, with a σ_1 oriented at N45°, then

only the NNE and NNW sets would show compatible kinematics since they could be interpreted as R and P synthetic shear fractures, respectively.

Furthermore, another interpretation can be proposed for the formation of the NNE faults. The location of segments of the active Fagnano Transform System at the Río Irigoyen valley, about 10 km westwards from the Cabo Malengüena area (Figs 1 & 3; Torres Carbonell *et al.* 2008b), and the estimated young age of the NNE faults, may suggest that these latter and the Fagnano Transform System are genetically related. Since the NNE set is oriented at 75° to the left-lateral east–west Transform System, it can be interpreted as an antithetic Riedel fracture set. Nevertheless, this interpretation is still preliminary since the main synthetic Riedel shear fractures, that should be oriented $N75^\circ$, are apparently lacking.

Cabo Leticia Anticline. The Cabo Leticia and La Barca Formations are involved in an asymmetrical anticline (Cabo Leticia Anticline), with a north–NE vergence, recognized at Cabo Leticia and partly at Río Malengüena (Figs 3 & 5). The structure is inferred to be continuous between both sites, with morphological expression along the southern border of the Sierra de Malengüena.

At Cabo Leticia the exposed core of the anticline is formed by subvertical beds of the Cabo Leticia Formation. Both limbs are formed by the La Barca Formation. The southern limb (backlimb) dips around 30° SE, and the northern limb (frontal limb) is subvertical to overturned, and is cut by many faults oriented east–west (Figs 6 & 7). The anticlinal hinge is recognized at Cabo Leticia, and reveals an axis plunging 20° to the east. In this site the fold has an interlimb angle of 60° (close fold), and exposed width of 3 km.

This anticline is related to the Cabo Leticia Thrust, which dips to the south with a moderate angle and is interpreted to root at the same décollement as the Malengüena Backthrust (within the Paleocene). The Cabo Leticia Thrust has several splays exposed from the northern coast of the eponymous cape up to the south of Punta Ainol, where, although the outcrops are scarce and isolated, a change in the fault attitude to a very gentle dip is revealed. Low dip fault splays are also exposed at Río Malengüena south of the Malengüena Backthrust trace, affecting overturned beds of the Punta Noguera Formation, which comprise the frontal part of the Cabo Leticia Anticline there (Fig. 6). Farther to the south along Río Malengüena, outcrops of the La Barca Formation (Ghiglione 2003; Olivero *et al.* 2007) may form part of the inner frontal limb of the anticline.

A drag fold is recognized in the footwall of the Cabo Leticia Thrust affecting beds of the Punta

Noguera Formation at Punta Ainol and at Río Malengüena as well. In the first site the drag fold is formed by overturned sandstones dipping from 40 – 11° S, revealing a strong rotation (Fig. 5). At Río Malengüena the Punta Noguera beds dip from 45 – 19° S also in overturned position (Fig. 6).

Río Bueno Syncline. The Río Bueno Syncline is a fold recognized between Cerro Ruperto and Punta Noguera. It is formed by the Punta Noguera and Cerro Ruperto Formations (Figs 3, 4 & 7), and is covered with an angular unconformity (u3) by the Río Bueno Formation (Fig. 9a).

The half-wavelength of the syncline is of c. 7 km in the northern limb. That limb comprises the Punta Noguera Formation, and has an average dip of

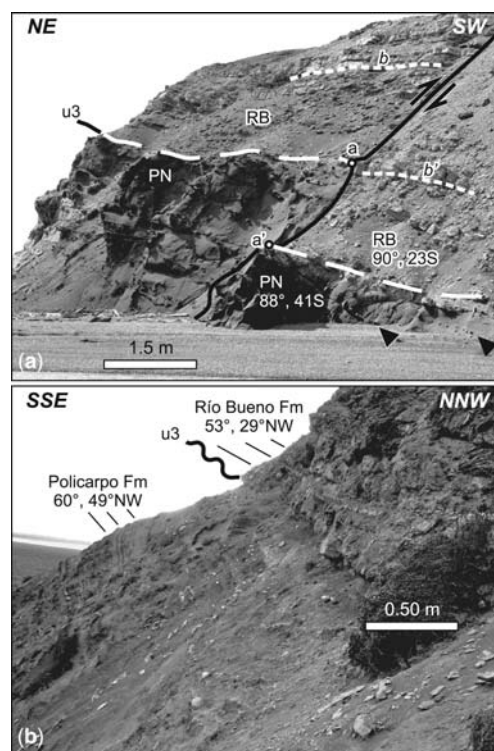


Fig. 9. (a) Angular unconformity (u3) in the northern limb of the Río Bueno Syncline (at Punta Noguera) between the Punta Noguera sandstones (PN) and the Río Bueno basal marls (RB). The dashed line *b* marks a reference horizon within the Río Bueno marls. A fault (subvertical, note that the angle of the photo generates an apparent dip to the left) affects both formations downthrowing the SW block. Note that this geometry could be caused either by a right-lateral or a dip-slip displacement. The black triangles mark horizons in the PN clearly truncated by the u3. (b) Detail of the angular unconformable contact between the Policarpo and Río Bueno Formations at Punta Donata.

37–40°SSE at Punta Noguera. The southern limb, although being obliterated by minor order deformation (see below), could be measured in the wave cut bench near Punta Cuchillo, where it dips *c.* 20°NW, and is formed by the Cerro Ruperto Formation (Fig. 10a). The Punta Noguera Formation comprises

the external part of the southern limb at Punta Ancla (Fig. 4). The interlimb angle is of *c.* 120° (open fold). The Río Bueno Syncline surface trace is located in the southern part of Punta Noguera, where it closes forming a rounded hinge with an axis plunging 27° to the SW.

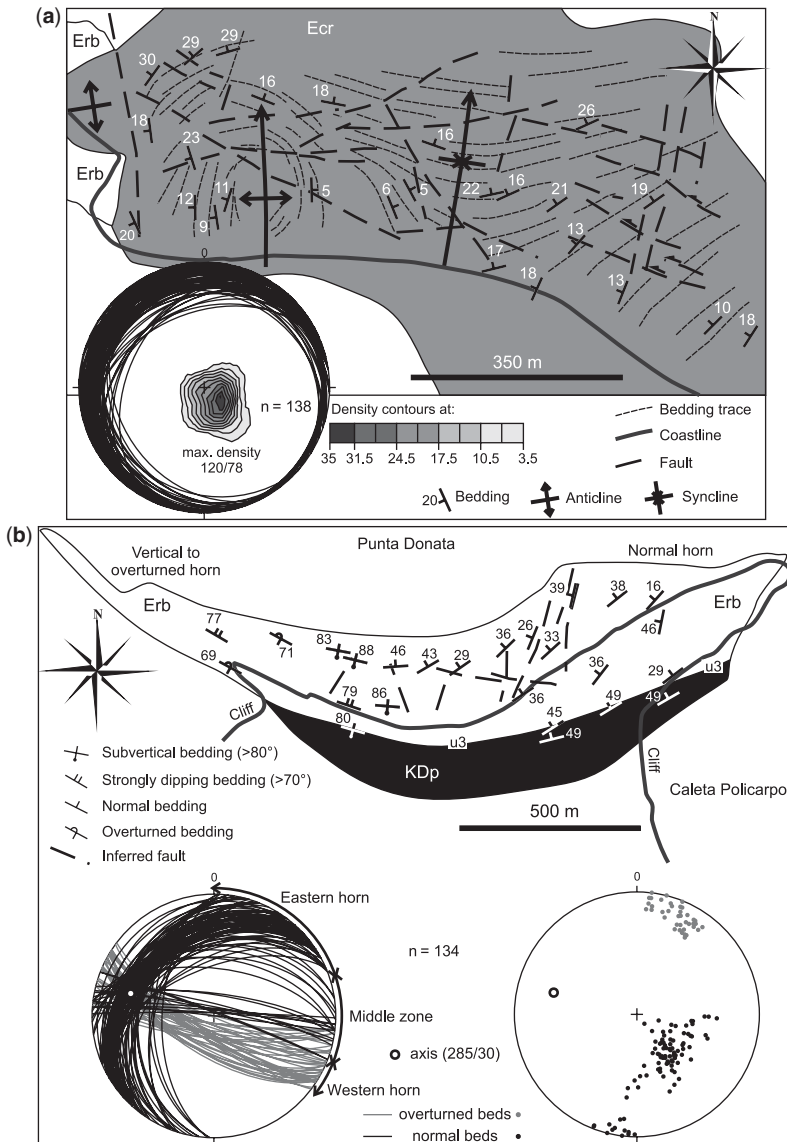


Fig. 10. (a) Geological map of Punta Cuchillo–Cerro Ruperto wave-cut bench, and lower hemisphere, equal area stereographic plot of the Cerro Ruperto Formation bedding (density contours for poles) showing an average moderate dip towards the NW. Erb, Río Bueno Formation; Ecr, Cerro Ruperto Formation. (b) Geological map of Punta Donata. Erb, Río Bueno Formation; KDp, Policarpo Formation. The stereonet are lower hemisphere, equal area projections of bedding planes (left diagram: planes; right diagram: poles) of the Río Bueno Formation at Punta Donata, indicating the polarity (normal, inverted) and location of the measured planes. The estimated axis of rotation of the beds in the western horn is shown.

The southern limb of the Río Bueno Syncline is affected by a gently dipping thrust, called Punta Ancla Thrust, related to low wavelength folds and minor fault splays that accommodate deformation above it. The Punta Ancla Thrust and its related minor structures partly obliterate the original geometry of the Río Bueno Syncline (Fig. 7), and although these structures are associated with a younger deformation stage (see below), they are described here since they form part of the southern limb of the Río Bueno Syncline.

The low wavelength folds related to the Punta Ancla Thrust (LWF in Fig. 7) affect the Punta Noguera, Cerro Ruperto and Río Bueno Formations. The most significant structures related to the Punta Ancla Thrust are the Punta Cuchillo Anticline and the Punta Ancla Anticline (Fig. 4). The first one is formed on beds of the Río Bueno Formation and cored by the Cerro Ruperto Formation; it is symmetrical with both limbs dipping 32° – 35° and a sub-horizontal axis trending $N243^{\circ}$, with a rounded hinge, a wavelength of about 500 m and an interlimb angle of 118° (open fold). The Punta Ancla Anticline is cored by the Punta Noguera Formation and flanked by the Río Bueno Formation; it is also nearly symmetrical, with limbs dipping 30° – 34° and an axis plunging 5° towards $N221^{\circ}$, a wavelength of about 850 m and an interlimb angle also of 118° . The limbs of the Punta Ancla Anticline are cut by several high-angle minor faults with probable normal dip–slip displacements. The south limb (back limb) of the Punta Ancla Anticline is also recognized in the hills located to the SW of Punta Ancla (Fig. 4). The north limb (frontal limb) of this anticline is cut by a splay of the Punta Ancla Thrust, which dips 60° SE and has striae plunging towards $N140^{\circ}$ – $N160^{\circ}$. The reverse displacement along this fault is indicated by drag folds in its footwall.

The inland area between Río Noguera and Río Bueno is characterized by low hills frequently topped by exposures of the Río Bueno Formation (Fig. 4). These exposures show low wavelength folding, equivalent to that recognized in the coast formed above the Punta Ancla Thrust. The most notable inland folds are the Cerro Las Vacas Anticline and the Cerro Piedra Syncline (Fig. 4). The first one is cored by siltstones here assigned to the Cerro Ruperto Formation, its south limb dips nearly 57° S, but its frontal limb is badly exposed, and its wavelength is in the order of 1000 m. The Cerro Piedra Syncline is formed by the Río Bueno Formation, with limbs dipping 30° SSE and 42° NNW, a subhorizontal axis gently plunging towards $N256^{\circ}$, an interlimb angle of 113° (open fold) and a wavelength of almost 300 m.

A recent different structural analysis of this region of Tierra del Fuego proposes reactivation of high-angle normal faults to explain this evidence

of contractional deformation, mainly based on the interpretation of the Punta Noguera Formation as a synrift succession. This interpretation is principally supported by apparent thickness variations of that formation at Punta Noguera (Ghiglione *et al.* 2008). These authors propose that the normal faults associated with the rifting stage were later inverted as reverse faults uplifting the Río Bueno Formation.

Nevertheless, the detailed stratigraphy (Furque & Camacho 1949; Olivero *et al.* 2002) and structural analysis at the Punta Noguera area reveal that: (a) the interpreted thickness variations in the Punta Noguera Formation are a consequence of an incorrect definition of the basal unconformity of the Río Bueno Formation (u3), since Ghiglione *et al.* (2008) wrongly assigned the basal marls of this later unit to the top of the Punta Noguera Formation, therefore incorrectly placing the u3 within the Río Bueno Formation; and (b) the normal faults, which are subvertical and strike north–NNE (data omitted by Ghiglione and collaborators), affect both the Punta Noguera and Río Bueno Formations with no evidence of inversion. They generate a neat apparent downdip displacement of c. 2–3 m to both formations (Fig. 9a). A more feasible interpretation, therefore, is that these faults postdate the Río Bueno Formation, instead of being synchronous with the Punta Noguera sandstones. Moreover, since no directional data (e.g. slickenline orientations) were presented by Ghiglione *et al.* (2008), a strike-slip component of displacement is also possible (Fig. 9a).

The interpretation of Ghiglione *et al.* (2008) also proposes a pop-up anticline in the Punta Noguera Formation with a trace located in the exact position where we place the axial trace of the Río Bueno Syncline. That interpretation is not even consistent with the data shown on their maps, which reveal the synclinal open hinge at Punta Noguera like our map does (Fig. 4). The clear evidence of contractional tectonics in northern Península Mitre during the Early Eocene (Ghiglione & Ramos, 2005; this work), for example, the Cabo Leticia Anticline that formed during or after deposition of the Punta Noguera Formation and before the development of the u3 unconformity, also argues against the interpretation of an extensional setting during these times.

Cordón Largo–Punta Donata Anticlinal Limb. Between the northern shore of Laguna Río Bueno, along Cordón Largo and towards the east up to Punta Donata, the Río Bueno Formation beds keep a dip of 50° – 35° N, NNE and NW (Fig. 4). These beds unconformably cover the Policarpo Formation (u3) with an angle of 20° at Punta Donata (Fig. 9b) and almost zero at Laguna Río Bueno. This long structure, with a general east–west orientation that varies from WNW to ENE, is interpreted as the

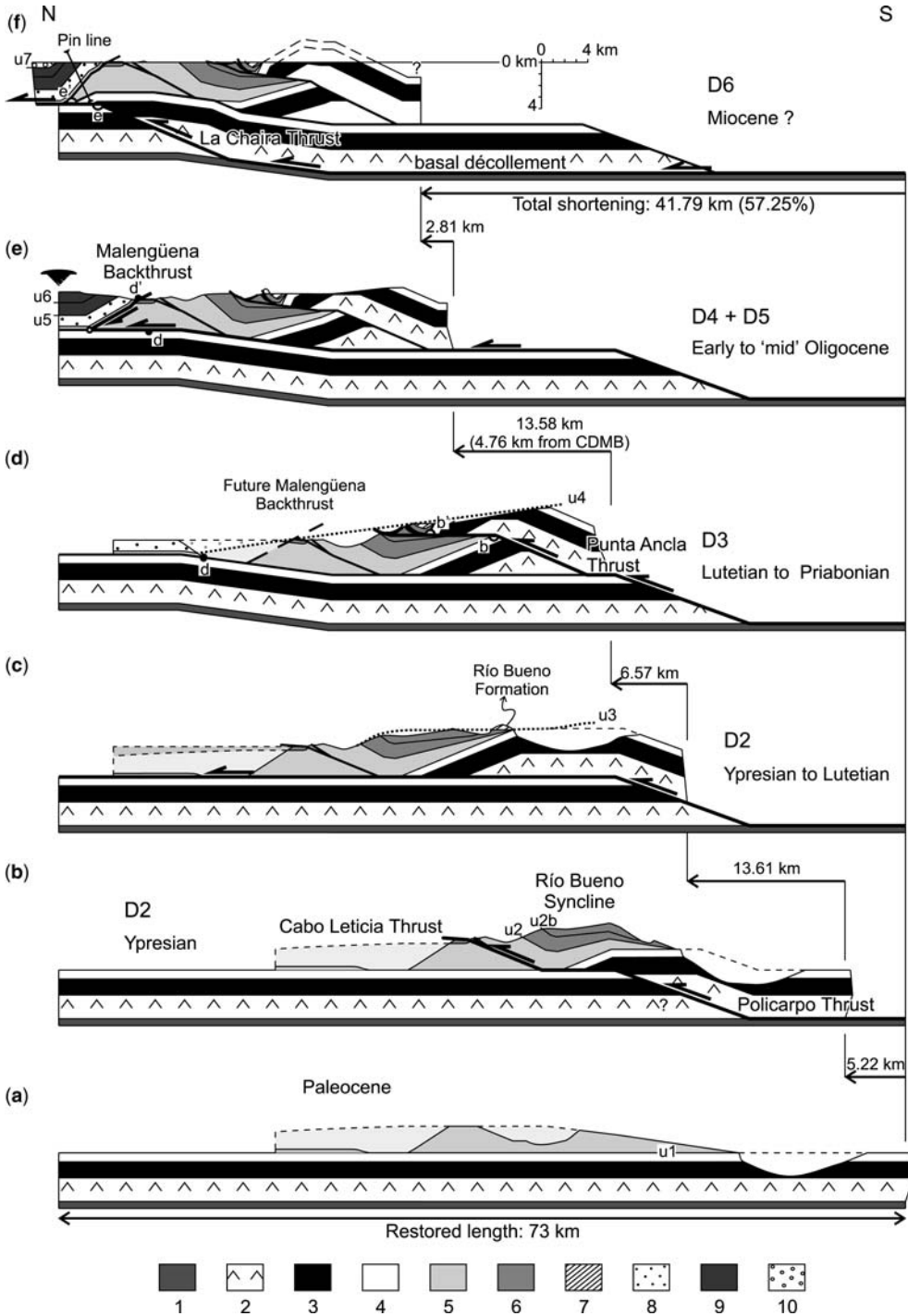


Fig. 11. Kinematic evolution of the balanced cross-section of Figure 7. CDMB, Campo del Medio Backthrust. Stratigraphic key: 1, ?Upper Jurassic; 2, ?Lower Cretaceous; 3, ?Upper Cretaceous; 4, Policarpo Formation; 5, Cabo Leticia and La Barca Formations; 6, Punta Noguera and Cerro Ruperto Formations; 7, Río Bueno Formation; 8, Leticia

frontal limb of an anticline. The core of this anticline is not exposed at the study area. The northern limit of the Cordón Largo–Punta Donata Anticlinal Limb is preserved at Cerro Donata, where an open syncline is recognized (Fig. 4). Part of this syncline is laterally represented by subhorizontal to gently dipping beds east of Punta Ancla, and towards Laguna Río Bueno, where the northern limb of the syncline steepens to form the backlimb of the Cerro Las Vacas Anticline.

The Cordón Largo–Punta Donata Anticlinal Limb reveals several changes in orientation along its strike. At Punta Donata, where this is more pronounced, this structure is arcuate and the bedding changes its strike from NE at the eastern salient to NW at the western salient, forming a map-view curve with its concave side facing north. The convex side of the curve is formed by the Policarpo Formation, whereas the concave part and both salients or horns are formed by the Río Bueno Formation (Figs 4 & 10b). The beds in the eastern horn dip moderately to the NW (30–40°), the middle zone varies from north-dipping to subvertical, and the beds in the western horn are slightly overturned, steeply dipping to the SW (Fig. 10b). This complex structure was previously interpreted as a syncline with a north–south oriented axis (Olivero *et al.* 2002; Ghiglione 2003), but it is here reinterpreted as part of an originally NW dipping succession (with its original attitude preserved only at the eastern horn) that has been bent by clockwise rotation of the beds in the western horn on a plunging axis. The possible axis of rotation, with 30° of plunge towards N285°, is obtained from the bedding stereogram (Fig. 10b).

Between Punta Ancla and Punta Duquesa, the Río Bueno Formation reveals flat lying beds affected by several faults and gentle parasitic folds, which define a folding axis plunging 6° towards N275° (Fig. 4). These gently folded beds are inferred to form part of the northern (frontal) syncline of the Cordón Largo–Punta Donata Anticlinal Limb.

It is here interpreted that the Cordón Largo–Punta Donata Anticlinal Limb constitutes the northern flank of an anticline formed in the Policarpo and Río Bueno Formations. This anticline is not exposed at the study area, but is recognized to the east at Caleta Falsa (Ghiglione & Ramos 2005), where its core crops out and has a SW trend. This anticline is interpreted in this paper as related to the Punta Ancla Thrust, which forms the upper segment of a fault-ramp that cuts the backlimb of the Río Bueno Syncline. The anticline was transported above that

thrust, and shortening in the hanging wall in front of the Cordón Largo–Punta Donata Anticlinal Limb generated the low wavelength folds and minor thrusts previously described in the backlimb of the Río Bueno Syncline. The Cordón Largo–Punta Donata Anticlinal Limb is connected to these low wavelength folds by means of its frontal syncline in the Río Bueno Formation, as observed between Punta Ancla and Punta Duquesa, and at Laguna Río Bueno where that syncline is tighter.

According to this interpretation, the time of formation of the Cordón Largo–Punta Donata Anticlinal Limb is the same as the Punta Ancla Thrust and its genetically related low wavelength folds, which postdate the u3 unconformity and the deposition of the Río Bueno Formation (D3). The deformation that obliterates the anticlinal limb and produces its rotation at Punta Donata, on the other hand, is considered to be produced by a later deformation stage. Due to the lack of exposures, the kinematics and structures related to this younger stage cannot be evaluated with certainty, so the geometry was simplified in the balanced cross-section (Fig. 7).

Balanced cross-section restoration and kinematics.

On the basis of the structural data, a balanced cross-section of northern Península Mitre was constructed (Fig. 7). It depicts an interpretation of the complex structures recognized in this part of the Fuegian Thrust–Fold Belt, constrained by the geometries already described. There is no local subsurface information (well-logs or seismic data) available in order to better constrain the geometries, but reasonable results were achieved with the data obtained by intensive mapping. In addition to these abundant structural data, the cross-section kinematics were time-calibrated with the biostratigraphic ages published elsewhere (Olivero & Malumián 2008; Torres Carbonell *et al.* 2009a).

For the construction of the cross-section and subsequent restoration, several geological assumptions concerning the mechanisms of deformation were made. Folding by flexural slip was assumed for the Paleocene–?Miocene beds, according to models by Suppe (1983) and Suppe & Medwedeff (1990). Restoration of these structures was made, therefore, assuming conservation of bed lengths. In the Cretaceous–Danian package, on the other hand, unknown amounts of internal strain are likely in highly deformed areas affected by more than one contractional stage. To restore these parts of the section, therefore, a combined bed length and area balancing technique was used (Fig. 11).

Fig. 11. (*Continued*) and Cerro Colorado Formations; 9, Puesto José Formation; 10, Malengüena Formation. Light shaded areas indicate eroded parts. Thicker lines indicate active faults and solid lines mark previous faults. Unconformities 1–7 (u1–u7) are indicated, as well as contractional stages D2–D6. See text for explanation.

Two main décollement levels are present in the cross-section. The shallower one has been already described, and is located within the Paleocene. A deeper décollement is placed at the base of the Cretaceous package. This layer does not crop out in nearby regions, but it was proposed as a detachment level in other parts of Tierra del Fuego (Klepeis 1994a). This inference is also necessary in order to be consistent with the approximate thickness of Cretaceous rocks in the Fuegian Andes (Klepeis 1994a; Olivero & Martinioni 2001).

The evolution of the structures shown in the cross-section starts in the Ypresian (late D2) with the propagation of the basal décollement of the thrust–fold belt from the deeper level to the Paleocene succession (Fig. 11a, b). The connection of both décollements implies the formation of a thrust-ramp called the Policarpo Thrust (Fig. 11b). The importance of the Policarpo Thrust in the evolution of the thrust–fold belt is here highlighted, since it ultimately connects the sole fault to the base of the post-Danian sedimentary fill of the foreland basin, leading to further accommodation of the tectonic shortening above the shallower décollement. Displacement over the Policarpo Thrust results in the formation of an anticline cored by the Policarpo Formation and older rocks (Fig. 11b). The emplacement of the Policarpo Thrust occurs after the initial phases of the D2 stage, which had already given birth to the u2 unconformity, and is probably synchronous with the deposition of the Punta Noguera and Cerro Ruperto Formations.

Part of the shortening transferred to the foreland by the emplacement of the Policarpo Thrust sheet (5.22 km) is accommodated above the shallower décollement by a fault-propagation fold (Cabo Leticia Anticline) that affects the Cabo Leticia, La Barca and Punta Noguera Formations (Fig. 11b). The Río Bueno Syncline is formed between the frontal limb of the Policarpo fault-bend fold and the Cabo Leticia Anticline, affecting also the Cerro Ruperto Formation. The Cabo Leticia Anticline evolves initially as a fault-propagation fold with a backlimb dip of *c.* 30°, and is later transported above a further thrust with a dip of 22° and a gently dipping upper flat. Beneath this thrust, a drag structure with overturned beds is formed in the footwall, as observed in the Punta Noguera Formation at Punta Ainol and at Río Malengüena. The two-stage evolution of the Cabo Leticia Anticline (first fault-propagation and then fault-bend folding) is consistent with models of deformation in heterolithic turbidite successions (Butler & McCaffrey 2004). The age of the Policarpo Thrust sheet and the Cabo Leticia Anticline during the D2 is constrained by the Early Ypresian age estimated for the Punta Noguera Formation. The D2 stage continues by the ongoing displacement above the Policarpo

Thrust, which accommodates a shortening of 13.6 km after the formation of the Cabo Leticia Anticline, transferring deformation to the foreland (Fig. 11c). Partial erosion of the D2 structures produces the unconformity observed at the base of the Río Bueno Formation (u3, Fig. 11c), which also constrains the earliest age of the D2 structures to the Late Ypresian, and defines a short period of erosion and sedimentation after D2.

Continued contraction after deposition of the Río Bueno Formation leads to renewed thrusting in an out-of-sequence scheme (D3), forming the Punta Ancla Thrust. This thrust is also rooted at the décollement in the Paleocene succession, and offsets the core of the earliest Policarpo Thrust sheet (Fig. 11d), accommodating almost 6.6 km. The stage D3, constrained in age between the Early Lutetian and 43.7 Ma (u4), is responsible for the uplift of the Policarpo Formation to a higher structural level, for the low wavelength folding of the Punta Noguera, Cerro Ruperto and Río Bueno Formations in the backlimb of the Río Bueno Syncline, and for favored erosion of the uplifted thrust–fold belt.

The enhanced erosion after D3 gives rise to the major unconformity u4, while the increase in tectonic load by the repetition of a thick Cretaceous–Danian package at the southern part of the section (imbrication of the Policarpo and Punta Ancla thrust sheets) enhances flexural subsidence (Fig. 11d). Since the amount of subsidence is unknown, and also difficult to estimate with the available data, we constrained it using the maximum reasonable slope for the u4 unconformity. This slope was calculated from the thickness of the sedimentary succession deposited above u4, taking into account the original position of that succession and its estimated pinch-out before the inferred kinematics of the Malengüena Backthrust, which later affects these rocks. The slope is consistent with the angle of truncation of the equivalent unconformity below the Middle Eocene in the foreland, offshore Tierra del Fuego (unconformity P3 of Galeazzi 1998). Although this constraint on the magnitude of subsidence may be somewhat inaccurate, the approximation is plausible, and allows good geometrical results that can be improved if coupled with geophysical information. Furthermore, a significant aeromagnetic and gravimetric low is observed to the north of the Cordón Largo–Punta Donata Anticlinal Limb (Lodolo *et al.* 2007; Ghiglione *et al.* 2008), supporting the inference of a flexural deflection in the sector.

The development of the u4 unconformity involves significant erosion of the previous succession, generating a chronostratigraphic hiatus that can reach up to 12 Ma (cf. chronostratigraphic chart by Gradstein *et al.* 2004). This is manifest

at Punta Ainol where the Leticia Formation covers the La Barca Formation. Following the development of the u4, a thick sedimentary succession is deposited during the Late Lutetian–Priabonian (Fig. 11d). After the deposition of the Leticia and Cerro Colorado Formations (*c.* 950 m) an unconformity (u5) is formed above the latter, caused by the contractional stage D4 that is characterized by backthrusting in the foreland (to the north of the area involved in Fig. 11) in the earliest Oligocene (Campo del Medio Backthrust, Torres Carbonell *et al.* 2008a). The deformation caused by the D4 is recognized by unconformities through the outer orogenic belt, with their best expression at the base of the earliest Oligocene Tchat-chii Conglomerate, which consists of up to 70 m of conglomerate and coarse sandstone with abundant clasts derived from Jurassic, Cretaceous and Palaeogene rocks of the Andean Cordillera (Malumián & Olivero 2006). The D4 is interpreted to be intimately related to the next contractional stage that affects the studied area (D5).

The stage D5 acts in the ‘mid’ Oligocene leading to the formation of a second backthrust (Malengüena Backthrust) generated in response to the delamination of the sequence above the décollement in the Paleocene rocks (Fig. 11e). The stage D5 is coincident with the development of u6 and the progradational deposition of the syntectonic upper part of the Puesto José Formation (Fig. 11e).

The Malengüena Backthrust evolves by displacement of the footwall towards the foreland, resembling the work of a chisel against the passive hanging wall. The backthrust’s branch line and the syncline above it are displaced towards the north (Fig. 11d, e). Such a backthrust sheet could not evolve without a basal décollement in continuous propagation in order to accommodate the tectonic push from the hinterland (Butler 1987). In this case, the necessary basal décollement formed during the late D2 by the continued emplacement of the Policarpo Thrust Sheet, after formation of the Cabo Leticia Anticline (Fig. 11c). Therefore, the backthrust is able to evolve by continuous delamination as long as other mechanical instabilities restrain further deformation.

The Campo del Medio and Malengüena Backthrusts accommodate *c.* 13.6 km of shortening, uplifting and exposing to erosion a thick succession of sedimentary rocks from the foreland basin fill. The shortening involved in the Campo del Medio Backthrust (*c.* 4.8 km) (Torres Carbonell *et al.* 2008a) is accounted for in Figure 11 by displacing the hanging wall of the décollement towards the north (cf. reference point ‘d’ in Fig. 11d, e), previous to the development of the Malengüena Backthrust (offset of reference point ‘d’ in Fig. 11e), which in turn accommodates *c.* 8.8 km. The estimated

shortening transferred to the foreland during D4, however, is poorly constrained since the structural disconnection between the northern and southern structures produced in the Neogene by the Fagnano Transform System (Torres Carbonell *et al.* 2008b) hinders the estimations. For this reason, the relative proportions of shortening of the Campo del Medio and Malengüena Backthrusts should be considered a rough approximation, while the total shortening produced by the combined result of both structures (13.6 km) is better constrained and more accurate.

Renewed deformation generates thrusting in the footwall of the basal décollement, within the Cretaceous–Danian sequence (D6; Fig. 11f). The new thrust branches from the lower flat of the Policarpo Thrust (deeper décollement) and rejoins the upper décollement forming a horse in the Cretaceous–Danian rocks (Figs 7 & 11f). This splay is called the La Chaira Thrust, and its lower flat forms the new sole for this portion of the thrust–fold belt. Displacement along the La Chaira Thrust produces further deformation of the already folded Paleocene–Oligocene successions. The stage D6 is responsible for the steepening of the Malengüena Backthrust sheet (see description), which is incorporated to the frontal limb of the La Chaira fault–bend anticline. The La Chaira Thrust sheet is emplaced after or during the formation of the u7 unconformity, covered by the ?Miocene Malengüena Formation, and it accommodates a shortening of less than 3 km, being probably the last stage of the contractional tectonic regime (Fig. 11f). Unfortunately, there is no accurate geochronological data to constrain the timing of this stage in relation to deformation in the foreland at the Early Miocene (Ghiglione 2002; Ponce *et al.* 2008). Additionally, the different amounts of shortening estimated for the La Chaira Thrust and the Late Oligocene–Early Miocene thrusting in the foreland (Torres Carbonell *et al.* 2008a), may suggest along-strike variations in the forward transference of shortening in the thrust–fold belt.

The structural geometry of the final cross-section can be depicted as a large duplex horse within the Cretaceous–Danian strata bounded by the La Chaira and Policarpo Thrusts and by a roof thrust within the Paleocene, above which there is a set of thrusts of opposite vergence. The total shortening estimated is of 41.8 km, which represents 57% of the initial section’s length. Analysing the kinematic history of this section, it is important to recall the out-of-sequence style of the propagated thrusts above the shallower décollement between D3 and D5, since it indicates a long-lived stage of internal deformation and thickening of the thrust wedge, explained below using the Coulomb wedge theory.

Kinematics of the eastern Fuegian Thrust–Fold Belt: progressive growth of a Coulomb thrust wedge

The structures of northern Península Mitre are here linked with previous work that depicts the geometry and kinematics of the eastern Fuegian Thrust–Fold Belt deformation front (Torres Carbonell *et al.* 2008a), which is located c. 50 km northwards (Fig. 1). This permits the description of the thrust–fold belt's complete structural history and to propose a model for the evolution of the thrust wedge in terms of the Coulomb wedge theory (Davis *et al.* 1983). The thrust sequence recorded at the thrust–fold belt leading edge, outside the study area (cf. Torres Carbonell *et al.* 2008a), can be summarized as follows: (a) folding of the Punta Torcida Formation (Ypresian) before the Late Lutetian, most probably during the Ypresian coinciding with the D2 stage; (b) backthrusting of the Punta Torcida, Leticia and Cerro Colorado Formations in the earliest Oligocene by development of the Campo del Medio Backthrust (D4), which branches from the basal décollement and evolves by delamination analogous to the Malengüena Backthrust; and finally (c) foreland and upward propagation of the sole fault and frontal thrusting between the latest Oligocene and the Early Miocene (D6?), forming an imbricate thrust system that is now exposed at the Punta Gruesa area in the Atlantic coast (Punta Gruesa Imbricates).

The thrust sequence observed reveals stages of forward propagation of the thrust front (D2 and D6?), separated by stages of out-of-sequence thrusting and backthrusting within the wedge (D3–D5, Fig. 12). This history of progressive deformation can be understood in terms of the Coulomb wedge theory, as a general approximation to the incremental buildup of the outer Fuegian orogenic belt. According to that theory, thrust–fold belts are considered analogous to a homogeneous wedge with a taper angle that is the sum of the topographic slope (α) and the basal décollement dip (β) (Davis *et al.* 1983). The taper angle is referred to a critical value, dependant on the coefficient of friction at the base of the wedge and the strength of the rocks that compose it. When the taper angle is below that value, the wedge is subcritical and deforms internally to increase taper, until the critical geometry is reached. If the critical wedge is forced to accrete new material (e.g. by syntectonic sedimentation) it will continuously deform to maintain its critical taper (Davis *et al.* 1983; Dahlen & Suppe 1988). Also, variations of the composition and basal friction of the wedge produce different critical taper angles, thus controlling its internal dynamics (Dahlen 1984). Physical factors such as erosion and sedimentation play an important role in changing

the taper angle, therefore affecting the state (critical or subcritical) of the wedge (Dahlen & Suppe 1988).

The model to be introduced here describes the Ypresian–Miocene history of the eastern Fuegian Thrust–Fold Belt. Before this period, the orogenic wedge had grown since the 'mid' Cretaceous, after the closure of the Late Jurassic–Early Cretaceous marginal basin (Dalziel & Palmer 1979; Nelson *et al.* 1980; Dalziel & Brown 1989; Kohn *et al.* 1995), and its thrust front was located southwards from the studied area (Ghiglione & Ramos 2005). This thrust front involved Upper Cretaceous to Paleocene sedimentary units deformed during the early stages of the D2 episode.

During the Ypresian, the incremental growth of the outer orogenic wedge begins with the foreland propagation of the sole décollement, which ramps from a previous deeper level at the base of the Cretaceous up to the Paleocene succession, forming the Policarpo Thrust (stage D2). The shortening becomes then accommodated above this shallower décollement by the development of thrust-related structures within the wedge (Cabo Leticia Thrust, Fig. 13a). The folding of the Punta Torcida Formation (Torres Carbonell *et al.* 2008a), here considered Ypresian, is assumed to accommodate the last pulse of emplacement of the Policarpo Thrust Sheet (Fig. 11c) during the end of the D2 stage (Fig. 13b). The D2 stage is the result of a critical wedge that grows towards the foreland by forward thrusting, accreting material (foreland sedimentary deposits) at its toe. The forward expansion of the wedge tends to decrease the angle β , while active sedimentation at its toe and erosion at the hinterland impede the proportional α increase to maintain the critical taper. This forms a very thin frontal orogenic wedge, with a low taper angle that causes it to become subcritical, restraining continued forward thrusting (Fig. 13a, b).

As no further horizontal growth is possible, the following thrusting stage (D3) tends to increase the taper angle in the Lutetian, deforming the clastic infill of the foreland basin in an out-of-sequence fashion (Punta Ancla Thrust, Fig. 13c). The D2 and D3 stages are coincident with a regional period of tectonic contraction, orogenesis and sedimentation in the Fuegian Andes (Klepeis 1994a; Kohn *et al.* 1995; Olivero & Martinioni 2001; Olivero & Malumíán 2008; Barbeau *et al.* 2009).

The emplacement of thrust sheets at the hinterland of the thrust wedge enhances tectonic load, which in turn leads to flexural subsidence increasing the décollement slope β . The flexural subsidence also favors the deposition of a thick clastic succession above the u4 unconformity during the Late Lutetian to Priabonian, adding fresh material at the front of the wedge which in turn flattens its upper slope (Fig. 13d).

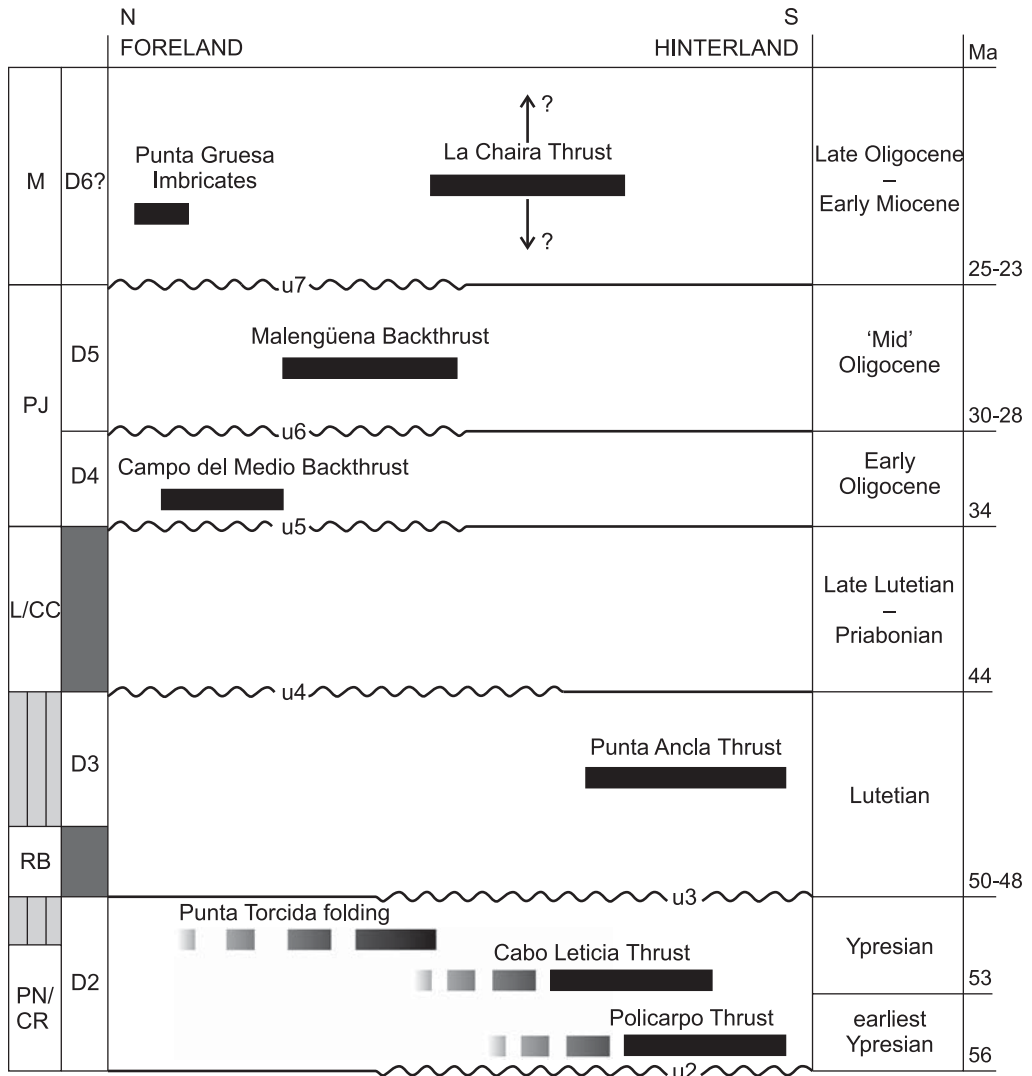


Fig. 12. Chronological evolution of the structures recognized in the eastern Fuegian Thrust–Fold Belt, constrained by the ages of the syntectonic successions and their bounding unconformities (u2–u7), and related to successive contractional stages (D2–D6?). Stratigraphic key: PN/CR, Punta Noguera and Cerro Ruperto Formations; RB, Río Bueno Formation; L/CC, Leticia and Cerro Colorado Formations; PJ, Puesto José Formation; M, Malengüena Formation. Vertical lined shading indicates hiatuses, dark shading indicates pauses between contractional stages. Note the cyclicity concerning the location of deformation within the thrust wedge.

Since the wedge continues to be subcritical, further contraction is accommodated above the sole décollement by backthrusting (D4 and D5), coincidentally with the deposition of the Oligocene package. Backthrusting evolves due to delamination in a piggyback fashion, forming a hinterlandward leading imbricate system (Fig. 13e). The first structure formed is the Campo del Medio Backthrust (D4), starting with a branch line several kilometres

south from the tip line of the décollement (previously formed during the D2 stage). The backthrust's branch line migrates northwards, folding the hanging wall succession until it reaches the décollement's termination, causing the backthrust to stick. Further deformation is then accommodated by the development of the Malengüena Backthrust (D5) towards the hinterland, which evolves in a similar way. The backthrusting stage in the

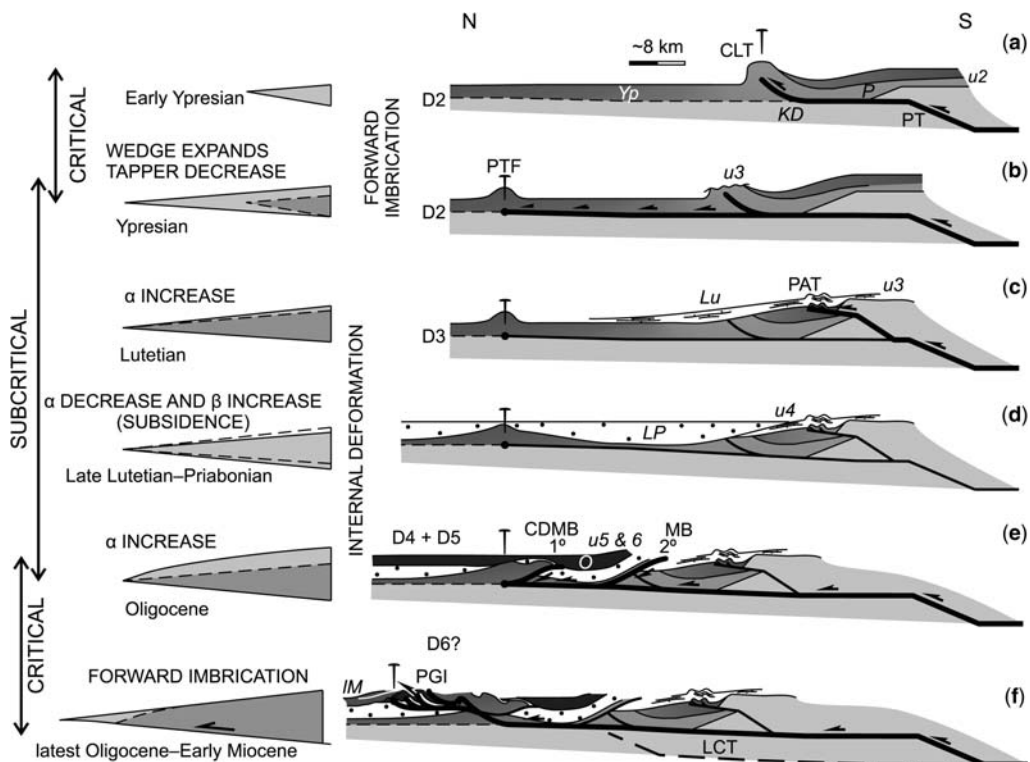


Fig. 13. Schematic evolution of the eastern Fuegian Thrust–Fold Belt through contractional stages D2–D6?, according to the Coulomb wedge theory. This cartoon shows the thrust wedge configuration before the emplacement of the Fagnano Transform System (cf. Torres Carbonell *et al.* 2008b). KD, Cretaceous–Danian; P, Paleocene; Yp, Ypresian; Lu, Lutetian; LP, Upper Lutetian–Priabonian; O, Oligocene; IM, Lower Miocene; PT, Policarpo Thrust; CLT, Cabo Leticia Thrust; PTF, folding of the Punta Torcida Formation; PAT, Punta Ancla Thrust; CDMB, Campo del Medio Backthrust; MB, Malengüena Backthrust; PGI, Punta Gruesa Imbricates; LCT, La Chaira Thrust. Thick lines indicate the active faults at each stage.

Oligocene accommodates a minimum shortening of *c.* 15% within the thrust–fold belt, significantly building up the surface slope of the orogenic wedge.

After the taper increase produced between D3 and D5, the wedge attains its critical geometry permitting foreland sliding over the sole décollement with deformation localized at the leading edge. The décollement termination propagates to a higher structural level, causing the development of the Punta Gruesa imbricate fan between the latest Oligocene and the Early Miocene (Fig. 13f), as recorded by syntectonic strata (Ghiglione 2002; Ponce *et al.* 2008). There is a possible correlation between the stage D6 that acts during the emplacement of the La Chaira Thrust in the ?Miocene and the development of the Punta Gruesa Imbricates. In that sense, the latest contractional pulses in the thrust front in the Early Miocene could be related to growth of the wedge with accretion below the sole by emplacement of the La Chaira Thrust, as a

way to maintain the taper. Nevertheless, the precise age of u7, which constrains the age of the La Chaira Thrust, has not been estimated yet, and its relative age in relation to the syntectonic Lower Miocene beds in the thrust front is therefore not known.

Conclusions

A detailed study of the structures at the eastern Fuegian Thrust–Fold Belt has led to an improved kinematic model that reveals a complex and distinct thrust-sequence for this portion of the Andes. The analysis of this model in terms of the Coulomb wedge theory reasonably explains the progressive deformation of the thrust wedge, linking it to sedimentation in the Austral foreland basin.

The eastern Fuegian Thrust–Fold Belt at northern Península Mitre reveals complex pro- and

retro-vergent structures rooted at the base of the Cretaceous and within the Paleocene, which affect the unconformity-bounded syntectonic sequences of the Austral foreland basin system. These structures accommodate a minimum shortening of c. 41.8 km, assuming fault-related folding mainly by flexural slip, restored by the combination of bed-length and area conservation techniques.

The kinematic evolution of the eastern Fuegian Thrust–Fold Belt unveils a progressive behaviour with several contractional stages: (a) during the Ypresian the décollement propagates into the foreland (Policarpo Thrust), ultimately connecting the sole fault to the base of the post-Danian sedimentary fill of the Austral Basin; (b) continuing in the Ypresian, thrusting occurs in a forward-directed fashion, expanding the wedge towards the foreland (Cabo Leticia Anticline and folding of the Punta Torcida Formation); (c) during the Lutetian, out-of-sequence thrusting acts hinterlandwards from the deformation front (Punta Ancla Thrust); (d) significant subsidence and sedimentation take place from the Late Lutetian–Oligocene; (e) backthrusting occurs in the Oligocene (Campo del Medio and Malengüena Backthrusts); (f) from the latest Oligocene to the Early Miocene, foreland-verging thrusting acts at the leading edge (Punta Gruesa Imbricates), probably related to renewed thrusting on Cretaceous–Danian rocks below the sole fault in the hinterland (La Chaira Thrust).

This progressive thrust sequence indicates critical Coulomb wedge behaviour during the Ypresian, with horizontal growth of the wedge by forward directed thrusting into the foreland syntectonic successions, which accretes new material. The increased length causes a diminished taper angle, and the subsequent subcritical wedge progressively grows by internal deformation from the Lutetian–Oligocene. Backthrusting in particular proves to be an important mechanism to accommodate significant shortening (c. 15%) during the subcritical stage. After the internal deformation and creation of the topographic slope, the thrust wedge again reaches a critical geometry in the Late Oligocene. The second critical stage causes renewed foreland propagation of the thrust front between the latest Oligocene and the Miocene. This last stage is short lived in comparison to the previous subcritical stage, and ends apparently during the Early Miocene.

The authors acknowledge A. Sobral (CADIC–CONICET) for help in the field and construction of petrographic sections; and N. Malumíán (SEGEMAR, CONICET) for providing unpublished biostratigraphic data. We are grateful to the owners and personnel of the Estancia Policarpo, specially N. Oyarzún and N. Ainol (†), who granted access and aid in the field. Kind collaboration and transport were provided by D. Muriel and A. Imbert.

We thank K. Klepeis (University of Vermont), V. Ramos (University of Buenos Aires) and J. Poblet (University of Oviedo) for their constructive comments, which substantially improved this article. Financed by CONICET PIP 5100 and 5506, ANPCYT–FONCYT PICTO 36315 and 841.

References

- ÁLVAREZ-MARRÓN, J., MCCLAY, K. R., HARAMBOUR, S., ROJAS, L. & SKARMETA, J. 1993. Geometry and evolution of the frontal part of the Magallanes foreland thrust belt (Vicuña area), Tierra del Fuego, Southern Chile. *American Association of Petroleum Geologists Bulletin*, **77**, 1904–1921.
- BARBEAU, D. L. JR, OLIVERO, E. B., SWANSON-HYSELL, N. L., ZAHID, K. M., MURRAY, K. E. & GEHRELS, G. E. 2009. Detrital-zircon geochronology of the eastern Magallanes foreland basin: implications for Eocene kinematics of the northern Scotia Arc and Drake Passage. *Earth and Planetary Science Letters*, **284**, 489–503.
- BIDDLE, K. T., ULIANA, M. A., MITCHUM, R. M. JR, FITZGERALD, M. G. & WRIGHT, R. C. 1986. The stratigraphy and structural evolution of the central and eastern Magallanes Basin, southern South America. In: ALLEN, P. A. & HOMEWOOD, P. (eds) *Foreland Basins*. International Association of Sedimentologists Special Publications, **8**, 41–66.
- BOYER, S. E. & ELLIOTT, D. 1982. Thrust systems. *American Association of Petroleum Geologists Bulletin*, **66**, 1196–1230.
- BRUHN, R. L. 1979. Rock structures formed during back-arc basin deformation in the Andes of Tierra del Fuego. *Bulletin of the Geological Society of America*, **90**, 998–1012.
- BUTLER, R. W. H. 1987. Thrust sequences. *Journal of the Geological Society, London*, **144**, 619–634.
- BUTLER, R. W. H. & MCCAFFREY, W. D. 2004. Nature of thrust zones in deep water sand-shale sequences: outcrop examples from the Champsaur sandstones of SE France. *Marine and Petroleum Geology*, **21**, 911–921.
- CAMINOS, R. 1980. Cordillera Fueguina. In: TURNER, J. C. (ed.) *Geología Regional Argentina 2. II Simposio de Geología Regional Argentina*. Academia Nacional de Ciencias, Córdoba, 1463–1501.
- DAHLEN, F. A. 1984. Noncohesive critical Coulomb wedges: an exact solution. *Journal of Geophysical Research*, **89**, B12, 10 125–10 133.
- DAHLEN, F. A. & SUPPE, J. 1988. Mechanics, growth, and erosion of mountain belts. In: CLARK, S. P. (ed.) *Processes in Continental Lithospheric Deformation*. Geological Society of America Special Paper, **218**, 161–178.
- DALZIEL, I. W. D. 1986. Collision and Cordilleran orogenesis: an Andean perspective. In: COWARD, M. P. & RIES, A. C. (eds) *Collision Tectonics*. Geological Society, London, Special Publications, **19**, 389–404.
- DALZIEL, I. W. D. & BROWN, R. L. 1989. Tectonic denudation of the Darwin metamorphic core complex in the Andes of Tierra del Fuego, southernmost Chile. Implications for Cordilleran orogenesis. *Geology*, **17**, 699–703.

- DALZIEL, I. W. D. & PALMER, K. F. 1979. Progressive deformation and orogenic uplift at the southern extremity of the Andes. *Bulletin of the Geological Society of America*, **90**, 259–280.
- DALZIEL, I. W. D., DE WIT, M. J. & PALMER, K. F. 1974. Fossil marginal basin in the southern Andes. *Nature*, **250**, 291–294.
- DALZIEL, I. W. D., DOTT, R. H., WINN, R. D. & BRUHN, R. L. 1975. Tectonic relations of South Georgia Island to the Southernmost Andes. *Geological Society of America Bulletin*, **86**, 1034–1040.
- DALZIEL, I. W. D., STOREY, B. C., GARRETT, S. W., GRUNOW, A. M., HERROD, L. D. B. & PANKHURST, R. J. 1987. Extensional tectonics and the fragmentation of Gondwanaland. In: COWARD, M. P., DEWEY, J. F. & HANCOCK, P. L. (eds) *Continental Extensional Tectonics*. Geological Society, London, Special Publications, **28**, 433–441.
- DAVIS, D., SUPPE, J. & DAHLEN, F. A. 1983. Mechanics of fold-and-thrust belts and accretionary wedges. *Journal of Geophysical Research*, **88**, B2, 1153–1172.
- EAGLES, G., LIVERMORE, R. A., FAIRHEAD, J. D. & MORRIS, P. 2005. Tectonic evolution of the west Scotia Sea. *Journal of Geophysical Research*, **110**, B2401, 1153–1172, doi: 10.1029/2004JB003154.
- FURQUE, G. & CAMACHO, H. H. 1949. El Cretácico Superior de la costa Atlántica de Tierra del Fuego. *Revista de la Asociación Geológica Argentina*, **4**, 263–297.
- GALEAZZI, J. S. 1998. Structural and stratigraphic evolution of the western Malvinas basin, Argentina. *American Association of Petroleum Geologists, Bulletin*, **82**, 596–636.
- GHIGLIONE, M. C. 2002. Diques clásticos asociados a deformación transcurrente en depósitos sinorogénicos del Mioceno inferior de la cuenca Austral. *Revista de la Asociación Geológica Argentina*, **57**, 103–118.
- GHIGLIONE, M. C. 2003. *Estructura y evolución tectónica del Cretácico-Terciario de la costa atlántica de Tierra del Fuego*. PhD thesis, Universidad de Buenos Aires.
- GHIGLIONE, M. C. & RAMOS, V. A. 2005. Progression of deformation and sedimentation in the southernmost Andes. *Tectonophysics*, **405**, 25–46.
- GHIGLIONE, M. C., RAMOS, V. A. & CRISTALLINI, E. O. 2002. Estructura y estratos de crecimiento en la faja plegada y corrida de los Andes Fueguinos. *Revista Geológica de Chile*, **29**, 17–41.
- GHIGLIONE, M. C., YAGUPSKY, D., GHIDELLA, M. & RAMOS, V. A. 2008. Continental stretching preceding the opening of the Drake Passage: evidence from Tierra del Fuego. *Geology*, **36**, 643–646.
- GRADSTEIN, F. M., OGG, J. G. & SMITH, A. G. 2004. *A Geologic Time Scale*. Cambridge University Press, Cambridge.
- HEUSSER, C. J. 2003. Ice age southern andes. A chronicle of paleoecological events. *Developments in Quaternary Science Series*, **3**, 1–240.
- KLEPEIS, K. A. 1994a. Relationship between uplift of the metamorphic core of the southernmost Andes and shortening in the Magallanes foreland fold and thrust belt, Tierra del Fuego, Chile. *Tectonics*, **13**, 882–904.
- KLEPEIS, K. A. 1994b. The Magallanes and Deseado fault zones: major segments of the South American-Scotia transform plate boundary in southernmost South America, Tierra del Fuego. *Journal of Geophysical Research*, **99**, 22 001–22 014.
- KLEPEIS, K. A. & AUSTIN, J. A. JR. 1997. Contrasting styles of superposed deformation in the southernmost Andes. *Tectonics*, **16**, 755–776.
- KOHN, M. J., SPEAR, F. S., HARRISON, T. M. & DALZIEL, I. W. D. 1995. Ar⁴⁰/Ar³⁹ geochronology and P-T-t paths from the Cordillera Darwin metamorphic complex, Tierra del Fuego, Chile. *Journal of Metamorphic Geology*, **13**, 251–270.
- KRAEMER, P. E. 2003. Orogenic shortening and the origin of the Patagonian orocline (56°S lat.). *Journal of South American Earth Sciences*, **15**, 731–748.
- LODOLO, E., LIPPAI, H., TASSONE, A., ZANOLLA, C., MENICCHETTI, M. & HORMAECHEA, J. L. 2007. Gravity map of the Isla Grande de Tierra del Fuego, and morphology of Lago Fagnano. *Geologica Acta*, **5**, 307–314.
- MALUMIÁN, N. & CARAMÉS, C. 2002. Foraminíferos de sedimentitas ricas en carbono orgánico: formación La Barca, Paleoceno superior, Tierra del Fuego, República Argentina. *Revista de la Asociación Geológica Argentina*, **57**, 219–231.
- MALUMIÁN, N. & OLIVERO, E. B. 2006. El Grupo Cabo Domingo, Tierra del Fuego, Argentina: bioestratigrafía, paleoambientes y acontecimientos del Eoceno-Mioceno marino. *Revista de la Asociación Geológica Argentina*, **61**, 139–160.
- MALUMIÁN, N., MASIUK, V. & RIGGI, J. C. 1971. Micro-paleontología y sedimentología de la perforación SC-1, Provincia de Santa Cruz, República Argentina. Su importancia y correlaciones. *Revista de la Asociación Geológica Argentina*, **26**, 175–208.
- MALUMIÁN, N., JANNOU, G. & NÁÑEZ, C. 2009. Serial planktonic foraminifera from the Paleogene of the Tierra del Fuego Island, South America. *Journal of Foraminiferal Research*, **39**, 316–321.
- MARTINIONI, D. R., OLIVERO, E. B. & PALAMARCZUK, S. 1999. Estratigrafía y discordancias del Cretácico Superior-Paleoceno en la región central de Tierra del Fuego. *Anales del Servicio Geológico Minero Argentino*, **33**, 7–16.
- NELSON, E. P., DALZIEL, I. W. D. & MILNES, A. G. 1980. Structural geology of the Cordillera Darwin. Collisional-style orogenesis in the southernmost Chilean Andes. *Eclogae Geologicae Helveticae*, **73**, 727–751.
- OLIVERO, E. B. & MALUMIÁN, N. 1999. Eocene stratigraphy of southeastern Tierra del Fuego island, Argentina. *American Association of Petroleum Geologists, Bulletin*, **83**, 295–313.
- OLIVERO, E. B. & MALUMIÁN, N. 2008. Mesozoic–Cenozoic stratigraphy of the Fuegian Andes, Argentina. *Geologica Acta*, **6**, 5–18.
- OLIVERO, E. B. & MARTINIONI, D. R. 2001. A review of the geology of the Argentinian Fuegian Andes. *Journal of South American Earth Sciences*, **14**, 175–188.
- OLIVERO, E. B., MALUMIÁN, N., PALAMARCZUK, S. & SCASSO, R. A. 2002. El Cretácico superior-Paleógeno del área del Río Bueno, costa atlántica de la Isla Grande de Tierra del Fuego. *Revista de la Asociación Geológica Argentina*, **57**, 199–218.
- OLIVERO, E. B., MALUMIÁN, N. & PALAMARCZUK, S. 2003. Estratigrafía del Cretácico superior-Paleoceno

- del área de bahía Thetis, Andes Fueguinos, Argentina: acontecimientos tectónicos y paleobiológicos. *Revista Geológica de Chile*, **30**, 245–263.
- OLIVERO, E. B., MALUMIÁN, N. & MARTINIONI, D. R. 2007. Mapa geológico de la Isla Grande de Tierra del Fuego e Islas de Los Estados, escala 1:500 000. Servicio Geológico Minero Argentino.
- PONCE, J. J., OLIVERO, E. B. & MARTINIONI, D. R. 2008. Upper Oligocene–Miocene clinoforms of the foreland Austral Basin of Tierra del Fuego, Argentina: stratigraphy, depositional sequences and architecture of the foredeep deposits. *Journal of South American Earth Sciences*, **26**, 36–54.
- ROSELLO, E. A., HARING, C. E., CARDINALI, G., SUÁREZ, F., LAFFITTE, G. A. & NEVISTIC, A. V. 2008. Hydrocarbons and petroleum geology of Tierra del Fuego, Argentina. *Geologica Acta*, **6**, 69–83.
- SCARPA, R. & MALUMIÁN, N. 2008. Foraminíferos del Oligoceno inferior de los Andes Fueguinos, Argentina: su significado tectónico-ambiental. *Ameghiniana*, **45**, 361–376.
- SUPPE, J. 1983. Geometry and kinematics of fault-bend folding. *American Journal of Science*, **283**, 684–721.
- SUPPE, J. & MEDWEDEFF, D. A. 1990. Geometry and kinematics of fault propagation folding. *Eclogae Geologicae Helveticae*, **83**, 409–454.
- TORRES CARBONELL, P. J., OLIVERO, E. B. & DIMIERI, L. V. 2008a. Structure and evolution of the Fuegian Andes foreland thrust–fold belt, Tierra del Fuego, Argentina: paleogeographic implications. *Journal of South American Earth Sciences*, **25**, 417–439.
- TORRES CARBONELL, P. J., OLIVERO, E. B. & DIMIERI, L. V. 2008b. Control en la magnitud de desplazamiento de rumbo del Sistema Transformante Fagnano, Tierra del Fuego, Argentina. *Revista Geológica de Chile*, **35**, 63–77.
- TORRES CARBONELL, P. J., MALUMIÁN, N. & OLIVERO, E. B. 2009a. El Paleoceno-Mioceno de Península Mitre: antifosa y depocentro de techo de cuña de la cuenca Austral, Tierra del Fuego, Argentina. *Andean Geology*, **36**, 197–235.
- TORRES CARBONELL, P. J., DIMIERI, L. V. & OLIVERO, E. B. 2009b. *Estructura de la faja del Cretácico Superior-Paleoceno de los Andes Fueguinos*. XIV Reunión de Tectónica, Libro de Resúmenes, **46**.
- TWISS, R. J. & MOORES, E. M. 2007. *Structural Geology*. Freeman and Co., New York.
- WILSON, T. J. 1991. Transition from back-arc to foreland basin development in the southernmost Andes: stratigraphic record from the Última Esperanza District, Chile. *Geological Society of America Bulletin*, **103**, 98–111.

Comparison of tectonic styles in the Mexican and Canadian Rocky Mountain Fold–Thrust Belt

ELISA FITZ-DIAZ¹*, PETER HUDLESTON¹ & GUSTAVO TOLSON²

¹*Department of Geology and Geophysics, University of Minnesota, 310 Pillsbury Drive SE, Minneapolis, MN, 55454, USA*

²*Depto. de Geología Regional, Instituto de Geología, Universidad Nacional Autónoma de México, Av. Universidad 3000, C. U., Coyoacán, México*

**Corresponding author (e-mail: fitzd008@umn.edu)*

Abstract: Despite the fact that most fold–thrust belts around the world share many features, successfully explained by the critical wedge model, the details of their geometric evolution and tectonic style development are poorly understood. In the classic section of the southern Canadian Rocky Mountains the dominant tectonic style consists of imbricate thrust sheets with relatively little internal deformation of the individual slices. In the Mexican fold–thrust Belt (Central Mexico), the age of deformation, the overall structural pattern and the total amount of shortening are similar, but the individual thrust sheets exhibit much more internal deformation as manifest by metre-scale buckle folds. One of the differences between these localities is the lateral variation of facies resulting in massive platform limestone separated by thinly-bedded basinal limestone in the Central Mexico section. Strain is concentrated toward the margins between platforms and basins. In Canada, thick platform carbonates form continuous resistant units across the Front Range. Possible reasons for the differences in tectonic style between the two sections include the dominant lithology, distribution of lithologies, taper angle of the tectonic wedges, amount of friction along the basal detachment and the degree of anisotropy of the basin facies rocks.

Fold–thrust belts are common features that developed on the edges of orogenic belts worldwide. Many have been well studied and their characteristic features established (Dahlstrom 1970; Chapple 1978; Boyer & Elliott 1982; Price & Fermor 1985; McClay 1992). These features include the classic notions of forward propagation of thrusts, piggy-back style, a basal *décollement*, and decreasing intensity of deformation towards the foreland. Most fold–thrust belts are wedge-shaped, and since the mid 1980s, the critical taper model of their development (Davis *et al.* 1983; Dahlen *et al.* 1984; Dahlen 1990) has become generally accepted. Analogue and numerical models have been developed that are able to capture many of the basic features of fold–thrust belts and that are broadly consistent with the critical taper theory (e.g. Huiqi *et al.* 1992; Stockmal *et al.* 2007). From early studies it has been clear that most of the large folds in fold–thrust belts are intimately related genetically to the thrusts, and extensive studies of thrust-related folds, in the field and in analogue and numerical models, have established the nature of this relationship (e.g. Dahlstrom 1969, 1970; Elliott 1976; Suppe 1983; McClay 1992; Wilkerson *et al.* 2002; Spratt *et al.* 2004).

Despite the many similarities among fold–thrust belts in general, there are significant differences

among belts and along strike within individual belts. These reflect, among other things, differences in the strength of the basal detachment and the composition and distribution of the rocks in the fold–thrust wedge. In this contribution we compare basic elements of the structures developed roughly synchronously in two widely separated parts of a single orogenic belt: the North American Cordillera. The sections we compare are a well-known section across the southern Canadian Rocky Mountains and a new section across the Sierra Madre Oriental in central Mexico. The dimensions of the fold–thrust belts in these two locations are similar, and both sections are dominated by carbonates. The structural style, however, is quite different. We compare structures in the two locations and speculate on what may be responsible for the differences.

Tectonic setting

The Rocky Mountain Fold–Thrust Belt (RMFTB) is located along the eastern edge of the North American Cordillera. Although it has a physiographic expression that is continuous from Alaska to southern Mexico (Fig. 1), it presents changes in width, structural style and age along strike. In southern Canada, the belt has a width between

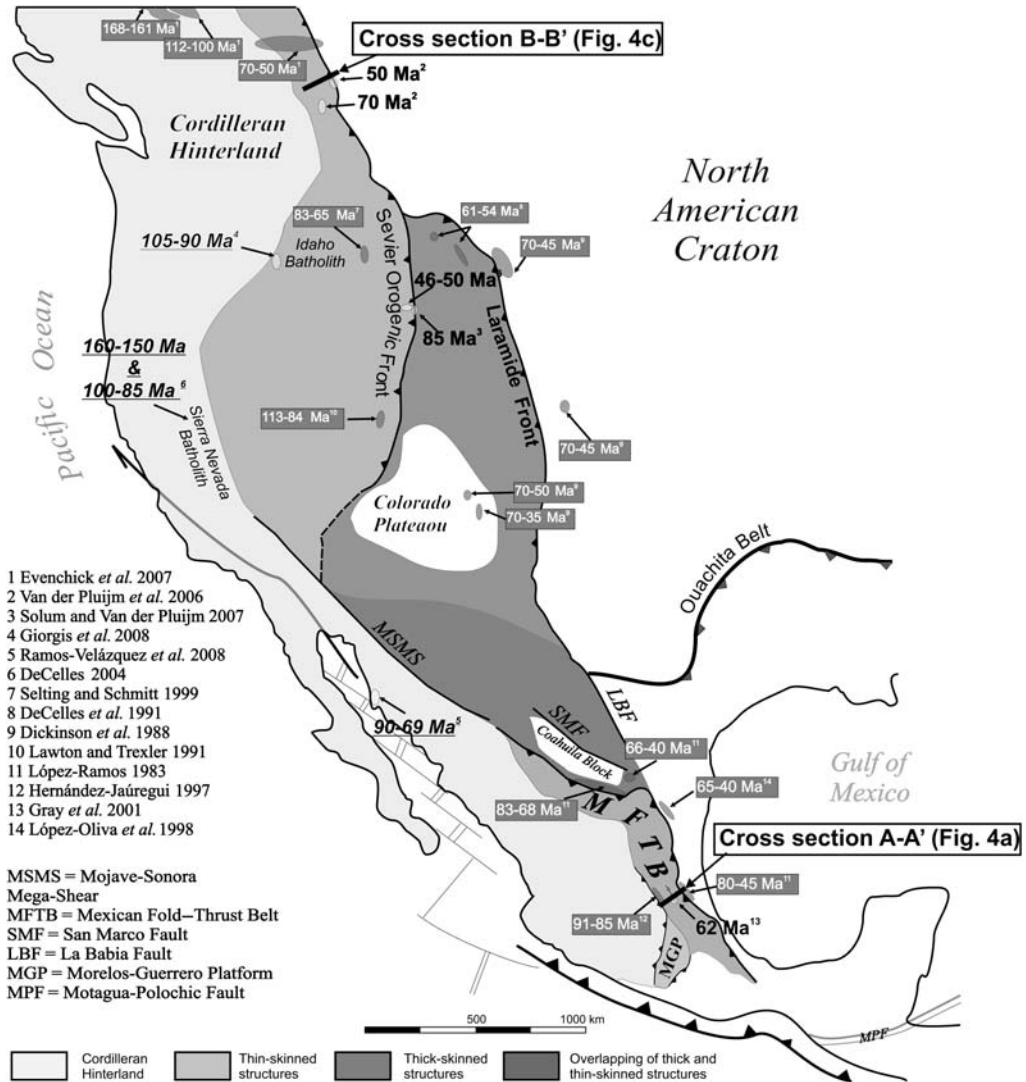


Fig. 1. Generalized tectonic map of the North American Cordillera showing the differences observed in the fold-thrust belt along its eastern edge, together with ages of syntectonic plutons, basins and absolute ages of deformation (based on various sources as indicated, and Armstrong 1974; Campa-Uranga 1983; Anderson & Silver 2005). The ages in grey boxes correspond to ages of syn-sedimentary basins, determined by means of biostratigraphy; underlined ages correspond to isotopic zircon ages from syn-tectonic intrusive rocks; and bold ages are fault-gouge illite Ar/Ar ages.

100–200 km, is thin-skinned and is fold dominated to the north (Thompson 1979, 1981) and thrust dominated to the south (Price 1981). In the SW USA, it widens to more than 1000 km and is divided into two parts: the Sevier and Laramide (Fig. 1, Armstrong 1974). The Sevier fold-thrust belt is thin-skinned and its front is to the west of the Colorado Plateau (Armstrong 1968; Yonkee 1992). Its original width is not well known because

it has been severely affected by Basin and Range extension in the Neogene. The Laramide province extends eastward of the Sevier fold-thrust belt into the continental interior from central Montana to northern Mexico. It is characterized by basement-involved or thick-skinned structures (Allmendinger *et al.* 1982; Brewer *et al.* 1982; Schmidt *et al.* 1993). It is not clear how the Sevier and Laramide tectonic fronts continue to the south, partly because the

traces of Laramide structures are not continuous for long distances along strike and partly because the Sevier structures seem to terminate along the trace of the Mojave–Sonora Megashear (Anderson & Silver 2005). However, in a broad area in northern Mexico (Fig. 1), thin-skinned structures are cut by high angle reverse faults that involve blocks of basement (e.g. San Marcos and La Babia faults, Chávez-Cabello *et al.* 2007), which suggests the presence of both Sevier and Laramide structural expressions. Farther south, the Sierra Madre Oriental is a clear topographical expression of the Mexican Fold–Thrust Belt (MFTB), a 100–250 km wide thin-skinned fold belt (Campa-Uranga 1983; Eguiluz *et al.* 2000). The MFTB extends from northern Mexico, where it is oriented NW–SE and its northern boundary coincides with the Mojave–Sonora Megashear trace, to central and southern Mexico, where it is narrower, changes orientation to north–south, and finally bifurcates, with one branch that continues along the Gulf of Mexico coast and the other that runs into the Morelos Guerrero platform (Fig. 1). One significant difference between the MFTB and its northern counterpart is the absence of a comparable continental foreland.

In addition to the striking variations in tectonic style along the North American Cordillera, there is a difference in deformation ages (Fig. 1). Detailed studies of plutonism and syn-orogenic basins in western Canada (Evenchick *et al.* 2007), suggest that deformation started in Late Jurassic and propagated to the east through the Cretaceous. In the western USA, intensive orogenic plutonism has been documented in the Late Jurassic and continued until Late Cretaceous (e.g. Sierra Nevada and Idaho Batholiths, DeCelles 2004; Giorgis *et al.* 2008). Stratigraphic–sedimentological studies in syn-tectonic piggyback basins, however, suggest an Albian–Maastrichtian age for the Sevier deformation and a Campanian–Eocene age for Laramide structures (Dickinson *et al.* 1988; DeCelles *et al.* 1991; Lawton & Trexler 1991; DeCelles *et al.* 1995). In central Mexico, the age of syn-tectonic turbidites indicates a Middle Turonian–Santonian age for the western boundary of the MFTB (Hernández-Jáuregui 1997) and Paleocene–Early Eocene age for the frontal structures (López-Ramos 1983; López-Oliva *et al.* 1998). Absolute ages of deformation by Ar/Ar dating of illite extracted from fault gouge in different major thrusts in the RMFTB in Canada (Van der Pluijm *et al.* 2006), Montana, USA (Solum & Van der Pluijm 2007) and in the MFTB in central Mexico (Gray *et al.* 2001), suggest that deformation along the front of the thin-skinned fold thrust belts from Canada to Mexico occurred between Maastrichtian and Early Eocene. Therefore, although there is no apparent physical continuity between the Sevier

and MFTB fronts, their ages of deformation are contemporaneous and they were active until the Early Cenozoic. This is perhaps expected from the fact that subduction occurred continuously along the western margin of the continent during Mesozoic and early–mid Tertiary times (Scotese & Golonka 1992). The subduction picture, however, is complicated by the presence of accreted terranes along the western margin of the continent, reflecting arc-parallel displacements during the Mesozoic of portions of crust now constituting the hinterland to the fold–thrust belt (e.g. Evenchick *et al.* 2007).

Detailed field observations of the MFTB in central Mexico have been made and the results synthesized in a geological map and cross section A–A' (Fig. 2), and we compare the structures displayed in this cross section with those of the classical cross section of the RMFTB in southern Canada (Fig. 3). The latter was chosen because of its similarity to the one in Mexico in width, amount of accommodated shortening, lithology (dominated by carbonates), and because they are both part of the same extensive orogenic belt and formed at least in part at the same time. It was also chosen because of the striking contrast in tectonic style. One important difference is the nature of the carbonates involved in the deformation. In Mexico they are Cretaceous in age with large lateral variations in facies over relatively short distances, while in Canada, they are Palaeozoic with a smooth westward transition from shallow to deeper water facies in the section studied, although elsewhere along-strike facies changes from platform to shaly facies occur (e.g. Spratt *et al.* 2004; Fig. 4).

Mexican Fold–Thrust Belt (MFTB) in Central Mexico

The cross section of the MFTB in central Mexico is well exposed and the surface geology has been quite well studied (Imlay 1944; Suter 1980, 1984, 1987; Carrillo-Martínez 1989, 1990, 1997; Contreras & Suter 1990; Carrillo-Martínez *et al.* 2001) (see the map in Fig. 2 and cross section in Fig. 4a). Except for two borehole records close to the line of cross section, no sub-surface information is available in this area.

The fold–thrust structures displayed in this cross section define a body of deformed rocks that is wedge shape, tapers to the east, and involves mostly Mesozoic units that are dominated by Cretaceous carbonates. One particularity of these carbonates in central Mexico is the abrupt lateral change from thick platform facies (delineating El Doctor and Valles–San Luís Potosí platforms) to thinner basinal facies (Zimapán and Tampico–Misantla Basins). The platforms and basins are

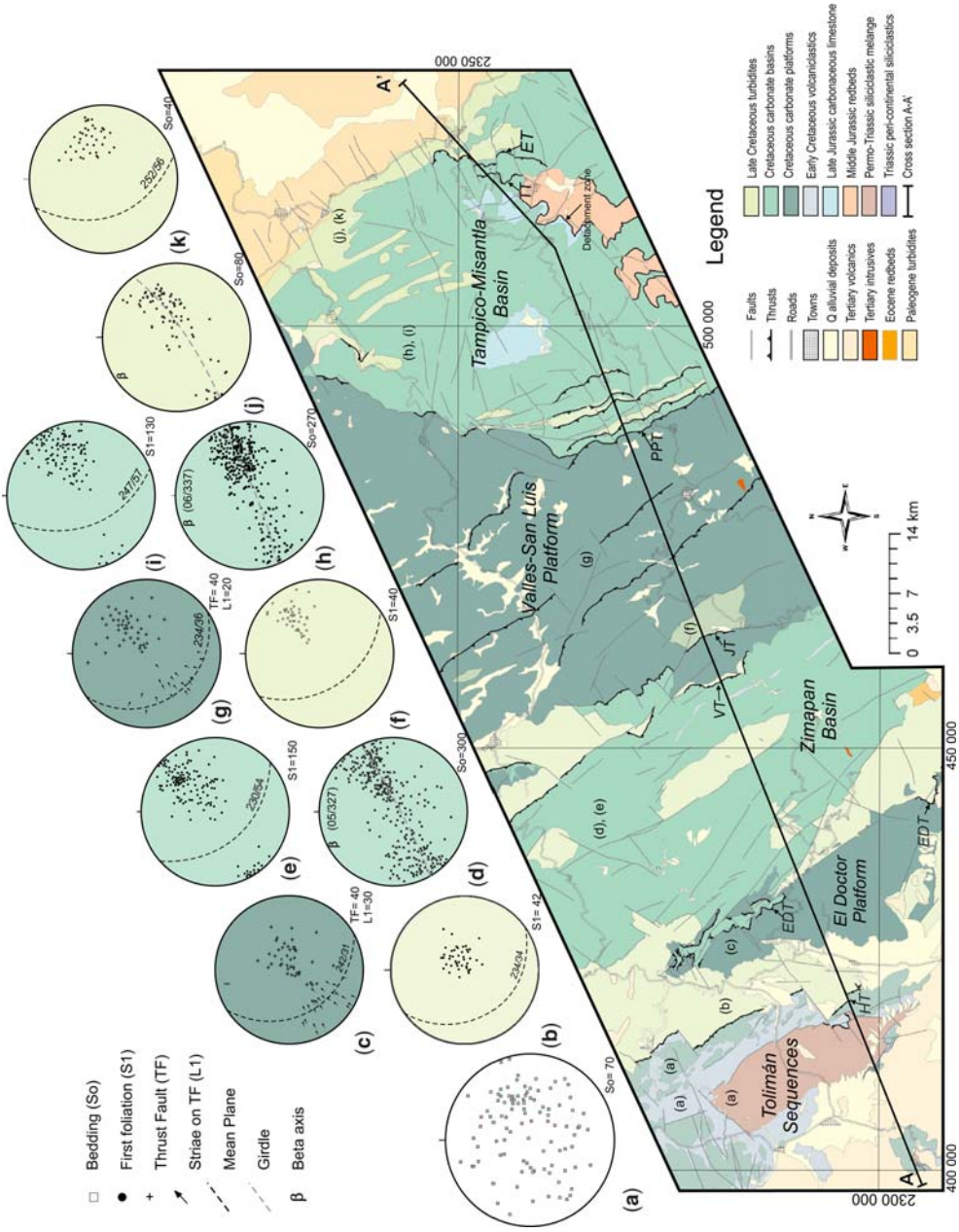


Fig. 2.

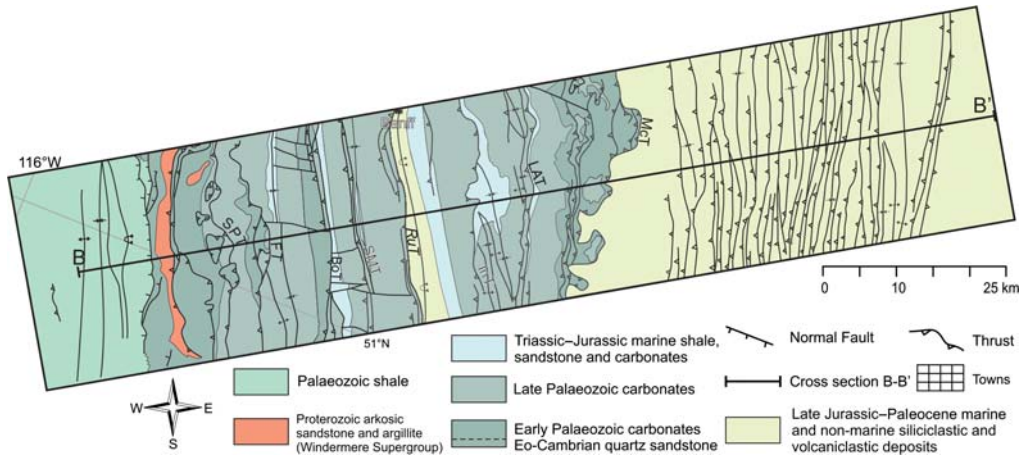


Fig. 3. Generalized geological map of the Southern Canadian Rocky Mountain Front Ranges and Foothills along the Highway 1 transect to the west of Calgary (taken from Price & Fermor 1985). Line B–B' corresponds to the section in Figure 4c. SPT, Simpson Pass Thrust; FT, Fatigue Thrust; BoT, Bourgeau Thrust; SMT, Sulphur Mountain Thrust; RuT, Rundle Thrust; InT, Inglismaldie Thrust; LAT, Lac des Arcs Thrust; McT, McConnell Thrust.

clearly defined on the geological map (Fig. 2) and cross section (Fig. 4a). A possible modern analogue would be the Bahamas carbonate platform and surrounding basins. The stratigraphic range of the units containing the carbonate banks extends from Neocomian to Cenomanian. In the Tampico–Misantla Basin (on the eastern side of the cross section) these rocks have a thickness of about 600 m and lie on top of Jurassic red beds (200–500 m thick). To the south these red beds rest on a Palaeozoic volcanic arc related sequence (Rosales-Lagarde *et al.* 2005) and in some areas, according to borehole records, directly on Grenville age granulite gneisses (Eguiluz *et al.* 2000). Lack of borehole data in the area and the considerable thickness of the Valles–San Luís Potosí Platform rocks, with an original thickness of more than 2 km, duplicated by thrusting, means it is not

possible to determine what happens to the pre-Cretaceous units to the west. Pre-Cretaceous rocks do reappear on the western edge of the cross section (Fig. 4a), but they are very different in character to those exposed or inferred to the east. They have been interpreted to be a siliciclastic Permo-Triassic *mélange* overlain by Early Cretaceous marine volcanoclastic strata that are in turn overlain by Albian–Aptian deep-water carbonates (debris flow and talus facies). These units together constitute the Tolimán Sequences (Figs 2 & 4a). They are separated from the Cretaceous carbonates to the east by the Higuierillas Thrust (HT in Figs 2 & 4a).

Within the Tolimán Sequences, the siliciclastic *mélange* possesses a fabric that predates the deformation associated with the MFTB. The two overlying Cretaceous units show more complex deformation than Cretaceous rocks east of the

Fig. 2. Simplified geological map of the area studied in Central Mexico to show the geometry and extent of structures in map view, as well as the location of the cross section in Figure 4a. In the upper part, equal-area lower hemisphere projections of structural data, measured along the line of section in different units, are keyed to map location, with the color of the stereoplot corresponding to the lithological unit in which measurements were made: (a) poles to bedding (So), Tolimán area; (b) poles to cleavage (S1) in Late Cretaceous turbidites in the footwall of Higuierillas Thrust; (c) poles to thrusts planes (TF) and slickenlines (L1) measured in El Doctor Platform; (d) poles to bedding (So) measured in mesoscopic folds in layers of Cretaceous carbonates of Zimapán Basin; (e) poles to axial plane cleavage (S1) of mesoscopic folds, in Cretaceous carbonates of Zimapán Basin; (f) poles to cleavage (S1) in Late Cretaceous turbidites in the footwall of Jiliapan Thrust; (g) poles to thrusts planes (FT) and slickenlines (L1) measured within Valles–San Luís Potosí Platform; (h) poles to bedding (So) measured in mesoscopic folds in Cretaceous carbonates layers of Tampico–Misantla Basin; (i) poles to axial plane cleavage (S1) in Cretaceous carbonates of Tampico–Misantla Basin; (j) poles to bedding (So) in Late Cretaceous turbidites to the front of the MFTB; (k) poles to axial plane cleavage (S1) in Late Cretaceous turbidites in the front of the MFTB. A–A' shows the line of cross section in Figure 4a. HT, Higuierillas Thrust; EDT, El Doctor Thrust; VT, Volantín Thrust; JT, Jiliapan Thrust; PPT, Puerto de Piedra Thrust; TT, Tetitla Thrust; ET, Enramaditas Thrust.

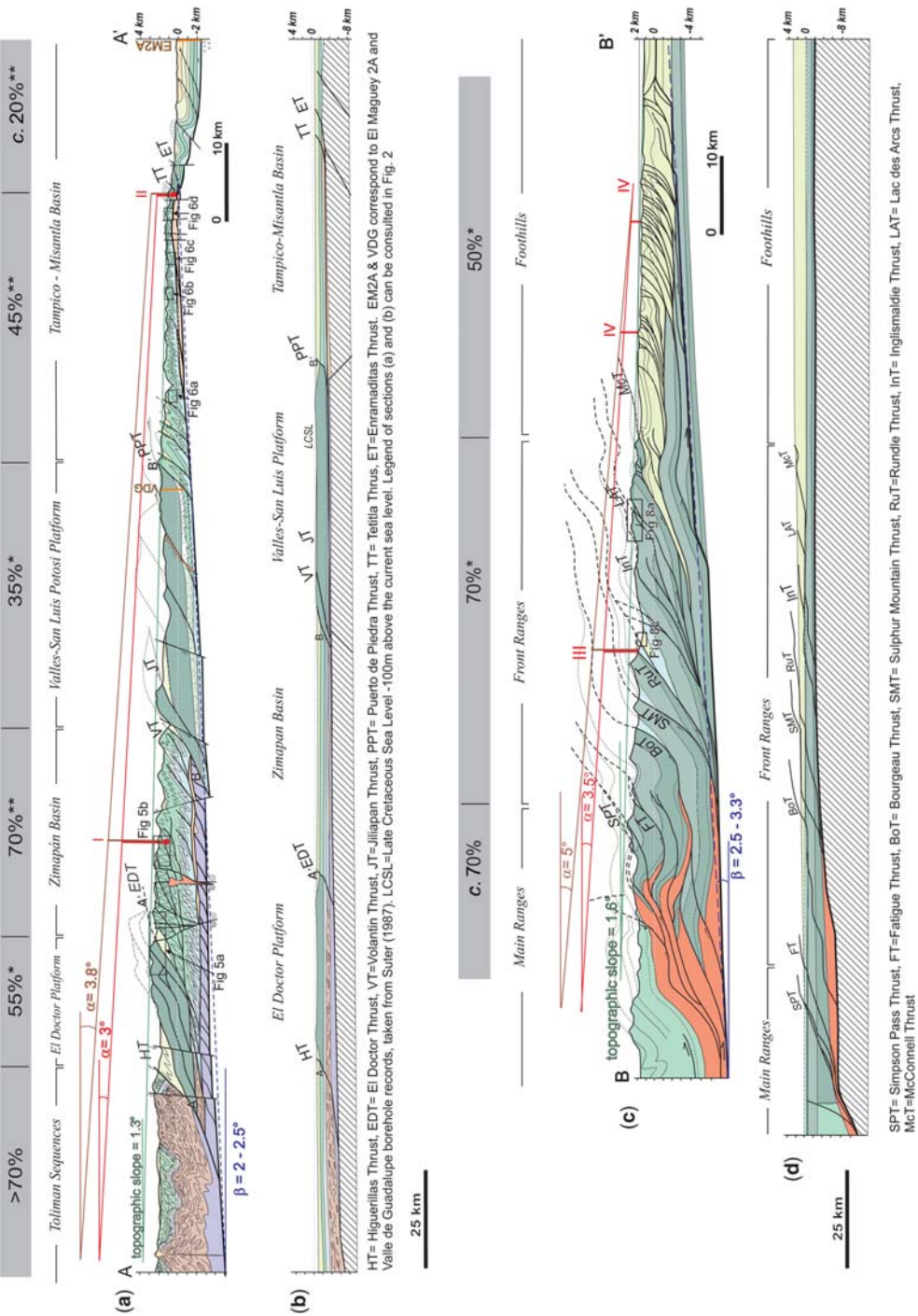


Fig. 4.

Higuerillas Thrust. They are strongly deformed, and are affected by at least two generations of folds: isoclinal folds refolded into asymmetrical open folds generally verging to the east. These folds are severely affected by later faults. The contact between the lower unit and the mélangé is strongly sheared, and that between the upper and lower units weakly sheared.

A possible reconstruction of carbonate facies distribution in the area suggests that the Higuerillas Thrust accommodates a stratigraphic separation on the order of 3 km, the largest such associated with a thrust along the entire cross section. Just east of this thrust, El Doctor Platform is mostly cut by thrusts with kilometre scale displacements (see Fig. 4a) and large-scale related folds, although there is also evidence of smaller scale internal deformation in the form of abundant tectonic stylolites and veins within the thrust slices. Because the rocks of the Tolimán Sequences are different in facies and show evidence of a more complex tectonic history than rocks to the east, the western boundary of the MFTB for the purpose of this study is taken as the Higuerillas Thrust, which thus is taken to separate foreland from hinterland.

To the east of El Doctor Platform, the rocks in the Zimapán Basin have been shortened by kilometre scale thrusting close to the contact with El Doctor Platform (Fig. 5a). The individual thrust slices, however, show very strong internal deformation (Fig. 5b). In thinly bedded limestone layers, this is in the form of metre scale tight folds (Fig. 5c,

d) and in the shaly layers, in addition to open folds, a pervasive axial plane pressure-solution cleavage is also observed (Fig. 5e). Tight mesoscopic folds with eastward vergence and associated cleavage are present all across the Zimapán Basin, with a diminishing of thrusting eastward (Fig. 4a).

Structures in the Valles–San Luís Potosí Platform, which is cut by several kilometre scale thrusts, are similar to those in El Doctor Platform (Fig. 5a); although a major difference is a striking decrease in the intensity of tectonic stylolites and veins at the mesoscopic scale.

At the eastern edge of the fold–thrust belt, in the Tampico–Misantla Basin, deformation is mostly accommodated by folds of chevron style (Fig. 6a). These folds are tight close to the boundary with the Valles–San Luís Potosí Platform, and become progressively more open towards the front of the belt. Most deformation here is accommodated by east verging folding and bedding-parallel slip with internal deformation mostly in fold hinges, with little variation in layer thickness from limb to limb (Fig. 6b–d). Axial planes are mostly steep across the basin (Figs 2i & 4a), but as the basal detachment zone is approached, they decrease in dip. The detachment zone is in a Late Jurassic carbonaceous horizon and is well exposed along a broad area (see map in Fig. 2). It separates folded Cretaceous carbonates above from slightly tilted Jurassic red beds below.

Near the western boundary of the Tampico–Misantla Basin the thrusts dip more steeply than

Fig. 4. Cross sections of the two fold–thrust belts in the foreland of the North American Cordillera. The locations and orientations of sections A–A' and B–B', with legends, are indicated in Figures 2 & 3. (a) Admissible and partly schematic cross section of the Mexican Fold–Thrust Belt (section A–A' in Figs 1 & 2) showing the variation of deformation style within the wedge. (b) Possible restoration of the section in (a) prior to deformation. Note the abrupt lateral changes in thickness and facies of the Cretaceous carbonates associated with the two platforms, and the disrupted basement at the east end of the cross section. (c) Balanced cross section of the Rocky Mountain Fold–Thrust Belt in southern Canada (Price & Fermor 1985) along line B–B' in Figures 1 and 3. (d) Palinspastic restoration of the sedimentary units (Proterozoic, Palaeozoic and Mesozoic strata) of section (c) before deformation (Price & Fermor 1985). Note the gradual increase in thickness of the different units towards the west. Figure 4a, c are at the same scale, which is twice that of the palinspastic restorations in (b) and (d). The amounts of shortening shown above (a) and (c) were determined using two methods (see the text and Fig. 7), one for thrust-dominated (*) and the other for fold-dominated segments (**). Blue lines in (a) and (c) show the average dip angle of the basal detachment zone inferred for the MFTB and reported in the CRMFTB. Red lines and brown lines in (a) and (c) show inferred paleo-topographic slopes for the end of the Cretaceous. In the MFTB the slope was determined using paleo-temperatures estimated at two localities (I and II), and calculating burial depth for a range of geothermal gradients. At locality I, a temperature (T) of 180 °C was calculated from an illite crystallinity index of 0.48 (average of 6 measured samples). The value falls in the range of temperature of homogenization (170–190 °C) of measured fluid inclusions in quartz of syn-tectonic veins from exactly the same locality. In locality II, a minimum burial temperature of 70 °C was calculated from an average illite crystallinity index of 1.54. If we consider a minimum geothermal gradient of 23 °C/km (Magoon *et al.* 2001) and a maximum geothermal gradient of 30 °C/km, we get estimates of burial depth of from 6.6–5.0 km for locality I and, from 2.2–1.5 km for locality II. Plotting these in cross section A–A', we obtain a gradient of from 3.0–3.8° to the east. For the CRMFTB, we used the thickness of the column (4.0–5.5 km) of rocks above the Lewis Thrust in Late Cretaceous calculated by Feinstein *et al.* (2007), and projected this as being directly above the Rundle Thrust on our line of section (point III in (c)). In the Foothills (point IV in (c)), we used the thickness of the overburden column calculated by Nurkowski (1984) for Late Cretaceous–Early Cenozoic times. We draw a line that approximately fits the burial depths and these values implying a range in gradient of 3.0–5.5° to the east. Labeled boxes in (a) and (b) show locations of photographs shown in Figures 5, 6 and 8.

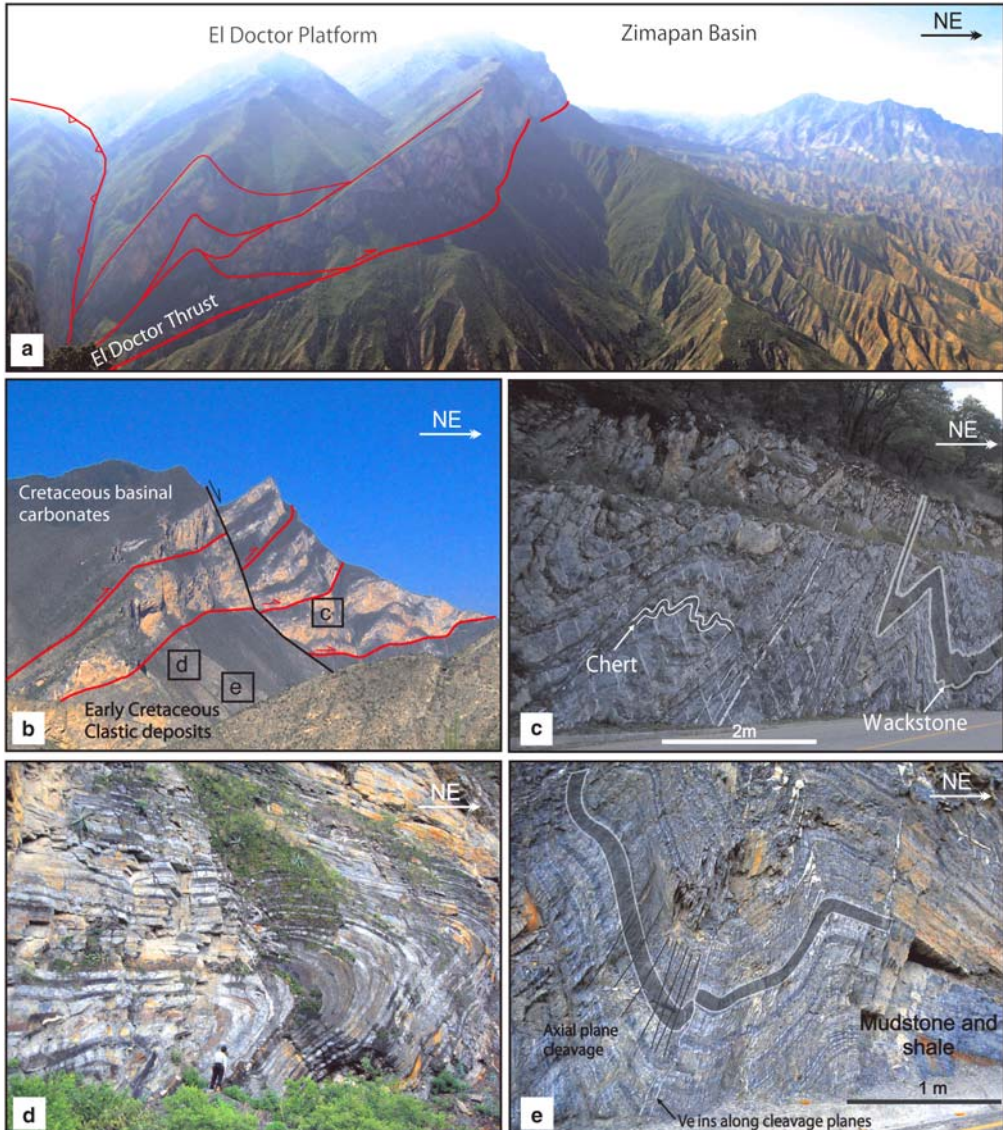


Fig. 5. Examples of structures from the Mexican Fold–Thrust Belt on the western part of the section (for locations see boxes in Fig. 4a). (a) Panoramic view of El Doctor Thrust from south of the Montezuma River. (b) Panoramic northward view of stacked thrust sheets of the Cretaceous Tamaulipas limestone in the Zimapán Basin, which at this scale does not seem to be internally deformed, but which in fact displays intense internal folding. (c) Tight mesoscopic folds in the interior of a thrust sheet of middle Cretaceous limestone, Tamaulipas Fm. Note the thickening in the fold hinges, except in the chert layers (to the left). (d) Gently inclined fold in Early Cretaceous shale and calcarenite layers. Note the variation in layer thickness around the fold. (e) Folds in layers of Early Cretaceous shale and mudstone. The folds are more open but the cleavage is more intense than in the limestone and sandstone layers. Note that the insets in (b) do not correspond to the actual locations of (c), (d) and (e), but rather indicate equivalent stratigraphic/structural positions where these folds are encountered.

they do to the east and appear to postdate folding, as suggested by thrusts cutting attenuated fore-limbs of folds, although no examples were observed in the field. Some of the thrusts could be coeval with the

folds. The same is also true for the Zimapán Basin, and is different to what is observed in the platforms. In general, the large-displacement thrusts along the cross section are located in the interiors of

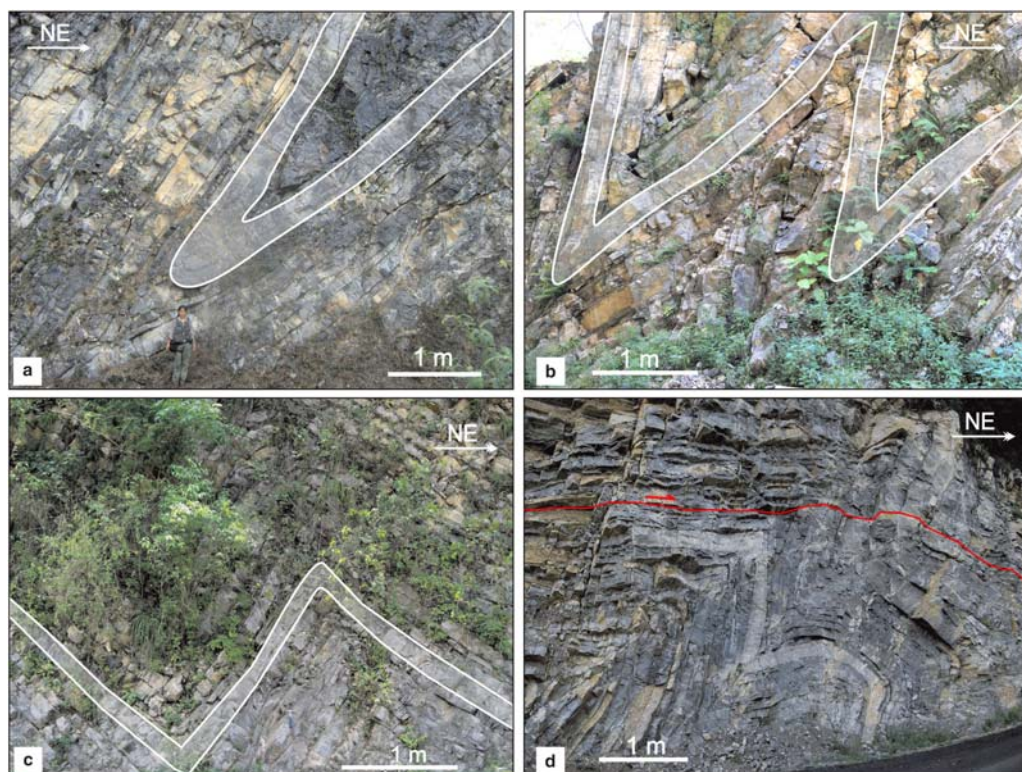


Fig. 6. Examples of meso-scale structures to show variation in fold style along the same horizon of Middle Cretaceous basinal carbonates (Tamaulipas Formation) across the Tampico–Misantla Basin (TMB, for locations see boxes in Fig. 4a). (a) Tight folds with thickened hinges, typically observed on the western boundary of the basin. (b) Close chevron folds typically observed in the centre of the basin. (c, d) Open folds observed towards the eastern side of the basin.

the two platforms or at their eastern boundaries, where they produce stratigraphic offsets on the order of hundreds of metres. This, together with field observations and fold analyses, suggests that most of the shortening in the basins is accommodated by folding.

The geometrical features described above are consistent with what is observed in cross sections to the north and to the south of the area (Eguiluz *et al.* 2000), which have borehole records to provide control at depth.

Shortening within the wedge across the two Cretaceous platforms was determined by three methods, using: (1) length of the base or top of the massive carbonate unit (see Fig. 6a); (2) comparing total widths of the platform in the unrestored, restored and palinspastically restored states; and (3) using the area occupied by the carbonate unit in the unrestored and restored states, assuming that both bed length and thickness (and thus area) are preserved and that all deformation is in the plane of the section. In the third method, the original thickness

of the unit is known from measurements in the field and in boreholes. This method is one of several described by Hossack (1979). These result in average estimates of shortening of *c.* 55% (corresponding to 20 km of shortening in the cross section) for El Doctor Platform and *c.* 35% (*c.* 23 km) for the Valles–San Luís Potosí Platform. The latter is less than the value of 42% reported by Suter (1987) and Contreras & Suter (1990) for exactly the same cross section. The difference reflects the conservative way in which the cross section has been constructed.

To determine shortening in the basins, we analyzed trains of at least 5 single layer buckle folds of mesoscopic scale in the same stratigraphic unit (Tamaulipas Fm, Figs 6c & 7b). We characterized the geometry of such folds in outcrop and calculated the minimum shortening by using the chord method. The chord method (Fig. 7b) was only applied to buckle folds in rocks that did not show significant internal deformation, such as chert layers (Fig. 5c). Folds were analyzed in 10 outcrops in the

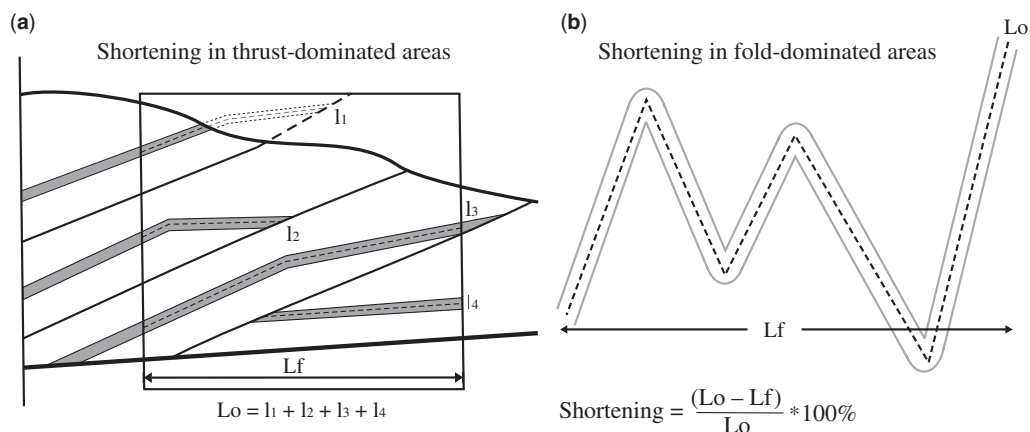


Fig. 7. Methods applied to determine shortening: (a) using line length in the platforms of the MFTB and for the CRMFTB where thrusts are the dominant structure, including eroded segments of the marker horizon; (b) in the basins, where the dominant structures are buckle folds, we used fold arc length to determine shortening. We applied the second method only in trains of upright folds in Cretaceous carbonates, in layers that did not show significant variations in thickness or a pervasive axial plane cleavage (in some horizons of limestone and chert).

Zimapán Basin, mostly on the eastern side (and the values obtained were extrapolated to the whole basin), and 14 outcrops in the Tampico–Misantla Basin, covering the whole width. Shortening (of 60–65%, at least 49 km) at the level of the Tamaulipas appears to be fairly uniformly distributed across the Zimapán Basin and to decrease (from 70–20%, with an average of 40%, *c.* 30 km) eastwards across the Tampico–Misantla Basin (Fig. 4a). Offsets on thrusts and local anomalous thickening give rough estimates of shortening due to thrusting in the two basins of 10 and 5%. These are added to the shortening estimates due to folding to arrive at the values of 70 and 45% for total shortening across the Zimapán and Tampico–Misantla basins, respectively.

The limited stratigraphic range and thickness of strata of the rocks exposed across the full length of the cross section indicate that the wedge must have been thin and must have had a relatively low taper angle, which is consistent with the 2–2.5° dip westward of the detachment zone exposed near the east side of the cross section. However, we do not have direct evidence of the position of the basement or the basal décollement to the west of the cross section.

The current average topographic slope along cross section A–A' (Fig. 4a) dips from 1–1.3° to the east. An inferred paleo-topographic slope based on the reconstruction of structures varies from 3.0–3.8° to the east (Fig. 4a). This is consistent with burial conditions in the Zimapán Basin, interpreted from temperature of deformation (*c.* 180 °C) in this basin and towards the front of the cross section A–A' (*c.* 70 °C), determined with illite

crystallinity analysis and considering a range of geothermal gradients from 23–30 °C (Fig. 4a).

Rocky Mountains Fold–Thrust Belt in Southern Canada (CRMFTB)

Because of the excellent exposure, arguably the best characterized cross section of a fold–thrust belt anywhere is the one that runs sub-parallel to Highway 1 in Alberta and British Columbia, in the southern Canadian Rocky Mountains. We focus our attention on the Front Ranges and eastern edge of the Main Ranges (Figs 3 & 4c), although data from the Foothills are also included. Cross section B–B' is based on a great deal of geological and geophysical information. The sedimentary rocks involved in the belt include a broad range of ages from Late Proterozoic–Late Cretaceous (Price 1981; Price & Fermor 1985). For the purposes of this paper these units are grouped into five suites. The first is a Proterozoic sequence of feldspathic to arkosic sandstone and argillite (Windermere Supergroup). The second consists of a Palaeozoic sequence of shale that is the dominant lithology exposed in the Main Ranges, to the west of the cross section (Fig. 4c). The third suite corresponds to Palaeozoic platform and shallow water carbonates that thicken and changes to deep-water facies (shale) westward. This consists of two packages of Early to Late Palaeozoic age that are represented separately in the map. These are the dominant lithologies in the Front Ranges (Figs 3 & 4c, d). The fourth suite consists of Triassic–Jurassic marine

shale, quartz sandstone and limestone. The fifth consists of Late Jurassic–Paleocene marine and non-marine siliciclastic and volcanoclastic deposits, which are dominant in the Foothills. Price (1981) suggested that these different units exert an important control on the nature and orientation of structures within the fold–thrust belt.

In the Foothills, closely spaced listric imbricate thrusts are observed in the Late Cretaceous units, and fault-related folds are also common (MacKay 1996). Associated with these folds are folds not directly related to faults (probably buckle folds) of variable style and often complex geometry (e.g. MacKay 1996; Soule & Spratt 1996; Stockmal *et al.* 2001). Wells reveal several large gently westward dipping thrust sheets of Palaeozoic strata below the east-directed imbricates (Bally *et al.* 1966). The eastern-most outcrops of the imbricates are marked by a triangle zone (Spratt *et al.* 1993; Spratt & Lawton 1996; Stockmal *et al.* 1996), which is blind to the east of Figure 4c (Slotboom *et al.* 1996) and better exposed in the Turner Valley structure, just to the south of the line of section in Figure 4c.

In the Front Ranges (Fig. 8a) the imbricate style is maintained, but the thrusts are more widely spaced and are developed in Palaeozoic platform carbonates. The structures are well exposed and the thrust slices are dominated by the thicker carbonate units that stand out in the landscape, often giving the superficial impression of homoclinal sequences of undisturbed beds (Fig. 8a). Large fault-related folds mark hanging wall or footwall cutoffs and thrust terminations (Fig. 8b). There is little internal deformation in most of the platform carbonates, except in the vicinity of faults, where locally some of the units may show intense internal folding, such as in the Middle Cambrian Eldon Fm limestones in the hanging wall of the McConnell thrust, near Mt. Yamnuska, or in the in the Jura-Cretaceous Kootenay Fm (interbedded sandstones, shale and coal, Fig. 8c) in the footwall of the nearby Rundle Thrust (Cant & Stockmal 1999).

In the Main Ranges, contemporaneous internal deformation in the Early Palaeozoic shale and clastic Proterozoic rocks is widespread and pronounced, with the development of a pervasive

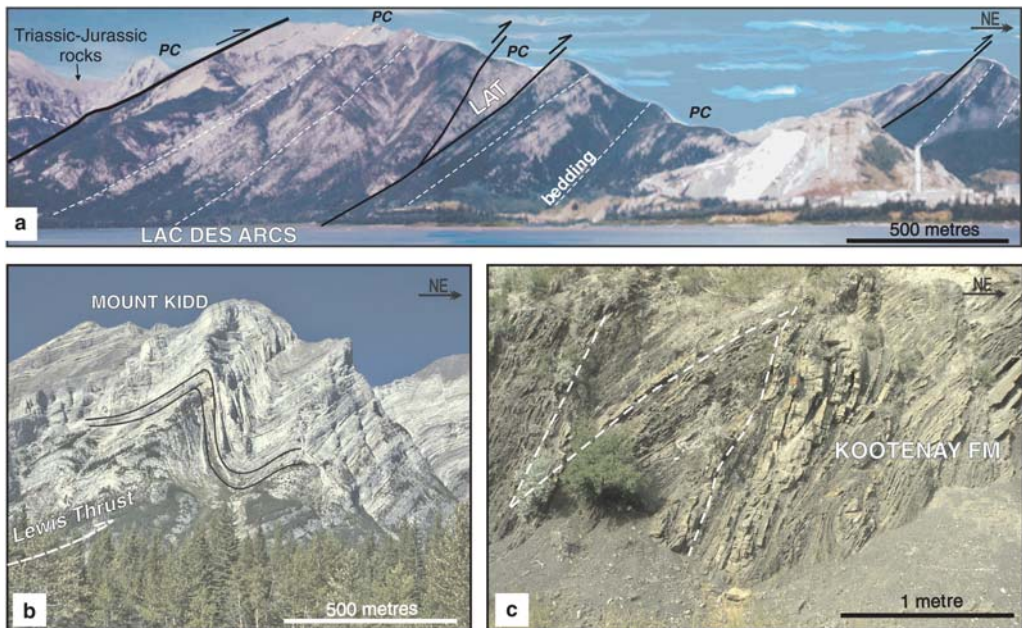


Fig. 8. Examples of structures in the Canadian Rocky Mountains (for locations see boxes in Fig. 4c). (a) Panoramic northward view of Front Range structures (across Lac Des Arcs) with repetition of mostly Upper Palaeozoic carbonates (PC) and little change in bedding dip (white dashed lines) across several thrusts. To the west, Triassic–Jurassic units cover the Palaeozoic units. Nowhere in the MFTB section is there such uniformity of dip on this scale. (b) Palaeozoic carbonates at Mount Kidd, folded in connection with the northern termination of the Lewis thrust. (c) Tight mesoscopic chevron folds in shale and sandstone layers of the Jurassic–Cretaceous Kootenay Fm. in the core of the Mount Allan Syncline, under the Rundle Thrust in the Front Ranges (see Cant & Stockmal 1999, for more photographs and description of the rocks and structures in this location).

cleavage and mesoscopic folds with vergence towards the east, which are more evident than large thrusts. With the exception of the Western Main Ranges, the deformation in cross section B–B' (Fig. 4c) is dominated by thrust slabs, mostly more than 1 km thick in the Front Ranges and less than 1 km thick in the Foothills, stacked to the east.

Shortening in the Front Ranges of cross section B–B' (Fig. 4c) was determined by the bed length method (Fig. 7a), selecting as the marker horizon the base of the Upper Devonian and vertical pin lines passing through the surface traces of the Fatigue and McConnell thrusts (Fig. 7a). The shortening thus derived is 70% (corresponding to c. 110 km). The same method was used for the Foothills, above the Palaeozoic rocks, using the Cretaceous Cardium Formation as the marker horizon, the trace of the McConnell thrust as the western end point and the eastern tip of the triangle zone as the eastern end (see Fig. 4d, the actual section used for the measurements was that of Price & Fermor 1985). The shortening is c. 50% (c. 50 km), although it is not uniformly distributed. In the central part of the Foothills, bounded by the traces of the Waiparous and Old Baldy thrusts, shortening is almost 80% (at least 100 km in the

studied cross section). Because of the presence of smaller scale thrusts and folds not accounted for in the cross section of Price & Fermor (1985), this estimate of shortening in the Foothills is certainly an underestimate.

An average dip of the detachment zone in the CRMFTB over the section studied is c. 3.3° with a minimum dip of 2.5° in the Foothills. The current topographic slope varies between 1.3 – 1.6° to the east (maximum dip is shown in Fig. 4c) and a minimum inferred paleo-topography based on structural reconstructions varies from 3.5 – 5° . Some structural features of the CRMFTB and the MFTB are compared in Table 1.

Horizontal shortening and wedge geometry

Values of shortening obtained for fold–thrust belts, with significant discontinuities in displacement across faults and little internal deformation between faults, depend on the scale at which the measurements are made. The most meaningful results are obtained when the measurement 'box' is wide compared with the displacements on

Table 1. Comparative table outlining the differences and similarities between the Mexican Fold–Thrust Belt (MFTB) and the Rocky Mountain Fold–thrust Belts in southern Canada (CRMFTB)

	CRMFTB section	MFTB section
Width	125 km	150 km
Dip of the detachment zone, β	2.5 – 3.3° to the west	2 – 2.5° to the west
Current surface slope	1.3 – 1.6° to the east	1 – 1.3° to the east
Inferred topographic slope, α	3.5 – 5°	3.0 – 3.8°
Inferred critical taper angle ($\alpha + \beta$)	6 – 8.3°	5 – 6.3°
Stratigraphic range of rocks involved in deformation	Proterozoic–Late Cretaceous	Triassic–Eocene
Dominant Lithology	Carbonates (Palaeozoic platform) in the Front Ranges, clastic units in the Foothills and Main Ranges	Carbonates (Cretaceous platforms and basins)
Lateral facies changes	Smooth-transitional at the scale of tens of km, except in transition from Front Ranges to Main Ranges (abrupt in the third dimension)	Abrupt at the scale of tens of km, associated with platforms
Amount of Shortening	70%	60% (minimum)
Maximum vertical displacement along thrusts	5 km	2.5 km
Scale of deformation	Typically kilometre scale in the Front Ranges	Typically metre scale
Dominant structures	Thrusts	Folds
Axial plane cleavage	Pressure-solution and slaty cleavage in the Main Ranges	Pressure-solution dominant to the rear and center of the cross section, but also present to the front

individual thrusts. The nature of thrust development also means that shortening between two vertical bounding lines may vary with stratigraphic level, typically decreasing with depth, as in-sequence thrusts are added from below (e.g. Lebel *et al.* 1996). We assume here that shortening measured at an appropriate stratigraphic level is characteristic of the segment under consideration. With the limitations of the methods in mind, the sections in Figure 4 show that in general, for both fold–thrust belts, shortening is greatest towards the hinterland and least towards the foreland. This phenomenon is predicted for critical taper models of subaerial wedges, since erosion in such wedges requires continued deformation – and thus shortening – throughout the wedge to maintain the critical angle (Davis *et al.* 1983). Continued displacement on older thrusts that develop in piggy back fashion is consistent with observations in the Front Range of the Canadian Rockies (Price 2001), and also with finite element simulations of fold–thrust belts by Stockmal *et al.* (2007) and analog models (Dixon & Liu 1992). In addition to an overall gradient in shortening, Figure 4 shows that the total shortening accommodated by the two fold–thrust belts is similar, within the uncertainties of the measurements – *c.* 55% for the MFTB and 65% for the CRFTB. A significant difference between the two is that the stratigraphic section in the MFTB contains two carbonate platforms flanked by more pelitic facies. The shortening of the MFTB Platform carbonates is significantly less (55 and 35%) than the shortening accommodated by the basinal strata (*c.* 70% close to the platform borders) on either side.

It is instructive to compare the overall shortening in the two sections with shortening in an idealized self-similar wedge and with the shortening pattern in finite element models (Stockmal *et al.* 2007). In an ideal wedge, the percentage of internal shortening for a given amount of displacement between the ‘backstop’ and the rigid substrate below the wedge is a function of the taper angle (surface slope α plus basal slope β) and the thickness of the section from which the wedge is built. Figure 9 shows the ideal total percentage of shortening for three values of wedge taper angle and the dimensionless displacement of the backstop (displacement divided by thickness of the undeformed section). For comparison, the progressive shortening displayed by Models 7 and 8 of Stockmal *et al.* (2007) are also shown. In the Stockmal *et al.* models, for which the Canadian Rockies section shown in Figure 4c provided a rough prototype, relative displacements between backstop and sub-wedge crust of 240 km are associated with values of shortening of *c.* 60% for taper angles of about 5.5–6.5° for model 7 and 5.0–5.5° for model 8. The taper angles of the fold–thrust belt in Canada

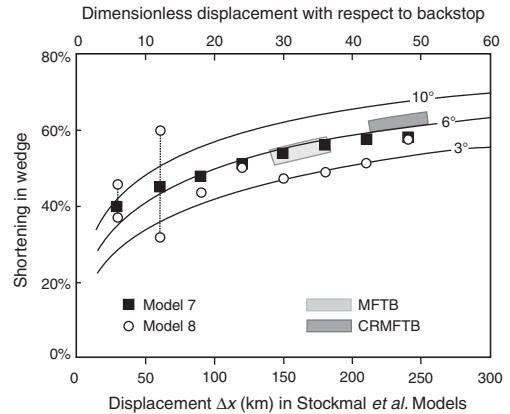


Fig. 9. Data for numerical models and approximate fields corresponding to the MFTB and CRMFTB compared with theoretical shortening in a self-similar critically tapered wedge for three different taper angles (surface slope α plus basal slope β : 3°, 6° and 10°) as a function of the relative displacement between the backstop and the rigid sub-wedge substrate, for wedge development from strata of uniform thickness and assuming no erosion. The black squares and open circles indicate the shortening developed in finite element Models 7 (three-detachment, with erosion and no sedimentation) and 8 (three-detachment, erosion and sedimentation to base level) respectively of Stockmal *et al.* (2007), for which the CRMFTB is a rough prototype. The two circles joined by dotted lines at 30 and 60 km displacement represent alternative positions of the toe at incipient development of a new thrust in the numerical models. The discrete nature of thrust spacing and displacement on a scale not markedly different from that of the displacement of the backstop result in considerable deviation of the data points from a smooth curve, especially towards the left of the figure, and especially for Model 8, involving erosion and sedimentation (see Stockmal *et al.* 2007, for more details of the models). Dimensionless displacement is displacement divided by thickness of the strata fed into the wedge at the toe. The shaded areas represent the ranges of inferred values of taper angles and internal wedge shortening for the two fold–thrust belts.

and Mexico have diminished since the cessation of tectonism due to erosion – estimates suggest that about 2 km of strata have been removed at the deformation front in Canada (Nurkowski 1984), and proportionately more would have been eroded farther back in the wedge. Thus, the current taper angles of about 4.0–5.0° for the CRMFTB and 3.5–4.0° for the MFTB are lower bounds to the values that existed at the time of wedge formation, for which our estimates are 6–8° and 5–7°, respectively. One piece of geological evidence that supports the notion that the taper angle was higher for the CRMFTB than for the MFTB is the stratigraphic

range of the rocks exposed at the surface in the two belts. In the CRMFTB these rocks are progressively older towards the hinterland whereas in the MFTB the strata exposed at the surface are of a much more restricted stratigraphic range. With a high taper angle there will be greater uplift and erosion at the back of the wedge, bringing deeper rocks to the surface. The estimates of total shortening and taper angle for the two fold–thrust belts are indicated on Figure 9. It should be noted that the displacement of the backstop (on the horizontal axis of the plot) applies just to the segments of the fold–thrust belts for which shortening data was obtained (Doctor platform to the Tampico–Mislantla basin in the case of the MFTB and Front Range and Foothills in the CRMFTB). In other words, the ‘backstop’ is locally defined within the larger orogenic belt.

In a Coulomb wedge taper is controlled by the angle of internal friction of the wedge material, friction at the base, and pore fluid pressure (Davis *et al.* 1983). Since the composition of the rocks in the two fold–thrust belts is similar (although the distribution of facies is different), it seems likely that the main reason for the difference in taper angle lies with basal friction: the lower the basal friction, the smaller the taper angle. Although only exposed in the middle of the Valles–San Luis Potosí Platform, there is good reason to believe from borehole data to the north and to the south of the area that (Neocomian) evaporites partially underlie the MFTB wedge and localize the basal detachment (Eguiluz *et al.* 2000). In the CRMFTB the basal detachment (sole thrust) lies at the basement cover interface under the Main Ranges and Front Ranges and steps up into the Palaeozoic section towards the Foothills, climbing further into the Mesozoic section towards the tectonic front. The *décollement* horizons involved are all in a carbonate/clastic units and will be associated with higher coefficients of friction than the inferred evaporite horizons under the MFTB.

It is instructive to explore what combinations of mechanical properties might satisfy the observed and inferred wedge geometries of the two fold–thrust belts. If we assume Coulomb behaviour and a homogeneous wedge, the only properties that affect the taper angle are internal friction within the wedge, basal friction, and pore fluid pressure (Davis *et al.* 1983) (although cohesion affects the frontal part of the wedge, resulting in a slightly concave upwards profile, Dahlen *et al.* 1984). The results of applying the wedge model of Dahlen *et al.* (1984), with various combinations of basal friction and internal friction, are shown in Figure 10, with the combinations that satisfy the geometry of the two fold–thrust belts, given the taper angles inferred from the geology. The range of values of internal

friction and basal friction that match the inferred taper angles for the two sections are realistic, and are consistent with a weaker basal detachment under the MFTB for a fluid pressure ratio of 0.7.

Major controls on tectonic style

The most striking difference in structural style between the two fold–thrust belts is in the relative partitioning of deformation between displacement on thrust faults and internal deformation of the rock units. In the CRMFTB much of the deformation is accommodated by slip on faults, with a relatively small amount of internal deformation within individual stratigraphic units. In the MFTB much of the deformation is taken up by internal deformation within each stratigraphic unit, accompanied by mesoscale fold and cleavage development, with correspondingly less deformation taken up by displacement on thrusts.

The large-scale folding in the CRMFTB is associated with hanging wall or footwall cutoffs (fault bend folds) and thrust terminations along strike or in the displacement direction (fault-propagation folds or detachment folds). The anisotropy of the layers certainly influenced the growth and geometry of these folds, with bedding-parallel slip a key component of the deformation, but the main factor that controls the location, general shape and orientation of folds is the geometric accommodation required to allow slip on thrust faults. Large-scale folds of this type in the MFTB are restricted to the platforms.

In general the mesoscale folding in the MFTB is not directly associated with thrust faults but reflects a buckling instability of layers of different composition subjected to layer-parallel compression. Intense folding within a stratigraphic unit without much folding of the unit itself, a common phenomenon in the MFTB, suggests what has been referred to by Biot (1965) as internal buckling. This requires the layer in which the folds develop to possess anisotropy, which is the case for a unit made up of alternating layers of differing stiffness or viscosity. This phenomenon has been well documented in experiment and in nature (e.g. Cobbold *et al.* 1971; Johnson & Fletcher 1994, ch. 6). The centrifuge models of Dixon (2004) nicely illustrate the difference in behaviour of juxtaposed massive units, simulating carbonate platforms, and strongly anisotropic softer units, simulating basinal facies. The massive units fail by thrusting and the anisotropic units by multilayer buckling. The models also show that the presence of platform facies cause partitioning of deformation in the wedge on a large scale, as is indicated for the MFTB in Figure 4a, with deformation concentrated in the basinal facies.

Very weak detachment ($\mu_b = 0.35$)																
φ	25				30				35				40			
β	2	2.5	3	3.5	2	2.5	3	3.5	2	2.5	3	3.5	2	2.5	3	3.5
α	3.8	3.6	3.5	3.4	3.1	3.0	2.8	2.6	2.5	2.3	2.1	1.9	1.9	1.7	1.4	1.1
$\alpha + \beta$	5.8	6.1	6.5	6.9	5.1	5.5	5.8	6.1	4.5	4.8	5.1	5.4	3.9	4.2	4.4	4.6

Intermediate detachment ($\mu_b = 0.5$)												
φ	30				35				40			
β	2	2.5	3	3.5	2.0	2.5	3.0	3.5	2.0	2.5	3.0	3.5
α	5.0	4.9	4.8	4.6	4.1	3.9	3.7	3.5	3.2	3.0	2.8	2.5
$\alpha + \beta$	7.0	7.4	7.8	8.1	6.1	6.4	6.7	7.0	5.2	5.5	5.8	6.0

Strong detachment ($\mu_b = 0.7$)												
φ	35				40							
β	2.0	2.5	3.0	3.5	2.0	2.5	3.0	3.5				
α	7.3	7.2	7.0	6.8	5.3	5.1	4.9	4.6				
$\alpha + \beta$	9.3	9.7	10.0	10.3	7.3	7.6	7.9	8.1				

Solutions for α and β in the range estimated for the MFTB

Solutions for α and β in the range estimated for the CRMFTB

Overlapping solutions

Fig. 10. Comparative table showing critical taper angles in an ideal subaerial wedge, and combinations of basal friction, μ_b , and internal friction, μ , that are consistent with inferred taper angles for the MFTB and CRMFTB. The taper angle ($\alpha + \beta$) is approximated by: $\alpha + \beta = \frac{\beta + (1 - \lambda_b)\mu_b}{1 + (1 - \lambda)K}$ (from eq. 21 in Dahlen *et al.* 1984). This equation is valid for non-cohesive wedges and to cohesive wedges far from the toe. β is the dip of the detachment; α is the topographic slope; λ and λ_b are the ratios of fluid pressure to total vertical pressure in the wedge and in the detachment, respectively. Taper angle is sensitive to pore fluid pressure, with fluid pressure build up in the detachment and the wedge itself having opposite effects on the taper angle. We have no direct evidence for what fluid pressure might have been at the time of wedge formation. Certainly it was elevated above hydrostatic ($\lambda \approx 0.44$), because of the abundance of veins in both the MFTB and CRMFTB. If fluid pressure is high just in the detachment (say $\lambda_b = 0.9$), taper angles are all too low. We take for this comparison $\lambda = \lambda_b = 0.7$. μ_b is the basal coefficient of friction. The coefficient of internal friction, $\mu = \tan \varphi$, is embodied in the coefficient K (see Dahlen *et al.* 1984, eq. 18a). Note that $\mu_b \leq \mu$ for a wedge to exist. To achieve the critical taper inferred for the MFTB we need a wedge with a weak detachment and relatively low φ or an intermediate-strength detachment and a high φ (shaded in pale gray). For the CRMFTB, we require a strong detachment and a relatively high φ , or an intermediate-strength detachment and an intermediate φ in the rock to achieve the inferred critical taper (shaded in deep grey). There is a small zone of overlap in conditions that matches both of the fold–thrust belts. Geological data suggest a weak detachment for the MFTB, and the range of matching φ for the inferred critical taper are typical for limestones ($\varphi = 25\text{--}30^\circ$, Sydney 1966). Stockmal *et al.* (2007) took a value of $\varphi = 38^\circ$ for the strongest material in their models, and values of basal friction consistent with such a value and the inferred tapers can be found for MFTB ($\mu_b = 0.5$) and CRMFTB ($\mu_b = 0.7$).

The normal decrease in deformation towards the toe in a homogenous wedge is changed by the presence of a carbonate platform which may act as a competent ram to concentrate deformation ahead of the platform towards the foreland. This is seen in front of both the Doctor and Valles–San Luís Potosí platforms in the MFTB and in Models MO15 and MO17 of Dixon (2004). Field examples of the lateral transition in structural style from reef facies to shales facies in rocks above a thrust are given by Spratt *et al.* (2004). This transition is orthogonal to the shortening direction rather than parallel to it as is the case for the MFTB.

All the folds illustrated in Figures 5 and 6 are internal to particular stratigraphic units, and many

of them can be characterized as either internal buckles or examples of true multilayer buckling (Schmid & Podladchikov 2006). In some cases deformation becomes localized in fold limbs to produce distinctly asymmetric folds with strong bed thinning (Fig. 5c). The fold style is similar to that observed in the intra-unit buckle folds developed in the anisotropic layers in the analog models of Spratt *et al.* (2004). It also appears to be similar to the style observed in Mesozoic strata above blind thrusts in the Foothills in northern Alberta (Gabrielse & Taylor 1982). The examples of natural folds described by Spratt *et al.* (2004) are long wavelength compared to the intra-unit folds in the basal formations of the MFTB, and most appear

to be fault related, unlike the small-scale folds in the models. Most of the mesoscale folds seen in the MFTB are buckles without ties to specific faults.

There are several possible reasons for the stark difference in structural style of the two fold–thrust belts. First, the presence of two carbonate platforms within the MFTB may have inhibited the development of long thrust slices and the large displacements associated with them. These two stiff platforms would have tended to localize deformation along their margins and inhibited large displacement thrusting. Second, the MFTB does not possess the equivalent of the extensive competent lithological units in the CRMFTB that provided stiffness to the sequence and resistance to internal buckling. In the CRMFTB the carbonates of the Devonian Palliser and Mississippian Rundle Group, sandwiching the shale-dominated Banff Formation, are generally considered to have formed a stiff beam that controlled thrust spacing and major folds (Currie *et al.* 1962; Spratt *et al.* 2004). If that was the case, it is unclear why the more anisotropic units in this package and in units above and below it, did not develop meso-scale buckle folds of the kind seen in the MFTB and, allowing for scaling to bed thickness, in the analog models of Dixon (2004) and Spratt *et al.* (2004). Third, the wedge geometry may have had an influence. In thin wedges with low taper angles there is less opportunity for thrust slices with long aspect ratios to develop. This is nicely shown in analog models. For example, in the sandbox models of Huiqi *et al.* (1992), the aspect ratio of the ‘thrust slices’ defined by shear bands in the sand increases with taper angle, which itself increases with basal friction (see Figs 7 & 8 in Huiqi *et al.* 1992). Thus the lower taper angle in the MFTB may have inhibited the development of large thrust sheets. These three factors, either separately or in combination, likely made the MFTB more susceptible to intra-formational deformation than the CRMFTB and the latter more susceptible to the development of long thrust slices and imbricate thrust faulting with large displacements and little internal deformation.

Conclusions

Variations among different fold-and-thrust belts as well as along the strike of individual belts are well documented but, with few exceptions (e.g. Spratt *et al.* 2004), the reasons for these differences have not been fully addressed systematically. By comparing and contrasting the style of deformation along two sections of the Rocky Mountain fold-and-thrust Belt we conclude that the broad geometry and structural evolution in both sections agrees with a critical wedge model. The major difference between the

two sections is the relative amount of strain accommodated by slip along regional scale thrust faults (Southern Canadian Rocky Mountains) compared with the strain associated with internal deformation within the thrust sheets themselves (Mexican Fold–Thrust Belt).

The variation of internal deformation across the Mexican fold-and-thrust Belt is associated with the spatial distribution of carbonate platforms and intervening basinal sequences resulting in the juxtaposition of massively bedded and thinly bedded limestone packages whose response to shortening is markedly different. The anisotropy of the latter is such that the development of mesoscale buckling instabilities is widespread and shortening is preferentially accommodated by internal folding. The more competent and more massively bedded units apparently favor the development of longer wavelength thrusting instabilities. The relative lack of meso-scale buckle folds in the Southern Canadian Rocky Mountain section, despite the existence of thinly bedded limestone packages that would favor their development, may be due to the shielding effect of an effectively stiff carbonate-dominated unit in the central part of the section.

Whether these differences in tectonic style are related to the taper angle of the critical wedge is unclear, although numerical and analogue modeling suggests that wedges with more taper tend to develop larger thrust sheets, which is in agreement with our observations. Considering a tectonic wedge of a given lithology, friction along the basal *décollement* is directly related to the taper of the wedge, with higher angles resulting from higher values of basal friction. Thus, thin wedges with low taper angles favor internal deformation of thrust slices while thicker wedges accommodate strain by the imbrication of thrust sheets along regional thrusts with little or no internal deformation.

The authors thank CONACyT, the Universidad Nacional Autónoma de México (PAPIIT grant 1210063) and the University of Minnesota for financial support to help carry out this research. They also sincerely thank B. Ortega, A. Serrano and D. Bolaños for their support during field work and for the information they have provided in the course of carrying out their graduate research. We thank P. Simony for sharing with us some of his extensive knowledge of the Canadian Rockies, but any misinterpretations of the geology are entirely ours. D. Spratt and J. Poblet provided most helpful reviews that have led to significant improvements in the manuscript.

References

- ALLMENDINGER, R. W., BREWER, J. A., BROWN, L. D., KAUFMAN, S., OLIVER, J. E. & HOUSTON, R. S. 1982. COCORP profiling across the Rocky Mountain Front

- in southern Wyoming; Part 2, Precambrian basement structure and its influence on Laramide deformation. *Geological Society of America Bulletin*, **93**, 1253–1263.
- ANDERSON, T. H. & SILVER, L. T. 2005. The Mojave–Sonora Megashield; field and analytical studies leading to the conception and evolution of the hypothesis. *Geological Society of America, Special Paper*, **393**, 1–50.
- ARMSTRONG, R. L. 1968. Sevier orogenic belt in Nevada and Utah. *Geological Society of America Bulletin*, **79**, 429–458.
- ARMSTRONG, R. L. 1974. Magmatism, orogenic timing, and orogenic diachronism in the Cordillera from Mexico to Canada. *Nature*, **247**, 348–351.
- BALLY, A. W., GORDY, P. L. & STEWART, G. A. 1966. Structure, seismic data, and orogenic evolution of southern Canadian Rocky Mountains. *Bulletin of Canadian Petroleum Geology*, **14**, 337–381.
- BIOT, M. A. 1965. Theory of viscous buckling and gravity instability of multilayers with large deformation. *Geological Society of America Bulletin*, **76**, 371–378.
- BOYER, S. E. & ELLIOTT, D. 1982. Thrust systems. *AAPG Bulletin*, **66**, 196–1230.
- BREWER, J. A., ALLMENDINGER, R. W., BROWN, L. D., OLIVER, J. E. & KAUFMAN, S. 1982. COCORP profiling across the Rocky Mountain Front in southern Wyoming; Part 1, Laramide structure. *Geological Society of America Bulletin*, **93**, 1242–1252.
- CAMPA-URANGA, M. F. 1983. The tectonostratigraphic terranes and the thrust belt in Mexican territory. *Stanford University Publications, Geological Sciences*, **18**, 44–46.
- CANT, D. J. & STOCKMAL, G. D. 1999. A field guide to portions of the Jurassic Fernie–Kootenay Trans-Canada Highway section, Banff, Alberta; new sedimentological and structural observations and interpretations. *Bulletin of Canadian Petroleum Geology*, **47**, 1–18.
- CARRILLO-MARTÍNEZ, M. 1989. Structural analysis of two juxtaposed Jurassic lithostratigraphic assemblages in the Sierra Madre Oriental fold belt of central Mexico. *Geofísica Internacional*, **28–5**, 1007–1028.
- CARRILLO-MARTÍNEZ, M. 1990. Geometría estructural de la Sierra Madre Oriental entre Peñamiller and Jalpan, Estado de Querétaro. *Revista del Instituto de Geología, UNAM*, **8**, 62–70.
- CARRILLO-MARTÍNEZ, M. 1997. Hoja Zimapán 14Q-e(7); resumen de la geología de la hoja Zimapán, estados de Hidalgo y Querétaro. *Carta Geológica de Mexico, Serie de 1:100 000*, **24**, 1–32.
- CARRILLO-MARTÍNEZ, M., VALENCIA, J. J. & VÁZQUEZ, M. E. 2001. Geology of the southwestern Sierra Madre Oriental fold-and-thrust belt, east-central Mexico; a review. *AAPG Memoir*, **75**, 145–158.
- CHAPPLE, W. M. 1978. Mechanics of thin-skinned fold-and-thrust belts. *Geological Society of America Bulletin*, **89**, 1189–1198.
- CHÁVEZ-CABELLO, G., ARANDA-GÓMEZ, J. J., GARZA-MOLINA, R. S., COSSIO-TORRES, T., ARVIZU-GUTIÉRREZ, I. R. & GONZÁLEZ-NARANJO, G. A. 2007. The San Marcos Fault; a Jurassic multireactivated basement structure in northeastern Mexico. *Geological Society of America, Special Paper*, **422**, 261–286.
- COBBOLD, P. R., COSGROVE, J. W. & SUMMERS, J. M. 1971. Development of internal structures in deformed anisotropic rocks. *Tectonophysics*, **12**, 23–53.
- CONTRERAS, J. & SUTER, M. 1990. Kinematic modeling of cross-sectional deformation sequences by computer simulation. *Journal of Geophysical Research*, **95**, 21 913–21 929.
- CURRIE, J. B., PATNODE, H. W. & TRUMP, R. P. 1962. Development of folds in sedimentary strata. *Geological Society of America Bulletin*, **73**, 655–674.
- DAHLEN, A. 1990. Critical taper model of fold and thrust belts and accretionary wedges. *Annual Reviews Earth Planetary Sciences*, **18**, 55–99.
- DAHLEN, A., SUPPE, J. & DAVIS, D. 1984. Mechanics of fold-and-thrust belts and accretionary wedges: cohesive Coulomb Theory. *Journal of Geophysical Research*, **89**, 10 087–10 101.
- DAHLSTROM, C. D. A. 1969. Balanced cross sections. *Canadian Journal of Earth Sciences*, **6**, Part 1, 743–757.
- DAHLSTROM, C. D. 1970. A structural geology in eastern margin of Canadian Rocky Mountains. *The American Association of Petroleum Geologists Bulletin*, **54**, 843.
- DAVIS, D., SUPPE, J. & DAHLEN, F. A. 1983. Mechanics of fold-and-thrust belts and accretionary wedges. *Journal of Geophysical Research*, **88**, 1153–1172.
- DECELLES, P. G. 2004. Late Jurassic to Eocene evolution of the Cordilleran thrust belt and foreland basin system, western USA. *American Journal of Science*, **304**, 105–168.
- DECELLES, P. G., GRAY, M. B., RIDGWAY, K. D., COLE, R. B., PIVNIK, D. A., PEQUERA, N. & SRIVASTAVA, P. 1991. Controls on synorogenic alluvial-fan architecture, Beartooth Conglomerate (Palaeocene), Wyoming and Montana. *Sedimentology*, **38**, 567–590.
- DECELLES, P. G., LAWTON, T. F. & MITRA, G. 1995. Thrust timing, growth of structural culminations, and synorogenic sedimentation in the type Sevier orogenic belt, Western United States. *Geology (Boulder)*, **23**, 699–702.
- DICKINSON, W. R., KLUTE, M. A., HAYES, M. J., JANECKE, S. U., LUNDIN, E. R., MCKITTRICK, M. A. & OLIVARES, M. D. 1988. Paleogeographic and paleotectonic setting of Laramide sedimentary basins in the central Rocky Mountain region. *Geological Society of American Bulletin*, **100**, 1023–1039.
- DIXON, J. M. 2004. Physical (centrifuge) modeling of fold–thrust shortening across carbonate bank margins – timing, vergence, and style of deformation. In: McCLAY, K. R. (ed.) *Thrust tectonics and hydrocarbon systems*. AAPG Memoir, **82**, 223–238.
- DIXON, J. M. & LIU, S. 1992. Centrifuge modelling of the propagation of thrust faults. In: McCLAY, K. R. (ed.) *Thrust Tectonics*. Chapman & Hall, London, 53–69.
- EGUILUZ, S., ARANDA-GÓMEZ, M. & MARRET, R. 2000. Tectónica de la Sierra Madre Oriental, México. *Boletín de la Sociedad Geológica Mexicana*, **LIII**, 1–26.
- ELLIOTT, D. 1976. The energy balance and deformation mechanisms of thrust sheets. *Philosophical Transactions of the Royal Society of London*, **283**, 289–312.
- EVENCHICK, C. A., MCMECHAN, M. E., MCNICOLL, V. J. & CARR, S. D. 2007. A synthesis of the Jurassic–Cretaceous tectonic evolution of the central and south-eastern Canadian Cordillera; exploring links across the

- orogen. *Geological Society of America, Special Paper*, **433**, 117–145.
- FEINSTEIN, S., KOHN, B., OSADETZ, K. & PRICE, R. A. 2007. Thermochronometric reconstruction of the pre-thrust paleogeothermal gradient and initial thickness of the Lewis thrust sheet, southeastern Canadian Cordillera foreland belt. *Geological Society of America, Special Paper*, **433**, 167–182.
- GABRIELSE, H. & TAYLOR, G. C. 1982. *Geological maps and cross sections of the northern Canadian Cordillera from southwest of Fort Nelson, British Columbia to Gravina Island, southeastern Alaska*. Open-File Report 864, Geological Survey of Canada.
- GORGIS, S., MCCLELLAND, W., FAYON, A., SINGER, B. S. & TIKOFF, B. 2008. Timing of deformation and exhumation in the western Idaho shear zone, mccall, Idaho. *Geological Society of America Bulletin*, **120**, 119–1133.
- GRAY, G. G., POTTORF, R. J., YUREWICZ, D. A., MAHON, K. I., PEVEAR, D. R. & CHUCHLA, R. J. 2001. Thermal and chronological record of syn-to-post-Laramide burial and exhumation, Sierra Madre Oriental, Mexico. *AAPG Memoir*, **75**, 159–181.
- HERNÁNDEZ-JÁUREGUI, R. 1997. *Sedimentación Sintectónica de la Formación Soyatal (Turoniano Medio-Campaniano) y Modelado Cinemático de la Cuenca de Flexura de Maconí, Querétaro-Syntectonic sedimentation of Soyatal Formation (Middle Turonian-Campanian) and kinematic modeling the Maconí Flexural Basin, Querétaro*. MSc thesis, Instituto Politécnico Nacional, ESIA.
- HOSSACK, J. R. 1979. The use of balanced cross-sections in the calculation of orogenic contraction: a review. *Journal of the Geological Society, London*, **136**, 705–711.
- HUIQI, L., MCCLAY, K. R. & POWELL, D. 1992. *Physical models of thrust wedges*. In: MCCLAY, K. R. (ed.) *Thrust Tectonics*. Chapman & Hall, London, 71–81.
- IMLAY, R. W. 1944. Correlations of the Cretaceous Formations of the Greater Antillas, Central America, and Mexico. *Bulletin of the Geological Society of America*, **55**, 1005–1046.
- JOHNSON, A. M. & FLETCHER, R. C. 1994. *Folding of Viscous Layers*. Columbia University Press, New York.
- LAWTON, T. F. & TREXLER, J. H. 1991. Piggyback basin in the Sevier orogenic belt, Utah; implications for development of the thrust wedge. *Geology (Boulder)*, **19**, 827–830.
- LEBEL, D., LANGENBERG, W. & MOUNTJOY, E. W. 1996. *Structure of the central Canadian Cordilleran thrust-and-fold belt, Athabasca-Brazeau area, Alberta; a large, complex intercutaneous wedge*. *Bulletin of Canadian Petroleum Geology*, **44**, 282–298.
- LÓPEZ-OLIVA, J. G., KELLER, G. & STINNESBECK, W. 1998. El límite Cretácico/Terciario (K/T) en el noreste de México; extinción de foraminíferos planctónicos. The Cretaceous–Tertiary boundary in northeastern Mexico; extinction of planktonic Foraminifera. *Revista Mexicana de Ciencias Geológicas*, **15**, 109–113.
- LÓPEZ-RAMOS, E. 1983. Estratigrafía Cretácica y tectónica de una porción del centro y noreste de México. Cretaceous stratigraphy and tectonics of a portion of the central and northeast of Mexico. *Boletín de la Sociedad Geológica Mexicana*, **44**, 21–31.
- MACKEY, P. A. 1996. The Highwood Structure; a tectonic wedge at the foreland edge of the southern Canadian Cordillera. *Bulletin of Canadian Petroleum Geology*, **44**, 215–232.
- MAGOON, L. B., HUDSON, T. L. & COOK, H. E. 2001. *Pimienta-Tamabra(!); a giant supercharged petroleum system in the southern Gulf of Mexico, onshore and offshore Mexico*. *AAPG Memoir*, **75**, 83–125.
- MCCLAY, K. R. (ed.) 1992. *Thrust Tectonics*. Chapman & Hall, London.
- NURKOWSKI, J. R. 1984. Coal quality, coal rank variation and its relation to reconstructed overburden, Upper Cretaceous and Tertiary plains coals, Alberta, Canada. *AAPG Bulletin*, **68**, 285–295.
- PRICE, R. A. 1981. The Cordilleran foreland thrust and fold belt in the southern Canadian Rocky Mountains. In: MCCLAY, K. R. & PRICE, N. J. (eds) *Thrust and Nappe Tectonics*. Geological Society, London, Special Publications, **9**, 427–448.
- PRICE, R. A. 2001. An evaluation of models for the kinematic evolution of thrust and fold belts; structural analysis of a transverse fault zone in the Front Ranges of the Canadian Rockies north of Banff, Alberta. *Journal of Structural Geology*, **23**, 1079–1088.
- PRICE, R. A. & FERMOR, P. R. 1985. Structure section of the Cordilleran Foreland thrust and fold belt west of Calgary, Alberta. *Geological Survey of Canada*, **84–14**, 1 sheet.
- RAMOS-VELÁZQUEZ, E., CALMUS, T., VALENCIA, V., IRIONDO, A., VALENCIA-MORENO, M. & BELLON, H. 2008. U/Pb and (super 40) Ar/ (super 39) Ar geochronology of the Coastal Sonora Batholith; new insights on Laramide continental arc magmatism. *Revista Mexicana de Ciencias Geológicas*, **25**, 314–333.
- ROSALLES-LAGARDE, L., CENTENO-GARCIA, E., DOSTAL, J., SOUR-TOVAR, F., OCHOA-CAMARILLO, H. & QUIROZ-BARROSO, S. 2005. The Tuzancoa Formation; evidence of an Early Permian submarine continental arc in east-central Mexico. *International Geology Review*, **47**, 901–919.
- SCHMID, D. W. & PODLADCHIKOV, Y. Y. 2006. Fold amplification rates and dominant wavelength selection in multilayer stacks. *Philosophical Magazine*, **86**, 3409–3423.
- SCHMIDT, C. J., CHASE, R. B. & ERSLEV, E. A. 1993. Laramide basement deformation in the Rocky Mountain foreland of the Western United States. *Geological Society of America, Special Paper*, **280**, 1–365.
- SCOTSE, C. & GOLONKA, J. 1992. *PALEOMAP Paleogeographic Atlas, PALEOMAP*. Progress Report No. 20, Department of Geology, University of Texas at Arlington, Arlington, Texas.
- SELTING, A. J. & SCHMITT, J. G. 1999. Carbonate sedimentation in a foreland basin lake system, Upper Cretaceous Beaverhead Group, Southwest Montana. *AAPG Bulletin*, **83**, 1188.
- SLOTBOOM, R. T., LAWTON, D. C. & SPRATT, D. A. 1996. Seismic interpretation of the triangle zone at Jumping Pound, Alberta. *Bulletin of Canadian Petroleum Geology*, **44**, 233–243.
- SOLUM, J. S. & VAN DER PLUJM, B. A. 2007. Reconstructing the Snake River-Hoback River Canyon section of the Wyoming thrust belt through direct dating of

- clay-rich fault rocks. *Geological Society of America, Special Paper*, **433**, 183–196.
- SOULE, G. S. & SPRATT, D. A. 1996. En echelon geometry and two-dimensional model of the triangle zone, Grease Creek Syncline area, Alberta. *Bulletin of Canadian Petroleum Geology*, **44**, 244–257.
- SPRATT, D. A., DIXON, J. M. & BEATTIE, E. T. 2004. Changes in structural style controlled by lithofacies contrast across transverse carbonate bank margins; Canadian Rocky Mountains and scaled physical models. *AAPG Memoir*, **82**, 259–275.
- SPRATT, D. A. & LAWTON, D. C. 1996. Variations in detachment levels, ramp angles and wedge geometries along the Alberta thrust front. *Bulletin of Canadian Petroleum Geology*, **44**, 313–323.
- SPRATT, D. A., LAWTON, D. C. & MACKAY, P. A. 1993. The Triangle Zone and Turner Valley Structure west of Calgary, Alberta. *Geological Association of Canada Field Trip A-1 Guidebook*, **41**.
- STOCKMAL, G. S., BEAUMONT, C., NGUYEN, M. & LEE, B. 2007. Mechanics of thin-skinned fold and thrust belts; insights from numerical models. *Geological Society of America, Special Paper*, **433**, 63–98.
- STOCKMAL, G. S., MACKAY, P. A., LAWTON, D. C. & SPRATT, D. A. 1996. The Oldman triangle zone: a complicated tectonic wedge delineated by new structural mapping and seismic interpretation. *Bulletin of Canadian Petroleum Geology*, **44**, 202–214.
- STOCKMAL, G. S., McMECHAN, M. E., LEBEL, D. & MACKAY, P. A. 2001. Structural style and evolution of the triangle zone and external foothills, southwestern Alberta; implications for thin-skinned thrust-and-fold belt mechanics. *Bulletin of Canadian Petroleum Geology*, **49**, 472–496.
- SUPPE, J. 1983. Geometry and kinematics of fault-bend folding. *American Journal of Science*, **283**, 684–721.
- SUTER, M. 1980. Tectonics of the external part of the Sierra Madre Oriental foreland thrust and fold belt Between Xilitla and the Moctezuma River (Hidalgo and San Luis Potosí states). *UNAM, Revista del Instituto de Geología*, **4**, 19–31.
- SUTER, M. 1984. Cordilleran deformation along the eastern edge of the Valles-San Luis Potosí carbonate platform, Sierra Madre Oriental thrust and fold belt, east-central Mexico. *Geological Society of America Bulletin*, **95**, 1387–1397.
- SUTER, M. 1987. Structural traverse across the Sierra Madre Oriental fold–thrust belt in east-central Mexico. *Geological Society of America Bulletin*, **98**, 249–264.
- SYDNEY, P. C. JR. 1966. *Handbook of Physical Constants*. Revised edn. Geological Society of America, Memoir, **97**, 587.
- THOMPSON, R. I. 1979. A Structural interpretation across a part of the northern Rocky Mountains, British Columbia, Canada. *Canadian Journal of Earth Sciences*, **6**, 1228–1241.
- THOMPSON, R. I. 1981. The nature and significance of large ‘blind’ thrusts within the northern Rocky Mountains of Canada. In: McCLAY, K. R. & PRICE, N. J. (eds) *Thrust and Nappe Tectonics*. Geological Society, London, Special Publications, **9**, 449–462.
- VAN DER PLUIJM, B. A., VROLIJK, P. J., PEVEAR, D. R., HALL, C. M. & SOLUM, J. 2006. Fault dating in the Canadian Rocky Mountains: evidence for late Cretaceous and early Eocene orogenic pulses. *Geology*, **34**, 837–840.
- WILKERSON, M. S., APOTRIA, T. & FARID, T. 2002. Interpreting the geologic map expression of contractional fault-related fold terminations; lateral/oblique ramps v. Displacement gradients. *Journal of Structural Geology*, **24**, 593–607.
- YONKEE, W. A. 1992. Basement-cover relations, Sevier orogenic belt, northern Utah. *Geological Society of America Bulletin*, **104**, 280–302.

Hinterland-foreland zonation of the Variscan orogen in the Central Pyrenees: comparison with the northern part of the Iberian Variscan Massif

J. GARCÍA-SANSEGUNDO^{1*}, J. POBLET¹, J. L. ALONSO¹ & P. CLARIANA²

¹*Departamento de Geología, Universidad de Oviedo, C/Jesús Arias de Velasco s/n, 33005 Oviedo, Spain*

²*Instituto Geológico y Minero de España, La Calera, Tres Cantos, Madrid, Spain*

**Corresponding author (e-mail: jgsanseg@geol.uniovi.es)*

Abstract: A new sequence of Variscan deformations is proposed for the Palaeozoic rocks of the Central Pyrenees. The non-metamorphic units include south-directed thrust systems and related folds with a poorly developed cleavage. In the metamorphic units north-verging, recumbent to inclined folds (D1), associated with a subhorizontal to south dipping cleavage, are refolded by south-verging, upright to inclined folds (D2), with a subvertical to north-dipping axial plane cleavage, and offset by south-directed thrusts approximately coeval with D2. The structural evolution of these units suggests a subdivision of the Variscan Central Pyrenees into two different regions consistent with the zones known for a long time in the core of the Ibero-Armorican or Asturian arc (northern part of the Iberian Variscan Massif). The structure of the Pyrenean non-metamorphic units has foreland affinities and is comparable to that of the Cantabrian Zone, whereas the deformation observed in the Pyrenean metamorphic units is characteristic of the hinterland and is consistent with the features of the West Asturian–Leonese Zone or Central–Iberian Zone. Since the Pyrenean non-metamorphic units are located southwards of the metamorphic ones and the Variscan thrusts are south-directed, we tentatively correlate the Variscan Pyrenees with the northern branch of the Ibero-Armorican or Asturian arc.

The Pyrenees are an ESE–WNW-trending, Alpine cordillera that resulted from collision between the Iberian and Euro-Asian plates from Late Cretaceous–Early Miocene. The collision induced tectonic inversion of previous Permian–Mesozoic extensional basins and incorporated Palaeozoic basement rocks in some Alpine thrust sheets. The resulting cordillera is an asymmetrical, double-verging belt consisting of large outcrops of Mesozoic and Cenozoic rocks deformed by mainly north-directed structures in the north part of the belt and involved in principally south-directed structures in the southern part of the cordillera, separated by a large strip of Palaeozoic rocks in the core of the Pyrenees (Seguret 1972, amongst others). The Pyrenees have been traditionally divided into the eastern, central and western Pyrenees, but the Alpine age structures mapped at surface, subsurface and offshore, enabled the identification of the western prolongation of the Pyrenean Chain along the onshore and offshore part of the north Atlantic margin of the Iberian Peninsula from the Basque–Cantabrian Basin to the Cantabrian Mountains (Alonso *et al.* 1996, amongst others).

The first systematic studies of the Palaeozoic rocks of the Central Pyrenees were conducted during the sixties and seventies by geologists of

Leiden University, The Netherlands (see Zwart 1979, and references therein) (Fig. 1). These studies provided a large number of geological maps and cross sections, and a great deal of stratigraphic, palaeontological, petrological and structural data. Since then, various aspects of the structures of the Palaeozoic rocks of the central Pyrenees and their origin have been a matter of debate between geologists from different schools. One of the most controversial aspects is the succession of deformation events proposed. Although most authors accept that the Variscan orogeny gave rise to a polyphase deformation and that some of the structures recognized in the Palaeozoic rocks were formed during the superimposed Alpine orogeny, the described features and order of the different deformation phases identified are extremely variable (e.g. Zwart 1960, 1964, 1968, 1979, 1981, 1986; Seguret & Proust 1968*a, b*; Matte 1969; Clin *et al.* 1970; Muller & Roger 1977; Soula 1982; Soula *et al.* 1986; Vissers 1992). Another major topic of debate concerns the occurrence of two structural domains, called ‘infrastructure’ and ‘suprastructure’, distinguished by their metamorphic grade and by the attitude of the main cleavage (Fig. 2). Most authors agree that the main cleavage has a flat-lying attitude and it is usually associated

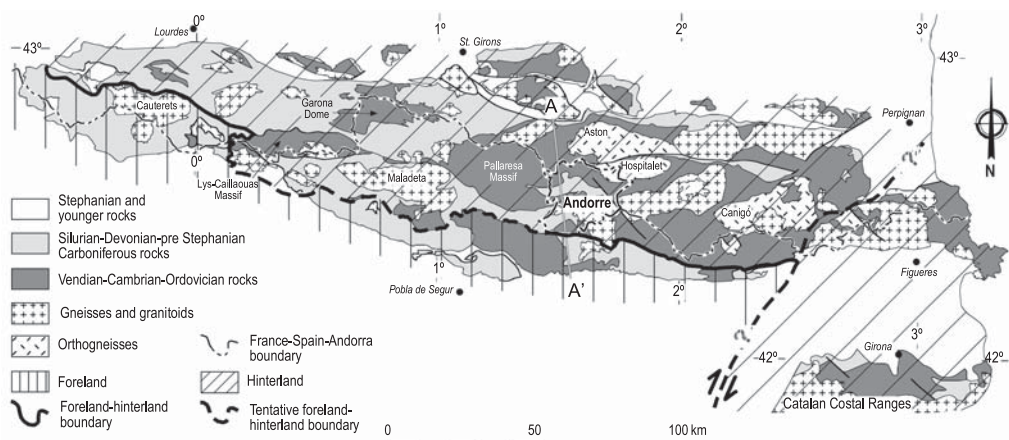


Fig. 1. Geological map of the Palaeozoic rocks of the Pyrenees showing the boundary between non-metamorphic regions to the south (foreland) and metamorphic regions to the north (hinterland). The occurrence of metamorphic Palaeozoic rocks in the north part of the Catalan Coastal Ranges may be tentatively explained by a kilometre-scale NE–SW fault located in the eastern part of the Pyrenees. A–A' geological cross-section illustrated in Figure 2.

with high temperature metamorphism in the 'infra-structure', whereas the cleavage is subvertical and was generated in low grade metamorphic conditions in the 'suprastructure', though the relative age and main structural features of these two structural domains has been extensively discussed (e.g. Zwart 1960, 1964, 1968, 1979, 1981, 1986; Seguret & Proust 1968*a, b*; Matte 1969; Clin *et al.* 1970; Van den Eeckhout & Zwart 1988; Vissers 1992). The last controversial matter is related to the contractional and/or extensional geodynamic settings and their relative age invoked to explain the origin of the Palaeozoic structures, sedimentation, metamorphism and magmatism in the Pyrenees (e.g. Wickham & Oxburgh 1985, 1986; Soula *et al.* 1986; Matte & Mattauer 1987; Van den Eeckhout & Zwart 1988; Pouget *et al.* 1989; Pouget 1991; Vissers 1992, 1993; Poblet & Casas 1993*a*).

In many of these studies, the Palaeozoic rocks of the Pyrenees were treated as an almost isolated massif unrelated to the Variscan orogenic system that extends all across Europe. Thus, the structural evolution, the structural domains and/or the geodynamic settings of the Variscan rocks of the Pyrennes proposed in many publications does not fit those observed in neighbouring portions of the Variscan orogenic belt, and, this lack of correspondence was hardly addressed. This aspect, together with the complex structure of the Pyrenean Palaeozoic basement resulting from the superposition of the Variscan deformation, a Mesozoic extensional event and a Tertiary contractional episode, led some authors to consider the Palaeozoic rocks of the Pyrenees as a geological anomaly, and therefore ignored it or did not attempt to correlate it with the

rest of the Variscan belt in their reconstructions of the geology during Palaeozoic times (Matte 1995, 1998, 2001 amongst many others).

Here, we propose a new sequence of Variscan deformations that has resulted from geological mapping and structural analyses for more than two decades in various regions along the central Pyrenees formed by different types of rocks of various ages and different metamorphic grades. This new structural evolution leads us to establish a zonation of this portion of the Variscan belt in two different regions, originally located in internal and external structural positions of the orogenic belt, and supplies us data to discuss the similarities and differences between some features of the Palaeozoic Pyrenean rocks and those observed in the Palaeozoic rocks that crop out in the northwest Iberian Peninsula, one of the most well known regions of the Variscan belt adjacent to the Pyrenees.

Lithostratigraphy

The main lithostratigraphic features of the Upper Proterozoic and Palaeozoic rocks that crop out in the Central Pyrenees (Fig. 1) are briefly described below. Although some stratigraphic units have been given different names in the literature, only the most accepted ones will be used in the summary below.

Vendian (Proterozoic)–Cambrian–early Ordovician

Pre-Upper Ordovician rocks consist mainly of a siliciclastic succession without fossil remains. In this

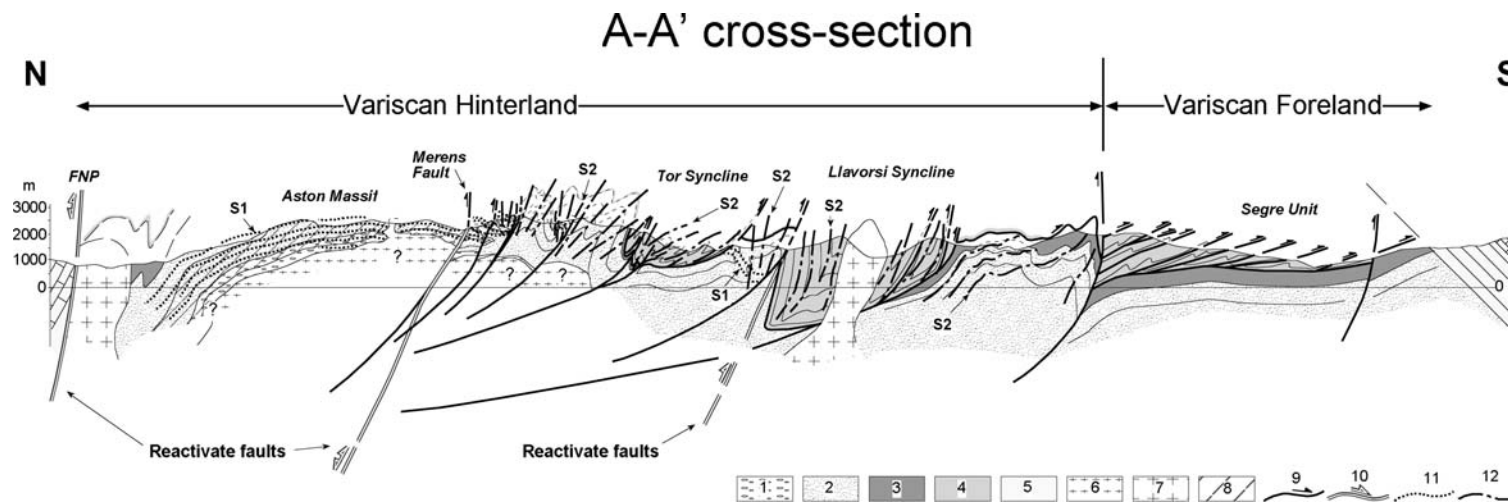


Fig. 2. Geological section across the Palaeozoic rocks of the Pyrenees showing the main Variscan structures and the Foreland–Hinterland boundary. 1, Lower Ordovician orthogneisses; 2, Pre-Upper Ordovician metasedimentary rocks; 3, Upper Ordovician rocks; 4, Silurian, Devonian and pre-Stephanian Carboniferous rocks; 5, Mesozoic rocks; 6, Synorogenic Variscan granitoids; 7, Late-Variscan granitoids; 8, Amphibolitic Variscan metamorphism; 9, Variscan thrusts; 10, Alpine thrusts; 11, S1 cleavage or schistosity; 12, S2 cleavage. The section is located in Figure 1. The geological cross-section is constructed using data from Zwart (1979), Casas *et al.* (1989), Poblet (1991) and Clariana & García-Sansegundo (2009).

section we will follow Cavet’s (1951, 1957, 1958) stratigraphic subdivisions (Table 1). The Canaveilles Group is the oldest stratigraphic unit and is a schist-greywacke sequence with intercalated limestone and volcanic rocks. The base of this group was dated as 580 Ma (Vendian age) using U–Pb radiometric data from zircons (Laumonier *et al.* 2004). In the Eastern Pyrenees, metavolcanic and plagioclastic gneisses coeval with sedimentary rocks have been dated by U–Pb as 580–540 Ma in age (Castiñeiras *et al.* 2008). The Jujols Group, assigned to the Cambrian and Early–Middle Ordovician (Laumonier *et al.* 2004), is basically an alternation of slates, sandstones and quartzites; its base is formed by two slate and sandstone olistostromes (Tregura Formation), whereas its top, when preserved underneath the Upper Ordovician unconformity, includes a slate succession (Poblet 1991). A limestone level intercalated within the Jujols Group called Lladore, Bentaillou, Boums, etc. divides the Jujols Group into lower and upper Jujols. Within the

Cambrian–Ordovician metasediments, orthogneiss bodies cropping out in the Aston, Hospitalet, Canigó, Nuria, and other massifs intruded during the Early Ordovician (Laumonier *et al.* 2004). Castiñeiras *et al.* (2008) dated these laccoliths of aluminous granitic orthogneisses as 475–460 Ma.

Late Ordovician

Upper Ordovician rocks lie unconformably on older Cambrian–Ordovician beds (Llopis 1965; Santanach 1972; Muñoz & Sàbat 1981; Laumonier & Guitard 1986; García-Sansegundo & Alonso 1989; Kriegsman *et al.* 1989; Poblet 1991; García-Sansegundo *et al.* 2004; Casas & Fernández 2007, amongst others). The most complete Upper Ordovician succession was described by Hartevelt (1970) (Table 1). From bottom to top, the following stratigraphic units can be distinguished: (1) the Rabassa Formation characterized by conglomerates and sandstones; (2) the Cava Formation consisting of

Table 1. Stratigraphic units defined in the lower Palaeozoic of the Cantabrian Zone, West Asturian–Leonese Zone and Central Iberian Zone (Iberian Massif) and in the Central Pyrenees. OSD, Ollo de Sapo Domain

AGE			Western Cantabrian Zone (Somiedo Unit)		Westasturian Leonese Zone	Eastern Central-Iberian Zone (OSD)	Axial Zone of the central Pyrenees		U-Pb Age
SILURIAN			Formigoso Fm.		Black shales	Black shales	Black shales		
O R D O V I C I A N	Upper	Ashgill	Hiatus	Limestones	Agüeira Fm.	La Aquiana limestones	Ansovell and Bar Fms.		
		Caradoc		Castro Fm.			Estana Fm.		
							Rabasa and Cava Fms.		
	Middle	Llandeilo	Luarca Fm.	Luarca Fm.	Luarca Fm.	U p p e r J u j o l s S e r i e s	Orthogneisses of Aston, Hospitalet, Canigó, Nuria		
		Llanvirn							
	Lower	Arenig	Barrios Fm.	Los Cabos Series	Armorican quartzites				468 my
					Ollo de Sapo Orthogneisses			*	473 my
		Tremadoc						*	488 my
C A M B R I A N	Upper	Oville Fm.							
	Middle								
	Lower	Láncara Fm.	Vegadeo Fm.						Boum, Bentaillou Lladorre, Ransol Ist.
		Herrería Fm.	Cándana Fm.				Lower Jujols Series		
							Tregura Fm.		
PRECAMBRIAN			Narcea shales		Villalba shales		Canaveilles Group		* 580 my

alternating greywackes and slates with volcanic intercalations, dated as Late Caradoc–Early Ashgill on the basis of palaeontological data (Hartvelt 1970); (3) the Estana Formation formed by calcareous shales and limestones with Middle Ashgill age (Hartvelt 1970); (4) the Ansovell Formation consisting of poorly bedded dark slates with scarce siliciclastic levels; and (5) the Bar Formation consisting of quartzites. In some regions not all these formations occur, in others there are no Upper Ordovician rocks and in others the lower part of the Upper Ordovician succession is basically a package of siliciclastic levels (Massana Formation) sometimes capped by calcareous rocks of the Estana Formation.

Silurian

The Silurian is represented by black shales, with local volcano-derived bodies, that include orthoceras limestone beds in the upper part (Table 1). Based mainly on graptolites collected in the black shales this succession extends in age from Llandovery to Early Ludlow, whereas the conodonts found in the limestone beds yielded a Ludlow–Early Gedinnian (Early Devonian) age (e.g. Degardin 1988).

Devonian-pre Stephanian Carboniferous

The Devonian rocks exhibit significant facies variations across the different Pyrenean structural units (e.g. Mirouse 1966; Mey 1967, 1968; Boersma 1973; Zwart 1979; Sanz-López 2004). In outline, three main Devonian–Carboniferous domains can be distinguished (Fig. 3). The northern and eastern domain is characterized by limestones, slates and marls, the former becoming nodular limestones in the Middle and Late Devonian. This domain includes the Compte Facies, the Northern Facies and the Northpyrenean Facies defined by Zwart (1979). These Devonian rocks have been interpreted as sedimentated in a hemipelagic moderately deep platform. In the western and southern domain, the lower Devonian rocks consist of shales, marls and limestones with local intrusions of hypabyssal rocks. The limestones are usually reefal and may reach Middle Devonian age in the western Pyrenees, whereas to the east the middle Devonian is made up of black shales. Upper Devonian rocks consist of limestones. This domain includes the Sierra Negra Facies and Baliera Facies defined by Mey (1968) and has been interpreted as deposited in a shallow platform. The central domain is located in between previous domains. The lower Devonian rocks of this domain are similar to those of the western and southern domain, but the main difference is the occurrence

of a thick siliciclastic succession of Middle and Late Devonian age. This domain corresponds to the Central Facies defined by Kleinsmiede (1960) and is assumed to correspond to an elongated and depressed region within the central part of the Devonian platform filled in by turbidites.

In the western part of the study area, where the pre-Stephanian Carboniferous sequence is more complete, it is composed of a lower part characterized by nodular red limestones and cherts underlying black limestones that reach Bashkirian ages (Perret 1993). The upper part, usually known as Culm facies, deposited contemporaneously with black limestones in the Central and Western Pyrenees (Devolvé & Perret 1989), consists of a siliciclastic package (sandstones, greywackes, slates and conglomerates) in which some olistostromes composed of underlying limestones occur.

Stephanian (Carboniferous)–Autunian (Permian)

Stephanian–Autunian rocks lie unconformably over deeply eroded older rocks through a marked angular unconformity (e.g. Mirouse 1959; Van den Lingen 1960; Roger 1965; Lucas 1968; Clin *et al.* 1970; Gisbert 1981) and consist of breccias, volcanic rocks, shales, conglomerates, sandstones and some coal and limestone beds intercalated. Based on the flora assemblages found, the time span covered by these stratigraphic units ranges from Stephanian B–Late Autunian (e.g. Broutin & Gisbert 1985).

Visean (Carboniferous)–Autunian (Permian) igneous rocks

Granitoid bodies of various dimensions, giving rise to contact metamorphism aureoles around them, and related dykes of hypabyssal rocks intruded in the pre-Stephanian succession. According to the radiometric ages yielded, these bodies were emplaced approximately during a time span from Visean (oldest age in the Lys Caillaouas massif; Majoor 1988)–Gzehelian (Romer & Soler 1995)–Autunian (youngest age in the Costabona massif; Vitrac-Michard & Allègre 1975).

Tectonic evolution

Pre-Variscan (Upper Ordovician) extensional faulting and cleavage

In pre-Upper Ordovician rocks a northward dipping cleavage, unrelated to folds and not developed in younger rocks, has been observed (García-Sansegundo & Alonso 1989; García-Sansegundo *et al.* 2004; Clariana & García-Sansegundo 2009).

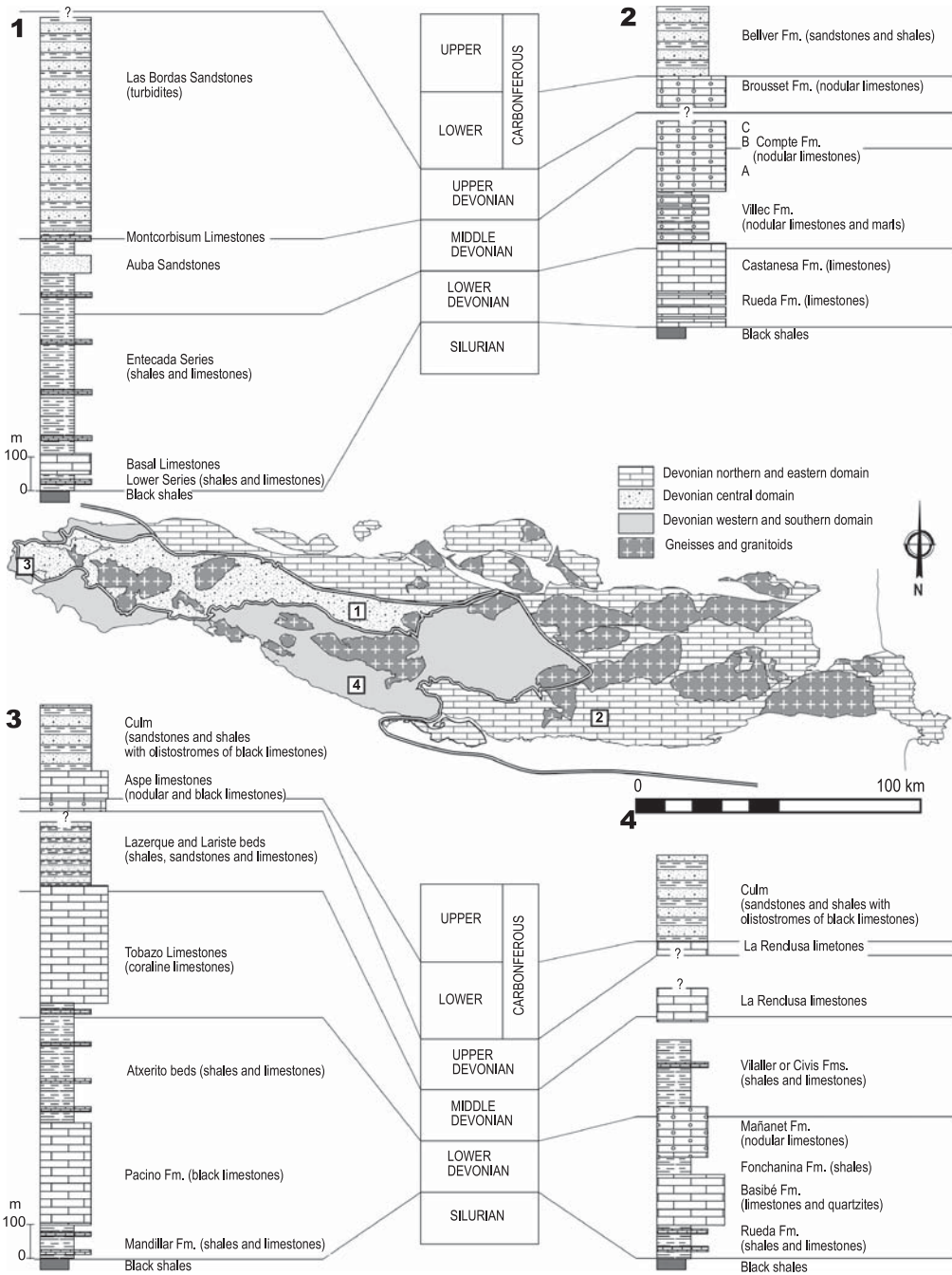


Fig. 3. Representative stratigraphic columns of the Devonian rocks of the Pyrenees. Sketch of the Palaeozoic rocks of the Central Pyrenees showing the different Devonian domains proposed here based on the observations of Mirouse (1966), Mey (1967, 1968), Boersma (1973), Zwart (1979), García-Sansegundo (1992) and Sanz-López (2004). The approximate position of the stratigraphic columns is indicated on the map using numbers.

In addition, the Upper Ordovician rocks lie unconformably on the underlying series (e.g. Llopis 1965) or they are absent in some places (Poblet 1991) and are cut and offset by some syn-sedimentary faults (Casas & Fernández 2007). This evidence of tectonic activity during Upper Ordovician times is supported by the occurrence of Upper Ordovician volcanism and ore deposits with a SEDEX origin related to an extensional regime.

Pre-Variscan (Silurian–Carboniferous) extensional faulting

Apart from the Upper Ordovician structures described above, the oldest structures recognized consist of centimetre- to kilometre-scale normal faults, causing stratigraphic omissions, offsetting infra-lower Devonian materials (e.g. Bichon 1986; Poblet & Casas 1993b). These faults might have been originated after the Late Silurian or Early Devonian (age of the youngest beds affected by the faults) and before the development of the main Variscan structures. Hypabyssal rocks intruded within Devonian rocks and affected by the main Variscan deformations support the occurrence of this extensional episode.

It is likely that the Upper Ordovician and the Silurian–Carboniferous extensional faults are tectonic evidences of the formation of the Palaeozoic sedimentary basin which later deformed during the Variscan orogeny. The initial orientation of these structures and their tectonic transport sense cannot be precisely discerned since they were strongly overprinted by younger sets of structures described below.

Variscan folding and thrusting

Two different types of structural units have been distinguished from the structural point of view; in the non-metamorphic structural units both folding and thrusting dominate and cleavage is not well developed, whereas in the metamorphic structural units metamorphism ranges from low to high grade and different generations of folds and pervasive cleavages are the most conspicuous structures accompanied by subordinate thrusting.

Non-metamorphic units. In outline, the structure of this region consists of several thrust sheets piled up (e.g. Muñoz 1985; Domingo *et al.* 1988; Casas *et al.* 1989; Poblet 1991). The thrust ramps are mainly developed within the Devonian–Carboniferous limestones, whereas the flats run along the Silurian, Devonian and Carboniferous slates (see southern part of Fig. 2). Small scale kinematic indicators, and the hanging wall and footwall ramps and flats and cut-off lines suggest a southward sense of

tectonic transport. In some regions, the movement of the lower thrust sheets causes deformation of the higher sheets, suggesting a piggy-back thrust sequence. Elsewhere some thrusts, propagated out-of-sequence, cutting and offsetting previously folded upper ones. Metre- to kilometre-scale folds with north-dipping axial planes occur and display an axial plane cleavage best developed in the slates. In some localities the cleavage is deformed by discrete shear zones in the vicinity of the thrust surfaces and some thrust surfaces cause stratigraphic omissions suggesting that thrusting post-dated folding, whereas some folds deform different thrust sheets pointing out thrusting prior to folding. These inconsistent timing relationships have been interpreted as a diagnostic feature of broadly coeval development of folds and thrusts.

Metamorphic units. First of all, two generations of folds are described below (D1 and D2) followed by a description of the thrusts (T), and eventually the temporal relationships between folds and thrusts is discussed (Fig. 4).

D1) This deformation episode consists of east–west-trending, recumbent to inclined folds that verge to the north and are developed at all scales (Casas & Poblet 1989; García-Sansegundo & Alonso 1989; Casas *et al.* 1989; Cirés *et al.* 1990; García-Sansegundo 1990, 1992, 1996; Poblet 1991; Clariana & García-Sansegundo in press) (Fig. 2). Structures possibly equivalent to the folds described here were identified by some authors in different regions of the Central Pyrenees (e.g. Zwart 1960, 1964, 1968, 1979, 1981, 1986; Seguret & Proust 1968a, b, Matte 1969; Muller & Roger 1977; Soula 1982; Soula *et al.* 1986; Clin *et al.* 1970) under the names of pre-cleavage, pre-main phase, early folds, etc. These folds are well developed and tighter in some regions in the north of the study area, where only pre-Silurian rocks affected by high grade metamorphism crop out. In these regions, D1 folds show a sub-horizontal S1 axial plane cleavage which is the main cleavage. In pre-Upper Ordovician rocks, S1 cleavage consists of a crenulation cleavage of the pre-Variscan cleavage. In low grade metamorphic regions, S1 may be absent.

D2) This deformation episode includes east–west-trending, upright to inclined folds developed from millimetre- to kilometre scale (Casas & Poblet 1989; Casas *et al.* 1989; Cirés *et al.* 1990; García-Sansegundo 1990, 1992, 1996; Poblet 1991; Clariana & García-Sansegundo 2009) (Fig. 2). These folds have been identified by all workers in the Variscan Pyrenees under different names such as main phase, main cleavage phase, etc. D2 folds verge to the south and exhibit a subvertical to moderately north dipping axial plane cleavage. D2 structures are scarce in areas composed

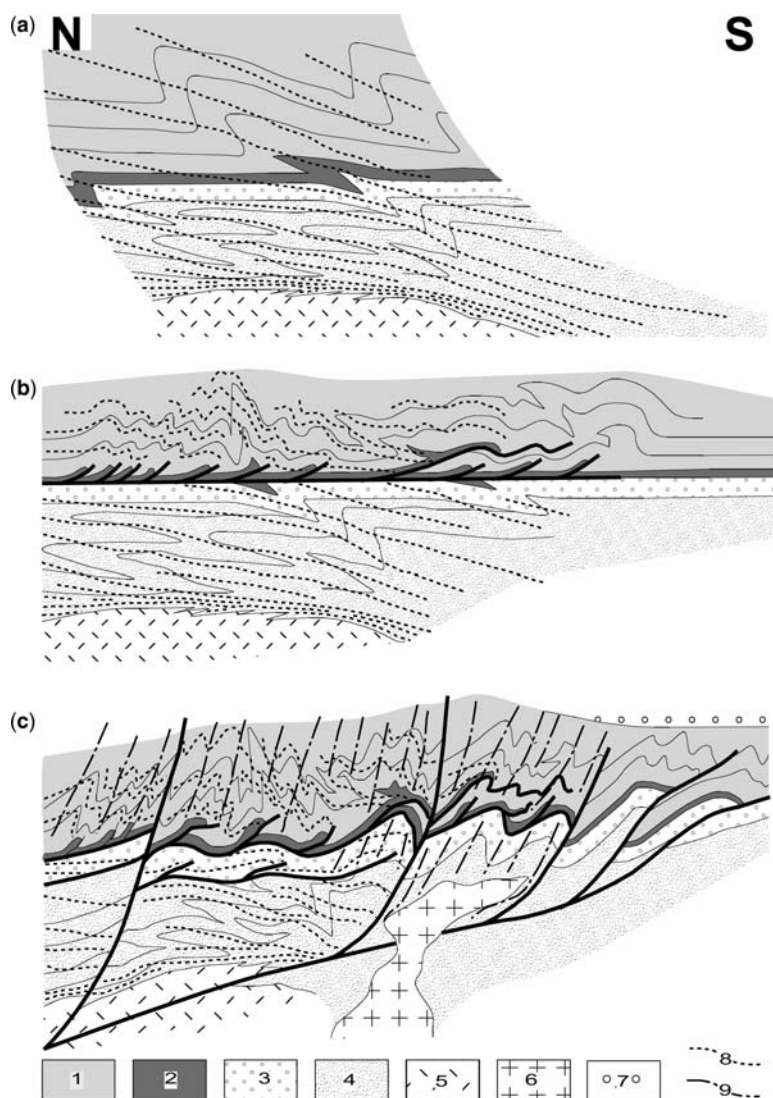


Fig. 4. Schematic evolution of the main Variscan structures involving the Palaeozoic rocks of the Pyrenean metamorphic regions. 1, Devonian-pre Stephanian Carboniferous rocks; 2, Silurian rocks; 3, Upper Ordovician rocks; 4, Vendian-Lower Ordovician rocks; 5, syn-orogenic granitoid bodies; 6, late-orogenic granitoid bodies; 7, Stephanian-Autunian rocks; 8, cleavage formed during D1; 9, cleavage formed during D2. (a) D1 north-verging folds with S1 cleavage associated and synorogenic granitoids, which deformed the S1 cleavage and produced extensional deformation around them. (b) D2 south-directed imbricate thrusts converging in the Silurian rocks and associated upright E-W folds, which deform D1 structures. (c) South-directed, out of sequence thrusts deforming previous structures and flattening D2 folds with their associated S2 cleavage. At the end of D2 episode, late granitoids intruded.

of high grade metamorphic rocks, but S2 is the main cleavage in low grade metamorphic areas. In those regions where D2 axial planes and cleavage are sub-vertical, D1 axial planes and cleavage are approximately flat-lying, whereas when D2 surfaces dip moderately towards the north, D1 surfaces dip moderately towards the south. Thus, the superposition of

D1 and D2 structures gave rise to type 3 fold interference patterns of Ramsay (1967).

T) A number of thrust faults, up to pluri-kilometre length-scale, emanate from detachment levels located in different stratigraphic positions (Mattauer *et al.* 1967; Muller & Roger 1977; Llac 1979; Majesté-Menjoulas 1982; Muñoz 1985;

Raymond 1986; Domingo *et al.* 1988; Casas & Poblet 1989; Casas *et al.* 1989; García-Sansegundo & Alonso 1989; Soliva *et al.* 1989; Cires *et al.* 1990; García-Sansegundo 1990, 1992, 1996; Poblet 1991, and many others). The recorded kinematic criteria indicate that these structures are mainly south-directed (Fig. 2). The oldest thrusts merge into detachment levels located within the Silurian slates. In some regions these thrusts are folded by east–west-trending, south-verging folds (e.g. Poblet 1991; Clariana & García-Sansegundo 2009). In other regions they are related to east–west-trending, south-verging folds, which are more abundant and show tighter geometries as they approach the thrust surfaces (e.g. Matte 1969; García-Sansegundo 1990, 1992, 1996). In other regions these thrusts offset the east–west-trending, south-verging folds and deform their associated cleavage (e.g. Casas & Poblet 1989; Casas *et al.* 1989; Poblet 1991). The youngest thrusts branch with deeper detachments located within Upper Ordovician and Cambrian–Ordovician rocks, exhibit steeper dips, are also related to east–west-trending, south-verging folds and are usually responsible for folding and/or offsetting the shallower thrusts developed in Silurian and overlying beds (e.g. García-Sansegundo 1990, 1992, 1996; Poblet 1991). The east–west-trending, south-verging folds are D2 structures, and the cross-cutting relationships between them and the thrusts have been interpreted as approximately coeval development of D2 folds and thrusts followed by subsequent flattening of D2 folds formed during the initial stages and development of new D2 folds caused by younger thrust propagation.

The fold and thrust systems described above developed during the contractional paroxysm of the Variscan orogeny and are responsible for crustal thickening of the Variscan cordillera in this region. These structures are post-dated by the late-Variscan granitoid bodies of Permian age and by the Stephanian–Autunian stratigraphic succession but involve all the underlying series. Further constraints on the age of the folds and thrusts are furnished by the intrusion of some syn-orogenic granitoids such as the Lys Caillaouas massif dated as Visean (Majoer 1988). Although some metamorphism occurred during development of D1 structures, the peak of Variscan regional metamorphism, which ranges from very low to high grade, is approximately contemporaneous with the deformation episode D2 and the south-directed thrusts.

In the metamorphic country rocks surrounding the upper parts of syn- and late-orogenic granitoid bodies, small scale folds, boudins, normal domino fault systems, stretching lineations and mylonitic normal faults are preserved. These structures, restricted to the contact metamorphic aureoles, are

evidence for local flattening of the older structures and resulted from extensional deformation conditions linked to the intrusion of these igneous masses (e.g. Zwart 1979; Poblet 1991; García-Sansegundo 1992; Mezger & Passchier 2003).

Late-Variscan and Alpine structures

All Variscan Pyrenean workers have identified several generations of structures developed after the fold and thrust episodes described above. They consist of folds with various orientations, some of them including axial plane cleavages that crenulate previous cleavages, kink-bands, faults and flattening of the rigid granitoid bodies. Although late folds and kink bands may be found in many places, in outline, they are relatively open, small scale structures responsible for gentle undulations of previous cleavages that did not cause significant modifications of the previous structural configuration, except at some scattered localities where late structures show an intense development. A similar situation occurs with respect to the faults and other structures.

Late-Variscan folding. Some of the late structures may be related to the last contractional stages of the Variscan cycle such as sets of folds developed prior to the intrusion of some late-Variscan batholiths of Permian age and their associated contact metamorphic aureole.

Late-Variscan faulting. Some faults, with a predominant normal component of displacement, exhibit evidence of syn-tectonic sedimentation and related volcanism of Stephanian–Autunian age (e.g. Gisbert 1983; Poblet 1991).

Alpine folding and thrusting. There is no doubt that some structures affecting the Palaeozoic rocks formed during the Alpine contraction of Late Mesozoic–Tertiary age that is responsible for the formation of the Pyrenean Chain. For instance, some thrusts, folds and associated crenulation cleavages affect both Palaeozoic and post-Palaeozoic rocks; some reactivated Palaeozoic faults cut and offset post-Permian rocks. In addition there is a 'progressive' tilting of the S2 cleavage from steeper attitudes to the north to gentler dips in the southern part (e.g. Zandvliet 1960) consistent with the overall geometry of the Pyrenean belt (e.g. Parish 1984).

Zonation of the Variscan Pyrenees

The structural, stratigraphic, metamorphic and magmatic features of Variscan age recognized in the Palaeozoic rocks of the Central Pyrenees allowed us to distinguish two different regions (Figs 1 & 2). In the non-metamorphic areas, the

Variscan structures consist of thrusts and thrust-related folds formed under non-metamorphic conditions, the cleavage is not very well developed and granitoid intrusions are scarce; these structural units fit in the Variscan orogen foreland. The metamorphic areas are characterized by well developed fold interference patterns, pervasive cleavages and subordinate thrusts generated under low to high grade metamorphic conditions and abundant granitoid bodies; these structural units would be located in more hinterland areas of the Variscan orogen.

In the eastern part of the Central Pyrenees, the boundary between the foreland and hinterland regions would correspond to Variscan, Alpine and Variscan thrusts partially reactivated during Alpine times (e.g. Casas *et al.* 1989, Poblet 1991), whereas in the western part of the Central Pyrenees, this boundary would be marked by Variscan thrusts, mapped by Majesté-Menjoulas (1979) north of Cauterets Massif, probably reactivated during the Alpine contractional event.

According to the present-day distribution, the regions with affinities to the Variscan foreland (non-metamorphic) are located to the south of the hinterland regions (metamorphic). The position of part of the non-metamorphic and metamorphic regions prior to the Alpine deformation has been a matter of debate; thus, some authors place some non-metamorphic regions (the structural unit called Noguères Zone) north of their present-day position but suggest that the relative position of the non-metamorphic and metamorphic regions remained constant (e.g. Seguret 1969, 1972; Zwart 1979, 1986), whereas others point out that part of the non-metamorphic regions were located to the north of some metamorphic regions before Alpine thrusting (e.g. Muller & Roger 1977; McClelland & McCaig 1988; Bates 1989; Casas *et al.* 1989; Muñoz 1992). The evidence used to support the different hypotheses are mainly based on comparisons of the Devonian stratigraphy in the non-metamorphic and metamorphic regions and the occurrence of faults within the metamorphic units in which the non-metamorphic units could be rooted, but, from our point of view, none of them are conclusive. Since the Pyrenean Variscan thrusts are south-directed it is likely that the non-metamorphic units were all together located southwards of all the metamorphic units during Variscan times rather than metamorphic regions surrounded northwards and southwards by non-metamorphic regions and vice versa. This hypothesis is based on the fact that in most cordilleras the thrusts motion is foreland-directed and assumes minimum shortening and no structural inversions.

Before the Alpine contraction, an extensional event of Permian–Cretaceous age, responsible for the rotation of Iberia and opening of the Bay of

Biscay, took place. According to the crustal scale sections across the Central Pyrenees (e.g. Coward & Dietrich 1989; Roure *et al.* 1989; Choukroune *et al.* 1990; Mattauer 1990; Muñoz 1992; Teixell 1998), the relative position of the different Variscan blocks was not modified during this event.

Pre-Devonian rocks exhibit approximately constant facies all along the Pyrenees whereas Devonian rocks vary as described above. The distribution of the Pyrenean Devonian facies suggests that their present-day palaeogeographic boundaries are oblique to the strike of the main Variscan structures (Fig. 3). From the sedimentological point of view, the shallowest Devonian facies are located in the southwestern part of the Pyrenees, which would be in accordance with a hinterland region located towards the NE.

Comparison of the Variscan Pyrenees and the Iberian Variscan Massif

The north portion of the Iberian Variscan Massif exposed in the NW Iberian Peninsula exhibits a tight oroclinal pattern in map view known as the Ibero-Armorican or Asturian arc (e.g. Lotze 1945; Julivert *et al.* 1972). The inner core of the arc is formed by regions initially located in the most external parts of the belt, that is, the foreland, whereas the outer part of the arc consists of hinterland regions (Fig. 5). In the northern branch of the arc, foreland zones occur south of hinterland ones, whereas in the southern branch of the arc, the foreland is located northwards with respect to the hinterland. The zonation of the Variscan orogen in the Central Pyrenees proposed here (foreland southwards of the hinterland) would enable it to be correlated westwards with the north branch of the Ibero-Armorican or Asturian Arc, as suggested by Matte (1986) and Julivert & Martínez (1983), rather than with the core of the arc (e.g. Ellenberger & Tamain 1980; Martínez-García 2006). According to this correlation the Pyrenean Variscan foreland should be equivalent somehow to the westernmost Cantabrian Zone (Variscan foreland in the Iberian Variscan Massif) (e.g. Julivert 1971, 1979, 1981, 1983a; Savage 1979, 1981; Pérez-Estaún *et al.* 1988, 1991; Pérez-Estaún & Bastida 1990; Alonso & Pulgar 1995; Bastida *et al.* 2004, and references therein), whereas the Pyrenean Variscan hinterland would be the prolongation of the West Asturian–Leonese Zone (region adjacent to the Variscan foreland in the Iberian Variscan Massif) and/or the northeastern part of the Central–Iberian Zone (Ollo de Sapo Domain) (e.g. Julivert 1983b; Martínez-Catalán *et al.* 1990; Pérez-Estaún *et al.* 1991; Bastida & Pulgar 1995; Marcos *et al.* 2004; Martínez-Catalán *et al.* 2004 and references

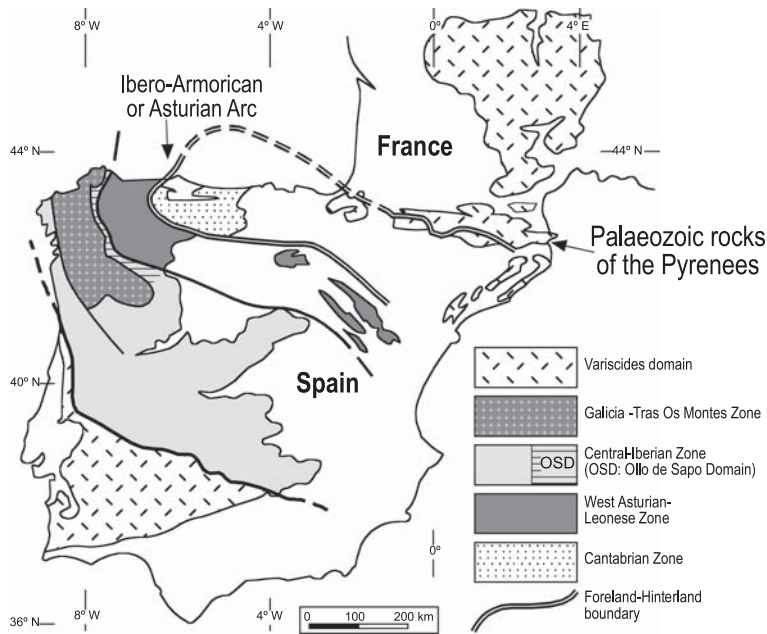


Fig. 5. Map depicting the present-day geometry of the Variscan belt in which the north branch of the Ibero-Armorican or Asturian Arc (Iberian Massif) is linked with the Palaeozoic rocks of the Pyrenees.

therein). To further check this hypothesis, the main features of the foreland and hinterland regions of the Variscan Pyrenees and Variscan Iberian Massif must be compared. Although the palaeogeographic patterns may not be necessarily parallel to the structural trends of the cordillera, and therefore, different facies may occur within a single, uniform structural domain, a synthetic comparison of the stratigraphy of the Pyrenees and that of the Iberian Massif is presented first in order to emphasize the main lithostratigraphic similarities (Table 1). After that, a structural comparison is discussed.

Regarding the stratigraphy, the Canaveilles Group could be equivalent to the Vendian series of the Iberian Massif (Laumonier *et al.* 2004). The limestone beds within the Jujols Group (Lladorre, Bentaillou, Boms or Lleret-Bayau limestones) could be lateral equivalents of the Lower–Middle Cambrian Vegadeo Formation (Barrois 1882), the upper part of the Jujols Group may correspond to the Cambrian–Lower Ordovician Cabos Series (Lotze 1958), and the uppermost slate part of this group may be an equivalent of the Middle–Upper Ordovician Luarca Formation of the West Asturian–Leonese Zone. The orthogneiss bodies of Lower Ordovician age within the Cambrian–Ordovician metasediments would correspond to the Ollo de Sapo gneisses of the eastern part of the Central–Iberian Zone. The Upper Ordovician Rabassa and Cava Formations consist of siliciclastic rocks with

volcano-sedimentary materials similar to the westernmost part of the Cantabrian Zone (Castro Formation in Table 1). The Estana Formation exhibits similarities with the La Aquiana Formation (Nollau 1966; Matte 1968; Pérez-Estaún 1978), the distal facies of the Upper Ordovician rocks of the Pyrenees could be represented by the Agüeira Formation (Jaritz & Walter 1970; Marcos 1970, 1973; Crimes *et al.* 1974; Pérez-Estaún & Marcos 1981), and the Bar Formation could be an equivalent of the ‘basal Silurian’ quartzites observed in some localities of the Iberian Massif (Gutiérrez-Marco *et al.* 2002) (Table 1). The Pyrenean Silurian rocks are almost identical to those mapped in many regions of the Iberian Massif. In the West Asturian–Leonese Zone and Ollo de Sapo Domain of the Central–Iberian Zone, Devonian–Carboniferous rocks are hardly represented, whereas in the Cantabrian Zone shallow Devonian–Carboniferous rocks are well represented (Barrois 1882; Comte 1959; Truyols *et al.* 1990; García-Alcalde *et al.* 2002). The lower and middle Devonian rocks of the Pyrenean western and southern domain and of the Pyrenean central domain are similar to those of the westernmost part of the Cantabrian Zone, because in both regions limestones and shales are common and include thick levels of reef limestones. In addition, the Carboniferous rocks of the western part of the Pyrenees, including from bottom to top red limestones and cherts, black limestones and a

siliciclastic sequence with limestone olistostromes, are also similar to the facies found in the Cantabrian Zone.

The structure of the external part of the Variscan Pyrenees resembles that observed in the northwestern Cantabrian Zone. Thus, both regions are dominated by the occurrence of thrusts and thrust-related folds, cleavage is poorly developed, the fold vergence and the thrust tectonic transport is consistent, and the structures formed under non-metamorphic conditions, except for very localized areas.

The West Asturian–Leonese Zone, the Central–Iberian Zone and the internal part of the Variscan Pyrenees also exhibit a number of similarities. The structural framework of both regions resulted from superposition of two principal folding episodes, with associated pervasive cleavages, and some thrusts, developed under higher metamorphic grades than in foreland areas. Both regions exhibit approximately orthogonal relationships between the axial surfaces and cleavages of the two folding deformation events and in both regions the folding episodes are coaxial, giving rise to type 3 interference fold patterns of Ramsay (1967). Regarding the timing of fold development, in both regions the steeper structures postdate the gentler structures. In addition, in both zones, thrusts are foreland-directed, the tectonic transport direction of the thrusts is approximately perpendicular to the fold trends of the two principal folding episodes and thrusting initiated after the first folding episode. A number of poorly developed late structures such as kink bands, etc. occur in both the West Asturian–Leonese Zone and the internal part of the Variscan Pyrenees.

However, there are some differences between the internal part of the Variscan Pyrenees and the West Asturian–Leonese Zone and the Ollo de Sapo Domain of the Central–Iberian Zone. Thus, in the Pyrenees the first folding event verge towards the hinterland, whereas in the West Asturian–Leonese Zone and Central–Iberian Zone the first folds verge towards the foreland. In addition, thrust development in the Pyrenees is approximately synchronous to second folding event, whereas thrust development in the West Asturian–Leonese Zone and Central–Iberian Zone ceased before the second folding event. Irrespective of these specific differences regarding the vergence of the first folding episode and the timing of the Variscan thrusts, most features of the structures observed in the Variscan Pyrenees and in the Iberian Massif are coincident, the position of the foreland and hinterland zones is consistent, and the thrust systems and the two folding episodes and thrusts developed in the foreland and hinterland of the Variscan Pyrenees respectively and the equivalent structures developed in the north branch of the Iberian

Massif are fully compatible with a roughly north–south shortening, supporting the correlation proposed between both portions of the Variscan belt (Fig. 5). If our correlation is correct, the Ibero-Armorican or Asturian arc is tighter than the arc depicted in some structural maps of this portion of the Variscan cordillera, and this may have implications in the mechanisms of oroclinal bending previously proposed to explain this large scale structure and in the reconstructions of the original disposition of this segment of the Variscan belt carried out through unfolding the arc using mainly palaeomagnetic data (e.g. Weil 2006 and references therein), but these topics are beyond the scope of our study.

Conclusions

The different sequences of Variscan structures identified in the non-metamorphic and in the metamorphic Palaeozoic rocks of the Central Pyrenees lead us to distinguish a foreland domain in which thrust systems and thrust-related folds with a poorly developed cleavage are the main structures, and an hinterland domain characterized by a two fold sets associated with pervasive cleavages and subordinate thrusts coeval to the second folding episode. At the present day, both domains are separated by thrusts of Variscan age, Alpine age or Variscan age reactivated during Alpine times. Except for the first folding episode in the hinterland domain that verges towards the north, all the structures have a southwards vergence sense consistent with the southwards position of the foreland domain with respect to the hinterland. The structures developed, the succession of deformations, the structures being consistent with a north–south shortening and the relative position of the foreland and hinterland suggest that the Variscan domains of the Central Pyrenees may be equivalent to the northern branch of the Ibero-Armorican or Asturian arc in the Iberian Massif. According to this correlation the Pyrenean Variscan foreland would be equivalent to the Cantabrian Zone, whereas the Pyrenean Variscan hinterland could correspond to the West Asturian–Leonese Zone and the Ollo de Sapo Domain of the Central–Iberian Zone.

The conclusions presented in this study are a preliminary attempt at correlation between the Variscan Pyrenees and the neighbouring largest outcrop of Variscan rocks, that is, the Iberian Massif, but further comparisons between the Palaeozoic rocks that crop out north (Mouthoumet Massif, Montagne Noir, etc.) and south (Catalonian Coastal Ranges, Balearic Islands, etc.) of the Pyrenees and the rest of domains of the Variscan realm are required to confirm the validity of hypothesis presented here.

We acknowledge financial support by projects CGL2008-03786/BTE, CGL2006-12415-C03-02/BTE, CSD2006-0041 and CGL2008-00463-E/BTE funded by the Spanish Ministry for Science and Innovation, and CNG08-15 funded by the Asturian Ministry for Science and Education. We are grateful to the reviewers R. Lisle and J. M. Casas, to J. A. Muñoz and A. Pérez-Estaún for fruitful discussions and M. Bulnes for their help in the last stages of the manuscript preparation.

References

- ALONSO, J. L. & PULGAR, J. A. 1995. La estructura de la Zona Cantábrica. In: ARAMBURU, C. & BASTIDA, F. (eds) *Geología de Asturias*. Editorial Trema, Gijón, 103–112.
- ALONSO, J. L., PULGAR, J. A., GARCÍA-RAMOS, J. C. & BARBA, P. 1996. Tertiary basins and Alpine tectonics in the Cantabrian Mountains (NW Spain). In: FRIEND, P. F. & DABRIO, C. J. (eds) *Tertiary Basins of Spain. The Stratigraphic Record of Crustal Kinematics*. Cambridge University Press, Cambridge, 214–227.
- BARROIS, C. 1882. Recherches sur les terrains anciens des Asturies et de la Galice. *Mémoires de la Société géologique du Nord*, **2**, 1–630.
- BASTIDA, F. & PULGAR, J. A. 1995. La estructura de la Zona Asturoccidental-leonesa. In: ARAMBURU, C. & BASTIDA, F. (eds) *Geología de Asturias*. Editorial Trema, Gijón, 113–122.
- BASTIDA, F., PÉREZ-ESTAÚN, A. ET AL. 2004. Zona Cantábrica. In: VERA, J. A. (ed.) *Geología de España*. Sociedad Geológica de España-Instituto, Geológico y Minero de España, Madrid, 42–49.
- BATES, M. 1989. Paleomagnetic evidence for rotations and deformation in the Noguera Zone, Central Southern Pyrenees. *Journal of the Geological Society, London*, **146**, 459–476.
- BICHON, F. 1986. *La tectonique distensive carbonifère dans les Pyrénées. Corrélations est-canadiennes et ouest-européennes*. PhD thesis, University of Bordeaux III, France.
- BOERSMA, K. TH. 1973. Devonian and lower Carboniferous conodont biostratigraphy, Spanish Central Pyrenees. *Leidse Geologische Mededelingen*, **49**, 303–377.
- BROUTIN, J. & GISBERT, J. 1985. Entorno paleoclimático y ambiental de la flora del Stephano-Autuniense del Pirineo catalán. *Actas del X Congreso Internacional de Estratigrafía y Geología del Carbonífero*, **3**, 53–66.
- CASAS, J. M. & FERNÁNDEZ, O. 2007. On the Upper Ordovician unconformity in the Pyrenees: new evidence from the La Cerdanya area. *Geologica Acta*, **5**, 193–198.
- CASAS, J. M. & POBLET, J. 1989. Essai de restitution de la déformation dans une zone avec plis et chevauchements: le “synclinal de Llavors” dans les Pyrénées centrales (Espagne). *Comptes Rendus de l'Académie des Sciences, Paris, Séries II*, **308**, 427–433.
- CASAS, J. M., DOMINGO, F., POBLET, J. & SOLER, A. 1989. On the role of the Hercynian and Alpine thrusts in the Upper Palaeozoic rocks of the Central and Eastern Pyrenees. *Geodinamica Acta*, **3**, 135–147.
- CASTIÑEIRAS, P., NAVIDAD, M., LIESA, M., CARRERAS, J. & CASAS, J. M. 2008. U-Pb zircon ages (SHRIMP) for Cadomian and Lower Ordovician magmatism in the Eastern Pyrenees: new insights in the pre-Variscan evolution of the northern Gondwana margin. *Tectonophysics*, **461**, 228–239.
- CAVET, P. 1951. Sur la stratigraphie du Paléozoïque de la zone axiale des Pyrénées orientales. *Comptes Rendus de l'Académie des Sciences, Paris, Séries II*, **232**, 747–745.
- CAVET, P. 1957. Le Paléozoïque de la zone axiale des Pyrénées orientales françaises entre le Roussillon et l'Andorre (étude stratigraphique et paléontologique). *Bulletin des Services de la Carte géologique de France*, **254**, 303–318.
- CAVET, P. 1958. Stratigraphie du Paléozoïque de la zone axiale des Pyrénées à l'E de l'Ariège. *Bulletin de la Société Géologique de France, Série 8*, 853–867.
- CHOUKROUNE, P., PINET, B., ROURE, F. & CAZES, M. 1990. Major Hercynian thrusts along the ECORS Pyrenees and Biscay lines. *Bulletin de la Société Géologique de France*, **8**, 313–320.
- CIRÉS, J., ALIAS, G., POBLET, J. & CASAS, J. M. 1990. La estructura del anticlinal de La Massana (Hercínico del Pirineo central). *Geogaceta*, **8**, 42–44.
- CLARIANA, P. & GARCÍA-SANSEGUNDO, J. 2009. Variscan structure of the eastern part of the Pallaresa massif, Axial Zone of the Pyrenees (NW Andorra). Tectonic implications. *Bulletin de la Société Géologique de France*, **180**, 501–511.
- CLIN, M., HEDDEBAUT, C., MIROUSE, R., MULLER, J., ROGER, P. & WATERLOT, M. 1970. Le cycle hercynien dans les Pyrénées. *Annales de la Société Géologique du Nord*, 253–276.
- COMTE, P. 1959. Recherches sur les terrains anciens de la Cordillère Cantabrique. *Memorias del Instituto Geológico y Minero de España*, **60**, 1–440.
- COWARD, M. & DIETRICH, D. 1989. Alpine Tectonics – an overview. In: COWARD, M. P., DIETRICH, D. & PARK, R. G. (eds) *Alpine Tectonics*. Geological Society, London, Special Publications, **45**, 1–29.
- CRIMES, T. P., MARCOS, A. & PÉREZ-ESTAÚN, A. 1974. Upper Ordovician turbidites in Western Asturias. A facies analysis with particular reference to vertical and lateral variations. *Palaeogeography Palaeoclimatology Palaeoecology*, **15**, 169–184.
- DEGARDIN, J. M. 1988. Le Silurien des Pyrénées. Biostratigraphie. Paléogéographie. *Publication de la Société Géologique du Nord*, **15**, 1–525.
- DEVOLVÉ, J. J. & PERRET, M. F. 1989. Variations de l'âge des sédiments calcaires et “Culm” carbonifère dans la chaîne varisque du sud de la France: migration de l'orogénèse varisque. *Geodinamica Acta*, **3**, 117–126.
- DOMINGO, F., MUÑOZ, J. A. & SANTANACH, P. 1988. Estructures d'encavalcament en els materials del sòcol hercinià del massís de la Tossa d'Alp (Pirineu oriental). *Acta Geològica Hispànica*, **23**, 141–153.
- ELLENBERGER, F. & TAMAIN, A. L. G. 1980. Hercynian Europe. *Episodes*, 22–23.
- GARCÍA ALCALDE, J. L., SOTO, F. & TRUYOLS-MASSONI, M. 2002. Cantabrian Mountains. In: GIBBONS, W. & MORENO, T. (eds) *The Geology of Spain*. Geological Society, London, 68–75.
- GARCÍA-SANSEGUNDO, J. 1990. Structure of the Palaeozoic in the Aran valley, Axial zone, central Pyrenees.

- Bulletin de la Société Géologique de France*, **8**, 229–239.
- GARCÍA-SANSEGUNDO, J. 1992. Estratigrafía y Estructura de la Zona Axial Pirenaica en la transversal del Valle de Arán y de la Alta Ribagorça. *Publicaciones especiales del Boletín Geológico y Minero, Madrid*, **102–103**, 1–167.
- GARCÍA-SANSEGUNDO, J. 1996. Hercynian structure of the Axial Zone of the Pyrenees: the Aran Valley cross-section (Spain-France). *Journal of Structural Geology*, **18**, 1315–1325.
- GARCÍA-SANSEGUNDO, J. & ALONSO, J. L. 1989. Stratigraphy and structure of the southeastern Garona Dome. *Geodinamica Acta*, **3**, 127–134.
- GARCÍA-SANSEGUNDO, J., GAVALDÁ, J. & ALONSO, J. L. 2004. Preuves de la discordance de l'Ordovicien supérieur dans la Zone Axiale des Pyrénées: exemple du Dôme de la Garonne (Espagne, France). *Comptes Rendus Geosciences*, **336**, 1035–1040.
- GISBERT, J. 1981. *Estudio geológico-petroológico del Estefaniense-Pérmico de la Sierra del Cadí (Pirineo de Lérida). Diagénesis y sedimentología*. PhD thesis, Universidad de Zaragoza, Spain.
- GISBERT, J. 1983. Las molasas tardihercínicas del Pirineo. In: COMBA, J. A. (ed.) *Libro Jubilar J.M. Ríos. Geología de España, Tomo II*. Instituto Geológico y Minero de España, Madrid, 168–185.
- GUTIÉRREZ-MARCO, J. C., ROBARDET, M., RÁBANO, I., SARMIENTO, G. N., SAN JOSÉ LANCH, M. A., HERRANZ, P. & PIEREN PÍDAL, A. P. 2002. Ordovician. In: GIBBONS, W. & MORENO, T. (eds) *The Geology of Spain*. Geological Society, London, 31–49.
- HARTEVELT, J. J. A. 1970. Geology of the Upper Segre and Valira valleys, Central Pyrenees, Andorra/Spain. *Leidse Geologische Mededelingen*, **45**, 167–236.
- JARITZ, W. & WALTER, R. 1970. Faciesuntersuchungen in Altpaläozoikum Nordwest-Spaniens/Asturien und Prov. Lugo. *Geologisches Jahrbuch*, **88**, 509–552.
- JULIVERT, M. 1971. Décollement tectonics in the Hercynian Cordillera of NW Spain. *American Journal of Science*, **270**, 1–29.
- JULIVERT, M. 1979. A cross-section through the northern part of the Iberian Massif: its position within the Hercynian fold belt. *Krystalinikum*, **14**, 51–67.
- JULIVERT, M. 1981. A cross-section through the northern part of the Iberian Massif. *Geologie en Mijnbouw*, **60**, 107–128.
- JULIVERT, M. 1983a. La estructura de la Zona Cantábrica. In: COMBA, J. A. (ed.) *Libro Jubilar J. M. Ríos. Geología de España, Tomo I*. Instituto Geológico y Minero de España, Madrid, 339–381.
- JULIVERT, M. 1983b. La estructura de la Zona Asturoccidental-Leonesa. In: COMBA, J. A. (ed.) *Libro Jubilar J. M. Ríos. Geología de España, Tomo I*. Instituto Geológico y Minero de España, Madrid, 381–408.
- JULIVERT, M., FONTBOTÉ, J. M., RIBEIRO, A. & CONDE, L. 1972. *Mapa tectónico de la Península Ibérica y Baleares*. Instituto Geológico y Minero de España, Madrid.
- JULIVERT, M. & MARTÍNEZ, F. J. 1983. Estructura de conjunto y visión global de la Cordillera Herciniana. In: COMBA, J. A. (ed.) *Libro Jubilar J. M. Ríos. Geología de España, Tomo I*. Instituto Geológico y Minero de España, Madrid, 612–631.
- KLEINSMIEDE, W. F. J. 1960. Geology of the Valle de Arán (Central Pyrenees). *Leidse Geologische Mededelingen*, **25**, 129–241.
- KRIEGSMAN, L. M., AERDEN, D. G. A. M., BAKKER, R. J., BROK, S. W. J. DEN & SCHUTJENS, P. M. T. M. 1989. Variscan tectonometamorphic evolution of the eastern Lys-Caillaouas massif, Central Pyrenees – evidence for a late orogenic extension prior to peak metamorphism. *Geologie en Mijnbouw*, **68**, 323–333.
- LAUMONIER, B. & GUITARD, G. 1986. Le Paléozoïque inférieur de la moitié orientale de la zone axiale des Pyrénées. Essai de synthèse. *Comptes Rendus de l'Académie des Sciences, Paris, Séries II*, **302**, 473–478.
- LAUMONIER, B., AUTRAN, A., BARBEY, P., CHEILLETZ, A., BOUDIN, T., COCHERIE, A. & GUERROT, C. 2004. Conséquences de l'absence de socle cadomien sur l'âge et la signification des séries pré-varisques (anté-Ordovicien supérieur) du sud de la France (Pyrénées, Montagne Noire). *Bulletin de la Société Géologique de France*, **175**, 643–655.
- LLAC, F. 1979. Les nappes tardi-hercyniennes entre Cerdagne et Llobregat (versant sud des Pyrénées catalanes). *Bulletin de la Société Géologique de France, Série 7*, **21**, 467–473.
- LLOPIS, N. 1965. Sur le Paléozoïque inférieur de l'Andorre. *Bulletin de la Société Géologique de France, Série 7*, 652–659.
- LOTZE, F. 1945. Zur gliederung der Varisziden in der Iberischen Meseta. *Geotektonische Forschungen*, **6**, 78–92.
- LOTZE, F. 1958. Zur stratigraphie des Spanischen kambriums. *Geologie*, **7**, 727–750.
- LUCAS, C. 1968. *Le grès rouge du Comminges et de la Bigorre (Pyrénées centrales). Etude géologique. Thèse 3ème. Cycle*, Université de Toulouse, Toulouse.
- MAJESTÉ-MENJOULAS, C. 1979. *Evolution alpine d'un segment de chaîne varisque: Nappe de Gavarnie, chevauchement Cinq-Monts-Gentiane (Pyrénées centrales et occidentales)*. Thèse Sci., Univ. Paul Sabatier, Toulouse.
- MAJESTÉ-MENJOULAS, C. 1982. L'unité paléozoïque de Bachebiro-Chinipro, témoin d'une tectonique tangentielle varisque dans les Pyrénées centrales. *Comptes Rendus de l'Académie des Sciences, Paris, Séries II*, **294**, 145–150.
- MAJOOR, F. J. M. 1988. *A geochronological study of the Axial Zone of the Central Pyrenees, with emphasis on Variscan events and Alpine resetting*. Verhandeling nr.6 zwo Laboratorium voor isotopen-geologie, Amsterdam.
- MARCOS, A. 1970. Sobre la presencia de un flysch del Ordovícico Superior en el Occidente de Asturias. *Breviora Geológica Astúrica*, **14**, 13–28.
- MARCOS, A. 1973. Las series del Paleozoico inferior y la estructura herciniana del Occidente de Asturias (NW de España). *Trabajos de Geología, Universidad de Oviedo*, **6**, 1–113.
- MARCOS, A., MARTÍNEZ-CATALÁN, J. R. ET AL. 2004. Zona Asturoccidental-Leonesa. In: VERA, J. A. (ed.) *Geología de España*. Sociedad Geológica de España-Instituto Geológico y Minero de España, Madrid, 49–68.
- MARTÍNEZ-GARCÍA, E. 2006. Proterozoic-Lower Paleozoic terrane accretion and Variscan domains in the

- Iberian Massif (Spain and Portugal). *Zeitschrift der Deutschen Gesellschaft für Geowissenschaften*, **157**, 559–574.
- MARTÍNEZ-CATALÁN, J. R., PÉREZ-ESTAÚN, A., BASTIDA, F., PULGAR, J. A. & MARCOS, A. 1990. West Asturian-Leonese Zone: structure. In: DALLMEYER, R. D. & MARTÍNEZ-GARCÍA, E. (eds) *Pre-Mesozoic Geology of Iberia*. Springer-Verlag, Berlin, 103–114.
- MARTÍNEZ-CATALÁN, J. R., MARTÍNEZ-POYATOS, D. & BEA, F. 2004. Zona Centro-Ibérica. In: VERA, J. A. (ed.) *Geología de España*. Sociedad Geológica de España-Instituto Geológico y Minero de España, Madrid, 68–132.
- MATTAUER, M. 1990. Une autre interprétation du profil ECORS Pyrénées. *Bulletin de la Société Géologique de France*, **8**, 307–311.
- MATTAUER, M., DALMAYRAC, B., LAURACHER, G. & VIDAL, J. C. 1967. Contribution à l'étude des tectoniques superposées dans la chaîne hercynienne: le 'synclinal' paléozoïque de Villefranche-de-Conflent (Pyrénées orientales). *Comptes Rendus de l'Académie des Sciences, Paris*, **265**, 1361–1364.
- MATTE, P. 1968. La structure de la virgation hercynienne de Galice (Espagne). *Revue de Géologie Alpine*, **44**, 1–128.
- MATTE, PH. 1969. Le problème du passage de la schistosité horizontale à la schistosité verticale dans le dôme de Garonne (Paléozoïque des Pyrénées Centrales). *Comptes Rendus de l'Académie des Sciences, Paris*, **268**, 1841–1844.
- MATTE, PH. 1986. La chaîne varisque parmi les chaînes paléozoïques péri – atlantiques, modèle d'évolution et position des grands blocs continentaux au Permo – Carbonifère. *Bulletin de la Société Géologique de France*, **8**, 9–24.
- MATTE, PH. 1995. Southern Uralides and Variscides: comparison of their anatomies and evolutions. *Geologie en Mijnbouw*, **74**, 151–166.
- MATTE, PH. 1998. Continental subduction and exhumation of HP rocks in Palaeozoic orogenic belts: Uralides and Variscides. *Geologiska Foreningen i Stockholm Forhandlingar*, **120**, 209–222.
- MATTE, PH. 2001. The Variscan collage and orogeny (480–290 Ma) and the tectonic definition of the Armorica microplate: a review. *Terra Nova*, **13**, 122–128.
- MATTE, PH. & MATTAUER, M. 1987. Hercynian orogeny in the Pyrenees was not a rifting event. *Nature*, **325**, 739–740.
- MCCLELLAND, E. A. & MCCAIG, A. M. 1988. Palaeomagnetic estimates of total rotation in basement thrust sheets, Axial Zone, Southern Pyrenees. *Cuadernos de Geología Ibérica*, **12**, 181–193.
- MEY, P. H. W. 1967. The Geology of the Upper Ribagorzana and Baliera valleys, Central Pyrenees, Spain. *Leidse Geologische Mededelingen*, **41**, 153–220.
- MEY, P. H. W. 1968. Geology of the Upper Ribagorzana and Tor valleys, Central Pyrenees, Spain. *Leidse Geologische Mededelingen Leidse*, **41**, 229–292.
- MEZGER, J. E. & PASSCHIER, C. W. 2003. Polymetamorphism and ductile deformation of staurolite-cordierite schist of the Bossòst dome: indication for Variscan extension in the Axial Zone of the central Pyrenees. *Geological Magazine*, **140**, 595–612.
- MIROUSE, R. 1959. Sur le 'Grés Rouge' des hautes du Gave d'Aspe et de l'Aragon Subordon. *Comptes Rendus de l'Académie des Sciences, Paris*, **248**, 2361–2363.
- MIROUSE, R. 1966. *Recherches géologiques dans la partie occidentale de la zone primaire des Pyrénées*. Mémoires pour servir à l'explication de la Carte Géologique détaillée de la France, Paris.
- MULLER, J. & ROGER, Ph. 1977. L'évolution structurale des Pyrénées (domaine central et occidental). Le segment hercynien, la chaîne de fond alpine. *Géologie Alpine*, **53**, 149–191.
- MUÑOZ, J. A. 1985. *Estructura alpina i herciniana a la vora sud de la zona axial del Pirineu oriental*. PhD thesis, Universitat de Barcelona, Spain.
- MUÑOZ, J. A. 1992. Evolution of a continental collision belt: ECORS-Pyrenees crustal balanced cross section. In: McCLAY, K. R. (ed.) *Thrust Tectonics*. Chapman & Hall, London, 235–246.
- MUÑOZ, J. A. & SÀBAT, F. 1981. El Paleozoic prehercinia de la Serra Cavallera. *Revista del Instituto de Investigaciones Geológicas de la Diputación Provincial de Barcelona*, **35**, 43–59.
- NOLLAU, G. 1966. El desarrollo estratigráfico del Paleozoico en el Oeste de la Provincia de León (España). *Nota de la Comisión del Instituto Geológico y Minero de España*, **88**, 31–48.
- PARISH, M. 1984. A structural interpretation of a section of the Gavarnie nappe and its implications for Pyrenean geology. *Journal of Structural Geology*, **6**, 247–255.
- PÉREZ-ESTAÚN, A. 1978. Estratigrafía y estructura de la rama sur de la Zona Astur-occidental Leonesa. *Memorias del Instituto Geológico y Minero de España*, **92**, 1–49.
- PÉREZ-ESTAÚN, A. & MARCOS, A. 1981. La Formación Agüeira en el Sinclinorio de Vega de Espinareda: Aproximación al modelo de sedimentación durante el Ordovícico superior en la Zona Astur – occidental – leonesa (NW de España). *Trabajos de Geología, Universidad de Oviedo*, **11**, 135–145.
- PÉREZ-ESTAÚN, A. & BASTIDA, F. 1990. Cantabrian Zone: structure. In: DALLMEYER, R. D. & MARTÍNEZ-GARCÍA, E. (eds) *Pre-Mesozoic Geology of Iberia*. Springer-Verlag, Berlin, 55–69.
- PÉREZ-ESTAÚN, A., BASTIDA, F. ET AL. 1988. A thin-skinned tectonics model for an arcuate fold and thrust belt: the Cantabrian Zone (Variscan Ibero-Armorican Arc). *Tectonics*, **7**, 517–537.
- PÉREZ-ESTAÚN, A., MARTÍNEZ-CATALÁN, J. R. & BASTIDA, F. 1991. Crustal thickening and deformation sequence in the footwall to the suture of the Variscan belt of north-west Spain. *Tectonophysics*, **191**, 243–253.
- PERRET, M. F. 1993. Recherches micropaléontologiques et biostratigraphiques (conodontes-foraminifères) dans le Carbonifère Pyrénéen. *Strata*, **2**, 1–597.
- POBLET, J. 1991. *Estructura herciniana i alpina del Vessant sud de la zona Axial del Pirineu Central*. PhD thesis, Universitat de Barcelona, Spain.
- POBLET, J. & CASAS, J. M. 1993a. Evidence for Devonian-Carboniferous extensional tectonics in the Central Pyrenees. *Geodinamica Acta*, **6**, 225–232.
- POBLET, J. & CASAS, J. M. 1993b. Variscan extension in the Pyrenees (comment). *Tectonics*, **12**, 1479–1481.
- POUGET, P. 1991. Hercynian tectonometamorphic evolution of the Bossost dome (French-Spanish central

- Pyrenees). *Journal of the Geological Society, London*, **148**, 299–314.
- POUGET, P., LAMOROUX, C. ET AL. 1989. Typologie et mode de mise en place des roches magmatiques dans les Pyrénées hercyniennes. *Geologische Rundschau*, **78**, 537–554.
- RAMSAY, J. G. 1967. *Folding and Fracturing of Rocks*. McGraw-Hill Book Company, New York.
- RAYMOND, D. 1986. Tectonique tangentielle varisque dans le paléozoïque supérieur de l'est des Pyrénées françaises: l'exemple du Pays de Sault (nord du granite de Quérigut, Aude et Ariège) et des régions voisines. *Bulletin de la Société Géologique de France*, Série 8, 479–485.
- ROGER, Ph. 1965. Etude stratigraphique et structurale de la zone des Nogueras entre l'Èsera et l'Isábena (Huesca-Espagne). *Actes de la Société Linnéenne de Bordeaux*, Série 3, **102**, 1–25.
- ROMER, R. L. & SOLER, A. 1995. U-Pb age and lead isotopic characterization of Au-bearing skarn related to the Andorra granite. *Mineralium Deposita*, **30**, 374–383.
- ROURE, F., CHOUKROUNE, P. ET AL. 1989. ECORS Deep Seismic data and balanced cross sections: Geometric constraints on the evolution of the Pyrenees. *Tectonics*, **8**, 41–50.
- SANTANACH, P. F. 1972. Sobre una discordancia en el Paleozoico inferior de los Pirineos orientales. *Acta Geológica Hispánica*, **7**, 129–132.
- SANZ-LÓPEZ, J. 2004. Silúrico, Devónico y Carbonífero pre- sin-varisco de los Pirineos. In: VERA, J. A. (ed.) *Geología de España*. Sociedad Geológica de España – Instituto Geológico y Minero de España, Madrid, 250–254.
- SAVAGE, J. F. 1979. The Hercynian orogeny in the Cantabrian Mountains, Northern Spain. *Krystalinikum*, **14**, 91–108.
- SAVAGE, J. F. 1981. Geotectonic cross-section through the Cantabrian Mountains, Northern Spain. *Geologie en Mijnbouw*, **81**, 3–5.
- SEGURET, M. 1969. Contribution à l'étude de la tectonique sud-pyrénéenne sur le style et importance des déplacements vers le sud des séries secondaire et tertiaire de la partie centrale du versant sud des Pyrénées. *Comptes Rendus de l'Académie des Sciences, Paris*, **268**, 907–910.
- SEGURET, M. 1972. *Etude tectonique des nappes et séries décollées de la partie centrale du versant sud des Pyrénées*. Publications de l'Université des Sciences et Techniques du Languedoc (USTELA), Série Géologie Structurale, **2**.
- SEGURET, M. & PROUST, F. 1968a. Contribution à l'étude des tectoniques superposées dans la chaîne hercynienne: l'allure anticlinale de la schistosité à l'Ouest du massif de l'Aston (Pyrénées Centrales) n'est pas originelle mais due à un replissement. *Comptes Rendus de l'Académie des Sciences, Paris*, **266**, 317–320.
- SEGURET, M. & PROUST, F. 1968b. Tectonique hercynienne des Pyrénées centrales: signification des schistosités redressées, chronologie des déformations. *Comptes Rendus de l'Académie des Sciences, Paris*, **266**, 984–987.
- SOLIVA, J., SALEL, J. F. & BRUNEL, M. 1989. Shear deformation and emplacement of the gneissic Canigou thrust nappe (Eastern Pyrenees). *Geologie en Mijnbouw*, **68**, 357–366.
- SOUZA, J. C. 1982. Characteristics and mode of emplacement of gneiss domes and plutonic domes in central-eastern Pyrenees. *Journal of Structural Geology*, **3**, 313–342.
- SOUZA, J. C., DEBAT, P., DERAMOND, J., GUCHERREAU, J. Y., LAMOROUX, Ch., POUGET, P. & ROUX, L. 1986. Evolution structurale des ensembles métamorphiques des gneiss et des granitoïdes dans les Pyrénées centrales. *Bulletin de la Société Géologique de France*, **8**, 79–93.
- TEIXELL, A. 1998. Crustal structure and orogenic material budget in the west central Pyrenees. *Tectonics*, **17**, 395–406.
- TRUYOLS, J., ARBIZU, M. A., GARCÍA-ALCALDE, J. L., GARCÍA LÓPEZ, S., MÉNDEZ BEDIA, I., SOTO, F. & TRUYOLS-MASSONI, M. 1990. The Asturian-Leonese Domain (Cantabrian Zone). In: DALLMEYER, R. D. & MARTÍNEZ GARCÍA, E. (eds) *Pre-Mesozoic Geology of Iberia*. Springer-Verlag, Berlin, 10–19.
- VAN DEN ECKHOUT, B. & ZWART, H. J. 1988. Hercynian crustal scale extensional shear zone in the Pyrenees. *Geology*, **16**, 135–138.
- VAN DER LINGEN, G. J. 1960. Geology of the Spanish Pyrenees, north of Canfranc, Huesca province. *Estudios Geológicos*, **16**, 205–242.
- VISSERS, R. L. M. 1992. Variscan extension in the Pyrenees. *Tectonics*, **6**, 1369–1384.
- VISSERS, R. L. M. 1993. Variscan extension in the Pyrenees (reply). *Tectonics*, **12**, 1369–1384.
- VITRAC-MICHARD, A. & ALLÈGRE, C. J. 1975. A study on the formation and history of a piece of continental crust by 87Rb–86Sr method: The case of the French oriental Pyrenees. *Contributions to Mineralogy and Petrology*, **50**, 257–285.
- WEIL, A. B. 2006. Kinematics of orocline tightening in the core of an arc: Paleomagnetic analysis of the Ponga Unit, Cantabrian Arc, northern Spain. *Tectonics*, **25**, TC3012.
- WICKHAM, S. M. & OXBURGH, E. R. 1985. Continental rifts as a setting for regional metamorphism. *Nature*, **318**, 330–333.
- WICKHAM, S. M. & OXBURGH, E. R. 1986. A rifted tectonic setting for Hercynian high-thermal gradient metamorphism in the Pyrenees. *Tectonophysics*, **129**, 53–69.
- ZANDVLIET, J. 1960. The geology of the upper Salat and Pallaresa valleys, Central Pyrenees, France/Spain. *Leidse Geologische Mededelingen*, **25**, 1–127, 1960.
- ZWART, H. J. 1960. Relations between folding and metamorphism in the Central Pyrenees and their chronological succession. *Geologie en Mijnbouw*, **22**, 163–180.
- ZWART, H. J. 1964. The structural evolution of the Palaeozoic of the Pyrenees. *Geologische Rundschau*, **53**, 170–205.
- ZWART, H. J. 1968. The Paleozoic crystalline rocks of the Pyrenees and their structural setting. *Krystalinikum*, **6**, 125–140.
- ZWART, H. J. 1979. The Geology of the Central Pyrenees. *Leidse Geologische Mededelingen*, **50**, 1–74.
- ZWART, H. J. 1981. Three profiles through the Central Pyrenees. *Geologie en Mijnbouw*, **60**, 97–104.
- ZWART, H. J. 1986. The Variscan geology of the Pyrenees. *Tectonophysics*, **129**, 9–28.

Kinematics of the Forcarei Synform (NW Iberian Variscan belt)

FRANCISCO JOSÉ FERNÁNDEZ*, FLORENTINO DÍAZ-GARCÍA[†] &
JORGE MARQUÍNEZ

*Departamento de Geología, Universidad de Oviedo, C/ Jesús Arias de Velasco s/n 33005
Oviedo, Spain*

**Corresponding author (e-mail: brojos@geol.uniovi.es)*

[†]Deceased

Abstract: The Forcarei Synform is a kilometric fold developed in the hinterland of the NW Iberian Variscan belt. A detailed analysis of the synform, based on quartz fabrics and kinematic markers, shows pervasively deformed rocks that have been continuously deformed during the last two main Variscan deformation phases (D₂ and D₃).

Variscan D₂ minor structures related to the synform were formed under general non-coaxial flow and have a sub-horizontal maximum finite stretching toward the SSE. Later a coaxial D₃ produced a sub-vertical crenulation cleavage, and type 2 and 3 refolded folds figures at the meso- and micro-scale. Consequently, the strike of the foliations (S₂ and S₃) become sub-parallel and lineation (L₂ and L₃) are sub-horizontal. The geometry of the synform and the related structures can be interpreted in the context of D₃. However the dominantly sinistral shear sense indicators, observed in both limbs of the synform (in map view), seem to be most probably developed during D₂. A model is proposed involving the progressive clockwise rotation of a sub-horizontal shear, with general top-to-the-south sense, during the simultaneous development of shear zone and foliation in agreement with the kinematic indicators.

The Variscan belt in NW Iberia has been divided into four major zones with different geological characteristics (Julivert *et al.* 1972; Farias *et al.* 1987) Cantabrian Zone, Westasturian–Leonese Zone, Central–Iberian Zone and Galicia–Trás-os-Montes Zone. The general trend of the structures in the belt describes the Ibero-Armorican arc. The Cantabrian Zone represents the external part of the orogen and forms the core of the Ibero-Armorican arc (Fig. 1a).

The Westasturian–Leonese Zone is located to the west of the Cantabrian Zone (Fig. 1a). This zone mainly consists of Lower Palaeozoic siliciclastic rocks and represents the transition to the hinterland of the orogen. The orogenic metamorphic grade increases westward up to amphibolite facies; granitoid outcrops occupy a large area in the western part of the zone. Deformation is polyphase, with three phases having been distinguished in the Westasturian–Leonese Zone (Marcos 1973). During the first deformation phase (D₁), close to tight folds (F₁), vergent towards the foreland with sub-horizontal fold axes and associated cleavage (S₁), were formed. During the second deformation phase (D₂), thrusts and ductile shear zones, also foreland-directed, were developed. During the third phase of deformation (D₃), upright open folds with associated crenulation cleavage (S₃) were formed; these folds are almost homoaxial with F₁ folds.

The sequence of deformation phases in the most hinterland zones (Central–Iberian and Galicia–Trás-os-Montes Zones) is comparable to that of the Westasturian–Leonese Zone (Pérez-Estaún *et al.* 1991), although in general F₃ folds are more developed (Matte 1968). The regional metamorphism ranges from the chlorite to the migmatite zone, with grade increasing toward the granitoid areas that occupy most of the domain. The metamorphic peak occurred mainly during the inter-phase D₂–D₃.

The Galicia–Trás-os-Montes zone is formed by two domains: (a) the lower allochthon and autochthon or Schist domain; and (b) the Allochthonous complexes. The lower allochthon and autochthon is formed by a thick succession of siliciclastic rocks, mainly metapelites, probably chiefly Ordovician in age (Farias & Marcos 2004; Valverde *et al.* 2005). The succession of deformation phases in this zone has been considered the same as that in the easternmost hinterland zones (Marquínez 1984; Farias 1990; Farias & Marcos 2004). However it has been interpreted that the main regional foliation is S₂. This foliation consists of a domainal cleavage with relict microfolds. D₁ structures are very scarce, for example, the Silleda syncline and the Carrio anticline (Martínez-Catalán *et al.* 1996). Major D₂ folds have never been described, whereas D₃ structures are common and easily recognizable.

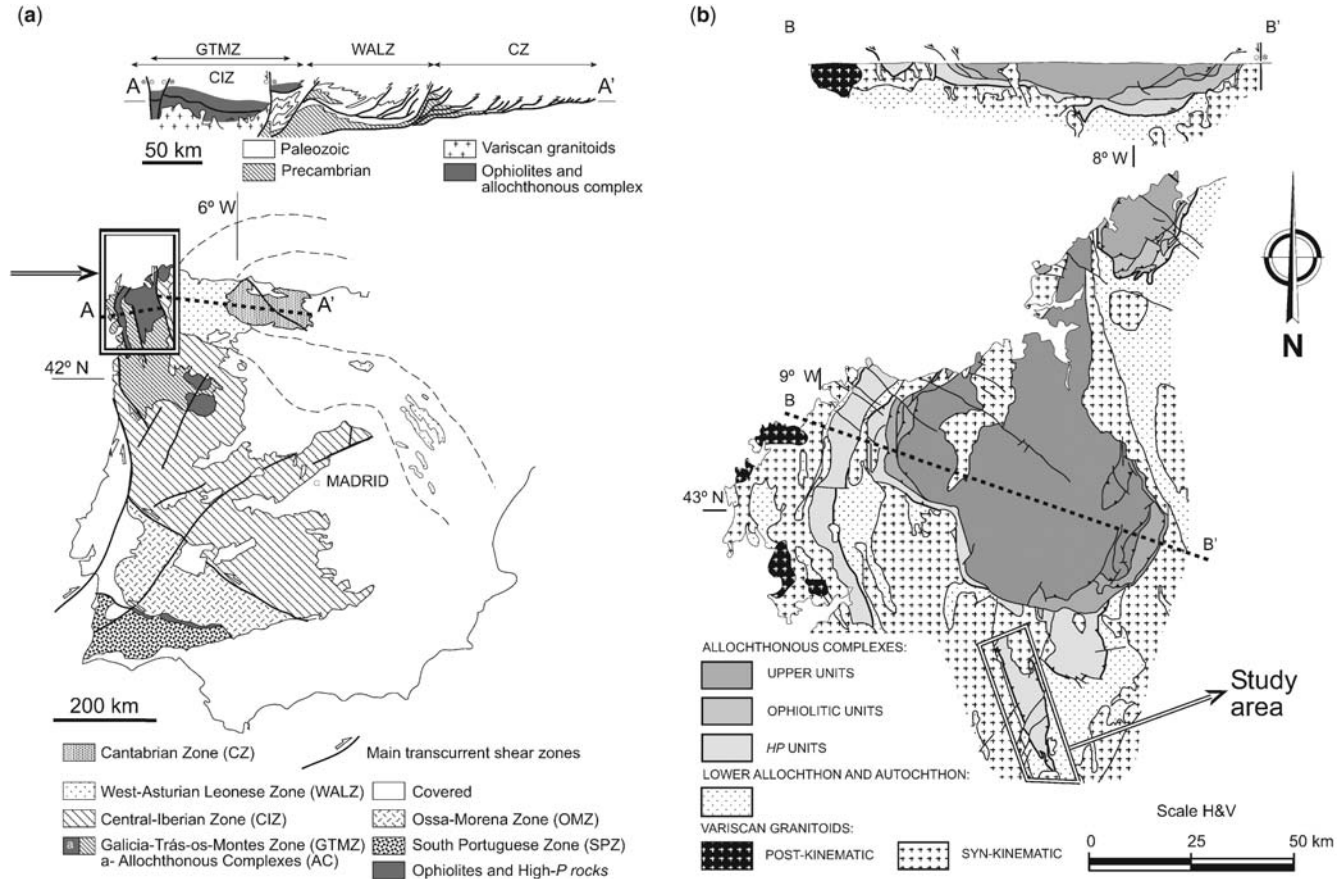


Fig. 1. (a) Simplified geological map of the Iberian Massif and cross section through the northern part after Pérez-Estaún *et al.* (1991) highlighting the location of figure in box b. (b) Simplified geological map of the Northern part of Galicia-Trás-os-Montes Zone and cross section through the Ordenes Complex after Martínez Catalán *et al.* (2002), highlighting the location of the Forcarei Synform study area (Fig. 2) and the major tectono-stratigraphic units.

The allochthonous complexes of Galicia-Trás-os-Montes appear isolated as great klippen in the cores of D_3 -synforms. They are formed by meta-sediments, mafic and ultramafic rocks that underwent high grade polymetamorphism, separated by

thrusts. Their internal structure is complex with a structural history longer than that of the underlying units. The amphibolite facies metamorphism dated at 390–380 Ma (Dallmeyer *et al.* 1997) was retrogressive in the upper allochthonous units.

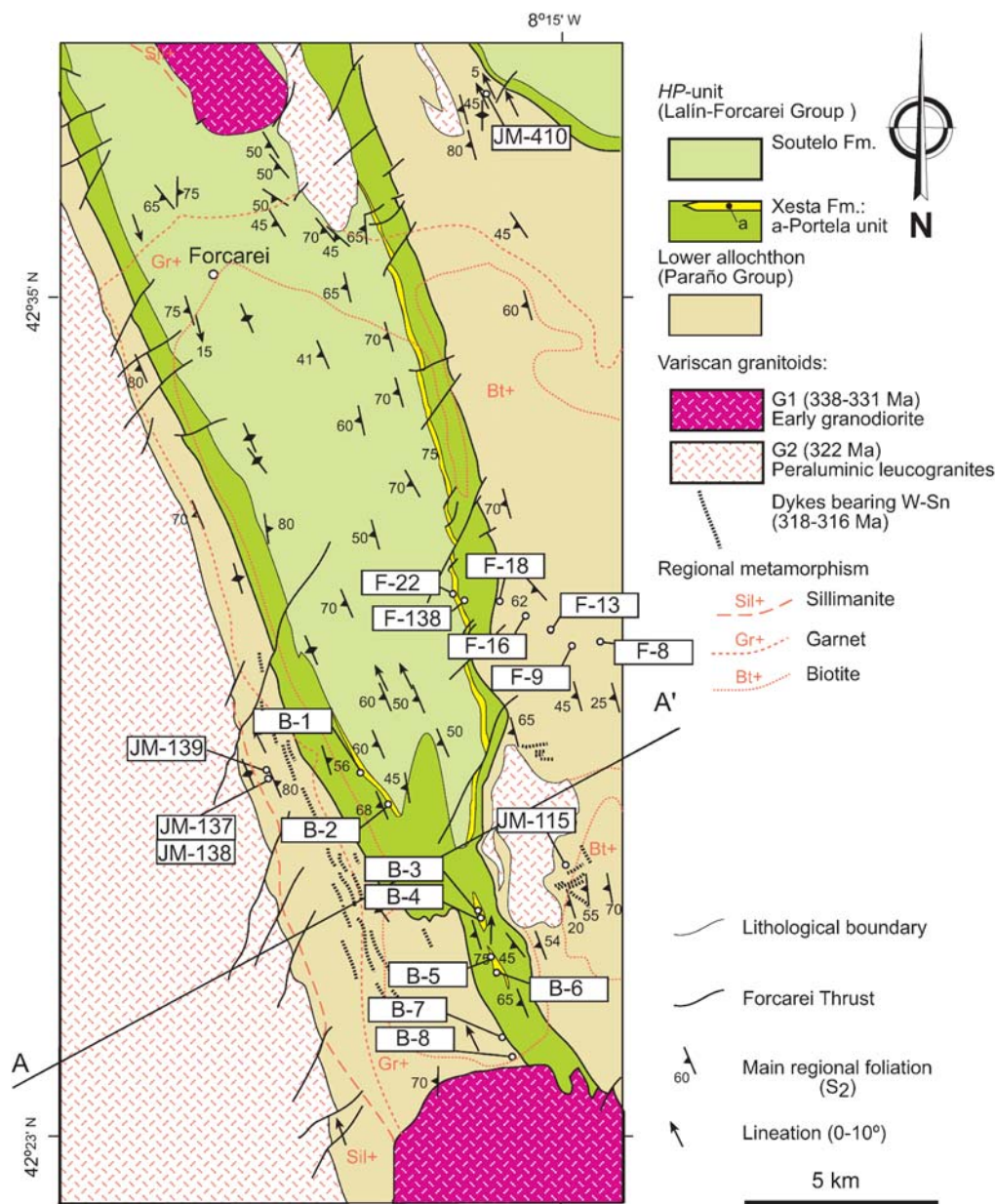


Fig. 2. Detailed geological map of the study area based on Marquínez (1984); note that almost all the samples have been collected along the periclinal termination of the major fold because of the higher quality of the outcrops. Grid numbers correspond to European Geodesic Grid 1950 (RE50). Variscan granitoids after González-Cuadra *et al.* (2006) and Gloaguen (2006), regional metamorphism after Marquínez & Klein (1982). Cross-section A–A' is in Figure 13.

One of the main features of the Galicia-Trás-os-Montes Zone is the development of large folds which formed at a relatively late stage of the formation of the Variscan orogen. The Forcarei Synform is a kilometric fold that affects the high pressure and the lower allochthon units, but it is not represented in the overlying units (Fig. 1b). It is assigned to the D₃ Variscan deformation event (Marquínez 1984).

A suite of samples of metaquartzites and quartz-schists have been collected from the Forcarei Synform for quartz *c*-axis fabric analysis in combination with shape fabric analysis and for the characterization of the flow type and deformation conditions of the main foliation (S₂). In addition, field mapping of other shear sense indicators and superimposed structures at outcrop scale are used to interpret the processes involved in fabric and folding evolution. From these data, the fold kinematics is discussed, in the context of the polyphase Variscan deformation.

Regional context of the Forcarei Synform

This section is focused on the arrangement of the thrust sheets and rock types of the two main units that lie along the Forcarei Synform (Fig. 1b).

The high pressure units, also named the basal units (Arenas *et al.* 1995; Martínez Catalán *et al.* 1996), form a fairly continuous thrust sheet consisting of schists and paragneisses alternating with felsic and mafic igneous rocks, of which granitic and peralkaline orthogneisses have yielded Rb–Sr and U–Pb ages of 490–470 Ma (Santos Zalduegui *et al.* 1995). Early-Variscan, high-*P* metamorphism in the basal units is deduced from eclogites, jadeite-bearing orthogneisses, and blueschists, and is interpreted as the result of subduction (Gil Ibarguchi 1995; Arenas *et al.* 1995, 1997; Rodríguez *et al.* 2003; Rodríguez Aller 2005; López Carmona *et al.* 2008). Peak pressure ranges between 1–1.65 GPa in the Órdenes Complex, where *P*–*T* gradients indicate a west-directed polarity for the subduction (Martínez Catalán *et al.* 1996). The palaeo-dip of the subduction zone has been estimated from the *P*–*T* conditions and thermal modelling to be between 15° and 20° (Alcock *et al.* 2005) from the *P*–*T* conditions and thermal modelling. The ophiolitic and high pressure units bear the imprint of the oceanic closure that preceded continental collision. According to isotopic data, subduction started before 376 Ma and ended at *c.* 365 Ma (Dallmeyer *et al.* 1997; Rodríguez *et al.* 2003). Subsequent underthrusting of more continental material blocked the subduction and triggered the ascent and exhumation of the basal units, whilst the convergence continued (Martínez Catalán *et al.* 1996).

The emplacement of high-*P* units in higher crustal levels over the lower allochthon, implies a horizontal displacement of at least 250 km and a rapid exhumation from depths from 60 to less than 30 km (Fig. 1a). During this tectonic stage, recumbent folds and thrusts developed, along with successive normal detachments. Compressional and extensional structures were synchronous or alternated in time and together induced the thinning and tapering of the orogenic wedge and its lateral spreading, and extended from *c.* 375–340 Ma (Martínez Catalán 2007). The unroofing took place locally under an inverted temperature gradient caused by a detachment which carried a part of the hot mantle wedge above the subduction zone over the subducted units (Martínez Catalán *et al.* 1996).

The lower allochthon unit has stratigraphic and igneous affinities with the Iberian autochthon (Valverde-Vaquero *et al.* 2005; Martínez Catalán *et al.* 2007). It does not show evidence of HP metamorphism and is considered a distal part of the Gondwana continental margin. The emplacement of the upper units over the ophiolitic units occurred across the Corredoiras shear zone at 376 Ma (Dallmeyer *et al.* 1997) and supplies a roughly top-to-the-SE emplacement (Díaz García *et al.* 1999).

In addition, crystallization-deformation relationships suggest the prograde metamorphic event occurred between S₂ and the intrusion of the Variscan granitoids (Marquínez & Klein 1982; Díaz García 1993). In the study area, the Beariz granite (Fig. 2) was emplaced at the final stages of the S₂ development, and was slightly folded into the upright Candán antiform showing top-to-the-south kinematic criteria (González-Cuadra *et al.* 2006).

Stratigraphy and structure of the study area

The study area is mainly occupied by the lower allochthon (Paraño Group), which is overlain by the high pressure unit (Lalín-Forcarei Group). These two sequences of rocks are separated by a tectonic contact parallel to the bedding, the Forcarei Thrust (Fig. 2). The Paraño Group is formed by a 3000 m thick succession of metapelites, with intercalations of thin layers of quartz-schists that are more frequent at the top of the succession. Whilst the Forcarei Thrust is not well exposed in the field, and the bottom of the Lalín-Forcarei Group is conventionally placed below the lowest layers of amphibolites, a 10 cm–5 m thick metaquartzite, the Portela unit (Hilgen 1971), appears clearly positioned on top of the amphibolites (Fig. 2). A detailed structural analysis was carried out essentially in the low grade southern limit of the Forcarei Synform. The Portela unit has been sampled because it is the most suitable rock type within the stratigraphic

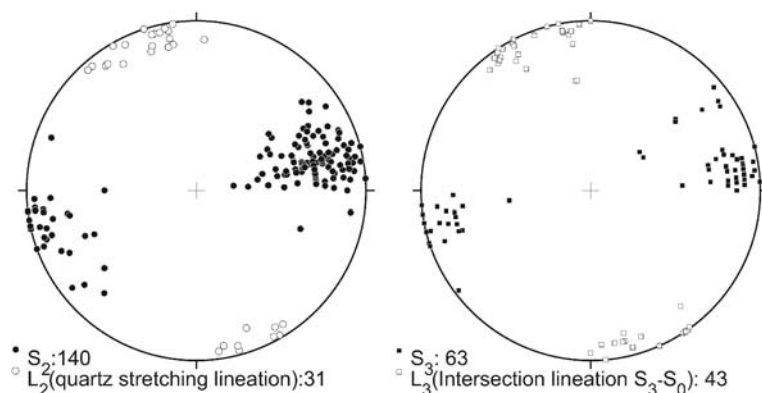


Fig. 3. Equal-area, lower-hemisphere projection of D_2 and D_3 foliation (S_2 , S_3) and lineation (L_2 , L_3) data within the study area.

sequence for quartz c -axis fabric analysis; complementarily quartz c -axis fabric from quartz-schists of the lower allochthon were also determined.

The Forcarei Synform is a gently plunging upright isoclinal fold outcropping within an area of $c. 275 \text{ km}^2$. Its axis trends NNW parallel to the trend of the fold belt and it is formed just beneath the ultramafic unit of the Órdenes complex (NW Iberian Variscan belt). Consequently, it affects exclusively the high pressure and the lower allochthon units, but it cannot be followed in the overlying units tectonically emplaced by movement along the Corredoiras shear zone (Figs 1 & 2). The main foliation (S_2) is a flat-lying schistosity spaced in domains Q (microlithons of quartz) and M (cleavage defined by micas). It seems to be more evolved in the HP-unit, where a earlier cleavage is preserved only in the porphyroblasts of albite and garnet, rather than in the lower allochthon (Díaz-García 1993).

The Portela unit has a regional S_2 with a subhorizontal mineral elongation lineation (Fig. 4a), which is parallel to the axes of rootless centimetric folds that appear in the upper part of the lower allochthon as sheath folds. This main foliation was later affected by an open upright fold, the Candán Antiform (Marquín 1984), that locally developed a spaced crenulation cleavage (S_3). S_3 often presents minor associated structures such as minor folds, conjugate shear bands and symmetric boudinage. Despite both S_2 and S_3 having the same strike on the scale of the map (Fig. 3), in some locations it is possible to observe F_3 folds superimposed on F_2 folds and forming Ramsay type 2 and type 3 interference patterns (Fig. 4b, c), where type 2 was formed by superimposed S_3 on D_2 minor sheath folds (Fig. 4b). The two foliations can only be differentiated because S_2 is more penetrative than S_3 and because the symmetry of the fabric and associated structures suggests that D_2 is characterized by

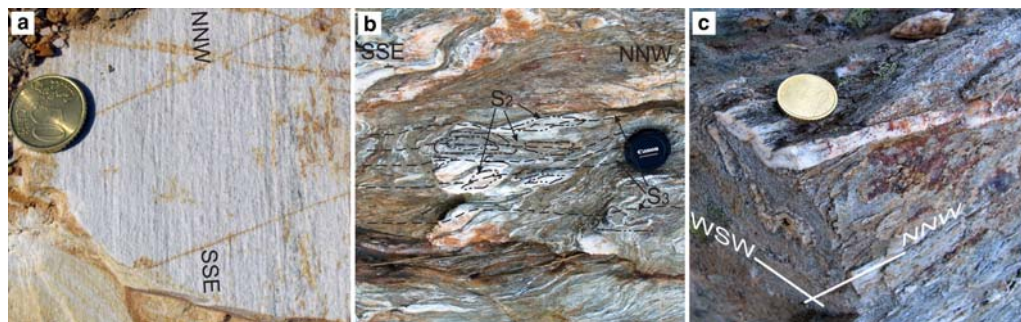


Fig. 4. Photographs of Variscan D_2 structures at outcrop-scale on metaquartzites of the Portela unit: (a) stretching lineation (samples B-3 and B-4 of Fig. 2). (b) Minor sheath folds F_2 located near sample B-2 of Figure 2. (c) Typical superposed fold F_2 - F_3 interference type 3 located between samples B-5 and B-6 of Figure 2. Coin is 24.25 mm and camera cap is 45 mm in diameter.

non-coaxial deformation, whereas D_3 is basically coaxial in character.

Rock microstructure

Twenty hand specimens have been used for the micro-structural analysis. Eight samples were collected from the Portela unit and the others from the lower allochthon in both limbs of the Forcarei Synform (Fig. 2). Metaquartzites and quartz-schist show a composite foliation (Fig. 5a) defined by coarse-quartz domains and fine-grained matrix domains composed of quartz (50–70%), biotite + muscovite \pm garnet \pm staurolite (20–40%) and feldspar (<10%). The coarse-grained domains are in fact quartz veins within the matrix, which presumably were formed during the earlier stages of D_2 . With the exception of samples B-1, B-2 and B-5, all samples were taken from areas of dominant S_2 regional foliation, where later deformation is not involved.

Grain shape fabric analysis in quartz was carried out in all of the studied sections from the hand drawings of the grains using the image processing package ImageJ, version 1.38 (public domain

program at <http://rsbweb.nih.gov/ij/>), and using the shape parameters which were defined following the procedure explained in Fernández *et al.* (2005). Additionally, c -axis fabrics were studied using a Zeiss U-stage in the XZ-section (perpendicular to the S_2 foliation and parallel to L_2) and in the YZ-section.

Three main types of quartz grains are found: ribbons (Fig. 5b), irregular grains (Fig. 5c) and polygonal grains (Fig. 5d). Undulose extinction and dynamic recrystallization are quite frequent. Some grain boundaries display bulging (Fig. 5c), so presumably they have been deformed at the high strain rate and low temperature corresponding to Regime 1 of Hirth & Tullis (1992). In general, however, the predominance of polygonal grains suggests recovery accommodated by grain boundary migration (Fig. 5a, b, d–f), which indicates a low strain rate and high temperatures (Regime 3 of Hirth & Tullis 1992). Despite the local preservation of microstructures indicating the operation of different deformation mechanisms, most of the quartz grains are modified or thermally grown later, probably during the emplacement of the Variscan granitoids.

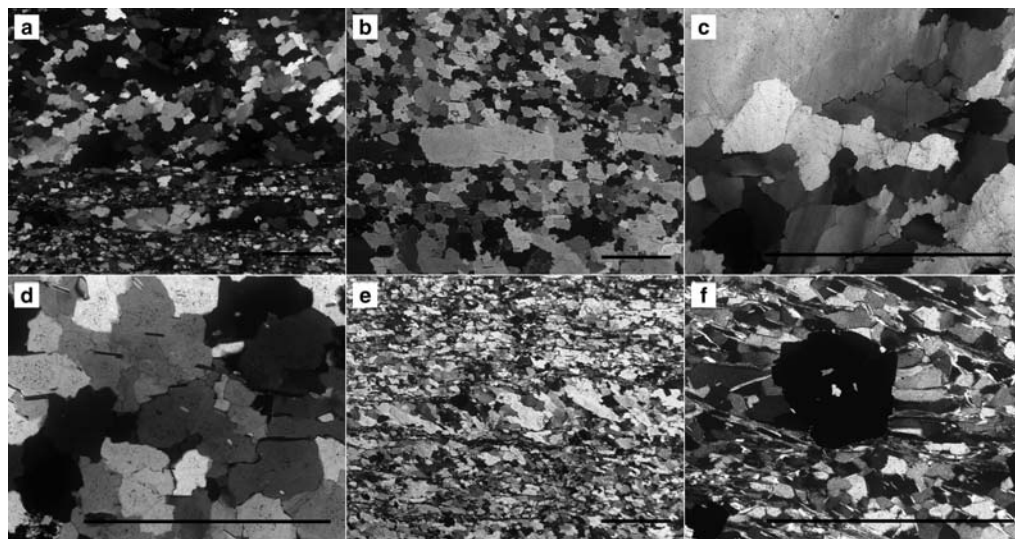


Fig. 5. Optical micrographs in transmitted light: (a) Spaced foliation composed of alternating domains of coarse- and fine-grained quartz and micas. Portela unit, sample B-4. (b) Spaced foliation composed of quartz ribbons and recrystallized quartz. Quartz-schist of Paraño Group, sample JM-410. (c) Irregular grain boundaries due to grain boundary migration and bulging recrystallization of quartz. Hosted quartz grains also present (oblique) deformation lamellae and undulose extinction. Portela unit, sample B-5A. (d) Polycrystalline quartz pinning by white mica. Quartz-schist of Paraño Group, sample JM-410. (e) Quartzite mylonite. The quartz is dynamically recrystallized and has developed an oblique foliation showing sinistral shear sense (top-to-the-south). Quartz-schist of Paraño Group, sample JM-139. (f) Strain shadows filled by quartz adjacent to a pentagonal pyrite showing dextral shear sense (top-to-the-north) during the latter stages of deformation. Quartz-schist of Paraño Group, sample FI-9. It may have modified the CPOs in quartz by superimposing c -axis quartz patterns of the type found in sample B-1 of Figure 11. All photographs are CPL and the scale-solid lines are 1 mm long.

Our observations indicate that shape and crystallographic fabrics were partially or totally reset during the progressive Variscan deformation and recovered by the thermo-metamorphic effect of

the granitoid intrusion, but it is still possible to compare the symmetry of shape and crystallographic fabrics, and then to interpret both in kinematic terms. The shear sense of the main S_2

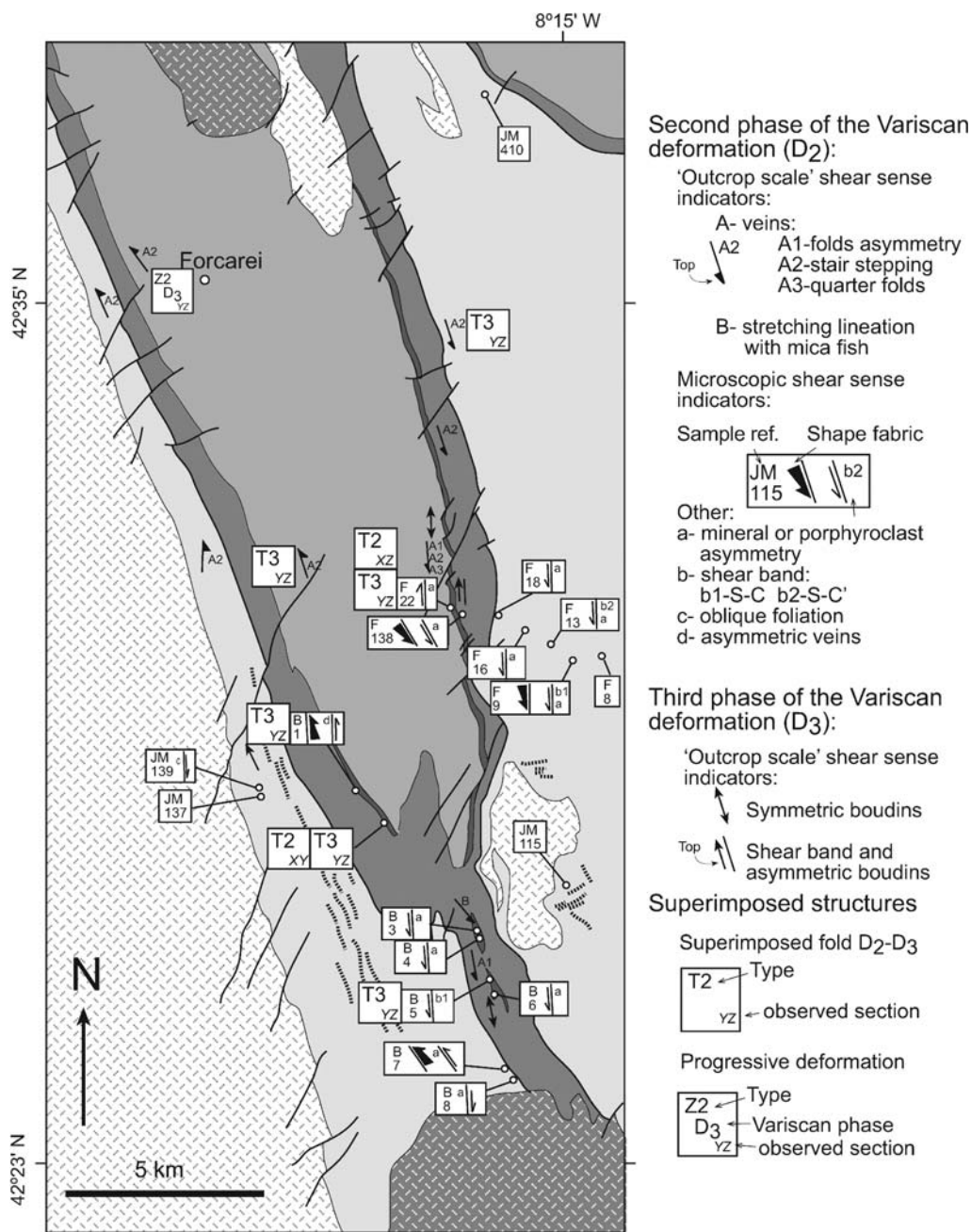


Fig. 6. Kinematic map of the study area showing the sample location and the shear sense indicators. Terminology for shear sense indicators as in Passchier & Trouw (2005). Ramsay's nomenclatures are used for the type of superimposed folds (Ramsay 1962) and for the type of progressive deformation (Ramsay 1967).

regional foliation has been determined using the asymmetry of the quartz *c*-axis preferred orientation together with additional kinematic indicators, such as the asymmetry of the shape fabric (SPO), fold asymmetry, shear veins, quarter fold veins, shear bands and oblique foliations. All the kinematic indicators are represented in Figure 6 and summarized in Table 1, and suggest a bulk sinistral shear sense during the development of the non-coaxial D₂ deformation. In the field, only a few sets of shear bands and boudins were found deforming the S₂ foliation, and indicating a local, dextral sense of shear. They have been interpreted as later D₃ structures related to a bulk extension parallel to the D₃ fold axis.

Grain shape fabric

Three main geometric features of the shape fabric have been analysed: the grain size, grain shape and grain orientation of the polycrystalline quartz grains aggregates. The grain size distribution has been characterized using two parameters: the percentage area of the different size ranges, and the size frequency. Most quartzites and quartz-schists deformed during D₂ have a tri-modal grain size distribution (Fig. 7) with an average grain area ranging from 2300 µm² (samples F-138, F-22, F-18, F-16, F-13, F-9 and F-8 collected from the

east limb and far from the large granitoid intrusion) to 60 000 µm² (samples from near the granitoid boundaries or from just below the ophiolite layer). Some grain size distributions correspond to samples with special deformational features; for example, the shape fabric of sample B-1 corresponds to later tension gash veins formed during the latter stage of the Variscan deformation, and samples B-2 and B-5 correspond to segregation veins affected by superposed D₂–D₃ folds.

The grain shape is analysed using two parameters: grain ellipticity and the shape parameter *S* (Fig. 8). Grain ellipticity is the aspect ratio of the largest ellipse that can be inscribed inside each grain. The shape parameter (*S*) is grain-size independent, and is equal to 1 if the grain is a perfect circle, otherwise *S* decreases from 1 as grain boundary irregularities increase (Fernández *et al.* 2005). The arithmetic mean of *S* (\bar{S}) ranges from 0.53–0.57 and ellipticity ranges from 1–5. Larger \bar{S} correspond to fabrics of polygonal grains, whereas lower \bar{S} and larger ranges of ellipticity correspond to fabrics of irregular boundaries developed during the latter stages of deformation (Sample B-1). Obviously, ellipticity is lower in the YZ section (Sample B-5B) than in the XZ section (Fig. 7).

The grain orientation is defined by the angle ϕ between the major axis of the greatest inscribed ellipse and the *X* direction (Fig. 9). The histograms

Table 1. Summarised shear sense indicators from quartz fabric analysis and local field observations (Fig. 2). Note sinistral, according to the stratigraphic way-up of units within the Forcarei Synform, is top-to-the south along the east limb, but is top-to-the north along its west limb

Sample	Quartz <i>c</i> -axes	Shape fabric	Porphyroclast asymmetry	Shear bands	Stair steeping
<i>West limb of the Forcarei Synform and east limb of the Candán Anticline:</i>					
JM-410	Sinistral	—	—	—	—
JM-137	Sinistral	—	—	—	—
JM-139	Sinistral	—	—	—	—
B-7	Sinistral	Sinistral	—	—	Sinistral
Other	—	—	—	Sinistral (in 1 locality)	Sinistral (in 4 localities)
B-1*	Sinistral	Sinistral	—	(*latter tension gash)	—
<i>East limb of the Forcarei Synform:</i>					
F-8	Sinistral	—	—	—	—
F-9	Sinistral	Sinistral	Sinistral	Sinistral	—
F-13	Sinistral	—	Sinistral	—	Sinistral
F-16	—	—	Sinistral	—	—
F-18	—	—	Sinistral	—	—
F-22	Sinistral	—	Dextral	—	—
F-138	—	Sinistral	Sinistral	Sinistral	—
JM-115	Sinistral	—	—	—	—
Other	—	—	—	Dextral (in 1 locality)	Sinistral (in 4 localities)
<i>Hinge zone of the Forcarei Synform:</i>					
B-3	Dextral	Sinistral	—	—	—
B-4	Sinistral	—	—	—	Sinistral
B-6	Sinistral	Sinistral	—	—	Sinistral

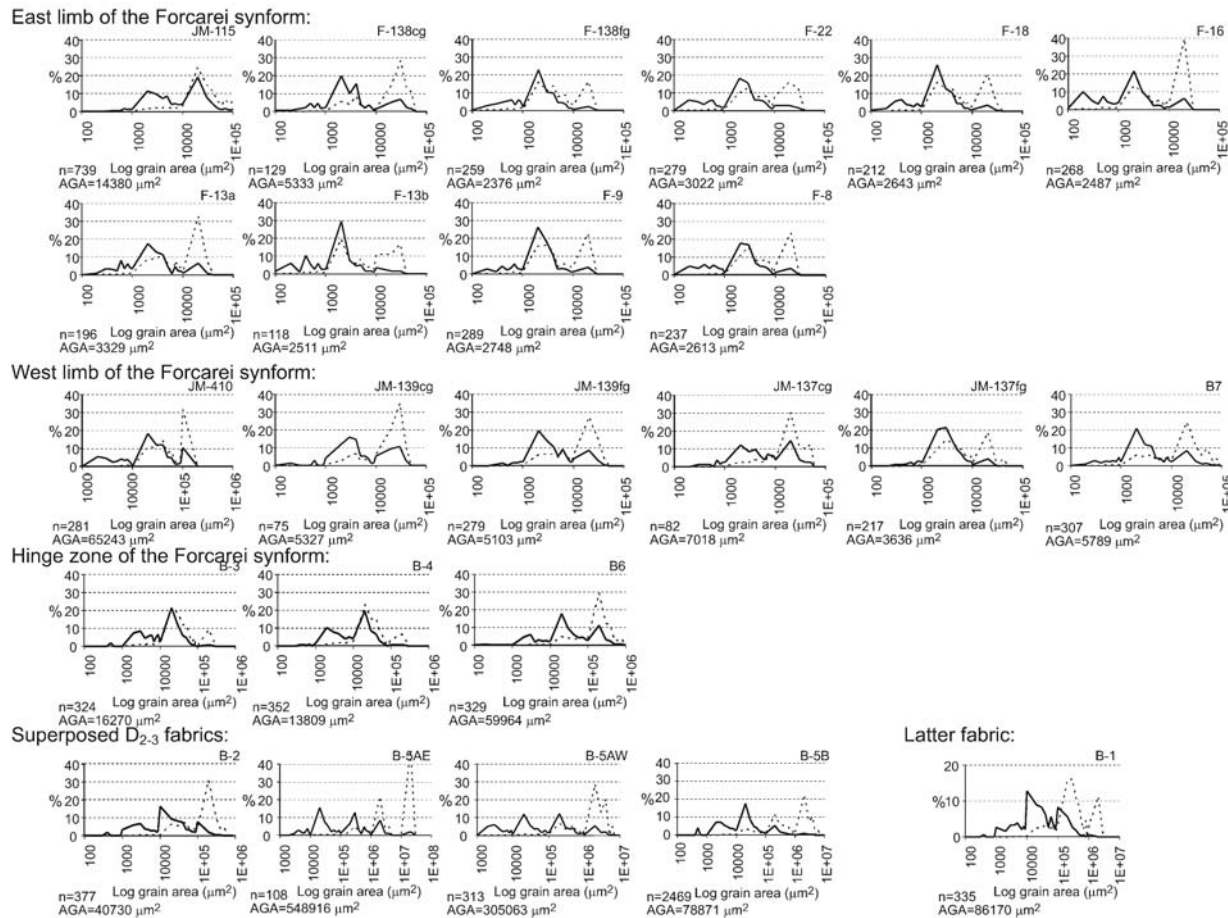


Fig. 7. Grain size distribution diagrams showing the size frequency (black line) and the area per cent (dashed line) of the different size ranges; n, number of quartz grains measured by sample; c.g., abbreviation of coarse grained domain; f.g., fine grained domain; AGA, average grain area.

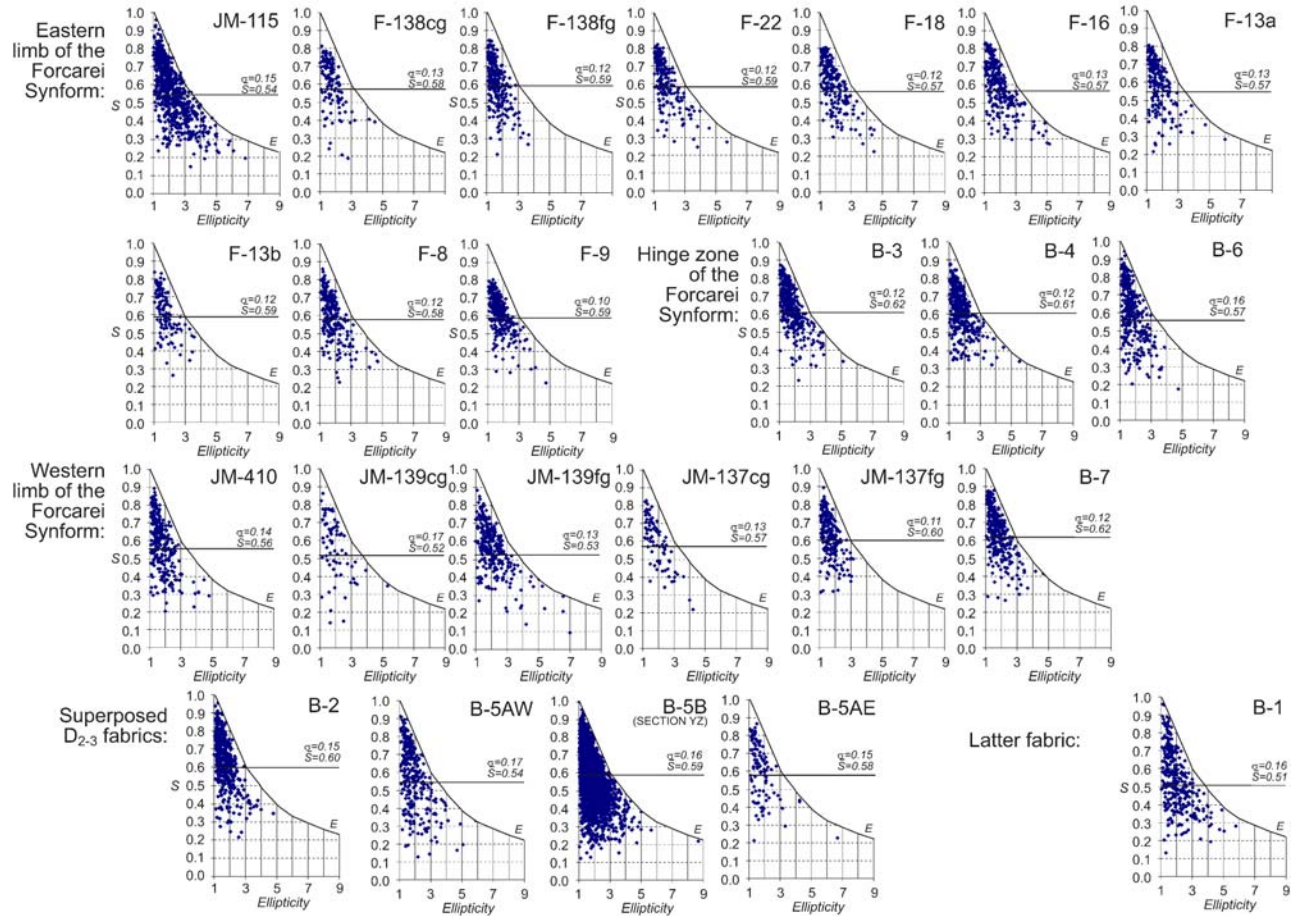
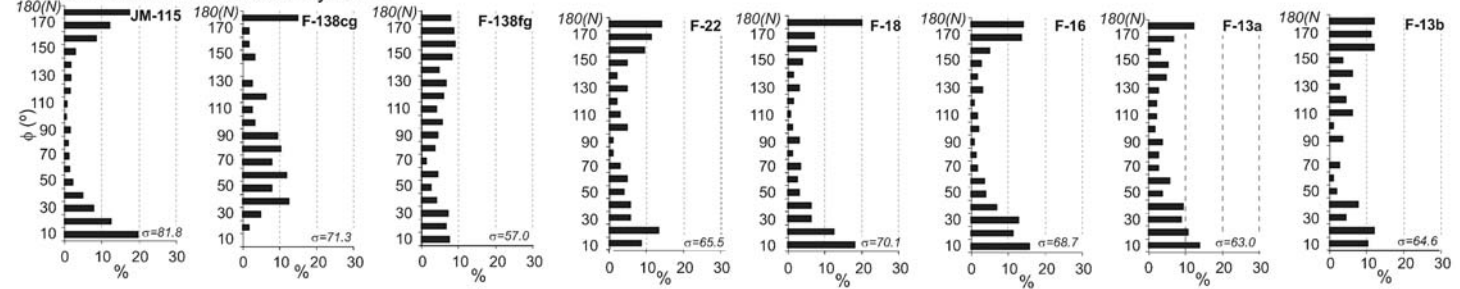
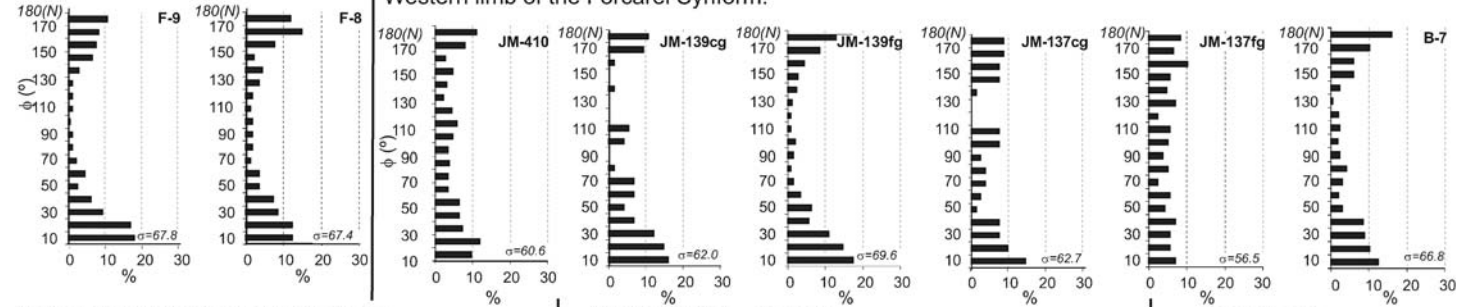


Fig. 8. Shape parameter (S) v. ellipticity diagrams; \bar{S} is noted by the horizontal black line and σ is the standard deviation. The curved line E is the continuous trace of an ellipse as its ellipticity increases, and is only plotted as a reference line.

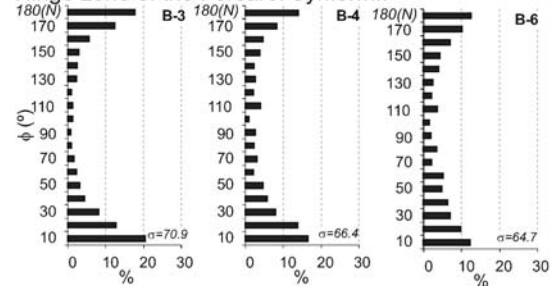
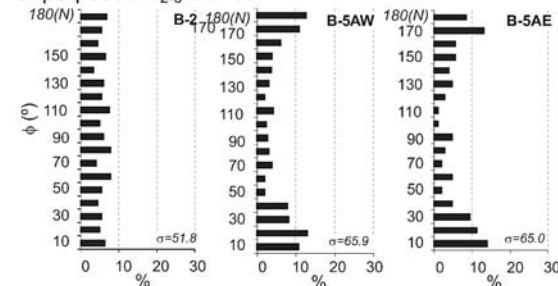
Eastern limb of the Forcarei Synform:



Western limb of the Forcarei Synform:



Hinge zone of the Forcarei Synform:

Superposed D₂₋₃ fabrics:

Latter fabric:

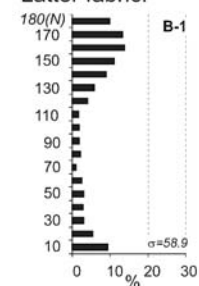


Fig. 9. Histograms showing the frequency of the orientation (ϕ) of the major ellipse inscribed in each grain. σ , standard deviation. X marked in abscises is oriented to the north.

of the grain orientation show a flat distribution in fabrics that are totally thermally recovered (Samples JM-410, JM-137 and B-2). A Gaussian distribution can be observed in fabrics with oblique orientations (samples JM-139 and F-138) or in fabrics of sigmoidal tension gashes (sample B-1), with the maximum frequency of grain orientation asymmetric with respect to X . However, the most common fabric shows a slightly asymmetric Gaussian distribution, with maxima close to the foliation plane. Consequently shape fabrics cannot be used as shear sense indicators (Fig. 9).

Quartz c -axis preferred orientation

In all samples the c -axes were measured separately within the domains of coarse- and fine-grained quartz, but no significant differences were found between domains (i.e. fabrics F-138 and JM-137 in Fig. 10). With the exception of the single girdles of the fabrics JM-115 and B-4, almost all the quartz c -axis preferred orientations are defined by unusual patterns. In most cases, the quartz c -axis corresponds to positions favourable for slip in the basal (maximum around Z) and prismatic planes (maximum on Y), indicating that they developed at temperatures ranging from 300 to 600 °C (Christie & Green 1964; Bouchez & Pêcher 1981; Takeshita & Wenk 1988) and consistent with reported D_2 metamorphic conditions (Fig. 2). The pattern obtained in sample F-138 is characterized by a quartz c -axis preferred orientation defining a great circle centred on Y . This anomalous fabric could be interpreted as 'usual' (it is a permutation of the position of the X and Y axes), suggesting that maximum stretching during the development of crystallographic fabric was normal to the shape fabric (Fig. 9). Another unusual quartz c -axis pattern is obtained in sample B-1 (Fig. 11), corresponding to a fabric formed during the development of a later tension gash vein. This is defined by a single point maximum around Z whose external asymmetry is consistent with the asymmetry of the shape fabric (Fig. 9). Both indicate top-to-the-north shear. The effect of the superposition of the Variscan deformational events on the crystallographic fabrics has been evaluated in samples B-2 and B-5 (Fig. 11), where S_2 foliation and sheath folds were refolded by F_3 folds with associated crenulation cleavage. In addition, the microstructure of the sample B-5B has allowed us to observe in more detail the c -axis patterns formed on the different limbs of a syn-kinematic vein progressively folded during D_2 , and refolded by F_3 folds. The c -axis fabric pattern in sample B-2 is similar to the partial patterns obtained on the limbs of the D_2 veins refolded during D_3 in sample B-5B (Fig. 12). These c -axis patterns generally show asymmetric fabrics

defining incomplete crossed girdles, or single girdles with a main maximum around Z .

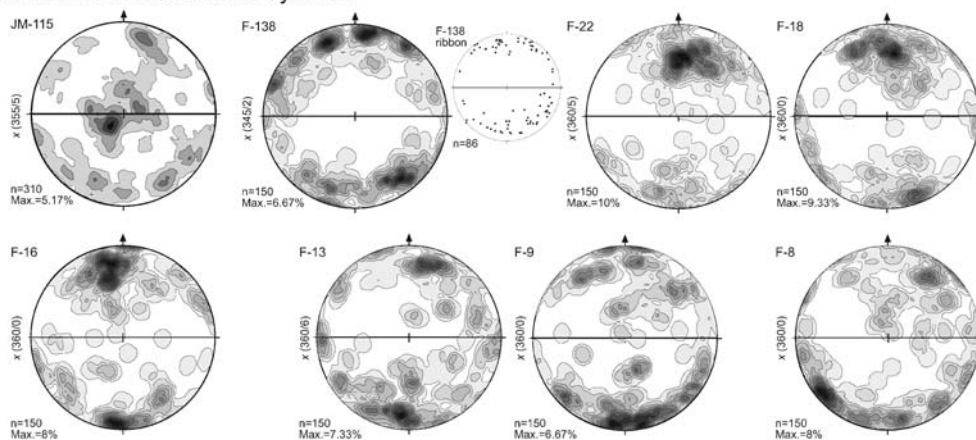
Usually quartz c -axis patterns show an asymmetry when they develop by non-coaxial progressive deformation, and this asymmetry can be used to deduce the sense of shear. It can be defined as an internal asymmetry, independent of other fabric elements, or as an external asymmetry with respect to S and L in the rock (Passchier & Trouw 2005). The internal asymmetry of c -axis girdles in some cases is in agreement with the external asymmetry of the patterns with respect to S_2 and L_2 , and generally indicates sinistral shear sense in both limbs of the Forcarei Synform; in other words, top-to-the-south along the east limb, and top-to-the-north along the west limb. However, within the superposed fabrics D_{2-3} of sample B-5B the opposite shear sense can be deduced within the different refolded D_2 limbs (Fig. 12). This is similar to the effect described by García Celma (1982) for fabrics showing kinematic domains smaller than thin-section scale. In the case of the sample B-5B, the change in shear sense demonstrates that c -axis preferred orientations were mainly developed during D_2 , and that shear sense changes disappear after fold restoration (Fig. 13a). In addition, the unequal distribution and intensity of homologous maxima in basal and prismatic position with respect to the S_2 and L_2 defines a third type of asymmetry, called here 'triclinic' because it is due to the apparent rotation of the pattern about the X and the Z axes. Indeed, some of these fabrics have apparent 'triclinic' symmetry, as with total-fabric B-5B (Fig. 11). However, when fabrics are measured in a single domain, c -axis fabrics with generally monoclinic symmetry are obtained (Fig. 12), suggesting that the 'triclinic' symmetry is a consequence of the folding/transposition in mylonites.

Discussion

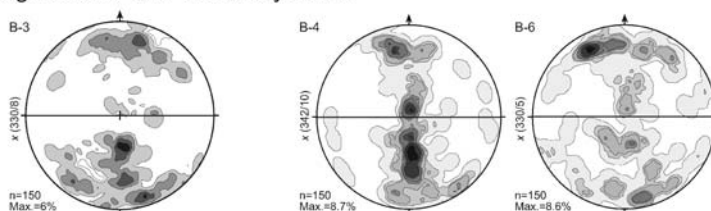
The structures and microstructures observed in the study area were formed by polyphasic deformation. The first episode of deformation can be observed only on the microscopic scale as a set of inclusion trails within the porphyroblasts, from which a map of isograds of inverted regional metamorphism M_1 was constructed by Arenas *et al.* (1995). Later a pervasive flat lying foliation was formed and then crenulated by a sub-vertical foliation. In the light of the kinematic data presented in this research, which indicate a general sinistral shear, the following interpretation could explain the development of the large-scale fold and the kinematic indicators (Fig. 13).

The widespread S_2 cleavage surfaces and the Forcarei Thrust, which are approximately parallel, are ascribed to the deformation event D_2 . This

Eastern limb of the Forcarei Synform:



Hinge zone of the Forcarei Synform:



Western limb of the Forcarei Synform:

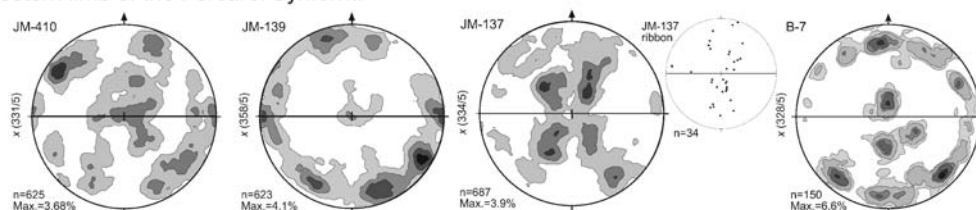


Fig. 10. Quartz *c*-axis textures from the regional D₂ Variscan fabric in parautochthonous quartz-schists and in metaquartzites from the basal unit. The location of the samples is shown in Figure 2. Pole figures are contoured in 1% intervals, starting from 1%, in equal area, lower hemisphere projections; the solid line is the rock foliation (normal to Z); X is horizontal (stretching lineation). North is approximately to the left.

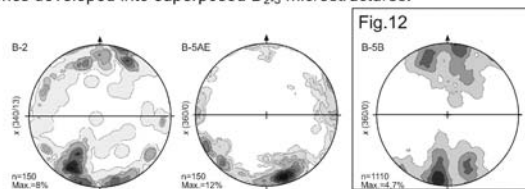
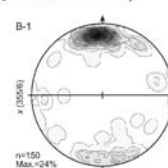
Fabrics developed into superposed D₂₋₃ microstructures:Later fabric (Post-D₃ strain shadows):

Fig. 11. Quartz *c*-axis preferred orientation from superposed D₂₋₃ Variscan fabric and later fabric in parautochthonous quartz-schists and in metaquartzites from the basal unit (Sample B-5B). Location of samples is shown in Figure 2. Pole figures are contoured in the same intervals and with the same reference frame as in Figure 10. The bulk data of sample B-5, plotted by domains in Figure 12, is in the box.

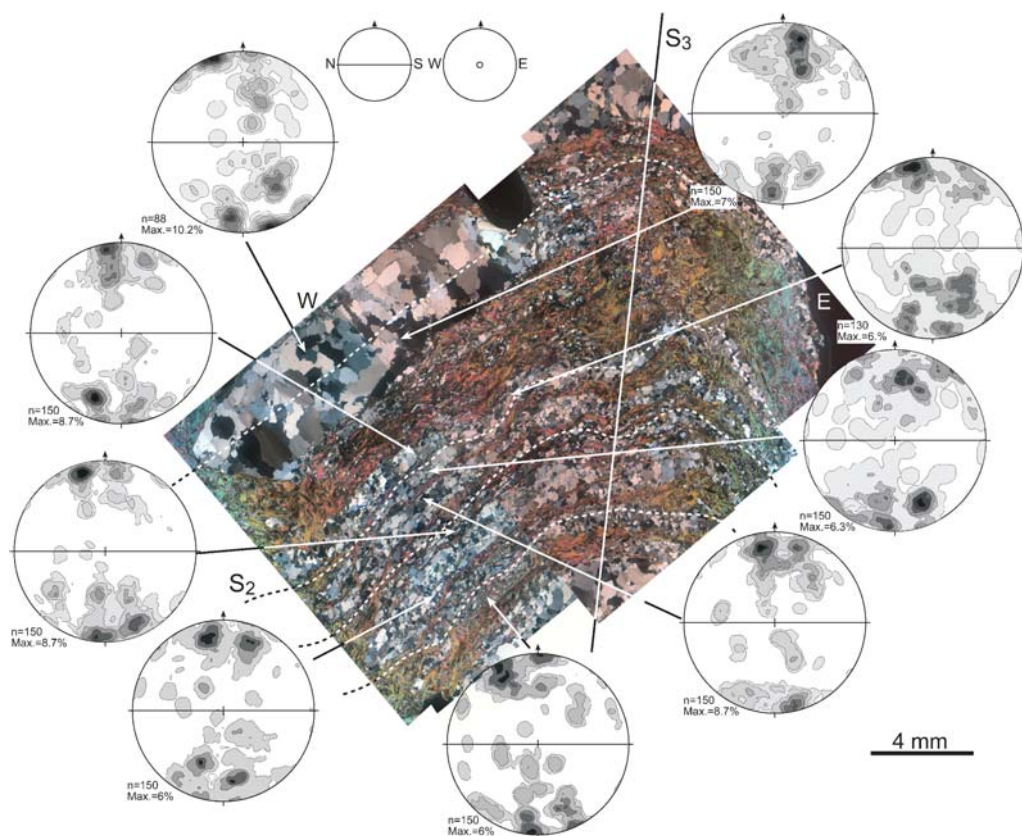


Fig. 12. Quartz *c*-axis preferred orientation pattern corresponding to quartz in Variscan D_2 veins refolded by D_3 microfolds. Different D_3 -limbs are plotted in Figure 11 (East limb is pattern B-5AE and west limb is pattern B5-AW). Note the orientation of the photomicrograph is west–east, whereas the orientation of the reference frame in the pole figures is defined by the north–south horizontal L_2 lineation. Pole figures are contoured in the same intervals and with the same reference frame as in Figure 10.

deformation event was also responsible for other related structures such as minor folds and the high strain recorded by the Portela unit. Although no conclusive evidence of the original orientation of the S_2 cleavage and the Forcarei Thrust is available, it is likely that both structures were generated in an almost flat-lying disposition. We suggest that this region underwent a notable amount of shear during D_2 , so that the S_2 cleavage developed in the initial stages of the second Variscan deformation event and was followed by propagation of the Forcarei Thrust. The hanging wall of the Forcarei Thrust moved southwards relative to its footwall together with a slight progressive clockwise rotation along a sub-vertical axis. This hypothesis is supported by the orientation of the stretching lineation developed in this region during D_2 (L_2), which is sub-horizontal and exhibits a slight dispersion from north–south to NW–SE trend (Fig. 3).

According to the present-day lineation trend, the hanging wall thrust motion would have initiated towards the SE and would have rotated progressively towards the south. If the Forcarei Synform is totally unfolded along its sub-horizontal fold axis, so that both fold limbs return to horizontal, the small-scale sinistral shear indicators related to D_2 measured in the east limb of the Forcarei Synform indicate top-to-the-south and agree with the southwards sense of motion along the Forcarei Thrust. However, the small-scale sinistral shear indicators related to D_2 measured in the west limb of the Forcarei Synform point out top-to-the-north and, apparently, they do not agree with the southwards sense of motion along the Forcarei Thrust. This may be explained if the clockwise rotation along a vertical axis solely prevails over the southward component of hanging wall thrust motion in the last stage of thrust motion before it becomes

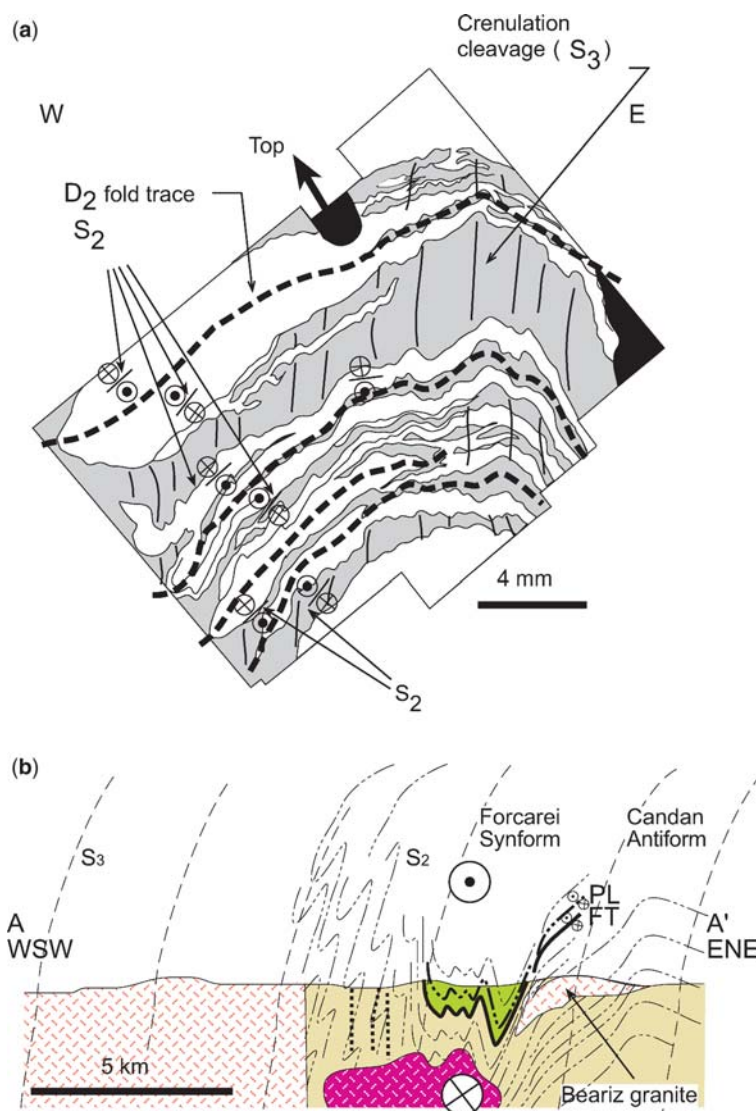


Fig. 13. (a) Interpretative sketch of the microstructure found in the thin section of sample B-5B shown in Figure 12. (b) Vertical cross-section A–A' to show the relationships between the main tectono-metamorphic features. The larger, late Variscan granitoid is bounded to the E by a later vertical strike-slip fault and is in contact with the adjacent Forcarei Synform. FT is the Forcarei Thrust and PL is the Portela unit. Location of cross-section A–A' is in Figure 2.

inactive. Thus, the sinistral kinematic indicators found in the west limb of the Forcarei Synform would have only recorded the very last stage of Forcarei Thrust movement, and this is the reason why they are much less developed than those found in the east limb of the synform. Later on, during the deformation event D_3 , the Forcarei Synform was formed, a sub-vertical crenulation cleavage (S_3) developed parallel to the axial plane of the Forcarei Synform, an intersection lineation (L_3) whose

orientation is almost equivalent to the L_2 lineation (Fig. 3) and other related structures such as minor folds also developed, and the D_2 structural elements (S_2 and Forcarei Thrust) were folded. Although this kinematic model is provocative, in our opinion it satisfactorily explains the large-scale framework, meso- and microstructures, and kinematic indicators mapped in this region and it agrees with the general features of the sequence of deformations observed in surrounding regions, that is, a sub-horizontal

cleavage developed in the early stages of the Variscan deformation and thrust faults subsequently folded by structures which display a steep S_3 crenulation cleavage parallel to their axial planes.

Conclusions

The Forcarei Synform is a kilometric-scale, upright isoclinal fold formed just beneath the ultramafic unit of the Ordenes complex (NW Iberian Variscan belt). The structural analysis performed suggests that, at least, two deformation events were recorded in this region. D_2 produced a pervasive cleavage, a stretching lineation, minor folds and other related structures, and also the Forcarei Thrust. Most of the quartz D_2 microstructures were thermally recovered later and probably during the emplacement of the Variscan granitoids. However some ductile D_2 microstructures survived as relicts, such as quartzitic veins folded within the matrix. The related quartz c -axis preferred orientation are in agreement with temperatures ranging from 600–300 °C. Quartz c -axis fabrics measured in single domain have generally monoclinic symmetry whereas apparent 'triclinic' symmetry is interpreted as a consequence of the folding/transposition in the pervasively deformed mylonites D_{2-3} . Quartz-SPOs, asymmetric microstructures and other 'field' shear sense indicators indicate general sinistral shear sense. This shear sense could be result of a southwards motion hanging wall of the Forcarei Thrust accompanied by progressive clockwise rotation along a sub-vertical axis before the Forcarei Synform was formed.

Later, coaxial horizontal shortening in an approximately ENE–WSW direction occurred during the third stage of the Variscan deformation and produced a crenulation cleavage parallel to the Forcarei Synform axial plane, boudinage extension parallel to L_2 , minor folds superposition, and the formation of the Forcarei Synform.

In memoriam of Florentino Díaz-García, the co-author who died on the 28th August 2009. The authors are grateful to J. Poblet, A. Ribeiro and especially to an anonymous reviewer for all their constructive review of the first version. Special thanks are due to the colleagues of the department J. Aller and F. Bastida for discussion of the final version. The present work was supported by Spanish CGL2008-03786-BTE project.

References

ALCOCK, J., ARENAS, R. & MARTÍNEZ CATALÁN, J. R. 2005. Shear stress in subducting continental margin from high-pressure moderate-temperature metamorphism in the Ordenes Complex. *Galicia, Northwest Spain, Tectonophysics*, **397**, 181–194.

ARENAS, R., RUBIO PASCUAL, F. J., DÍAZ GARCÍA, F. & MARTÍNEZ CATALÁN, J. R. 1995. High pressure micro-inclusions and development of an inverted metamorphic gradient in the Santiago Schists (Ordenes Complex, Northwest Iberian Massif, Spain): evidence of subduction and syncollisional decompression. *Journal of Metamorphic Geology*, **13**, 141–164.

ARENAS, R., ABATI, J., MARTÍNEZ CATALÁN, J. R., DÍAZ GARCÍA, F. & RUBIO PASCUAL, F. J. 1997. P–T evolution of eclogites from the Agualada Unit (Ordenes Complex, Northwest Iberian Massif, Spain): implications for crustal subduction. *Lithos*, **40**, 221–242.

BOUCHEZ, J. L. & PÊCHER, A. 1981. The Himalayan Main Central Thrust pile and its quartz-rich tectonics in central Nepal. *Tectonophysics*, **78**, 23–50.

CHRISTIE, J. M. & GREEN, H. W. 1964. Several new slip mechanisms in quartz. *EOS*, **45**, 103.

DALLMEYER, R. D., MARTÍNEZ CATALÁN, J. R. ET AL. 1997. Diachronous Variscan tectonothermal activity in the Northwest Iberian Massif: evidence from $^{40}\text{Ar}/^{39}\text{Ar}$ dating of regional fabrics. *Tectonophysics*, **277**, 307–337.

DÍAZ GARCÍA, F. 1993. Análisis comparativo de la foliación regional y estructuras asociadas en el Dominio de Santiago y su autóctono relativo (Galicia, Northwest de España). *Revista de la Sociedad Geológica de España*, **6**, 105–114.

DÍAZ GARCÍA, F., MARTÍNEZ CATALÁN, J. R., ARENAS, R. & GONZÁLEZ CUADRA, P. 1999. Structural and kinematic analysis of the Corredoiras Detachment: evidence for early Variscan synconvergent extension in the Ordenes Complex, Northwest Spain. *International Journal of Earth Sciences*, **88**, 337–351.

FARIAS, P. 1990. *La Geología de la región del sinforme de Verín (Cordillera Herciniana, NW de España)*. Laboratorio Xeolóxico de Laxe, Serie Nova Terra 2, A Coruña.

FARIAS, P. & MARCOS, A. 2004. Dominio Esquistoso de Galicia-Tras-os-Montes. In: VERA, J. A. (ed.) *Geología de España*. SGE-IGME, Madrid, 135–138.

FARIAS, P., GALLASTEGUI, G. ET AL. 1987. Aportaciones al conocimiento de la litoestratigrafía y estructura de Galicia Central. *Memórias-Museo e Laboratório Mineralógico e Geológico Faculdade de Ciências, Universidade do Porto*, **1**, 411–431.

FERNÁNDEZ, F. J., MENÉNDEZ-DUARTE, R., ALLER, J. & BASTIDA, F. 2005. Application of Geographical Information Systems to shape-fabric analysis. In: BRUHN, D. & BURLINI, L. (eds) *High-Strain Zones: Structure and Physical Properties*. Geological Society, London, Special Publications, **245**, 409–420.

GARCÍA CELMA, A. 1982. Domainal and fabric heterogeneities in the Cap de Creus quartz mylonites. *Journal of Structural Geology*, **4**, 443–456.

GIL IBARGUCHI, J. L. 1995. Petrology of jadeite metagranite and associated orthogneiss from the Malpica-Tuy allochthon (Northwest Spain). *European Journal of Mineralogy*, **7**, 403–415.

GLOAGUEN, E. 2006. *Apports d'une étude intégrée sur les relations entre granites et minéralisations filoniennes (Au et Sn-W) en contexte tardi orogénique (Chaîne Hercynienne, Galice centrale, Espagne)*. PhD thesis, University d'Orléans, France.

- GONZÁLEZ-CUADRA, P., DÍAZ GARCÍA, F. & CUESTA FERNÁNDEZ, A. 2006. Estructura del granito de Beariz (Ourense, Galicia). *Geogaceta*, **40**, 151–154.
- HILGEN, J. D. 1971. The Lalín unit; a new structural element in the Hercynian orogen of Galicia (Northwest Spain). *Proceedings of the Koninklijke Nederlandse Akademie van Wetenschappen*, **74**, 398–407.
- HIRTH, G. & TULLIS, J. 1992. Dislocation creep regimes in quartz aggregates. *Journal of Structural Geology*, **14**, 145–159.
- JULIVERT, M., FONTBOTE, J. M., RIBEIRO, A. & CONDE, L. N. 1972. *Mapa tectónico de la Península Ibérica y Baleares, E. 1:1.000.000*. Instituto Geológico y Minero de España, Madrid.
- LÓPEZ CARMONA, A., ABATI, J. & RECHE, J. 2008. Metamorphic evolution of the HP/LT Ceán schists (Malpica-Tui Unit, Northwest Iberian Massif). *Geogaceta*, **43**, 3–6.
- MARQUÍNEZ, J. 1984. *La geología del Área Esquistosa de Galicia Central (Cordillera Herciniana, Northwest de España)*. Memorias del Instituto Geológico y Minero de España 100/231.
- MARQUÍNEZ, J. & KLEIN, E. 1982. Evolución temporal y distribución del metamorfismo en el área esquistosa de Galicia Central (NO de España). *Trabajos de Geología*, **12**, 227–242.
- MARCOS, A. 1973. Las series del Paleozoico inferior y la estructura herciniana del occidente de Asturias (NW de España). *Trabajos de Geología*, **6**, 3–113.
- MARTÍNEZ CATALÁN, J. R., ARENAS, R., DÍAZ GARCÍA, F., RUBIO PASCUAL, F. J., ABATI, J. & MARQUÍNEZ, J. 1996. Variscan exhumation of a subducted Paleozoic continental margin: the basal units of the Ordenes Complex. *Galicia, Northwest Spain. Tectonics*, **15**, 106–121.
- MARTÍNEZ CATALÁN, J. R., DÍAZ GARCÍA, F. ET AL. 2002. Thrust and detachment systems in the Ordenes Complex (Northwest Spain). In: MARTÍNEZ CATALÁN, J. R., HATCHER, R. D., ARENAS, R. & DÍAZ GARCÍA, F. (eds) *Variscan-Appalachian Dynamics: The Building of the Late Paleozoic Basement*. Geological Society of America, Special Papers, **364**, 163–182.
- MARTÍNEZ CATALÁN, J. R., ARENAS, R. ET AL. 2007. Space and time in the tectonic evolution of the Northwestern Iberian Massif: implications for the Variscan belt. In: HATCHER, R. D. JR, CARLSON, M. P., MCBRIDE, J. H. & MARTÍNEZ CATALÁN, J. R. (eds) *4-D Framework of Continental Crust*. Geological Society of America, Memoir, **200**, 403–423.
- MATTE, P. 1968. La structure de la virgation hercinienne de Galicie (Espagne). *Extrait des travaux du laboratoire de géologie de la Faculté des Sciences de Grenoble*, **44**, 1–228.
- PASSCHIER, C. W. & TROUW, R. A. J. 2005. *Microtectonics, 2nd Revised and Enlarged Edition*. Springer-Verlag, Berlin.
- PÉREZ-ESTAÚN, A., MARTÍNEZ CATALÁN, J. R. & BASTIDA, F. 1991. Crustal thickening and deformation sequence in the footwall to the suture of the Variscan belt of Northwest Spain. *Tectonophysics*, **191**, 243–253.
- RAMSAY, J. G. 1962. Interference patterns produced by the superposition of folds of 'similar' type folds. *Journal of Geology*, **60**, 466–481.
- RAMSAY, J. G. 1967. *Folding and Fracturing of Rocks*. McGraw-Hill, New York.
- RODRÍGUEZ, J., COSCA, M. A., GIL IBARGUCHI, J. I. & DALLMEYER, R. D. 2003. Strain partitioning and preservation of $^{40}\text{Ar}/^{39}\text{Ar}$ ages during Variscan exhumation of a subducted crust (Malpica-Tui complex, Northwest Spain). *Lithos*, **70**, 111–139.
- RODRÍGUEZ ALLER, J. 2005. Recristalización y deformación de litologías supracorticales sometidas a metamorfismo de alta presión (Complejo de Malpica-Tuy, NO del Macizo Ibérico). *Series Nova Terra*, **29**/572.
- SANTOS ZALDUEGUI, J. F., SCHÄRER, U. & GIL IBARGUCHI, J. I. 1995. Isotope constraints on the age and origin of magmatism and metamorphism in the Malpica-Tuy allochthon, Galicia, Northwest-Spain. *Chemical Geology*, **121**, 91–103.
- TAKESHITA, T. & WENK, H. R. 1988. Plastic anisotropy and geometric hardening in quartzites. *Tectonophysics*, **149**, 345–360.
- VALVERDE-VAQUERO, P., MARCOS, A., FARIAS, P. & GALLASTEGUI, G. 2005. U–Pb dating of Ordovician felsic volcanism in the Schistose Domain of the Galicia-Trás-os-Montes Zone near Cabo Ortegal (Northwest Spain). *Geologica Acta*, **3**, 27–37.

Tectonic style and structural analysis of the Puebla de Guzmán Antiform (Iberian Pyrite Belt, South Portuguese Zone, SW Spain)

ELENA M. MANTERO^{1*}, FRANCISCO M. ALONSO-CHAVES¹,
ENCARNACIÓN GARCÍA-NAVARRO¹ & ANTONIO AZOR²

¹*Departamento de Geodinámica y Paleontología, (Universidad de Huelva),
Campus 'El Carmen', 21007 Huelva, Spain*

²*Departamento de Geodinámica, (Universidad de Granada), Campus de Fuentenueva,
18002 Granada, Spain*

**Corresponding author (e-mail: elena.mantero@dgyp.uhu.es)*

Abstract: In the South Portuguese Zone (Iberian Massif), thin-skinned tectonics linked to the collision with the Ossa-Morena Zone produced the inversion of previous extensional basins in Carboniferous times. Its central domain, namely the Iberian Pyrite Belt, underwent two deformation phases at mostly low-grade metamorphic conditions linked to a progressive deformation migrating upwards from a basal detachment and from north to south. The Puebla de Guzmán Antiform is one of the most outstanding cartographic structures in the Iberian Pyrite Belt, representing a imbricate fan thrust system developed during the second regional deformation phase. In the Puebla de Guzmán Antiform, the first deformation phase gave rise to a penetrative slaty cleavage (S_1), which is also recognized in the whole Iberian Pyrite Belt and constitutes the main foliation all over the region. Its genesis is possibly linked to the coetaneous development of thrusts at deeper crustal levels and SSW-vergent folds at all levels above these thrusts. First phase structures were deformed by large-scale imbricated thrust systems with lateral (NNE–SSW) and frontal (WNW–ESE) ramps, which constitute the most relevant regional cartographic structures. This second deformation phase generated thrusts, two set of folds with WNW–ESE and NNE–SSW-oriented axes, as well as two related axial plane crenulation cleavages. These relatively brittle to ductile-brittle second phase structures have been identified in many areas of the Iberian Pyrite Belt, and especially in the southern limb of the Puebla de Guzmán Antiform. The second phase thrusts reported from the Puebla de Guzmán Antiform have not been folded according to both the geological map of the area and the analysis of maximum shortening and stretching axes.

Introduction and geological setting

Foreland fold-and-thrust belts are typical features in the external zones of most orogenic belts. They generally involve only the sedimentary cover (i.e. thin-skinned style), although sometimes both the basement and the cover are deformed (i.e. thick-skinned style). In the case of thin-skinned fold-and-thrust belts, the entire deformation process occurs on top of a sole fault (basal detachment) and rises through the stratigraphic pile towards the foreland. Thus, imbricate thrust systems appear in many of these belts, most faults being asymptotic to the basal detachment at depth (e.g. Mitra 1988; Muñoz 1992; Martínez *et al.* 1997).

The South Portuguese Zone in the SW Iberia Variscides (Fig. 1) shows the characteristic features of a foreland fold-and-thrust belt dominated by thin-skinned tectonics (Ribeiro & Silva 1983; Silva *et al.* 1990). This zone shows a general SSW vergence, being constituted by Upper Palaeozoic low- to very low-grade metamorphic rocks (Munhá

1990; Abad *et al.* 2001, 2002; Simancas 2004). The South Portuguese Zone is limited to the north by mafic rocks, namely the Beja-Acebuches Amphibolites, displaying both an oceanic affinity and an intense deformation (Fig. 2).

Three major tectonic domains can be defined in the South Portuguese Zone (Fig. 1). Across a north–south transect these are, in structural descending order: (a) the Northern Domain, including the units outcropping in the Pulo do Lobo Antiform and their lateral equivalent in the easternmost sector: the Sierra Norte of Sevilla Batholith and their metasedimentary and volcanic hosted rocks (Fig. 1); (b) the Iberian Pyrite Belt (or Central Domain), which includes the Baixo Alentejo Flysch Group defined by Portuguese authors (Oliveira *et al.* 1979); and (c) the Southern Domain which includes the Southwestern Portugal Units (Oliveira *et al.* 1979). In the Spanish segment of the South Portuguese Zone, only the first two domains crop out. The boundaries between these three tectonic domains are thrusts rooted to the

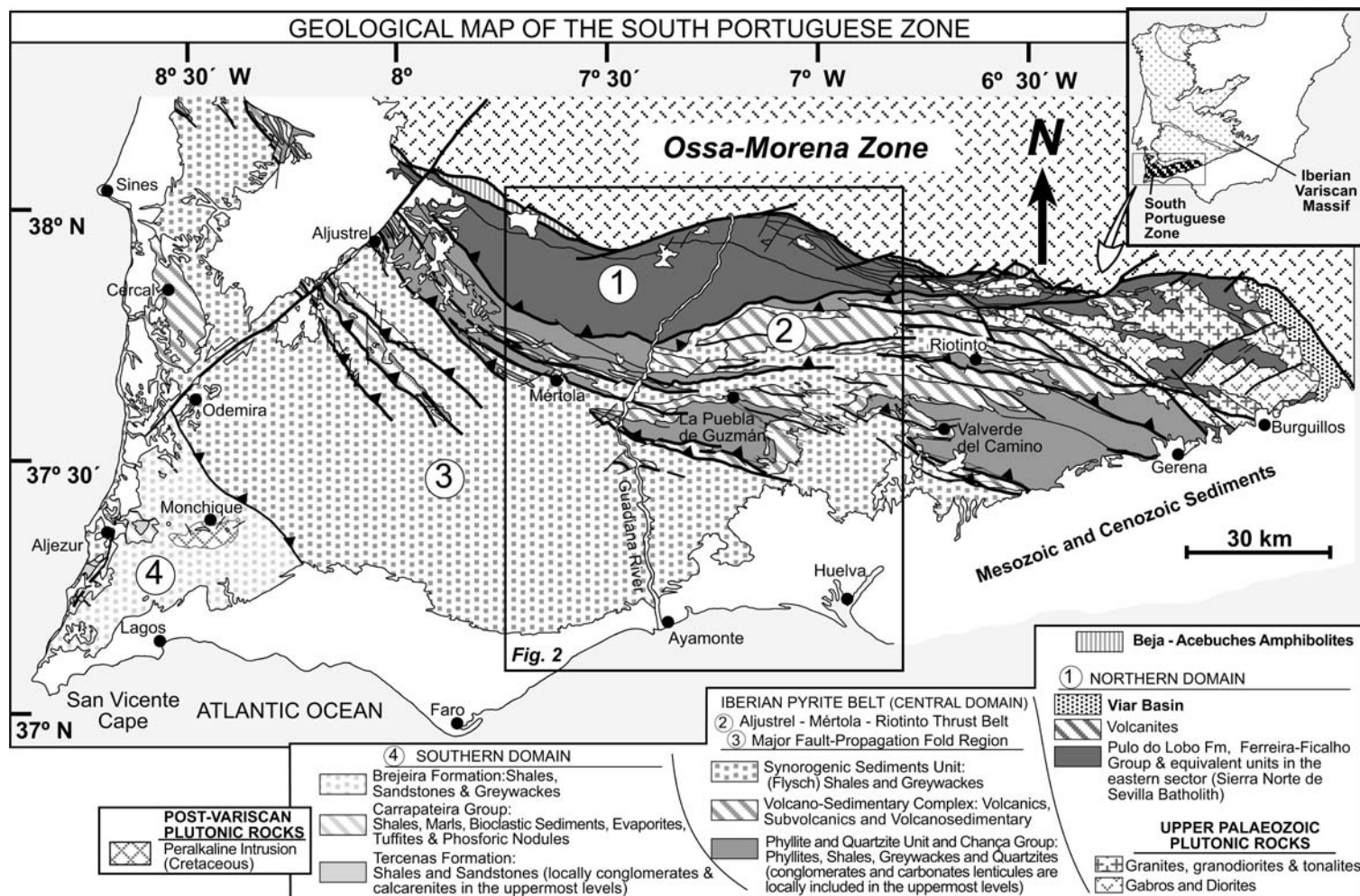


Fig. 1. Geological map of the South Portuguese Zone (Iberian Variscan Massif) showing the setting of the Puebla de Guzmán Antiform. The lateral equivalents to the Pulo do Lobo Antiform Units include the rocks of Sierra Norte of Sevilla Batholith and their hosting metasedimentary and metavolcano-sedimentary sequences.

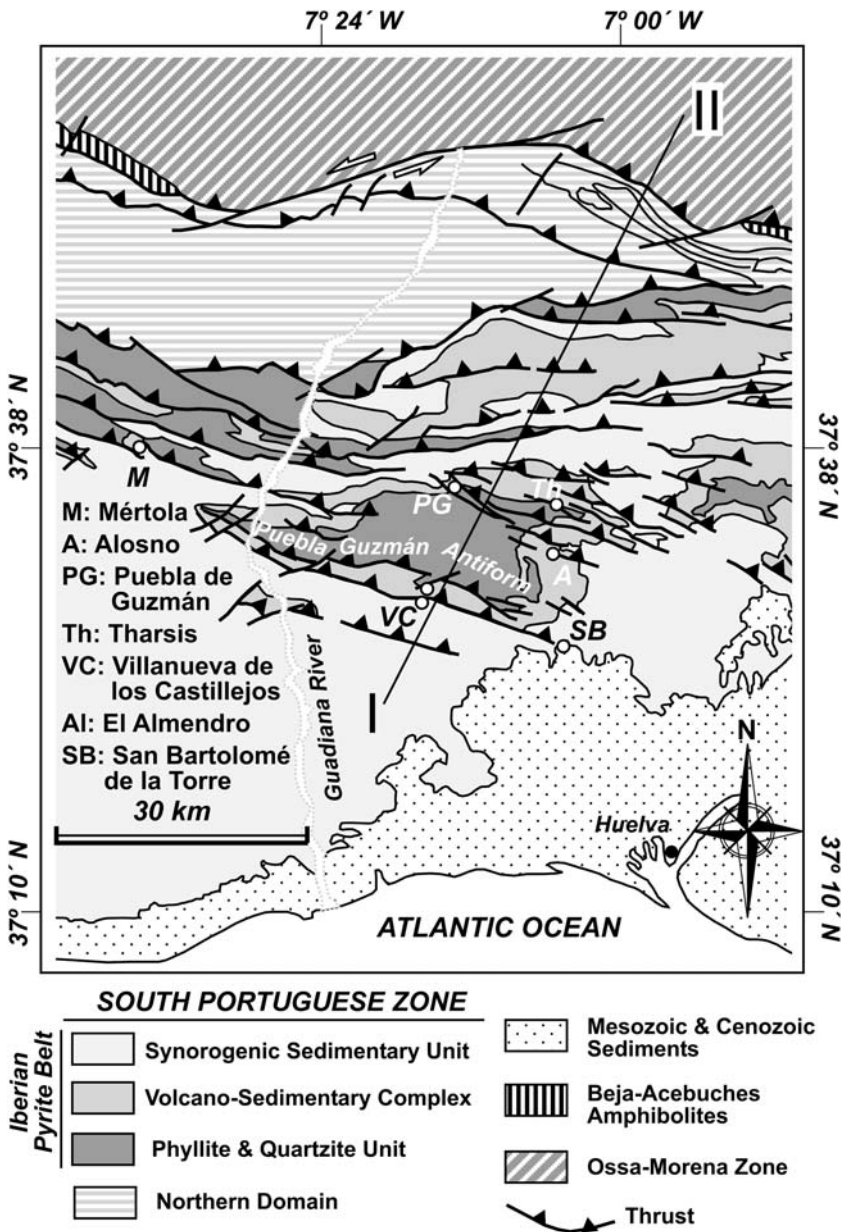


Fig. 2. Geological map of the Puebla de Guzmán Antiform and surrounding areas. The position of the geological cross-section (I–II) shown in Figure 3 has been indicated. The location of each sector showed on Figure 10 has also been indicated.

north (Fig. 3). The structural grain in the South Portuguese Zone changes progressively from NW–SE in the west to east–west in the central and easternmost parts.

The Iberian Pyrite Belt can be divided into two sub-domains according to their cartographical and

structural characteristics (Mantero *et al.* 2007): Aljustrel–Mértola–Riotinto Thrust Belt (the northernmost one) and Major Fault–Propagation Fold Region (Figs 1–3). The former constitutes a band of nearly 15 km width, which is parallel to the Northern Domain border. It is formed by repetition

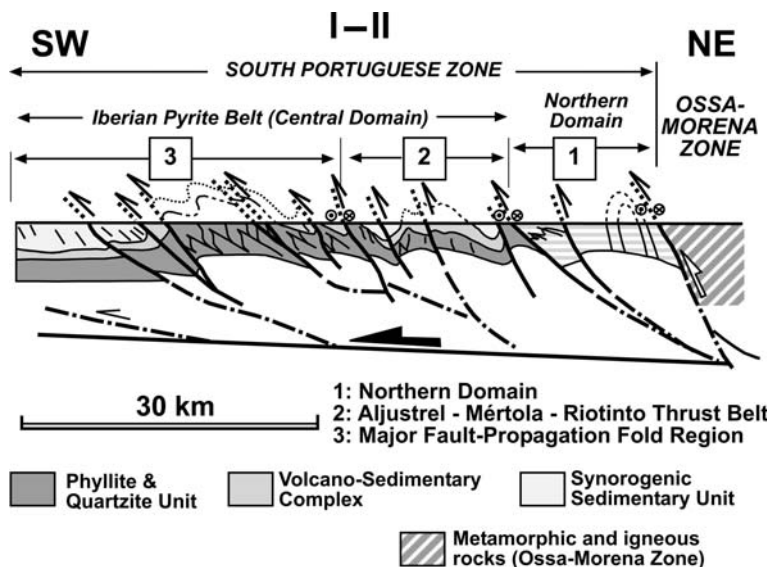


Fig. 3. Geological cross-section of the South Portuguese Zone along the transect of the Puebla de Guzmán Antiform. The cross-section shows the structure of the Iberian Pyrite Belt (including the Aljustrel–Mértola–Riotinto Thrust Belt and most of the Major Fault-Propagation Fold Region), the Northern Domain and the contact with the Ossa-Morena Zone. The position of this cross-section (I–II) has been indicated in Figure 2.

of several tectonic sheets varying in number and stratigraphy for different transects (older units are more abundant to the west). The Major Fault-Propagation Fold Region comprises two major structures, namely the Puebla de Guzmán and Valverde del Camino Antiforms. It is characterized by very low metamorphic grade (prehnite–pumpellite facies to anchizone/intense diagenesis; Abad *et al.* 2004), while the Aljustrel–Mértola–Riotinto Thrust Belt is characterized by the transition to greenschist facies conditions.

This paper mainly deals with the analysis of the progressive deformation in the central domain of the South Portuguese Zone, namely, the Iberian Pyrite Belt. Specifically, the present paper revisits the claims previously made by some authors regarding the differentiation of tectonic phases involved in the tectonic configuration of this zone. New data are provided which enable us to discuss some aspects of the general models for the stratigraphy and the structure of the region. Observations are distributed in different sectors of the Puebla de Guzmán Antiform (Fig. 2), with special attention to the study of deformation in the Filón Norte Open Pit in the Tharsis area.

Lithostratigraphic sequence

The Iberian Pyrite Belt (Fig. 4) is made up of three tectostratigraphic units (Schermerhorn 1971). The basal unit is the Phyllite and Quartzite Unit, which

basically comprises phyllites, shales and quartzites. High energy deposits, including conglomerates, limestones and other sediments typical of shallow-water sedimentary environments, have been locally reported at the top of this unit (Moreno & Sáez 1990; Moreno *et al.* 1995, 1996). They are lateral equivalents of dark shales deposits of deeper sedimentary environments. Conodonts and other fossils indicate a Late Famennian age for the uppermost Phyllite and Quartzite Unit (Boogaard & Schermerhorn 1980). The Phyllite and Quartzite Unit is exposed in the core of the two major regional antiforms in the eastern South Portuguese Zone (Figs 1 & 2). In Filón Norte Open Pit, the transition between the Phyllite and Quartzite Unit and the Volcano–Sedimentary Complex is characterized by dark shales, with minor intercalations of sandstones, attributed to uppermost Famennian LN spore Biozone (González *et al.* 2002). The contact between the Phyllite and Quartzite Unit and the overlying Volcano–Sedimentary is an essentially stratigraphic contact, though locally affected by some minor faults.

The Volcano–Sedimentary Complex consists of volcanic rocks interfingering in a sedimentary sequence including volcanoclastic rocks and siliceous deposits (chert, jasper) located at different stratigraphic levels. Felsic and mafic volcanics, as well as some minor andesites have been described (Routhier *et al.* 1980; Mitjavila *et al.* 1997; Thiéblemont *et al.* 1998). Diabase dykes are intruded into

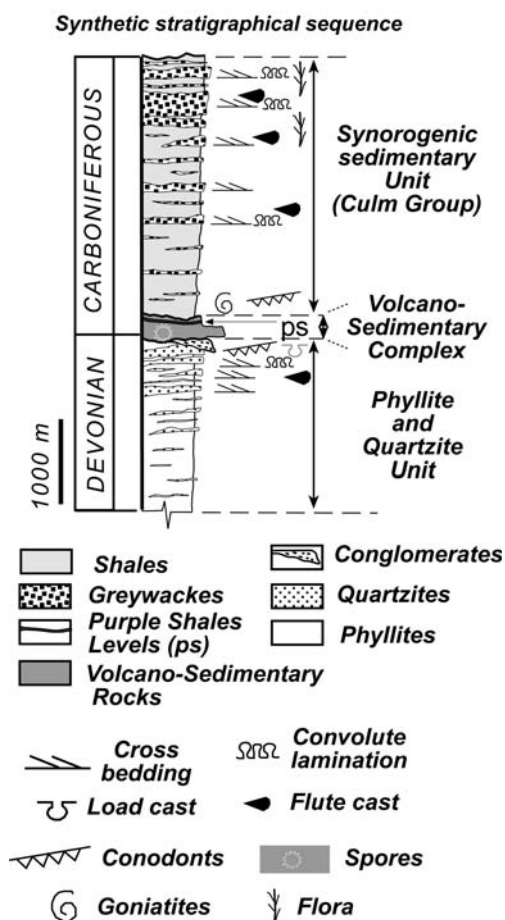


Fig. 4. Synthetic stratigraphic series for the Iberian Pyrite Belt.

the upper levels of the Phyllite and Quartzite Unit and the lower part of the Volcano-Sedimentary Complex. Particularly important is the presence in the Volcano-Sedimentary Complex of thick polymetallic massive sulfide deposits. Some of these have been mined for many years (Riotinto, Neves Corvo, Aljustrel, Aznalcóllar, Sotiel and Tharsis mines). The basal part of the Volcano-Sedimentary Complex has been dated as Late Famennian (Oliveira 1983; Pereira *et al.* 1996). Recently, González *et al.* (2002) and Moreno *et al.* (2003) have established the beginning of the volcanic activity in the area, as well as the age of several massive sulfide deposits intercalated in a sequence of dark shales, which contain spores of the LN Biozone (Figs 4 & 5). The age estimated by these authors is consistent with Re-Os isotopic studies in massive sulfides and stockwork mineralizations,

which indicate an age of 348.6 ± 12.3 Ma (Nieto *et al.* 2000a) and 353 ± 44 Ma (Mathur *et al.* 1999) in the Tharsis area, 346 ± 26 Ma (Mathur *et al.* 1999) in Riotinto and Tharsis areas, and 350.75 ± 8.52 Ma (Nieto *et al.* 2000b) in the Aznalcóllar area.

In the Filón Norte Open Pit, the Volcano-Sedimentary Complex is composed of a dark shale succession with interfingering felsic and mafic igneous rocks (volcanic or subvolcanic origin) and two massive sulfide lenses which are lateral equivalents. This implies sharp lateral changes in the sedimentary environment, which reflects a division – probably of tectonic nature – of the main basin. An outstanding feature is a pervasive hydrothermal alteration of the whole outcropping sequence (carbonatization, silicification, chloritization, and sericitization). The sequence includes two massive sulfide lenses (Filón Norte and San Guillermo) whose position and geometry is structurally controlled, showing sharp changes in thickness along strike and dip. The former is 850 m-long and has 60 m of maximum thickness, while San Guillermo body is 380 m-long showing in its uppermost part changes of thickness (5–25 m). Despite its intense deformation, some primary features are preserved, including framboidal and colophorm textures, as well as laminations and breccias.

The Volcano-Sedimentary Complex has a controversial geotectonic interpretation. It has been interpreted as the result of a transtensional setting in a geodynamic scenario of continental collision (Silva *et al.* 1990; Quesada *et al.* 1991; Mitjavila *et al.* 1997; Soriano 1997). Other authors have suggested, by contrast, that it could have been part of a magmatic arc (Onézime *et al.* 2003).

The uppermost Iberian Pyrite Belt unit is a thick flyschoid deposit, namely, the Synorogenic Sedimentary Unit (Culm Group), consisting of shales and greywackes (Figs 4 & 5). It contains goniatite and conodont fauna, which yields a Late Viséan to Namurian age (Oliveira 1990).

Tectonic framework of the Iberian Pyrite Belt

In the South Portuguese Zone, diachronous structures have been reported as being linked to the progressive deformation of the orogenic wedge in the most external and southern sector of the Variscan Orogenic Belt (Silva *et al.* 1990; Onézime *et al.* 2002; Soriano & Casas 2002; Mantero *et al.* 2004). They resulted from a progressive deformation process, which migrated from north to south, and rose from deep (the basal detachment is located about 12–15 km depth, Simancas *et al.* 2003) to more superficial levels of the continental

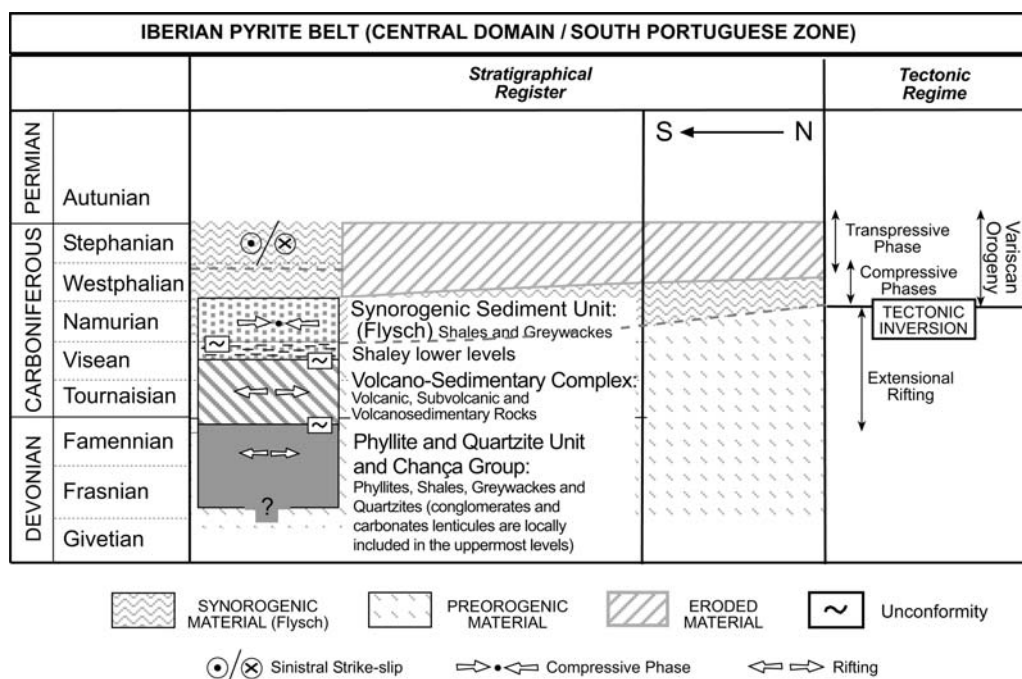


Fig. 5. Chronostratigraphical chart for the Iberian Pyrite Belt (or Central Domain), supported by several geological data (Mantero *et al.* 2007).

crust following a piggy-back propagation mode, though some out-of-sequence thrusts have also been described (Ribeiro & Silva 1983; Silva *et al.* 1990; Quesada 1998; Soriano & Casas 2002). The main structures show a southward vergence (Figs 2 & 3). However, retrovergent structures were also developed, mainly during the last deformation stages.

Characterization of deformation phases

The shortening of the orogenic wedge in the Iberian Pyrite Belt can be interpreted as the result of two deformation phases. The first one is characterized by inclined overturned folds vergent to the south at different scales. These folds exhibit a very penetrative axial plane cleavage (S_1) with northward dip. Nevertheless, upright folds were formed in some areas such as the Riotinto Syncline. S_1 is a slaty cleavage, very penetrative in shaley sequences but less developed in the more competent quartzites, greywackes and igneous rocks. S_1 is a consistent feature of the whole sequence, its usual orientation being N120°E/60°N (Fig. 6a). These first phase folds are hanging wall folds related to deeper thrusts of the same phase (first phase thrusts outcrop only in the Northern Domain). In superficial levels of the Puebla de Guzmán Antiform, there are

minor folds of this first phase, which do not reach cartographical dimensions.

The second deformation phase is represented by kilometre scale thrust surfaces with associated frontal, lateral, and oblique ramps and flats, which are generated by the rising and propagation of deeper thrusts to the foreland. They constitute thrust imbricated fan systems, which are rooted in a middle crust sole fault (main detachment) located at 12–15 km depth (Fig. 3) according to a seismic reflection profile (Simancas *et al.* 2003). The general southward movement of these thrust sheets produced folds of varied geometric configurations within each sheet. On a local scale, domes and basins of the second deformation phase were formed. Two crenulation cleavage sets related to second phase folds (S_{2a} and S_{2b} ; Fig. 6b) overprint the structures related to the first phase. They are steep-dipping cleavages, differing from each by other about 60° in strike. S_{2a} shows a rather parallel strike to the main thrusts, with an average N125°E direction and a dip of 60°SW (Fig. 6b). By contrast, S_{2b} is strongly oblique (about 45–50°) to the main thrusts, displaying an average orientation of N160°E/70°W (Fig. 6b), being more conspicuously developed near the eastern closure of the Puebla de Guzmán Antiform. Crenulation folds are kink-like

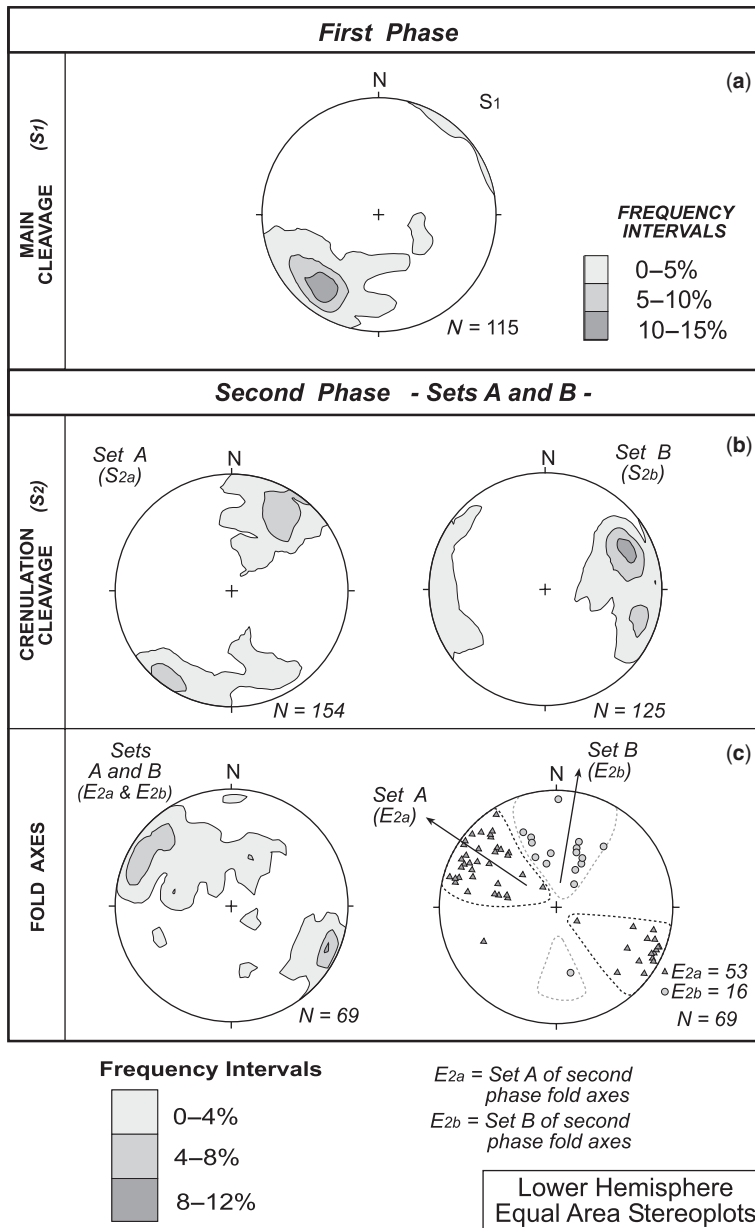


Fig. 6. Stereoplots showing the orientation of the first phase cleavage or main cleavage (a) and of the second phase structures (b, c) observed in the Filón Norte Open Pit. Two creunulation cleavage sets have been recognized (b), both of them being axial plane foliations of second phase folds (c).

and upright or highly inclined. The majority of them are related to S_{2a}, showing slightly plunging axes to the NW and SE (Fig. 6c). A second less abundant group of folds is related to S_{2b}, having axes plunging c. 50° to the north (Fig. 6c). These S_{2b}-related folds become predominant in the eastern closure of the

Puebla de Guzmán Antiform. Second phase structures are the most conspicuous tectonic elements in the whole Puebla de Guzmán Anticline.

In the eastern closure of the Puebla de Guzmán Antiform, the second deformation phase structures are minor brittle thrust surfaces and a set of

reverse north–south striking faults. According to the method by Marret & Allmendinger (1990), the kinematic analysis of the thrusts oriented N100°E/40°NE shows a subvertical stretching axis and a subhorizontal shortening axis (Fig. 7). A maximum horizontal shortening axis with NNE–SSW orientation can be deduced (Fig. 7). This direction is almost perpendicular to S_{2a} (Fig. 6b) and also to

the main frontal thrust ramp in the southern limb of the Puebla de Guzmán Antiform. On the other hand, the reverse faults striking north–south are congruent with a maximum horizontal shortening axis of WNW–ESE direction (Fig. 7), and therefore are perpendicular to the secondary lateral ramps in the easternmost closure of the Puebla de Guzmán Antiform. This fact, together with the initial

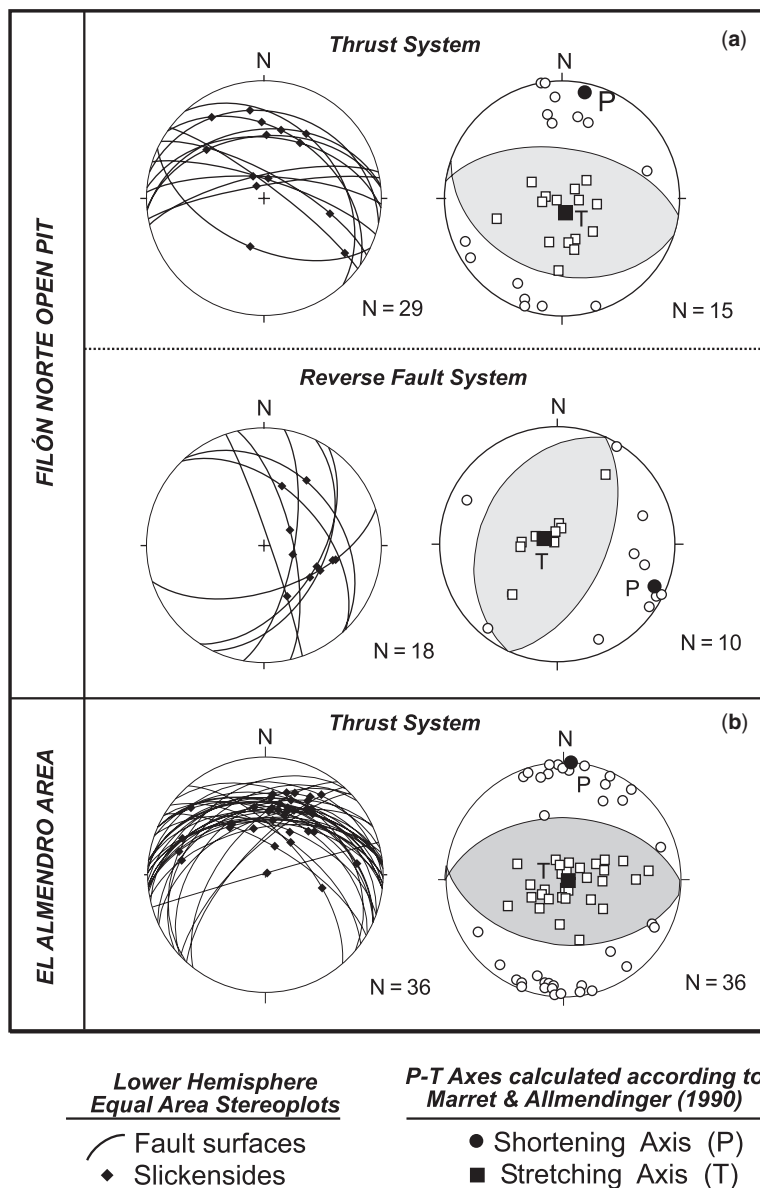


Fig. 7. Equal area lower hemisphere projection of thrust surfaces belonging to main thrust systems and secondary reverse faults described in Filón Norte Open Pit (a) and El Almendro area (b). Calculations of Shortening (P)–Stretching (T) axes for each system according to Marret & Allmendinger (1990) are also shown.

northerly dip of S_1 , must be taken into account for the formation of S_{2b} and related folds. The maximum stretching axis, deduced for both sets of reverse faults is subvertical (Fig. 7), which suggests that second phase thrusts are not folded in this sector of the Iberian Pyrite Belt. The slight deviation from the vertical is due to the existence of only one fault family, displaying the same strike and dip directions. The absence of conjugate faults could produce these slight vertical deviations as discussed by Twiss & Unruh (1998). The existence of two shortening axes can explain the simultaneous formation of two crenulation cleavage sets (constriction-type strain).

Structure of the Puebla de Guzmán Antiform

The Puebla de Guzmán Antiform is an antiformal structure developed in relation to the formation of a south vergent thrust system along its southern limb. This thrust system is made up of a set of thrust surfaces with an imbricate fan configuration (Fig. 8), which are rooted in deeper levels towards the north. Each thrust produced the tectonic repetition of a portion of the stratigraphic section. Thus, the Phyllite and Quartzite Unit, located in the core of the antiform, overrides the younger

rocks of the Volcano–Sedimentary Complex by means of a thrust. Numerous minor thrust surfaces and Riedel faults dipping *c.* 30° to the north were generated during the propagation of the deformation to the footwall. They cause internal repetitions in the Volcano–Sedimentary Complex, which, in turn, is also tectonically placed over the Synorogenic Sedimentary Unit (Fig. 8).

The displacement related to the thrust system originated a fault-propagation fold in its hanging wall. The southern limb of this fault-propagation fold shows minor asymmetrical folds with overturned forelimbs. This geometry produces local inversions of the stratigraphic polarity in the southernmost outcrops of the Phyllite and Quartzite Unit (Figs 9a & 10a). However, each thrust slice in the southern limb of the Puebla de Guzmán Antiform generally contains rocks with normal stratigraphic polarity, except for these local-scale overturned forelimbs of minor folds. Structural criteria generally indicate the presence of normal limb relationships inside the thrust sheets that constitute the imbricate fan for both the first and second deformation phases (Fig. 9b, c). In fact, the enveloping surfaces of folds dip very gently (10 – 20°) to the north in most of the sheets (Fig. 9b). S_0 within the thrust sheets has an average strike of about $N125^\circ E$ (Fig. 10b). S_1 is oriented $N125$ – $140^\circ E$ / $55^\circ NE$ on average, thus indicating a normal

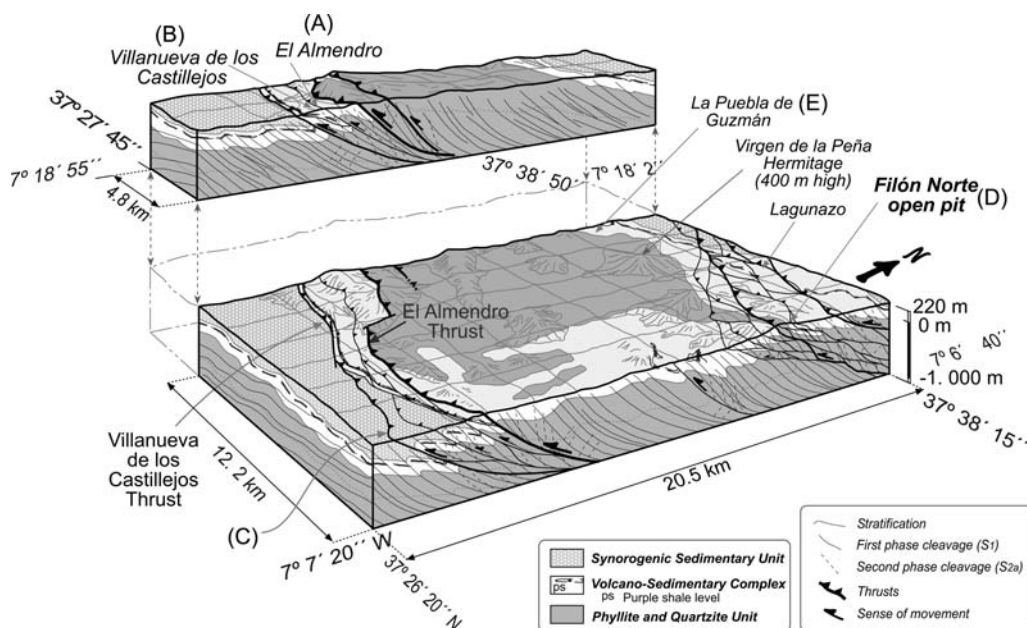


Fig. 8. Block diagram showing the structure of the eastern-middle part of the La Puebla de Guzmán Antiform. The location of the schematic drawings in Figure 9 along with the position of the main geographical places of reference which are mentioned in the text has been indicated.

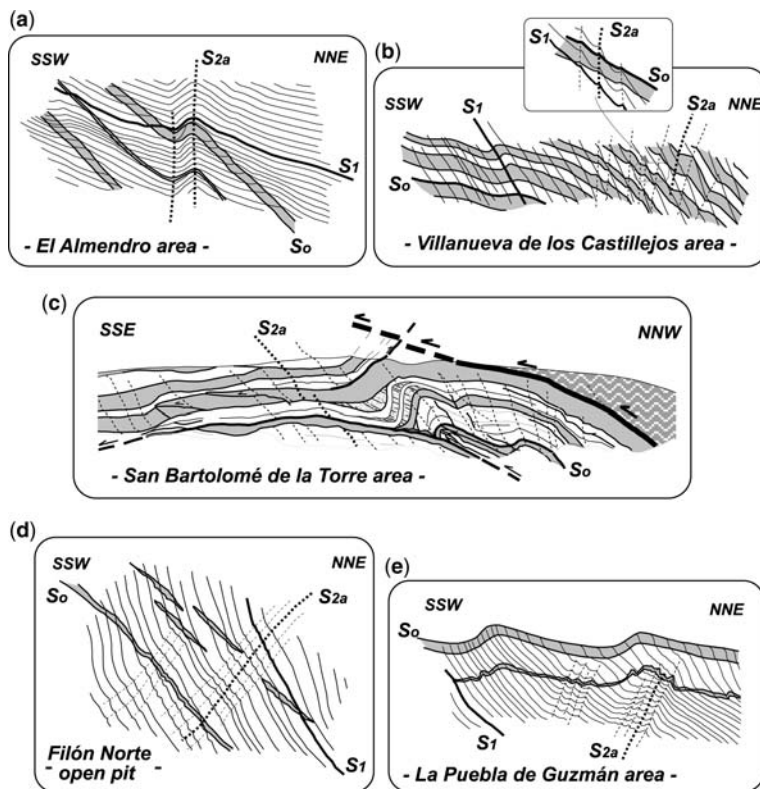


Fig. 9. Schematic drawings (not to scale) illustrate S_0 - S_1 - S_{2a} relationships in different points of the Puebla de Guzmán Antiform. The location of each point can be found in Figure 8.

structural polarity for the first deformation phase. S_2/S_1 relationships indicate a second phase normal limb structural position. In the hanging wall of the thrust system, rocks of the Phyllite and Quartzite Unit lie on felsic rocks of the Volcano-Sedimentary Complex (e.g. El Almendro area, see Fig. 8). In this sector (Fig. 10a), both S_0 and S_1 have an almost east-west strike with northward dips of about 80° and 65° respectively in the first phase reverse forelimbs of minor folds that can be locally observed. These folds also show a normal limb, where S_0 and S_1 have an east-west average strike and dip *c.* 50° N and 70° N respectively. S_2 usually exhibits steeper dips than S_1 and S_0 , thus indicating the prevalence of normal second phase fold limbs. Following the method by Marret & Allmendinger (1990), the kinematic analysis of the thrusts in the southern limb of the Puebla de Guzmán Antiform imbricated system (El Almendro area, Fig. 7) indicates a maximum subvertical stretching axis. This fact can be taken to support the claim that second phase thrusts are not folded within the area under study here.

In the easternmost part of the southern limb of the Puebla de Guzmán Antiform near San Bartolomé de la Torre (Fig. 9c), the Synorogenic Sedimentary Unit has exclusively registered the second deformation phase (Fig. 10c), while the older units (Phyllite and Quartzite Unit and Volcano-Sedimentary Complex) have registered the superposition of the two deformation phases.

The northern limb of the Puebla de Guzmán Antiform (Fig. 9d, e) generally features normal structural and stratigraphic polarity. Nevertheless, this general framework is locally modified by second phase structures, which give rise to an overthrusting of tectonic sheets (e.g. in the Filón Norte Open Pit). This second phase yielded a significant thickening of the Volcano-Sedimentary Complex in the Lagunazo area (thrusts involving a length of 5–10 km). Open folds of the second phase with slight asymmetry and south vergence have been developed (Figs 9e & 10d). The S_0 orientation in these folds is almost east-west, with dips of about 30° to the north or south depending on the limb (Fig. 10d). The S_1 cleavage (Fig. 10d) has a strike

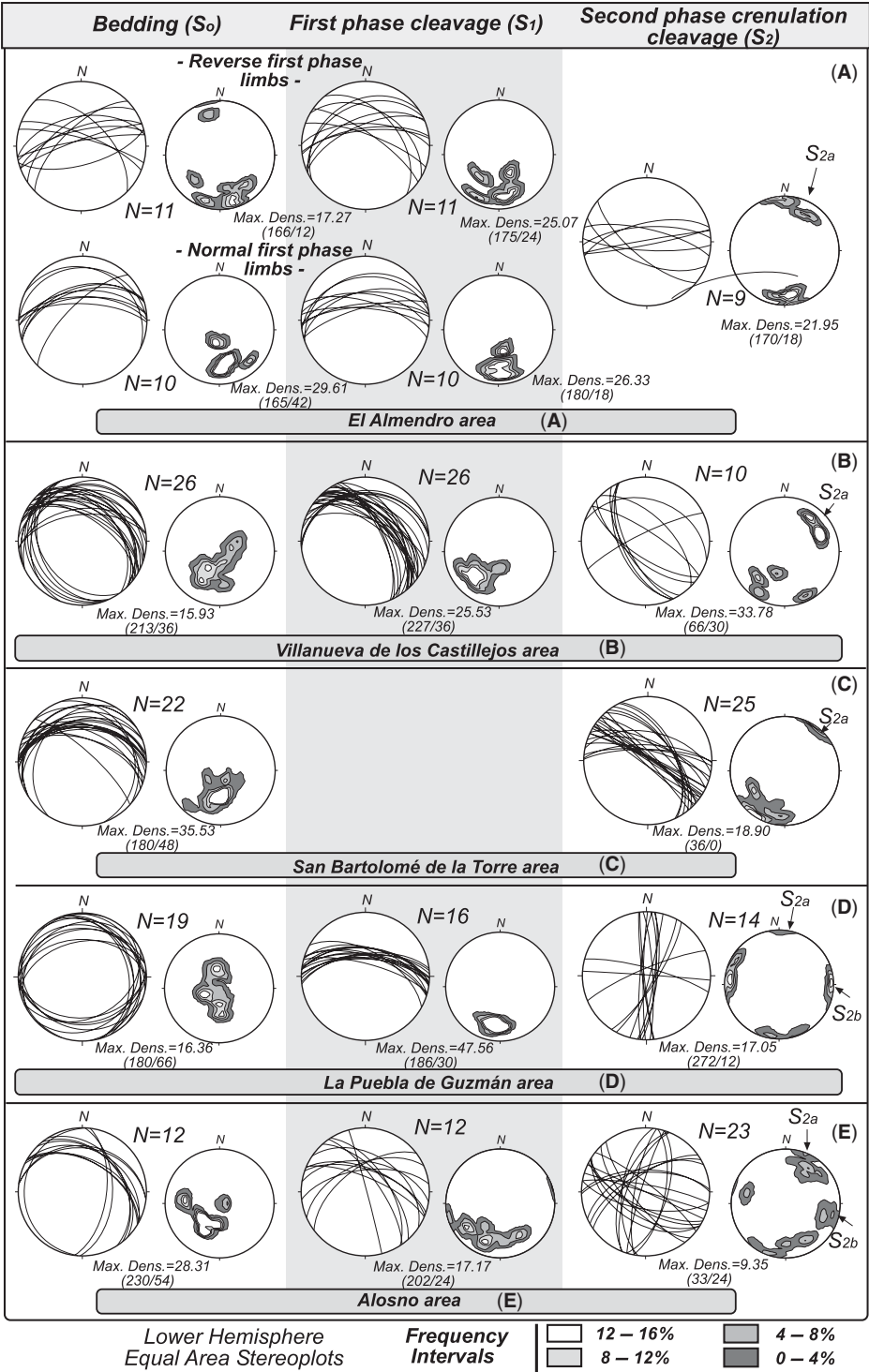


Fig. 10. Orientation of bedding, as well as first and second phase cleavages in several sectors of the Puebla de Guzmán Antiform. Equal area lower hemisphere projection and density contour stereoplots are shown. The location of each sector is indicated on Figure 2.

of around N95°E and a dip of 60° to the north. The S₂ cleavage (Fig. 10d) is represented by two families, the one oriented north–south/80°E (S_{2b}) being more developed in the easternmost end of this limb than the family S_{2a} which is oriented N100°E/80°N. Later local-scale deformation produced open and kink-band folds, which may locally have an associated crenulation foliation.

To the east, near the Tharsis mining district (Figs 8 & 9d), the tectonic structure of the northern limb of the Puebla de Guzmán Antiform is somewhat more complex (e.g. the structure in Filón Norte Open Pit), because of the presence of a thrust system related to the second deformation phase. This system produced the thickening of the stratigraphic units. This is particularly conspicuous in the Volcano–Sedimentary Complex (Fig. 4), a thin stratigraphic unit (about 300 m-thick), which has been considerably thickened. This thrust system mainly consists of faults with anastomosing morphologies defining duplex structures at all scales (Fig. 8). Thrust zones with 10–30 m of thickness and brittle–ductile behaviour produced repetitions of the lithological sequence. However, the displacement along the different thrusts in the area of Tharsis is probably less than the one which took place along the thrust system of the southern limb of the Puebla de Guzmán Antiform. The development of thrust surfaces, Riedel shears and the tectonic stacking occurred over a sequence previously folded during the first deformation phase, which is responsible for a moderate dip to the north of the S₀ prior to the second deformation phase. This fact has been crucial in the final structural configuration, in which bedding surfaces show higher dips than the thrusts, thus pointing to the formation of a ramp zone related to a thrust system affecting a sequence previously tilted and folded during the first phase.

Over a short distance, only a few kilometres south of Filón Norte Open Pit and near Alosno village (Figs 2 & 8), the average S₀ orientation dramatically changes (Fig. 10e). This sector, coincident with the eastern closure of the Puebla de Guzmán Antiform (Figs 2 & 8), shows a general NNW–SSE strike for the S₀. Folds have limbs with N140°E/35°NE and north–south orientations. The S₁ cleavage is c. N115°E/65°N, while the S₂ cleavage is represented by two sets (S_{2a} and S_{2b}) of N125°E/65°SW and N20°E/75°W orientation. Structural criteria generally are consistent with normal limbs for both the first and second deformation phases. Numerous fold axes plunging north have been identified. These data show an unusual orientation for the minor structures in this area with a strong change in the general strike of the S₀, suggesting lateral constraints on deformation propagation.

Structure of the Filón Norte Open Pit (Tharsis)

Thrust systems define the main structures at both regional and local scales. In Filón Norte Open Pit, the main criterion for structural division are the existence of thrust zones cross-cutting the lithostratigraphic sequence. These thrusts define three tectonic units with tabular or wedge-shaped geometry (Figs 11 & 12). Sigmoidal structures at all scales (Fig. 13a, b) are often developed within each structural unit, indicating a top-to-the-SSW sense of movement. The stacking of these three local units defined by structural criteria is due to the development of two main thrusts, the North Thrust Zone (NTZ) and the South Thrust Zone (STZ) (Figs 11 & 12), which belong to an imbricated fault system. Minor faults produced small repetitions within each unit, especially in the Northern Unit (Fig. 12).

Both brittle–ductile to brittle thrust zones have an approximately east–west strike (Fig. 11) and dip to the north about 20° (NTZ) or 40° (STZ), see Figure 12. Deformation linked to these thrusts is mainly evident in the dark shales because of their low competence with respect to other lithologies such as felsic and mafic igneous rocks. Accordingly, thrust zones define dark shaly bands of 10–15 m for the NTZ and up to 30 m-thick for the STZ. These intensely deformed shale bands (referred to as phyllonites by Tornos *et al.* 1998) concentrate most of the tectonic deformation associated with the second deformation phase. In some areas, especially those surrounding the thrust surfaces, syntectonic quartz veins commonly invade dark shales.

Each thrust zone comprises numerous fault surfaces showing an anastomosing morphology and defining north-dipping tectonic duplexes. Such duplexes are the main feature of both the geological map of the area (Fig. 11) and the cross-section (Fig. 12). Minor sigmoidal false S–C structures (Figs 11–13b), drag sense of S₁ planes and dip-slickenlines on the main thrust planes (Fig. 7) indicate a top-to-the-SSW sense of movement.

Despite its small size, the Northern Unit is the most complex one. Three sectors are distinguishable within the Northern Unit on the basis of structural criteria (Fig. 12). Sector B is characterized by the presence of minor splays of the NTZ (Figs 11 & 12) which caused repetitions of the original stratigraphic sequence (dark shales and felsic volcanics). They may well have a similar relevance to that of the STZ and NTZ. All of these faults would constitute a system of anastomosing thrust surfaces developed on a kilometre-scale (Fig. 8). East of the open pit, in the zone where they converge with the NTZ, a strong deformation has resulted in the generation of sigmoidal structures (Figs 11 & 12). However,

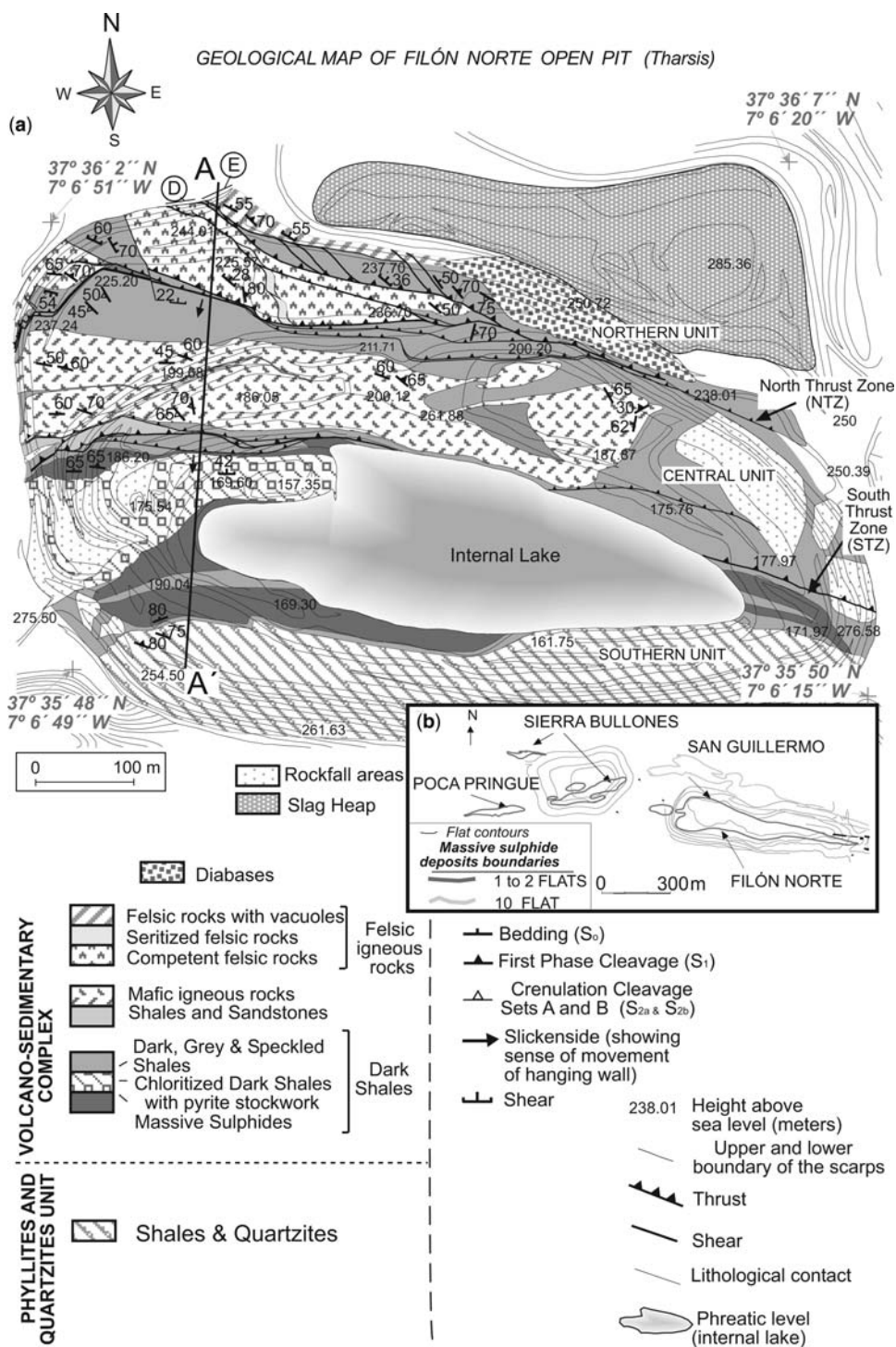


Fig. 11. (a) Geological map of the Filón Norte Open Pit (Tharsis). (b) Sketch modified from Strauss (1970), showing the position of the massive sulfide bodies in Filón Norte Open Pit and surrounding areas. The position of the geological cross-section (A–A') showed in Figure 12 has been indicated.

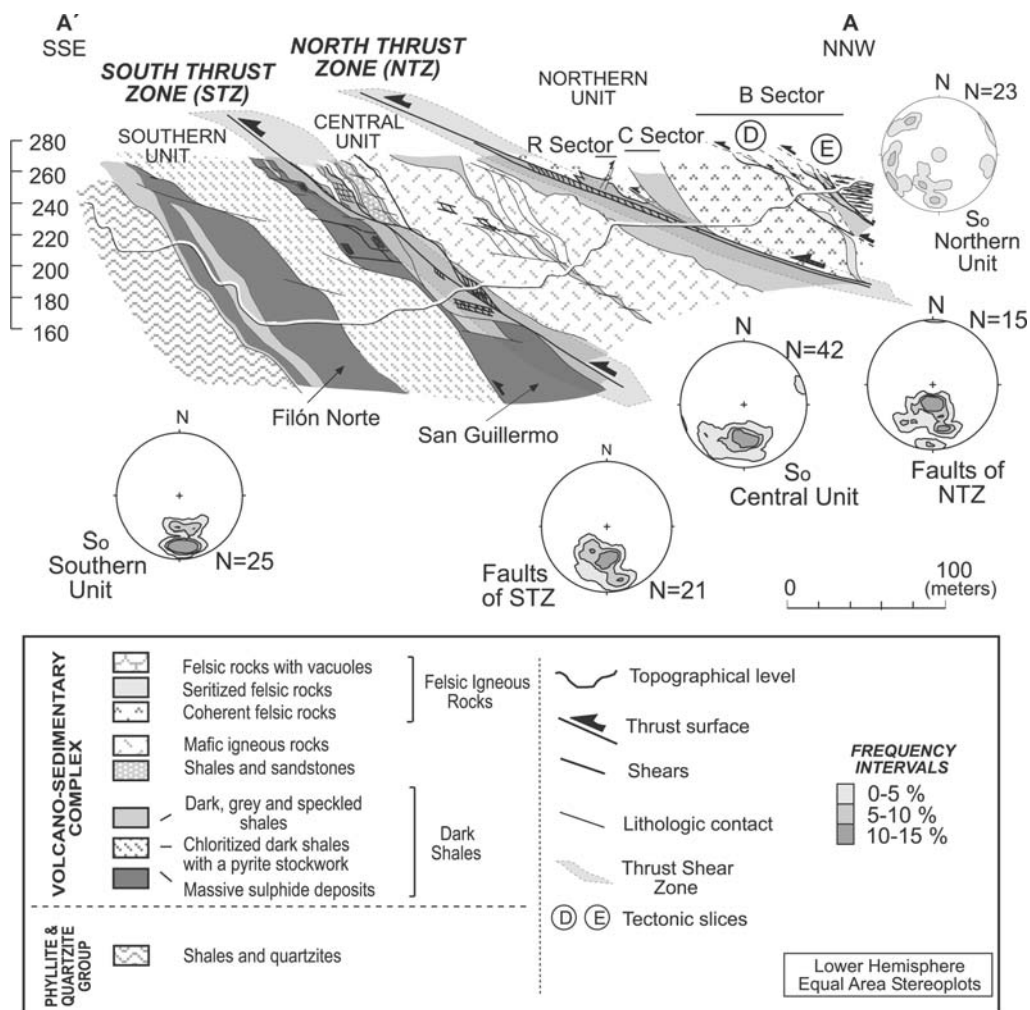


Fig. 12. Synthetic geological cross-section of the Filón Norte Open Pit (Tharsis). The orientation of the two main thrust zones is shown in density contour stereoplots, together with the orientation of the bedding (S_0) in each thrust sheet. The position of this cross-section has been indicated in the Figure 11 (A–A'). Three sectors are distinguishable within the Northern Unit on the basis of structural criteria. Sector B includes minor splays of the NTZ. Sector R shows a set of back-vergent structures (thrusts and main cleavage). Sector C includes thrusts striking north–south and dipping steeply to the east.

the subvolcanic diabase body included within the Northern Unit (Fig. 11) is not disrupted by the main thrusts. In Sector R, the NTZ exhibits a set of back-vergent structures in the hanging wall, including thrusts and main foliation planes dipping southward. These back-vergent structures are concentrated in a narrow band (Sector R; Fig. 12) parallel to the NTZ. Sector C is characterized by thrust surfaces striking north–south and dipping steeply to the east (Figs 7 & 12). They postdate the main thrusts of NTZ (Fig. 11).

The two massive sulfide masses (Filón Norte and San Guillermo) included in the Southern Unit show sharp lateral and vertical thickness changes (Figs 11 & 12). Drilling data (Strauss & Gray 1986; Strauss & Beck 1990) indicate that the Filón Norte progressively thins at depth. Conversely, the San Guillermo thickens considerably at depth towards the north (Fig. 12). The present-day morphology of Filón Norte and San Guillermo massive sulfide bodies has a strong structural control, as evidenced by stretching linked to thrust movement, which

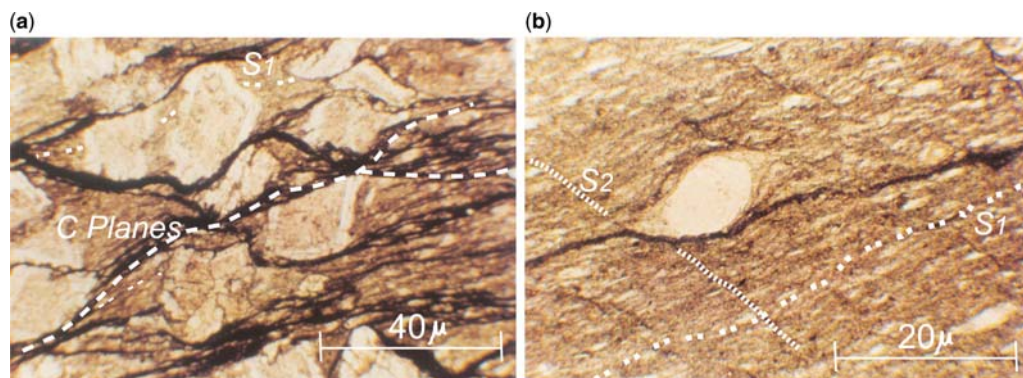


Fig. 13. (a) Carbonate idiomorphic crystals in a dark shale matrix. First phase cleavage (S_1) and later shear planes (C planes) were developed during deformation. (b) Penetrative first phase cleavage (S_1) and more spaced second phase cleavage (S_2) in a fine-grained rock.

resulted in a pinch-and-swell geometry. This is especially conspicuous in the San Guillermo body, whose extreme thinning (Figs 11 & 12) is due to its proximity to the lower part of the STZ.

Tectonostratigraphic evolution

Filón Norte Open Pit, despite its relatively restricted size, reflects very well the complex evolution of the sedimentary basins during the Devonian–Carboniferous transition in the Iberian Pyrite Belt. The tectonostratigraphic model proposed here (Fig. 14) is based on data collected from the Filón Norte Open Pit and surrounding areas of the Tharsis mining district and Puebla de Guzmán Antiform.

In a first stage of evolution, an accumulation of shales and sandstones (Phyllite and Quartzite Unit) occurred on a passive, marginal, relatively shallow platform environment (Moreno & Sáez 1990). Stratigraphic and palaeogeographic data suggest the existence of high and low offshore topographic areas, controlled by normal faults related to an incipient extensional tectonic setting (Fig. 14a). The sedimentary environment envisaged for the overlying Volcano–Sedimentary Complex (Routhier *et al.* 1980; Sáez *et al.* 1996; Sáez *et al.* 1999) also supports this interpretation. This extensional tectonic event compartmentalized the original basin, giving way to the bimodal magmatism and the hydrothermal activity that characterized the Volcano–Sedimentary Complex (Fig. 14a).

The Volcano–Sedimentary Complex is considerably thinner than both the Phyllite and Quartzite Unit and the Synorogenic Sedimentary Unit. The striking diversity of rapidly accumulated sediment and igneous rocks in this unit probably illustrates the complex evolution of the sedimentary

basins during the Devonian–Carboniferous transition in this region and indicates a significant tectonic activity. This tectonism may well have been extensional (or transtensional?), resulting in the sub-basin division of the basin in which the Phyllite and Quartzite Unit accumulated.

The inferred existence of the sub-basins during Volcano–Sedimentary Complex deposition presumably was tectonically controlled, resulting in a horst and half-graben system (Fig. 14a). Normal faults may well have been used as conduits for magma ascent. These early faults have not been well preserved in the South Portuguese Zone (Simancas *et al.* 2003) due to the intense later deformation and their existence (Moreno *et al.* 1996; Sáez *et al.* 1996; Sáez *et al.* 1999; Tornos *et al.* 2002) and orientation can only tentatively be considered to have been sub-parallel to main contractive later structures (thrusts). Therefore, an extensional or transtensional regime may have prevailed at this time, its precise origin being a controversial issue. Recent hypotheses favour this extensional/transtensional setting to have been brought about by a mantle plume interfering with a general oblique collisional tectonic regime (Simancas *et al.* 2003). Other hypotheses suggest their formation in a back-arc basin context (Onézime *et al.* 2003), but the absence of data to argue for the existence of a subduction zone south of the Ossa-Morena Zone–South Portuguese Zone boundary makes this interpretation highly questionable.

Irrespective of the interpretation to be invoked, the extensional/transtensional episode seems to have been very ephemeral, being succeeded by a longer compressional regime which caused tectonic inversion (Fig. 14b, c). This contractive regime initiates in the South Portuguese Zone in Early–Middle Viséan times (Simancas *et al.* 2003). The

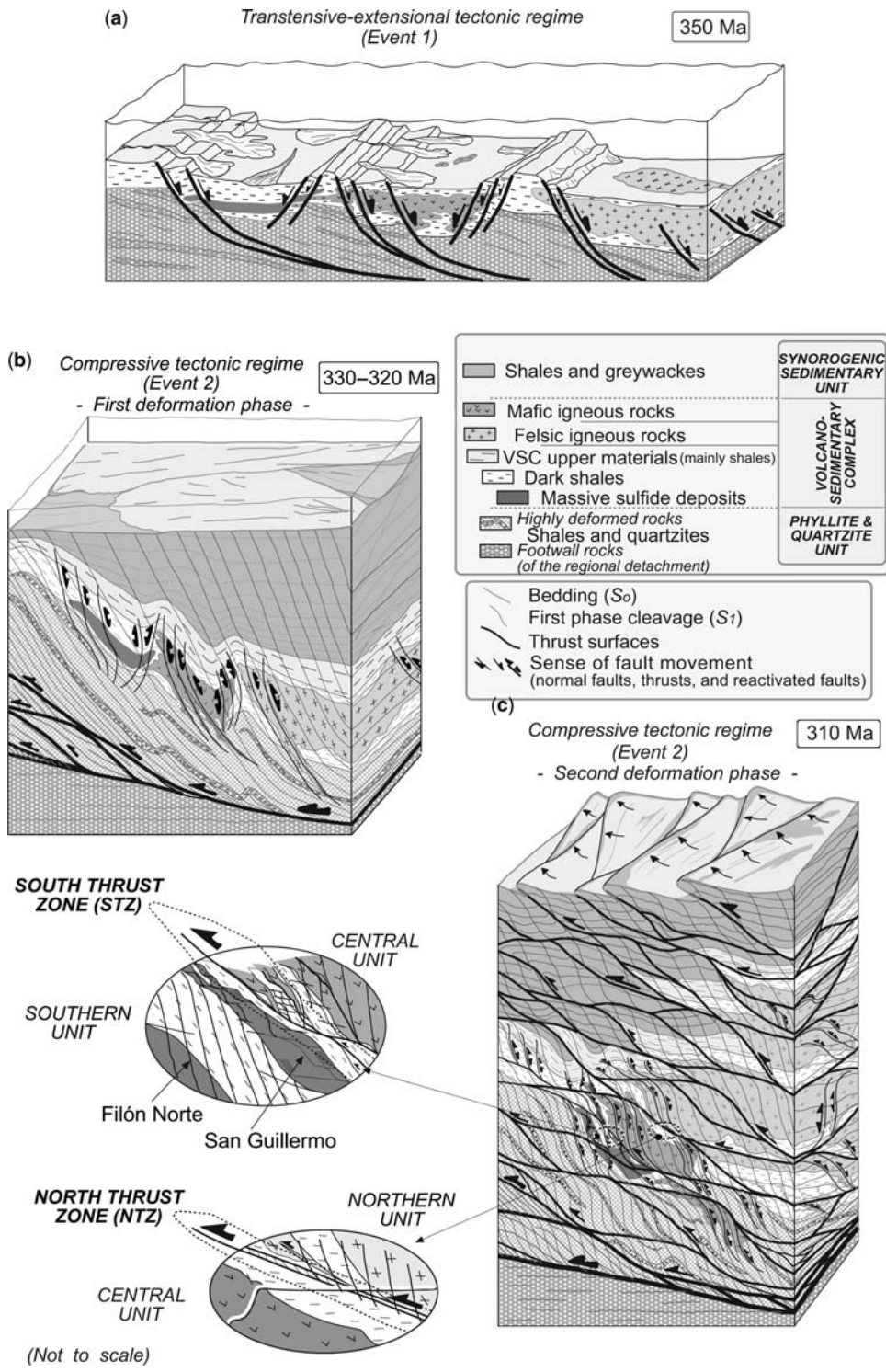


Fig. 14. Tectonostratigraphical evolutionary model for the Filón Norte Open Pit (diagrams are not to scale). (a) Event 1: transensional-extensional tectonic regime. (b) Event 2: first deformation phase of compressive tectonic regime. (c) Event 2: second phase of the compressive tectonic regime.

contractional deformation progressed from north to south, producing an important shortening of the sub-basins, where the Volcano–Sedimentary Complex was formed. It also led to a thickening of the pre-existing sedimentary sequence and to a topographic uplift in some areas, mainly in the northern sector of the South Portuguese Zone, which provided synorogenic sediments (Flysch deposits of Culm facies, the Synorogenic Sedimentary Unit). Thus, flows of sediment, which had a major WNW–ESE direction and a secondary NE–SW one in the Puebla de Guzmán Antiform (Moreno 1993), progressively blanketed the Volcano–Sedimentary Complex (Fig. 14b). A considerable number of thrust zones were generated at this time implying different displacements. Thrust development produced repetitions of the original lithological sequence and a tectonic transport of sheets from their original northern location towards the south.

Discussion

The main tectonic structures, such as the S_1 (main cleavage) and the thrusts in the southern boundary of Puebla de Guzmán Antiform have been attributed to a second contractional deformation phase (D2 of Soriano & Casas 2002). However, the new structural data obtained in the Puebla de Guzmán Antiform suggest that both structures are not linked to a single deformation phase. The main cleavage seems to have been generated in a first deformation phase, as axial plane foliation of disarmonical south-vergent folds linked to deep detachments located at different levels in the upper crust; the basal detachment is situated at 12–15 km depth. Subsequently, second phase thrusts generated the Puebla de Guzmán Antiform and the Valverde del Camino Antiform in the southern sector of the Iberian Pyrite Belt, thus cross-cutting the former regional cleavage (S_1). The second phase is therefore responsible for the generation of most of the structures in this part of the Iberian Pyrite Belt. Other structures linked to the generation of second phase thrusts (Soriano & Casas 2002; Mantero & Alonso-Chaves 2004) are two sets of crenulation cleavage (S_{2a} and S_{2b}) and folds (F_{2a} and F_{2b}). The existence of lateral ramps related to the thrusts has been previously proposed (Quesada 1998; Alonso-Chaves *et al.* 1999; Soriano & Casas 2002). The major development of one set with respect to the other one seems to be controlled by the presence of frontal (S_{2a} and F_{2a}) or lateral ramps (S_{2b} and F_{2b}) of second phase thrusts.

First phase folds developed above a detachment level, thus modifying the orientation of the multi-layer sequence bedding. Nevertheless, the prevalence of normal long limbs over overturned or

subvertical ones kept the series with a general normal stratigraphic polarity (Alonso-Chaves *et al.* 1999; Soriano & Casas 2002; Mantero *et al.* 2003). Local stratigraphic inversions are more common near the regional-scale thrust ramps. The lack of reverse limbs (both for second and first deformation phases) in the southern and central part of the Iberian Pyrite Belt (Puebla de Guzmán Antiform) is an interesting feature of the region. The mechanical weakness of stratigraphic pile constituted basically by Devonian argillites and mudstones determined the development of an important strain in the whole sequence (three cleavage sets have been recognized). It also determined the formation of wide thrust imbricated fan systems containing multiple thrust surfaces, each of them accommodating short displacements, rather than a discrete thrust surface or detachment accumulating long displacements (nappes). The distribution of tectonic displacements among multiple thrust surfaces must have caused a minor deformation inside each thrust sheet.

In the Puebla de Guzmán Antiform, first phase thrusts have not been recognized in the field. However, imbricate fan thrust systems developed during the second contractional deformation phase. In the northernmost sectors of the Iberian Pyrite Belt, thrusts attributed to the first phase crop out and are folded by second phase structures (Ribeiro & Silva 1983; Quesada 1998). The way of propagation of the deformation in orogenic wedges and the presence of first phase cleavage and folds, which usually develop in the hanging wall of first phase thrusts, strongly suggest the presence of first phase thrusts at deeper structural levels under the Puebla de Guzmán Antiform.

In the Volcano–Sedimentary Complex, the position and thickness of each individual pack of highly competent rocks (igneous rocks or massive sulphide bodies enclosed in a mostly slaty sequence) exerted a notable influence on the mechanical behaviour of the whole rock sequence during deformation. In general, a correlation can be established between a high competence contrast and the greater wavelength and amplitude of the folds. Competence contrast also controls the more penetrative development of cleavages (S_1 and S_2) in the slaty levels, as well as the refraction of foliation and the changes in the style of folds in multilayered sequences (Alonso-Chaves *et al.* 1999). Moreover, the high competence contrast between different levels of the Volcano–Sedimentary Complex, together with the low original thickness of this unit (about 300 m), favoured the formation of many thrust surfaces in it. These thrusts produced tectonic repetitions and also a considerable thickening of the Volcano–Sedimentary Complex in some zones, thus provoking some confusion in its thickness

estimates (Strauss 1970; Schermerhorn 1971; Strauss *et al.* 1977; Contreras-Vázquez *et al.* 1982; Ramírez-Copeiro *et al.* 1982; Oliveira 1990; Soriano & Martí 1999).

Conclusions

Two main deformation phases have been recognized in the Puebla de Guzmán Antiform. The structural features generated during the first and second deformation phases in the southern and central parts of the Iberian Pyrite Belt show very similar orientations. Both phases reflect a progressive deformation process associated with the growing of an orogenic wedge represented by the South Portuguese Zone.

In the Puebla de Guzmán Antiform, the first phase has manifest itself in two different ways. First of all, this phase is expressed by the presence of a widespread and pervasive slaty cleavage (S_1), which is also recognized in the whole Iberian Pyrite Belt and constitutes the main foliation all over the region. Its genesis is possibly linked to the coetaneous development of thrusts at deeper crustal levels and folds at all levels above these thrusts (the generation of thrusts during the first tectonic phase was restricted to rather deep levels and/or to the northernmost areas of the Iberian Pyrite Belt). The second effect of the first deformation phase can be deduced from the analysis of the tectonic stacking of thrust sheets in places as the Filón Norte Open Pit, which reveals that the stratigraphic series had a relatively steep angle of dip before the second deformation phase.

The structure of the Puebla de Guzmán Antiform mainly results from the second deformation phase. This phase generated thrusts, folds (F_{2a} and F_{2b}) with WNW–ESE and NNE–SSW axes respectively, as well as their related axial plane crenulation cleavages (S_{2a} and S_{2b}). These relatively brittle to ductile–brittle second phase structures have been identified in many areas of the Iberian Pyrite Belt, and especially in the southern limb of the Puebla de Guzmán Antiform. This southern limb mainly consists of an imbricate thrust system (Soriano & Casas 2002; Mantero *et al.* 2006), including numerous thrust zones such as El Almendro or Villanueva de los Castillejos thrusts. The second phase thrusts reported from the Puebla de Guzmán Antiform have not been folded according to both the geological map of the area and the analysis of maximum shortening and stretching axes.

The main structures of both deformation phases generally show an *c.* N100°E strike in the Iberian Pyrite Belt. However, other structures, including reverse faults, folds and a set of crenulation cleavage display a north–south mean strike. The

development of these structures are related to the presence of lateral ramps. Thus, the two sets of crenulation cleavages (S_2) could have been simultaneously formed due to local deformation processes. In the Puebla de Guzmán Antiform, these processes relate to the presence of a frontal ramp (WNW–ESE oriented) ahead of its southern limb and a lateral ramp (NNE–SSW oriented) in its eastern closure.

Despite the widespread presence of folds in the Iberian Pyrite Belt, the enveloping surfaces of these folds are sub-horizontal in most cases. The thrust systems display a geometrical configuration with ramps and flats. Only in the surroundings of frontal or lateral ramps does the bedding show steeper angles of dip, as a consequence of the generation of fault-propagation folds. There are only very local inversions in the original stratigraphic sequence, which are more often located in the hanging wall of major thrust systems, where minor folds of fault-propagation-folds with a reverse or sub-vertical southern limb can be found.

The tectonic repetitions of the stratigraphic sequence are mainly due to thrusts development. The tectonic transport is distributed along a large number of faults (imbricate fan thrust systems), rather than as discrete displacements along a unique thrust surface. It must be emphasized that thrusts are grouped in thrust zones having several kilometres of width. The stacking of thrust sheets produced an important thickening of the original sequence in the Iberian Pyrite Belt. This geometry is also strongly supported by the seismic image of the South Portuguese Zone (Simancas *et al.* 2003), which fits in well with the presence of these imbricate fan thrust systems rising upward from a basal detachment level located at a 12–15 km depth.

This work has been financed by project BTE2003-09544-C02-02, the research group RNM-316 and a grant awarded by the Junta de Andalucía. A. A. has received financial support through the Spanish Ministry of Science and Innovation grants CGL2007-63101/BTE and TOPO-IBERIA CONSOLIDER-INGENIO CSD2006-00041. Reviews by G. Draper, the editors and an anonymous reviewer are greatly acknowledged. We thank F. González García for reviewing our English text.

References

- ABAD, I., MATA, M. P., NIETO, F. & VELILLA, N. 2001. The phyllosilicates in diagenetic-metamorphic rocks of the South-Portuguese Zone, Southwestern Portugal. *The Canadian Mineralogist*, **39**, 1571–1589.
- ABAD, I., NIETO, F. & VELILLA, N. 2002. Chemical and textural characterization of diagenetic to low-grade metamorphic phyllosilicates in turbidite sandstones of the South Portuguese Zone: a comparison between metapelites and sandstones. *Schweizerische*

- Mineralogische Petrographische Mitteilungen*, **82**, 303–324.
- ABAD, I., NIETO, F., VELILLA, N. & SIMANCAS, J. F. 2004. Metamorfismo. Zona Sudportuguesa. In: VERA, J. A. (ed.) *Geología de España*. Sociedad Geológica de España and Instituto Geológico y Minero de España, Madrid, 209–211.
- ALONSO-CHAVES, F. M., GARCÍA-NAVARRO, E. & CAMACHO, M. 1999. Deformación progresiva de la Zona Sudportuguesa: plegamiento y cizallamiento de secuencias multicapa. *Geogaceta*, **25**, 11–14.
- BOOGAARD, M. V. & SCHERMERHORN, L. J. G. 1980. Conodont faunas from Portugal and southwestern Spain. Part 4 – A Famennian conodont fauna near Nerva (Rio Tinto). *Scripta Geologica*, **56**, 1–14.
- CONTRERAS-VÁZQUEZ, F., NODAL-RAMOS, T. & MANSILA, H. 1982. *Mapa Geológico de España (Serie Magna, E: 1/50.000) de Calañas*. Sheet no. 959, 9–39. Instituto Geológico y Minero de España. Servicio de Publicaciones Ministerio de Industria y Energía, Madrid, 1–87.
- GONZÁLEZ, F., MORENO, C., SÁEZ, R. & CLAYTON, G. 2002. Ore genesis age of the Tharsis Mining District (Iberian Pyrite Belt): a palynological approach. *Journal of the Geological Society, London*, **159**, 229–232.
- MANTERO, E. M. & ALONSO-CHAVES, F. M. 2004. Control estructural de las masas de sulfuros masivos en la corta minera de Filón Norte (Tharsis, Faja Pirítica Ibérica). *Geotemas*, **6/3**, 81–84.
- MANTERO, E. M., ALONSO-CHAVES, F. M. & AZOR, A. 2003. El abanico imbricado de Valverde del Camino (parte meridional de la Zona Sudportuguesa, Huelva). *Geogaceta*, **34**, 175–178.
- MANTERO, E. M., GARCÍA-NAVARRO, E. & ALONSO-CHAVES, F. M. 2004. Pliegues de propagación de falla transportados en la zona frontal de un cabalgamiento de la Faja Pirítica Ibérica (San Bartolomé de la Torre, Huelva). *Geotemas*, **6/3**, 85–88.
- MANTERO, E. M., ALONSO-CHAVES, F. M. & AZOR, A. 2006. Geometría y Cinemática de un Sistema Imbricado de Cabalgamientos en la Faja Pirítica Ibérica (Zona Sudportuguesa). *Geogaceta*, **39**, 47–50.
- MANTERO, E. M., GARCÍA-NAVARRO, E., ALONSO-CHAVES, F. M., MARTÍN PARRA, L. M., MATAS, J. & AZOR, A. 2007. La Zona Sudportuguesa: propuesta para la división de un bloque continental en dominios. *Geogaceta*, **43**, 27–30.
- MARRETT, R. & ALLMENDINGER, R. W. 1990. Kinematic analysis of fault slip data. *Journal of Structural Geology*, **12/8**, 973–986.
- MARTÍNEZ, A., RIVERO, L. & CASAS, A. 1997. Integrated gravity and seismic interpretation of duplex structures and imbricate thrust systems in the southeastern Pyrenees (NE Spain). *Tectonophysics*, **282**, 303–329.
- MATHUR, R., RUIZ, J. & TORNOS, F. 1999. Age and sources of the ore at Tharsis and Rio Tinto, Iberian Pyrite Belt, from Re-Os isotopes. *Mineralium Deposita*, **34**, 790–793.
- MITJAVILA, J., MARTÍ, J. & SORIANO, C. 1997. Magmatic evolution and tectonic setting of the Iberian Pyrite Belt Volcanism. *Journal of Petrology*, **38**, 727–755.
- MITRA, S. 1988. Three-dimensional geometry and kinematic evolution of the Pine Mountain thrust system, southern Appalachians. *Geological Society of America Bulletin*, **100**, 72–95.
- MORENO, C. 1993. Postvolcanic Paleozoic of the Iberian Pyrite Belt: an example of basin morphologic control on sediment distribution in a turbidite basin. *Journal of Sedimentary Petrology*, **63/6**, 1118–1128.
- MORENO, C. & SÁEZ, R. 1990. Sedimentación marina somera en el devónico del anticlinorio de Puebla de Guzmán, Faja Pirítica Ibérica. *Geogaceta*, **8**, 62–64.
- MORENO, C., SIERRA, S. & SÁEZ, R. 1995. Mega-debris flows en el tránsito Devónico-Carbonífero de la Faja Pirítica Ibérica. *Geogaceta*, **17**, 9–11.
- MORENO, C., SIERRA, S. & SÁEZ, R. 1996. Catastrophism evidence in the Famennian-Dinantian limit of the Iberian Pyrite Belt. In: STROGEN, P., SOMMERVILLE, I. D. & JONES, G. L. (eds) *European Dinantian Environments*. Geological Society, London, Special Publications, **107**, 153–162.
- MORENO, C., GONZÁLEZ, F., SÁEZ, R. & SIERRA, S. 2003. Inicio del vulcanismo en el sector de Calañas (Faja Pirítica Ibérica). *Caracterización y datación en base a palinomorfos*. *Geogaceta*, **33**, 67–70.
- MUNHÁ, J. 1990. Metamorphic evolution of the South Portuguese/ Pulo do Lobo Zone. In: DALLMEYER, R. D. & MARTÍNEZ GARCÍA, E. (eds) *Pre-Mesozoic Geology of Iberia*, Springer-Verlag, Berlin, 363–369.
- MUÑOZ, J. A. 1992. Evolution of a continental collision belt: ECORS-Pyrenees crustal balanced cross-section. In: MCCLAY, K. R. (ed.) *Thrust Tectonics*. Chapman & Hall, London, 235–246.
- NIETO, J. M., ALMODÓVAR, G. R., PASCUAL, E., SÁEZ, R. & JAGOUTZ, E. 2000a. Evidencias isotópicas sobre el origen de los metales en los sulfuros masivos de la Faja Pirítica Ibérica. *Cuadernos del Laboratorio Xeológico de Laxe*, **25**, 139–142.
- NIETO, J. M., ALMODÓVAR, G. R., PASCUAL, E., SÁEZ, R. & JAGOUTZ, E. 2000b. Estudio isotópico con el sistema Re-Os de las mineralizaciones de sulfuros de la Faja Pirítica Ibérica. *Geogaceta*, **27**, 127–129.
- OLIVEIRA, J. T. 1983. The marine Carboniferous of South Portugal: a stratigraphic and sedimentological approach. In: SOUSA, M. J. L. & OLIVEIRA, J. T. (eds) *The Carboniferous of Portugal*. Memórias Serviço Geológico, Portugal, **29**, 3–37.
- OLIVEIRA, J. T. 1990. Stratigraphy and synsedimentary tectonism. In: DALLMEYER, R. D. & MARTÍNEZ GARCÍA, E. (eds) *Pre-Mesozoic Geology of Iberia*. Springer-Verlag, Berlin, 334–347.
- OLIVEIRA, J. T., HORN, M. & PAPROTH, E. 1979. Preliminary note on the stratigraphy of the Baixo Alentejo Flysch Group, Carboniferous of Portugal, the palaeogeographic development compared to corresponding units in northwest Germany. *Communicaciones Serviço Geológico, Portugal*, **65**, 151–168.
- ONÉZIME, J., CHARVET, J., FAURE, M., CHAUVET, A. & PANIS, D. 2002. Structural evolution of the southernmost segment of the West European Variscides: the South Portuguese Zone (SW Iberia). *Journal of Structural Geology*, **24**, 451–468.
- ONÉZIME, J., CHARVET, J., FAURE, M., BOURDIER, J. L. & CHAUVET, A. 2003. A new geodynamic interpretation for the South Portuguese Zone (SW Iberia) and the Iberian Pyrite Belt genesis. *Tectonics*, **22/4**, 1027, doi: 10.1029/2002TC001387.

- PEREIRA, Z., SÁEZ, R., PONS, J. M., OLIVEIRA, J. T. & MORENO, C. 1996. Edad devónica (Struniense) de las mineralizaciones de Aznalcollar (Faja Pirítica Ibérica) en base a palinología. *Geogaceta*, **20**, 1609–1612.
- QUESADA, C. 1998. A reappraisal of the structure of the Spanish segment of the Iberian Pyrite Belt. *Mineralium Deposita*, **33**, 31–44.
- QUESADA, C., BELLIDO, F. ET AL. 1991. Terranes within the Iberian Massif: correlations with West African sequences. In: DALLMEYER, R. D. & LÉCORCHÉ, J. P. (eds) *The West African Orogens and Circum-Atlantic Correlations*. Springer, Berlin-Heidelberg, 267–293.
- RAMÍREZ-COPEIRO, J., NAVARRO-VÁZQUEZ, D., NODAL-RAMOS, T., MANSILLA, H., CASTROVIEJO, R. & MENA-ROMERO, F. 1982. *Mapa Geológico de España (Serie Magna, E: 1/50.000) de Valverde del Camino. Hoja no. 960, 10-39*. Instituto Geológico y Minero de España, Servicio de Publicaciones Ministerio de Industria y Energía, Madrid, 1–77.
- RIBEIRO, A. & SILVA, J. B. 1983. Structure of the South Portuguese Zone. *Memórias dos Serviços Geológicos de Portugal, Lisboa*, **29**, 83–89.
- ROUTHIER, P., AYE, F., BOYER, C., LÉCOLLE, M., MOLIÉRE, P., PICOT, P. & ROGER, G. 1980. La ceinture Sud-Ibérique à amas sulfurés dans sa partie espagnole médiane. *Bureau de Recherches Géologiques et Minières. Mémoires*, **94**, 221.
- SÁEZ, R., ALMODÓVAR, G. R. & PASCUAL, E. 1996. Geological constraints on the massive sulfide genesis in the Iberian Pyrite Belt. *Ore Geology Reviews*, **11**, 429–451.
- SÁEZ, R., PACUAL, E., TOSCANO, M. & ALMODÓVAR, G. R. 1999. The Iberian type of volcano-sedimentary massive sulphide deposits. *Mineralium Deposita*, **34**, 549–570.
- SCHERMERHORN, L. J. G. 1971. An outline stratigraphy of the Iberian Pyrite Belt. *Boletín Geológico y Minero*, **82**, 239–268.
- SILVA, J. B., OLIVEIRA, J. T. & RIBEIRO, A. 1990. Structural outline. South Portuguese Zone. In: DALLMEYER, R. D. & MARTÍNEZ GARCÍA, E. (eds) *Pre-Mesozoic Geology of Iberia*. Springer-Verlag, Berlin, 348–363.
- SIMANCAS, J. F. (coordinator) 2004. Zona Sudportuguesa. In: VERA, J. A. (ed.) *Geología de España*. Sociedad Geológica de España and Instituto Geológico y Minero de España, Madrid, 199–222.
- SIMANCAS, J. F., CARBONELL, R. ET AL. 2003. Crustal structure of the Transpressional Variscan Orogen of SW Iberia: SW Iberia Deep Seismic Reflection Profile (IBERSEIS). *Tectonics*, **22/6**, 1062, doi: 10.1029/2002TC001479, 2003.
- SORIANO, C. 1997. *Vulcanisme i estructura de la Faja Pirítica Ibérica. Zona Sud-Portuguesa*. PhD thesis, Universitat de Barcelona (Spain), 265.
- SORIANO, C. & CASAS, J. M. 2002. Variscan tectonics in the Iberian Pyrite belt, South Portuguese Zone. *International Journal of Earth Sciences*, **91**, 882–896.
- SORIANO, C. & MARTI, J. 1999. Facies analysis of volcano-sedimentary successions hosting massive sulfide deposits in the Iberian Pyrite Belt, Spain. *Economic Geology*, **94**, 867–882.
- STRAUSS, G. K. 1970. Sobre la Geología de la Provincia Pirítica del Suroeste de la Península Ibérica y de sus yacimientos, en especial sobre la mina de pirita de Lousal (Portugal). *Memoria. Instituto Geológico y Minero de España*, **77**, 266.
- STRAUSS, G. K. & BECK, J. S. 1990. Gold mineralisations in the SW Iberian Pyrite Belt. *Mineralium Deposita*, **25**, 237–245.
- STRAUSS, G. K. & GRAY, K. G. 1986. Base metal deposits in the Iberian Pyrite Belt. In: FRIEDRICH, G. H., GENKIN, A. D., NALDRETT, A. J., RIDGE, J. D., SILLITOE, R. H. & VOKES, F. M. (eds) *Geology and Metallogeny of Copper Deposits*. Society for Geology Applied to Mineral Deposits, Special Publications, **4**, 304–324.
- STRAUSS, G. K., MADEL, J. & FERNÁNDEZ-ALONSO, F. 1977. Exploration practice for stratabound volcano-genic sulphide deposits in the Portuguese-Spanish Pyritic belt. In: KLEMM, D. D. & SCHNEIDER, H. J. (eds) *Time and Stratabound Ore Deposits*. Springer-Verlag, Berlin, Heidelberg, New York, 55–93.
- THIÉBLEMONT, D., PASCUAL, E. & STEIN, G. 1998. Magmatism in the Iberian Pyrite Belt: petrological constraints in a metallogenic model. *Mineralium Deposita*, **33**, 98–110.
- TORNOS, F., GONZÁLEZ CLAVIJO, E. & SPIRO, B. 1998. The Filon Norte orebody (Tharsis, Iberian Pyrite Belt): a proximal low-temperature shale-hosted massive sulphide in a thin-skinned tectonic belt. *Mineralium Deposita*, **33**, 150–169.
- TORNOS, F., CASQUET, C., RELVAS, J., BARRIGA, F. & SÁEZ, R. 2002. Transpressional tectonics and ore deposit formation: the southwestern margin of the Iberian Variscan belt. In: BLUNDELL, D., NEUBAUER, F. & VON QUADT, A. (eds) *The Timing and Location of Major Ore Deposits in an Evolving Orogen*. Geological Society, London, Special Publications, **206**, 179–198.
- TWISS, R. J. & UNRUH, J. R. 1998. Analysis of fault-slip inversions: do they constrain stress or strain rate? *Journal of Geophysical Research*, **103**, 12 205–12 222, doi: 10.1029/98JB00612.

Polyphase deformation of the Variscan accretionary wedge: an example from the southern part of the Moravian Karst (Bohemian Massif, Czech Republic)

JIRÍ REZ*, ROSTISLAV MELICHAR & JIRÍ KALVODA

*Department of Geological Sciences, Masaryk University, Kotlářská 2, 61137,
Brno, Czech Republic*

**Corresponding author (e-mail: dobcina@post.cz)*

Abstract: The presence of two different coeval pre-flysch carbonate facies juxtaposed in numerous profiles in the southern part of the Moravian Karst proves that the Variscan nappe tectonics affected the pre-flysch basement of the main Culmian flysch nappes. Two main thrust events were recognized: (1) a 'thin-skinned' event, during which two sedimentary facies were juxtaposed along bedding sub-parallel thrusts, and (2) a 'thick-skinned' event, which generated younger thrusts oblique to bedding, involved crystalline rocks of the Brno Massif, and resulted in refolding of the older thrusts.

The Variscan accretionary wedge originated during the collision of the Armorican terrane assemblage with the passive margin of Laurussia (in the Czech Republic, the Moldanubian and Saxothuringian terranes collided with the Brunovistulian Terrane along the Moldanubian thrust; Fig. 1). Extensive research during the last two decades has provided a kinematic scenario of the Variscan collision involving internal parts of the orogenic belt (e.g. Rajlich 1990; Schulmann *et al.* 1991; Fritz & Neubauer 1993), nappes of syn-orogenic flysch sediments and their pre-orogenic basement also involved in the nappe stack (e.g. Čížek & Tomek 1991; Hladil *et al.* 1999; Hartley & Otava 2001).

Variscan externalites in the Czech Republic are built of the Moravo-Silesian Palaeozoic Zone sequences. The Moravo-Silesian Palaeozoic Zone, which is regarded as the continuation of the Rhenohercynian Zone (Franke 1995; Kalvoda *et al.* 2002, 2003), was formed by pre-orogenic pre-flysch and syn-orogenic flysch sequences (Culmian facies, e.g. Zúkalová & Chlupáč 1982). Different pre-flysch facies of the Moravo-Silesian Palaeozoic Zone – the basinal Drahany facies, transitional Ludmírov facies and platform carbonate facies of the Moravian Karst were juxtaposed and incorporated into the Variscan nappes (e.g. Bábek *et al.* 2006). The facies of the Moravian Karst was recently divided into Northern and Southern tectonic units based on their sedimentological and thermal history (Bábek *et al.* 2006).

The deformation history of the Moravian Karst has been a matter of discussion during the last hundred years. The thrust tectonic idea was proposed early on by Kettner (e.g. 1949). However,

tectonic models based on vertical movements of crustal blocks prevailed (e.g. Dvořák & Pták 1963; Dvořák 1967). The southern part of the Moravian Karst was considered as a more or less isolated basin with distinct sedimentary and deformation history, separated from the rest of the Moravian Karst by a large horst structure called the Říčanice-Ochoz elevation (Fig. 2; e.g. Dvořák 1989). Dvořák recognized rapid facies changes in numerous profiles in the southern part of the Moravian Karst, which reflected differentiation of facies of the basin mainly during Famennian to Viséan. These abrupt facies changes were interpreted as changes of depositional environment *in situ* caused by synsedimentary vertical movements of tectonic blocks not larger than about 500 × 300 m. While some blocks were relatively uplifted under shallow water sedimentation, on the subsided blocks deeper-water sediments were deposited. The relative vertical position of the blocks changed several times because both the deeper water and the shallow water coeval facies are often present within the blocks. The newly deposited unlithified sediments were deformed during vertical movements by gravitational sliding forming recumbent folds. During the Lower Viséan, the tectonic regime of the basin inverted. The NE–SW compression caused diapiric extrusion of the Líšeň bivergent anticlinal structure of the Horákov ridge (NE-vergent in the NE and SW-vergent in the SW; Dvořák 1967; Horákov *anti-form* in this paper).

In the last two decades thrust tectonic models have been proposed, which are supported by detailed geological mapping (Hladil 1987a) and data on facies (Kalvoda 1989; Hladil 1991; Hladil

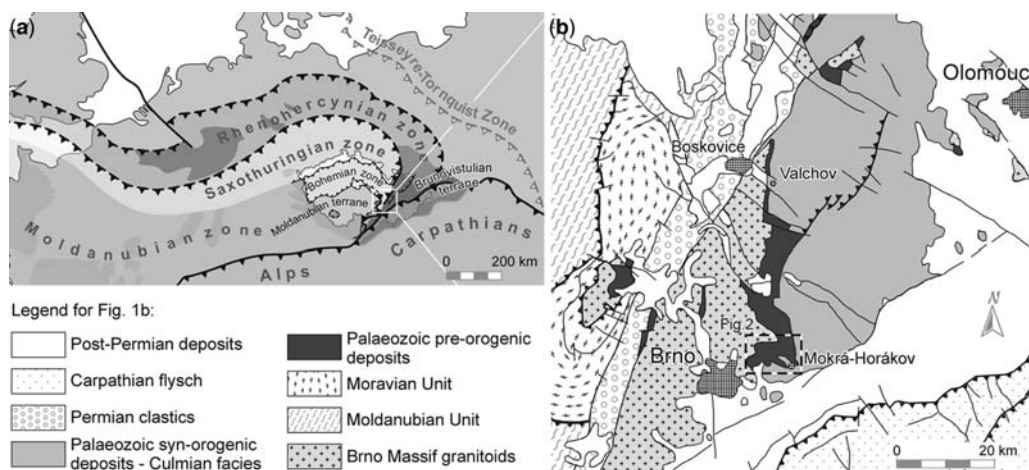


Fig. 1. (a) Tectonic position of the area of interest within European Variscides (modified after Gee & Zeyen 1996). (b) Schematic geological sketch of the SE part of the Bohemian Massif (modified after Kodým *et al.* 1968).

et al. 1991). In order to unravel the character and geometry of thrust faults and outline the possible deformation history of the southern part of the Moravian Karst, a summary of the existing data in light of new observations is provided below.

Geological setting and stratigraphy

The area of interest, the southern part of the Moravian Karst, is situated to the NE of the town of Brno in the eastern part of the Czech Republic in the southernmost part of the Moravo-Silesian Palaeozoic Zone. Devonian to Carboniferous sedimentary sequences of the Moravo-Silesian Palaeozoic Zone can be divided in three different facies: (1) basinal Drahaný facies represented by shales, calciturbidites, and bimodal volcanic rocks; (2) reefoid carbonate facies of the Moravian Karst; and (3) transitional Ludmírov facies (Zukalová & Chlupáč 1982). The rocks of these three facies form more or less continuous belts along the eastern margin of the crystalline rocks of the Bruno-vistulian Terrane and are incorporated into Variscan flysch nappes.

The basement formed by Precambrian granitoids and metabasites of the Brno Massif is overlain by Cambrian and Devonian 'basal' clastics (arkoses, sandstones and conglomerates).

The carbonate sedimentation of the Moravian Karst facies begun in the Upper Eifelian with the deposition of the Macocha Formation (Zukalová & Chlupáč 1982; Hladil 1983) represented by the Lažánky and the Vilémovice limestones. The Lažánky Limestone is a thick-bedded, grey to dark grey micritic limestone with rich *Amphipora* fauna. The Vilémovice Limestone is a massive, rarely

bedded, light-grey, biomicritic to biotrital limestone, forming biohermal bodies. The Macocha Fm was deposited in four cycles, which are characterized by alternation of Vilémovice and Lažánky limestones (Hladil 1983). The thickness and presence of each cycle varies along the belt of the Moravian Karst. The three lower cycles are well developed in the northern part forming a sequence hundreds of metres thick. However, the deposits of the fourth cycle exhibit disproportionately smaller thicknesses in the north (Hladil 1983). In contrast, the fourth cycle is well developed in the southern part of the Moravian Karst, whereas the other cycles are thinner and the first cycle is not present at all. Two different types of the Vilémovice Lst. in the fourth Upper Frasnian cycle can be distinguished (Fig. 3), reflecting differentiation of the carbonate sedimentation, which is more clearly expressed in the Líšeň Formation (see below; Hladil 1983).

The subsidence rate of the carbonate platform accelerated in the Late Frasnian. This process led to differentiation of the basin during the Famennian–Lower Visean, resulting in facies variability of the Líšeň Formation (e.g. Prantl 1947; Dvořák 1967; Kalvoda 1996). In the southern part of the Moravian Karst the Líšeň Fm reaches much greater thicknesses than in the north. This formation has two formal members: (1) biomicritic nodular or brecciated Křtiny Limestone and biotrital calciturbidites; and (2) the Hády-Říčka Limestone (Zukalová & Chlupáč 1982). However, the situation in the field is more complex. Two main facies of the Líšeň Fm can be distinguished in the southern part of the Moravian Karst: (1) shallower Hostěnice facies; and (2) deeper Horákov facies (Kalvoda 1996). Both the Křtiny and Hády-Říčka limestones

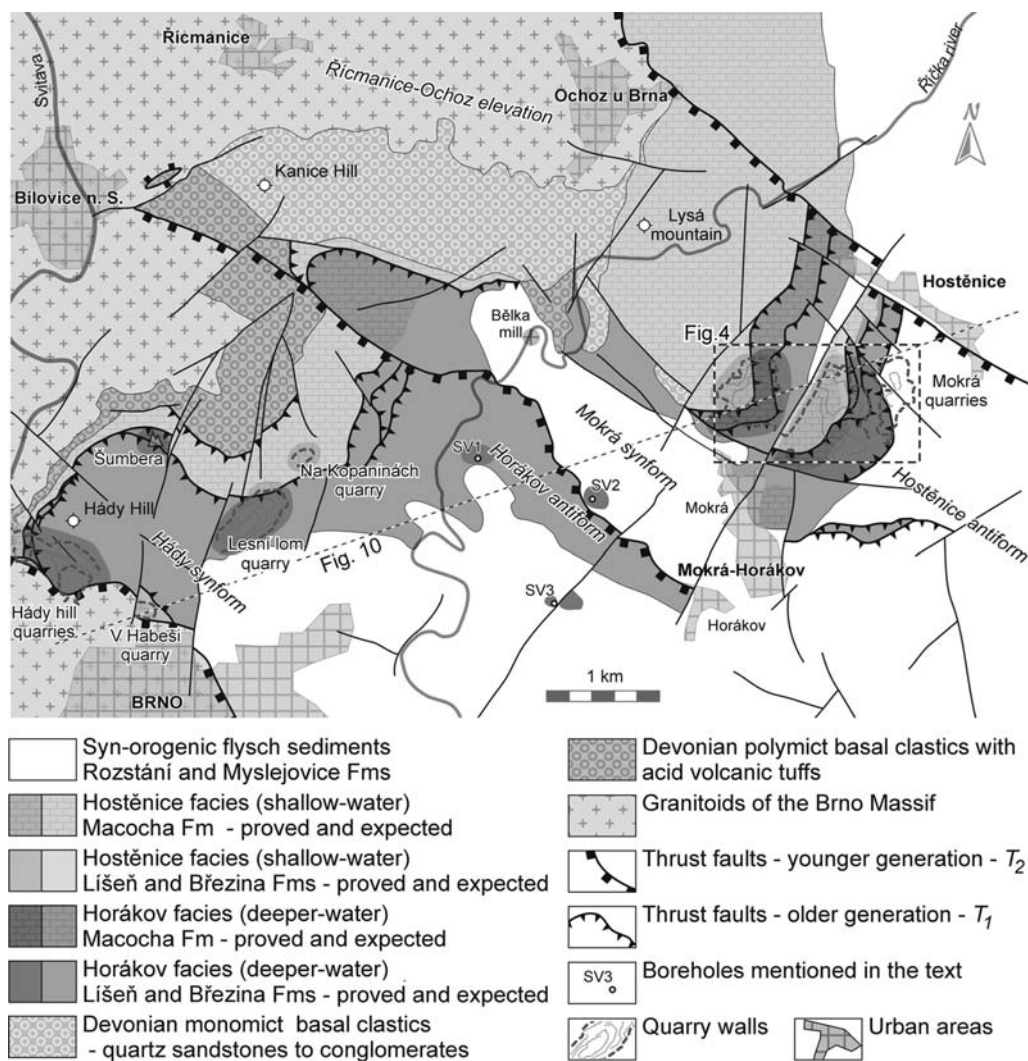


Fig. 2. Schematic geological map of the southern part of the Moravian Karst (Hladil 1991, modified using geological maps by Hladil 1987a; Dvořák 1997 and the authors' geological mapping in the Mokrá, Lesní lom and Hádý hill quarries). For location see Figure 1.

occur repeatedly in both facies in different structural and stratigraphical positions. To distinguish between them, informal lithostratigraphical units are used.

The *Hostěnice facies* represents upper slope condensed sedimentation with dominant micritic to biomicritic limestone deposition during Famennian–Middle Tournaisian (lower Křtiny Limestone). These limestones are mostly nodular as an effect of deformation that occurred during several phases. Growing tectonic activity in the Late Tournaisian–Middle Visean resulted in deposition of brecciated to sandy limestones of the Březina Formation (Fig. 3).

The *Horákov facies* represents lower slope calciturbiditic sedimentation. During the Famennian, dark grey, biotrital to biomicritic limestones were deposited (lower Hádý-Říčka Limestone). After a global eustatic fall in the Earliest Tournaisian (Kalvoda & Kukal 1987), the deposition of predominantly skeletal calciturbidites changed to mud calciturbidites and hemipelagites with higher percentage of clay (upper Křtiny Limestone), which are also nodular. In the Middle Tournaisian biotrital to biomicritic calciturbidites with variable amount of cherty concretions or brecciated cherty layers (upper Hádý-Říčka Limestone) were

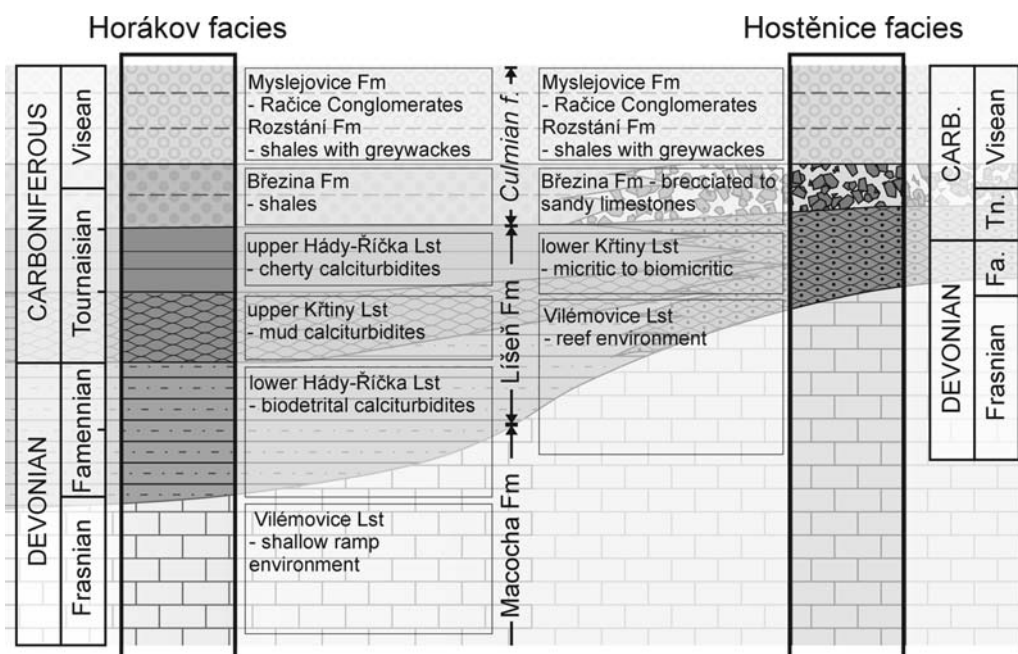


Fig. 3. Stratigraphic scheme of the southern part of the Moravian Karst (after Kalvoda 1996).

deposited indicating a global eustatic rise (Isaacson *et al.* 1999). In the Late Tournaisian–Middle Visean, the flyschoid Březina Formation deposited. It is characterized by alternating limestones, brecciated limestones, sandstones and limey shales (Fig. 3). The percentage of shales grows towards the top.

These two different facies (Horákov and Hostěnice) were juxtaposed during Variscan deformation events: the deeper Horákov facies was thrust over the shallower Hostěnice facies. The thrust zone is well exposed in the Mokrá quarries and can be observed in structural boreholes through the Horákov antiform (e.g. SV-1 and SV-2; Dvořák 1989; Kalvoda 1989). The known outcrops of both facies are indicated in Figure 2.

The sedimentary sequence is topped by allochthonous flysch sediments of the Culmian facies, which is represented in the area of interest by Middle Visean Rozstání and Myslejovice formations. The Rozstání Fm is composed of greenish shales with minor greywacke and conglomerate intercalations. The Upper Visean Myslejovice Formation is represented by greywackes and the polymict Račice Conglomerate with a greywacke matrix (e.g. Hladil 1987b).

Structural framework and data on facies

The following paragraphs are based on detailed structural and lithostratigraphical analysis of key

outcrops from the area (mainly the Mokrá quarries) and revision and reinterpretation of existing lithostratigraphical and structural data (case studies including several structural boreholes and the primary documentation of the geological mapping by Hladil 1987b).

Mokrá quarries

Three big quarries near Mokrá-Horákov village, about 2 km NE from Brno, allow a full 3D view of the structural pattern in the southern part of the Moravian Karst. Sections studied in the western, middle and eastern quarries (total length of 1800 m) provided evidence of polyphase deformation including folding, thrusting and faulting. In each profile detailed lithologic and structural mapping was calibrated using biostratigraphic data based on the study of conodonts and foraminifers (by J. Kalvoda; Fig. 4).

The western quarry profile shows thick bedded Vilémovice Lst. to the west overlain by Lower Famennian micritic nodular lower Křtiny Lst. (Fig. 5a; Friáková *et al.* 1985; Hladil 1987b). The contact between the Vilémovice Lst. and the lower Křtiny Lst. was affected by bedding-parallel slip and mylonitization. Detachment folds also developed in the lower Křtiny Lst. Another mylonitic bedding-parallel shear zone is located c. 80 m under the Vilémovice/Křtiny limestones contact

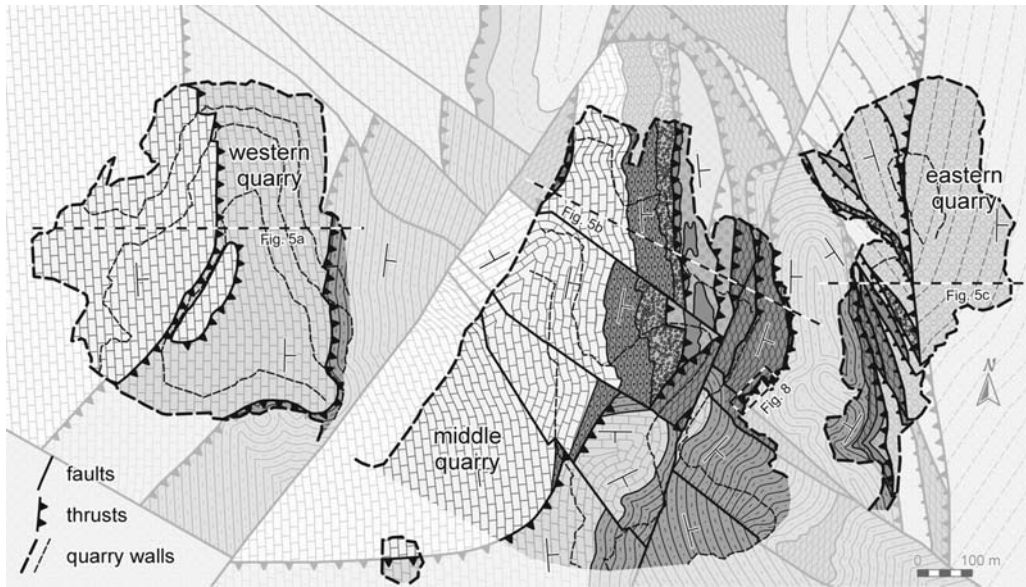


Fig. 4. Schematic map of the Mokrá quarries (note that the map is slightly shaded between quarries to highlight the structure exposed by the quarries). For legend see Figure 3, for location see Figure 2.

suggesting detachment of the overlying strata (Figs 4 & 5).

The most complete section is displayed in the middle quarry (Fig. 5b). From NW–SE it begins with Upper Frasnian Vilémovice Lst. of the Hostěnice facies, building up the western wall of the quarry, dipping to the east. They are overlain by folded nodular or thin bedded, Lower

Famennian–Middle Tournaisian lower Křtiny Lst., comprising c. 50 m of apparent thickness. The Hostěnice facies sequence is terminated by a few metres of Upper Tournaisian brecciated limestone. This parautochthonous sequence is in tectonic contact with the deep-water Horákov facies. The internal structure of the allochthonous body is very complex and includes several stratigraphical duplications.

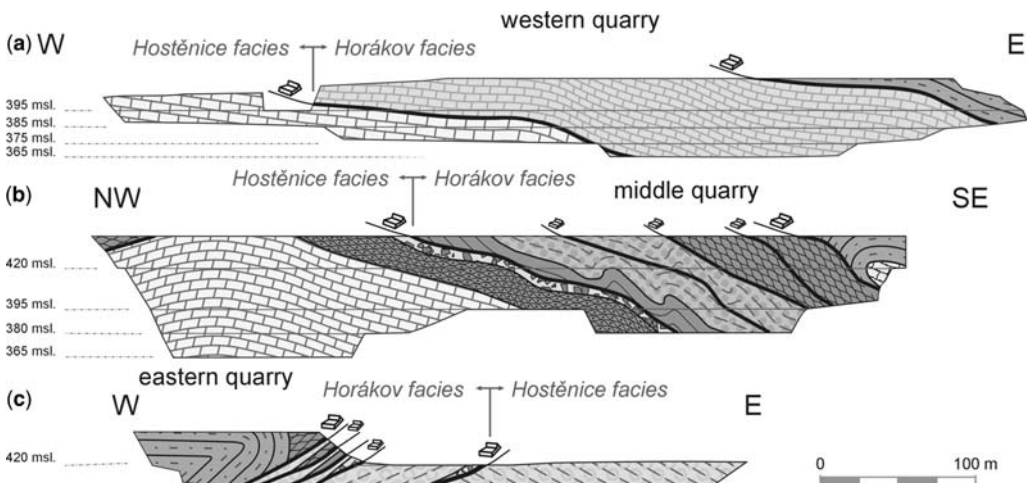


Fig. 5. Schematic geological sections through the western (a), middle (b) and eastern (c) Mokrá quarries. Young faults are not displayed in order to highlight the geometry of the older structures. For legend see Figure 3. See Figure 4 for approximate location of the sections.

The orientation of bedding planes varies, but the main overturned orientation trend can be recognized. At the bottom, directly on the paraautochthonous sequence are Upper Tournaisian upper Hádý-Říčka Lst. overlain by the Upper Tournaisian–Lower Visean rocks of the Březina Fm. The sediments of the Březina Fm are intensely folded, forming a tectonic sheet up to 80 m thick. To the east an imbricate stack of Lower Tournaisian upper Křtiny Lst., where sequences of normal as well as overturned orientation alternate, is thrust over the tectonic sheet formed by the Březina Fm. Tectonic slices of older limestones (Famennian lower Hádý-Říčka and Frasnian Vilémovice limestones) up to one metre thick are also involved in the imbricate stack structure. This imbricate stack of upper Křtiny Lst. can be considered as a detached and duplicated overturned limb of a NE-vergent recumbent anticline of Famennian biodetrital lower Hádý-Říčka and Vilémovice limestones, whose hinge zone crops out at the SE end of the profile (Fig. 5b).

The eastern quarry cuts across from west–east a complete sequence of the Horákov facies in reverse stratigraphic order dipping to the west, forming an overturned anticline that was thrust over the shales of the Rozstání Fm along a duplex zone including numerous tectonic sheets of upper Křtiny, upper Hádý-Říčka and Upper Tournaisian brecciated limestones incorporated in the Rozstání shales (Figs 4 & 5c).

The sedimentary complex exposed in the Mokrý quarries is affected by folding, faulting and thrusting. Two generations of folds with distinct fold-axis orientation and geometry are present. The older and dominant folds (F_1) are mostly tight, gently inclined to recumbent with fold-axes plunging to the SE (mean plunge is 150/28; Fig. 6c). Constant true thickness of folded beds and striae on bedding planes suggest a flexural slip folding mechanism. The F_1 folds are NE-vergent, which in combination with the striae trend suggests movement towards NE (Fig. 6). The younger folds (F_2), which gently re-fold

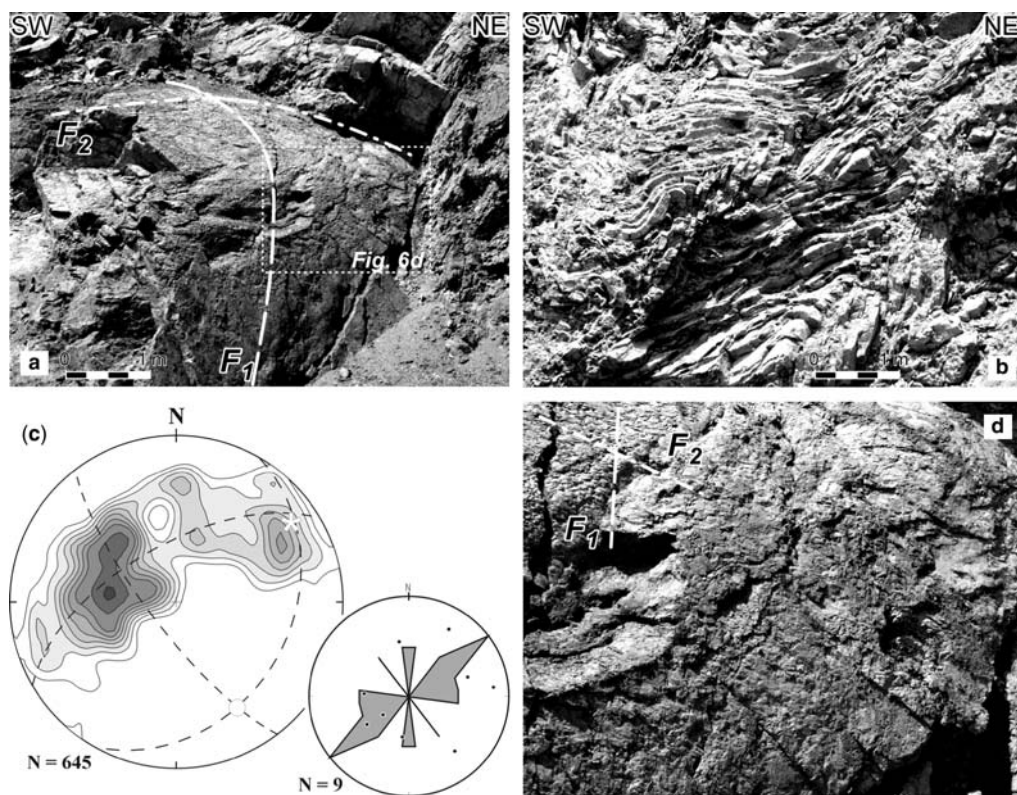


Fig. 6. (a) Gently inclined F_1 fold reformed by a F_2 upright fold (lower Křtiny Lst., middle quarry), (b) NE-vergent F_1 folds in the upper Hádý-Říčka Lst., (c) contoured equal area plot of bedding planes (1% contours, lower hemisphere) and a rose diagram of bedding plane striae orientation; dashed great circles indicate principal planes of the orientation matrix, small circle indicates the mean F_1 fold axis, the asterisk indicates the mean F_2 fold axis, (d) enlarged section of Figure 6a showing relationship of F_1 and F_2 striae (F_2 striae cross-cut F_1 striae).

the F_1 generation, have fold axes almost perpendicular to the F_1 ones (approximate plunge is 60/15). The F_2 generation folds are open and symmetric with upright axial surfaces and several times larger wavelengths than F_1 folds. F_2 striae along bedding planes, which evidently cross cut F_1 striae (Fig. 6d), indicate movement along the NW–SE direction.

As suggested above, sequences of Horákov and Hostěnice facies are tectonically juxtaposed. The thrust zone developed as a 30–80 m thick duplex zone with complex internal structure where each tectonic sheet is delimited by thrust faults. These faults are zones of intense deformation 2 cm–2 m thick (Fig. 7), which exhibit well developed schistosity with lineation. Most of the volume of these highly strained rocks was dissolved by pressure solution during thrusting which enriched them in siliciclastic and graphitic insoluble material originally dispersed in the sheared limestone. Progressive stages of this process can be observed in the Mokrá quarries from the initial stage (Fig. 7d), to moderate stage, in which remnants of the original limestone are present (Fig. 7f), to final stages, where all the limy material was dissolved and the shear zone has a black slate character (Fig. 7e). These rocks can be best described as mylonites. These mylonitic thrust faults bear asymmetric structures (Fig. 7), which in combination with the NE–SW-trending lineation prove top-to-NE movement.

Several tectonic sheets of deep-water Horákov facies separated by minor thrust faults lie on top of the Hostěnice facies rocks (Fig. 5). The middle quarry profile described above shows that in general the strata within the duplex zone are overturned. Moreover, an anticline of the upper Hádý-Říčka and Vilémovice Limestones was thrust over the duplex zone (Figs 4 & 5). These two facts suggest that the allochthonous body is a large-scale anticline and the duplex zone is the overturned limb that was highly strained and duplicated during thrusting.

The main thrust fault that separates the two facies is sub-parallel or slightly oblique to the bedding in the footwall, which is well observable in the middle quarry. It ramps up from the Vilémovice Lst. in the SW (the third cycle is thrust over the fourth one) to the Middle Tournaisian brecciated limestones in the NE (Fig. 4). In the eastern quarry the allochthonous sequences are thrust over the Viséan flysch sediments of the Rozstání Fm.

The geometry of the thrust faults was modified by folding. The thrust faults are folded by both generations of folds as suggested by identical orientation of the eigen vectors of the orientation matrices, the resemblance of the equal area plots in Figures 6c and 7c, and field observations. The relative timing of thrusting and folding phases is

complex. The thrust faults are folded by the F_1 folds, as suggested above, but they also crosscut F_1 folds (Fig. 8). Identical striae directions as well as the shear sense of both, thrusts and F_1 folds, suggest that both structures are approximately coeval and originated during NE-vergent shear. The thrust faults developed on the overturned limbs of the F_1 folds during progressive stages of F_1 folding. This fold/thrust structure was further folded during F_1 folding into F'_1 folds, which are alike the F_1 folds, and then refolded by F_2 folds.

This complex thrust-fold structure is further complicated by brittle tectonics. Beyond minor fault generations, two main systems exist which cross-cut the older fold/thrust structures dividing the area into several blocks with different erosion level (Fig. 4). The first system is represented by NNE–SSW-trending SE steeply dipping strike-slip faults. The second generation of faults is represented by WNW–ESE-trending strike-slip faults steeply dipping to the NE. Striae observed on fault planes show evidence of fault reactivation. The orientation of these faults as well as their relationships to other structures (Fig. 4) suggests that they originated during a younger, post-folding deformation phase, probably of Alpine age.

3D structure of the southern part of the Moravian Karst

The tectonic structure of the Mokrá quarries can be generalized for the whole southern part of the Moravian Karst. It bears identical traits including facies juxtaposition along thrust faults, two generations of folds, and a dominant generation of folds with axes plunging to the SE which folded the thrust faults, etc.

The diversity of facies documented in the Mokrá quarries can also be observed in other places all over the southern part of the Moravian Karst. The outcrops of both coeval facies are indicated in Figure 2 (based mainly on existing field documentation by Hladil 1987b; Dvořák 1989).

The Mokrá quarries provided evidence of juxtaposition of the two facies. Similar structure was documented in structural boreholes, mainly in the boreholes SV-1, SV-2 and SV-3, drilled in the tectonically most interesting area of the Horákov anti-form (Fig. 2). All three boreholes started in sequences of the Horákov facies. At depth a deformation zone marked by a black slaty horizon separates the deeper-water sequences from a tectonic mélange of variable thickness (e.g. 76 m in the SV-1 borehole), with an overall reversed stratigraphic order with a black mylonitic zone underneath. The footwall of this fault zone is made up of the Hostěnice facies sequences. This thrust zone

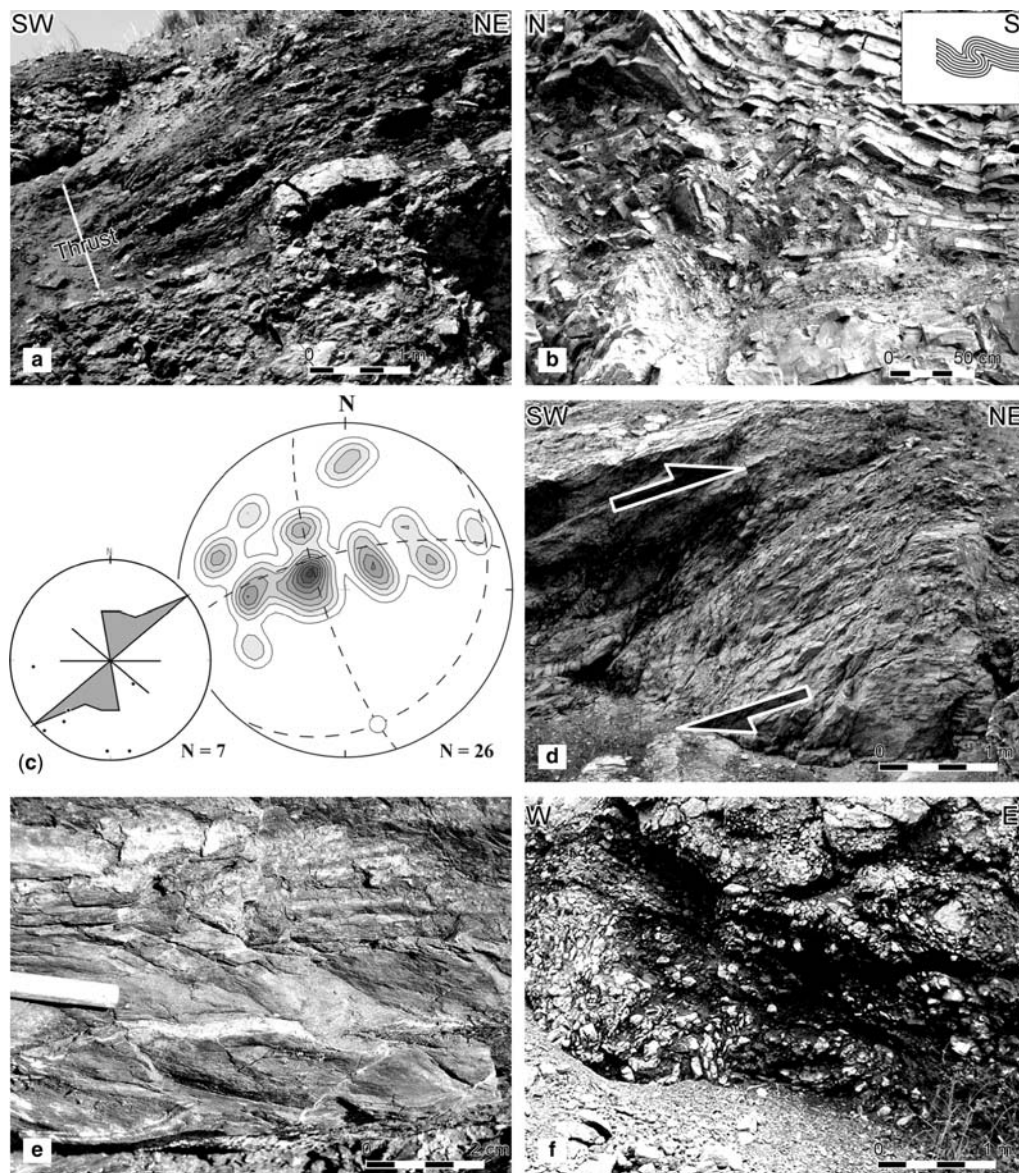


Fig. 7. (a) Thrust fault in the eastern quarry (shales of the Rozstání Fm are thrust over Visean brecciated limestone), (b) a thrust fault folded into a NE-vergent F_1 fold (upper Hádý-Ríčka Lst., middle quarry), (c) contoured equal area plot of thrust faults (1% contours, lower hemisphere) and a rose diagram of striae orientation; dashed great circles indicate principal planes of the orientation matrix, small circle indicates the mean F_1 fold axis, (d) mylonitic thrust fault in initial stage showing strong dextral asymmetry (lower Hádý-Ríčka Lst., eastern quarry), (e) detail of the mylonitic thrust fault (middle quarry), (f) thrust fault in a moderate stage of mylonitization and pressure solution – remnants of the limestone are present (eastern quarry).

has an identical structure to the thrust zone exposed in the Mokrá quarries.

Even though large thicknesses of the Hádý-Ríčka Lst. forming the major parts of the Lesní lom quarry link the sequence to the Horákov

facies, brecciated limestones in the NW corner of the quarry overlying the Vilémovice Limestones underneath a thrust fault can be regarded as a sequence of the Hostěnice facies. Also several bedding-parallel detachments in the Horákov

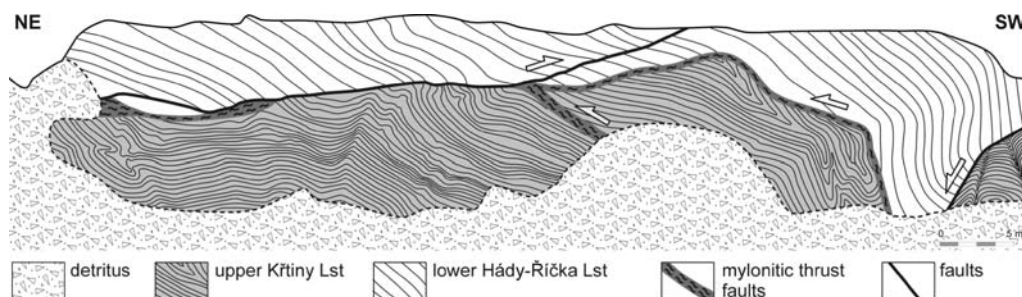


Fig. 8. A schematic view of the NE uppermost edge in the middle quarry (for location see Fig. 4). Upper Famennian lower Hádý-Říčka Lst. is thrust over Lower Tournaisian upper Křtiny Lst. The thrust plane cuts the F_1 folds and is folded by coaxial F_1 folds.

facies sequence in the eastern part of the quarry suggest the proximity of a thrust. The strata exposed in the Na Kopanínách quarry definitely belong to the Hostěnice facies. A rather complex pattern of facies can be observed in the Hádý hill area. Profiles across the Šumbera, north of the Hádý hill, and across the eastern part of the Hádý hill quarries show typical sequences of the Horákov facies. On the other hand, the V Habeši quarry and the western part of

the Hádý hill quarries show the shallower Hostěnice facies (Fig. 2).

Detailed investigation of the 3D geometry in the Mokrá quarries reveals that the thrust faults separating different facies are slightly oblique to the bedding (they ramp up from Vilémovice Lst.–Březina Fm) and are folded by both generations of folds. The structural map in Figure 9 shows two main antiform and two synform structures

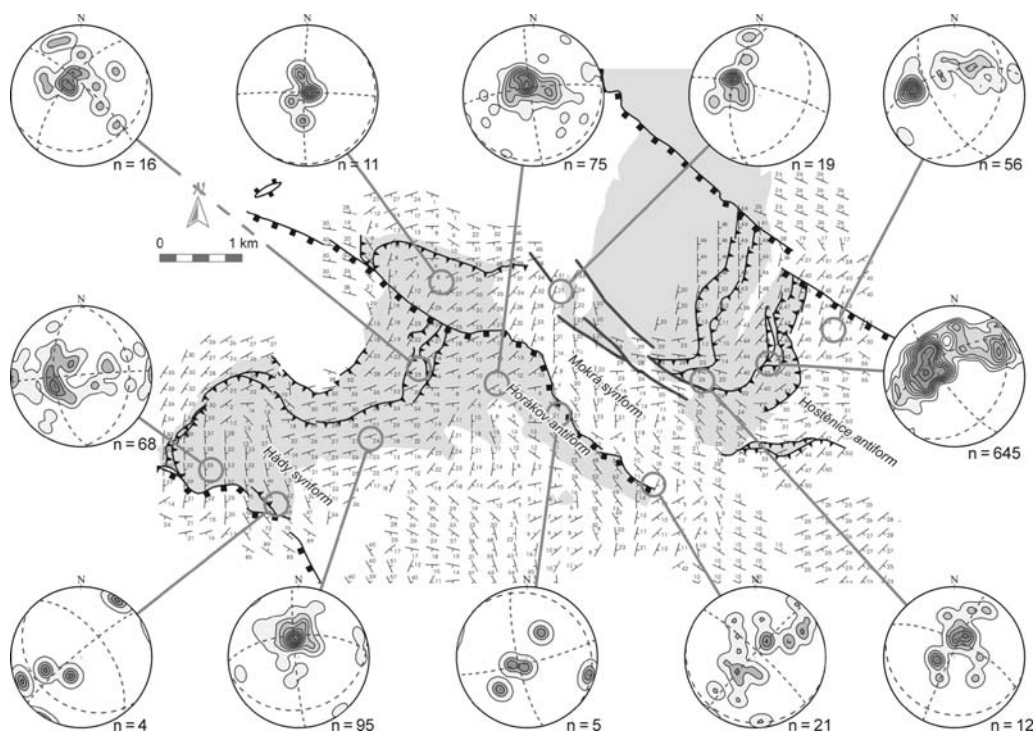


Fig. 9. Structural map of the southern part of the Moravian Karst showing the main fold structure (spatially averaged orientations of bedding planes by SpheriStat software). Contoured equal area plots show bedding planes compass data from the nearest area used for the space averaging (1% contours, lower hemisphere). Dashed great circles indicate principal planes of the orientation matrix. Limestones are in grey, see Figure 2 to distinguish thrust generations.

belonging to the F_1 fold generation – Hostěnice and Horákov antiforms and Mokrá and Hádý synforms (modified terms by Dvořák 1967). These structural data combined with existing patchy data on facies from outcrops and boreholes allowed tracing of the thrust faults in the map.

The thrust zone in the Mokrá quarries is folded into an antiform structure following the main fold configuration (Figs 4 & 9). Furthermore, a well documented thrust in the Vilémovice Lst. (second cycle Vilémovice Lst. are thrust over the third-cycle Vilémovice Lst.) SE of Kanice hill (Fig. 2; Hladil 1987*a, b*) has a synformal geometry. This thrust is most probably the continuation of the thrust zone that crops out in the Mokrá quarries, considering the occurrence of a NW–SE-trending fault zone between Mokrá and Říčanice villages separating two parts of this S-shaped folded thrust fault (Fig. 2).

A thrust fault separating two different facies with S-shaped folded geometry can be traced also west of the Horákov antiform (Fig. 2). The thrust zone is not exposed as in the Mokrá quarries but it has been documented in the SV-1 and SV-3 boreholes (Hladil 1987*b*; Dvořák 1989). The overall fold geometry (Fig. 9) suggests that the thrust zone should be exposed WNW of the SV-1 borehole. The thrust was also documented in the NW part of the Lesní lom quarry. A typical sequence of the shallow-water Hostěnice facies is exposed in the V Habeši quarry, but since the top of the Hádý hill is composed of the deeper-water Horákov facies, a thrust fault has to be located north of the V Habeši quarry. The situation in the Hádý hill quarries is more complex. Most of the limestones are heavily strained and stacked with abundant black mylonitic zones. The main thrust is probably located in the Famennian lower Křtiny Lst. or in the Vilémovice Lst. in the westernmost part of the quarries, analogically to the Mokrá quarries.

In addition to these folded S-shaped thrust faults, rather straight, gently folded WNW–ESE-trending S-dipping thrust faults can be traced. These thrusts are folded only by the open F_2 folds with relatively large wavelengths. These thrusts affect not only carbonate rocks, but also flysch siliciclastics and crystalline rocks of the Brno Massif. The thrust that places granitoids of the Brno massif and the basal clastics over the Vilémovice and lower Křtiny Lst. in the southern part of the Hádý hill quarries is well known (Fig. 2; e.g. Hladil 1987*b*). Another example is the NE marginal fault of the Horákov antiform in the Říčka river valley SW of the Bělka mill (Fig. 2). Famennian biotrital lower Hádý-Říčka Lst. are thrust over Březina and Rozstání Fm along a flat thrust fault. These straight thrusts are oblique to bedding, but obviously are related to the large fold structure as they are parallel to

the main fold axes (Fig. 9). These thrusts can also be traced deep into the Brno Massif, forming mylonitic zones several metres thick.

Discussion

Detailed structural research in the field supported by sedimentological and biostratigraphical data allowed a critical revision of the old, but still used tectonic model for the southern part of the Moravian Karst (e.g. Dvořák 1967; Dvořák *et al.* 1987). New data as well as well-known facts not consistent with this model are discussed in following paragraphs.

There are two phenomena responsible for the fold structure of the southern part of the Moravian Karst according to previous authors (e.g. Dvořák 1967, 1989): (1) gravitational sliding of unlithified sediments from numerous small north-tilted crustal blocks giving rise to recumbent folds; and (2) bivergent folding of lithified sediments caused by diapiric extrusion of the Horákov antiform during NNE–SSW compression.

Some facts contradict Dvořák's model and these are discussed below. Štelcl (1957) used orientations of calcite *c*-axes to prove that tectonic processes, not gravitational sliding, were responsible for the development of the recumbent folds. Furthermore, the folds of both generations have constant true thickness (1B type after Ramsay & Huber 1987) and uniform orientation of fold axes. These facts show that the strata were not folded by gravitation sliding but after lithification during NNE–SSW compression by flexural slip mechanism. There is no evidence that SW of the Horákov antiform the folds are mostly SW-vergent and NE of the Horákov antiform the folds are NE-vergent as stated by Dvořák (1967). Instead there is a major NE vergence trend all over the area.

In the area of interest, bands of black slaty rocks are present (e.g. Dvořák *et al.* 1987) and were formerly considered as black shales with minor intercalations or pebbles of limestones. Their deformation features and structural position suggest a tectonic origin. These bands are zones of strong deformation and pressure solution. While the carbonate component of the limestones dissolved during deformation, the amount of siliciclastic and graphitic material was relatively enriched, causing the slaty character and black coloration of these mylonitic zones. The limestone 'pebbles' are undissolved remnants of the original limestone. One-metre scale tectonic sheets incorporated in the mylonitic zones are well documented from the Mokrá and Hádý hill quarries (e.g. Dvořák 1989). These mylonitic zones bear strong evidence of simple shear strain: asymmetric structures and stretching lineations. Their structural setting suggests that the

mylonitic zones represent thrust faults, because they juxtapose coeval stratigraphical sequences of different facies.

Frequent changes of facies observed in the field were formerly explained by variation in sedimentation *in situ* resulting from non-uniform subsidence rate of the pre-Devonian basement divided into numerous small blocks (not bigger than 300–500 m in the Mokrá quarries) separated by an orthogonal net of very steeply inclined faults (Dvořák 1987). The newly deposited unlithified sediments folded by gravitation sliding during syn-sedimentary movements along the marginal faults of the blocks.

It has been demonstrated here that the folds were caused by tectonics. Moreover, other facts support the thrust juxtaposition of the facies. First, the area of the blocks (300–500 m) seems to be insufficient for such changes of facies. It is hard to imagine almost vertical slopes hundreds of metres high separating areas with shallow-water and deeper-water sedimentation. Second, the planar marginal faults cross-cut the fold-and-thrust structures and therefore are definitely younger. These facts prove that the sequences of different facies were deposited in different areas and were juxtaposed tectonically. The deeper-water lower slope Horákov facies was thrust over the shallower upper slope Hostěnice facies. This is observed in several outcrops and boreholes all over the area of the southern part of the Moravian Karst.

As suggested above, two generations of thrust faults are recognized. T_1 thrusts are folded by F_1 folds and hence S-shaped, consistent with the main fold structure (Fig. 9). They juxtaposed two different carbonate facies (Fig. 2). A second generation of planar almost unfolded thrust faults T_2 cross-cuts T_1 thrusts and hence is younger. The T_2

generation thrusts superpose mainly the carbonate rocks upon the Culmian ones, but also involves crystalline rocks of the Brno Massif (e.g. in the Hádý Hill quarry, Fig. 2). The T_2 thrust faults are parallel to the F_1 fold axes and to the main anticlinal and synclinal structures (Fig. 9). Moreover, a systematic relationship of anticlines and synclines of the T_1 thrusts and the T_2 thrusts can be observed (Figs 2 & 9): antiforms are in the hanging walls and synforms in the foot walls of the T_2 thrusts. This geometrical relation suggests that the folds (with fold axes parallel to the F_1 folds, hence are designated as F'_1 folds) originated during the T_2 phase of thrusting (drag-folds? fault-bend folds?; Fig. 10). It seems likely that in some state of compression T_2 thrust faults originated causing folding of the T_1 ones. However, identical striae orientation of both thrust generations, as well as identical orientation of fold axes (F_1 and F'_1 ones) suggest, that the T_2 thrusting did not reflect a change of stress field orientation, but an increase in stress intensity. Whereas the T_1 generation of thrust faults represents a thin-skinned tectonic event, when only cover rocks were affected by thrusting, the T_2 generation of thrust faults represents a thick-skinned tectonic event because the basement crystalline rocks of the Brno Massif were also involved in the thrust structure. The F_2 -folding phase, probably also Variscan, refolded then gently all D_1 (F_1 and T_1) and D_2 (F'_1 and T_2) structures.

Such a complex thrust/fold structural pattern is not unique along the western margin of the Bruno-vistulian terrane. Similar structure was identified in the Němčice-Vrátkov Zone in the northern part of the Brno Massif (Melichar & Kalvoda 1997) where two generations of thrusts are also present, the older one is cross-cut and folded by a younger one. In the northern part of the Moravian Karst some thrusts associated with recumbent folds are

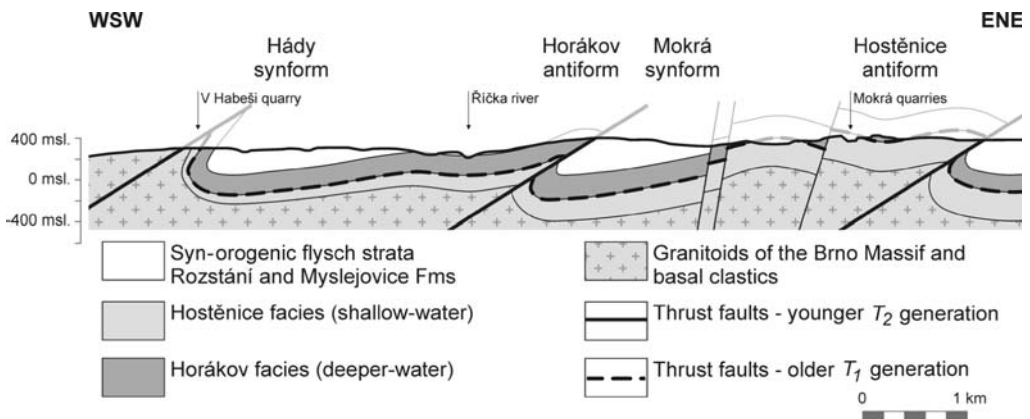


Fig. 10. Schematic cross-section across the southern part of the Moravian Karst. For location see Figure 2.

present, suggesting a complex fold/thrust structure of the area (Dvořák & Melichar 2002). Finally, folded thrust faults within the granitoids of the Brno Massif, marked by tectonic sheets of Devonian rocks near Valchov (Melichar & Kalvoda 1997), Vavřinec (Slavík & Melichar 1996) and Adamov (Rez & Melichar 2002) suggests that, even though individual tectonic units differ slightly in thermal regime during deformation (e.g. Bábek *et al.* 2006) which resulted in a different overprint of older structures, the whole eastern margin of the Brno Massif between Brno in the south and Boskovic in the north bears a similar polyphase deformation imprint.

An idealized deformation sequence for the area of interest during the Variscan orogeny can be outlined using the observations mentioned above:

- (1) The first phase of NE–SW compression (D_1) is represented by NE-vergent recumbent F_1 -folding and T_1 -thrusting. After the recumbent folds were in place, no more compression could be accommodated by folding, and therefore, T_1 thrusts developed. This thin-skinned D_1 deformation event caused the sedimentary sequences of deeper-water facies originally located to the SE to be displaced at least five kilometres and thrust over the shallow-water paraautochthonous facies (Kalvoda 1989). These processes were coeval with the main thrusting of the Variscan flysch nappes, caused by oblique collision of the Moldanubian and Saxothuringian terranes with the Brunovistulian Terrane (along the Moldanubian Thrust; e.g. Schulmann *et al.* 1991; Fritz & Neubauer 1993; Schulmann & Gayer 2000). The pre-orogenic units were also involved in the nappe stack (e.g. Čížek & Tomek 1991), forming a thrust package underlying the main Culmian nappes. Deep-water Drahany and transitional Ludmírov facies were thrust over platform carbonates of the Moravian Karst facies.
- (2) In later stages of the convergence (D_2), the structural style changed to thick-skinned. Newly developed T_2 thrusts, also involving Brunovistulian basement, penetrated and offset the older D_1 structures (F_1 and T_1) and folded them into F'_1 folds. This late stage of thrusting may be connected with the dextral strike-slip movements along the Moravian shear zone (e.g. Rajlich 1990; Schulmann *et al.* 1991). The basement rocks of the Brunovistulian terrane together with formerly stacked Palaeozoic nappes and paraautochthonous strata were sliced by thrust faults into numerous tectonic sheets and thrustured over the Palaeozoic sequences to the NE

(e.g. Melichar & Kalvoda 1997; Schulmann & Gayer 2000; Bábek *et al.* 2006).

Conclusions

Recent structural and lithostratigraphical research in the southern part of the Moravian Karst confirms the presence of two distinct facies of the Upper Devonian to Lower Carboniferous pre-flysch strata and the tectonic juxtaposition of these coeval sequences. Lithological differences between these two facies suggest that they underwent displacements greater than 5 km (Kalvoda 1989).

The 3D study of the geometry of the nappes has revealed a folded character of the T_1 thrust faults separating the two facies. Simultaneously some thrust faults (T_2) were unfolded and crosscut the T_1 thrust faults. This suggests two phases of thrusting, when the younger T_2 thrusts crosscut the older T_1 nappes, which were folded by dragging. The resemblance of the top-toward-NE movement of both thrust fault generations suggests progressive deformation during a single stress orientation. The folded T_1 thrust faults represent a thin-skinned contractional event. The younger T_2 thrusts and associated folds represent a thick-skinned event that involved the crystalline rocks of the Brno Massif as well as cross-cutting and refolding of the T_1 thrusts. Following F_2 folds gently refolded D_1 and D_2 structures.

Later (probably Alpine) brittle tectonics represented by normal faults as well as strike-slip faults divided the area into numerous smaller blocks with different erosion levels.

This study was supported by Ministry of Education, Youth and Sports of the Czech Republic grant project MSM0021622412.

References

- BÁBEK, O., TOMEK, Č., MELICHAR, R., KALVODA, J. & OTAVA, J. 2006. Structure of unmetamorphosed Variscan tectonic units of the southern Moravo-Silesian zone, Bohemian Massif: a review. *Neues Jahrbuch für Geologie und Paläontologie – Abhandlungen*, **239**, 39–75.
- ČÍZEK, P. & TOMEK, Č. 1991. Large scale thin-skinned tectonics in the eastern boundary of the Bohemian Massif. *Tectonics*, **10**, 273–286.
- DVOŘÁK, J. 1967. Vývoj synsedimentárních struktur jižní části moravského krasu. *Časopis pro Mineralogii a Geologii*, **12**, 237–246.
- DVOŘÁK, J. 1989. *Geologie sovrství líšeňského a jeho nadloží v jižní části Moravského krasu (vyhodnocení tří strukturálních vrstev Horákov)*. Archive of the Czech Geological Survey.
- DVOŘÁK, J. 1997. *Základní geologická mapa ČR 24-413 Mokrý-Horákov*. Czech Geological Survey map.

- DVOŘÁK, V. & MELICHAR, R. 2002. Nástin tektonické stavby severní části Moravského krasu. *Geologické výzkumy na Moravě a ve Slezsku v roce 2001*, 51–54.
- DVOŘÁK, J. & PRÁK, J. 1963. Geologický vývoj a tektonika devonu a spodního karbonu moravského krasu. *Sborník geologických věd, Geologie*, **3**, 49–84.
- DVOŘÁK, J., FRIÁKOVÁ, O., HLADIL, J., KALVODA, J. & KUKAL, Z. 1987. Geology of the Palaeozoic rocks in the vicinity of the Mokrá cement factory quarries (Moravian Karst). *Sborník geologických věd, Geologie*, **42**, 41–88.
- FRANKE, W. 1995. III.B.1 Stratigraphy. In: DALLMEYER, R. D., FRANKE, W. & WEBER, K. (eds) *Pre-Permian Geology of Central and Eastern Europe*. Springer, Berlin, 33–49.
- FRIÁKOVÁ, O., GALLE, A., HLADIL, J. & KALVODA, J. 1985. A lower Famennian fauna from the top of the reefoid limestones at Mokrá (Moravia, Czechoslovakia). *Newsletter on Stratigraphy*, **15**, 43–56.
- FRITZ, H. & NEUBAUER, F. 1993. Kinematics of crustal stacking and dispersion in the south-eastern Bohemian Massif. *Geologische Rundschau*, **82**, 556–565.
- GEE, D. G. & ZEYEN, H. J. (eds) 1996. *EUROPROBE 1996 – Lithospheric Dynamics: Origin and Evolution of Continents*. Publication by the EUROPROBE Secretariate, Uppsala University, Sweden.
- HARTLEY, A. J. & OTAVA, J. 2001. Sediment provenance and dispersal in deep marine foreland basin: the lower carboniferous Culm Basin, Czech Republic. *Journal of the Geological Society, London*, **158**, 137–150.
- HLADIL, J. 1983. Cyklická sedimentace v karbonátech macošského souvrství. *Zemní Plyn a Nafta*, **28**, 1–14.
- HLADIL, J. 1987a. *Základní geologická mapa ČSSR 24-413 Mokrá-Horákov*. Czech Geological Survey map.
- HLADIL, J. 1987b. *Vysvětlivky k základní geologické mapě ČSSR 24-413 Mokrá-Horákov*. Archive of the Czech Geological Survey.
- HLADIL, J. 1991. Násunové struktury v jižním uzávěru Moravského Krasu. *Zprávy o geologických výzkumech v roce 1989*, 80–81.
- HLADIL, J., KREJČÍ, Z., KALVODA, J., WINTER, M., GALLE, A. & BEROUNSEK, P. 1991. Carbonate ramp environment of Kellwasser time interval (Lesní lom, Moravia, Czechoslovakia). *Bulletin de la Société Belge de Géologie*, **100**, 57–199.
- HLADIL, J., MELICHAR, R. ET AL. 1999. The Devonian in the easternmost Variscides, Moravia: a holistic analysis directed towards comprehension of the original context. *Abhandlungen der Geologischen Bundesanstalt*, **54**, 27–47.
- ISAACSON, P. E., HLADIL, J., SHEN, J. W., KALVODA, J. & GRADER, G. 1999. Late Devonian Famennian glaciation in South America and marine offlap on other continents. *Abhandlungen der Geologischen Bundesanstalt*, **54**, 239–257.
- KALVODA, J. 1989. *Foraminiferová zonace svrchního devonu a spodního karbonu moravskoslezského paleozoika*. PhD thesis, Masaryk University, Brno, Czech Republic.
- KALVODA, J. 1996. *Stratigrafie vápenců v lomu mokerské cementárny*. Department of Geological Sciences, Masaryk University.
- KALVODA, J. & KUKAL, Z. 1987. Devonian-Carboniferous boundary in the Moravian Karst at Lesní lom Quarry, Brno-Líšeň, Czechoslovakia. *Courier Forschungsinstitut Senckenberg*, **98**, 95–117.
- KALVODA, J., MELICHAR, R., BÁBEK, O. & LEICHMANN, J. 2002. Late Proterozoic–Paleozoic tectonostratigraphic development and paleogeography of Brunovistulian Terrane and comparison with other terranes at the SE margins of Baltica-Laurussia. *Journal of the Czech Geological Society*, **47**, 32–41.
- KALVODA, J., LEICHMANN, J., BÁBEK, O. & MELICHAR, R. 2003. Brunovistulian Terrane (Central Europe) and Istanbul Zone (NW Turkey): Late Proterozoic and Paleozoic tectonostratigraphic development and paleogeography. *Geologica Carpathica*, **54**, 139–152.
- KETTNER, R. 1949. Geologická stavba severní části Moravského krasu. *Rozpravy Československé Akademie Věd a Umění, Třída II*, **59**, 1–29.
- KODYM, O., FUSÁN, O. & MATĚJKA, A. 1968. *Geologická mapa ČSSR (odkrytá)*. Czech Geological Survey map.
- MELICHAR, R. & KALVODA, J. 1997. *Strukturně-geologická charakteristika německo-vratkovského pruhu*. Sborník II. semináře České tektonické skupiny, 51–52.
- PRANTL, F. 1947. Stratigraficko-paleontologický výzkum devonu na Hádech u Brna. *Věstník státního geologického ústavu ČSR*, **23**, 173–180.
- RAJLICH, P. 1990. Strain and tectonic styles related to Variscan transpression and transtension in the Moravo-Silesian Culmian basin, Bohemian Massif, Czechoslovakia. *Tectonophysics*, **174**, 351–367.
- RAMSAY, J. G. M. & HUBER, M. I. 1987. *Techniques of Modern Structural Geology*. Academic press, London.
- REZ, J. & MELICHAR, R. 2002. Tektonika výskytu devonu u Adamova. *Geologické výzkumy na Moravě a ve Slezsku v roce 2001*, 57–61.
- SCHULMANN, K. & GAYER, R. 2000. A model for a continental accretionary wedge developed by oblique collision: the NE Bohemian Massif. *Journal of the Geological Society, London*, **157**, 401–416.
- SCHULMANN, K., LEDRU, P., AUTRAN, A., MELKA, R., LARDEAUX, J. M., URBAN, M. & LOBKOWICZ, M. 1991. Evolution of nappes in the eastern margin of the Bohemian Massif: a kinematic interpretation. *Geologische Rundschau*, **80**, 73–92.
- SLAVÍK, L. & MELICHAR, R. 1996. Styk brněnského masivu a devonu moravského krasu a jeho tektonický význam. *Geologické výzkumy na Moravě a ve Slezsku v roce 1995*, 120–122.
- ŠTELCL, J. 1957. K povaze vrás z moravského a slezského devonu (mikrostrukturní analýza). *Sborník k osmdesátinám akademika Františka Slavíka*, 435–451.
- ZUKALOVÁ, V. & CHLUPÁČ, I. 1982. Stratigraphic classification of non-metamorphic Devonian of the Moravo-Silesian region (In Czech). *Časopis pro Mineralogii a Geologii*, **9**, 225–247.

Thrust tectonics of the Upper Jurassic limestones in the Pavlov Hills (Outer Western Carpathians, Czech Republic)

IVAN POUL^{1,2*}, ROSTISLAV MELICHAR³ & JIŘÍ JANEČKA⁴

¹*Czech Geological Survey (branch office Brno), Leitnerova 22, 658 69 Brno, Czech Republic*

²*Institute of Geotechnics, Faculty of Civil Engineering, Brno University of Technology, Veveří 331/95, 602 00 Brno, Czech Republic*

³*Department of Geological Sciences, Faculty of Science, Masaryk University, Kotlářská 2, 611 37 Brno, Czech Republic*

⁴*Institute of Rock Structure and Mechanics, Academy of Sciences of the Czech Republic, v.v.i, V Holešovičkách 41, 182 09 Praha 8, Czech Republic*

**Corresponding author (e-mail: istvan@igeo.cz)*

Abstract: The Pavlov Hills are formed by separated limestone blocks previously identified as klippen. A new flat-ramp-flat thrust model of the Pavlov Hills is formulated in this paper. The main tectonic detachment is located at the base of the limestone plate and other subsidiary detachments are located within the nodular limestone horizon and also at the base and top of the Upper Cretaceous deposits. The ramps are situated in the Klentnice Fm and Ernstbrunn Lst. The ramp angle was determined by structural evidence combined with interpretation of seismic profiles. Two parallel antiformal structures plunging to the NE are recognized within the study area. The antiformal fold axes are gently plunging to the NE so the anticlines are not ideal for 3-point hydrocarbon trap setting. These anticlines were subsequently cut by sinistral strike-slip faults perpendicular to the fold axis which resulted in the formation of a large-scale pseudo en-echelon structure in an approximate north-south direction.

The Western Carpathians and the associated fore-deep are located in the area of south-eastern Czech Republic (south Moravia) and north-eastern Austria. These areas are relatively rich in hydrocarbon resources when compared to other local discoveries. This area represents the westernmost segment of Carpathian Orogenic Belt which is closely connected to the geological evolution of the Eastern Alps which has proven to contain structures that are suitable for hydrocarbon genesis, migration, and trapping in both stratigraphic and structural settings. All known oil and gas fields in the Western Carpathians are located both in the flysch nappes and in the Neogene basins. However, in our study area only the Neogene sediments hold the known hydrocarbon accumulations.

The aim of this paper is to unravel the present structure and tectonic evolution of the Pavlov Hills as a frontal part of the Ždánice Nappe (Fig. 1) in order to better explain the absence of oil and gas fields in an area which has significant structural and stratigraphic trap possibilities when compared to an area that has been subjected to a similar geological and tectonic evolution. This research will take into account known structural data as well as utilizing seismic data. As the Jurassic limestones

in this unit are easily discernable in lithological and geomorphological respects, this research utilized this marker as the basis of the structural interpretations. The current study area was recently mapped at 1:10 000 by Ivan Poul in 2002–2006. Field, borehole, structural and stratigraphic data were supplemented and supported by new geological interpretations of two perpendicular seismic profiles. Balanced cross sections were hand-drawn and their construction was completed with AutoCAD software. Conservation of bed length and area principles were assumed following the studies of Suppe (1983), Marshak & Mitra (1988), amongst others.

Regional setting

The study area is situated in south-eastern Moravia in the frontal portion of the Carpathian accretionary wedge (Figs 1 & 2). This wedge involves two nappe groups (Krosno and Magura groups) which are formed by several flysch nappe units, which consist mainly of Cretaceous to Palaeogene siliciclastic flysch sediments but also contain Mesozoic pre-flysch sediments. These sediments were folded and thrust during the Neo-Alpine Orogenesis.

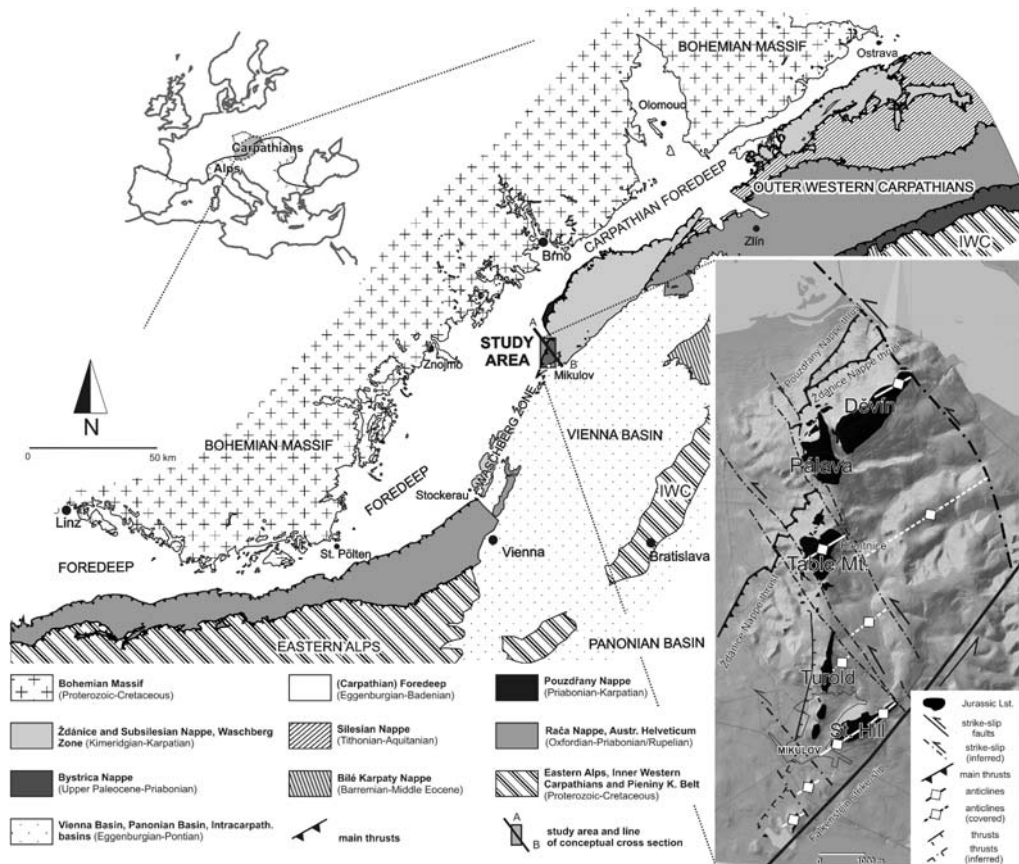


Fig. 1. Structural map showing the location of the study area (box in the central portion of the map) in the northern margin of the Waschberg Zone, Outer Western Carpathians (based on Fusán *et al.* 1967; Beck *et al.* 1980, simplified and modified by authors); IWC, Inner Western Carpathians. See Figure 2 for conceptual cross section A–B.

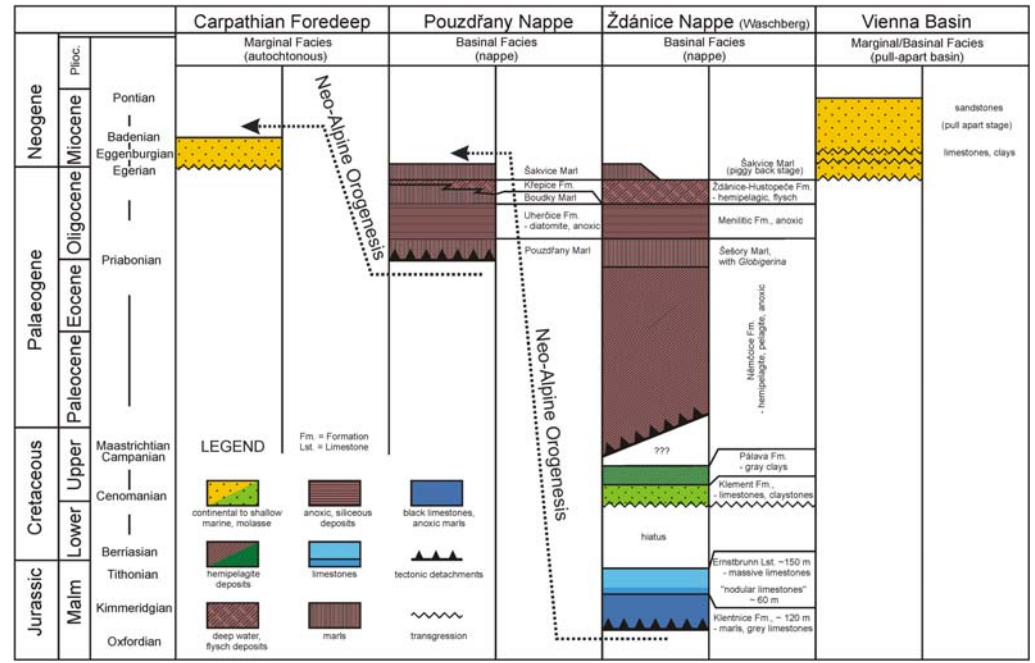
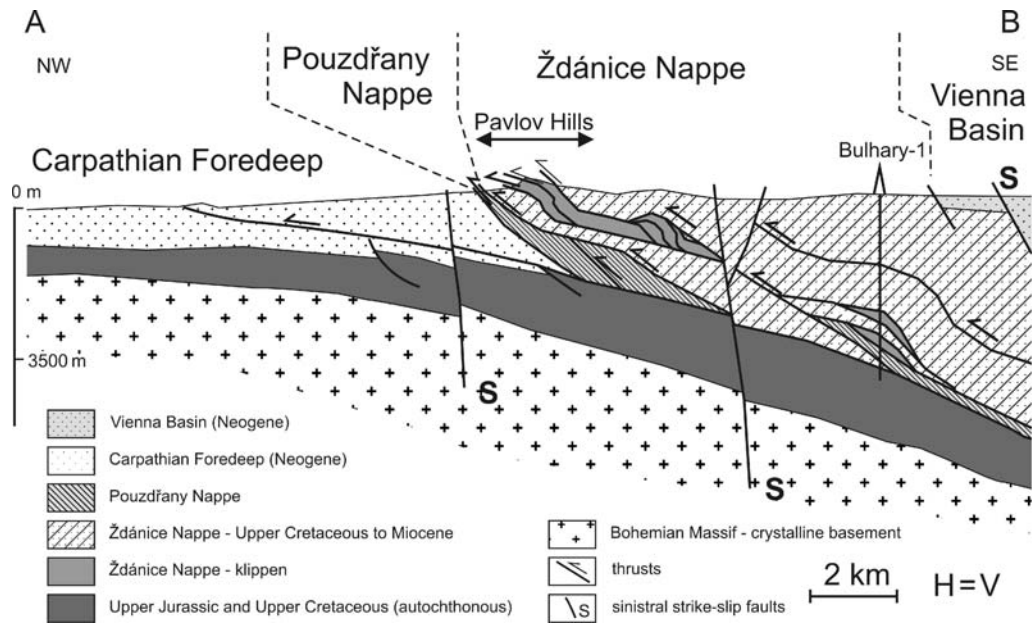
The typical direction of the fold axes is NE–SW while transversal faults are typically perpendicular to the fold axes trend.

In the south of Moravia, the Krosno Nappe Group is composed of the Pouzdrany Nappe and the overlying Ždánice Nappe which are mostly composed of hemipelagic and flysch sequences (Stráník *et al.* 1999). These nappes are surrounded by younger Neogene basins; the Carpathian Foredeep in the west and the Vienna Basin in the east. Both Neogene and Palaeogene sediments are friable and easy erodable, which results in a flat landscape of the study area. The only exception to this is the Waschberg Zone: a chain of small morphological elevations arranged into a longitudinal NNE–SSW belt (Fig. 1). The Waschberg Zone starts in the Danube river valley in Austria close to the town of Stockerau and ends in the Thaya river valley in the south Moravia near the town of Mikulov. The northernmost (Moravian) part of this ridge with an

anomalous north–south direction is called the Pavlov Hills located in Czech Republic.

Such elevations, which are normally underlain by the Upper Malm carbonates, were found at several localities in the Outer Western Carpathians and the term ‘klippen’ is usually employed for their description. As these large eye-catching limestone bodies are set in the younger Palaeogene flysch sediments on a regional scale, their emplacement mechanism has been the focus of several authors concerned with an exact explanation of the formation.

The first speculations were introduced by Suess in the 19th Century, who considered these limestone bodies as a relict of an island ridge which had ascended from the Palaeogene sandstones to the surface (Andrusov 1959). Another hypothesis introduces the concept that perhaps limestone were derived as hard exotic bodies from the basement and ‘flowing’ in younger soft sediments (Uhlig 1903;



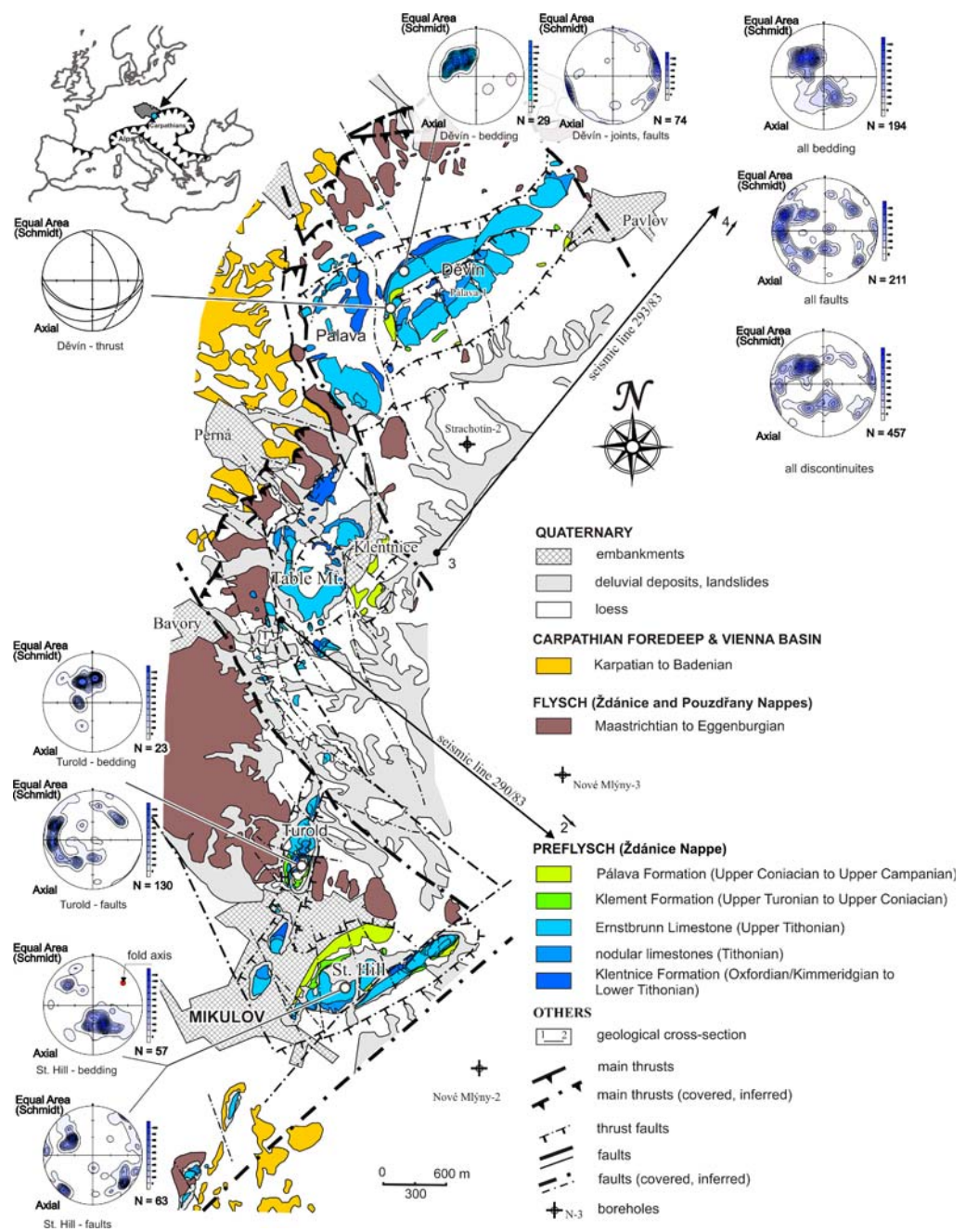


Fig. 4. New geological map of the Pavlov Hills (based on authors' detail geological mapping 1:10 000, simplified). Equal area projections (lower hemisphere) show orientation of structural elements. See Figures 6 and 8 for seismic profiles 1–2 and 3–4 respectively.

Jüttner 1940; Wessely 2006). A more allochthonous hypothesis was presented by Stejskal (1935), who suggested that the limestones cover the Palaeogene sediments and form only the upper parts of

elevations as 'caps' which are cut off by subhorizontal thrusts. Ideas of a sedimentary origin of the limestones emplacement were formulated during the 1960s by Eliáš & Stráňk (1963), who recognized

olistoliths which are located in the Silesian Nappe (northern Moravia); this idea was recently developed by Golonka *et al.* (2006). Glaessner (1931) regarded limestone bodies as small tectonic slices at the base of the Ždánice Nappe and his idea is still currently accepted (Stráník *in* Hanzlíková 1965; Stráník *et al.* 1979, 1999). In a published geological map of the Pavlov Hills (Čtyroký *et al.* 1988, 1995; scale 1:25 000), the limestone blocks are interpreted as tectonic blocks bounded by two post-thrust perpendicular systems of faults in west–east and north–south directions which do not agree with the other tectonic features in the Outer Western Carpathians regions.

Stratigraphy

The lowest part of the Ždánice Nappe is composed of Jurassic calcareous sediments (Fig. 3). The latter sediments are divided into three distinct lithostratigraphic units: Klentnice Formation (?Oxfordian/Kimmeridgian–Lower Tithonian), nodular limestones (Tithonian) and Ernstbrunn Limestone (Upper Tithonian). The Klentnice Fm consists of dark-grey, deep-marine calcareous claystones, marls and limestones (Glaessner 1931; Jüttner 1940; Eliáš 1992). The Ernstbrunn Lst. is typically light coloured, shallow-marine, massive calcareous rocks (Eliáš 1962; Eliáš & Eliášová 1984, 1985, 1986). Problematic transitional beds between these formations are termed ‘nodular limestones’ in this article. These nodular limestones are represented by clayey limestones, usually brecciated. The Upper Cretaceous siliciclastic sediments (Klement and Pálava Formations) unconformably overlie the Jurassic limestones (Glaessner 1931; Stráník *et al.* 1996). The Jurassic and Upper Cretaceous rocks are surrounded by Palaeogene hemipelagic and flysch claystones and sandstones (Abel 1907; Jüttner 1940; Stráník *et al.* 1979; Pícha *et al.* 2006).

Structures

Bedding is very distinct in the Klentnice Fm as well as in the nodular limestones. However, bedding recognition has proven to be problematic in the Ernstbrunn Lst. The absence of distinct bedding is the reason why we used small-scale and microscopic geopetal structures for the determination of bedding-orientation. Bedding in the area strikes mostly in the NE–SW direction and dips either to the SE or to the NW (Fig. 4). The opposite dip directions are interpreted to be a result of large-scale folding. Maxima of preferred bedding orientation are fairly sharp (Fig. 4) and, consequently, folds are classified as closed chevron folds with axial plane steeply dipping to NW.

Large antiformal structures are recognized in three locations: (1) the northernmost one at the northern edge of the Pavlov Hills (Děvín Hill; see Fig. 5); (2) the central one to the southwest of Klentnice village (Table Mt. [Stolová hora]; Stráník *in* Hanzlíková 1965); and (3) the southernmost one to the east of the town of Mikulov (Saint Hill [Svatý kopeček]; Poul & Melichar 2006).

As the fold axes plunge gently to the NE, the limestone outcrop narrows and ends in this direction. In addition, it was possible to recognize a sub-surface antiformal structure by the interpretation of the seismic profile 290/83 at a depth of c. 500 m (see Figs 4 & 6). As the geological interpretation of the seismic profile includes young strike-slip faults, the cross section was not balanced as a single geological section but rather in separated blocks. During hydrocarbon prospecting, the antiformal structure was penetrated by the Nové Mlýny-3 borehole (Adámek 1979; Table 1). There were no hydrocarbon accumulations that were discovered by this well and an anomalous thickness of the Klentnice Fm was interpreted as a hinterland dipping duplex system in the core of the antiform. The Upper Cretaceous sediments found in outcrops or in other local boreholes (Nové Mlýny-2,



Fig. 5. View of NE slope of the Děvín Hill with remarkable antiformal structure (Ernstbrunn Lst.).

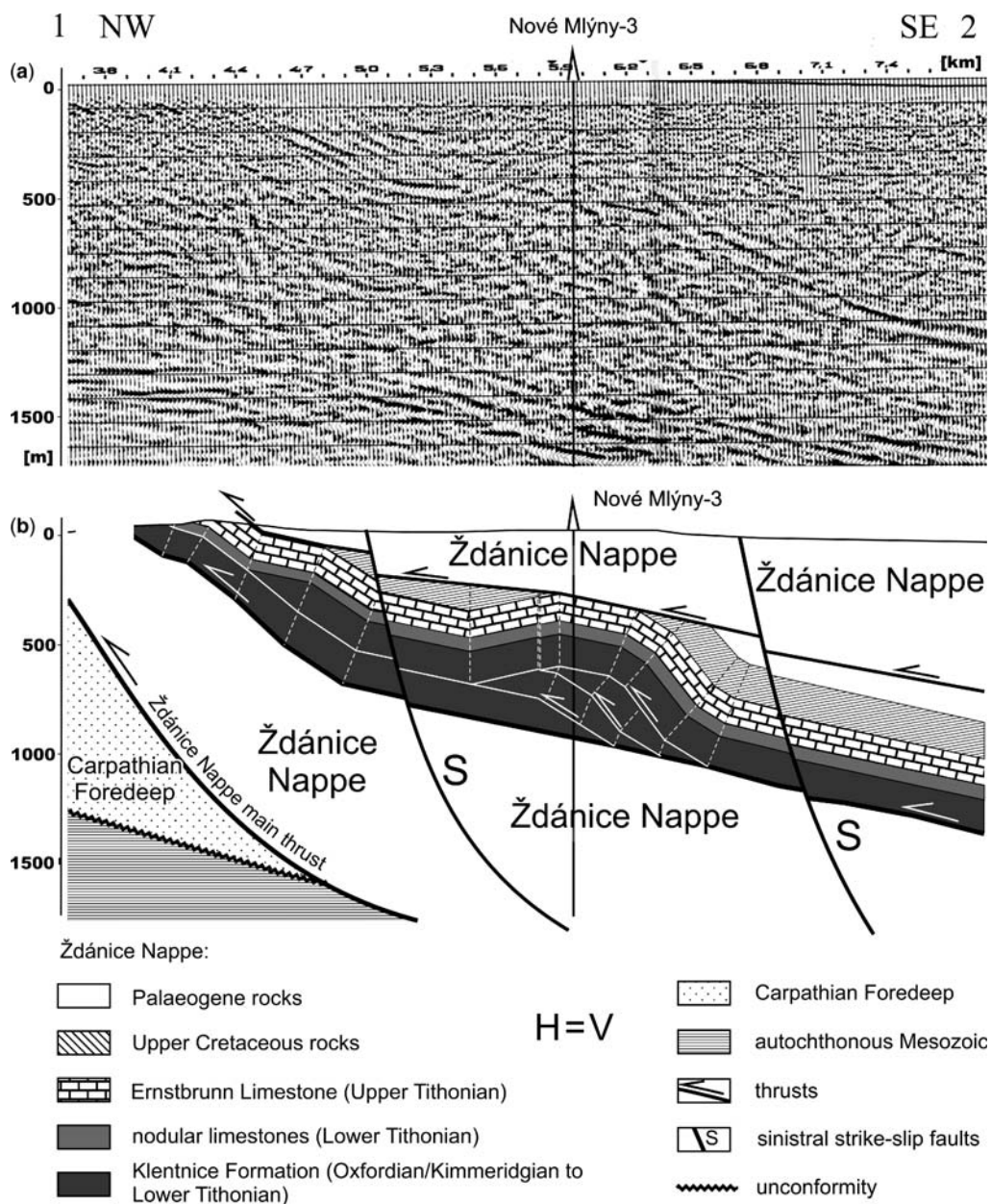


Fig. 6. Transversal seismic profile 290/83 including a projected borehole (a) and locally balanced cross section (b) obtained from the geological interpretation of the seismic profile shown in (a). See Figure 4 for location of line 1–2.

Strachotín-2; Table 1) are absent in the Nové Mlýny-3 borehole. This can be explained by the presumable presence of an out of sequence thrust that cuts down-sequence.

Thrust faults were identified by either stratigraphic inversions or repetitions of stratigraphic

sequences, as Jurassic rocks are found to be physically on top of Cretaceous or Palaeogene sediments. A well-exposed thrust is situated on the Děvín Hill, where the Jurassic limestones (nodular limestones and Klentnice Fm) overlie the Upper Cretaceous beds (Jüttner 1933; see Fig. 7). This

Table 1. *Boreholes profiles*

			Nové Mlýny-3		
Bulhary-1			0	– 180 m	Ždánice-Hustopeče Fm.
	– 1192 m	Ždánice-Hustopeče Fm.		– 343 m	Němčice Fm.
	– 1303 m	Upper Eocene – Oligocene (Menilite Fm., Němčice Fm.)		–	thrust
	– 1402 m	Němčice Fm.		– 485 m	Ernstbrunn Lst.
	–	thrust		– 559 m	Kurdějov Lst.
	– 1428 m	Eocene		– 1087 m	Mikulov Marl
	– 1488 m	Němčice Fm.		–	thrust
	–	thrust		– 1690 m	Němčice Fm.
	– 1619 m	Eocene		–	thrust
	– 1664 m	Menilite Fm.		– 1925 m	Ždánice-Hustopeče Fm.
	– 1817 m	Němčice Fm.		– 2031 m	Němčice Fm. + slivers of Upper Jurassic marls
	–	thrust		–	Ždánice Nappe thrust
	– 2210 m	Eocene		– 2247 m	autochthonous Middle + Upper Cretaceous (equiv. Klement Fm.)
	– 2260 m	Němčice Fm.		– 2692 m	Kurdějov Lst.
	–	thrust		– 3258 m	Mikulov Marl
	– 2295 m	Eocene		– 3299 m	Vranovice Carbonates
	–	thrust		– 3350 m	Nikolčice Fm.
	– 2391 m	Upper Jurassic	Pálava-1		
	–	thrust	0	– 5.6 m	Quaternary
	– 2688 m	Němčice Fm.		– 20 m	Ernstbrunn Lst.
	–	thrust		– 32 m	Nodular limestones (dip 52°)
	– 2706 m	Upper Jurassic, Boudky Marl (Pouzďfany Nappe)		– 147 m	Klentnice Fm.
	–	thrust		–	thrust
	– 3119 m	Němčice Fm. (Ždánice Nappe)		– 150 m	Upper Cretaceous + Paleogene
	–	thrust		–	thrust
	– 3126 m	Oligocene, Uherčice Fm. (Pouzďfany Nappe)		– 152.3 m	Klentnice Fm.
	–	thrust		–	thrust
	– 3231 m	Němčice Fm. (Ždánice Nappe)		– 153 m	Ernstbrunn Lst.
	–	Ždánice Nappe thrust		–	thrust
	– 3500 m	autochthonous Jurassic		– 157 m	Klement Fm.
				–	thrust
				– 285 m	Ernstbrunn Lst. (dip 40°)
				– 288.15 m	Nodular limestones
				–	thrust
				– 323.6 m	Klentnice Fm. (dip 35°)
				–	thrust
				– 356.25 m	Nodular limestones
				– 436 m	Klentnice Fm. (dip 60°)
Nové Mlýny-2			Strachotín-2		
0	– 100 m	Upper Badenian	0	– 100 m	Ždánice-Hustopeče Fm.
	– 455 m	Middle Badenian		– 450 m	Němčice Fm. + slivers of Mesozoic and Pouzďfany Nappe
	– 1225 m	Ždánice-Hustopeče Fm.		–	thrust
	– 2193 m	Němčice Fm. + slivers of Jurassic and Cretaceous rocks:		– 485 m	Upper Cretaceous (Klement Fm., Pálava Fm. + slivers of Němčice Fm.)
		1292–1316 m Ernstbrunn Lst.		– 660 m	Ernstbrunn Lst.
		1350 m Upper Cretaceous (drilling fluid)		– 805 m	Klentnice Fm. + slivers of Upper Cretaceous
		1595–1612 m Ernstbrunn Lst.		–	Ždánice Nappe thrust
		1450 m Albian (drilling fluid)		–	Pouzďfany Nappe
	–	Ždánice Nappe thrust		–	Pouzďfany Nappe thrust
	– 2385 m	autochthonous Upper Cretaceous		– 1675 m	autochthonous Upper Cretaceous
	– 2425 m	Upper Albian (Nové Mlýny Lst.)		– 1880 m	(Turonian–Coniacian)
	– 2852 m	Kurdějov Lst.		– 2208 m	Kurdějov Lst.
	– 3265 m	Mikulov Marl		– 2750 m	Mikulov Marl
	– 3340 m	Vranovice Carbonates		– 2910 m	Vranovice Carbonates
	– 3397 m	Nikolčice Fm.		– 2997 m	Nikolčice Fm.
	– 3500 m	crystalline basement (granitoids)		– 3075 m	Gresten Fm.
				– 3147 m	crystalline basement (granitoids)

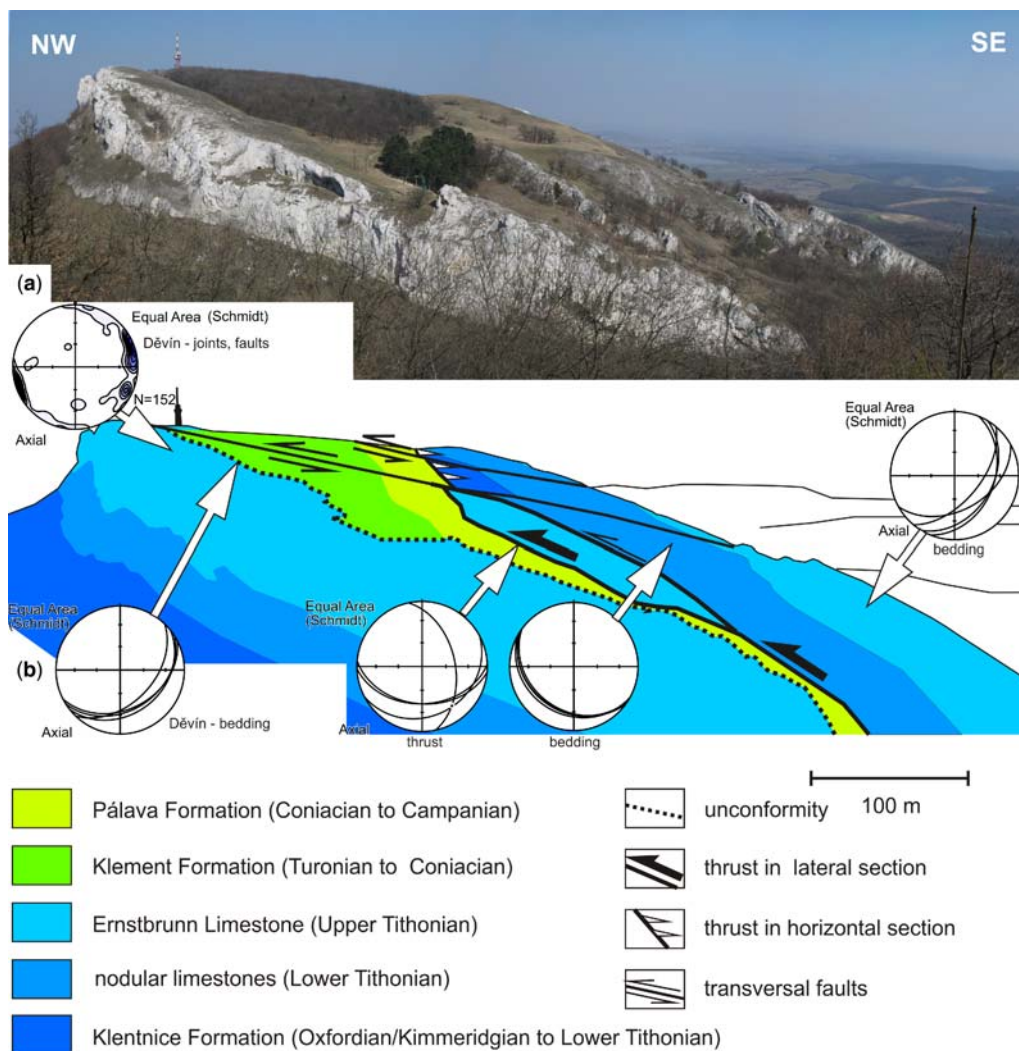


Fig. 7. View of SW slope of the Děvín Hill (a) and geological interpretation of the photograph shown in (a) as backlimb of an antiformal structure including a thrust (b). Equal area projections (lower hemisphere) show orientation of structural elements.

particular thrust dips to the SSE. The tectonic movement appears to be top-to-the NW. This same thrust is recognized at a depth of 147 m in the Pálava-1 borehole (Stráník *in* Hanzlíková 1965; Stráník *et al.* 1979; see Table 1, Fig. 4). This thrust separates slices in an antiformal stack whose NW limb was partially eroded. The main thrust of the study area (basal thrust of the Žďánice Nappe) was recognized in the Strachotín-2 borehole (Table 1, Figs 4 & 8) at a depth of 805 m and in the seismic profile 293/83. Other thrusts were identified from disrupted stratigraphic contacts interpreted from the geological map.

The thrusts are accompanied by anticlines that have compatible structural patterns and are developed in the thrust hanging walls. The main thrusts occur in the frontal portions of the anticlines and the strike of these thrusts is *c.* parallel to the subhorizontal fold axes. We interpret these anticlines as fault-related folds. The large fold interlimb angle ($110\text{--}140^\circ$) suggests that a fault-bend fold mechanism is responsible for their formation (Suppe 1983, 1985; Merle 1998; Savage & Cooke 2003). The interpretation of the seismic profile displayed in Figure 6 shows the same type of folding mechanism.

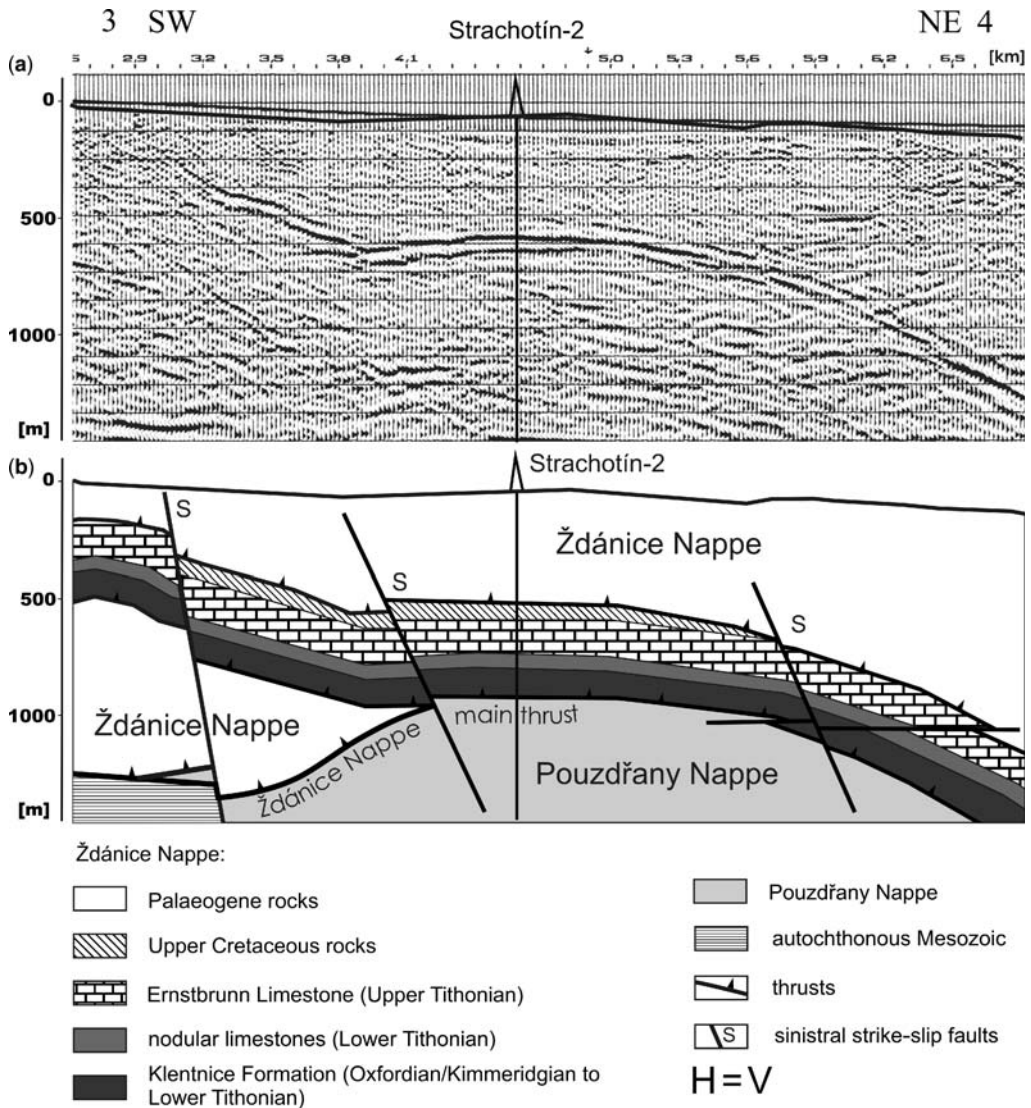


Fig. 8. Longitudinal seismic profile 293/83 including a projected borehole (a) and locally balanced cross section (b) obtained from the geological interpretation of the seismic profile shown in (a). See Figure 4 for location of line 3–4.

Small-scale transversal strike-slip faults have developed in several directions within the study area (Fig. 4). Two main directions have been identified: the strike of these faults is either parallel (NE–SW) or perpendicular to the fold axes (NW–SE). These faults are either vertical or steeply to moderately inclined, forming a pair of maxima with opposite dip directions (Fig. 4). Faults striking in the NW–SE direction are common along the whole western margin of the West Carpathians (Roth 1980). Sinistral strike-slip

movements along these subvertical faults planes were proved by sinistral kinematic indicators on parallel small-scale faults and by offsets in map; the largest offset of which in map view is *c.* 1200 m. A local but distinct system of steep faults was also found in the Turold quarry (dip direction 110°, Fig. 4) and St. Hill (dip direction 330°, Fig. 4). Very distinct striae and asymmetric markers (accretionary steps and/or *P*- and *T*-shears) indicate sinistral normal movement along these faults.

Tectonic model for the isolated limestone blocks

The new geological map shows patterns with two similar and approximately parallel continuous limestone belts which strike in a SW–NE direction (Děvín in the north, St. Hill in the south, Fig. 4). These two continuous belts are connected by a discontinuous chain of limestone bodies, which are separated by depressions occupied by the Palaeogene rocks which are less resistant to erosion. The presence of separated limestone blocks tends to validate the hypothesis of individual independent blocks (flowing blocks or olistoliths; Wessely 2006) but their repeated pattern and more or less identical structural style in different limestone outcrops, especially parallel fold axes of the large anticlines, are in contradiction with the hypothesis and are in favour of the thrust model. The geological interpretation of a longitudinal seismic profile (Fig. 8) demonstrates that the limestone body is a large approximately continuous plate which is cut by steep faults. Thus, problematic discontinuous distributions of limestone bodies may be explained as a result of post-thrust strike-slip faulting.

The original structure of the recently separated limestone bodies could be interpreted as a result of movements along the flat-ramp thrusts which are accompanied by fault-bend folds, that is, antiformal structures (Fig. 9a). Based upon the previously described thrust observations, the main detachment (flat) is interpreted to be situated in the basal part of the Klentnice Fm and the other subsidiary flats are located in the younger nodular limestones and also

above the uppermost part of the Ernstbrunn Lst. Competent portions of Mesozoic rocks (Klentnice Fm and Ernstbrunn Lst.) are crosscut by the thrust ramps. The original angle between the detachment and the thrust ramps was around 20° . This value was verified by field compass measurements of bed orientation as well as in the geological interpretation of the seismic profiles that image that particular structure. Differences in dip direction and angle of beds measured in two small slices in the Děvín Hill (different dips 32° and 50°), in the St. Hill (50° and 72°) and in several slices in the seismic profile (Fig. 6b) can be explained assuming the same original ramp angle modified by thrust sheet stacking.

Two main anticlines, or antiformal stacks, are also recognized. The first large anticline was found in two distinct locations: Table Mt. and in the frontal position of Děvín Hill. This originally continuous anticline was cut by a sinistral strike-slip fault so that fault blocks moved in relation to each other. In their current day position, these blocks are separated by wide regions which are underlain by Palaeogene rocks. The second large anticline is situated to the east of Mikulov town in the St. Hill. The antiformal structure interpreted in the Nové Mlýny-3 borehole (Fig. 6b) may be considered to be a continuation of the anticline along the NE plunging fold axis. The disrupted axial trace of these two structures may be explained by the presence of sinistral strike-slip faulting. There were recognizable sinistral strike-slip faults which offset the anticlines and also two other equivalent faults were inferred at the SW and NE edges of

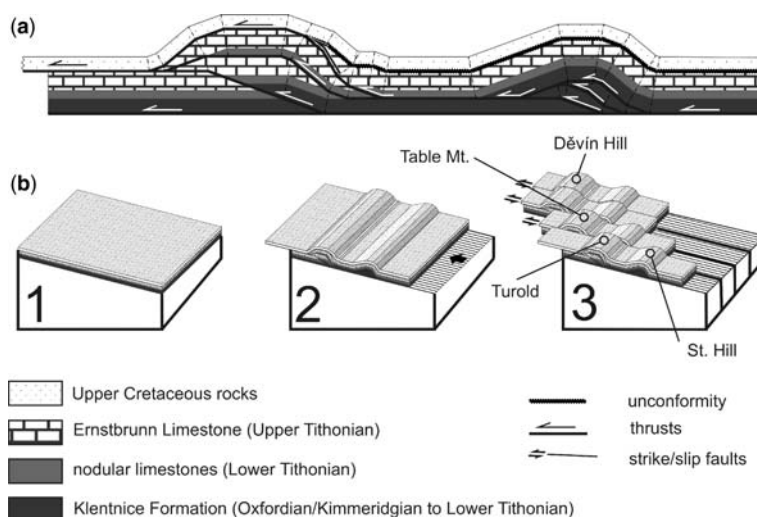


Fig. 9. Schematic model of thrust tectonics suitable for the Pavlov Hills (a) and principal stages of its evolution (b). Only Mesozoic rocks are presented, any Tertiary sediments covering this structure are not shown.

the study area. These faults, which strike in the NW–SE direction, are approximately perpendicular to the main fold axes.

Two main tectonic events could be derived from the model geometry (Fig. 9b). Originally a continuous plate of competent limestone was incorporated into the Ždánice Nappe due tectonic movements. As a result of thrusting, the plate was cut down by flats and at the ramp position was folded to antiformal structures. After that, at least two anticlines were cut by several sinistral strike-slip faults and separated. These faults rearranged the separated limestone blocks with antiformal structures into an approximate north–south-trending ‘klippen zone’, which is, in fact, a large-scale pseudo en-echelon structure.

Conclusions

In this study, we have proposed a new model of the tectonic architecture of the Pavlov Hills. It is shown that flat-ramp-flat geometry of thrusts and subsequent sinistral strike-slip faulting adequately explains the current geological arrangement of the area as a large limestone plate incorporated into the existing accretionary wedge. This model is in better accordance with the general structures found in the Outer Western Carpathians than other previously published models as it accepts the same principles of thrust tectonics and the same direction of transversal faults.

In the Mesozoic rocks, the main detachment of the thrusts is located at the base of the Klentnice Fm and the second order faults are located in the nodular limestones and at the base of the Upper Cretaceous rocks, whereas the ramps are situated in the competent Klentnice Fm and Ernstbrunn Lst. Their position is marked by large antiformal structures; the fold axis of which is gently plunging to the NE. This gentle plunge may be a possible escape route for the migrating hydrocarbons and may potentially be the reason why no hydrocarbon accumulations have been found in this seemingly favourable antiformal structure. Pseudo en-echelon arrangements of the limestone elevations are explained as a result of displacement along the sinistral strike-slip faults which strike in the NW–SE direction, for example, perpendicularly to fold axes of antiformal structures. Finally, the limestone elevations create chains in an approximate north–south direction.

We would like to thank P. Kopal (RWE co.) for seismic data and Cameron R. Sheya for his proofreading and linguistic correction. This study was supported by the GA CR Project TOP/08/E014.

References

- ABEL, O. 1907. *Geologische Spezialkarte Auspitz und Nikolsburg 1:75 000*. Geologische Reichsanstalt, Wien.
- ADÁMEK, J. 1979. Pynové ložisko Dolní Dunajovice a geologická stavba jižní části karpatské předhlubně. *Zemní plyn a nafta*, **24**, 69–76.
- ANDRUSOV, D. 1959. *Geologia československých Karpát II*. Slovenská akadémia vied. Bratislava.
- BECK, H., SPENGLER, E., VETTERS, H., WAAGEN, L. & WINKLER, A. 1980. *Geologische Karte der Republik Österreich und Nachbargebiete*. Geologische Bundesanstalt, Wien.
- ČTYRÝ, P. (ed.), HAVLÍČEK, P., DORNÍČ, J., STRÁNÍK, Z. & ZEMAN, A. 1988. *Základní geologická mapa ČSSR*. List 34-142 Mikulov. Ústřední ústav geologický, Praha.
- ČTYRÝ, P., HAVLÍČEK, P., STRÁNÍK, Z. & PÁLENSKÝ, P. 1995. *Geologická a přírodovědná mapa CHKO a BR Pálava 1:25 000*. Český geologický ústav, Praha.
- ELIÁŠ, M. 1962. Zpráva o sedimentárně petrografickém výzkumu klentnických vrstev a ernstbrunnských vápenců. *Zprávy o geologických výzkumech v roce*, **1961**, 196–198.
- ELIÁŠ, M. 1992. Sedimentology of the Klentnice formation and the Ernstbrunn Limestone. *Věstník Ústředního ústavu geologického*, **67**, 179–196.
- ELIÁŠ, M. & ELIÁŠOVÁ, H. 1984. Facies and palaeogeography of the Jurassic in the western part of the outer Flysch Carpathians in Czechoslovakia. *Sborník geologických věd, Geologie*, **39**, 105–170.
- ELIÁŠ, M. & ELIÁŠOVÁ, H. 1985. New biostratigraphic material from the Mesozoic of Flysch Carpathians and their foreland. *Věstník Ústředního ústavu geologického*, **60**, 105–108.
- ELIÁŠ, M. & ELIÁŠOVÁ, H. 1986. Elevation facies of Malm in Moravia. *Geologica Carpathica*, **37**, 533–550.
- ELIÁŠ, M. & STRÁNÍK, Z. 1963. K původu štramberských vápenců. *Věstník Ústředního ústavu geologického, Praha*, **38**, 133–136.
- FUSÁN, O., KODYM, O., MATĚJKA, A. & URBÁNEK, L. 1967. *Geological map of Czechoslovakia 1:500 000*. Geological Survey of Czechoslovakia, Praha.
- GLAESSNER, M. F. 1931. Geologische Studien in der ausseren Klippenzone. *Jahrbuch der Geologischen Bundesanstalt*, **81**, 1–25.
- GOLONKA, J., CIESZKOWSKI, M. & WAŚKOWSKA-OLIWA, A. 2006. Geodynamic evolution of the Subsilesian Realm. *Geolines*, **20**, 39–40.
- HANZLÍKOVÁ, E. 1965. The Foraminifera of the Klentnice Beds (Malm). *Sborník geologických věd, Paleontologie*, **5**, 39–100.
- JÜTTNER, K. 1933. Zur Stratigraphie und Tektonik des Mesozoikums der Pollauer Berge. *Verhandlungen des Naturforschenden Vereines in Brünn, Brno*, **64**, 15–31.
- JÜTTNER, K. 1940. Erläuterungen zur geologischen Karte des unteren Thayalandes. *Mitteilungen des Reichsamts für Bodenforschung, Zweigstelle, Wien*, **1**, 1–57.
- MARSHAK, S. & MITRA, G. 1988. *Basic Methods of Structural Geology*. Prentice-Hall, Englewood Cliffs, NJ.
- MERLE, O. 1998. *Emplacement Mechanisms of Nappes and Thrust Sheets*. Kluwer Academic Publishers, Norwell.

- PÍCHA, J., STRÁNÍK, Z. & KREJČÍ, O. 2006. Geology and hydrocarbon resources of the Outer Western Carpathians and their foreland, Czech Republic. In: GOLONKA, J. & PÍCHA, J. (eds) *The Carpathians and their Foreland: Geology and Hydrocarbon Resources*. American Association of Petroleum Geologists' Memoirs, **84**, 49–176.
- POUL, I. & MELICHAR, R. 2006. Flat-ramp-flat thrust geometry in the external Western Carpathians (Pálava Hills, Czech Republic). *Volumina Jurassica*, **4**, 62–63.
- ROTH, Z. 1980. *Západní Karpaty – terciární struktura střední Evropy*. Ústřední ústav geologický, Praha.
- SAVAGE, H. M. & COOKE, M. L. 2003. Can flat-ramp-flat fault geometry be inferred from fold shape? a comparison of kinematic and mechanical folds. *Journal of Structural Geology*, **25**, 2023–2034.
- STEJSKAL, J. 1935. Geologická stavba Pavlovských vrchů se zřetelem na stratigrafii a tektoniku flyše, II. *Věstník Státního geologického ústavu Československé republiky*, **11**, 15–29.
- STRÁNÍK, Z., ADÁMEK, J. & CÍPRYS, V. 1979. Geologický profil karpatskou předhlubní, flyšovém pásmem a Vídeňskou pánví v oblasti Pavlovských vrchů. In: MAHEL', M. (ed.) *Tektonické profily Zapadných Karpát*. Geologický ústav Dionýsa Štúra Bratislava, 7–14.
- STRÁNÍK, Z., BUBÍK, M., ČECH, S. & ŠVÁBENICKÁ, L. 1996. The upper Cretaceous in South Moravia. *Věstník Českého geologického ústavu*, **71**, 1–20.
- STRÁNÍK, Z., ČTYROKÝ, P. & HAVLÍČEK, P. 1999. Geologická minulost Pavlovských vrchů. *Sborník geologických věd, Geologie*, **49**, 5–32.
- SUPPE, J. 1983. Geometry and kinematics of fault-bend folding. *American Journal of Science*, **283**, 684–721.
- SUPPE, J. 1985. *Principles of Structural Geology*. Prentice-Hall, Englewood Cliffs, NJ.
- UHLIG, V. 1903. Über die Tektonik der Karpaten. *Sitzungsberichte der Kaiserlichen Akademie der Wissenschaften, Mathematisch-naturwissenschaftliche Klasse*, **116**, 871–982.
- WESSELY, G. 2006. *Geologie der Österreichischen Bundesländer, Niederösterreich*. Geologische Bundesanstalt, Wien.

Index

Page numbers in *italic* refer to Figures. Page numbers in **bold** refer to Tables.

- abrasion, horst and graben 7
- accommodation space 3
- accretionary prisms 3, 6–7
- accretionary wedges 1–2, 11, 237
 - Variscan 223
- Ainsa Basin 13
- Aliaga basin 78, 79, 80, 81, 83, 85, 91
- Aljostrel–Mértola–Riotinto Thrust Belt 206
- Almazán basin 80
- Alpine Orogeny, Pyrenees 169
- Alps crystalline thrust belt 3, 72
- Altiplano 72
- Amaro Mount 27
- Andes 3, 9, 10, 72
 - see also* Fuegoan Andes
- anisotropy of magnetic susceptibility (AMS) 100–101
 - Tethyan Himalaya
 - methods of analysis 105, 107
 - results 107, **108**, 109, 110, 111, 112–115
 - results discussed 115–117
 - summary 117–118
- Ansovell Formation 172, 173
- antiformal stacks 3
- Apennines 3, 14, 26, 72
 - see also* Maiella Mountain
- Appalachians 11, 14, 15
- Appalachians crystalline thrust belt 3
- Apulia Platform 27
- Aquitaine Basin 72
- Arguis Formation 46, 48, 52
- Aston orthogneiss 172
- Asturian arc 5, 178, 179, 180
- Austral Basin 123, 124

- back-vergent folds 11
- backthrusts and backthrusting 6, 11
- Baixo Alentejo Flysch Group 203
- Bar Formation 172, 173, 179
- Barbados prism 3, 7
- Barrême Basin (Alps) 72
- basal detachment 3
- basement, fabric and structural style 9
- basement-cover relations, role in fold and thrust belt
 - evolution 2
- basement-involved belts 9
- Belsué-Atarés Formation 48, 52
- bivergent folding 232
- blueschist 7
- Bohemian Massif 9
 - see also* Moravian Karst
- Bolivian Subandes 72
- Bolognano Formation 27
- Borneo 3
- Bourgeau Thrust 153, 154
- bow-and-arrow rule 77, 78, 92–93
- box fold 85
- Brazil offshore 3
- break-forward sequence 11
- break-thrust fold 32
- Březina Formation 225, 226, 228, 232
- British Caledonides 3
- brittle deformation 3
- Brunovistulian terrane 223, 224
- buckle folds 157–158, 159
- buckling 72, 162
- burial and fold and thrust belt evolution 2
- Busk method 65, 66

- c* axis analyses 190, 196, 197, 198, 232
- Cabo Leticia Anticline 128, 135, 145
- Cabo Leticia Formation 125, 126, 127, 128, 132, 133, 135, 138
- Cabo Leticia Thrust 128, 135, 138, 144
- Calatayud basin 80
- calcite *c* axis analysis 232
- Campo del Medio Backthrust 138, 143, 144, 145
- Campodarbe Formation 48, 52
- Campos anticline 79, 81, 85
- Campos Basin (Brazil) 8
- Canadian Rocky Mountains Fold–Thrust Belt 3, 4, 9, 15
 - cross section 154
 - displacement v. deformation 162–164
 - map 153
 - shortening model 160–162
 - stratigraphy 158–159
 - structure 159–160
 - compared with Mexican Fold–Thrust Belt **160**
- Canaveilles Group 172, 179
- Candán Antiform 189
- Canigó orthogneiss 172
- Cantabrian Mountains 15
- Cantabrian Zone 5, 6, 178, 179–180, 185, 186
- Caramonico fault 32
- carbonate platform, Maiella Mountain 27–28
- Cardium Formation 160
- Carpathian accretionary wedge 237
- Carpathian Orogenic Belt 237
- Carpathians 3, 13, 72
- Cava Formation 172–173, 179
- Cellino Formation 27
- Central Clare Group 63, 64
- Central Iberian Zone 185, 186
- Cerro Colorado Formation 126, 127, 128, 129, 131, 133, 142
- Cerro Las Vacas Anticline 128
- Cerro Piedra Syncline 128
- Cerro Ruperto Formation 125, 126, 127, 128, 136, 137, 138
- China, intraplate regions 3
- Cima delle Murelle Formation 27, 30
- Clare Shale Formation 63, 67, 69, 70, 73
- compaction and decompaction 67
- competent bedding 13
 - Pico del Águila 48, 49, 50
 - discrete-element modelling 51
 - method 51–52
 - results 53–54
 - results discussed 55–58

- Cona Graben 103
 contractional structures 8
 Cordón Largo–Punta Donata Anticlinal Limb 128,
 137–139
 Corredoiras shear zone 189
 cosmogenic nuclides 2
 Costabona massif 173
 Coulomb wedge theory 2
 application in Fuegan Andes 142–144
 controls on taper 162
 cover-basement relations, role in fold and thrust
 belt evolution 2
 critical taper theory 11, 149, 163
 cross-sections
 balanced and restored 1, 25
 Fuegan Andes 139–141
 Maiella Mountain
 construction 30–32
 restoration 34–37
 use in strain simulation 26
 Western Irish Namurian Basin
 construction 65–66
 retro-deformation 68
 crystalline thrusts 3, 6
 Culm Group 207
 curvature analysis 25
 cyclothem sedimentation, Western Irish Namurian
 Basin 64
 Czech Republic *see* Moravian Karst *also* Pavlov Hills
- Dala granitoids 103
 Dead Sea transform 3
 decompaction, Western Irish Namurian Basin 67
 deformation
 rate and timing, role in fold and thrust belt
 evolution 2
 relation to displacement 162–164
 simulation by strain ellipses 26
 thick-skinned 9, 150, 203, 223
 Maiella Mountain model 30, 34
 thin-skinned 9, 72, 150–151, 203, 223
 Canadian Rocky Mountains 150
 Fuegan Andes Thrust–Fold Belt 123, 124
 Maiella Mountain model 29–30
 deformation front 70
 delta progradation 8
 deposition, role in fold and thrust belt evolution 2
 depth-to-detachment methods 1
 detachment folds 46, 85, 226
 detachments
 relation to taper angle 163
 type and depth 2
 Dėvín Hill 242, 244, 246
 diapiric extrusion 232
 diapirs 7
 dip domain method 65, 66
 discrete-element modelling (DEM)
 method 50–51
 use in Pico del Águila anticline
 model set-up 51–52
 results 52–53
 model (1) 53–54
 model (2) 54–55
 results discussed 55–58
- displacement, relation to deformation 162–164
 Drahany facies 224
 ductile deformation 3
 Duero basin 80
 duplex 3, 6, 241
 Moravian Karst 229
 Western Irish Namurian Basin 66, 68, 70
- Eastern Cordillera 72
 Eastern Syntaxis 99
 Ebro Basin 46, 72, 80
 El Doctor Platform 151, 154, 155, 157
 El Doctor Thrust 156
 Eldon Formation 159
 ellipticity coefficient 38, 39
 ellipticity of grains 192
 elongation axes, Maiella Mountain 40
 Eohimalayan phase 101
 Ernstbrunn Formation 241, 243, 244, 245, 246
 erosion, role in fold and thrust belt evolution 2
 error handling in cross-section manipulation 70–71
 Escucha Formation 80
 Estana Formation 172, 173, 179
 evaporates and structural style 9, 13
 extension faults 13
 External Sierras *see* Pico del Águila
- Fatigue Thrust 153, 154
 fault restoration
 Maiella Mountain 34, 35, 36, 38–49
 Western Irish Namurian Basin 66–67
 fault splay 3
 fault-bend folds 13, 85
 Canadian Rocky Mountains 162
 Maiella Mountain 32
 fault-parallel flow (FPF), Western Irish Namurian
 Basin 66
 fault-propagation folds 13, 46, 85, 204, 206, 210
 fault-related folds 45, 159
 finite-element modelling 50
 fission track analysis (FTA) 2
 flexural-slip folding 228, 232
 flexural-slip unfolding (FSU), Western Irish Namurian
 Basin 66, 67, 68, 70
 flysch 204, 208
 see also magnetic fabric study
- fold and thrust (FAT) belts
 classification 1–2
 accretionary prisms 6–7
 crystalline thrusts 3, 6
 foreland belts 3, 4, 5
 toe thrust belts 7–9
 evolution 11–13
 factors affecting 2
 fold-thrust interaction 13–15
 structural styles 9–11
 fold restoration
 Maiella Mountain 34, 35, 36, 38–39
 Western Irish Namurian Basin 66
 fold style, Western Irish Namurian Basin 73
 fold-thrust interaction 13–15
 foliations 3
 Forcarei Synform 186
 rock microstructure 190–192

- grain shape fabric 192–196
 - quartz *c* axis orientation 196
 - significance of results 196–200
- setting 188
- stratigraphy 188–190
- summary 200
- Forcarei Thrust 187, 188, 198, 199
- foreland basins 85
- foreland fold and thrust belts 3, 11
- forward modelling 25
- fracture density, Maiella Mountain 40
- fracture zones 7
- friction and taper angle 163
- frontal accretion 6
- frontal ramps 13
- Fuegan Andes Thrust–Fold Belt
 - maps 127, 128
 - stratigraphy 125, 126, 129
 - structural evolution 124–125
 - structure at Península Mitré
 - application of Coulomb wedge theory 142–144
 - balanced and restored cross section 139–141
 - geometry and kinematics 131
 - Cabo Letica Anticline 135
 - Cordón Largo–Punta Donata Anticlinal Limb 137–139
 - Malagüena Backthrust 131–133
 - Punta Isleta Fault System 133–135
 - Río Bueno Syncline 135–137
 - unconformities and contraction 129–131
- Galicia–Trás-os-Montes Zone 185, 186, 187–188
- geochronology 2
- geometrical variations 9–11
- geomorphological techniques 2
- geopetal structures 241
- geophysical techniques 2
- Gessoso Solifera Formation 27
- glide complex 7
- GPS mapping, Western Irish Namurian Basin
 - 64–65
- grain shape fabric analysis 192–196
- gravitational sliding 232
- gravity, role in transport 7
- Great Counter Thrust 100, 101, 103
- Greater Himalayan Sequence 101
- growth strata 45, 52
- Guara Formation 46, 48, 50, 52
- Gull Island Formation 63, 64, 66, 67, 68, 69, 70, 72, 73
- Gyrong–Kangmar Thrust 101, 103
- Hády-Říčka Limestone 224, 225, 228, 229, 230, 232
- Hellenides 72
- Highwood structure (Alberta, Canada) 6
- Higuerillas Thrust 153, 155
- Himalayas 2–3, 11, 72, 99
 - tectonic elements 100, 101
- Tethyan Himalayan Sequence 101
 - deformation 101–103
 - intrusions 103, 105
 - metamorphism and structure 105
 - Triassic flysch 103
 - AMS analysis
 - methods
 - mineralogy 107
 - sampling 105, 107
 - results 107, 108, 109, 110, 111, 112–115
 - results discussed 115–117
 - summary 117–118
- Horákov facies 224, 225, 226, 227, 228, 229, 231, 232
- horst and graben abrasion 7
- horst restoration, Maiella Mountain 35, 36
- Hospitalet orthogneiss 172
- Hostěnice facies 224, 225, 226, 229, 231, 232
- hydrocarbon industry 2
 - deformation studies and exploration 25
- hydrofracturing 7
- hysteresis 107
- Iapetus Suture 63
- Iberian Chain 78, 80
- Iberian Peninsula 5, 6
- Iberian Pyrite Belt 203, 206
 - evolution
 - described 217–219
 - interpreted 219–220
 - summary 220
 - lithostratigraphy 206–207
 - sub-domains 206
 - tectonic framework 208
 - deformation phases 208–210
 - structure
 - Filón Norte Open Pit 213–217
 - Puebla de Guzmán Antiform 210–213
- Iberian Variscan Belt 185–188
- Iberian Variscan Massif 13, 15, 204, 205
 - compared with Pyrenean Variscan structure 178–180
- Iberian Variscides *see* Forcarei Synform *also*
 - Puebla de Guzmán Antiform
- Ibero-Armorican arc 5, 11, 178, 179, 180, 185
- incompetent bedding 13
 - Pico del Águila 48, 49, 50
 - discrete-element modelling 51
 - method 51–52
 - results 53–54
 - results discussed 55–58
- Indus Yarlung Suture Zone 101, 103
- infrastructure, Pyrenean 169–170
- Inglismaldie Thrust 153, 154
- intercutaneous wedges 3
- intraplate folds 14
- intraplate regions 3
- Ireland *see* Western Irish Namurian Basin
- isoclinal folds 3
- isothermal remanant magnetism 107
- isotope analysis 2
- Italy *see* Apennines *also* Maiella Mountain
- Jujols Group 172, 179
- Jura Mountains 72
- Kilkee Cyclothem 63, 66, 67, 68, 69, 70, 71
- Killarney–Mallow Fault 61, 69
- kinematic modelling *see* Utrillas thrust
- kink bands 3, 6
- kink-band folds 212
- Klement Formation 241, 243, 244

- Klentnice Formation 241, 242, **243**, 244, 245, 246
 Kootenay Formation 159
 Krosno Nappe Group 238
 Křtiny Limestone 224, 225, 226, 227, 228, 232

 La Aquiana Formation **172**, 179
 La Babia fault 151
 La Barca Formation 125, 126, 127, 128, 131, 132, 133, 135, 138
 La Chiara Thrust 138, 143, 144
 La Despedida Group 126
 La Rambla normal fault 83
 Lac des Arcs Thrust 153, 154, 159
 Lalín-Forcarei Group 188
 landscape evolution 2
 landslides 13
 Laramide Province 150
 Laramide uplifts 9
 Las Parras normal fault 83
 Las Parras subbasin 83
 lateral faults 7
 lateral ramps 13
 Laurussia 62, 223
 Lažánky Limestone 224
 leading edge folds 14
 Lesser Himalayan Sequence 101
 Leticia Formation 126, 127, 128, 129, 131, 132, 133, 142
 Lewis Thrust 159
 Lhunze Fault 103
 Líšeň Formation 224, 225
 lithosphere, elastic thickness, role in fold and thrust belt evolution 2
 Lomas de Olmedo Trough 10
 Luarca Formation **172**, 179
 Ludmírov facies 224
 Lys Caillaouas massif 173

 McConnell Thrust 153, 154, 159
 Macocha Formation 224, 225
 Maestrazgo Basin 80
 magnetic fabric in Himalayan Triassic flysch
 methods of analysis 105, 107
 results 107, **108**, **109**, 110, 111, 112–115
 results discussed 115–117
 summary 117–118
 magnetostratigraphy 2
 Mahakam delta (Kalimantan) 11
 Maiella Massif 30
 Maiella Mountain
 analogue model summary 40–41
 cross-section construction 30–32
 cross-section restoration 34–37
 field observations 32–33
 geological setting 27–28
 maps 26, 28
 strain simulation 37–40
 stratigraphy 27
 structural interpretations 28–30, 34
 thrust detachment level 33–34
 Maiella Mountain anticline 14, 30
 forelimb and backlimb stratigraphy 32
 Main Boundary Thrust 100, 101
 Main Central Thrust (MCT) 100, 101

 Major Fault-Propagation Fold Region 206
 Malagüena Backthrust 128, 131–133, 138, 142, 143, 144, 145
 Malagüena Formation 126, 127, 128, 129, 131, 132, 133, 134
 Massana Formation 173
 mechanical heterogeneity *see* competent bedding *also* incompetent bedding
 mechanical properties and deformation 3
 modelling *see* discrete-element modelling, Pico del Águila
 Meilin anticline (Taiwan) 15
 melanges 7
 metamorphism, low grade 3
 Mexican Fold–Thrust Belt
 cross section 154
 displacement v. deformation 162–164
 map 152
 shortening model 160–162
 structure 151, 153, 156, 157, 158
 compared with Canadian Rocky Mountains **160**
 Mexico, Gulf of 3
 Miravete anticline 79, 85
 Mojave-Sonora Megashear 151
 Moldanubian terrane 223
 Moldanubian thrust 223
 Molise Allochthonous nappes 30
 Montalbán basin 80, 81, 85, 91
 Moravia *see* Pavlov Hills
 Moravian Karst
 geological setting 224
 research history 223
 stratigraphy 224–226
 structure
 3-D analysis 229–232
 field mapping 226–229
 results discussed 232–234
 summary 234
 Moravo-Silesian Zone 223, 224
 Morrone di Pacentro Formation 27, 30
 Mount Allan Syncline 159
 Mt Jangsang Lhamo 103
 mud diapirs 7
 Munster Basin 61, 62
 mylonitic zones 232–233
 Myslejovice Formation 225, 226

 Nankai accretionary prism 6
 nappes 3
 natural remanent magnetism (NRM), Tethyan Himalaya 107, **108**, **109**, 110
 Neohimalayan phase 101
 Niger Delta 3
 Nittany anticlinorium 14
 North American Cordillera 150–151
 see also Canadian Rocky Mountain Fold and Thrust Belt *also* Mexican Fold–Thrust Belt
 North Himalayan gneiss domes 103
 North Thrust Zone 213, 216, 218
 Nuria orthogneiss 172

 oblique collision 3
 oblique ramps 13
 Oklahoma fold and thrust belt 2

- Old Baldy Thrust 160
 Old Red Continent 62
 Ollo de Sapo Domain 178, 179, 180
 Orfento Formation 27, 30
 orientation of grains 192, 195, 196
 oroclines 11
 orogenic polarity 11
 out-of-sequence thrusts 11
 overstep 3
- P–T–t* data 2
 Pálava Formation 241, **243**, 244
 Palmyride Belt 3
 Paraño Group 188, 190
 parasitic folds 3
 Pavlov Hills
 setting 238, 239, 240, 241
 stratigraphy 241, **243**
 structure 241–242, 244–245
 tectonic model 246–247
 Península Mitre *see* Fuegan Andes
 pervasive cleavage 15
 phyllite 3
 Phyllite and Quartzite Unit 206, 207, 210, 216, 217
 Pico del Águila detachment anticline 14
 discrete-element modelling 50–51
 model set-up 51–52
 results 52–53
 model (1) 53–54
 model (2) 54–55
 results discussed 55–58
 geological setting 46, 48, 50
 map 47
 stratigraphy 46, 48
 piggy-back basins 3, 6, 85
 piggy-back sequence 11, 175
 Pindos **72**
 Pine Mountains Thrust 15
 plate convergence-collision regions 2–3
 plate tectonics, role in fold and thrust belt evolution 2
 Policarpo Formation 125, 126, 127, 128, 132, 133, 135, 136, 138
 Policarpo Thrust Sheet 138, 142, 143, 144
 Portalrubio thrust sheet 81, 82, 83
 Portalrubio–Vandellós fold and thrust belt 80
 Portela unit 188, 189, 190
 Pouzdřany Nappe 238, 239, 245
 Puebla de Guzmán Antiform 206, 219
 deformation 208, 210, 220
 map 205
 structure 210–213, 214
 Puesto José Formation 126, 127, 128, 129, 131, 132, 133, 134
 Pulo do Lobo Antiform 203
 Punta Ancla Anticline 128, 137
 Punta Ancla Thrust 137, 138, 142, 143, 144, 145
 Punta Cuchillo Anticline 128, 137
 Punta Gruesa Imbricates 142, 143, 144, 145
 Punta Isleta Fault System 128, 133–135
 Punta Noguera Formation 125, 126, 127, 128, 132, 133, 135, 137, 138
 Punta Torcida Formation 142, 143, 144, 145
 Puri anticline (Papua New Guinea) 15, 16
 Pyrenean thrust 46
 Pyrenees 11, 13, 15, **72**
 cross section 171
 history of research 169–170
 setting 169
 see also Pico del Águila
 Pyrenees, Central
 igneous bodies 173
 lithostratigraphy 174
 Ordovician 172–173
 Silurian–Permian 173
 Vendian–Early Ordovician 170, 172
 tectonic evolution
 Alpine 177
 Ordovician 173, 175
 Silurian–Carboniferous 175
 Variscan 175–177
 Variscan structures
 compared with Iberian Variscan Massif 178–180
 zonation 177–178
 pyrite 107
 pyrrhotite 107
- quantitative structural geometry 1
 quartz *c* axis analysis 190, 196, 197, 198
- Rabassa Formation 172, 179
 ramp geometry 13
 reactivated thrusts 11
 rear accretion 6
 recesses 9, 11
 reciprocal strain ellipse 37
 recumbent folds 6, 232
 reentrants 9, 11
 relay zone 11
 retro-deformation 61
 study in Western Irish Namurian Basin
 methods 66–67
 results 68–70
 results discussed 70–73
 summary 73–74
 Rhenohercynian Zone 62, 223
 Ricmanice-Ochoz elevation 223
 Riedel shears 212
 Río Bueno Formation 126, 127, 128, 129, 133, 136, 137, 138, 139
 Río Bueno Syncline 128, 135–137, 138, 139
 Río Claro Group 126
 Riotinto Syncline 208
 Rocky Mountains *see* Canadian Rocky Mountain Fold and Thrust Belt; Canadian Rocky Mountains
 Ross Sandstone Formation 63, 65, 66, 67, 68, 69, **70**, 73
 Rozstáni Formation 225, 226, 228, 229, 230, 232
 Rundle Thrust 153, 154, 159
- salients 9, 11
 San Andreas transform 3
 San Marcos fault 151
 sand-box modelling 8, 12, 50
 Santa Barbara System 10
 Santo Domingo detachment anticline 46
 Santo Domingo thrust 46
 saturation isothermal remanent magnetism (SIRM), Tethyan Himalaya 107

- Saxothuringian terrane 223
 Scandinavian crystalline thrust belt 3
 seamounts 7
 sedimentation effects 2
 seismic sections 242, 245
 seismic techniques 2
 serpentinite diapirs 7
 Sevier fold-thrust belt 150
 Shannon Group 63
 Shannon Lineament 62–63
 shape parameter for grains 192, 194
 shear sense indicators 192
 shear strain distribution, Pico del Águila 53–54
 shortening
 factors affecting measurement 160–161
 methods of measuring 158
 rates in fold and thrust belts **72**
 Sierra Madre Oriental *see* Mexican Fold and Thrust Belt
 Simpson Pass Thrust 153, 154
 Siwalik molasses 101
 slate belt 3
 slaty cleavage 3, 14
 slumping 13
 software tools 2
 data projection 65
 retro-deformation 66, 67
 sequential restoration 34
 SpheriStat 231
 sole fault 203, 208
 sole thrust 3
 Somiedo thrust sheet 6
 South Munster Basin 62
 South Portuguese Zone 203, 204, 205 206, 208
 see also Puebla de Guzmán Antiform
 South Pyrenean thrust 45
 South Thrust Zone 213, 216, 218
 South Tibetan Detachment System 101, 103
 Spain *see* Forcarei Synform; Iberian Pyrite Belt; Iberian Variscan Massif; Pico del Águila; Pyrenees; Utrillas thrust
 S. Spirito Formation 27, 30
 strain
 predictive methods 25
 quantification by strain markers 25
 simulation by cross-section restoration 26
 Maiella Mountain 37–40
 strain ellipses 26, 38
 stratigraphy, role in fold and thrust belt evolution 2
 strike-slip *see* transcurrent faults
 structural analysis
 methods 1
 techniques 2
 Subandean Ranges 10
 subduction erosion 6
 subsidence effects 2
 Sulphur Mountain Thrust 153, 154
 suprastructure, Pyrenean 169–170
 surficial processes 2
 syn-kinematic sedimentation
 discrete-element modelling 51
 method 52
 results 54–55
 results discussed 55–58
 Synorogenic Sedimentary Unit 207, 210, 217, 219
 syntaxis 9, 11
 Taiwan **72**
 Tajo basin 80
 Tamaulipas Formation 156, 157
 Tampico–Misantla Basin 151, 153, 154, 155, 158
 taper angles 142, 161–162
 tear faults 11
 techniques in structural analysis 2
 tectonic underplating 6
 Tethyan Himalayan Sequence 101
 deformation 101–103
 intrusions 103, 105
 metamorphism and structure 105
 Triassic flysch 103
 AMS analysis
 methods
 mineralogy 107
 sampling 105, 107
 results 107, **108**, **109**, 110, 111, 112–115
 results discussed 115–117
 summary 117–118
 thermal subsidence 73
 thick-skinned deformation 9, 150, 203, 223
 model for Maiella Mountain 30, 34
 thin-skinned deformation 9, 72, 150–151, 203, 223
 Canadian Rocky Mountains 150
 Fuegan Andes Thrust–Fold Belt 123, 124
 model for Maiella Mountain 29–30
 thrust flats 13
 thrust ramp fold 32
 thrust ramps 13
 thrust restoration, Maiella Mountain 34, 35, 36, 38–39
 thrust wedge 11, 13
 Tian Shan **72**
 Tibetan Plateau 99, 104
 Tierra del Fuego *see* Fuegan Andes
 toe thrust belts 3, 7–9, 11
 Tolimán Sequences 153, 155
 trailing edge folds 14
 transcurrent faults 3
 transfer faults 11
 transfer zone 11
 transform faults 3
 transport directions for thrusts 77
 see also Utrillas thrust kinematic modelling
 transpression 3
 Tre Grotte Formation 27, 30
 Tregura Formation 172
 triangle zones 3
 Trinidad thrust belt 3
 Tullig Cyclothem 63, 64, 66, 67, 69, **70**, **71**, 72, 73
 uplift effects 2
 USA Cordillera 9
 Utrillas Formation 80
 Utrillas thrust
 geological setting 80
 kinematic modelling
 measurements
 deformation 85
 geometry 82–85

- tectonosedimentary relations 85–86
 - transport directions 86–87
- results discussed
 - horizontal slip 92–93
 - integrated slip model 90–92
 - macro- and meso-structures 87–98
 - total displacement 94
- summary 94–95
- maps 78, 79
- transport directions 77–78
- Valle dell'Inferno Formation 27, 30
- Valles-San Luís Potosí Platform 151, 154, 155, 157
- Valverde del Camino Antiform 206
- Variscan accretionary wedge 223
 - see also* Moravian Karst
- Variscan Orogeny and Orogen 5, 6
 - Iberian Variscan Belt 185–188
 - Iberian Variscan Massif 13, 15, 204, 205
 - Iberian Variscides *see* Forcarei Synform; Iberian Pyrite Belt; Puebla de Guzmán Antiform
- Pyrenees 169
 - compared with Iberian Variscan Massif 178–180
 - folding and thrusting 175–177
 - zoning of structures 177–178
- SW Ireland 62–63, 73
- Vegadeo Formation 172, 179
- Venezuela Basin 8
- Vilémovice Limestone 224, 226, 227, 228, 229, 232
- virgations 9
- Volcano-Sedimentary Complex 204, 205, 206, 207, 210, 212, 216, 217, 219
- Waiparous Thrust 160
- Wales, slate belt 3
- Waschberg Zone 238, 239
- water retention and deformation 72
- West Asturian Leonese Zone 178, 179, 180, 185, 186
- Western Irish Namurian Basin (WINB) 15
 - map 62
 - retro-deformation study
 - methods
 - cross-section construction 65–66
 - data projection 65
 - decompaction 67
 - displacement analysis 67
 - GPS mapping 64–65
 - retro-deformation 66–67
 - results 68–70
 - results discussed
 - basin geometry 73
 - comparisons 71–72
 - error estimates 70–71
 - fold style 73
 - folding and sedimentation 72–73
 - summary 73–74
 - stratigraphy 63–64
 - Variscan Orogen 62–63
- Western Ordos 3
- Western Syntaxis 99
- Windermere Supergroup 158
- Yala Xiangbo 103
- Yinshan 3
- Zagros fold and thrust belt 2, 3, 72
- Ždánice nappe 238, 239, 242, 245
 - stratigraphy 241
 - tectonic model 246–247
- Zimapán Basin 151, 154, 155, 156, 158

Fold-and-thrust belts occur worldwide, have formed in all eras of geological time, and are widely recognized as the most common mode in which the crust accommodates shortening. Much current research on the structure of fold-and-thrust belts is focused on structural studies of regions or individual structures and on the geometry and evolution of these regions employing kinematic, mechanical and experimental modelling. In keeping with the main trends of current research, this title is devoted to the kinematic evolution and structural styles of a number of fold-and-thrust belts formed from Palaeozoic to Recent times. The papers included in this book cover a broad range of different topics, from modelling approaches to predict internal deformation of single structures, 3D reconstructions to decipher the structural evolution of groups of structures, palaeomagnetic studies of portions of fold-and-thrust belts, geometrical and kinematical aspects of Coulomb thrust wedges and structural analyses of fold-and-thrust belts to unravel their sequence of deformations.